IMPERIAL

Multi-scale and multi-fidelity numerical study of microfluidics and complex interfacial phenomena

Paula Pico

November, 2024

Department of Chemical Engineering

Imperial College London

Submitted in part fulfilment of the requirements for the degree of
Ph.D. in Chemical Engineering of Imperial College London
and the Diploma of Imperial College London

Declaration of Originality

I hereby certify that the material in this thesis is the result of my own original research. All consulted materials have been properly acknowledged and the literature used referenced.

I acknowledge the use of ChatGPT 3.5/4.0 (OpenAI) for assistance solely in grammar checking and text styling this thesis. I affirm that no AI-generated content has been presented as my own work; all discussions, results, and conclusions are entirely my own.

Copyright Statement

The copyright of this thesis rests with the author. Unless otherwise indicated, its contents are licensed under a Creative Commons Attribution-NonCommercial 4.0 International Licence (CC BY-NC). Under this licence, you may copy and redistribute the material in any medium or format. You may also create and distribute modified versions of the work. This is on the condition that: you credit the author and do not use it, or any derivative works, for a commercial purpose. When reusing or sharing this work, ensure you make the licence terms clear to others by naming the licence and linking to the licence text. Where a work has been adapted, you should indicate that the work has been changed and describe those changes. Please seek permission from the copyright holder for uses of this work that are not included in this licence or permitted under UK Copyright Law.

Abstract

Multiphase flows are crucial to various industrial applications and are an ubiquitous part of the natural world. Particularly significant are multiphase flows characterised by complex interfacial phenomena, such as surface-active contamination and interface breakup, as well as those involving disperse phases exhibiting variability in their properties, known as multiphase polydisperse systems. Accurately predicting the behaviour of these systems poses various challenges due to their tremendous complexity, involving multiscale phenomena, interactions between inertia, viscosity, gravity, and surface tension, nonlinear dynamics, and multiphysics mechanisms.

This thesis presents an in-depth computational investigation of three multiphase systems that exemplify these complexities. The first study examines reactive microscale flows through the chemical synthesis of silver nanoparticles. The second centres around the poorly-documented phenomenon of surfactant-laden drop encapsulation within a propagating bubble in a capillary channel. Lastly, this study examines the mechanisms leading to aerosol release from bursting bubbles at a liquid-gas interface, with a focus on the action of surfactants.

Regarding nanoparticle synthesis, a modelling framework integrating computational fluid dynamics with population balance (CFD-PBM) is proposed, extending traditional models developed for well-mixed systems to open-flow microchannels, where mixing dynamics critically influence the particle size distribution. The model has been rigorously validated against experimental and numerical data from multiple sources and under various operating conditions, offering insights into the relationships between kinetic and hydrodynamic phenomena affecting the system's outcomes.

Drop encapsulation events in propagating bubbles and bursting bubbles are investigated using high-fidelity CFD simulations employing a hybrid front-tracking/level-set approach. Through a comprehensive analysis of various surfactant properties, this work introduces a regime map categorising the observed encapsulation behaviours and demonstrates how surface tension reductions and Marangoni stresses delay encapsulation. For bursting bubbles, a quantitative assessment of surfactant-induced wave retardation and its impact on aerosol suppression is presented, along with a phenomenological mechanism explaining wave delays.

Acknowledgements

I would like to express my immense gratitude to my PhD supervisor, Prof. Omar K. Matar, for giving me the opportunity to pursue this long-held dream. His exceptional mentorship, guidance, support, and motivation over these past four years have been invaluable and have helped me to grow as a researcher. I would also like to thank my two academic co-supervisors, Dr. Lyes Kahouadji and Dr. Alessio Lavino, for their continuing teachings, advice, and encouragements. I am grateful for the time we spent discussing a wide range of scientific—and not-so-scientific—topics, from bursting bubbles and baking cakes to population balances and OpenFoam. A special mention to Prof. S. Shin, Dr. D. Juric, and Dr. J. Chergui for their assistance with simulation setups.

Next, I would like to thank our collaborators from the PREMIERE (EP/T000414/1) Programme grant, Prof. Mark Simmons, Dr. Nina Kovalchuk and Konstantia Nathanael from the University of Birmingham, and Prof. Panagiota Angeli, Dr. Loïc Chagot and Dr. Maria Kalli from University College London for their scientific input, fruitful collaboration, and experimental insights. A special mention to Prof. Sibo Cheng for his support and teachings about Machine Learning.

I would like to extend my gratitude to all the Quaisr team, especially Dr. Lachlan Mason, Dr. Indranil Pan, Dr. Assen Batchvarov, Dr. Morgan Kerhouant, and Dr. Gabriel Gonçalves, for their warm and supportive welcome to the team.

I would also like to acknowledge the Colombian Ministry of Science and Technology (MINCIENCIAS) for their "PhD Abroad Scholarship", which partially funded my PhD and made this work possible, and my first academic supervisor, Prof. Nicolás Ríos Ratkovich, for introducing me to the world of CFD and fluid mechanics.

A very special thanks to all past and present MFG members, especially Fuyue, Nausheen, Andrius, Debashis, Abdullah, and Zinelis, for making the office a fun and friendly place to be and with whom I've shared many laughs over much-needed coffee breaks and conference dinners. Those moments have been among the most enjoyable of my PhD.

A heartfelt thanks to a special PhD colleague of mine, Juan Pablo, for his friendship, com-

panionship, encouragement, and above all, love. Thank you for being a foundational pillar in my life over the past six years and for standing by me through everything. What a journey we've had together.

Last but certainly not least, I would like to thank my parents, Manuel and Lilia, and my sister, Laura, for their unconditional love. Thank you for your life lessons, sacrifices, unwavering support, and belief in me, which make me feel like I can achieve anything; there is nothing I want more in this world than to make you proud.

Dedication

To my family,

for their love and support.

Scientific output

Listed below are the publications in which I participated during my PhD that form the foundation of this thesis:

Chapter 2.3, which provides a literature review on AgNPs, its applications, and modelling approaches, is partially based on:

- Nathanael, K., **Pico, P.**, Kovalchuk, N.M., Lavino, A.D., Simmons, M.J.H. and Matar, O.K. (2022). *"Computational modelling and microfluidics as emerging approaches to synthesis of silver nanoparticles – A review"*. **Chem. Eng. J.**, 436, p.135178

Chapter 4, exploring the synthesis process of AgNPs via PBM-CFD in both microfluidic channels and well-mixed reactors, is based on:

- **Pico, P.**, Nathanael, K., Lavino, A.D., Kovalchuk, N.M., Simmons, M.J.H. and Matar, O.K. (2023). *"Silver nanoparticles synthesis in microfluidic and well-mixed reactors: A combined experimental and PBM-CFD study"*. **Chem. Eng. J.**, 474, p.145692

Chapter 5, which studies the dynamics of surfactant-laden multiphase flow in microchannels via high-fidelity CFD simulations, is based on:

- **Pico, P.**, Kahouadji, L., Shin, S., Chergui, J., Juric, D. and Matar, O.K. (2024). *"Drop encapsulation and bubble bursting in surfactant-laden flows in capillary channels"*. **Phys. Rev. Fluids.**, 9, p.034001

Chapter 6, presenting a CFD study of bursting bubbles in the presence of surfactant at large Bond number, is based on:

- **Pico, P.**, Kahouadji, L., Shin, S., Chergui, J., Juric, D. and Matar, O.K. *"Surfactant-laden bubble bursting: dynamics of capillary waves and Worthington jet at large Bond number"*. **Phys. Rev. Fluids.**, 9, p.83606

Besides the publications listed above, I have also participated in the following publications during my PhD:

- Kalli, M., **Pico, P.**, Chagot, L., Kahouadji, L., Shin, S., Chergui, J., Juric, D., Matar, O.K. and Angeli, P. (2023). *"Effect of surfactants during drop formation in a microfluidic*

channel: a combined experimental and computational fluid dynamics approach". **J. Fluid Mech.**, 961, p.A15

- Basha, N. et al. (2024). *"Machine Learning and Physics-Driven Modelling and Simulation of Multiphase Systems"*. **Int. J. Multiph. Flow**, 179, P.104936

Additionally, I have participated in the creation of the following repositories, the first of which was used to generate the data presented in the preliminary results of chapter 7, and the second contains the implementation of the PBM-CFD formulation proposed in chapter 4:

- Valdes, J. P., Liang, F., and **Pico, P.** (2024). HAMPPSterS: Hybrid PC-HPC Automated Monitoring and Post-processing: Parametric Study Scheduler for Simulations (Version 6.1) [Computer software].
- **Pico, P.** (2023). AgNPs: Predicting the Particle Size Distribution of AgNPs using PBM-CFD Simulations (Version 0.1) [Computer software].

Some of the work of this thesis has also been disseminated in the following international conferences (presenter marked with an asterisk):

- **Pico, P.***, L. Kahouadji, S. Shin, J. Chergui, D. Juric and O. K. Matar. *"Surfactant-laden bursting bubbles: Marangoni effects on capillary waves and Worthington jet formation at large Bond number"*. The 26$^{\text{th}}$ International Congress of Theoretical and Applied Mechanics. Daegu, South Korea (August 2024).
- **Pico, P.***, L. Kahouadji, S. Shin, J. Chergui, D. Juric and O. K. Matar. *"Surfactant-induced Marangoni effects on capillary waves and Worthington jets in bursting bubbles"*. Bifurcations and Instabilities in Fluid Dynamics. Edinburgh, UK (June 2024).
- **Pico, P.***, K. Nathanael, N. M. Kovalchuk, A. D. Lavino, O K. Matar and M.J.H. Simmons. *"Predicting the PSD of AgNPs: Coupled PBM-CFD Simulations and Experiments"*. ChemEngDayUK. London, UK (April 2024).
- **Pico, P.***, L. Kahouadji, S. Shin, J. Chergui, D. Juric and O. K. Matar. *"Fully 3-D simulations of bursting bubbles and jet droplets: effect of large Bond number"*. 76$^{\text{th}}$ Annual Meeting of the APS Division of Fluid Dynamics. Washington D.C, USA (November 2023).
- **Pico, P.***, L. Kahouadji, A. Batchvarov, S. Shin, J. Chergui, D. Juric and O. K. Matar. *"Dynamics of microfluidics in complex scenarios: surfactants, singularities, and non-circular geometries"*. The 11$^{\text{th}}$ International Conference on Multiphase Flow. Kobe, Japan (April 2023).
- **Pico, P.***, L. Kahouadji, A. Batchvarov, S. Shin, J. Chergui, D. Juric and O. K. Matar. *"Flow of elongated bubbles in microchannels under high We conditions: cavity formation,*

drop encapsulation, and bubble rupture". 75th Annual Meeting of the APS Division of Fluid Dynamics. Indianapolis, Indiana, USA (November 2022).

- **Pico, P.***, L. Kahouadji, A. Batchvarov, S. Shin, J. Chergui, D. Juric and O. K. Matar. *"Effect of surfactants on elongated bubbles in rectangular capillary channels: liquid encapsulation and bursting"*. 2022 AIChE Annual Meeting. Phoenix, Arizona, USA (November 2022).

- **Pico, P.***, K. Nathanael, N. M. Kovalchuk, A. D. Lavino, M. J. H. Simmons and O. K. Matar. *"Effect of Operating Conditions on the Chemical Synthesis of Silver Nanoparticles in Microfluidics: coupled PBM-CFD Simulations"*. 9th World Congress on Particle Technology. Madrid, Spain (September 2022).

- M. Kalli, **Pico, P.***, L. Chagot, L. Kahouadji, S. Shin, J. Chergui, D. Juric, O. K. Matar and P. Angeli. *"Effect of surfactants on the flow dynamics of liquid drops in complex microchannel geometries"*. 8th European Congress on Computational Methods in Applied Sciences and Engineering. Oslo, Norway (June 2022).

- **Pico, P.***, A. Lavino, and O. K. Matar. *"Numerical simulations of Polydisperse Particles in Multiphase Flows: Gas Hydrates in Flow Assurance Applications"*. 74th Annual Meeting of the APS Division of Fluid Dynamics. Phoenix, Arizona, USA (November 2021).

Contents

1 Introduction **1**

1.1 Context and motivation 1

1.2 Scope and objectives 3

1.3 Thesis outline 5

2 Literature review and background **7**

2.1 Overview 8

2.2 Brief fundamentals on interfacial systems and surfactants 8

2.3 Synthesis of AgNPs: applications, synthesis methods, and microfluidic production 15

2.4 Elongated bubbles in micro- and capillary channels 27

2.5 Bursting bubbles: capillary waves and Worthington jets 36

3 Numerical modelling of multiphase flows: multi-scale and multi-fidelity approaches **48**

3.1 Overview 48

3.2 Mesoscale PBM approaches for polydisperse particles in multiphase flows 49

3.3 High-fidelity CFD methods for interfacial phenomena with surfactants 58

4 Silver nanoparticles synthesis in microfluidic and well-mixed reactors: a PBM-CFD study **79**

4.1 Motivation and overview 80

4.2 Problem formulation and summary of experimental dataset 81
4.3 Numerical methods and model description 85
4.4 Results and discussion 99
4.5 Concluding remarks 118

5 Drop encapsulation and bubble bursting in surfactant-laden flows in capillary channels 122

5.1 Motivation and overview 123
5.2 Numerical methods and problem formulation 124
5.3 Mesh independence 129
5.4 Validation in square capillaries 134
5.5 Results and discussion 136
5.6 Concluding remarks 159

6 Surfactant-laden bubble bursting: dynamics of capillary waves and Worthington jet at large Bond number 162

6.1 Motivation and overview 163
6.2 Formulation and problem statement 164
6.3 Bursting bubble validation and drop size/velocity in the presence of surfactant . . 172
6.4 Results and discussion 174
6.5 Concluding remarks 195

7 Conclusions and future outlooks 198

7.1 Conclusions and main contributions 198
7.2 Future outlooks 202

Bibliography 214

A Derivation of the Finke-Watzky expression 243

B Literature PSD predictions using higher-order reconstructions **245**

List of Figures

1.1 Schematic representation of the modelling approaches that comprise the work of this thesis 4

2.1 Schematic representation of surfactant molecules and their interactions with interfaces: 10

2.2 Schematic representation of the primary surfactant phenomena in a rising bubble system within an aqueous phase 13

2.3 Summary of the various applications of AgNPs across a variety of fields 15

2.4 Simplified schematic of reduction-based fabrication methods of AgNPs 17

2.5 Illustration of the dynamics described by the F-W two-step mechanism 23

2.6 Schematic representation of microfluidic channels 26

2.7 Dynamics of elongated bubbles travelling through liquid-filled small-scale channels 29

2.8 Unique interfacial features of elongated bubbles in non-circular capillaries under $We_b << 1$ conditions 31

2.9 Representation of an elongated bubble in the presence of a low-solubility surfactant 33

2.10 Conceptual representation of the liquid infiltration and drop encapsulation phenomena in systems under large Ca_b and Re_b conditions 34

2.11 Encapsulation regime map proposed by Atasi et al. [17] for a surfactant-laden bubble travelling in a circular microchannel under vanishing inertial effects. 36

2.12 Production of aerosol droplets via bursting bubble phenomena 39

2.13 Schematic representation of a bubble resting on a free interface 40

2.14 A dominant capillary wave with wavelength λ^* propagating across the bubble domain under vanishing Bo conditions 43

2.15 Compilation of literature data on first ejected drop capillary and Laplace numbers (velocity and size, respectively) as a function of La (or Oh) and Bo, as compiled by Berny et al. [34] 44

2.16 Bubble collapse and Worthington jet interfacial self-similarity proposed in the work of Lai et al. [158] 46

2.17 Qualitative representation of surfactant-induced wave retardation in (a)-(b) and jet stabilisation in (c)-(d) in the fluid mechanics problem of bursting bubbles, as elucidated in the experimental study of Pierre et al. [227] 47

3.1 Conceptual illustration of birth and death events of a specific internal coordinate ξ_i, represented by the red spheres, due to agglomeration and breakup 53

3.2 Outline of a mesoscale description of a polydisperse multiphase system using PBM 57

3.3 Schematic representation of a stationary control volume V, an infinitesimal control volume δV encompassing a portion of the interface, and a small surface element . . 60

3.4 Schematic illustration of interface capturing and interface tracking methods 67

3.5 Schematic representation of the Level Contour Reconstruction Method 69

3.6 Schematic representation of interface merging/breakup in the context of the Level Contour Reconstruction Method in 2-D 70

3.7 Representation of a triangular Lagrangian element of area A_e and its geometrical information 76

4.1 Microfluidic synthesis of AgNPs via chemical reduction 82

4.2 Code validation against the numerical results of Perala and Kumar [221] and the experimental data of Watzky and Finke [309] for IrNPs 89

4.3 Mass diffusion coefficient of AgNPs as a function of particle size according to the Stokes-Einstein equation (S-E), the modification considering the Knudsen number ($Kn = 0.01$) [187], and the Wilke-Chang correlation (W-C) of Wilke and Chang [314]. The magenta marks represent the experimental data of Ung et al. [295] . . . 93

4.4 Results of mesh independence study under the operating conditions specified in figure 4.11(a) for a channel length of 0.25 m 97

4.5 Influence of the discretisation scheme for the convective term under the operating conditions specified in figure 4.11(a) for a channel length of 0.25 m 98

4.6 Effect of pH and TC_0 on the temporal evolution of A and B and comparison between the experimental measurements of Nathanael et al. [204] (marks) and F-W-based PBM predictions (dashed lines) for AgNPs in a well-mixed reactor, showing how F-W predicts well the behaviour at $pH = 7$ but not at $pH = 12$ . . . 100

4.7 Effect of pH and TC_0 on the PSD after full precursor consumption and comparison between experimental measurements, normal distribution fitting of said measurements, and F-W-based PBM predictions for AgNPs in a well-mixed reactor, highlighting the limitations of F-W for $pH = 12$ 102

4.8 Effect of the ratio $k_2 A_0/k_1$ on a few relevant parameters of the system in a well-mixed reactor, as predicted by the F-W two-step mechanism 106

4.9 Prediction of PSD in a well-mixed reactor by using two parameters: the ratio $k_2 A_0/k_1$ and d_{crit}, as predicted by the F-W model 107

4.10 Influence of hydrodynamic parameters on the steady-state concentration of AgNPs precursor (or silver ions) along the T-junction microchannel 109

4.11 Steady-state simulation contour profiles in the T-junction microchannel 111

4.12 Influence of inlet flow rate on the PSD along the T-junction microchannel 114

4.13 Influence of inlet flow rate on the spatial distribution of AgNPs in the T-junction microchannel 119

5.1 Schematic of simulation setup, re-entrant liquid jet penetrating the bubble, and encapsulated drop 127

5.2 Results of mesh independence study for surfactant-free and surfactant-laden elongated bubbles, showcasing the temporal evolution of kinetic energy, interfacial area, and axial location of the bubble nose 131

5.3 Elongated bubble-liquid interfacial profiles across time in the vicinity of a pinch-off event denoted by $\tilde{t}_{p-o}$ and comparison between different mesh resolutions for Case 0 133

5.4 Validation elongated bubbles travelling in square capillary channels and under $We > 1$ conditions in terms of (a) bubble nose velocity relative to average liquid phase velocity, and (b) gas phase area fraction 135

5.5 Effect of Ca on bubble characteristics for surfactant-free cases at $\tilde{t} = 0.76$ 138

5.6 Temporal evolution of interface characteristics in surfactant-free cases 139

5.7 Neck thinning analysis for the "back pinch-off" event of a surfactant-free interface 142

5.8 Neck thinning analysis for the "interior pinch-off" event of a surfactant-laden case characterised by $k = 0.25$ ($Da = 0.4$) 144

5.9 Effect of Marangoni stresses on re-entrant liquid jet formation and encapsulation . 145

5.10 Effect of β_s on re-entrant liquid jet formation and encapsulation 148

5.11 Effect of Bi on re-entrant liquid jet formation and encapsulation 150

5.12 Impact of surfactant parameters on pinch-off dynamics and evolution of first encapsulated drop for a highly desorptive surfactant ($k = 0.1$) 152

5.13 Effect of k and Da on re-entrant liquid jet formation and encapsulation 154

5.14 Effect of Re on re-entrant liquid jet formation and encapsulation 155

5.15 Encapsulation and bursting regime maps in the (a) β_s-k and (b) Bi-k spaces . . . 157

6.1 3-D computational domain in a Cartesian coordinate system $\mathbf{x} = (x, y, z)$ and initial bubble shapes 164

6.2 Interfacial tension isotherm and equilibrium interfacial concentration as a function of bulk surfactant concentration for SDS surfactant, as measured experimentally in Vega and Montanero [297], Pierre et al. [227], Néel and Deike [206] 171

6.3 Comparison of surfactant-free simulations results for varying Bo and La against the scaling (red lines) and numerical simulations (red squares) of Lai et al. [158] and the numerical data of Constante-Amores et al. [55] at $Bo \sim O(10^{-3})$ (black circles) using the same numerical approach employed here 174

6.4 Comparison of the dynamics of the first released drop obtained with surfactant-free (a,b) and surfactant-laden (d,e) simulations against previous work 175

6.5 Bubble bursting dynamics in surfactant-free interfaces: comparison of pressure fields and interface shape at the same T for a moderate $Bo = 0.5$ on the left half and a large $Bo = 5$ on the right half 176

6.6 Dynamics of capillary wave velocity and interfacial shape in surfactant-free interfaces: effect of Bo and Oh 177

6.7 Temporal evolution of (a) kinetic energy, (b) interfacial area, (c) viscous dissipation energy, and (d) maximal vertical location of the interface in surfactant-free cases (i.e., vertical position of the Worthington jet/released drops for $(\tilde{t} - \tilde{t}_0)/\tilde{t}_0 > 0$) . . 179

6.8 Surfactant-driven capillary wave motion delay: comparison of temporal evolution (at the same $\tilde{t}$) of pre-collapse bubble for surfactant-free interfaces on the left half and insoluble surfactant ($Bi = 0$, $\beta_s = 0.3, Ma = 93.43$) on the right half. 181

6.9 Effect of insoluble surfactant ($Bi = 0$, $\beta_s = 0.3, Ma = 93.43$) on the dynamics of the capillary wave velocity 183

6.10 Effect of surfactant solubility at $\beta_s = 0.3$ ($Ma = 93.43$) on capillary wave dynamics: (a,d,g,j) interface shape; (b,e,h,k) surfactant concentration along the interface; (c,f,i,l) Marangoni stresses along the interface 186

6.11 Effect of surfactant elasticity at $Bi = 0$ in the range $\beta_s = 0.3 - 0.7$ ($Ma = 93.43 - 218.01$) on capillary wave dynamics 188

6.12 Interface collapse under varying Bi and β_s conditions according to the scaling proposed in Lai et al. [158] in the range $t_0 - t \approx 6t_{pre} - 10t_{pre}$ 189

6.13 Compilation of Bi and β_s effects on average dominant capillary wave velocity and collapse time under varying Bo conditions 191

6.14 Effect of insoluble ($Bi = 0$) surfactant on Worthington jet dynamics: (a)-(h) comparison of temporal evolution (at the same T) of interface shape and pressure fields for surfactant-free interfaces on the left half and insoluble surfactant on the right half; the operating conditions for both the clean and surfactant case are identical to those in figure 6.8 193

6.15 Influence of bubble cap and hole opening location on Worthington jet 195

7.1 Effect of gravity on encapsulation dynamics for a surfactant-free case under the same operating conditions as figure 5.5 ($Ca = 0.0693$) 204

7.2 Effect of Lagrangian particles on bubble collapse under conditions of $Bo = 0.5$ and $Oh = 3.21 \times 10^{-3}$ ($La = 9.7 \times 10^4$) 205

7.3 Setup of the interfacial oscillations system and validation against the simulations of Farsoiya et al. [85] 208

7.4 Comparison between true and predicted $\tilde{a}_{k0}$ data, segregated by their corresponding dimensionless time $\tilde{t}$ and error dispersion for training (left columns) and testing (right columns) sets 210

7.5 Comparison between original images from CFD simulations and predicted-reconstructed images at different dimensionless times for a sample case exhibiting fully damped behaviour, characterised by $\epsilon = 1.03$, $\rho_r = 3.06$, $\mu_r = 1.69$, $La = 1 \times 10^4$, and $Bo = 0$. 212

7.6 Comparison between original images from CFD simulations and predicted-reconstructed images at different dimensionless times for a sample case exhibiting simple jetting behaviour, characterised by $\epsilon = 1.46$, $\rho_r = 6.96$, $\mu_r = 3.49$, $La = 1 \times 10^4$, and $Bo = 10.2$ 212

7.7 Comparison between original images from CFD simulations and predicted-reconstructed images at different dimensionless times for a sample case exhibiting complex jetting behaviour, characterised by $\epsilon = 1.46$, $\rho_r = 595.92$, $\mu_r = 661.10$, $La = 738.29$, and $Bo = 9.78$ 213

B.1 Influence of the order of the moments selected to compute d and σ^{SD} using the conditions of Perala and Kumar [221] 246

B.2 Temporal evolution of (a) d, (b) σ^{SD}, and (c) precursor concentration, obtained by using a volume-weighted mean, showcasing how a much closer prediction of PSD to the experimental data is obtained without deteriorating the precursor consumption predictions 247

List of Tables

2.1 Compilation of selected works utilising reduction-based methods for the chemical synthesis of AgNPs in well-mixed reactors 18

2.2 Compilation of selected works on microfluidic synthesis of AgNPs 25

2.3 Compilation of selected experimental and numerical studies reporting instances of re-entrant jet formation or drop encapsulation in liquid-liquid or gas-liquid flow within small-scale channels. 35

4.1 F-W two-step mechanism fitting parameters according to the experimental measurements of Nathanael et al. [204] and summarised in §4.2.3 in a well-mixed reactor for the chemical synthesis of AgNPs 99

4.2 Effect of pH and TC_0 on d, σ^{SD}, and $PDI = (\sigma^{SD}/d)^2$ after full precursor consumption and comparison between experimental measurements, normal distribution fitting of said measurements, and F-W-based PBM predictions for AgNPs in a well-mixed reactor 103

5.1 Additional features of the mesh resolutions tested in surfactant-free and surfactant-laden elongated bubbles, including computing time, minimum cell size, and maximum volume variation in both the gas and liquid phases 131

5.2 Recorded $\tilde{t}_{inv}$, $\tilde{t}_{p-o,bk}$, and $\tilde{t}_{p-o,int}$ for the two mesh resolutions tested 132

5.3 Interfacial area (A_d in mm^2) of encapsulated drop post pinch-off 132

6.1 Comparison of capillary wave velocity in clean interfaces and in the presence of insoluble surfactant ($Bi = 0$, $\beta_s = 0.3, Ma = 93.43$) 183

6.2 Effect of Bi (at constant $\beta_s = 0.3$) and β_s (at constant $Bi = 0$) on the exponent of a power-law fit of the form $\tilde{\theta} \sim \tilde{t}^{\alpha}$ of the $\tilde{\theta}$ vs. $\tilde{t}$ data 190

7.1 Model input features and their corresponding ranges used for training, testing, and validation 207

7.2 Hyperparameter search space, best configuration, and performance metrics in testing dataset, where MAE stands to mean absolute error, and MSE for mean squared error 209

Notation

All symbols and abbreviations used in this thesis are defined at their first occurrence and are summarised in the list below. For the reader's convenience, the definitions of certain key symbols and abbreviations introduced in earlier chapters are occasionally reiterated in subsequent chapters.

Abbreviations

AgNPs Silver nanoparticles

AuNPs Gold nanoparticles

CFD Computational fluid dynamics

CFL Courant-Friedrichs-Lewy

CMC Critical micelle concentration

DL Deep learning

DNS Direct numerical simulations

ENO Essentially non-oscillatory

F-W Finke-Watzky

GMRES Generalised Minimal Residual

GPBE Generalised population balance equation

IC Inertial-capillary

ID Internal diameter

IV Inertial-viscous

LCRM Level Contour Reconstruction Method

LHS Left-hand side

IrNPs Iridium nanoparticles

LSW Lifshitz-Slyozov-Wagner

MAC Marker-and-Cell

MAE Mean absolute error

MSE Mean squared error

ML Machine learning

MLP multilayer perceptron

MPI Message passing interface

MW Molecular weight

NDF Number density function

NP(s) Nanoparticle(s)

PBE Population balance equation

PBM Population balance modelling

PCA Principal component analysis

PDI Polydispersity index

PISO Pressure-Implicit-of-Split-Operations

PLIC Piece-wise linear interface calculation

PSD Particle size distribution

PTFE Polytetrafluoroethylene

QBMM Quadrature-based moments method

QMOM Quadrature method of moments

RF Random forest

RHS Right-hand side

SAXS Small-angle X-ray scattering

SDS Sodium dodecyl sulphate

S-E Stokes-Einstein

SSIM Structural similarity index measure

SLIC Simple line interface calculation

SN Silver nitrate

TA Tannic acid

TC Trisodium citrate

TX100 Triton X-100

W-C Wilke-Chang

XGBoost eXtreme Gradient Boosting

2-D, 3-D Two- and three-dimensional, respectively

VOF Volume of fluid

Roman letters

$a(\xi_i)$	Breakup kernel of a discrete entity with internal coordinate ξ_i in chapter 3
a_{k0}	Interfacial location at the domain's midpoint in chapter 7
A	Area or precursor species in the well-mixed reactor in the AgNPs case-study
$\mathbf{A}$	Collected diffusive, convective, and gravitational terms in the context of Chorin [52]'s projection method
A_e	Area of a triangular element in the Lagrangian grid in the context of LCRM
A_s	Interfacial area
$\mathbf{A_p}$	Combined forces per unit mass acting on a particle
$Ag_{(l)}$	Reduced silver atoms in the T-junction reactor
$Ag_{(s)}$	Silver nuclei species in the T-junction reactor
$Ag_{(s2)}$	Silver NPs species in the T-junction reactor
Ag^0	Elemental silver atoms
Ag^+	Silver ions in solution
$b(\xi_i\|\xi_j)$	Probability density function of the formation of ξ_i from the breakup of ξ_j in chapter 3
B	Precursor species in the NPs in the well-mixed reactor
$\mathcal{B}$	Total birth rate of a given internal coordinate
$\mathcal{B}(L_i)^{agg}$	Total birth rate of size L_i due to aggregation
$\bar{\mathcal{B}}(\xi_i)^{agg}$	Pair-wise birth rate of ξ_i due to aggregation
$\bar{\mathcal{B}}(\xi_i)^{bk}$	Pair-wise birth rate of ξ_i due to breakup
$Cv_{k+1,k}$	Coefficient of variation of the distribution calculated using m_{k+1} and m_k
C	Bulk surfactant concentration or contour boundary
Co	CFL condition
C_j	Molar concentration of the j^{th}
C_s	Surfactant concentration in bulk sub-phase

C_{SS}	Supersaturated monomer concentration
C_∞	Reference bulk surfactant concentration
d	Average diameter of the distribution
d_{crit}	Critical nucleation radius
$\mathrm{d}l, \mathrm{d}s, \mathrm{d}v$	Line, surface and volume infinitesimal element
$d_{k+1,k}$	Average diameter of the distribution calculated using m_{k+1} and m_k
d_m	Atomic diameter
D	Diffusion coefficient or diameter
$D_{s,c}$	Interfacial and bulk surfactant diffusion coefficients, respectively
$\mathcal{D}$	Total death rate of a given internal coordinate
$\mathcal{D}(L_i)^{agg}$	Total death rate of size L_i due to aggregation
$\bar{\mathcal{D}}(\xi_i)^{agg}$	Pair-wise death rate of ξ_i due to aggregation
$\bar{\mathcal{D}}(\xi_i)^{bk}$	Pair-wise death rate of ξ_i due to breakup
e	Electron
E	T-junction channel diameter
E_k	Kinetic energy
E_σ	Excess energy of the system or Gibbs modulus
E_0	Marangoni modulus
E_μ	Viscous dissipation energy
$f(L,t)$	NDF with particle size L as internal coordinate in chapter 4
$\mathbf{f_g}$	Gravitational body forces
$\mathbf{f}_\sigma$	Interfacial tension forces
$\mathbf{F}$	Surface tension term in the context of Chorin [52]'s projection method
g	Gravity
$G(y_j, L)$	Size-dependent growth rate as a function of the mass fraction of the j^{th} species
$\mathbf{G}$	Geometric information distribution
h	Liquid film thickness in the context of bubble propagation in liquid-filled channels
$h(\boldsymbol{\xi}, \mathbf{x}, t)$	Discrete events in the context of the PBE in chapter 3
$\mathcal{H}(\mathbf{x}, t)$	Heaviside function
H	T-junction channel length
$\mathbf{I}, \mathbf{I}_s$	Identity and surface identity tensors, respectively
$J(y_j)$	Nucleation rate as a function of the mass fraction of the j^{th} species
J_D	Diffusive surfactant mass flux
$J_{a,d}$	Surfactant mass flux due to adsorption and desorption, respectively
J_0	Zero$^{\text{th}}$-order Bessel function of the first kind
k	Wave number
k_B	Boltzmann constant
$k_{a,d}$	Kinetic constant of adsoption and desorption, respectively
k_V	Volumetric shape factor in the context of the AgNPs case-study

$k_{1,2}$	Kinetic constant of nucleation and growth, respectively
l_c	Capillary length scale
l_{vis}	Viscous length scale
L	Particle size or Length
L_{jet}	Worthington jet length
m_k	k^{th}-order moment of the PSD
$n(\boldsymbol{\xi}, \mathbf{x}, t)$	Number density function
$\mathbf{n}$	Unit normal vector
N	Number of surfactant molecules or number of nodes in the quadrature approximation in the context of PBM
N_{av}	Avogadro number
N_p	Number of particles
$\mathcal{N}$	Total nucleation rate
p	Pressure
p_{ref}	Reference pressure
$\mathbf{p}$	Binormal unit vector
Q	Volumetric flow rate of either channel inlet in the T-junction
r	Radial coordinate
$\dot{r}$	Rate of reaction
R	Radius or reducing agent species in the T-junction microchannel in the context of the AgNPs case-study
R_h	Hydraulic radius
R_0	Bubble radius in the context of the bursting bubble case-study
$\mathcal{R}$	Ideal gas constant
S	Surface
S_j	Mass-based source term representing the nucleation and growth
S_Γ	Source term modulating interface surfactant adsorption/desoption
$\mathbf{S}$	Rate-of-strain tensor
u_{d1}	Radius of first ejected drop
t	Time
t_0	Bubble collapse time in the bursting bubble case-study
$\mathbf{t}$	Tangential unit vector
T	Temperature or dimensionless comparative time in chapter 6
T_0	Wave oscillation period in chapter 7
$\mathbf{T}$	Symmetric stress tensor
$\mathbf{T}_s^\sigma$	Surface tension tensor
$\mathbf{u}$	Velocity vector field $[u, v, w]^T$
u_c	Capillary velocity scale
u_{d1}	Velocity of first ejected drop
u_{jet}	Worthington jet ejection velocity

u_{ref}	Reference velocity
u_θ	Average velocity of the dominant capillary wave
$\mathbf{u}_s$	Surface velocity
$\mathbf{u_t}$	Tangential velocity vector projection of $\mathbf{u}_s$
u_{vis}	Viscous velocity scale
U_a	Average channel's velocity
U_b	Bubble propagation velocity
U_{ch}	Characteristic velocity
U_{set}	Stokes particles settling velocity
U_{n}	Normal velocity to an interface
V	Volume
$\mathbf{V}_f$	Interface velocity interpolated from the Eulerian grid in the context of LCRM
w	Weight of the quadrature
W	Channel inlet length in the T-junction
$\mathbf{x}$	Cartesian coordinate vector $[x, y, z]^T$
$\mathbf{x}_f$	Location in the Lagrangian grid in the context of LCRM
y_j	Mass fraction of the j^{th} species
$z_{\max}$	Maximal interface location in the computational domain

Greek letters and operators

α	Scaling exponent in chapters 2 and 6
β	Scaling exponent in chapter 2
β_{clean}	Viscous damping rate in clean interfaces in chapter 2
β_s	Surfactant elasticity
$\beta(\xi_i - \xi_j, \xi_j)$	Aggregation kernel between two disperse entities in chapter 3
$\beta_{Br}(L_i, L_l)$	Brownian aggregation kernel between two particles with sizes L_i and L_l in chapter 4
Γ	Interfacial surfactant concentration
Γ_∞	Maximum packing of interfacial surfactant species (saturation concentration)
δ	Dirac delta function or liquid film thickness in chapter 6
δ_S	Surface distribution delta function
ϵ	Gas area fraction in chapter 5 and dimensionless initial wave amplitude in chapter 7
ϵ_σ	Minimum dimensionless surface tension
η	Wave interface in chapter 7
θ	Angular location of dominant capillary wave in chapters 2 and 6
κ	Curvature
λ	Wavelength
μ	Viscosity

ν	Stoichiometric coefficient in chapter 4 and kinematic viscosity in §2.2 and §2.5
ξ	Mixture fraction
$\boldsymbol{\xi}$	Internal coordinate
Π	Surface pressure
ρ	Density
σ	Interfacial tension (general)
σ_s	Interfacial tension in clean interfaces
σ^{SD}	Standard deviation of the distribution in the context of the AgNPs case-study
$\sigma^{SD}_{k+1,k}$	Standard deviation calculated by using m_{k+1} and m_k
τ	Stress
ϕ	Volume fraction or colour function in the VOF method, or dimensionless parameter as a function of La the bursting bubble case-study
ϕ_2	Mass fraction
ψ	Level-set distance function
ω	Vorticity
Δ	Delta difference operator
∇, $\nabla_{\mathbf{x}}$	Nabla operator in physical space
$\nabla_{\boldsymbol{\xi}}$	Nabla operator in phase space in the context of PBM
∇_h	Spatially discrete Nabla operator
∇_s	Surface gradient operator

Dimensionless numbers

Bi	Biot number
Bo	Bond number
Ca	Capillary number
Da	Damköhler number
k	Adsorption depth
La	Laplace number
Ma	Marangoni number
Oh	Ohnesorge number
$Pe_{c,s}$	Bulk and surface Péclet numbers, respectively
Re	Reynolds number
Se	Sedimentation number
St	Stokes number
We	Weber number

General rules

- Tildes ($\tilde{}$) are used to refer to the dimensionless version of a given variable.

- The subscript $_b$ denotes the bubble phase, while $_l$ and $_g$ refer to the liquid and gas phases, respectively. In certain cases, the subscripts $_g$ and $_b$ may be used interchangeably, depending on which is more contextually appropriate.
- The subscripts $_s$ and $_c$ are typically used to refer to the surface and bulk quantities of given parameters, respectively.
- The subscripts $_a$ and $_d$ are typically used to refer adsoprtion and desorption, respectively.
- The subscript $_0$ is typically used to refer to an initial or base state, unless stated otherwise. In the context of the bursting bubble case-study, it is used to refer to the bubble collapse time; the subscript $_f$ is used to refer to a final state.
- In the context of the F-W mechanism (refer to §2.3.3 and chapter 4), the subscripts $_{\text{ind,j}}$ and $_{\text{ind,p}}$ represent two distinct interpretations of induction time in a well-mixed reactor. The subscripts $_{\max}$ and $_{\text{plateau}}$ correspond to the maximum rate of consumption or production and the state at which complete precursor consumption is achieved, respectively.
- Beyond the context of the F-W mechanism, the subscript $_{\max}$ signifies a general maximum value.
- The subscripts $_m$, $_t$, and $_n$ denote Marangoni, tangential, and normal components, respectively. These notations are primarily employed in the context of Marangoni stresses, as well as tangential and normal viscous stresses.
- The subscript $_d$ denotes the dispersed phase, while $_p$ refers to the particles. In certain cases, these subscripts may be used interchangeably, depending on which is more contextually appropriate.
- In the context of PBM and the AgNPs case study, the subscript $_k$ denotes the k^{th} order, primarily in reference to the moment set.
- In the context of PBM and the AgNPs case study, the subscripts $_L$ and $_V$ denote length-based and volume-based quantities, respectively.
- In chapter 4, the subscript $_{res}$ denotes residence time, $_{trav}$ signifies transversal, in reference to the transversal Péclet number, $_{mix}$ refers to mixing, $_{conv}$ refers to convection, the index $_{rxn}$ is used as an index to indicate a given chemical reaction, and the subscript $_r$ refers to the reduction chemical reaction.
- The subscripts $_{nuc}$ and $_g$ typically refer to nucleation and growth, respectively.
- In the context of chapter 5, the subscript $_{p-o}$ signifies pinch-off, with $_{p-o,int}$ and $_{p-o,bk}$ denoting "interior" and "back" pinch-off, respectively.
- In the context of chapter 5, the subscript $_{jet}$ signifies the re-entrant jet penetrating the bubble's domain.

Chapter 1

Introduction

Contents

1.1 Context and motivation 1
1.2 Scope and objectives 3
1.3 Thesis outline 5

1.1 Context and motivation

Multiphase flows encompass a vast array of fluid mechanics problems that have fascinated both researchers and non-researchers for centuries. Their appeal lies in both their intricate and captivating behaviour, as well as their phenomenological complexity and pervasiveness in the natural world and advanced technology. Understanding how drops, bubbles, and particles interact amongst each other and with a continuous phase forms the pillar of a wide range of engineering applications. These span the realms of environmental science, meteorology, food processing, the oil and gas (O&G) industry, nuclear energy, aerospace engineering, pollution control, drug delivery, manufacturing processes, and irrigation systems, among many others [187, 290, 324, 67]. In fact, as eloquently put by the authors of Tryggvason et al. [290], it is not difficult to state that nearly all industrial operations involve multiphase flows in one way or another.

Disperse multiphase flows represent an important category of multiphase flows wherein at least one phase comprises well-defined discrete sub-structures (particles, droplets, or bubbles) within one or more carrier phases [23, 88]. In numerous applications, the attributes characterising the disperse phase—such as size, shape, temperature, velocity, and composition—may exhibit significant variability among the sub-structures, thereby making the system *polydisperse* with a *distribution* over its characterising attributes [187]. Examples of such flows in industrial applications can be found in spray drying, spray casting, cyclone separators for pollution control, fluidised beds, pneumatic conveyers, bubble columns, pipelines in the O&G industry, mixing operations,

emulsifiers, flame reactors, abrasive water jet cutters, and microchannels. In natural systems, polydisperse multiphase flows are observed in sediment transport in rivers and oceans, blood flow, mudflows and landslides, hailstorms, dust storms, and volcanic eruptions [61, 324, 187].

Multiphase flows in practical applications exhibit an exceptional level of complexity from both mathematical and modelling perspectives, attributable to their *multiscale*, *multiphysics*, and *highly nonlinear* characteristics. Moreover, precise characterisation of these phenomena frequently requires an explicit determination of the positions of phase boundaries or "interfaces," which, in addition to being infinitesimally thin, introduce discontinuities in the properties of the fluids. The multiscale nature of multiphase flows is evident in phenomena spanning a wide range of spatio-temporal scales—ranging from microscale droplets and bubbles to large-scale oceanic currents—where interactions across these scales significantly impact the dynamics of the system. Furthermore, the interaction of numerous physical phenomena can substantially affect the system's evolution through mechanisms including heat and mass transfer, chemical reactions, electromagnetic effects, surface-active contaminants, structural interactions, complex rheology, and phase transitions [290].

Correctly characterising polydisperse multiphase flows poses further challenges and complications as their modelling involves the consideration of two key aspects. The first is the correct coupling of the dynamics of the multiphase flow itself with the spatio-temporal evolution of the polydisperse properties of the disperse phase [187]. The second aspect corresponds to the broad range of interacting phenomena across different length and time scales that are encompassed in multiphase polydisperse systems [324, 88]. These aspects require the need for developing and applying theoretical and computational frameworks able to describe simultaneously the complex interactions between the continuous and the disperse phases, as well as the distribution of the disperse phase over a given property within a multi-scale formulation.

Significant effort has been devoted over the past decades to develop robust and reliable computational approaches for modelling the underlying physical phenomena of multiphase flows and polydisperse systems [290, 113, 88]. These efforts have incorporated a variety of mathematical and computational techniques designed to balance trade-offs between computational cost, robustness, and accuracy. The approaches have spanned from theoretical investigations in simplified scenarios using linear stability analysis [2], lubrication theory [43], and scaling analyses [100], to high-fidelity Direct Numerical Simulations (DNS) employing Eulerian-Eulerian [24] or Eulerian-Lagrangian [75] techniques to handle interfacial dynamics. Mesoscale models, including Population Balance Models (PBMs), have been proposed as an alternative to purely Lagrangian tracking of dispersed entities in polydisperse flows, enabling researchers to instead track the evolution of the distribution of the discrete entities' properties [187]. The advent of low-cost computational resources in recent decades has elicited growing interest in the application of data-driven approaches, including Machine Learning (ML) and Deep Learning (DL) algorithms, to multiphase flows in various engineering disciplines [215, 27].

The appropriateness of each aforementioned modelling approaches for a specific fluid mechanics problem is highly contingent upon the characteristic scales of the multiphase system, the interacting transport phenomena, the chemical properties, and the initial and boundary conditions. Although theoretical analyses offer vital insights into multiphase systems, their application has largely been confined to simplified scenarios, such as axisymmetric flows, inviscid systems, conditions of negligible inertia, free-surface flows, and systems devoid of contaminants. DNS, on the other hand, offer a high-fidelity, physics-driven representation of all continuum scales but require intense computations that have rendered complex large-scale engineering problems, especially those related to turbulence, out of reach for DNS. Mesoscale models are capable of offering significant insights into the spatio-temporal evolution of the disperse phase and the distribution of its properties, while incurring lower computational costs compared to purely Lagrangian approaches. However, these models typically necessitate detailed kinetic and mechanistic information about the system, which can be challenging to acquire experimentally, as will be discussed in this thesis. Lastly, ML and DL approaches, although frequently producing highly accurate predictions, exhibit notable limitations when tasked with extrapolating beyond the training data [215, 27, 187, 290, 12].

1.2 Scope and objectives

This thesis is an in-depth and systematic exploration of various fluid mechanics problems involving general multiphase flows and polydisperse multiphase systems through computational and numerical approaches. The specific case studies investigated feature complex interfacial phenomena and flows at the microscale within a multiphysics and multiscale context. The interfacial phenomena considered herein involve intricate topological changes to the interface, interfacial singularities arising from capillary breakup, highly confined and free-surface flows, and the presence of surface-active contaminants. This work specifically targets conditions far from ideality, such as non-negligible inertial and gravitational forces, or an intricate combination of capillarity, inertia, viscosity, gravity, and Marangoni effects, as they induce the development of intriguing dynamics that have not been previously characterised.

The findings presented in this thesis are centred around three case studies, with their modelling approaches and general scales depicted schematically in figure 1.1. The first case study addresses the engineering challenge of achieving size monodispersity during the synthesis of nanoparticles (NPs) in microfluidic channels, and examines how these dynamics differ from those in well-mixed batch reactors. In this case study, a modelling formulation based on a hybrid mesoscale-macroscale representation of the system is proposed. This formulation incorporates numerical simulations wherein population balances are employed to represent the NPs and to solve for the spatio-temporal evolution of their size distribution. Concurrently, computational fluid dynamics (CFD) techniques are utilised to represent the continuous phase. These approaches are integrated

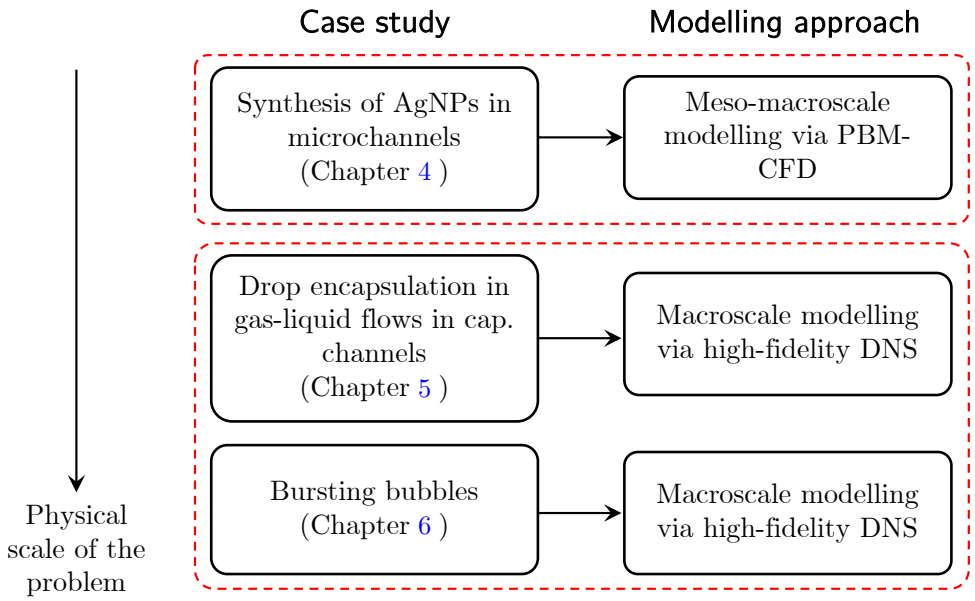

Figure 1.1: Schematic representation of the modelling approaches that comprise the work of this thesis

and coupled via experimentally validated chemical reaction kinetics.

Continuing with the examination of confined flows at micro- and capillary scales, the second case study explores the evolution of bubble-liquid flow in a square capillary channel through high-fidelity DNS. This study specifically addresses the less understood regime characterised by non-negligible inertial forces and the presence of surface-active agents. In this regime, substantial variations in bubble propagation are observed, including a series of interfacial singularities that result in the entrapment of liquid droplets within the bubble's domain.

The third and final case study shifts the focus from confined flows to the classic fluid mechanics problem of bubbles bursting through a liquid-gas interface, also investigated via high-fidelity DNS. This investigation emphasises the influence of non-negligible gravitational forces and the presence of surface-active contaminants on the temporal evolution of capillary waves that form around the collapsing bubble, ultimately governing the ejection of a Worthington jet. The study also investigates the breakup of this jet via the Rayleigh-Plateau instability, leading to the release of highly contaminated droplets into the atmosphere, within the context of mass exchange between the oceans and the atmosphere. The interfacial complexity inherent in the latter two case studies necessitates careful tracking of the interface topology in three dimensions, particularly during capillary breakup events, as well as monitoring the evolution of the spatial distribution of surfactants at the interface and within the bulk phase. These flow characteristics demand high-fidelity simulations and a special treatment of the interface.

1.3 Thesis outline

The rest of this thesis is organised as follows:

- Chapter 2 provides a contextual framework for this thesis by discussing the fundamental concepts that underpin its findings and the current state-of-the-art relevant to each case study. Concepts related to the various interpretations of surface tension, surface-active agents, Marangoni flows, equilibrium surfactant dynamics, and Gibbs-Marangoni moduli are covered alongside key investigations on nanoparticle synthesis, microfluidic channels, bubbles travelling in capillary channels, and bursting bubbles.

- Chapter 3 presents a comprehensive overview of the modelling and simulation approaches employed in this thesis. It begins with an exploration of relevant theoretical concepts, including mesoscale modelling of polydisperse systems, population balance models, the population balance equation, agglomeration and breakup events, and the quadrature method of moments, which is the technique selected in this work to solve the population balance equations in chapter 4. Subsequently, the chapter briefly reviews various computational fluid dynamics techniques proposed for handling multiphase flows, such as the volume of fluid method, front-tracking, and level-set methods. Special emphasis is placed on the level contour reconstruction method (LCRM), the numerical method utilised in this work to manage the interface and its coupling with the governing equations for surfactants in chapters 5-6.

- Chapter 4 delves into the synthesis of silver nanoparticles (AgNPs) within both microfluidic and well-mixed reactors. It commences with a thorough description of the proposed modelling and computational framework, which has been implemented using open-source code. This framework is based on the well-established Finke-Watzky two-step mechanism [309], originally designed for well-mixed reactors, and extended in this work to be applicable to open-flow domains, such as microfluidics, where mixing dynamics largely govern the system. A thorough validation of the model is presented, comparing the model predictions against experimental data available in the literature and data measured by our collaborators at the University of Birmingham [204, 224] in both well-mixed and microfluidics channels. Subsequent sections of the chapter provide a detailed analysis of the effects of various operating conditions, such as pH, reactant concentration, and flow rate, on the particle size distribution of the AgNPs.

- Chapter 5 is dedicated to the second case study, which examines an elongated bubble travelling through a liquid-filled capillary channel in the presence of surfactants. Following a brief introduction to the problem, the chapter addresses the poorly-understood conditions of large capillary numbers, Ca, under which the bubble's rear end undergoes curvature inversion, permitting the liquid phase to penetrate the bubble domain. In certain scenarios, this penetration results in the liquid jet breaking via the Rayleigh-Plateau instability, leading

to the entrapment or "encapsulation" of liquid drops within the bubble. The chapter investigates the influence of various surfactant parameters on this encapsulation phenomenon and proposes a regime map summarising all observed behaviours.

- Chapter 6 is devoted to the third case study — bubbles bursting through a liquid-gas interface in the presence of surfactants. This chapter focuses on understanding the effects of gravitational forces, quantified here by the Bond number (Bo), as well as various surfactant parameters on the velocity of capillary waves generated during bubble collapse. A mechanism based on the evolution of Marangoni stresses is proposed to rationalise the surfactant-induced wave retardation phenomena observed.

- Chapter 7 concludes this work by offering final remarks, perspectives, and various avenues for future research.

Chapter 2

Literature review and background

Contents

2.1 Overview **8**

2.2 Brief fundamentals on interfacial systems and surfactants **8**

2.2.1 Interfacial tension: a working definition 8

2.2.2 Surface-active agents and interfaces at equilibrium 9

2.2.3 Dynamic properties of surfactants 12

2.2.4 Marangoni flows 14

2.3 Synthesis of AgNPs: applications, synthesis methods, and microfluidic production **15**

2.3.1 Applications of AgNPs and fabrication methods 15

2.3.2 Influence of operating conditions on the properties of AgNPs 17

2.3.3 Mechanistic modelling of AgNPs 19

2.3.4 Microfluidic synthesis 24

2.4 Elongated bubbles in micro- and capillary channels **27**

2.4.1 Dynamics of elongated bubbles under idealised conditions 27

2.4.2 Effects of non-idealities: curvature reversals and drop encapsulation . . . 30

2.5 Bursting bubbles: capillary waves and Worthington jets **36**

2.5.1 The role of bursting bubbles on aerosol droplets 37

2.5.2 Initial shape of a bubble resting on a free interface 38

2.5.3 Jet drops: main findings in uncontaminated scenarios 41

2.5.4 The role of surface-active contaminants on bursting bubbles 45

2.1 Overview

The upcoming chapter presents an in-depth review of the fundamental theoretical concepts and key literature that underpin this thesis, providing essential context for the results in chapters 4 through 6. The review begins with §2.2, which dives into the most significant aspects of surfactant systems and related interfacial mechanisms, serving as an introduction to the state-of-the-art on surfactant-laden elongated bubbles in capillary channels and bursting bubbles, explored in §2.4 and §2.5. These sections form the basis for the results presented in chapters 5 and 6. Next, §2.3 presents an overview of AgNPs in §2.3, highlighting their relevance across various cutting-edge industries, fabrication methods, computational modelling, and microfluidic synthesis—a primary focus of chapter 4.

2.2 Brief fundamentals on interfacial systems and surfactants

2.2.1 Interfacial tension: a working definition

A classic definition of surface tension, σ_s, attributes this interfacial property to the imbalance of mutually attractive forces experienced by molecules at the interface compared to those in the bulk [184]. Molecules within the fluid bulk experience no net force due to the symmetric distribution of attractive forces from their neighbours. Conversely, molecules near the interface experience a net force directed towards the fluid bulk, resulting in an energetically unfavourable state. This unfavourable state prompts the system to minimise its interfacial area, thereby reducing its free energy [184, 290]. Consequently, surface tension can be conceptualised as the energy required to create additional interfacial area. From this lens, surface tension is also defined as the minimum amount of work required to expand an interface and create new area or the energetic difference between bulk and interface molecules [245].

Alternatively, and as elaborated in §3.3, surface tension can also be interpreted from a mechanical perspective. In this view, surface tension is the mechanical force per unit length that acts to "pull" the interface perpendicularly to any line segment along the interface [290]. These definitions of surface tension are encapsulated in Eq. (2.1):

$$\sigma_s = \frac{\text{Work}}{\mathrm{d}A} = \frac{\mathrm{d}E_\sigma}{\mathrm{d}A} = \frac{F}{L}, \tag{2.1}$$

where $\mathrm{d}A$ represents an infinitesimal surface area increment, E_σ the excess energy of the system, F the pulling force, and L the "pulled" length.

Another definition of surface tension, which becomes particularly relevant when discussing surfactants in the next subsection, is its characterisation as an isotropic surface stress, analogous to a negative pressure in three dimensions [184]. Let us imagine a situation where a gas bubble

A of initial radius R, immersed in a liquid B, is increasing its volume and thus its surface area. This situation is modelled by the well-known Laplace pressure jump expression of Eq. (2.2):

$$\Delta p = p_A - p_B = \frac{2\sigma_{AB}}{R}, \tag{2.2}$$

where p_A and p_B correspond to the pressures inside and outside the bubble, respectively. The above equation suggests that larger interfacial tensions or curvatures would require larger bulk pressures to maintain equilibrium; smaller bubbles have a higher internal pressure [184]. The classic Young-Laplace expression offers a more general view of these observations:

$$\Delta p = \sigma_{AB} \nabla_s \cdot \mathbf{n}, \tag{2.3}$$

where ∇_s is the surface gradient operator, $\mathbf{n}$ is a unit vector pointing away from the gas bubble, and $\nabla_s \cdot \mathbf{n}$ is the mean curvature of the interface. The mathematical definition of ∇_s is discussed in §3.3.

2.2.2 Surface-active agents and interfaces at equilibrium

Surfactants, or surface-active agents, are organic molecules of an often "amphiphilic" nature, capable of adsorbing onto surfaces and distinctly altering their free energies [245]. Their amphiphilic properties stem from the presence of both hydrophilic and hydrophobic groups within their molecular structure. These molecules are typically conceptualised as having hydrophilic "heads" and hydrophobic "tails", as shown in figure 2.1(a). Surfactants enable a reduction of surface tension by exerting a "surface pressure", Π, which counteracts the pulling forces of surface tension. In this way, surfactants reduce surface tension according to the expression of Eq. (2.4):

$$\sigma(\Gamma) = \sigma_s - \Pi(\Gamma), \tag{2.4}$$

where Γ is surfactant concentration at the interface. Henceforth, σ and σ_s are used to refer to surface tension in general, and σ_s as surface tension in "clean" interfaces, respectively.

Adsorbed surfactants typically form an ordered monolayer at the interface, with the hydrophilic heads oriented toward the aqueous phase and the hydrophobic tails facing an organic or gaseous phase. This adsorption process incurs an energetic cost, as surfactant molecules in the bulk liquid enjoy a greater range of rotational and translational micro-states compared to those at the interface. The reduced entropy per molecule of the adsorbed molecules is offset by the avoidance of unfavourable surfactant interactions at the molecular level when they are in the bulk. As a consequence, the equilibrium between adsorbed molecules, with a concentration given by Γ, and dissolved molecules at the bulk, with a concentration given by C, is represented by a balance between a favourable *enthalpy* change and an unfavourable *entropy* reduction during adsorption

[184]. Figure 2.1(b) schematically represents an ordered surfactant monolayer adsorbed to the interface in equilibrium with surfactants at the bulk of an aqueous phase.

Conceptually, an increase in bulk concentration C will promote surfactant adsorption, thereby increasing Γ to maintain equilibrium. As C continues to rise, the dissolved surfactant molecules begin to self-assemble into more energetically favourable structures, known as micelles [245]. The concentration at which this occurs is termed the critical micelle concentration (CMC). Beyond this point, the surfactant monolayer becomes saturated, and further increases in surfactant concentration no longer result in a reduction of surface tension, as schematically encapsulated in figure 2.1(c). Although intriguing dynamics emerge above the CMC [128, 227, 297], they lie beyond the scope of this investigation.

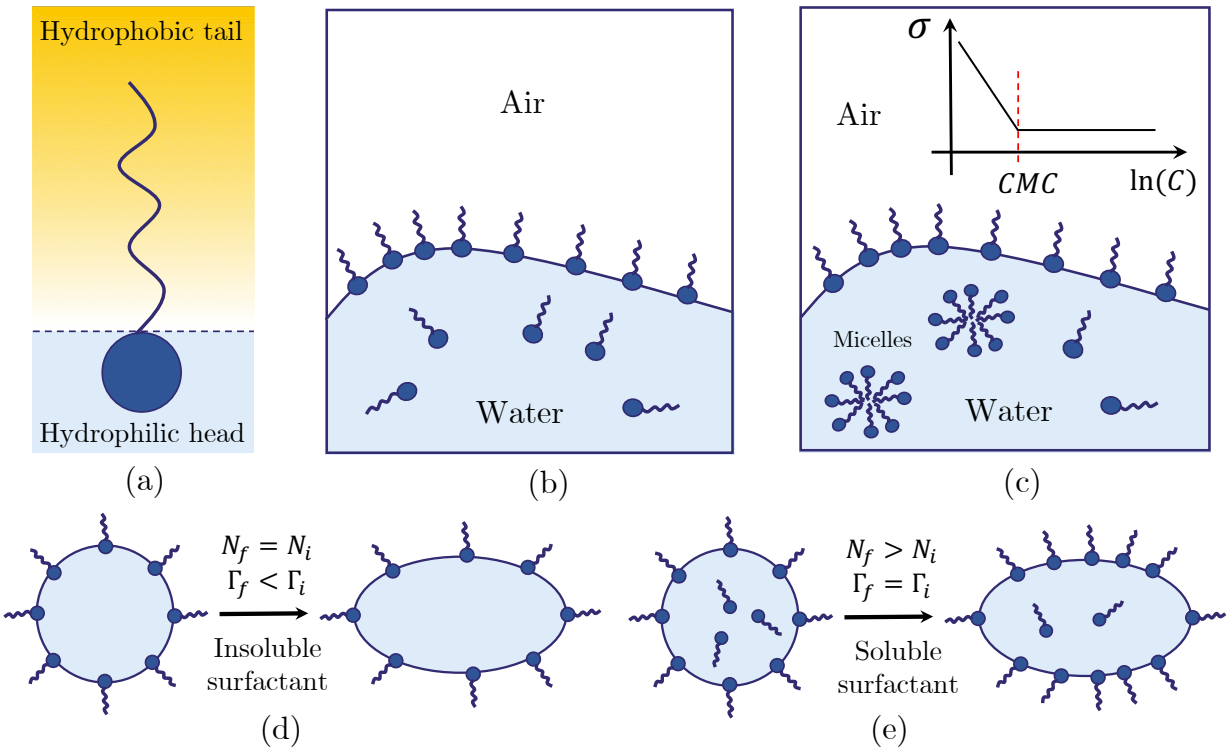

Figure 2.1: Schematic representation of surfactant molecules and their interactions with interfaces: (a) a simplified surfactant molecule, showcasing its hydrophilic head and hydrophobic tail; (b) an adsorbed surfactant monolayer in equilibrium with surfactant molecules in a bulk aqueous phase; (c) a saturated interface and micelle formation at the bulk liquid phase, where the schematic plot depicts a halt in surface tension reduction with surfactant concentration at CMC; (d)-(e) a water drop covered in insoluble and soluble surfactants, respectively, being deformed to increase its surface area. Here, the subscripts f and i denote final and initial conditions, respectively. Figure adapted from Manikantan and Squires [184]

2.2.2.1 Surfactant solubility and equations of state

Solubility is a crucial parameter in the characterisation of surfactants, significantly influencing their interfacial behaviour. Purely insoluble surfactants are those whose molecular structures

favour aggregate formation over dissolution in the bulk phase and therefore surfactant desorption from the interface is heavily restricted. According to Manikantan and Squires [184], surfactants with larger hydrophobic components generally exhibit lower solubilities. Common examples of insoluble surfactants in an organic phase include Sodium dodecyl sulfate (SDS) and DTAB [245]. Conversely, soluble surfactants can dissolve into the bulk phase, creating a dynamic equilibrium between adsorbed molecules at the interface and those dissolved in the bulk. In such systems, the free energy required to add a surfactant molecule to the interface must be identical to the energy released when a molecule is removed from the bulk, thereby maintaining equilibrium.

Monolayers comprising insoluble surfactants are typically referred to as "Langmuir monolayers", while those made of soluble surfactants are termed "Gibbs monolayers." To illustrate the conceptual difference between these two types of surfactants, figure 2.1(d)-(e) depicts a scenario where a surfactant-covered water drop is deformed from its initial state, with N_i adsorbed surfactant molecules and interfacial area A_i, to a final state with an increased interfacial area A_f ($A_f > A_i$). The strong resistance to desorption characteristic of insoluble surfactants ensures that the number of adsorbed molecules remains unchanged, leading to a decrease in interfacial surfactant concentration ($\Gamma = \frac{N}{A}$, with $\Gamma_f < \Gamma_i$) and an increase in surface tension. Conversely, soluble surfactants strive to maintain their equilibrium state upon deformation. Any potential reduction in Γ below equilibrium due to an increase in A will be counteracted by surfactant adsorption from the bulk. Consequently, after steady state is reached, both Γ and σ will remain unchanged.

The equilibrium dynamics between Γ and C are represented by adsorption isotherms, which are used to derive equations of state linking σ to Γ and C. Over the years, numerous isotherms of varying complexity have been proposed. Manikantan and Squires [184] provide a comprehensive overview and compilation of some of the most relevant adsorption isotherms in their perspectives manuscript. As mentioned in §3.3, this work employs the well-known Langmuir isotherm (see Eq. (3.35)) to model the variation of σ with Γ in chapters 5-6. The Langmuir isotherm is based on the organisation of non-interacting, finite-sized surfactant molecules in lattice structures [184].

2.2.2.2 Gibbs-Marangoni moduli

A relevant aspect of surfactant-laden interfacial dynamics is the tendency of an interface to resist compression. This is measured by the surface compressional modulus or Gibbs modulus, E, which is governed by Eq. (2.5) [184]:

$$E = -A\frac{\partial \Pi}{\partial A}. \tag{2.5}$$

As previously mentioned, insoluble surfactant monolayers, upon compression/expansion, maintain a constant number of surfactant molecules, leading to the Marangoni modulus, defined in

Eq. (2.6):

$$E_0 = \Gamma \frac{\partial \Pi}{\partial \Gamma}\Big|_N. \tag{2.6}$$

The Marangoni modulus quantifies the overall work required to compress surfactant molecules together [184]. The significance of this and other moduli in relation to the dynamic response of surfactant-covered interfaces and Marangoni flows will be elucidated in the upcoming subsections. §3.3 demonstrates the intimate connection between the Marangoni modulus and the surfactant parameters examined in chapters 5-6, as well as the resulting interfacial rigidification observed therein.

2.2.3 Dynamic properties of surfactants

Up to this point, the dynamic equilibrium between bulk and interface has been treated as an instantaneous event. In reality, the phenomena involved in this dynamic equilibrium have a temporal component. This temporal component is responsible for a number of distinct interfacial and bulk mechanisms which significantly influence the system's behaviour. The mathematical description of these mechanisms in the context of the CFD simulations conducted is elucidated in §3.3 (Eqs. (3.30)-(3.35)). Here, a general conceptual definition is provided.

2.2.3.1 Competition between convective and diffusive interfacial dynamics

Excluding Marangoni-induced flows, which are analysed is detail in the next subsection, the transport of surfactants across the interface is largely governed by two distinct mechanisms: convection, resulting from an imposed velocity field on the interface or bulk, and natural diffusion due to surfactant concentration gradients. The former mechanism sweeps surfactants in the direction opposite to the motion of the interface. This sweeping effect is responsible for the elevated surfactant concentration observed in the rear region in classic problems of rising bubbles [282] and bubbles in capillary channels (see §2.4 [31]). Conversely, diffusion seeks to minimise concentration gradients by imposing a net flow that opposes bulk convection. As highlighted in chapters 5-6, this work quantifies the competition between these mechanisms by defining an interfacial Péclet number, Pe_s (see Eq. (5.9) and Eq. (6.9) for its mathematical definition).

Figure 2.2(a)-(b) contains an illustrative sketch spotlighting the mechanistic differences between interfacial convection and diffusion in the context of a rising bubble, a system closely related to the elongated bubble studied in chapter 5. Surfactant interfacial convection is proportional to $\mathbf{u}\Gamma$, where $\mathbf{u}$ denotes velocity, as seen in the second term on the LHS of Eq. (3.30). In contrast, diffusive phenomena are typically modelled via Fickian flux equations: $\mathbf{J}_D = -D_s \nabla_s \Gamma$ (see first term on the RHS of Eq. (3.30), equal to $-\nabla_s \cdot (\mathbf{J}_D)$). In this expression, D_s is the diffusive coefficient, and $\mathbf{J}_D$ represents the net diffusive flux [184, 290]. Details on the implications of utilising a diffusive Fickian flux are provided in Manikantan and Squires [184].

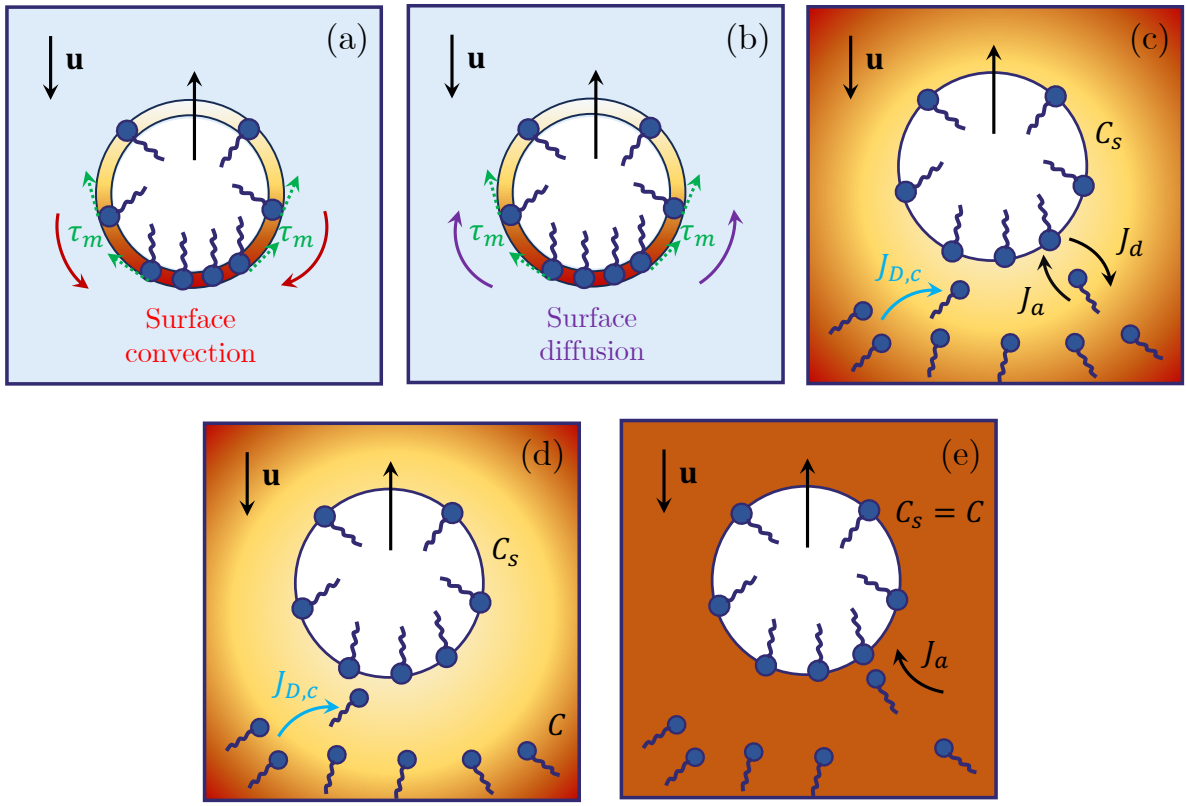

Figure 2.2: Schematic representation of the primary surfactant phenomena in a rising bubble system within an aqueous phase: (a)-(b) surface convection sweeps surfactant molecules towards the bubble's rear, while surface diffusion, driven by concentration gradients, counteracts this transport. The interface is thickened for illustrative purposes, with high interface concentration in red and low concentration in light yellow. Green dashed arrows indicate the tangential direction of Marangoni stresses; (c) bulk diffusion transports surfactants to and from the bulk sub-phase, where adsorption and desorption phenomena take place. Here, the bulk liquid phase is coloured by surfactant concentration; (d)-(e) depictions of diffusion-limited and adsorption-limited systems, respectively. Figure adapted from Manikantan and Squires [184]

2.2.3.2 Competition between sorptive dynamics and bulk diffusion

Surfactant interfacial adsorption is a complex process that is appreciably influenced by the dynamic interplay between surfactant desorption and diffusion across the bulk. This diffusive phenomenon is responsible from transporting surfactants from regions distant from the interface to a region, denoted as C_s, in the vicinity of the interface (also termed as bulk "sub-phase"), where surfactant exchange occurs via the kinetic mechanisms of adsorption and desorption, as depicted in figure 2.2(c). In situations of high surfactant interfacial coverage, a desorptive flux is prompted into the sub-phase, where surfactants can migrate through diffusion back into the bulk.

Adsorption-desorption interactions are given by a kinetic flux of the form $J_k = J_a(\Gamma, C_s) - J_d(\Gamma, C_s)$, which simply quantifies the difference between adsorptive and desorptive fluxes (see also Eq. (3.33), where J_k is denoted by the symbol S_Γ). A bulk diffusion flux based on Fick's law is given by $J_{D,c} = -D_c \mathbf{n}\cdot\nabla C\big|_{\text{interface}}$ (see also Eq. (3.34)), where D_c represents a surfactant diffusion coefficient at the bulk. Employing a simple surfactant conservation argument [184, 290, 245], one

reaches the conclusion that the diffusive flux must balance the kinetic flux.

In any multi-step process, the dynamics of surfactant-covered interfaces are determined by the interplay between the characteristic time scales of the phenomena involved. In diffusion-limited systems, the time scale associated with adsorption kinetics is negligibly small compared to that of diffusion. This is illustrated in figure 2.2(d), where slow bulk surfactant diffusion creates large bulk concentration gradients, and the molecules at C_s are adsorbed immediately. Conversely, adsorption-limited systems, depicted in figure 2.2(e), feature rapid diffusion that quickly equalises bulk concentration variations, resulting in $C \approx C_s$, where C represents surfactant concentration far way from the sub-phase.

2.2.4 Marangoni flows

The topics of Marangoni flows and Marangoni stresses have been extensively studied over the years, with numerous contributions across various fluid mechanics problems. This sub-section is not meant to offer a comprehensive historical overview of all contributions. Instead, it aims to highlight the most pertinent aspects of Marangoni flows and how they relate to the problems explored in this thesis.

Marangoni flows emerge due to surface tension gradients, which can arise due to temperature, electrical charge, or surfactant concentration gradients [184, 290]. This work focuses on the latter factor, which is also typically termed "solutal Marangoni effects". From a thermodynamic perspective, solutal Marangoni stresses can be understood as spatial gradients in chemical potential that drive surfactants along these gradients. Marangoni stresses, τ_m, can also be related to surface pressure through the Gibbs adsorption relation [184], leading to the definition shown in Eq. (2.7):

$$\tau_m = -\nabla_s \Pi = \nabla_s \sigma = -\frac{\partial \Pi}{\partial \Gamma} \nabla_s \Gamma. \tag{2.7}$$

The above equation suggests that imbalances in surfactant concentration, and consequently surface tension, will induce Marangoni stresses that drive a surface flow to counteract these imbalances, as illustrated by the green arrows in figure 2.2(a)-(b). As previously mentioned, non-uniform surfactant distributions across the interface can also be mitigated by diffusive phenomena, which tend to diminish the effects of Marangoni stresses.

A crucial feature of Marangoni-induced flows corresponds interface rigidification and augmented resistances to deformation [47, 58, 31]. The resistance to deformation of a surfactant-laden system can be quantified by the Marangoni number, Ma, which relates the characteristic time of the main flow, L_{ch}/U_{ch}, to that of Marangoni stresses, $\nu L_{ch}/E_0$, as shown in Eq. (2.8)

[213, 184]:

$$Ma = \frac{E_0}{\nu U_{ch}}. \tag{2.8}$$

In the above, L_{ch} and U_{ch} correspond, respectively, to the characteristic length and velocity of the system, and ν to the kinematic viscosity. In the $Ma >> 1$ limit, Marangoni flows develop much faster than the system's convective flows, allowing surfactant molecules to strongly resist compression and rigidify the interface.

2.3 Synthesis of AgNPs: applications, synthesis methods, and microfluidic production

2.3.1 Applications of AgNPs and fabrication methods

Over the past two decades, silver nanoparticles (AgNPs) have gained substantial prominence in both academia and industry due to their unique physicochemical properties, making them ideal for a wide array of applications. These applications, summarised in figure 2.3, include food preservation [319], localised drug delivery coatings [219], sterile textile fabrication [25], water disinfection [311], treatment of specific fungal and viral infections [63, 177], surface-enhanced Raman scattering (SERS) [176], electronics printing [162], and catalysis of organic reactions [71]. Due to these diverse applications, the global market for AgNPs was valued at $1.8 million in 2019 and is projected to reach $4.1 billion by 2027 [203]. Given their antibacterial and antiviral properties, it is anticipated that the pharmaceutical industry will experience the fastest AgNPs usage growth rate in terms of volume and revenue during this forecast period. The successful application of Ag-

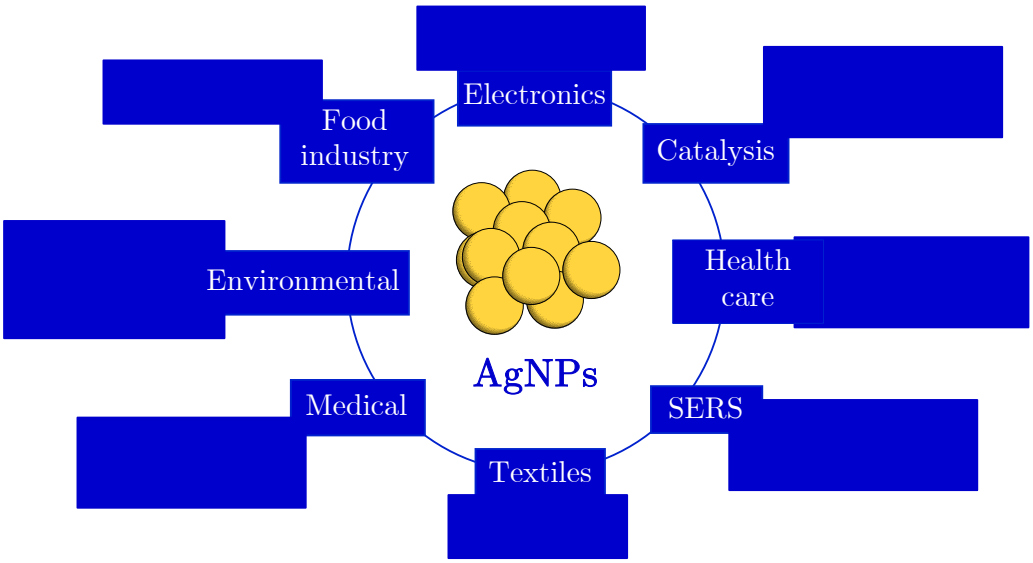

Figure 2.3: Summary of the various applications of AgNPs across a variety of fields. Adapted from Nathanael et al. [203]

NPs in many of the aforementioned fields is intrinsically tied to a highly controlled and reliable fabrication process. This process must be capable of rapidly synthesising nanoparticles (NPs) with extremely precise sizes and shapes, while also minimising polydispersity, reagent consumption, and environmental impact [271, 224]. Various synthesis methods have been proposed over the years, broadly categorised into two main approaches: *top-down* and *bottom-up*.

Top-down methods start with bulk material and progressively reduce its size to the nanoscale, typically ranging from 1–100 nm [329]. These methods are predominantly based on physical mechanisms, such as laser ablation, evaporation-condensation, electrical irradiation, thermal decomposition, gamma irradiation, and lithography [117]. In contrast, bottom-up methods construct complex nanostructures from atomic, molecular, or ionic components, utilising various chemical, biological, and physical mechanisms. While the detailed exploration of these fabrication methods is beyond the scope of this thesis, interested readers may refer to the work of Zahoor et al. [329] and Yaqoob et al. [323] for an in-depth analysis.

2.3.1.1 Chemical synthesis of AgNPs

Chemical synthesis is perhaps the most widely utilised method for fabricating AgNPs. Examples of chemical synthesis protocols include photochemical, electrochemical, thermal decomposition, and reduction-based methods. Photochemical techniques rely on electromagnetic radiation to induce chemical reactions, while electrochemical methods primarily trigger chemical changes through the movement of electrons [164].

Reduction-based synthesis in liquid phase, the primary focus of the present investigation, is an exceedingly well-documented process in the literature, with a vast wealth of published research demonstrating its effectiveness in producing monodispersed particles, even in large-scale scenarios [203]. Three main actors are involved in reduction-based processes: i) metal-based silver precursors, ii) capping/stabilising components, and iii) reducing agents [323].

Reduction-based synthesis processes typically begin with dissolving the silver precursor in a liquid phase, creating a solution of silver ions, Ag^+. These ions are then rapidly reduced to elemental silver atoms, Ag^0, by the reducing agent. This reduction is followed by the nucleation of silver clusters of a critical size, typically ranging from 0.7 to 1.2 nm (Ag_{13} to Ag_{55} clusters) [284]. The clusters (or nanoparticle nuclei) continue to grow until they reach the desired nanoparticle size. Throughout this process, stabilising/capping agents prevent particle agglomeration and stabilise the solution via steric or electrostatic mechanisms. A conceptual diagram of these steps can be found in figure 2.4, and their mathematical description is the subject of §2.3.3. Throughout the years, multiple reduction synthesis protocols, encompassing various silver precursors and reducing/stabilising agents, have been proposed and utilised for an effective synthesis of AgNPs. Examples of commonly-used reducing agents include Borohydrides, boranes, hydrazine hydrate and aniline, which are strong reducing agents, as well as glycose and tannic acid, which are weak

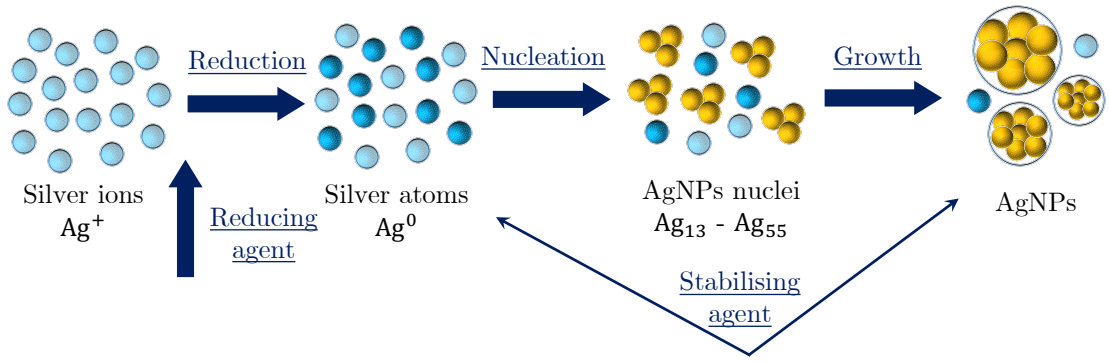

Figure 2.4: Simplified schematic of reduction-based fabrication methods of AgNPs, highlighting the reduction, nucleation, and growth steps. Here, the light blue spheres represent silver ions in solution, the dark blue spheres are the ions that have reduced into silver atoms, and the yellow spheres are NP nuclei that grow into AgNPs. Adapted from Pico et al. [224]

reducing agents. Although various salts have been used as silver precursors, including AgClO4, AgCF3COO, AgCH3COO or (PPh3)n Ag-R (R = Cl, Br or NO3 and n = 1 or 3), silver nitrate ($AgNO_3$) remains the most commonly utilised precursor as a consequence of its low cost and chemical stability [91].

Stabilising agents are crucial in the synthesis of AgNPs, garnering significant research attention due to their role in ensuring kinetic stability by preventing uncontrolled nanoparticle growth and limiting particle aggregation [201]. These agents include surface-active molecules like CTAB [138], polymers such as poly(vinylpyrrolidone) (PVP) and poly(ethylene glycol) (PEG), as well as thiols [5] and certain citrates [157]. Molecular dynamics simulations have provided valuable insights into the intricate behaviours of these stabilisers at the molecular level, elucidating their influence on nanoparticle morphology. Notably, studies by Tsuji et al. [292] and da Silva et al. [62] have demonstrated PVP's capability to selectively bind to specific facets of growing nanoparticles, thereby controlling the formation of diverse shapes such as cubes, nanosheets, nanoplates, and nanowires. A comprehensive review discussing the pivotal role of molecular dynamics simulations in elucidating NP-stabiliser interactions is presented in Nathanael et al. [205].

Table 2.1 presents a compilation of various investigations on AgNPs synthesis, where the wide variety of chemical components used, and their effects on the final NPs' size, can be appreciated. A more in-depth discussion of the impact of selecting a specific synthesis protocol and the influence of operating conditions on particle size can be found in §2.3.2.

2.3.2 Influence of operating conditions on the properties of AgNPs

Multiple factors significantly influence the properties of AgNPs synthesised via chemical reduction. Rather than exhaustively covering the literature, this subsection offers a general overview of the effects of various operating parameters. This context will be pertinent to the results presented in Chapter 4.

Table 2.1: Compilation of selected works utilising reduction-based methods for the chemical synthesis of AgNPs in well-mixed reactors. Here, the entries are organised in decreasing order of reducing agent strength; DDA: Dodecanoic acid, PVP: poly(vinylpyrrolidone), TC: Trisodium citrate, TX-100: Triton-100, CTAB: cetyltrimethylammonium bromide, AOT: Sodium bis (2-ethylhexyl) sulfosuccinate, SDS: Sodium dodecyl sulfate, and TA: Tannic acid. Table adapted and modified from Nathanael et al. [203]

Silver precursor	Red. agent	Stab. agent	Particle size	Particle shape	Application	Reference
$AgNO_3$	$NaBH_4$	DDA	≈ 7 nm	Spherical	Electrodes in printed circuit boards	[162]
$AgNO_3$	$NaBH_4$	PVP	9 ± 2.1 nm	Spherical	Thin films	[165]
$AgNO_3$	$NaBH_4$	TC	≈ 9.94 nm	Spherical and semispherical	Antimicrobial activity	[233]
$AgNO_3$	$NaBH_4$	TX-100	≈ 8 nm	Disc-shaped	Antimicrobial activity	[308]
$AgClO_4$	$NaBH_4$	-	$5 - 8$ nm	Spherical	-	[229]
$AgClO_4$	$NaBH_4$	PVP	$5 - 7$ nm	Spherical	-	[229]
$AgNO_3$	$NaBH_4$	Biosurfactant	$6 - 15$ nm	Spherical	-	[320]
$AgNO_3$	$NaBH_4$	CTAB	≈ 40 nm	Cubic	Antimicrobial activity	[308]
$(PPh_3)AgNO_3$	TBAB	1-dodecanethiol	2.5 nm	Spherical	-	[14]
$(PPh_3)AgCl$	TBAB	1-dodecanethiol	4.8 nm	Spherical	-	[14]
$(PPh_3)AgBr$	TBAB	1-dodecanethiol	3.4 nm	Spherical	-	[14]
$AgNO_3$	$N_2H_4 \cdot H_2O$	PVP	$50 - 200$ nm	Triangular	SERS	[165]
$AgNO_3$	$N_2H_4 \cdot H_2O$	AOT	$2 - 5$ nm	Spherical	Antimicrobial activity	[332]
$AgNO_3$	$N_2H_4 \cdot H_2O$	SDS and isoamylalchohol	$6.5 - 12.1$ nm	Spherical	-	[333]
$AgNO_3$	Aniline	CTAB	$10 - 30$ nm	Spherical	-	[138]
$AgNO_3$	TA	TC	≈ 46 nm	Spherical	-	[239]
$AgNO_3$	Glucose	PVP	$20 - 80$ nm	Spherical	-	[304]
$AgNO_3$	Ethylene glycol	PVP	17 ± 2 nm	Spherical	-	[142]
$AgNO_3$	Citrus sinensis peel extract		≈ 35 nm	Spherical	Antimicrobial activity	[135]
$AgNO_3$	*Melia dubia* leaf extract		≈ 7.3 nm	Spherical	Anticancer activity	[134]
$AgNO_3$	Fruit extract *Sterculia acuminata*		≈ 10 nm	Spherical	Catalysis	[153]
$AgNO_3$	Fruit extract of *Phyllanthus emblica*		≈ 39 nm	Spherical	Antimicrobial activity	[191]
$AgNO_3$	Seed extract of *Alpinia katsumadai*		≈ 12.6 nm	Quasi-spherical	Cytotoxic effects	[109]

The chemical nature and concentration of the silver precursor play a pivotal role in determining particle size, as illustrated by the works of Sobczak-Kupiec et al. [274] and Andrieux-Ledier et al. [14]. In the former, elevated concentrations of silver nitrate precursor led to the formation of larger particles, attributed to higher collision rates. The latter study fabricated AgNPs by utilising various silver phosphine precursors in the presence of TBAB and thiols. The authors found that increased redox potentials of the silver precursor (NO_3Ag (PPH_3) > $BrAg$ (PPH_3) > $ClAg$ (PPH_3)) were linked to smaller particle sizes, a result of enhanced nucleation rates that yield a reduction in *average* particle size. Similarly, Demchenko et al. [69] reported changes in particle size with varying reducing agents. Specifically, higher reducing agent activities and redox potentials were found to produce lower particle sizes.

Temperature significantly impacts both the particle size and shape of AgNPs. Skrabalak et al. [273] investigated a polyol-based synthesis route and proposed a mechanism to explain the

generation of nanoparticles with well-controlled shapes. According to this mechanism, elevated temperatures increase the oxidation rate of ethylene glycol to glycolaldehyde, thereby producing nanoparticles of various shapes. Experimental results by Kaviya et al. [135] and Liu et al. [175] demonstrated that higher temperatures typically result in smaller particle sizes. The latter study attributes this to the differing reaction rates of nucleation versus growth; while the nucleation rate increases sharply with temperature, the growth rate increases only linearly, leading to smaller particle sizes.

The work of Alqadi et al. [8] suggested the existence of an inverse relationship between pH and particle size by using a synthesis protocol involving ascorbic acid and sodium citrate. This finding has been corroborated by Marciniak et al. [188] and Qin et al. [232]. These investigations have explained their findings by proposing a mechanism whereby alkaline conditions increase the reducing power of the reducing agent, increasing the rate of nucleation, and leading to smaller particles. Dong et al. [70] explored how pH affects NPs shape, using citrate reduction of silver nitrate. They found that high pH engenders spherical and rod-like AgNPs due to rapid reduction rates, while low pH yields triangular and polygonal particles due to slower reduction.

Although much less understood, mixing conditions have been found to introduce additional dynamics to the system that serve to alter particle size. By using a rotating packed reactor and a green synthesis method, the authors of Ng et al. [208] detected a more uniform PSD with a lower average particle size when increasing the rate of mixing. Similar findings were reported in Kisyelova et al. [144] with stirred tank and spinning disk reactors.

Other factors influencing the properties of AgNPs include the concentration, chemical nature, and action mode of the stabilising agent [246], storage time, and exposure to light [119]. While these aspects fall outside the scope of this work, they are thoroughly reviewed by Nathanael et al. [203].

2.3.3 Mechanistic modelling of AgNPs

The following subsection provides a concise overview of three traditional mechanisms employed to model the synthesis of NPs from a phenomenological perspective. While the results of chapter 4 primarily focus on the Finke-Watzky two-step mechanism, the inclusion of the other two models serves to offer a comparative analysis, highlighting their distinct characteristics relative to the Finke-Watzky approach.

2.3.3.1 LaMer mechanism

One of the very first attempts at characterising the synthesis of NPs is credited to the work of Lamer and Dinegar [159] on the formation of sulphur sols through the decomposition of sodium

thiosulfate. This mechanism involves three primary steps: i) a rapid increase in the concentration of free sulphur monomers due to sodium thiosulfate until the system reaches supersaturation, ii) a "burst" nucleation, typically modelled using classical nucleation theory, during which the monomer concentration significantly decreases, and iii) NP growth events that are entirely controlled by monomer diffusion [286]. A mathematical expression for the growth of a nucleus with radius x within a spherical volume enclosed by an impenetrable shell of radius h is presented in Eq. (2.9) [313]:

$$\frac{\mathrm{d}(x^2)}{\mathrm{d}t} = (C_{SS} - C_S(t))\,\frac{2D}{\rho} - \frac{2D}{h^3}x^3, \tag{2.9}$$

where C_{SS} is the supersaturation concentration of sulphur monomers, $C_S(t)$ the instantaneous sulphur concentration above saturation at time t, D the diffusion coefficient of sulphur monomers, and ρ the bulk density of elemental sulphur.

The three major steps outlined above, along with the growth equation, underscore the key assumptions of this mechanism. Specifically, LaMer's mechanism posits that nucleation occurs instantaneously at the onset after supersaturation is achieved, and that the kinetics of monomer incorporation into nanoparticles are significantly faster than monomer diffusion. As will be discussed in the subsequent subsections, these assumptions are contrary to experimental observations in the synthesis of AgNPs.

2.3.3.2 The Ostwald ripening mechanism

In mechanisms based on Ostwald ripening, also known as "coarsening", smaller particles, owing to their higher surface energy and consequently larger solubility (in accordance with the Gibbs-Thomson relation), re-dissolve and redeposit onto larger ones. This process results in the growth of larger particles "at the expense" of smaller ones [286, 300]. The Lifshitz-Slyozov-Wagner (LSW) theory, developed by Lifshitz and Slyozov [168] and Wagner [301], mathematically describes this phenomenon. According to the LSW theory, the average particle size increases over time as $\sim t^{1/3}$, while the number of particles decreases as $\sim t^{-1}$ [288]. The essence of the LSW theory is encapsulated in Eq. (2.10), where r represents the particle radius, D the diffusion coefficient, $a = 2\sigma v C_\infty/\mathcal{R}T$, and $\Delta = C - C_\infty$ the concentration deviation from saturated conditions, C_∞; σ denotes surface tension, v the solute volume, $\mathcal{R}$ the ideal gas constant, T temperature, and $R_c = \alpha/\Delta$ is the critical radius [168]:

$$\frac{\mathrm{d}r}{\mathrm{d}t} = \frac{D}{r}\left(\Delta - \frac{a}{r}\right) = \frac{D}{r}\left(\frac{a}{R_c} - \frac{a}{r}\right). \tag{2.10}$$

The above equation models Ostwald ripening as a process in which particles smaller than R_c will dissolve, while particles larger than R_c will grow. The rate of dissolution of smaller particles will therefore be larger than the rate of growth of larger particles. Further information on Ostwald ripening can be found in Tokuyama et al. [288].

Experimental evidence has been put forward to suggest that AgNPs produced by photochemical methods follow an Ostwald ripening mechanism [270].

2.3.3.3 The Finke-Watzky two-step mechanism

The *Finke–Watzky two-step mechanism* (henceforth referred to as F-W) is one of the most successful and widely used models for the synthesis of transition-metal NPs. Originally proposed in 1997 by Watzky and Finke [309], the F-W mechanism is predicated on a *slow* and *continuous* pseudo-first-order nucleation process (Eq. (2.11)) occurring under conditions far from supersaturation, followed by an autocatalytic, pseudo-elementary growth reaction (Eq. (2.12)). The nucleation step encompasses all processes leading to the formation of the first NP nucleus, including the chemical reduction of the precursor, denoted as A.

$$Nucleation: A \xrightarrow{k_1} B; \quad \dot{r}_1 = k_1[A], \tag{2.11}$$

$$Growth: A + B \xrightarrow{k_2} 2B; \quad \dot{r}_2 = k_2[A][B], \tag{2.12}$$

where B represents the NPs and $[\cdot]$ indicates the molar concentration of each species; k_1 and k_2 are the kinetic constants governing nucleation and growth, respectively. From these expressions, and assuming that all of A is consumed into B ($[B] = [A]_0 - [A]$, with $[A]_0$ being the initial concentration of A), the temporal evolution of $[A]$ and $[B]$ is given by Eq. (2.13):

$$-\frac{\mathrm{d}[A]}{\mathrm{d}t} = \frac{\mathrm{d}[B]}{\mathrm{d}t} = k_1[A] + k_2[A][B] = k_1[A] + k_2[A]([A]_0 - [A]). \tag{2.13}$$

The assumptions of the F-W two-step mechanism, manifested in the above equations, have deep implications on the understanding of the underlying dynamics of NP synthesis and on the general applicability of the model to various scenarios. Crucially, in the original F-W mechanism, it is presumed that the growth step is kinetically limited by the incorporation (or "reaction") of new material into (with) an existing NP and not by the spatial diffusion of this material to reach an available reacting site (i.e., very fast mixing rates are imposed in the system). Multiple experimental [243, 197] and modelling [103, 228] investigations involving systems under fast mixing conditions for colloidal NPs are found in the literature, confirming this reaction-limited growth. Additional assumptions include a proportional relationship between the growth rate and material concentration in the NPs (Eq. (2.12)), implying the availability of the entire NP domain (entire particle volume) as a reacting site instead of the surface area only [221], and the generation of NP nuclei directly from the precursor, eliminating the explicit dependence on reduction- and reducing agent-related phenomena.

The features of F-W stand in opposition to other classic mechanisms, including LaMer and Ostwald ripening. Notably, the continuous nucleation and reaction-limited growth of F-W contradict the pulse-like appearance of NP nuclei and diffusion-controlled particle growth of LaMer and

supersaturation-driven process of Ostwald ripening [103]. In F-W, the attainment of uniform-sized NPs (despite a continuous nucleation process that constantly adds small-sized nuclei to the dispersion) is explained by assuming that the system adheres to a significantly longer (by approximately two orders of magnitude) nucleation step than growth; this large kinetic disparity separates nucleation from growth.

In a closed and perfectly-mixed system, the F-W mechanism predicts a long induction time (originally envisaged as proportional to $1/k_1$ [309] and later proved to be proportional to $\ln(k_2[A]_0/k_1)/(k_1+k_2[A]_0)$ [33]) that precedes a fast sigmoidal precursor consumption. For the duration of induction, the precursor concentration remains essentially constant while nucleation takes place. A plot of a typical temporal evolution of the precursor concentration, as proposed in F-W, is depicted in figure 2.5(a), and its mathematical description is given by Eq. (2.14) [309]:

$$[A] = \frac{[A]_0 + k_1/k_2}{1 + (k_1/k_2[A]_0)\exp(t(k_1 + k_2[A]_0))}, \tag{2.14}$$

which, under the assumptions $k_2[A]_0/k_1 >> 1$ and $[A] < [A]_0$, transforms into its well-known linearised form:

$$\ln\left(\frac{[A]_0 - [A]}{[A]}\right) = \ln\left(\frac{k_1}{k_2[A]_0}\right) + k_2[A]_0 t. \tag{2.15}$$

The full derivation of Eq. (2.14) from Eq. (2.13) can be found in Appendix A.

By assuming fully spherical particles, complete separation of nucleation and growth (i.e, the number of nuclei will not change after the induction period is finalised), and equally-sized nuclei, Watzky and Finke [309] proposed a simple F-W-based expression for the temporal evolution of *average* particle size after the induction time, t_{ind} (Eq. (2.16)). Explicit analytic formulas for t_{ind} (Eq. (2.17)-(2.18)), the time at the maximum rate of consumption/production, t_{max} (Eq. (2.19)), and the time at which the plateau (or full consumption) stage is reached, t_{plateau} (Eq. (2.20)), were derived by Bentea et al. [33] from the F-W rates of consumption/production (Eq.(2.13)):

$$L_{\text{F-W}} = L_{\text{F-W,f}}\left(\frac{[A]_0 - [A]}{[A]_0}\right)^{1/3} \quad (t \geq t_{\text{ind}}), \tag{2.16}$$

$$t_{\text{ind,j}} = \frac{\ln\left((2-\sqrt{3})\,\frac{k_2[A]_0}{k_1}\right)}{k_1 + k_2[A]_0}, \tag{2.17}$$

$$t_{\text{ind,p}} = \frac{k_1 + k_2[A]_0}{(k_1 - k_2[A]_0)^2}\ln\left(\frac{k_2[A]_0}{k_1}\right) + \frac{2}{k_1 - k_2[A]_0}, \tag{2.18}$$

$$t_{\text{max}} = \frac{\ln\left(\frac{k_2[A]_0}{k_1}\right)}{k_1 + k_2[A]_0}, \tag{2.19}$$

$$t_{\text{plateau}} = \frac{\ln\left((2+\sqrt{3})\frac{k_2[A]_0}{k_1}\right)}{k_1 + k_2[A]_0}, \tag{2.20}$$

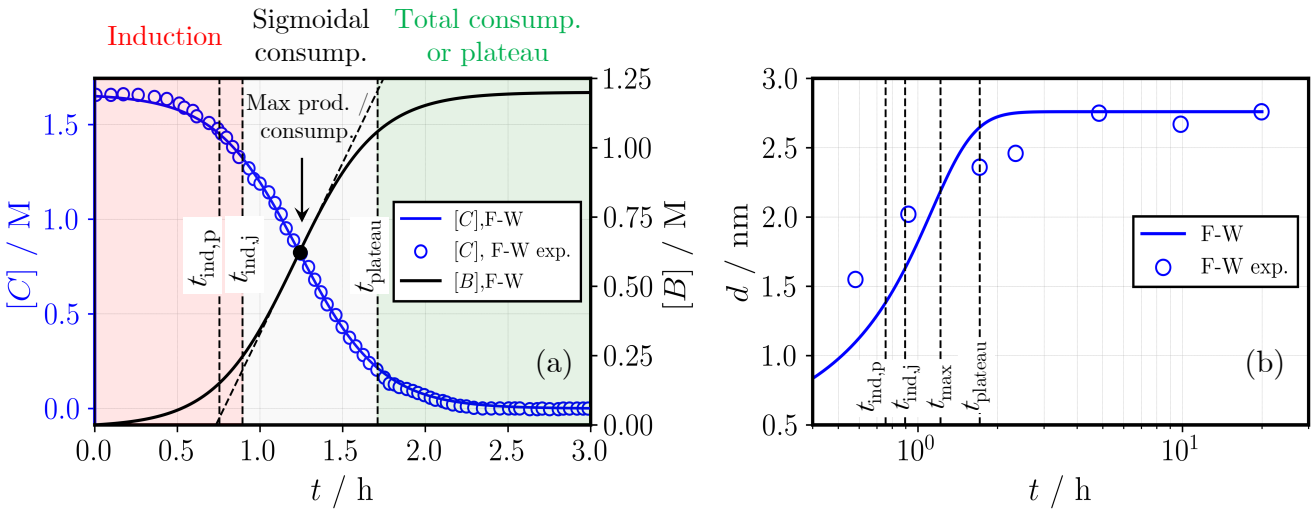

Figure 2.5: Illustration of the dynamics described by the F-W two-step mechanism: (a) temporal consumption of a reporter species, C (left axis in blue), initially present at a concentration 1375 times higher than the silver precursor, A, alongside the production of species B (right axis in black). The continuous lines represent the F-W mechanism (Eq. (2.13) - (2.14)), while the circular markers correspond to the experimental data from Watzky and Finke [309]; (b) temporal evolution of the average particle diameter as predicted by the F-W mechanism (Eq. (2.16)) and experimental data from Watzky and Finke [309]. The dotted vertical lines indicate the induction, maximum consumption, and plateau times, as predicted by Eq. (2.17) - (2.20) [33]. For this system, $k_1 = 0.0282$ h^{-1}, and $k_2 = 3.379 \times 10^3$ M^{-1}h^{-1}.

where $L_{\mathrm{F-W,f}}$ represents particle size after full precursor consumption, intended to be measured experimentally; $t_{\mathrm{ind,j}}$ and $t_{\mathrm{ind,p}}$ account for slightly different interpretations of the induction time, the former being defined as the point of maximum acceleration in the consumption of $[B]$ ($\mathrm{d}^3[B]/\mathrm{d}t^3 = 0$) and the latter as the intersection between the tangents at the initial and maximum $\mathrm{d}[B]/\mathrm{d}t$ points (see Bentea et al. [33] for their full derivation and detailed differences and figure 2.5(b) for a visual representation of these times).

The F-W two-step mechanism has been proven highly successful in explaining the experimentally-observed fast precursor consumption that follows an induction period in a diverse array of systems (see Handwerk et al. [103] and references therein), including the synthesis of Ir, Au, and AgNPs under different reducing and stabilising agent conditions (refer to Nathanael et al. [203] for a compilation of typical values of k_1 and k_2 for AgNPs). Nevertheless, the applicability of this model, at least in its original form, to predict the intricacies of particle size and particle size distribution (PSD) is still under debate. As will become apparent in the following paragraphs, the exact reason for the inapplicability of F-W to accurately capture all the intricacies related to PSD, as well as potential enhancing adjustments to the model, are highly contested topics in the literature, where multiple, and often contradicting, assertions are made.

The work of Perala and Kumar [221] assessed the performance of F-W in the context of Iridium nanoparticles (IrNPs) through a population balance framework. This work presented evidence to suggest that, while the closure parameters of the model can be optimised to fit the experimental

mean particle size of Watzky and Finke [309], it considerably over-predicts the standard deviation of the PSD (up to approximately 150%). The authors proposed and tested a few variations to the original F-W mechanism, including the growth term dependence on particles surface area instead of their volume, implementation of a reduction reaction to delay the onset of nucleation, a higher-order nucleation dependence on species concentration, and a nucleation expression derived from classical nucleation theory. They showed that the NPs nuclei formation, though slow, artificially increases the size polydispersity, especially when growth is much faster than nucleation.

Handwerk et al. [103, 104] and collaborators provided an alternative interpretation of the limited applicability of F-W for estimating the PSD based on a mechanism-enabled population balance model. The model relies on the assumption that monodisperse particles can be obtained in a continuous-nucleation environment if the nucleated particles grow at a faster rate than the larger particles. Based on this, the authors proposed an extension of F-W to a 3-step mechanism given by: $A \xrightarrow{k_1} B$, $A + B \xrightarrow{k_2} C$, and $A + C \xrightarrow{k_3} 1.5C$, where B represents the small-sized nuclei and C the larger particles ($k_2 > k_3$). The authors report a satisfactory agreement between the experimental and numerical evolution of the PSD for IrNPs with their 3-step model while also maintaining the excellent predictions of precursor concentration of the original model.

Mozaffari et al. [197], on the other hand, suggested that ligand activity and their binding to the NPs' surface predominately govern both nucleation and growth in the synthesis of PdNPs. In their PBM and experimental study, the authors devised a growth expression directly dependent on the number of free binding sites per unit area, translating into a growth suppression (enhancement) of the larger (smaller) particles and thus a monodisperse sample within the framework of continuous nucleation. UV-vis spectrophotometry and transmission electron microscopy (TEM) measurements [11] revealed a reversible reaction to the original F-W expression for nucleation, stating that a continuous disintegration of a portion of the NP nuclei better explains their experimental observations on AgNPs synthesis.

2.3.4 Microfluidic synthesis

Microfluidic-based methods have lately emerged as a promising alternative to traditional large-scale, batch-like systems for the synthesis of NPs. These miniaturised versions of large continuous-flow reactors have proven successful in the synthesis of numerous types of NPs, including gold [259], cadmium sulfide [76], cadmium selenide [48], silica [137], liposomes [121], and indeed, Ag [169], among others. On account of their small working volumes ($O(10^{-12})$ - $O(10^{-6})$ L), and spatial scales ($O(10^{1})$ - $O(10^{2})$ μm) [235], microfluidic channels allow for a high throughput operation under precisely-controlled hydrodynamic conditions, low reagents and energy requirements, high reaction yields, and reduced generation of waste products [234]. Depending on the mode of operation, microfluidics are well-known to also induce higher rates of heat and mass transfer in the system [155], as well as generally higher mixing rates due to smaller diffusion paths. Table

2.2 offers a summarised view of the range of particle sizes obtained during microfluidic synthesis of AgNPs.

Table 2.2: Compilation of selected works on microfluidic synthesis of AgNPs; DMAB: Borane dimethylamine, PVA: Polyvinyl alcohol, PVP: poly(vinylpyrrolidone), TC: Trisodium citrate, TA: Tannic acid, BMIM − BH_4: 1-Butyl-3-methylimidazolium borohydride, EDTA: Ethylenediaminetetraacetic acid. Table adapted and modified from Nathanael et al. [203]

Microfluidic type	Silver precursor	Red. and stab. agents (or other reagents)	Flow rates	Particle size	Reference
Drop-based: T- and Y-junction straight channels	$AgNO_3$	DMAB/PVA and tween 80	AP: 1 mL/h OP: 5 mL/h	2.5 ± 0.5 nm	[315]
Drop-based: Y-junction straight and serpentine channels	$AgNO_3$	TA/TC	AP: $16 - 32$ μL/h OP: $60 - 80$ μL/h	$12.8 - 22.3$ nm	[133]
Continuous-flow	$C_3AgF_5O_2$	Trioctylamine and isoamylether	$0.08 - 0.7$ mL/min	$3 - 12$ nm	[170]
Continuous-flow	$AgNO_3$	$NaBH_4$/TC	$1 - 14$ mL/min	$3.1 - 5.6$ nm	[19]
Drop-based: Multi-inlet T-junction straight channel	$AgBF_4$	BMIM − BH_4	AP: 0.5 mL/h OP: 10 mL/h	3.73 ± 0.77 nm	[161]
Drop-based: T-junction straight channel	$AgNO_3$	$NaBH_4$/PVP and EDTA	AP: $10 - 30$ mL/h OP: $10 - 30$ mL/h	$4.9 - 7.6$ nm	[321]

Continuous-flow [183] and drop-based [260] production are two primary operational modes in microfluidic synthesis. In continuous-flow production, a monophasic liquid system containing the reactants (e.g., precursor, reducing agent, and stabilisers) in aqueous solutions is employed, as illustrated in figure 2.6(a). A key drawback of continuous-flow microfluidic reactors is the laminar parabolic flow profile that emerges across the channel radius, leading to varied fluid residence times and potential particle deposition, fouling, or channel blockage. Enhancements in continuous-flow reactor performance have been achieved by incorporating channels with twists and turns [318] to promote mixing or by utilising droplet-based operations. In drop microfluidics, discrete droplets are created and manipulated, generating an immiscible segmented liquid–liquid multiphase flows inside the microchannels. Typically, one phase is an aqueous solution of the reactants, while the other is an inert oil phase that transports the droplets through the channel, as depicted in figure 2.6(b). A significant challenge in drop-based synthesis lies in developing reliable computational models, due to the complex interplay between chemical reactions and multiphase flows. This difficulty has been highlighted as a critical drawback of drop-based reactors in the literature [203].

The steps preceding synthesis reactions in drop-based microfluidics are well-explored topics in the literature. Numerous experimental and numerical studies have focused on understanding the emergence of various mixing patterns within the channel. These studies have elucidated the interplay between capillary, viscous, and inertial forces on mixing efficiency, provided insights into

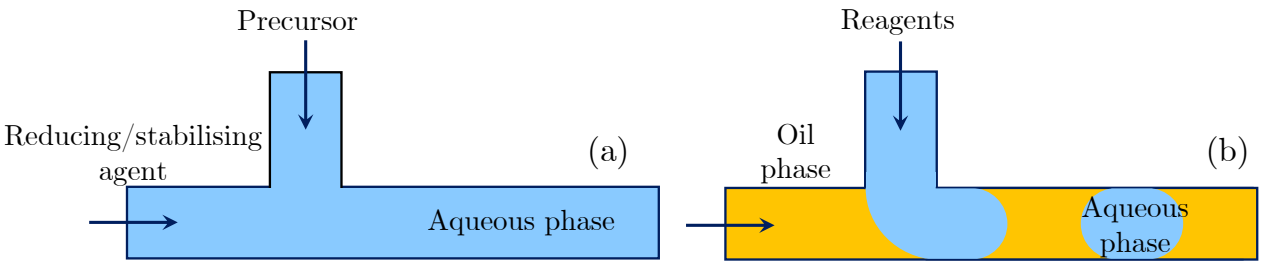

Figure 2.6: Schematic representation of microfluidic channels: (a) continuous-flow synthesis; (b) drop-based synthesis. Figure adapted from Shembekar et al. [260]

controlling flow patterns, and optimised channel geometry to enhance overall mixing [133, 293, 198, 148, 149, 125]. Comprehensive reviews of experimental drop-based microfluidic synthesis can be found in the work of Seemann et al. [256] and collaborators. For a critical review of numerical and computational studies on drop microfluidics, primarily in the absence of chemical reactions, refer to Nathanael et al. [203], particularly table 4, which offers a thorough compilation of computational studies on mixing in drop-based microfluidics.

The focus of the present investigation, continuous-flow synthesis in microfluidic devices, presents considerable challenges for developing accurate kinetic models to predict the PSD of AgNPs. These challenges stem from the intricate spatial and phase-dependent dynamics inherent in these systems, where reagents are not completely mixed at the onset of operation. Recent progress has been made in the estimation of the PSD of NPs synthesised via microfluidics and other continuous-flow channels, including SiO_2 [22, 21], CdSe [154], and ibuprofen [253] NPs. These investigations have elucidated the critical role of the system's hydrodynamics on the temporal progression of the system, and how the interplay between reactants' diffusion and residence times, phase interactions, and reaction kinetics greatly influences the PSD.

The experimental campaign and simulations of Bal and Bandyopadhyaya [22] revealed a dominant role of laminar shear and particle-particle chemical interactions on the agglomeration of colliding NPs in a low Reynolds ($Re \sim 2.54$) microfluidic operation. The PBM-CFD numerical results of Kumar and Ganesan [154] have uncovered a substantial heterogeneity in the distribution of the nucleation/growth rates and size polydispersity along the main axis of the microchannel, where the regions in the vicinity of the outlet exhibit significantly higher average particle sizes and standard deviations, explained by the comparatively higher flow residence times at the channel outlet. Although interesting, these investigations dive into synthesis processes entirely based on crystallisation and precipitation phenomena, which are well-known to be supersaturation-driven events [160]. As detailed previously, the synthesis of AgNPs is completely incompatible with these premises as it is a reduction-driven process under low saturation conditions (see §2.3.1.1).

To the best of the author's knowledge, Liu et al. [174] is the only attempt to explicitly model a reduction-based NP synthesis in microfluidic devices. This work carried out a series of Population Balance Model and Computational Fluid Dynamics (PBM-CFD) simulations in

commercial code considering a two-way coupled liquid-solid multi-component flow and a kinetic formulation similar to that of the F-W two-step mechanism. The reactive system included a simplified reduction reaction, $AgNO_3 + e \rightarrow Ag_{(l)}$, that leads up to nucleation and growth. In their PBM-CFD simulations, however, the authors neglected the contribution of particle diffusion and agglomeration on the PSD, which does not allow for a complete characterisation of the links between hydrodynamics and kinetics, and how these influence particle size.

From the preceding literature review it is clear that, while much progress has been made in the area of NP synthesis and its mechanistic modelling, multiple aspects remain elusive. Notably, a unifying scheme is needed to bridge the realm of the well-mixed systems considered in models akin to the F-W two-step mechanism and that of the continuously interdependent hydrodynamic phenomena inherent to continuous-synthesis reactors, including microfluidic channels, where little has been explored in terms of modelling reduction-based NP production. Moreover, and as explicitly remarked in Perala and Kumar [221], the field would greatly benefit from additional assessments of the capabilities of the F-W mechanism in explaining the temporal evolution of the PSD in well-mixed reactors through the systematic testing of different types of NPs.

2.4 Elongated bubbles in micro- and capillary channels

Equipped with a foundation of microfluidic technology (§2.3.4) and surfactant dynamics (§2.2), the present review of the literature proceeds to dive into the background and context behind the results of chapter 5.

2.4.1 Dynamics of elongated bubbles under idealised conditions

Systems involving gas bubbles propagating in confined capillary channels in Poiseuille flows have been the subject of extensive theoretical, experimental, and numerical investigation (see Etminan et al. [84] and references therein). In addition to being a classic problem in fluid mechanics, as seen in the now-seminal works of Taylor [285], Bretherton [43], Hyman and Skalak [116], and Schwartz et al. [254], these flows are central to multiple applications in technology development and are found in several real-life systems. To name a few examples, gas-liquid interfaces in the micro- and capillary scale are involved in two-phase coolers [132], micro-evaporators [140], CO_2 sequestration and storage microdevices [262], obstructed pulmonary airways [111], volcanic conduits [44], and have been proposed as a potential method for bacterial detachment and cleaning [141].

Since the early works mentioned above, extensive efforts have been undertaken to understand the phenomena dictating the bubble's behaviour along with the surrounding thin liquid film, largely through an idealisation of the operating conditions and the morphology of the bubble itself as a flat cylinder bounded by two hemispherical menisci (see figure 2.7(a)). These phenomena

are notably influenced by the bubble's capillary, Ca_b, Reynolds, Re_b, and Weber, We_b, numbers, which are defined below in Eqs. (2.21) - (2.23):

$$Ca_b = \frac{\mu_l U_b}{\sigma_s}, \tag{2.21}$$

$$Re_b = \frac{\rho_l U_b D}{\mu_l}, \tag{2.22}$$

$$We_b = Ca_b Re_b = \frac{\rho_l U_b^2 D}{\sigma_s}, \tag{2.23}$$

where μ_l and ρ_l denote the dynamic viscosity and density of the liquid phase, respectively, σ_s is surface tension, D the hydraulic diameter of the channel, and U_b is the bubble propagation velocity. Under conditions where buoyancy and inertial effects are negligible, surface tension primarily governs the flow characteristics. Consequently, the bubble phase occupies most of the channel cross-section, resulting in an exceedingly thin liquid film between the bubble and the channel walls, which remains independent of the bubble length [180]. Furthermore, the front and rear menisci are expected to be perfectly semi-circular, with identical curvature ($\kappa_{\text{back}} = \kappa_{\text{front}}$) [251]. Moreover, the bubble's velocity approaches that of the mean flow in the liquid phase ($U_b \approx U_l$) [140].

Accurately characterising and predicting the liquid film thickness, h, has been a focal point of academic research for decades, supported by extensive experimental and theoretical work. Bretherton [43] employed lubrication theory to study an inviscid gas bubble travelling through a small circular channel, neglecting gravity and inertia. Bretherton discovered that the thickness of the flat region of the bubble scales as $h \sim Ca_b^{2/3}$ within the realms of vanishing $Ca_b < 10^{-3}$ and Re_b. Building on this, Aussillous and Quéré [18] proposed an empirical fit to the experimental data of Taylor [285], resulting in an expression of the form $h \sim Ca_b^{2/3}/(1 + Ca_b^{2/3})$ for $Ca_b < 2$ and $Re_b << 1$. This expression is commonly referred to as "Taylor's law".

As inertial effects become non-negligible, Han and Shikazono [102] introduced a correction to the scaling exponents of Ca_b and incorporated We_b into the scaling law expression. This correlation has been shown to predict experimental data with a deviation of up to 15% for $Re_b < 2000$. de Ryck [66] also dived into inertial effects and suggested a correction to Bretherton [43]'s expression to account for the film thickening dynamics observed in low viscosity fluids. A compilation of the mathematical expressions proposed in the above investigations can be found in Eqs. (2.24) - (2.26):

$$\text{Bretherton [43]:} \quad \frac{h}{R} = 1.34 Ca_b^{2/3}, \tag{2.24}$$

$$\text{Aussillous and Quéré [18]:} \quad \frac{h}{R} = \frac{1.34 Ca_b^{2/3}}{1 + 2.5 \times 1.34 Ca_b^{2/3}}, \tag{2.25}$$

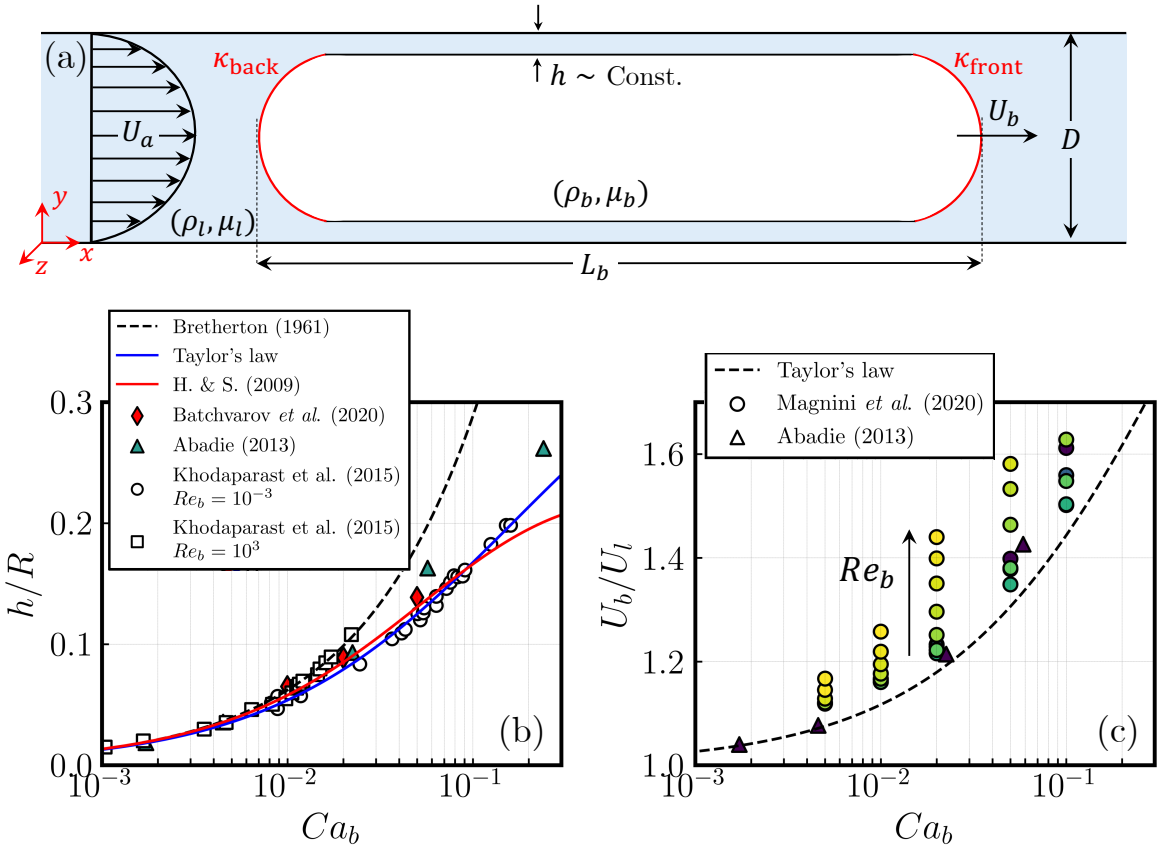

Figure 2.7: Dynamics of elongated bubbles travelling through liquid-filled small-scale channels: (a) schematic representation of the bubble under idealised conditions of vanishing Ca_b and Re_b, highlighting its most important characterising parameters; (b) effects of Ca_b on liquid film thickness, as proposed in Bretherton [43] (Eq. (2.24)), Aussillous and Quéré [18] (Taylor's law, Eq. (2.25)) and Han and Shikazono [102] (at $Re_b = 443$, Eq. (2.26)). Selected experimental and numerical data points from Batchvarov et al. [31] ($Re_b = 443$), Abadie [1] ($Re_b \approx 10^{-3}$), and Khodaparast et al. [140] are included for reference; (c) effects of Ca_b and Re_b on bubble velocity relative to the average liquid velocity. The dashed black line represents Eq. (2.27) and Eq. (2.25). Data from Magnini and Matar [179] (circles) were obtained at $Re_b = 1 - 2000$ and from Abadie [1] (triangles) at $Re_b \approx 10^{-3}$. In (c), lighter colours denote higher Re_b

Han and Shikazono [102]:
$$\frac{h}{R} = \frac{1.34 Ca_b^{2/3}}{1 + 3.13 Ca_b^{2/3} + 0.504 Ca_b^{0.672} Re_b^{0.589} - 0.352 We_b^{0.629}}, \quad (2.26)$$

where R represents the channel radius. Note that Eq. (2.26) will, for the most part, yield larger h/R than Eq. (2.25) due to the negative sign that accompanies We_b. This effectively captures the phenomenon of film thickening observed at high Re in comparison to the idealised scenario. A comparative analysis of the film thickness behavior, as predicted by these equations and corroborated by literature data, is illustrated in figure 2.7(b).

Bubble velocity is another crucial parameter in the study of elongated bubbles in small-scale channels. The works of Taylor [285] and Goldsmith and Mason [98] have proposed an expression relating their experimental measurements of bubble velocity to those of liquid thickness, leading

to Eq. (2.27):

$$\frac{U_b}{U_l} = \frac{1}{\left(1 - \frac{h}{R}\right)^2}. \tag{2.27}$$

This equation accurately reflects a large body of experimental and numerical research (see Magnini and Matar [179], Han and Shikazono [102] and references therein), indicating that conditions leading to film thickening—large Ca_b or Re_b—correspond to higher bubble velocities relative to the liquid phase. By combining Eq. (2.27) with Eqs. (2.24) - (2.26), one can obtain an expression relating U_b/U_l to Ca_b [1]. An example of this sort of expression using Eq. (2.27), along with literature data, are illustrated in figure 2.7(c). This figure shows a clear increase in U_b/U_l with both Ca_b and Re_b.

Considerable attention has also been devoted to exploring the influence of Ca_b and We_b on the development of stationary undulatory structures in the bubble's rear meniscus. The theory of Bretherton [43] yields a prediction of minimum film thickness in the undulatory regions of $0.716h_0$, with h_0 being the liquid thickness at the bubble's centre point in the main axis. It also predicts a scaling for the undulations' wavelength, λ, of the form $\sim h_0 Ca_b^{-1/3}$. This theoretical framework, however, has shown significant deviations from numerical simulations, even at moderate Ca_b ($Ca_b < 10^{-2}$) and $Re_b << 1$ [96, 77]. More recent research pursuits [140] have observed increased wave amplitudes and decreased wavelengths under conditions of $Re_b >> 1$. The recent CFD and theoretical work of Magnini et al. [180] offers predictions of the bubble's profile in conditions of finite inertia and accounting for the curvature of the channel wall. Their study revealed a marked decrease in the decay rate of the trailing undulations at $We_b > 10^{-1}$.

In addition to the above mentioned parameters, the elongated bubble community has also been interested in accurately mapping the full topological profiles of the bubble under varying conditions of Ca_b and We_b [66], uncovering the behaviour of the streamlines downstream from the bubble nose [96, 110], predicting pressure drop [317, 151], and characterising the front meniscus.

2.4.2 Effects of non-idealities: curvature reversals and drop encapsulation

Other researchers have delved into the elongated bubble problem by deviating from the traditional idealised assumptions of circular and straight channels, absence of surface-active materials, fully dominating capillary forces, and spherical menisci. These studies have elucidated critical differences between the steady-state and axisymmetrical features of idealised bubbles (see figure 2.7(a)) and those that adhere to more realistic scenarios.

For square or rectangular channel cross sections, the experiments of Chen et al. [49, 50] and numerical simulations of Magnini and Matar [179] and Magnini et al. [182] have uncovered significant angular and axial non-uniformities in the liquid film thickness, whereby the effects of the rigid walls tend to flatten the interface at the channel's centre-line ($h \sim Ca_b$), depleting it

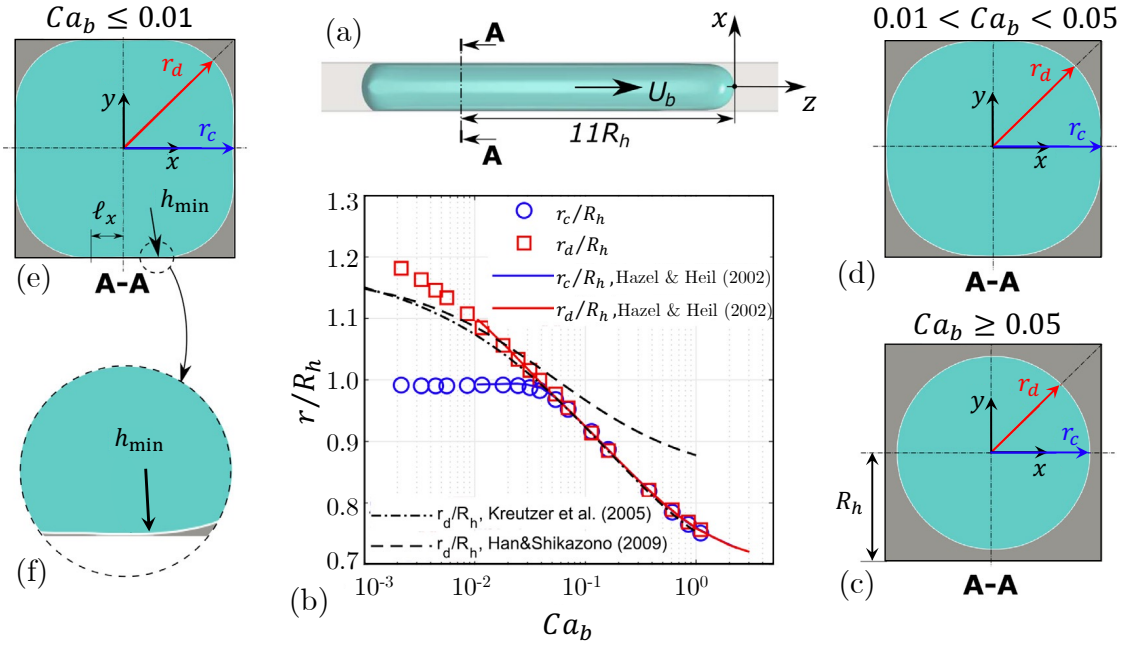

Figure 2.8: Unique interfacial features of elongated bubbles in non-circular capillaries under $We_b << 1$ conditions, as observed in the computational investigation of Magnini and Matar [179]: (a) schematic of elongated bubble; (b) comparison of centre-line vs. diagonal bubble radius in the channel cross section for varying Ca_b and comparison against Han and Shikazono [102], Hazel and Heil [108], Kreutzer et al. [150]; (c)-(f) bubble cross section across different Ca_b ranges. In (e)-(f), the regime developed at low Ca_b, l_x represents the distance from the centre-line where $h_{\min}$ is found. Figure reproduced from Magnini and Matar [179]

of the liquid phase, and inducing the formation of large lobes protruding towards the channel corners in the cross-section ($h \sim Ca_b^{0.445}$). More specifically, Magnini and Matar [179] identified three regimes in square capillaries based on the difference between the diagonal, r_d, and centre-line, r_c, bubble radius in the channel cross-section, as depicted in figure 2.8. In the first regime ($Ca_b \geq 0.05$), the previously mentioned thickening effects induced by large Ca_b conditions ensure that $r_d = r_c$ (figure 2.8(c)). As Ca_b decreases and falls within the range $0.01 < Ca_b < 0.05$, the bubble's centre-line growth is constrained by the channel walls, resulting in a non-axisymmetric bubble morphology ($r_d > r_c$) with the minimum film thickness, $h_{\min}$, located precisely at the channel's centre line (see figure 2.8(d)). At even lower $Ca_b \leq 0.01$, channel confinement effects become fully pronounced, causing a curvature reversal at the centre line and shifting the location of $h_{\min}$ (see figure 2.8(e)-(f)).

Besides radial effects on film thickness, non-circular channels promote an exponential thinning of the liquid film along the bubble length from the nose to the rear section, as reported in Lister et al. [173] and Magnini and Matar [179]. The latter study proposed an empirical equation for relating minimum liquid film thickness and axial location in the stream-wise direction of the form $h_{\min} \sim (z_N - z)^{-\beta}$, where z_N is the location of the nose, z is the stream-wise coordinate (see axis in figure 2.8(a)), and the β parameter is weakly influenced by Ca_b. The effects of other non-ideal geometries have been examined by Sauzade and Cubaud [252], who carried out an

experimental campaign to study the distortion of a train of bubbles in a constricting-expanding microchannel under varying Ca_b and bubble packing conditions. This study provided evidence for the occurrence of bubble width-to-length ratio hysteresis across the sinusoidal structures of the channel, and the attenuation of these effects with decreasing Ca_b.

A wide array of investigations have focused on illustrating the effects of (in)soluble surfactants on liquid-gas confined flows, placing particular emphasis on their influence on liquid film thickness, bubble deformation, and pressure drop (see Olgac and Muradoglu [213] and references). The literature largely agrees that, under typical surfactant characteristics and negligible inertia, the liquid film displays a thickening response to surfactants of the order of 1 to $4^{2/3}$ times that predicted by Bretherton [43]'s expression for uncontaminated interfaces. This thickening has been reported to vary with Ca_b, surface elasticity, surfactant solubility, and across the bubble length due to Marangoni-related mechanisms, which act in opposition to liquid drag forces as they push surfactant towards the bubble rear region. Nonetheless, it should be noted that Ghadiali and Gaver [95]'s numerical results in the context of pulmonary airways suggest the possibility of liquid film thinning surfactant actions under conditions of large bulk Péclet number, $Pe_c >> 1$, and $Ca_b > 10^{-1}$ due to a bifurcation and enhancement of Marangoni stresses, which drive fluid away from the thin film region and towards the bubble nose. In terms of pressure drop and bubble velocity, it has been shown that surfactants tend to increase the pressure drop across the dispersed phase [97, 178] and significantly reduce the bubble's mobility in the length-wise direction [39].

Batchvarov et al. [31] carried out a comprehensive computational exploration of multiple surfactant characteristics and dimensionless groups with the novelty of introducing inertial effects ($Re = 443 - 728$) to the analysis. A key finding of this work is the surfactant-induced dampening of the bubble's rear interfacial oscillatory structures, typical of systems with non-negligible inertia (see §2.4.1), together with the evidence provided to affirm that this process is entirely Marangoni-driven rather than a consequence of localised lowered surface tension. Moreover, this investigation addressed the effect of low-solubility surfactants, detecting a clear arrangement of the bubble's morphology into two separate regions; one fully covered in surfactant and of substantially reduced mobility, extending from the bubble rear to a portion in the stream-wise direction that depends on Pe_c, and one of diminished surfactant concentration that stretches to the bubble nose, behaving similarly to clean interfaces (see figure 2.9(a)). The authors of this work attributed this surfactant-induced mobility reduction to the well-known interfacial rigidification phenomena brought about by Marangoni stresses, as exemplified in figure 2.9(b). In this figure, the surfactant-covered region, besides exhibiting a much larger film thickness, reaches an almost zero velocity (relative to the nose) at the interface.

A noteworthy sequence of events transpires in the bubble as Ca_b is increased to a critical value that strongly depends on its length and Re_b. As reported in a number of investigations [2, 251, 283, 96], the combination of reduced dominance of capillary forces (given by larger Ca_b)

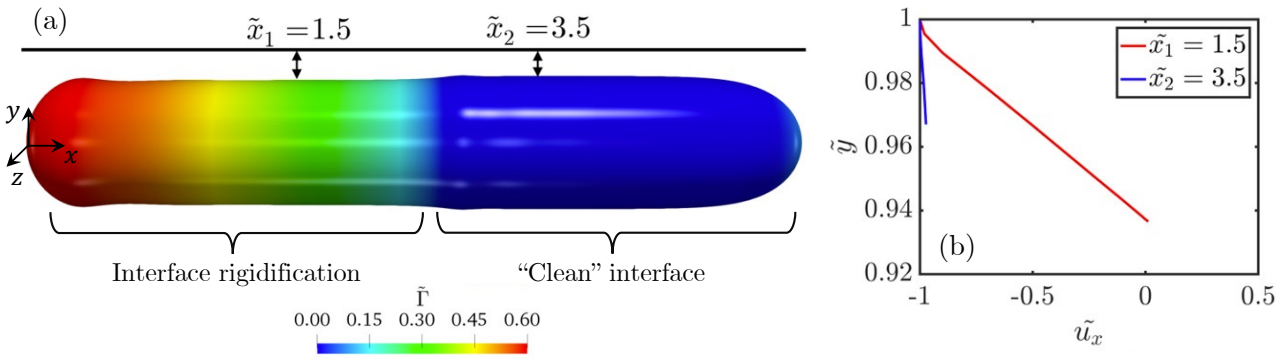

Figure 2.9: Representation of an elongated bubble in the presence of a low-solubility surfactant: (a) interface surfactant coverage, illustrating the division of the bubble morphology into two distinct regions: one characterised by high surfactant concentration and a rigid interface, and the other nearly devoid of surfactant; (b) stream-wise velocity (relative to the bubble nose) across the thin liquid film profile in the y-direction for the two primary bubble regions. The scenario depicted corresponds to $Ca_b = 0.0089$ and $Re_b = 443$. Figure adapted from Batchvarov et al. [31]

and heightened inertia (given by larger Re, leading to larger $We_b = Ca_b Re_b$) has a distorting impact on the curvature of the front and back menisci, dragging both interfaces towards the main flow direction and causing the bubble to adopt an elongated, "bullet-like" shape. With the continued increase in inertial and viscous forces, the bubble's rear undergoes a curvature inversion, enabling the liquid phase to infiltrate the bubble's domain and form a small re-entrant liquid jet. The threshold conditions that induce this curvature inversion phenomenon have been reported to be $We_b \approx 20$ for $Re_b \sim O(10^1)$ in circular channels by Giavedoni and Saita [96] and $Ca_b \gtrapprox 1$ for $Re_b \to 0$ in circular/square channels by Sauzade and Cubaud [251], Taha and Cui [283], and Martinez and Udell [189]. As briefly shown in the results of §5.5.1, the surfactant-free simulations performed allow us to place the threshold within the range $17 < We_b < 20$ for $Re_b \sim O(10^2)$ in square capillaries.

The fate of the liquid infiltrating the bubble is highly influenced by a complex interplay of phenomena that might culminate in a continuous growth in the main axial or radial direction, or in its capillary breakup via a Rayleigh-Plateau instability to encapsulate and entrap liquid drops within the bubble. Figure 2.10 provides a conceptual description of the liquid infiltration and drop entrapment process and a comparison against non-encapsulating conditions. This liquid infiltration process shares qualitative similarities with other systems relevant to engineering applications, such as sheet cavitation. In this type of cavitation, the adverse pressure gradient induces the development and spreading of a re-entrant liquid jet in the upstream direction underneath the cavity sheet, separating it from the solid surface [220].

The type of encapsulation described above has been observed experimentally in the works of Goldsmith and Mason [98] and Olbricht and Kung [212] in liquid-liquid flows. Similar findings are reported in a limited number of numerical pursuits on multiphase confined flows, including the investigations of Tsai and Miksis [291] and Izbassarov and Muradoglu [120] for contract-

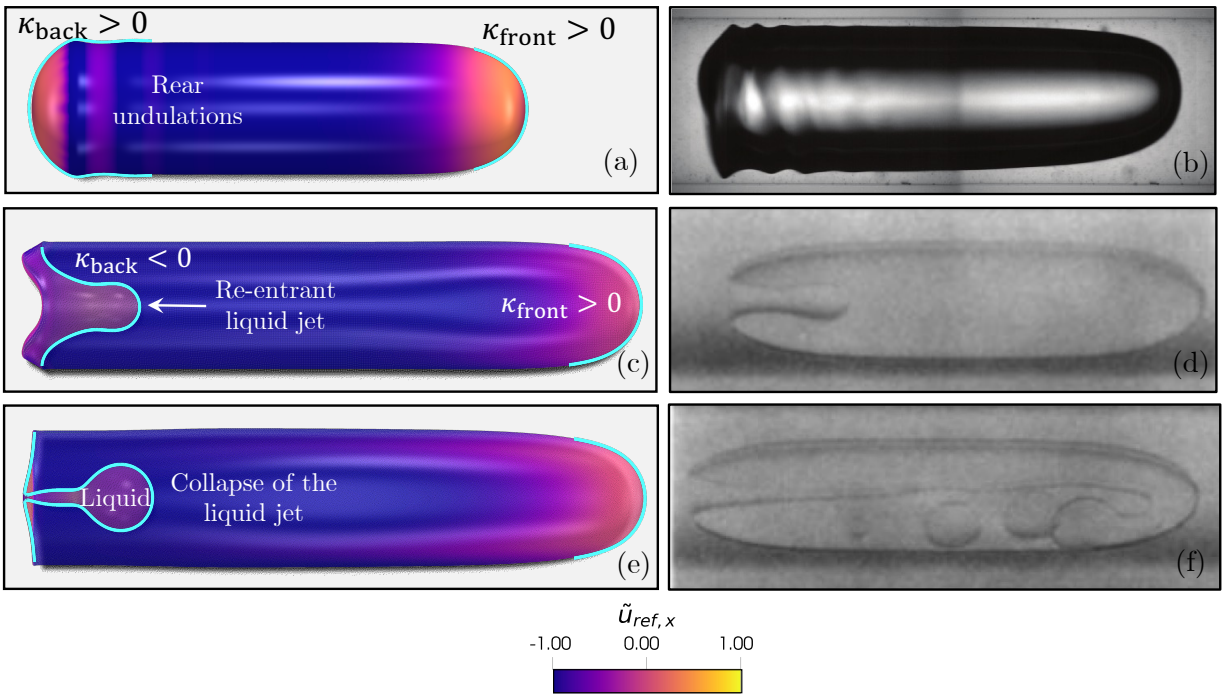

Figure 2.10: Conceptual representation of the liquid infiltration and drop encapsulation phenomena in systems under large Ca_b and Re_b conditions: (a)-(b) system characterised by non-negligible inertial dynamics, wherein back undulations develop but both front and back curvatures remain positive; (c)-(f) examples of systems under sufficiently high Ca_b and Re_b conditions ($17 < We_b < 20$ for $Re_b \sim O(10^2)$), leading to liquid phase infiltration into the bubble and the subsequent encapsulation of liquid droplets within the bubble's domain. The images in (a,c,e) correspond to numerical simulations conducted by the author of this thesis, while those in (b,d,f) correspond to experimental results published in Khodaparast et al. [140] for (b) and Olbricht [211] for (d,f). The colour scale in (a,c,e) represents interface velocity relative to the nose in the stream-wise direction, $u_{ref,x}$. These images are not to scale and are intended to provide a qualitative comparison only

ing/expanding capillaries in Newtonian and viscoelastic fluids, respectively, Pozrikidis [230] for buoyancy-driven flows of viscous drops, Nath et al. [202] for liquid drops in creeping flow, and Andredaki et al. [13] and Atasi et al. [17] for gas bubbles in the absence/presence of surfactants, respectively. A compilation of numerical and experimental studies where curvature inversion or full encapsulation events were observed is provided in table 2.3.

The studies by Nath et al. [202], Andredaki et al. [13], and Atasi et al. [17] are particularly noteworthy for their examination of the encapsulation process. These investigations have not only identified the specific conditions that induce this phenomenon but also elucidated the underlying mechanisms and provided an overview of the encapsulation aftermath. Nath et al. [202] have remarked that, in the inertialess limit and considering fully circular channels, there exists a critical Ca_b beyond which drop breakup and entrapment events will occur. The authors found this critical value to decrease (increase) with the initial drop-to-channel radius (dispersed-to-continuous phase viscosity). Andredaki et al. [13] and Atasi et al. [17] have recently laid the groundwork for the formulation of general encapsulation and breakup regime maps for $Re_b << 1$,

Table 2.3: Compilation of selected experimental and numerical studies reporting instances of re-entrant jet formation or drop encapsulation in liquid-liquid or gas-liquid flow within small-scale channels. Studies organised chronologically from oldest to most recent

Reference	System	Type of study	Main observations
Goldsmith and Mason [98]	Liquid-liquid with surfactants	Experimental	Re-entrant jet and encapsulation observed
Martinez and Udell [189]	Liquid-liquid in a straight channel	Numerical (boundary integral method)	Re-entrant jet formed at $Ca_b \approx 0.75$
Olbricht and Kung [212]	Liquid-liquid in a straight channel	Experimental	Re-entrant jet and encapsulation phenomena depend on viscosity ratio and Ca_b
Pozrikidis [230]	Liquid-liquid (vertical channel)	Numerical	Re-entrant jet and encapsulation observed
Tsai and Miksis [291]	Liquid (gas)-liquid in a constricting channel	Numerical	Re-entrant jet and encapsulation observed
Giavedoni and Saita [96]	Gas-liquid in a straight channel	Numerical	Curvature inversion at the bubble rear
Taha and Cui [283]	Gas-liquid in a square channel	Numerical	Curvature inversion at the bubble rear
Harvie et al. [107]	Viscoelastic liquid-liquid in a constricting channel	Experimental and numerical	Encapsulation observed in experiments but not in simulations
Sauzade and Cubaud [251]	Liquid-liquid in a square channel	Experimental	Rear curvature flattening with increasing Ca_b
Izbassarov and Muradoglu [120]	Viscoelastic liquid-liquid in a constricting channel	Numerical	Re-entrant jet and encapsulation observed in highly viscous drops
Nath et al. [202]	Liquid-liquid in a straight channel	Numerical	Existence of a critical Ca_b above which encapsulated drops burst the external drop
Atasi et al. [17]	Gas-liquid with surfactants	Numerical	First encapsulation regime maps depending on Ca_b and surfactant parameters
Andredaki et al. [13]	Gas-liquid in a straight channel	Experimental and numerical	Encapsulation regime maps depending on We_b and the Froude number
Abubakar and Matar [2]	Gas-liquid in a straight vertical channel	Numerical	Curvature inversion at the bubble rear

bounded by We_b and the relationship between inertia and pressure drop across the channel in the former, and Ca_b and the relative importance of interface surfactant adsorption/desorption in the latter case.

The regime map proposed by Atasi et al. [17] identifies three distinct modes of bubble behaviour involving curvature flattening/inversion and bubble bursting, as illustrated in figure 2.11 (Regions I, II, and III). In Regions I and II (depicted in green and defined by $Ca_b > 0.45$ and $k < 2$), capillary forces fail to maintain the semispherical front and rear menisci shapes characteristic of low Ca_b systems (see figure 2.7 and 2.9). In Region III, rear curvature inversion evolves into a re-entrant jet that rapidly advances to the bubble nose, leading to interfacial breakage events.

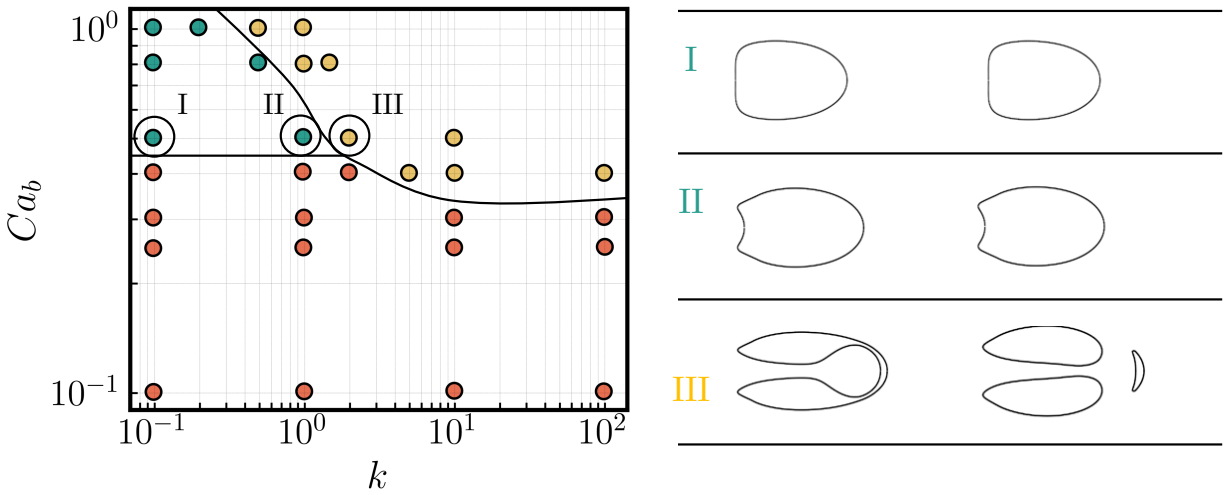

Figure 2.11: Encapsulation regime map proposed by Atasi et al. [17] for a surfactant-laden bubble travelling in a circular microchannel under vanishing inertial effects. Here, k, defined in Eq. (5.9), represents the competition between surfactant adsorption and desorption time scales. Regions I, II, and III denote behavioural modes where both Ca_b and k are sufficiently large to induce rear curvature flattening/inversion or bubble bursting events through drop encapsulation. The orange data points indicate instances where no rear curvature inversion was observed. Figure adapted from Atasi et al. [17]

Despite these initial efforts, much remains unknown and unexplored about these encapsulation events. Notably, a quantitative and phenomenological description of the underlying dynamics that govern each step of the process is needed, in combination with a thorough inspection of the re-entrant liquid jet characteristics. It is also crucial to address the multiple examples of interfacial singularities inherent to the system at hand, which have yet to be analysed from the perspective of the well-established problem of capillary breakup, from which multiple parallels naturally emerge between our system and others (e.g., contracting liquid ligaments and inkjet printing). Likewise, an analysis of the evolution of the drops beyond pinch-off is required as it is a topic much less understood than the steps that precede it [190] and could be crucial to potential applications [120]. Finally, and as will be seen in this chapter 5, extending the set of surfactant parameters explored from those of Atasi et al. [17] uncovers new encapsulation and breakup outcomes, which allows us to expand and enhance the original regime maps. The main objective of chapter 5 is therefore to carry out an extensive characterisation of the re-entrant liquid jet formation and (post) pinch-off dynamics, taking into account the interaction between surfactants and inertia, capillarity and viscosity in a non-circular channel geometry, which correspond to non-idealities of interest, as seen in the foregoing literature review.

2.5 Bursting bubbles: capillary waves and Worthington jets

The present review of the literature now proceeds to focus on the classic fluid mechanics problem of aerosol drops released by the action of bursting bubbles. This subsection provides the background

that contextualises the results of chapter 6.

2.5.1 The role of bursting bubbles on aerosol droplets

Aerosol droplets, arising from the bursting of bubbles at a liquid-gas interface, hold a crucial position at the confluence of diverse natural phenomena, industrial applications, and daily activities. Consider, for instance, the effervescence in sparkling drinks like champagne, where the bubbles that nucleate at the glass walls and eventually burst at the surface release the aromas experienced by the human senses [93]. In atmospheric physics, marine aerosol plays a pivotal role in governing the overall mass and heat exchange process between the oceans and the atmosphere. This stems from the liberated liquid drops, formed from an estimated $10^{18}-10^{20}$ bursting bubbles per second across the oceans [257] and capable of transporting an array of often surface-active substances, including salts, dissolved gases, biological material (e.g., harmful pathogens), microplastics, and toxic chemicals. Spanning a broad size range, from a few nanometers to several millimetres [298], marine aerosol actively participates in atmospheric chemical reactions, acts as nuclei for cloud and fog condensation, and can influence the cyclone intensity [298, 68]. Bursting bubbles are also relevant in other large-scale phenomena, such as volcanic eruptions and nuclear reactors, as reported in Sanjay et al. [249], Yu et al. [327].

The aforementioned significance of aerosol droplets generated via bursting of bubbles has made the system a notable problem within the realm of fluid mechanics, witnessing substantial advancements since the latter half of the previous century. In the absence of contaminants, the dynamics of an isolated bursting bubble of radius R_0 are governed by the interplay amongst buoyancy, surface tension, and viscosity, quantified by the Laplace, La (which can also be defined as Ohnesorge, Oh, $La = Oh^{-2}$) and the Bond, Bo, numbers, defined in Eq. (2.28). In this equation, ρ, μ, σ_s, and g correspond to density, viscosity, surface tension, and gravity, respectively, and the subscript l represents the continuous liquid phase; l_c and u_c denote the capillary length and velocity scales, respectively.

$$La = \frac{\rho_l \sigma_s R_0}{\mu_l^2} = \frac{1}{Oh^2}, \quad Oh = \frac{\mu_l}{\sqrt{\rho_l \sigma_s R_0}}, \quad Bo = \frac{\rho_l g R_0^2}{\sigma_s}, \quad l_c = \sqrt{\frac{2\sigma_s}{\rho_l g}}, \quad u_c = \sqrt{\frac{\sigma_s}{\rho_l R_0}}. \tag{2.28}$$

A typical initiation of an isolated bursting event involves a spherical bubble rising in a liquid medium, reaching the surface, and creating a thin liquid film or "cap" (characterised by a length scale $\delta/R_0 \sim O(10^{-6}) - O(10^{-3})$) that separates the bubble from the atmosphere. In situations where $R_0 < l_c$ [299, 163], this thin film undergoes drainage at an exponential or algebraic rate [327] until its ultimate collapse, triggering the development of capillary waves that propagate on two fronts: across the bubble's domain, and away from the cavity (see figure 2.14(a) or figure 6.1(a)). The bubble's capillary waves converge at the cavity's origin at a time denoted by t_0 and induce a far-field flow which accelerates the liquid phase towards the axis of symmetry [99] and causes a reversal of the bubble-liquid interface, bringing about the ejection of a high-velocity (up

to 50 times the capillary velocity, u_c) Worthington jet. Depending on the conditions, this jet may break up via a Rayleigh–Plateau instability to release one, or multiple, liquid drops into the atmosphere; these are typically referred to as "jet drops".

In scenarios where $R_0 > l_c$, the liquid film may be destabilised by a Rayleigh-Taylor instability arising from the film's centripetal acceleration. This instability leads to the fragmentation of the liquid film and the release of drops into the atmosphere, commonly referred to as "film drops". Film drops are typically much larger than jet drops, with minimum sizes of approximately 10 μm and 0.1 μm, respectively [299, 327]. The generation of film versus jet drops is highly dependent on bubble size; larger bubbles, which create longer films, are more likely to result in film drops. Figure 2.12 conceptually illustrates all phenomena involved in the release of aerosol drops via bursting bubbles, whether from the breakage of the liquid film (figure 2.12(b)) or the destabilisation of the Worthington jet (figure 2.12(c)). This thesis exclusively examines the operating conditions that result in jet drops, with the formation of film drops and the broader dynamics of the liquid film lying beyond the scope of this study.

Before proceeding with the present sub-section, it is important to acknowledge the significant variability in the measurement and reporting of data on bursting bubbles due to the extensive body of research in this area. This variability is particularly evident in the reporting of jet drop and Worthington jet size and velocity. Notably, some researchers report their data in terms of Oh, while others adhere to using La to represent the interplay between capillary and viscous forces. In this thesis, the most suitable dimensionless number is employed for clarity in each context. The reader should note that both Oh and La can be used almost interchangeably (see Eq. (2.28)) by noticing that increased Oh (decreased La) denotes increased influence of viscosity relative to surface tension.

2.5.2 Initial shape of a bubble resting on a free interface

The shape of a bubble that has risen to the liquid pool-atmosphere interface is determined by the interplay between capillary pressure, σ_s/R_0, and gravitational forces, $\rho_l g R_0$. This shape can be theoretically computed by adhering to the Young-Laplace equation, which demands a hydrostatic quasi-equilibrium between surface tension and gravity. The procedure for computing the initial bubble shape based on the Young-Laplace equation is complex but extensively documented in several publications, with various open-source numerical codes available for such computations[1]. This sub-section provides only a brief summary of the most relevant aspects of this procedure. Readers interested in detailed derivations of each equation and their implications are encouraged to refer to the works by Lhuissier and Villermaux [163], Boulton-Stone and Blake [41], Ghabache [92], and Toba [287].

For the calculation of the interface shape of a bubble resting on a free interface, it is useful to

[1] http://www.basilisk.fr/sandbox/aberny/bubble/bubbleShape.h

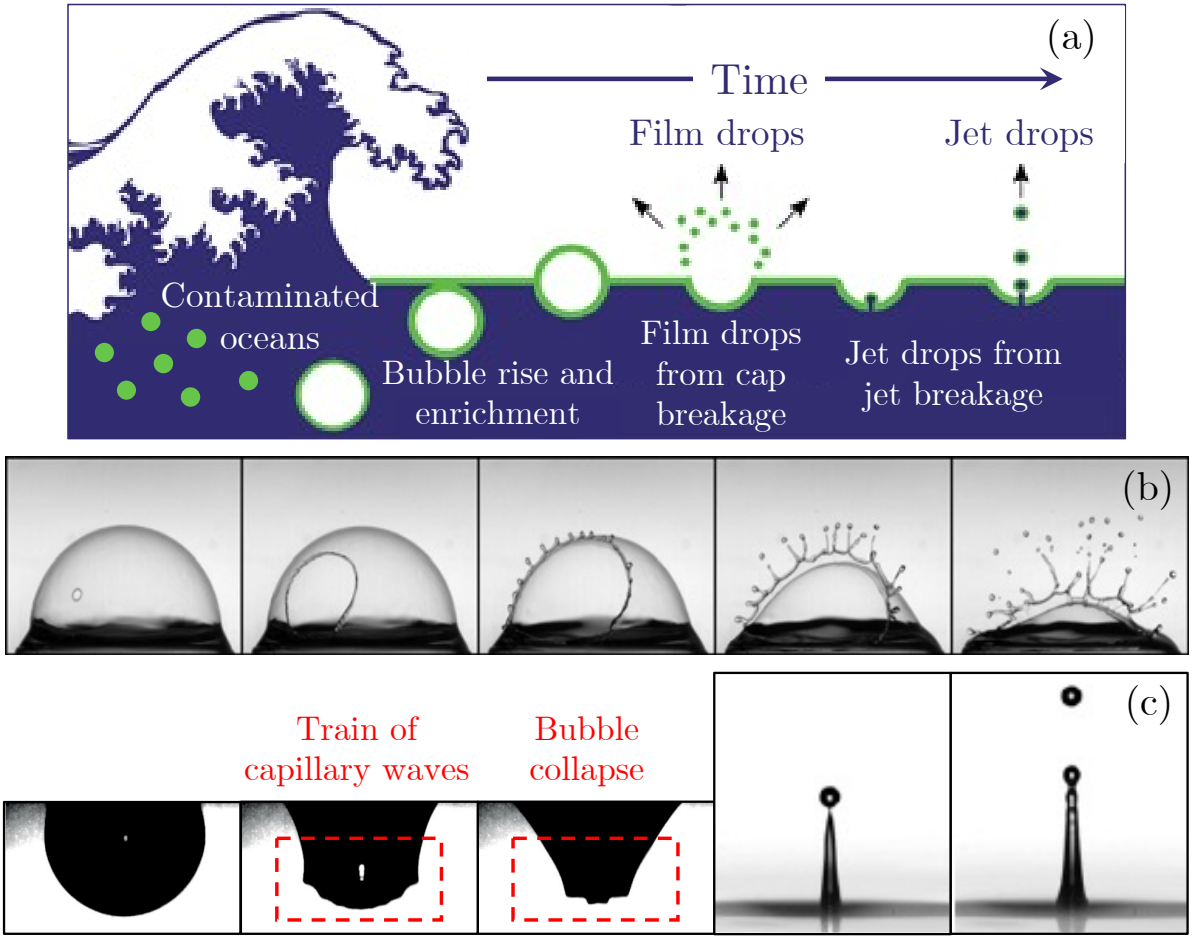

Figure 2.12: Production of aerosol droplets via bursting bubble phenomena: (a) schematic of bubble entrapment due to the action of contaminated oceanic waves, bubble rise, contaminant enrichment, liquid film formation, and drop release to the atmosphere. The production of drops can originate from the liquid film via a Rayleigh-Taylor instability or from a Worthington jet via a Rayleigh-Plateau instability; (b) formation of film drops via liquid film breakage, as observed experimentally by Lhuissier and Villermaux [163]; (c) formation of jet drops via capillary wave propagation and Worthington jet breakage, as observed experimentally by Pierre et al. [227] and Séon and Liger-Belair [257]

sub-divide the bubble domain into three regions: i) the submerged bubble or cavity, ii) the liquid film (cap) separating the bubble from the atmosphere, and iii) the bubble "tail" or meniscus. As portrayed in figure 2.13(a), these three regions converge at a single point, denoted here as "C" [92, 55, 325]. The basis of the solution is based on a shooting method in which the location of C is set arbitrarily and adjusted progressively. Using Laplace's law, and assuming a weightless liquid cap (vanishing thickness) and constant surface tension, each of the above regions is described by the expressions of Eqs. (2.29) - (2.31):

$$\text{Region i:} \quad p_b - (p_0 - \rho_l g z) = \sigma_s \kappa, \tag{2.29}$$

$$\text{Region ii:} \quad p_b - p_{\text{atm}} = \frac{4\sigma_s}{R_{\text{cap}}}, \tag{2.30}$$

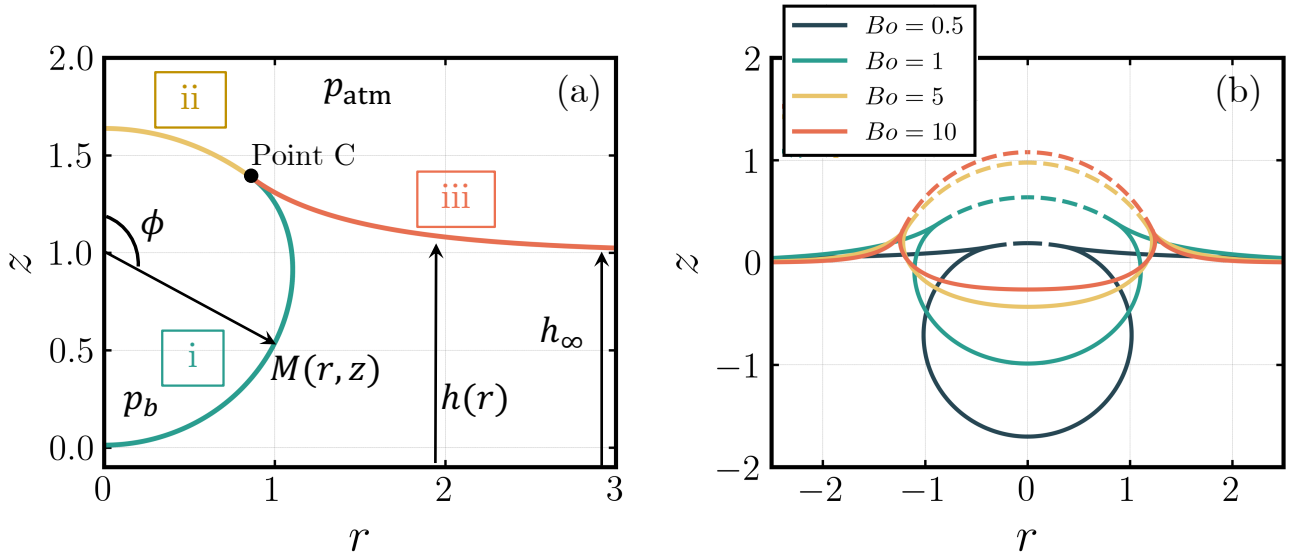

Figure 2.13: Schematic representation of a bubble resting on a free interface: (a) illustration the three main regions that comprise the system, highlighting the most important parameters used in the computation of the interface according to the Young-Laplace equation. The point C represents the intersection between the cap, the cavity, and the meniscus, at a location marked by the angle ϕ_c and height h_c; (b) example of interface computation for various Bo, with the cap depicted in dotted lines and the cavity and meniscus in continuous lines. The vertical position has been adjusted from (a) so that $h_\infty = 0$

$$\text{Region iii:} \quad p_{\text{atm}} - (p_{\text{atm}} - \rho_l g(h - h_\infty)) = \sigma_s \kappa, \tag{2.31}$$

where p_b is the bubble's pressure, p_{atm} the atmospheric pressure, p_0 the pressure underneath the bubble at the (0,0) point, and R_{cap} is the cap's radius; κ, the mean curvature is equal to $\kappa = 1/(R_1 + R_2)$, with R_1 and R_2 representing the principal radii of curvature.

By applying Eq. (2.29) to the point (0,0), one obtains $p_b - p_0 = 2\sigma_s/R_0$. Substituting this expression back into Eq. (2.29) yields $2\sigma/R_0 + \rho_l g z = \sigma_s \kappa$. At any given point $M(r, z)$ located at the bubble cavity, the interfacial curvature can be expressed by using the following equation in cylindrical coordinates (see figure 2.13(a)):

$$\kappa = \frac{\sin\phi}{r} + \frac{\mathrm{d}\sin\phi}{\mathrm{d}r}. \tag{2.32}$$

By replacing Eq. (2.32) into our updated expression for region i, Eq. (2.33) is obtained:

$$\frac{2\sigma}{R_0} + \rho_l g z = \frac{\sigma_s}{r}\frac{\mathrm{d}(r\sin\phi)}{\mathrm{d}r}, \tag{2.33}$$

which transforms into Eq. (2.34) by non-dimensionalising r and z using $r = \tilde{r}R_0$ and $z = \tilde{z}R_0$ (tildes denote dimensionless parameters):

$$\frac{1}{\tilde{r}}\frac{\mathrm{d}(\tilde{r}\sin\phi)}{\mathrm{d}\tilde{r}} = 2 + Bo\tilde{z}, \tag{2.34}$$

where $Bo = \rho_l g R_0^2/\sigma_s$, with $\phi = \phi(r, z)$ being the dependent variable in this equation. The

solution of the above expression necessitates an additional equation, which corresponds to the geometric definition of the angle ϕ, $\mathrm{d}z/\mathrm{d}r = -\tan\phi$. This expression, alongside Eq. (2.34) form a set of differential equations that represents region i. This set is depicted in Eq. (2.35) in parametric form using ϕ:

$$\begin{cases} \frac{\mathrm{d}\tilde{r}}{\mathrm{d}\phi} = \frac{\tilde{r}\cos\phi}{\tilde{r}(2+Bo\tilde{z})-\sin\phi}, \\ \frac{\mathrm{d}\tilde{z}}{\mathrm{d}\phi} = -\frac{\mathrm{d}\tilde{r}}{\mathrm{d}\phi}\tan\phi. \end{cases} \tag{2.35}$$

For region ii, the assumptions of weightless cap and uniform surface tension demand that the cap curvature be uniform, with a profile given by the arc of a circle. This circle is given by:

$$\begin{cases} r = R_{cap}\sin\phi, \\ z = h_c - R_{cap}\cos\phi_c + R_{cap}\cos\phi, \end{cases} \tag{2.36}$$

where the cap's radius is set to be equal to the curvature at the point C, which is set to be continuous in all three regions: $\tilde{R}_{cap} = \tilde{r}_c/\sin\phi_c$.

Without further demonstration, the interface shape for region iii is obtained by integrating Eq. (2.37) subject to the boundary conditions $\tilde{h}(\tilde{r}_c) = \tilde{h}_c$ and $\tilde{h}'(\tilde{r}_c) = -\tan\phi_c$ (see Ghabache [92] for the full derivation):

$$Bo(\tilde{h}(r) - \tilde{h}_\infty) = \frac{\tilde{h}'}{\tilde{r}(1+\tilde{h}'^2)^{1/2}} + \frac{\tilde{h}''}{(1+\tilde{h}'^2)^{3/2}}. \tag{2.37}$$

The above mentioned iteration of the location of point C continues until $\lim_{r\to\infty} h(r) = h_\infty$ is satisfied. Figure 2.13(b) showcases the computed interfacial bubble shape for various Bo, where it is clearly demonstrated how increasing Bo reduces the sphericity of the cavity and extends the length of the liquid cap.

2.5.3 Jet drops: main findings in uncontaminated scenarios

The fundamental dynamics governing the formation of jet drops from bursting bubbles are well-established in scenarios devoid of any contaminant material, with significant understanding extending from very low Bond numbers ($Bo \sim O(10^{-3})$) to higher Bond numbers up to $Bo \approx 1$. Among many notable contributions to the field, outlined in a recent review by Yu et al. [327], the interrelation between the nature of the capillary waves and the ejection of the Worthington jet is now well-understood as a result of the works of Gordillo and Rodríguez-Rodríguez [100], Blanco-Rodríguez and Gordillo [38] and collaborators. The theoretical models proposed in these references suggest that the Worthington jet forms due to the system's selection of a dominant capillary wave with wavelength λ^* during thin film retraction. This wavelength, which scales with Oh as $\lambda^* \sim Oh^{1/2}$ (for $Oh \leq 0.02$) and $\lambda^* \sim Oh^{4/5}$ (for $Oh > 0.02$), corresponds to that of the smallest wavelength not fully attenuated by viscous effects and the first one to reach the bottom of the cavity.

Noteworthy of mention are the time-scales involved in the bubble collapsing process. In collapsing bursting bubbles, according to Gordillo and Rodríguez-Rodríguez [100]'s theory, the time-scale associated with viscous damping in clean interfaces, $1/\beta_{\text{clean}}$ with β_{clean} being the damping rate, must be at least equal to the capillary time-scale t_c. Given that $\beta_{\text{clean}} \sim 1/\lambda^2$ (see Eq. (2.38) [184]), the wave that reaches the bottom first must be the smallest one not attenuated by viscosity (i.e., the one that satisfies $1/\beta_{\text{clean}} \approx t_c$). Since $\beta_{\text{clean}} \sim Oh$, this dominant wavelength, λ^*, must increase with Oh to compensate. This analysis explains the above mentioned λ^* and Oh scalings:

$$\beta_{\text{clean}} = -2\nu k^2, \tag{2.38}$$

where, β_{clean} is the wave damping rate, ν kinematic viscosity, and k the wave number of a given capillary wave ($\sim 1/\lambda$).

Gordillo and Rodríguez-Rodríguez [100] and Blanco-Rodríguez and Gordillo [38] have also uncovered the constant behaviour of the angular velocity of the dominant capillary wave, $|u_{\theta,lin}| \approx 5u_c$, as it propagates across the bubble. This angular velocity has also been demonstrated to be unaffected by Oh up to $Bo \approx 0.7$ [38]. Figure 2.14 offers a compilation of some of the most important findings of the numerical investigation by Blanco-Rodríguez and Gordillo [38], including how λ^* scales with Oh (figure 2.14(a,b,d,e)) and the average velocity of the capillary wave (figure 2.14(c)). It is noteworthy that figure 2.14(c) displays a single Oh data series for simplicity. However, all cases in the complete dataset, covering $0.004 < Oh < 0.04$, align on the same line, demonstrating the negligible influence of Oh on $|u_{\theta,lin}|$.

Through extensive experiments and numerical simulations, various authors [74, 68, 100, 90, 93, 158, 42, 302, 34] (see also references cited therein) have contributed to characterising the size and velocity of the first ejected drop and the Worthington jet, and how these variables are influenced by Oh (or La, see Eq. (2.28)) and Bo. A substantial portion of these investigations report the size of the first ejected drop, R_{d1}, in terms of the drop's Laplace number, defined as $La_{d1} = \frac{\rho_l \sigma_s R_{d1}}{\mu_l^2}$. Additionally, they report the drop velocity, u_{d1}, in terms of the drop's capillary number, $Ca_{d1} = \frac{u_{d1}\mu_l}{\sigma_s}$. Other studies directly report the values of R_{d1} and u_{d1} or the jet ejection velocity, u_{jet}.

Particularly noteworthy are the works of Gordillo and Rodríguez-Rodríguez [100] and Gañán-Calvo [90], which propose relationships between Oh and u_{jet} in the case of the former and Oh and u_{d1} in the case of the latter. Both studies do so by utilising scaling arguments and relating the time, velocity, and length scales characteristic of the pre-collapse dynamics to those in the post-collapse stages. Deike et al. [68] proposed an empirical correction to the equation of Gañán-Calvo [90] to account for the effect of Bo. A summary of these scaling relationships can be found in Eq. (2.39) - (2.42), where $Oh_* \approx 0.043$ denotes the Oh value above which viscous effects preclude the

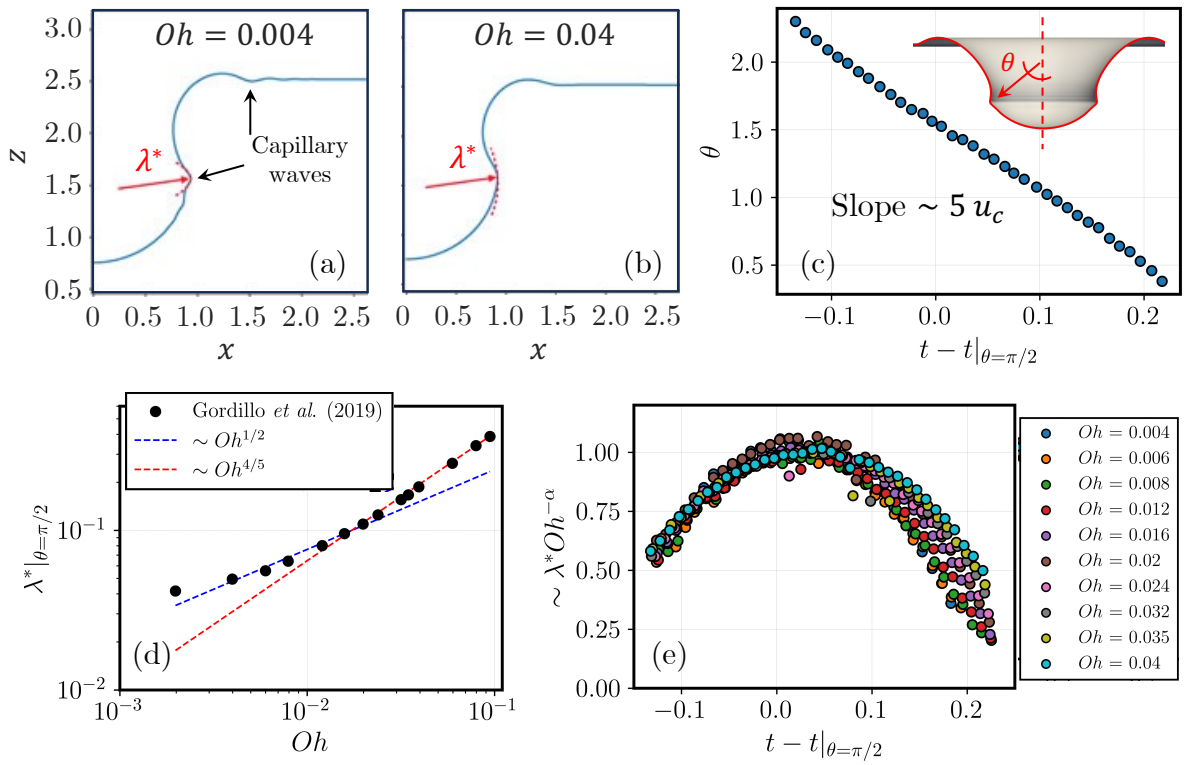

Figure 2.14: A dominant capillary wave with wavelength λ^* propagating across the bubble domain under vanishing Bo conditions. Its angular location at time t corresponds to θ: (a)-(b) sample interfacial shapes from the simulations of Gordillo and Rodríguez-Rodríguez [100], illustrating how increased damping effects at higher Oh necessitate a larger λ^*; (c) sample θ measurements from the same reference at $Oh = 0.004$, demonstrating the linear relationship between θ and t, and suggesting a constant wave propagation velocity of approximately $5u_c$; (d) numerical measurements of λ^* when $\theta = \pi/2$ from the same reference, alongside the scaling proposed; (e) temporal evolution of λ^* for various Oh values and data collapse utilising the scaling of the same reference, where $\alpha = 1/2$ for $Oh \leq 0.02$ and $\alpha = 4/5$ for $Oh > 0.02$.

jet from breaking ($La_* \approx 540$ would be the value *below* which no jet breaking would be observed):

$$\text{Gordillo and Rodríguez-Rodríguez [100]:} \quad u_{jet} \sim Oh^{1/2}(1-(Oh/Oh_*)^{1/2})^{-3/2} \ \ (Oh << Oh_*), \tag{2.39}$$

$$\text{Gordillo and Rodríguez-Rodríguez [100]:} \quad u_{jet} \sim (1-(Oh/Oh_*)^{1/2})^{-1/2} \ \ (Oh \approx Oh_*), \tag{2.40}$$

$$\text{Gordillo and Rodríguez-Rodríguez [100]:} \quad u_{jet} \sim Oh^{-1} \ \ (Oh > Oh_*), \tag{2.41}$$

$$\text{Gañán-Calvo [90]:} \quad u_{d1} \sim Oh^{1/2}(Oh_* - Oh)^{-3/4}. \tag{2.42}$$

In terms of the first ejected drop size, R_{d1}, numerous experimental and numerical studies have corroborated the scaling derived by Gañán-Calvo [90] as presented in Eq. (2.43):

$$\text{Gañán-Calvo [90]:} \quad R_{d1} \sim [(Oh_* - Oh)Oh^{-2}]^{5/4}. \tag{2.43}$$

More recently, Berny et al. [34] have furthered the field's understanding by extending prior analyses to include subsequent drops following the initial pinch-off. Their research demonstrates a consistent reduction in velocity with increasing number of produced drops. Figure 2.15 provides a compilation by Berny et al. [34] of various datasets from the literature, depicting the velocity of the first ejected drop/jet and the size of the first ejected drop for different La (Oh) and Bo values. Chapter 6 delves deeper into the influence of Oh on the velocity of the first ejected drop, distinguishing it from the jet ejection velocity, and also examines the impact of surfactants on these parameters.

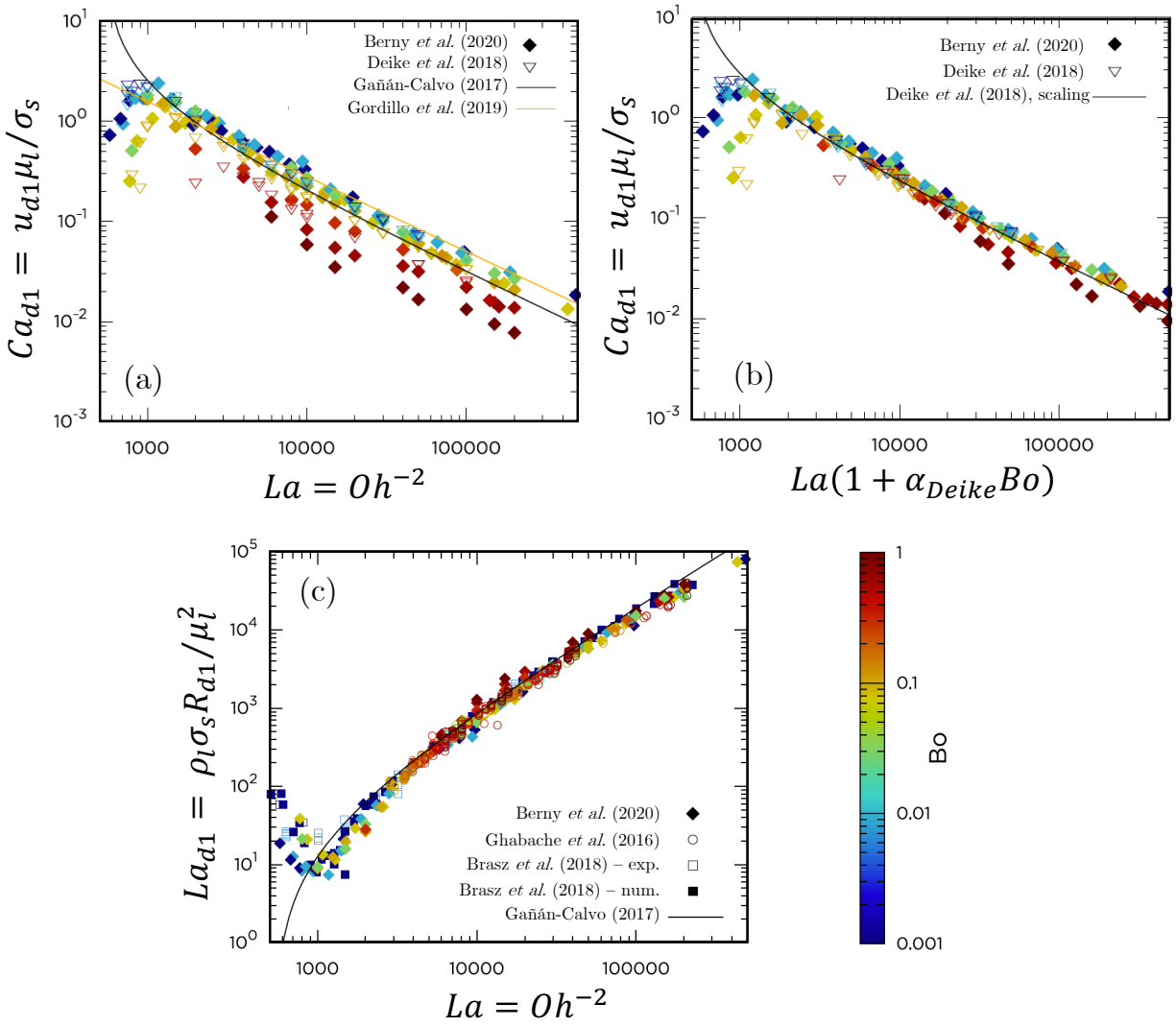

Figure 2.15: Compilation of literature data on first ejected drop capillary and Laplace numbers (velocity and size, respectively) as a function of La (or Oh) and Bo, as compiled by Berny et al. [34]: (a) Ca_{d1} experimental/numerical data from Berny et al. [34], Deike et al. [68], alongside the scalings of Gordillo and Rodríguez-Rodríguez [100] (Eq. (2.39) - (2.41)) and Gañán-Calvo [90] (Eq. (2.42)) without considering the effects of Bo; (b) collapse of the data in (a) by using the relationship proposed in Deike et al. [68], with $\alpha_{Deike} = 2.2$; (c) La_{d1} experimental/numerical data from [34, 93, 42] and scaling by Gañán-Calvo [90] (Eq. (2.43)). Figure adapted from Berny et al. [34]

The simulations and theoretical pursuits of Lai et al. [158] have suggested that both the

collapsing bubble and the nascent Worthington jet in uncontaminated scenarios follow an inviscid scaling of the form $|t - t_0|^{2/3}$, where t_0 is the bubble collapse time. This scaling, valid for $La \approx 1000 - 5000$, hints at interfacial self-similarity in bursting bubbles. The proposed scalings are depicted in mathematical form in Eqs. (2.44) - (2.45):

$$\text{Pre-collapse } (t < t_0): \quad \frac{z - z_0}{l_{vis}\phi} = \left(\frac{t_0 - t}{\phi^{3/2} l_{vis}/u_{vis}}\right)^{2/3} g_b \left[\frac{x}{l_{vis}\phi}\left(\frac{t_0 - t}{\phi^{3/2} l_{vis}/u_{vis}}\right)^{-2/3}\right], \tag{2.44}$$

$$\text{Post-collapse } (t > t_0): \quad \frac{z - z_b}{l_{vis}\phi} = \left(\frac{t - t_0}{\phi^{7/4} l_{vis}/u_{vis}}\right)^{2/3} g_a \left[\frac{x}{l_{vis}\phi}\left(\frac{t - t_0}{\phi^{7/4} l_{vis}/u_{vis}}\right)^{-2/3}\right]. \tag{2.45}$$

In the above, the radial direction is represented by x and the vertical axis by z (see, for instance, figure 2.14(a)). z_0 denotes the vertical location of the interface at the instance of collapse (interfacial curvature reversal), whilst z_b is the vertical location of the jet. g_b and g_a are the dimensionless interface profiles before and after collapse, respectively. The remaining parameters of Eqs. (2.44) - (2.45) are defined as follows:

$$l_{vis} = \frac{\mu_l^2}{\rho_l \sigma_s}, \quad u_{vis} = \frac{\sigma_s}{\mu_l}, \quad \phi = La(La_*^{-1/2} - La^{-1/2}) = Oh^{-2}(Oh_* - Oh), \tag{2.46}$$

where l_{vis}, and u_{vis} correspond to the viscous length and velocity scales, respectively. Figure 2.16 provides an example of the universal profiles obtained by the proposed scaling of Lai et al. [158], depicted both before (panels (a)-(b)) and after (panels (c)-(d)) bubble collapse. These plots demonstrate that the proposed universality ceases to hold for $La > 5000$ during bubble collapse. Furthermore, the theory accurately predicts the temporal evolution of the jet, except in regions near the bulbous tip of the jet. Similar scaling relationships in the pre-collapse region have been proposed by Duchemin et al. [74] and Ghabache et al. [94].

2.5.4 The role of surface-active contaminants on bursting bubbles

The structurally complex interfacial phenomena that arise from surface-active material have been the subject of a handful of recent investigations. The experimental and numerical work of Pierre et al. [227], Vega and Montanero [297], Ji et al. [123], Néel et al. [207], Constante-Amores et al. [55] for $Bo \to 0$ have reported dramatic modifications to all steps leading to jet breakup, revealing intricate relationships between the system's outcomes and surfactant properties due to the comparable nature of surfactant-related time-scales and those of bubble bursting. The most notable of these modifications involves a consistent temporal retardation of bubble collapse with the addition of insoluble surfactant (SDS). This retardation increases in prominence as the surfactant concentration increases but remains below the critical micelle concentration (CMC). Additionally, previous experimental measurements have reported a notable decrease in the number of ejected drops or complete prevention of jet breakup in the presence of insoluble surfactant [227, 297].

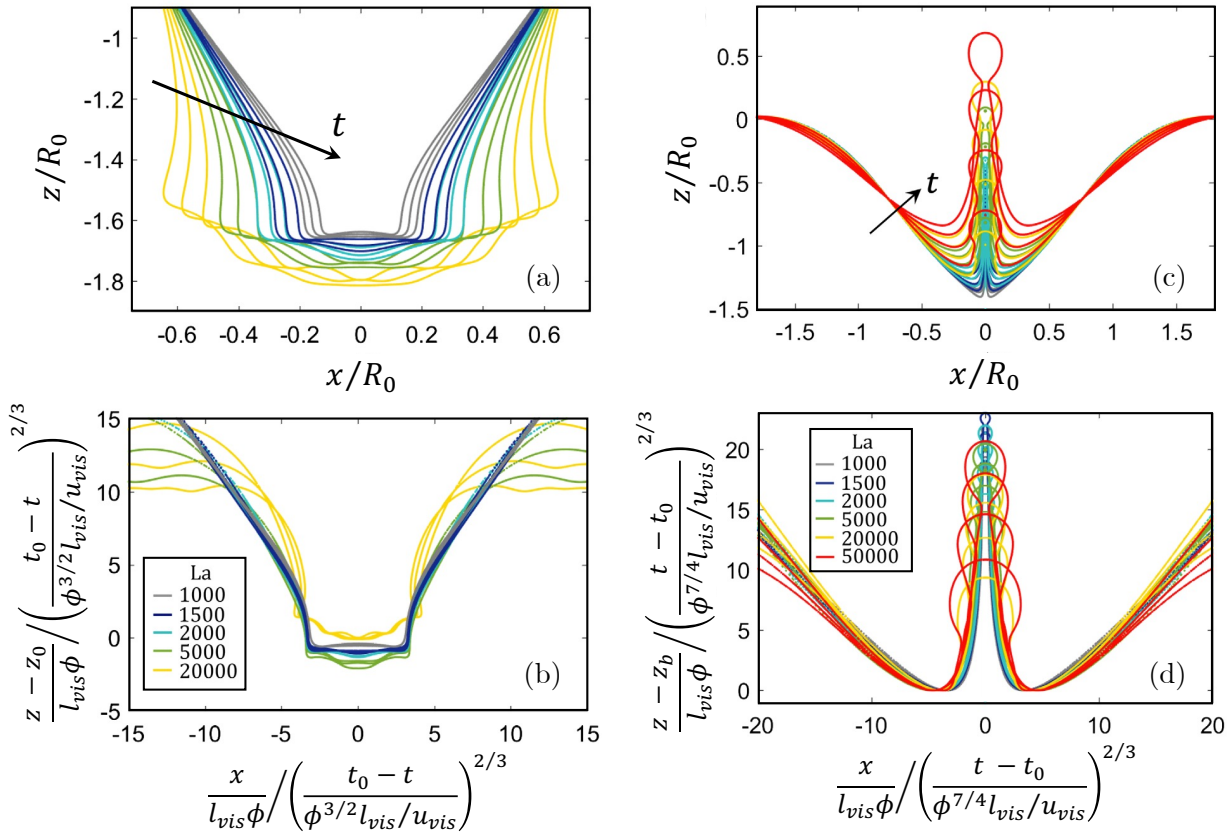

Figure 2.16: Bubble collapse and Worthington jet interfacial self-similarity proposed in the work of Lai et al. [158] and shown in Eqs. (2.44) - (2.45): (a)-(b) depict the pre-collapse dynamics, while (c)-(d) illustrate the nascent Worthington jet dynamics. In these plots, lines of the same colour represent different time instants: $t_0 - t = 6t_{pre}, 8t_{pre}, 10t_{pre}$, where $t_{pre} = \phi^{3/2} l_{vis}/u_{vis}$ before collapse. Post-collapse profiles are shown at $t - t_0 = t_{pos}, 3/2t_{pos}, 2t_{pos}, 5/2t_{pos}$, where $t_{pos} = \phi^{7/4} l_{vis}/u_{vis}$. Figure adapted from Lai et al. [158]

These phenomena are elucidated in figure 2.17.

Simulations by Constante-Amores et al. [55] have provided initial insights into the complex role of Marangoni stresses and reduced surface tension on the retardation dynamics. This study reported the development of a toroidal capillary wave carrying a large surfactant concentration across the bubble's domain, leading to a low surface tension bubble collapse (larger local Oh) and a fast jet ejection ($u_{jet} \sim Oh^{1/2}$ [100]) that is subsequently delayed by the action of Marangoni stresses. Other surfactant-induced effects unveiled in the literature relate to a reduction in the number and size of ejected drops below the CMC [227, 297].

The recent experiments and theoretical framework presented in Ji et al. [123] expose the marked influence of surface viscoelasticity and its unequivocal departure from Newtonian surface behaviour in surfactant-laden flows. This study introduces a new bursting regime featuring secondary daughter bubble entrapment during collapse and jetting suppression, which uniquely originate from the action of dilatational elastic stresses rather than Marangoni stresses. A similar jetting suppression phenomenon has been observed in bursting bubble systems in non-Newtonian liquid media and surfactant-free interfaces [249].

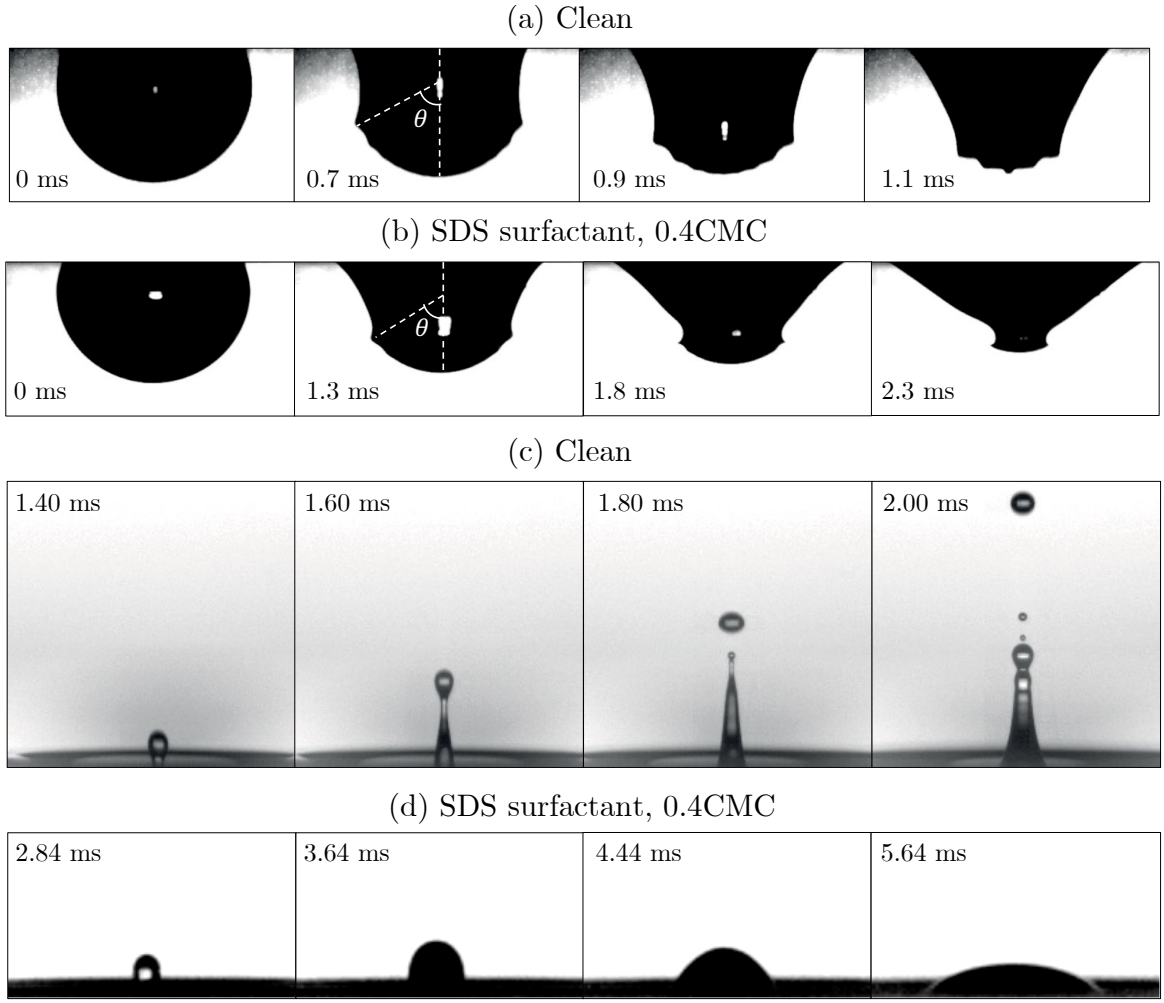

Figure 2.17: Qualitative representation of surfactant-induced wave retardation in (a)-(b) and jet stabilisation in (c)-(d) in the fluid mechanics problem of bursting bubbles, as elucidated in the experimental study of Pierre et al. [227]. The clean cases shown in (a,d) correspond to pure water under conditions of $Bo \approx 0.17$ and $Oh = 3.21 \times 10^{-3}$. The surfactant cases of (c,d) share the same Bo. Figure adapted from Pierre et al. [227]

Despite recent strides in untangling the rich interfacial phenomena that unfold in the presence of surface-active contaminants, a few critical aspects remain elusive. While experimental observations have detected a delay in capillary wave motion, enabling estimations of capillary wave velocity in surfactant-laden systems, temporal information on the evolution of the angular position of the dominant capillary wave, θ, akin to the insights provided by Gordillo and Rodríguez-Rodríguez [100] for clean interfaces, has not been reported before.

As demonstrated in this thesis, uncovering the dependence of θ on t is paramount to understanding the system's dynamics, representing the inherent nonlinearity and complexity of surfactant flows that are heavily influenced by surfactant parameters. Additionally, and as stated by Pierre et al. [227], Vega and Montanero [297], the exact mechanism by which the motion retardation comes about, as well as the unique influence of Marangoni stresses, is still unclear and challenging to access experimentally.

Chapter 3

Numerical modelling of multiphase flows: multi-scale and multi-fidelity approaches

Contents

3.1 Overview 48

3.2 Mesoscale PBM approaches for polydisperse particles in multiphase flows 49

3.2.1 Population balance model, the mesoscale, and multiphase flows 50

3.2.2 The moment transformation, the closure problem, and the quadrature method of moments 53

3.3 High-fidelity CFD methods for interfacial phenomena with surfactants 58

3.3.1 A brief introduction to interfacial fluid mechanics 58

3.3.2 Transport equations for soluble surfactant 63

3.3.3 Numerical methods for interfacial flows 64

3.3.4 The Level Contour Reconstruction Method (LCRM) 67

3.1 Overview

The following chapter offers a detailed account of the computational methodologies employed in this investigation. As discussed in §1, the inherent complexity of multiphase flows, particularly those involving polydisperse structures and complex interfaces, necessitates the careful formulation and implementation of numerical models that can accurately predict their behaviour. The chapter begins with §3.2, which offers a general overview of the principles underlying population balance modelling (PBM) and the meso-scale modelling of multiphase systems. This discussion

lays the groundwork for the hybrid PBM-CFD approach proposed in §4 for understanding the synthesis of AgNPs. Following this, §3.3 delves into the CFD methodologies and formulations used to handle interfacial flows, including the specific approach employed in this work, as discussed in chapters 5 through 6.

3.2 Mesoscale PBM approaches for polydisperse particles in multiphase flows

This section lays out the theoretical and numerical frameworks that form the basis of the mesoscale modelling approach used to describe the synthesis of AgNPs in chapter 4. Although a thorough description of the most relevant aspects is provided here, a more comprehensive account of mesoscale modelling, polydisperse multiphase flows, and PBM can be found in the foundational texts of Ramkrishna [237], Marchisio et al. [187], and Yeoh and Tu [324].

As outlined in chapter 1, polydisperse multiphase flows represent a distinct category within multiphase flows wherein the constituting entities of the disperse phase(s) exhibit variations in their physical properties or velocities. The type and relevance of the potential interactions that may arise between the disperse and continuous phases are largely dictated by the system's flow regime, typically quantified by the disperse phase's Stokes number, $St_d = t_d/t_c$, its volume fraction, ϕ_p, and its mass fraction, $\phi_2 = \phi_d\rho_d/(\phi_c\rho_c)$, with ρ denoting the density of each phase. St_p relates the characteristic or relaxation time of the disperse phase, t_d, to that of the main flow, t_c. In turbulent conditions, the Kolmogorov time scale serves as the natural representative timescale for the primary flow. However, in laminar flows, this timescale becomes highly system-dependent, with examples including residence time in batch and continuous-flow reactors, and nucleation times in crystallisation processes.

Very dilute regimes, also called "one-way coupling" are found when both $\phi_d << 1$ and $\phi_2 << 1$. In these situations, interactions between the continuous and disperse phase, as well as between discrete entities are not relevant due to the large average distance between discrete entities. Within the very dilute regime, $St_d << 1$ indicates that the disperse phase can be thought of as a passive contaminant which always follows the local velocity of the continuous phase. *Dilute* regimes arise when $\phi_d << 1$ and $\phi_2 \geq 1$, leading to non-negligible coupling between the continuous and disperse phase or "two-way coupling". In this regime, new flow instabilities not seen in very dilute regimes may emerge, owing to the momentum coupling between phases [187]. As ϕ_d increases, and we transition into *dense* regimes, the system's motion becomes largely controlled by sustained collisions between dispersed entities. In chapter 4 it is demonstrated that our AgNPs synthesis protocol in both reactors features systems within highly diluted conditions, allowing us to safely adopt a one-way coupling framework.

In the context of multiphase polydisperse flows, the term *macroscale* refers to a fully hydro-

dynamic description of all the phases present in the system, including the disperse phase [187]. These models consider a fixed control volume and reference frame where the flow properties are quantified as they are transported in and out of the control volume [240]. In turn, a *microscale* model is based on the full resolution of all the time and length scales related to individual particles, including boundary layers surrounding the particles and direct inter-particle interactions. Examples of microscale modelling are full-atom molecular dynamic simulations [89]. *Mesoscale* models attempt to bridge together the micro and macro scales by describing the disperse phase not as individual entities or as a continuous system but as a *population* with distributions over specific properties [187].

3.2.1 Population balance model, the mesoscale, and multiphase flows

The population balance framework is a mesoscale model that seeks to describe the behaviour of a population of discrete entities or sub-structures that interact with their environment [238]. These entities are characterised by a finite vector of states or properties, also called *coordinates*. A distinction between *internal* and *external* coordinates is typically made to denote the difference between those properties inherent to the particles (internal coordinates) and those related to their position in physical space (external coordinates) [237, 187]. Common internal properties are particle size, temperature, mass, enthalpy, and velocity. In this thesis, the vector $\boldsymbol{\xi} \equiv (\xi_1, \xi_2, ..., \xi_M)$ represents a set of M internal coordinates that characterise the elements of the disperse phase, while $\mathbf{x} \equiv (x, y, z)$ is the vector of external coordinates (position in physical space). These coordinates comprise the *particle state vector*, $(\boldsymbol{\xi}, \mathbf{x})$. Throughout this thesis, references will be made to the concepts of *physical* and *phase* spaces. Physical space corresponds to the domain of the particle position in the real, three-dimensional physical space, while phase space is an abstract representation of the domain of the internal coordinates of the particles [238]. In PBM formulations, two entities are said to be different only if their coordinates are different. Otherwise, they are considered to be identical.

The concept of *number-density function* (NDF) plays a crucial role in the population balance formulation. The NDF is related to the number of particles per unit volume with a given set of values for the mesoscale properties. The NDF, $n(\boldsymbol{\xi}, \mathbf{x}, t)$, is defined in such a way that $n(\boldsymbol{\xi}, \mathbf{x}, t)d\mathbf{x}d\boldsymbol{\xi}$ corresponds to the number of particles expected to be found in an infinitesimal volume $d\mathbf{x}$ in physical space and in an infinitesimal "volume" in phase-space $d\boldsymbol{\xi}$. As an example, for an NDF with the particle size L representing the internal coordinates, the value of $n(L_i, \mathbf{x_i}, t_i)$ would be equal to the number of particles per unit volume that can be found at a specific point $\mathbf{x_i}$ in physical space at time t_i with specific size L_i [237, 187]. In most traditional PBM approaches, only one internal coordinate is considered. In these cases, it is said that the NDF is *univariate*.

3.2.1.1 The population balance equation

The population balance equation, PBE, is a continuity statement for the NDF that accounts for its evolution in time, physical space, and phase space. The rigorous derivation of this equation can be found in the original works of Ramkrishna [237] and Marchisio et al. [186]. As PBEs provide a deterministic representation of a set of well-defined discrete entities, these equations are valid for populations containing a large number of these entities. Eq. (3.1) shows a generalised version of the PBE for particles embedded in a continuous flow and with a given set of internal coordinates $\boldsymbol{\xi}$:

$$\underbrace{\frac{\partial n(\boldsymbol{\xi},\mathbf{x},t)}{\partial t}}_{\text{Accumulation}} + \underbrace{\underbrace{\nabla_{\mathbf{x}}\cdot[\dot{\mathbf{x}}n(\boldsymbol{\xi},\mathbf{x},t)]}_{\text{Conv. in physical space}} + \underbrace{\nabla_{\boldsymbol{\xi}}\cdot[\dot{\boldsymbol{\xi}}n(\boldsymbol{\xi},\mathbf{x},t)]}_{\text{Conv. in phase space}} - \underbrace{\nabla_{\mathbf{x}}\cdot[D\nabla_{\mathbf{x}}n(\boldsymbol{\xi},\mathbf{x},t)]}_{\text{Diffusion}}}_{\text{Continuous events}} = \underbrace{h(\boldsymbol{\xi},\mathbf{x},t)}_{\text{Discrete events}} \quad , \tag{3.1}$$

where $\nabla_{\mathbf{x}} \equiv (\partial/\partial x, \partial/\partial y, \partial/\partial z)$, $\nabla_{\boldsymbol{\xi}} \equiv (\partial/\partial \xi_1, ..., \partial/\partial \xi_M)$, $\dot{\mathbf{x}} = \mathrm{d}\mathbf{x}/\mathrm{d}t = \mathbf{u_p}$, and $\dot{\boldsymbol{\xi}} = \mathrm{d}\boldsymbol{\xi}/\mathrm{d}t$; $\mathbf{u_p}$ represents the particle velocity vector. The basis of this equation is the notion that the dynamics of the NDF are specifically influenced by multiple phenomena of varying nature. The second and third terms on the LHS are advection terms that represent the rate of change of the NDF due to "motion" in either physical space or phase space, respectively. This concept of motion is denoted by a rate of change of the coordinate in time (i.e., $\dot{\mathbf{x}}$ and $\dot{\boldsymbol{\xi}}$). While the physical meaning of $\dot{\mathbf{x}}$ is the velocity of the disperse phase, the physical meaning of $\dot{\boldsymbol{\xi}}$ depends on the internal coordinate. For example, in the case of an internal coordinate representing a given size L, $\dot{\boldsymbol{\xi}}$ would correspond to the growth rate of the disperse phase. The fourth term on the LHS is related to the rate of change of the NDF due to diffusion processes, which are mediated by a diffusivity coefficient D. The terms shown on the LHS of Eq. (3.1) represent continuous events (advection and diffusion). In contrast, the term $h(\boldsymbol{\xi},\mathbf{x},t)$ on the RHS is a jump function that accounts for the rate of change of the NDF due to discrete events, such as aggregation, breakage, coalescence and nucleation. In this context, a "continuous" event shall be understood as an event in which the coordinates change in a time scale significantly smaller than that of the solutions of the PBE [186, 324]. In contrast, "discrete" events occur at time scales comparable to the general scale of the process.

Eq. (3.1) can be slightly reorganised to introduce the concepts of "births" and "deaths". Discrete events, such as particle aggregation and breakage, can be understood as processes that induce either the creation or the elimination of a particular value of $\boldsymbol{\xi}$. As an example, let us consider a case involving a univariate NDF in which the particle size L is the internal coordinate. A specific particle size L_i can "die" by the aggregation of two particles of sizes L_i and L_j. On the other hand, the size L_i could "be born" by the collision of two particles of sizes L_j and L_k (provided that $L_j + L_k = L_i$). The same logic applies to other discrete events. The PBE in terms of births and deaths is presented in Eq. (3.2) [237]. The dependencies on time, phase, and

physical space have been dropped in this equation for simplicity:

$$\frac{\partial n}{\partial t} + \nabla_{\mathbf{x}} \cdot [\dot{\mathbf{x}} n] + \nabla_{\boldsymbol{\xi}} \cdot [\dot{\boldsymbol{\xi}} n] - \nabla_{\mathbf{x}} \cdot [D \nabla_{\mathbf{x}} n] = \mathcal{B} - \mathcal{D} + \mathcal{N}, \tag{3.2}$$

where $\mathcal{B}$, $\mathcal{D}$, and $\mathcal{N}$ represent the rates of birth, death, and nucleation, respectively. Although nucleation is also a discrete phenomenon, it is written here as a separate term given that the concepts of births and deaths do not fully apply to nucleation. Instead, the birth and death terms are used for events related to coalescence/aggregation and breakup.

In the above equations, the internal coordinates vector has been contemplated as a general mathematical concept that applies to an arbitrary type of internal coordinate. It is relevant to note here that a special treatment is considered when the internal coordinate corresponds to particle velocity. Even though the mathematical formulation of the PBE remains unchanged, profound conceptual differences emerge when $\boldsymbol{\xi} = \mathbf{u_p}$ as opposed to, say $\boldsymbol{\xi} = L$ (i.e., when the particles are not subjected to a single velocity field but are characterised by a given velocity *distribution*). In such cases, the NDF is not transported passively by the velocity field, but actively interacts with the continuous phase through the advection term in phase space ($\dot{\boldsymbol{\xi}} = \mathrm{d}\mathbf{u_p}/\mathrm{d}t = \mathbf{A_p}$). This formulation, often termed the generalised population balance equation (GPBE) assigns $\mathbf{A_p}$ as the particle acceleration or the force per unit mass acting on the particles. These forces (e.g., drag, lift, gravity, virtual mass) embody the manner by which the continuous and disperse phase exchange momentum in systems governed by non-negligible inertia in the dispersed phase. Concerning discrete events, the GPBE rationalises collision or breakup instances as instantaneous events that induce changes in the discrete phase's velocity.

As elucidated in chapter 4, within the system under examination, the highly diluted conditions ensure that particles always follow the path of the continuous phase. Consequently, particle velocity ceases to be a relevant internal coordinate to describe the system's dynamics, thus confining our focus solely to the formulation of the PBE in this study. Further details on the GPBE and explicit momentum couplings between the continuous and disperse phase can be found elsewhere [186, 187].

3.2.1.2 Birth and death functions

As previously described, the constituting entities of the disperse phase can undergo fluctuations in their state vectors due to discrete births and deaths. Figure 3.1 depicts a conceptual representation of the birth/death of a specific internal coordinate value, ξ_i, due to agglomeration/coalescence and breakup events. It is illustrative to think of ξ_i as a specific mass or volume of the disperse phase entities (e.g., particles, bubbles, or droplets). Mathematical descriptions of

these concepts in a pair-wise context are written in Eqs. (3.3)-(3.6):

$$\bar{\mathcal{B}}(\xi_i)^{agg} = \frac{1}{2}\int_0^{\xi_i} [\beta(\xi_i - \xi_j, \xi_j) n(\xi_i - \xi_j) n(\xi_j)]\, \mathrm{d}\xi_\mathrm{j}, \tag{3.3}$$

$$\bar{\mathcal{D}}(\xi_i)^{agg} = \int_0^{\infty} [\beta(\xi_i, \xi_j) n(\xi_i) n(\xi_j)]\, \mathrm{d}\xi_\mathrm{j}, \tag{3.4}$$

$$\bar{\mathcal{B}}(\xi_i)^{bk} = \int_{\xi_i}^{\infty} [a(\xi_j) b(\xi_i|\xi_j) n(\xi_j)]\, \mathrm{d}\xi_\mathrm{j}, \tag{3.5}$$

$$\bar{\mathcal{D}}(\xi_i)^{bk} = a(\xi_i) n(\xi_i). \tag{3.6}$$

In the above, aggregation events create ξ_i from two entities of internal coordinates $(\xi_i - \xi_j)$ and ξ_j colliding and aggregating and destroy ξ_i from collisions between itself and another entity represented by ξ_j. In a similar manner, breakup events create ξ_i from a fragmenting entity represented by ξ_j and destroy ξ_i from its fragmentation. In what remains of this subsection, dependencies on physical space and time have been omitted, leaving only those related to the internal coordinates; $\beta(\xi_i - \xi_j, \xi_j)$ is typically referred to as the aggregation kernel and denotes the collision frequency between $(\xi_i - \xi_j)$ and ξ_j. Conversely, $a(\xi_j)$ is the breakage frequency or kernel of ξ_j and $b(\xi_i|\xi_j)$ represents the probability density function of the formation of ξ_i from the breakup of ξ_j.

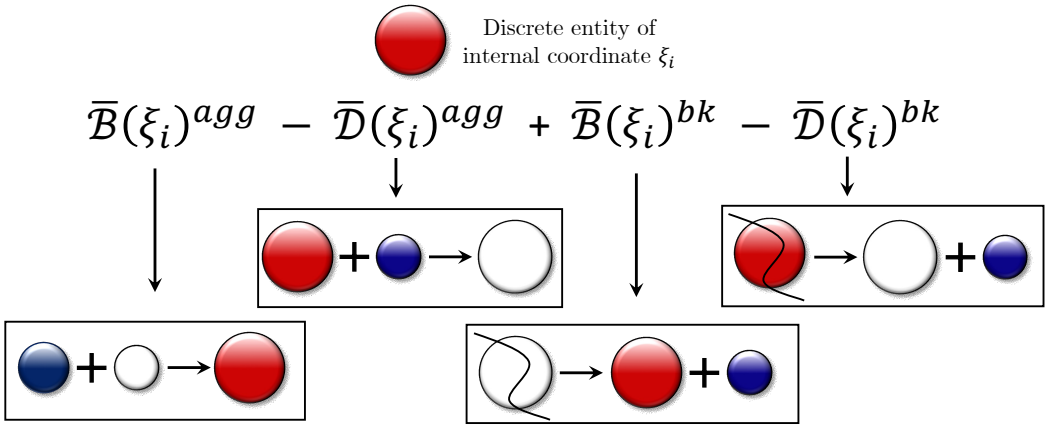

Figure 3.1: Conceptual illustration of birth and death events of a specific internal coordinate ξ_i, represented by the red spheres, due to agglomeration and breakup. The blue and white spheres represent discrete entities with other values of ξ [209]. Definitions for the birth and death functions are provided in Eq. (3.3)-(3.6)

3.2.2 The moment transformation, the closure problem, and the quadrature method of moments

The solution of the PBE is a topic of intensive and continuous research. Multiple approaches have been proposed in the past few decades, including Monte-Carlo [171], class [7], and moments-based methods [216]. For a recent review of the existing PBE solution methods, the reader is referred

to Shiea et al. [261]. As is mentioned in chapter 4, the present work focuses on moments-based methods to solve the PBE. As will become evident in the upcoming paragraphs, the advantage of using such methods, and specifically quadrature-based moments methods, is twofold: they solve only a limited number of scalar transport equations for each moment, lowering the corresponding computational cost compared to class- and Monte-Carlo-based methods; second, the moments set represents physical measurable quantities of interest, making the PBM readily compatible with macroscopic modelling through CFD [187].

Moments methods revolve around the central idea of the moment transformation of the PBE. A general definition of the k^{th}-order moment vector for a multivariate NDF is shown below in Eq. (3.7):

$$m_{\mathbf{k}}(\mathbf{x},t) \equiv \int_{\Omega_\xi} \xi_1^{k_1} ... \xi_M^{k_M} n(\boldsymbol{\xi},\mathbf{x},t)\,\mathrm{d}\boldsymbol{\xi}, \tag{3.7}$$

where the vector $\mathbf{k}$ corresponds to the order of the M moments with respect to each M internal variables, and Ω_ξ to the domain encompassing each internal variable ξ. By applying this operation to a given univariate NDF with particle size L as the internal coordinate, the physical meaning of the first few moments is revealed. Eqs. (3.8)-(3.10) show three important physical quantities represented by the moments:

$$N_p = m_0(\mathbf{x},t) \equiv \int_0^\infty L^0 n(L,\mathbf{x},t)\,\mathrm{d}L, \tag{3.8}$$

$$\phi_p = k_V m_3(\mathbf{x},t) \equiv k_V \int_0^\infty L^3 n(L,\mathbf{x},t)\,\mathrm{d}L, \tag{3.9}$$

$$d_{k+1,k} = \frac{m_{k+1}(\mathbf{x},t)}{m_k(\mathbf{x},t)} \equiv \frac{\int_0^\infty L^{k+1} n(L,\mathbf{x},t)\,\mathrm{d}L}{\int_0^\infty L^k n(L,\mathbf{x},t)\,\mathrm{d}L}. \tag{3.10}$$

The above set of equations indicates that, for a length-based NDF, the zeroth-order moment corresponds to the number of particles per unit volume in the system, N_p, and the third-order moment is proportional to the volume fraction of the disperse phase, ϕ_p. k_V, a volumetric shape factor, is the proportionality constant between ϕ_p and m_3. Moreover, the mean particle size, $d_{k+1,k}$, can be obtained by the operation m_{k+1}/m_k for all values of k (Eq. (3.10)).

Applying the moment transformation of Eq. (3.7) to the PBE depicted in Eq. (3.1), the *moment-transport equation* is obtained in Eq. (3.11). The dependencies on time, phase, and physical space have been neglected for simplicity:

$$\begin{aligned} \frac{\partial m_{\mathbf{k}}}{\partial t} + \nabla_{\mathbf{x}} \cdot (\mathbf{u_p} m_{\mathbf{k}}) - \nabla_{\mathbf{x}} \cdot [D \nabla_{\mathbf{x}} m_{\mathbf{k}}] = \\ - \int_{\Omega_\xi} (\xi_1^{k_1} ... \xi_M^{k_M}) \nabla_{\boldsymbol{\xi}} \cdot (\dot{\boldsymbol{\xi}} n)\,\mathrm{d}\boldsymbol{\xi} + \int_{\Omega_\xi} (\xi_1^{k_1} ... \xi_M^{k_M}) h\,\mathrm{d}\boldsymbol{\xi}. \end{aligned} \tag{3.11}$$

In moments-based solution methods, the primary objective therefore is to solve the moments-transport equation and to subsequently reconstruct the NDF from the computed moments. This procedure is often referred to as *moment inversion*, in which a reconstructed NDF, n^*, is obtained.

This n^* does not exactly correspond to the original NDF, but to one which shares its same moments. An essential aspect to notice from Eq. (3.11) is that, while the terms on the LHS depend only on $m_{\mathbf{k}}$ (provided that $\mathbf{u_p}$ is known), the terms on the RHS are dependent on the NDF ($h(\boldsymbol{\xi}, \mathbf{x}, t)$ functions are usually written in terms of $n(\boldsymbol{\xi}, \mathbf{x}, t)$) and cannot be expressed in terms of the moments unless other simplifications are made, such as assuming that $\dot{\boldsymbol{\xi}}$ is independent of $\boldsymbol{\xi}$. This gives rise to the moment closure problem, which consists of finding approximations to all the terms on the RHS.

Quadrature-based methods of moments, QBMOM, are a set of methods and algorithms based on a quadrature approximation of the NDF to tackle the closure problem. An overview of some of the existing QBMOM can be found in Yuan [328]. The quadrature method of moments, QMOM, originally proposed by McGraw [194], is centred around the approximation of the NDF by a summation of Dirac delta functions, as illustrated in Eq. (3.12). From now on, unless stated otherwise, the NDF will be considered univariate with an internal coordinate ξ. A rigorous derivation and description of QMOM can be found in Marchisio et al. [187]. Here, only a few characteristics of the method that are relevant to this project are provided.

$$n(\xi, \mathbf{x}, t) \approx \sum_{i=1}^{N} w_i(\mathbf{x}, t)\delta(\xi - \xi_i(\mathbf{x}, t)) \quad s.t. \quad m_k(\mathbf{x}, t) \approx \sum_{i=1}^{N} w_i(\mathbf{x}, t)\xi_i^k(\mathbf{x}, t), \tag{3.12}$$

where w_i, ξ_i, and N correspond to the weights, the abscissas, and the number of nodes of the quadrature, respectively, and $\delta(\xi - \xi_i)$ is a Dirac delta function. By applying this quadrature approximation, the problem is reduced to finding the N weights and the N abscissas. A quadrature approximation of order N will be sufficient to calculate the first $2N$ moments [186]. That is, a set of $\{m_k\}$ with $k = [0, 2N - 1]$.

The determination of the weights and abscissas in the context of QMOM is not trivial and has also been the subject of extensive research, resulting in multiple algorithms being proposed over the years. The rigorous mathematical underpinnings and detailed derivations associated with these moment-inversion algorithms are outside the scope of this work, but can be found in Marchisio et al. [187]. In chapter 4, the moment inversion is achieved by employing the Wheeler algorithm [312], which leverages the fact that the nodes of the quadrature correspond to the zeros of a set of polynomials, $\{P_0(\xi), P_1(\xi), ..., P_\alpha(\xi), ...\}$ with $P_\alpha(\xi) = k_{\alpha,0}x^\alpha + k_{\alpha,1}x^{\alpha-1} + ... + k_{\alpha,\alpha}$, which are orthogonal within Ω_ξ with respect to the NDF. Three consecutive polynomials can be related with a recurrence formula of the form $P_{\alpha+1}(\xi) = (\xi - a_\alpha)P_\alpha(\xi) - b_\alpha P_{\alpha-1}(\xi)$, where $\alpha = 0, 1, 2, ...$, $P_{-1}(\xi) \equiv 0$, and $P_0(\xi) \equiv 1$. Knowledge of these recurrence coefficients facilitates the computation of orthogonal polynomial roots, thereby determining the nodes or abscissas of the quadrature [216].

Irrespective of the specific moment-inversion algorithm employed, the computed nodes and abscissas must satisfy three fundamental conditions, as per the definition of an NDF [187]:

1. **positivity condition:** The reconstructed NDF must be positive for all values of its independent variables (time, phase, and physical space)
2. **realisability condition:** The reconstructed NDF must be non-zero only for realisable values of the internal coordinates. That is, only for physically-possible values
3. **extendibility condition:** The algorithm should be capable of extending the order of the moments to an arbitrary order. The reconstructed NDF should converge to the real NDF as k goes to infinity

As will be elaborated upon in chapter 4, this thesis employs a univariate NDF with particle size $L = [0, \infty]$ as the only internal coordinate. In consideration of this, a generic equation governing the moments set that describes the system discussed in chapter 4 is derived from the general expression of Eq. (3.11) as follows [187, 216]:

$$\begin{aligned} \frac{\partial m_k(\mathbf{x},t)}{\partial t} + \nabla_{\mathbf{x}} \cdot [\mathbf{u_p}\, m_k(\mathbf{x},t)] - \nabla_{\mathbf{x}} \cdot [D(L)\nabla_{\mathbf{x}} m_k(\mathbf{x},t)] = \\ k \int_0^{\infty} L^{k-1} G(L) n(L,\mathbf{x},t)\, \mathrm{d}L + \mathcal{B}(L)^{agg} - \mathcal{D}(L)^{agg} + \mathcal{B}(L)^{bk} - \mathcal{D}(L)^{bk} + \mathcal{N}. \end{aligned} \tag{3.13}$$

In the above, $G(L) = \dot{L} = \mathrm{d}L/\mathrm{d}t$ denotes the growth rate; $\mathcal{B}$ and $\mathcal{D}$ represent the aggregation/breakup birth and death functions, respectively, which are modified from Eqs. (3.3) - (3.6) through the application of the moment transformation; and $\mathcal{N}$ signifies the transformed nucleation term. The specific mathematical formulations used to model nucleation, growth, agglomeration, diffusion, and breakup, along with the application of the quadrature approximation (Eq. (3.12)) to Eq. (3.13), are comprehensively detailed in Chapter 4.

Figure 3.2 presents an overview of the logic behind employing a mesoscale description to model polydisperse multiphase flows, the formulation of the PBE and its solution via the QMOM. In a mesoscale description using PBM, the disperse phase is conceptualised as a population characterised by a given NDF, which represents the distribution of the population across various properties over both time and physical space. The PBE, a continuity equation written in terms of the NDF, can be solved through multiple approaches oftentimes computationally expensive as the domain of the internal variables is large. QBMOMs apply moment transformations to the PBE in order to reduce the equations set to just a few equations in terms of lower-order moments, aiming to alleviate computational complexity. One major implication and assumption of QBMOM is that a reconstructed NDF, n^*, can be obtained from the set of computed moments. This n^* must adhere to the criteria outlined by the NDF definition. Namely, n^* must be non-negative and realisable. QMOM resolves the closure problem that arises from the moment transformation of the PBE by approximating the NDF as a summation of Dirac delta functions with N nodes (N weights and N abscissas). Consequently, the task shifts from directly solving for the NDF in the PBE to determining the appropriate weights and abscissas, defining the moment set, and subsequently reconstructing the NDF.

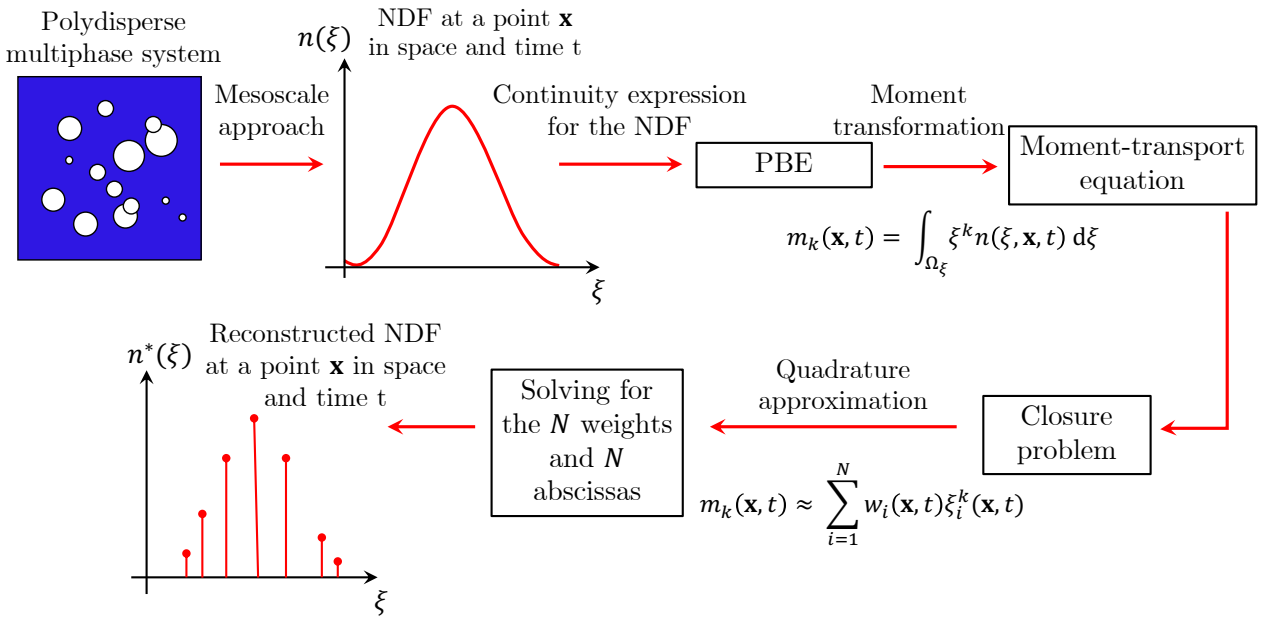

Figure 3.2: Outline of a mesoscale description of a polydisperse multiphase system using PBM: The population is described by an NDF, for which a continuity statement can be written, leading to the PBE, Eq. (3.1). Applying the moment transformation, Eq. (3.7), to the PBE, a series of unclosed transport equations for the first k moments is obtained in Eq. (3.11). QMOM circumvents the closure problem by applying a Gaussian quadrature approximation, Eq. (3.12), whereby solving for N nodes and N abscissas permits the reconstruction of the NDF

The conceptual illustration of the mesoscale and PBM modelling concepts elucidated above serves as an introduction to the modelling framework proposed in chapter 4 to inspect the dynamics of AgNPs synthesised in micro- and well-mixed reactors. This chapter provides a comprehensive overview of the framework's methodology, detailing the specific models for nucleation, growth (advection in phase space), diffusion, and agglomeration that underpin the moments transport equation presented in Eq. (3.11). Furthermore, this methodology outlines the novel approach proposed in this thesis for coupling PBM with CFD single-phase multi-species flow equations to model reduction-based systems in open-flow geometries, where mixing phenomena exert a significant influence on the system.

3.3 High-fidelity CFD methods for interfacial phenomena with surfactants

The following section presents a summary of the most relevant numerical methods and theory associated with a purely macroscopic depiction of multiphase systems via high-fidelity CFD simulations. Topics covered include the Navier-Stokes equations, surface tension phenomena, diverse methodologies proposed over time for modelling interfacial flows, the influence of surface-active contaminants on the governing equations, and the Level Contour Reconstruction Method. The latter method serves as the cornerstone of the modelling approach adopted in chapters 5 and 6.

3.3.1 A brief introduction to interfacial fluid mechanics

3.3.1.1 General principles and conservation equations

Three fundamental principles underpin the derivation of the governing equations describing multiphase flows with interfaces [290, 29]:

- **the continuum hypothesis**: fluids are conceptualised as continuous entities rather than discrete molecules. This assumption allows for the approximation of the fluid properties (e.g., density and viscosity) as smoothed average functions without accounting for the large molecular fluctuations that take place at small scales. It also facilitates the derivation of equations of motion that remain independent of the fluid's molecular structure
- **the sharp interfaces hypothesis**: this hypothesis leads to a sharp separation (infinitesimally thin interface) between immiscible fluids or thermodynamic phases of different material properties
- **the neglect of intermolecular forces**: by neglecting intermolecular forces, this principle simplifies the representation of forces acting on the fluid to solely body and surface forces; it circumvents the need to explicitly account for all potential intermolecular forces within the system. Those forces which play an important role in the system's dynamics, Van der Waals forces for instance, are included in the model by considering their most important effect, capillarity

In addition to the assumptions of continuity, sharp interfaces, and the non-consideration of molecular forces, this thesis further assumes that the systems involved are isothermal, Newtonian, and fully isotropic. These assumptions imply that the energy conservation equation is excluded, that viscosity remains unaffected by variations in shear rate, and that the fluid's properties are uniform in space.

Drawing upon the above principles, conservation equations for mass and momentum can be formulated in integral form with respect to a stationary reference frame encompassing a defined volume, V, and surrounded by a surface, S, amidst a velocity field, $\mathbf{u}(\mathbf{x}, t)$ (refer to figure 3.3(a)). Within this context, changes in mass inside V arise only due to the inflow and outflow across its surface element, $\mathrm{d}s$, with an outward normal vector, $\mathbf{n}$. This statement, which is articulated in integral form in Eq. (3.14), transforms into Eq. (3.15) upon application of the divergence theorem and taking into account that V is fixed in space [290, 29]; the latter equation further transforms into Eq. (3.16) for incompressible flows:

$$\frac{\mathrm{d}}{\mathrm{d}t}\int_V \rho \,\mathrm{d}v = -\oint_S \rho(\mathbf{u}\cdot\mathbf{n})\,\mathrm{d}s, \tag{3.14}$$

$$\frac{\partial \rho}{\partial t} + \nabla\cdot(\rho\mathbf{u}) = 0, \tag{3.15}$$

$$\nabla\cdot\mathbf{u} = 0. \tag{3.16}$$

At the heart of the momentum equation lies the momentum-conservation principle, which dictates that the rate of momentum change in V must be equal to the total momentum flux traversing through S plus the net forces exerted on V, corresponding to the net body and surface forces [324]. This statement is written in integral form in Eq. (3.17), which transitions into Eq. (3.18) through application of the divergence theorem [290, 29]:

$$\frac{\mathrm{d}}{\mathrm{d}t}\int_V \rho\mathbf{u} \,\mathrm{d}v = -\oint_S \rho\mathbf{u}(\mathbf{u}\cdot\mathbf{n})\,\mathrm{d}s + \int_V \mathbf{f_b}\,\mathrm{d}v + \oint_S \mathbf{n}\cdot\mathbf{T}\,\mathrm{d}s, \tag{3.17}$$

$$\frac{\partial \rho\mathbf{u}}{\partial t} = -\nabla\cdot(\rho\mathbf{u}\mathbf{u}) + \mathbf{f_b} + \nabla\cdot\mathbf{T}. \tag{3.18}$$

In the above, the second-to-last and last terms on the RHS represent the body and surface forces, respectively. Here, $\mathbf{f_b} = \rho\mathbf{g}$ represents the gravitational body forces per unit volume, whereas $\mathbf{T}$ is a symmetric stress tensor, whose definition can be found in Eq. (3.19) for a Newtonian fluid and an incompressible isotropic flow [67].

$$\mathbf{T} = -p\mathbf{I} + 2\mu\mathbf{S}, \tag{3.19}$$

where $\mathbf{S} = \frac{1}{2}(\nabla\mathbf{u} + \nabla\mathbf{u}^{\mathrm{T}})$ is the rate-of-strain tensor, $\mathbf{I}$ is the unit tensor, p is pressure, and μ is the fluid's viscosity. Insightful discussions about the nature of the surface forces and the rate-of-strain tensor can be found in Bird et al. [36] and Batchelor [29].

3.3.1.2 Interfacial boundary conditions

Armed with a general understanding of macroscale modelling of multiphase flows, it is pertinent at this point to delineate the interface conditions that couple fluid motion for different phases with the dividing interface. These conditions encompass the continuity of velocity and stresses

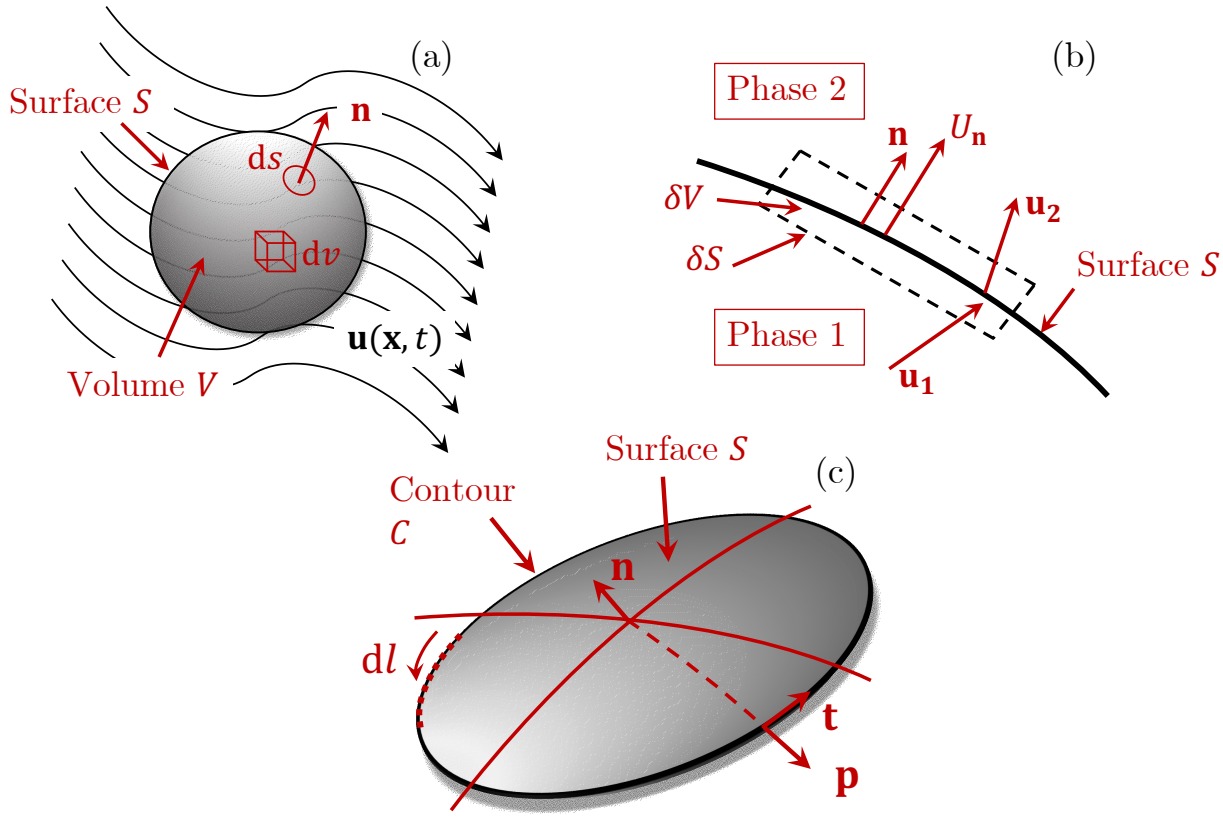

Figure 3.3: Schematic representation of a stationary control volume V, an infinitesimal control volume δV encompassing a portion of the interface, and a small surface element: (a) a control volume embedded into a velocity field, $\mathbf{u}(\mathbf{x}, t)$; (b) an infinitesimal δV with an interface separating two phases; (c) top view of a small surface element with a contour edge C from which a perpendicular unit vector $\mathbf{p}$ is defined, also referred to as binormal unit vector. Adapted from [290, 67]

across the interface in the presence of surface tension. Figure 3.3(b) depicts a thin control volume, δV, surrounding a section of the interface between two phases, "Phase 1" and "Phase 2", whose velocities are denoted by $\mathbf{u}_1$ and $\mathbf{u}_2$, respectively. The boundary of this control volume is given by δS, with $U_\mathrm{n} = \mathbf{u} \cdot \mathbf{n}$ being the interface normal velocity. A mass balance over a vanishingly small δV dictates a no-accumulation condition within our control volume, assuming no phase change occurs. Mathematically expressed as $\rho_1(\mathbf{u}_1 \cdot \mathbf{n} - U_\mathrm{n}) = \rho_2(\mathbf{u}_2 \cdot \mathbf{n} - U_\mathrm{n})$, this condition demands continuity in the normal velocities of the phases.

Regarding tangential velocities, it is a well-established fact that in fluids with finite viscosities and under typical operating conditions for engineering applications, there exists no relative motion between phases at the interface, thereby enforcing a no-slip condition [290]. Eqs. (3.20)-(3.21) portray the appropriate interfacial conditions governing normal and tangential velocity components [231, 290, 67]:

$$\textbf{Normal velocity (no-penetration)}: \quad \mathbf{u}_1 \cdot \mathbf{n} = \mathbf{u}_2 \cdot \mathbf{n}, \tag{3.20}$$

$$\textbf{Tangential velocity (no-slip)}: \ \mathbf{u}_1 \cdot \mathbf{t} = \mathbf{u}_2 \cdot \mathbf{t}. \tag{3.21}$$

A linear momentum balance over the control volume, akin to that shown in Eq. (3.17), but with an extra term representing surface tension forces, defined below in the classic expression of Eq. (3.22), and in the limit of vanishing δV, leads to the stress jump condition for interfacial flows, illustrated by Eq. (3.23) [67]:

$$\mathbf{f}_\sigma = \sigma\kappa\mathbf{n} + \nabla_s\sigma, \tag{3.22}$$

$$\mathbf{n} \cdot [\mathbf{T}_1 - \mathbf{T}_2] = \sigma\kappa\mathbf{n} + \nabla_s\sigma. \tag{3.23}$$

In the preceding discussion, σ represents surface tension, κ twice the mean interface curvature, and $\nabla_s = (\mathbf{I} - \mathbf{nn}) \cdot \nabla$ signifies the surface gradient operator.

From a mechanical standpoint, the surface tension term in the Navier-Stokes equation represents the forces per unit length acting perpendicularly on any line segment in the surface. Figure 3.3(c) showcases the top view of a small surface element surrounded by a contour line C, from which a unit vector $\mathbf{p}$, perpendicular to the edge of the element and tangential to the interface, can be defined. Surface tension forces can be conceived as generating "pulling" forces per unit length in the direction of $\mathbf{p}$, amounting to $\sigma\mathbf{p}$, and enabling the stretching of the interface. These forces can also be expressed as $\mathbf{T}_s^\sigma \cdot \mathbf{p}$, where $\mathbf{T}_s^\sigma$ is the surface tension tensor, defined as $\mathbf{T}_s^\sigma = \sigma\mathbf{I}_s$. Here, $\mathbf{I}_s = (\mathbf{I} - \mathbf{nn})$ represents the tangential projection of the 3-D identity tensor [290, 67].

By constructing an integral of $\mathbf{T}_s^\sigma \cdot \mathbf{p}$ over the entire interface edge line C, one can find the total "pulling" force exerted on a surface element, as depicted in Eq. (3.24) [290]:

$$\delta\mathbf{f}_\sigma = \oint_C \mathbf{T}_s^\sigma \cdot \mathbf{p} \ \mathrm{d}l = \int_S \nabla_s \cdot \mathbf{T}_s^\sigma \ \mathrm{d}s. \tag{3.24}$$

Taking the limit of the above equation as the surface area is shrunk to a singular point, a working definition of surface force per unit area arises in Eq. (3.25):

$$\mathbf{f}_\sigma = \nabla \cdot \mathbf{T}_s^\sigma = \nabla \cdot \sigma\mathbf{I}_s = \sigma\nabla_s \cdot \mathbf{I}_s + \mathbf{I}_s \cdot \nabla_s\sigma. \tag{3.25}$$

Since $\nabla_s \cdot \mathbf{I}_s = -\mathbf{n}\nabla_s \cdot \mathbf{n} \equiv \mathbf{n}\kappa$, and $\mathbf{I}_s \cdot \nabla_s\sigma = \nabla_s\sigma$, Eq. (3.22) is recovered from Eq. (3.25) [289].

Conceptually, the first term on the RHS of Eq. (3.22) constitutes the normal forces acting upon the interface due to the average local surface tension. These forces become negligible in fully planar interfaces. The second term symbolises tangential forces on the interface due to gradients in surface tension, which can arise from temperature variations or the non-uniform concentration of surface-active materials. The latter factor is an extensive focus of the present study. Although outside the current scope, it is appropriate to highlight that Eq. (3.23) represents a special case of a more general relation derived by Scriven [255]. This relation includes the effects of

dilatational and shear viscosity coefficients, which are a function of surfactant concentration and induce viscous resistance to interfacial deformation. These effects are known as surface viscosity effects and are further discussed in chapter 7 as a future research avenue.

3.3.1.3 The one fluid formulation

The interfacial jump conditions previously discussed rely on a distinct set of governing equations for each phase. This thesis, however, adopts the "one-fluid formulation," wherein a single set of governing equations is applied to the entire flow domain. This approach treats the multiple phases as a single fluid, with properties that change abruptly from one phase to another. To account for surface tension forces at the interface, singular terms (δ- functions) are added to the Navier-Stokes equations, which can be thought of as a counterpart to the jump conditions in the "multi-fluid" formulation.

The derivation of the governing equations in a one-fluid context is based on the same principles and considerations previously delineated, with the caveat that surface tension must be added as a body force to the momentum equation. For a given control volume that includes an interface, this body force is equal to an integral of the surface tension forces (see Eq. (3.22)) over the enclosed surface S, as shown in the LHS of Eq. (3.26):

$$\int_S \mathbf{f}_\sigma \, \mathrm{d}s = \int_{\delta V} \mathbf{f}_\sigma \delta_f \, \mathrm{d}v. \tag{3.26}$$

The volume integral shown in the RHS is obtained by employing a δ-function, defined as $\delta_f = \delta_f(\mathbf{x} - \mathbf{x}_f)$ [290]; $\delta_f(\mathbf{x} - \mathbf{x}_f)$ vanishes everywhere except for the interface, which is parameterised by $\mathbf{x}_f$. The above term is added to Eq. (3.18) by making use of the consideration that the volume integral can only be zero for an arbitrary control volume if the integrand is also zero [290], resulting in Eq. (3.27):

$$\frac{\partial \rho \mathbf{u}}{\partial t} + \nabla \cdot (\rho \mathbf{u}\mathbf{u}) = -\nabla p + \rho \mathbf{g} + \nabla \cdot [\mu(\nabla \mathbf{u} + \nabla \mathbf{u}^{\mathrm{T}})] + \mathbf{f}_\sigma \delta_f. \tag{3.27}$$

The above equation is the one-fluid version of Eq. (3.18), with the surface forces terms expanded for clarity. The final version of the momentum equation for an incompressible flow used in the present work is depicted in Eq. (3.28), which utilises the fact that $\mathbf{f}_\sigma \delta_f = \int_{A_e} \mathbf{f}_\sigma \delta(\mathbf{x} - \mathbf{x}_f) \, \mathrm{d}A$, where A_e corresponds to an interface surface element [290]:

$$\rho \left(\frac{\partial \mathbf{u}}{\partial t} + \mathbf{u} \cdot \nabla \mathbf{u} \right) = -\nabla p + \rho \mathbf{g} + \nabla \cdot [\mu(\nabla \mathbf{u} + \nabla \mathbf{u}^{\mathrm{T}})] + \int_{A_e} [\sigma \kappa \mathbf{n} + \nabla_s \sigma] \delta(\mathbf{x} - \mathbf{x}_f) \, \mathrm{d}A. \tag{3.28}$$

In biphasic flow, the abrupt change in the fluids' density and viscosity is governed by Eq. (3.29), which makes use of a Heaviside function, $\mathcal{H}(\mathbf{x}, t)$, defined as one in phase 1 and zero in

phase 2:

$$\begin{aligned}\rho\left(\mathbf{x},t\right) &= \rho_2 + (\rho_1 - \rho_2)\mathcal{H}(\mathbf{x},t),\\ \mu\left(\mathbf{x},t\right) &= \mu_2 + (\mu_1 - \mu_2)\mathcal{H}(\mathbf{x},t).\end{aligned} \tag{3.29}$$

3.3.2 Transport equations for soluble surfactant

Surfactant flows take centre stage in the present work in chapters 5 and 6. The mass and momentum interfacial equations described previously are coupled with transport equations governing the spatiotemporal evolution of surfactant concentration at the interface (which can be subjected to significant deformation and topological changes) and surfactant concentration at the bulk phase. The symbols utilised hereafter to refer to these variables are Γ (in surfactant mass or moles per unit area) and C (in surfactant mass or moles per unit volume); their transport is controlled by Eqs. (3.30)-(3.31), according to the well-established formulation by Stone [278], Eggleton and Stebe [82], Muradoglu and Tryggvason [199] (and references therein):

$$\frac{\partial \Gamma}{\partial t} + \nabla_s \cdot (\Gamma \mathbf{u}_\mathrm{t}) = D_s \nabla_s^2 \Gamma + S_\Gamma, \tag{3.30}$$

$$\frac{\partial C}{\partial t} + \mathbf{u} \cdot \nabla C = \nabla \cdot (D_c \nabla C), \tag{3.31}$$

$$\mathbf{u}_\mathrm{t} = (\mathbf{u}_s \cdot \mathbf{t})\mathbf{t}, \tag{3.32}$$

where $\mathbf{u}_\mathrm{t}$ in Eq. (3.32) represents the tangential projection of the surface velocity, $\mathbf{u}_s$, and $D_{s,c}$ correspond to the surfactant diffusion coefficients along the interface (s subscript) and in the bulk phase (c subscript). S_Γ denotes the source term modulating surfactant exchange between the interface and the bulk due to adsorption/desorption mechanisms; its definition is found in Eq. (3.33):

$$S_\Gamma = k_a C_s(\Gamma_\infty - \Gamma) - k_d \Gamma. \tag{3.33}$$

Here, $k_{a,d}$ correspond to the adsorption and desorption coefficients, Γ_∞ is the "maximum packing" or saturation concentration, and C_s is the bulk concentration of the region immediately adjacent to the interface; this formulation presumes that surfactant exchange between the bulk and interface can only transpire at these adjacent regions. The relationship between S_Γ and C is dictated by the condition expressed mathematically in Eq. (3.34):

$$\mathbf{n} \cdot \nabla C|_\mathrm{interface} = \frac{\partial C}{\partial \mathbf{n}}|_\mathrm{interface} = -\frac{S_\Gamma}{D_c}. \tag{3.34}$$

As mentioned in chapter 2, multiple equations of state have been proposed throughout the years to describe the variation of surface tension with surfactant concentration. This work makes use of the Langmuir expression, shown in Eq. (3.35) [184]:

$$\sigma(\Gamma) = \sigma_s - \Pi(\Gamma) = \sigma_s + \mathcal{R}T\Gamma_\infty \ln\left(1 - \frac{\Gamma}{\Gamma_\infty}\right), \tag{3.35}$$

where $\Pi(\Gamma)$ denotes surface pressure (see §2.2), σ_s designates surface tension in the absence of surface-active material, $\mathcal{R}$ is the ideal gas constant, and T is the absolute temperature.

By non-dimensionalising the Langmuir expression of Eq. (3.35) using σ_s, one arrives at Eq. (3.36):

$$\frac{\sigma(\Gamma)}{\sigma_s} = 1 + \beta_s \ln\left(1 - \frac{\Gamma}{\Gamma_\infty}\right), \tag{3.36}$$

where $\beta_s = \mathcal{R}T\Gamma_\infty/\sigma_s$. This dimensionless parameter will play a significant role in the results of chapters 5-6. Although the concept of β_s has predominantly been utilised in numerical studies [199, 213], it has also been employed in experimental research to characterise different surfactants at the interface. For example, $\beta_s \approx 0.1 - 0.18$ for SDS and $\beta_s \approx 0.1$ for Triton X-100 [126, 128].

The parameter β_s, often referred to as "surfactant elasticity" or "surfactant strength" [82, 199, 213], serves as a measure of how variations in surfactant concentration influence surface tension. It has multiple alternative interpretations and significantly impacts various quantities of interest in surfactant-laden systems, including the Marangoni modulus E_0, Marangoni stresses τ_m, and Marangoni number Ma (refer to §2.2 for further details on their physical meanings). By invoking the mathematical definition of E_0 (Eq. (2.6)) and applying Eq. (3.35), an important interpretation of β_s emerges in Eq. (3.37):

$$\frac{E_0}{\sigma_s} = \frac{\beta_s \Gamma}{\Gamma_\infty(1 - \Gamma/\Gamma_\infty)}. \tag{3.37}$$

The equation above illustrates that β_s is integral to the Marangoni modulus (or Marangoni elasticity, as it is sometimes termed [184]). For identical values of Γ, higher β_s values lead to greater resistance to interfacial compression, resulting in increased interfacial "rigidification" or "immobilisation" [184], as corroborated in previous numerical work [31, 58].

Marangoni stresses, whose definition can be found in Eq. (2.7), can also be written as a function of β_s such that:

$$\tau_m = -\frac{\beta_s \sigma_s}{\Gamma_\infty(1 - \Gamma/\Gamma_\infty)} \nabla_s \Gamma. \tag{3.38}$$

The above elucidates that β_s can also be interpreted as a modulator of the strength of Marangoni stresses in conjunction with spatial gradients of surfactant concentration. As explained in the introduction to Eq. (2.8) [184], Ma depends directly on E_0 and quantifies the rate at which Marangoni flows develop relative to convection. Since E_0 itself is a function of β_s (Eq. (3.37)), it becomes clear that β_s plays a critical role in influencing multiple surfactant-related parameters.

3.3.3 Numerical methods for interfacial flows

As elucidated in chapter 1, accurately predicting the location and intricate morphology of the interface is one of the primary challenges of modelling multiphase flows via macroscale CFD approaches. The presence of surface-active material and its interactions with the interface am-

plifies this complexity. This sub-section aims to offer a concise overview of the most prevalent numerical approaches proposed in the literature to model interfacial fluid dynamics problems. While a general outline of these methods is provided here, this is done mostly with the objective of contextualising the Level Contour Reconstruction Method, which is explained in detail in the following sub-section and heavily used in chapter 5 and 6. References are provided for those readers interested in diving deeper into other modelling strategies.

In broad terms, methods for computing the interface between immiscible fluids can be categorised into two main families: i) *interface-capturing*, and ii) *interface-tracking* methods. Popular interface capturing methods include volume of fluid (VOF), level-set, and the phase-field method, while well-known interface tracking methods comprise front tracking and immersed boundary method. These two families exhibit profound differences in modelling approaches, endowing each with specific advantages and disadvantages over the other. Interface capturing methods typically utilise an indicator function, which is directly advected with the fluid, to distinguish between phases [290, 324]. In contrast, interface tracking methods explicitly trace the interface by employing connected marker particles on the interface. Traditionally, the main difficulty of interface capturing methods is obtaining a sharp interface from which a well-defined curvature can be extracted and surface tension can be computed. Interface tracking methods, on the other hand, have typically had difficulties in handling complex interface topological changes, such as capillary breakup and coalescence[290, 289].

The volume of fluid method:

VOF stands as one of the most commonly-used techniques in the fluid mechanics community. It operates on a scalar colour function, denoted by ϕ, representing the volume fraction of one phase within a range of $[0, 1]$, and is passively advected by the flow according to: $\frac{\partial \phi}{\partial t} + \mathbf{u} \cdot \nabla \phi = 0$. In this formulation, a cell containing only the reference phase is characterised by $\phi = 1$, while $\phi = 0$ designates a cell exclusively filled with the other phase. Consequently, the interface is situated within cells exhibiting fractional values of ϕ (see figure 3.4(a)). Various approaches have been proposed to derive a sharp interface from ϕ, including the simple line interface calculation (SLIC) and the piece-wise linear interface calculation (PLIC). In the former, the interface is approximated by a sequence of line segments parallel to the grid coordinates. In the latter, it is reconstructed by lines (in 2-D) or planes (in 3-D) whose orientation is determined by the neighbouring cells [139, 12].

By their very nature, VOF methods are inherently conservative and lend themselves well for parallelisation. However, challenges arise in the discretisation of the convective term of the ϕ transport equation, leading to diffuse and smeared interfaces, thereby complicating the computation of surface tension [290, 324].

The level-set method:

This method, originally introduced in Osher and Sethian [214], employs a smooth distance function, $\psi(\mathbf{x}, t)$, which signifies the minimum distance to the interface. Typically, $\psi(\mathbf{x}, t) < 0$ represents one phase, $\psi(\mathbf{x}, t) > 0$ denotes the other, and $\psi(\mathbf{x}, t) = 0$ is the interface. Thus, the interface is represented by a contour of a smooth function (i.e., $\psi(\mathbf{x}, t) = const$, see figure 3.4(b)). In the absence of phase change, $\psi(\mathbf{x}, t)$ evolves in space and time similarly to ϕ in VOF. Unlike VOF, however, $\psi(\mathbf{x}, t)$ is a smooth function, facilitating the treatment of topological changes. Despite its advantages with respect to formulation simplicity, early implementations of the level-set method encountered considerable issues with enforcing mass conservation, compromising the entire solution [290]. Consequently, several pure level-set with higher-order convection schemes and hybrid VOF/level-set methods have been proposed to mitigate these challenges. For further insights into these methods, please refer to Sussman and Fatemi [279], Sussman and Puckett [280].

The front tracking method:

Front tracking employs a dual formulation wherein the interface is described by a piecewise linear (in 2-D) or triangular (in 3-D) Lagrangian grid, while the flow is characterised by a fixed Eulerian grid. The interface, also referred to as "front," comprises a series of interconnected marker points whose trajectories are dictated by the fluid's motion (refer to figure 3.4(c)). Two primary considerations underlie any front-tracking algorithm: maintaining the front as it stretches, deforms, or compresses, and ensuring accurate coupling of the interface's information with the fixed grid of the flow. This information transfer can be achieved via Peskin [222]'s immersed boundary method, whereby information from the Eulerian grid is interpolated to the front, and front information is distributed to the fixed grid via a smooth distribution function. This method is described in more detail in the following sub-section.

While front-tracking methods have traditionally yielded highly precise sub-grid predictions of interface morphology, they typically entail a higher computational expense compared to interface-capturing methods. One of the main drawbacks of front-tracking methods lies in their challenge in tracking coalescence or interfacial breakup events, in which markers need to be constantly deleted or added [290, 324].

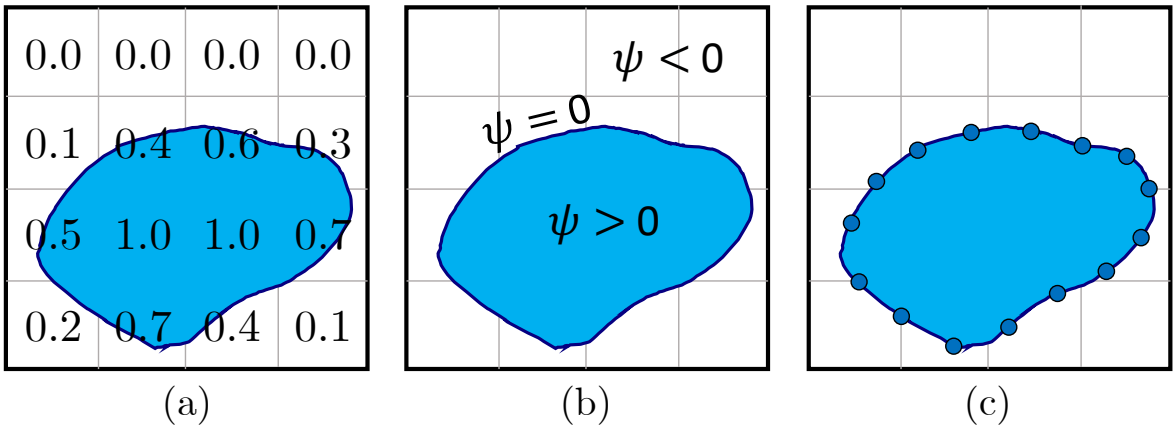

Figure 3.4: Schematic illustration of interface capturing and interface tracking methods, where the area in blue represents one phase, the area in white the other phase, and the blue curve the interface: (a) Volume of fluid (interface capturing); (b) Level-set (interface capturing); (c) Front tracking (interface tracking), showcasing the logically-connected markers on the interface

3.3.4 The Level Contour Reconstruction Method (LCRM)

The LCRM is a hybrid front-tracking/level-set technique designed to harness the strengths of both approaches while mitigating their respective drawbacks. Initially introduced by Shin and Juric [263] in 2002, LCRM has been significantly refined to address the complexities of surfactant-laden flows [268]. Notable enhancements include a more precise representation of surface tension to suppress parasitic currents [247], a higher-order reconstruction method to substantially reduce spurious currents [264], the calculation of an indicator function, $\mathcal{H}$, from a level-set function computed from the front [265], and adaptations for massively parallelised computations [267]. LCRM has proven successful in multiple scenarios of interest to the broader fluid mechanics community, including drop coalescence [58], ligament breakup [54], turbulent jets [56], microfluidics [128], falling film [30], elongated bubbles [31, 225] and bursting bubbles [55].

The fundamental distinction between LCRM and traditional front-tracking methods [289] lies in the use of Lagrangian marker points that are *physically-linked* rather than *logically-connected* to track the interface's geometry and motion. Logically-linked marker points are utilised in the original front tracking formulation as a way of "bookkeeping" or "keeping tabs" on neighbouring points' information. This bookkeeping of markers' connectivity requires a series of complex data operations, especially in the event of topological changes requiring the addition, merging, or deletion of marker points in 3-D [263, 265, 266, 267]. In an LCRM context, front elements are linked by their physical position at the interface rather than by logical connections. This feature allows LCRM-based computations to be easily parallelised and naturally handle topological transitions [267], as elaborated below.

The hybrid nature of LCRM is manifested in its dual representation of the interface: i) explicitly tracked marker points and ii) an indicator function, $\mathcal{H}$, whose isocontours denote the

interface within the fixed Eulerian grid, akin to traditional level-set methods. Consequently, LCRM can either generate a set of interface elements based on the isocontour of the indicator function or determine the indicator function using geometric information from the front elements. The latter was initially accomplished by solving the Poisson expression presented in Eqs. (3.39) - (3.40) [263]:

$$\nabla^2 \mathcal{H} = \nabla \cdot \mathbf{G}, \tag{3.39}$$

$$\mathbf{G} = \int_{A_e} \mathbf{n}\delta(\mathbf{x} - \mathbf{x}_f)\, dA, \tag{3.40}$$

where $\mathbf{G}$ contains geometric information computed directly on the interface [264]. In the revised formulation, the determination of the indicator function using geometric information from the front elements is achieved by employing a vector level-set distance function, ψ, as detailed by Shin and Juric [265].

In a typical simulation based on the LCRM formulation, the interface is explicitly tracked by Lagrangian marker points at each time step, following the traditional front tracking approach. From the positions of these markers, which are subsequently discarded, isocontour levels of the indicator function are drawn across each Eulerian grid cell to represent the interface in a level-set context. New marker points are then generated from these isocontours using either linear interpolation or a high order spline kernel [264]. As a consequence of this interpolation, neighbouring elements will share the same endpoint location and move with the same velocity, making them physically connected and eliminating the need for logical connections. The crucial interface reconstruction step with the indicator function is precisely what allows LCRM to naturally and robustly model interfacial singularities, whilst still retaining the accuracy and appropriate mass conservation provided by explicitly tracking the interface in a front tracking fashion. It avoids the above mentioned drawbacks of level-set since the distance function plays no part in advecting the interface. Instead, the Lagrangian elements of the interface are advected by integrating the expression in Eq. (3.41) [263, 265, 266, 267]:

$$\frac{\mathrm{d}\mathbf{x}_f}{\mathrm{d}t} = \mathbf{V}_f, \tag{3.41}$$

where $\mathbf{V}_f$ represents the interface velocity, interpolated from the velocity field in the Eulerian grid. This integration is accomplished using a second-order Runge-Kutta method. The exchange of information between the Eulerian and Lagrangian grids is facilitated by employing the immersed boundary method, as will be briefly explained in the following sub-section.

Figure 3.5 offers a conceptual representation of the revised LCRM process in both two and three dimensions. In the latter case, the Eulerian cells are subdivided into five tetrahedra, which are intersected with the isocontours of the distance function field to generate triangular elements, as presented in figure 3.5(b).

Given the critical role of complex topological changes at the interface—such as interface

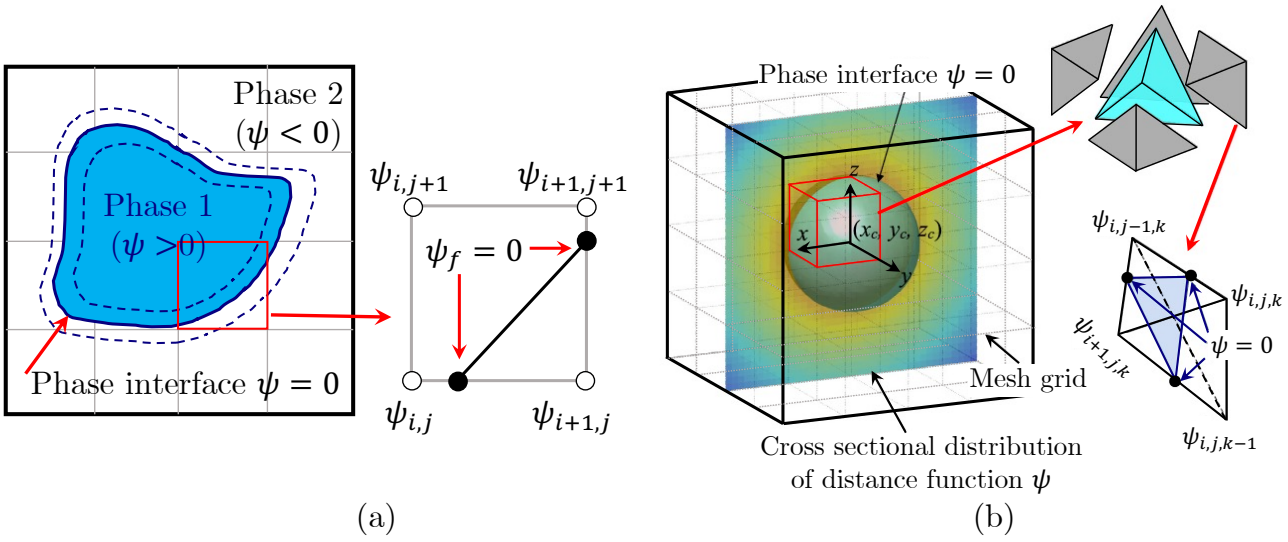

Figure 3.5: Schematic representation of the Level Contour Reconstruction Method, showcasing the definition of new marker points (represented by the black dots) from the reconstructed iso-contours of the distance function field ψ: (a) two-dimensional case; (b) three-dimensional case, in which the Eulerian cells are sub-divided into five tetrahedra and an intersection between them and the isocontour is located. Image adapted from Shin et al. [268, 267]

breakup—in the results presented in Chapters 5 and 6, the following paragraphs describe how these events are numerically handled within the context of the LCRM. For a comprehensive account of these intricacies, the reader is referred to Shin et al. [266]. As previously mentioned, the LCRM is based on a hybrid representation of the interface, utilising either Lagrangian grid elements, as in pure front-tracking, or an indicator function on the Eulerian grid, as in traditional level-set methods (see figure 3.5). The communication between these two grid representations is detailed in the following sub-sections. The implicit representation of the interface via a signed distance function, rather than a collection of Lagrangian markers, endows level-set methods with the ability to handle interfacial singularities easily and naturally without any special treatment. The LCRM leverages these features of level-set techniques by utilising the Eulerian representation of the interface to manage events of interface breakup and merging instead of relying on the Lagrangian representation. It is important to reiterate, however, that the level-set representation of the interface does not have any effect on the advection of the interface, for which the Lagrangian representation is used (see Eq. (3.41)).

Figure 3.6 schematically illustrates how the LCRM leverages the level-set representation of the interface to handle interfacial merging and breaking events. It subsequently reconstructs the Lagrangian front from the updated distance function, as depicted in figure 3.6(c-d). The correct capture of these complex topological changes, in accordance with universal pinch-off scaling laws, is detailed in Chapter 5 and in previous works [58, 54]. To finalize these notes on interface breakup and merging in the context of the present investigation, it is pertinent to mention that the numerical methods used in Chapters 5 and 6 impose a purely macroscopic representation of the system, wherein the continuum hypothesis is assumed to be valid (see §3.3.1.1), and molecular

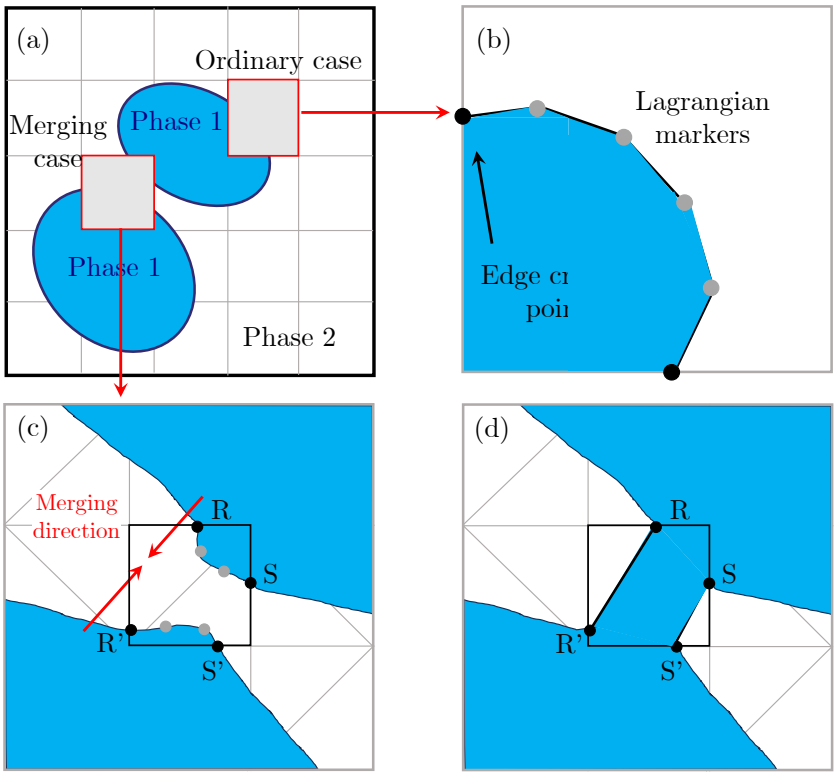

Figure 3.6: Schematic representation of interface merging/breakup in the context of the Level Contour Reconstruction Method in 2-D: (a) Eulerian representation of the interface, illustrating both an ordinary case and an interfacial merging event; (b) Lagrangian interfacial elements in an ordinary case, with black circles indicating elements at the edges of the Eulerian grid; (c) interface merging scenario, with edge Lagrangian elements labelled S and R; (d) resulting merged interface. Image adapted from Shin et al. [266]

interactions are neglected, even during interface breakup. Previous numerical investigations [146] of interface breakup via molecular dynamics simulations have reported qualitative agreement in the pinch-off behaviour between molecular and continuum calculations, suggesting minimal molecular effects on these phenomena despite their small-scale dynamics.

3.3.4.1 Information exchange between the Eulerian and Lagrangian grids: immersed boundary method

Communication between the stationary Eulerian grid and the moving Lagrangian grid in LCRM employs a methodology akin to traditional front-tracking methods, specifically leveraging Peskin's well-established immersed boundary method [222]. This technique approximates the infinitesimally thin interface using a smooth distribution function, which distributes source terms at the interface across multiple grid points [263]. Additionally, this distribution function facilitates the interpolation of flow variables from the Eulerian grid to the front [290]. To ensure stability and smoothness, the front is assigned a thickness approximately equal to one grid cell, as shown schematically in figure 3.5(a) [263].

To elucidate this information transfer, let us first define ϕ_f^l as any given variable at the front at a location l on the Lagrangian grid, $\mathbf{x}_f = (x_f^l, y_f^l, z_f^l)$. Conversely, $\phi_{i,j,k}$ represents a given variable located at $\mathbf{x} = (i, j, k)$ on the Eulerian grid, which consists of uniform cells of size $\Delta\mathbf{x} = (\Delta x, \Delta y, \Delta z)$. The aforementioned interpolation of Eulerian variables to the front is mathematically represented by a weighted summation of the variable's values at the grid points nearest to the front, as expressed in Eq. (3.42) [290, 289]:

$$\phi_f^l = \sum_{ijk} w_{i,j,k}^l \phi_{i,j,k}, \tag{3.42}$$

where $w_{i,j,k}^l$ is the weight of each Eulerian grid point with respect to l. These weights are defined to ensure that the interpolated quantity remains bounded by the corresponding grid values and matches the grid value if the marker location coincides with the grid point. Additionally, the sum of all weights with respect to a marker point must equal unity [290].

Information that exists on the interface (e.g., the surface tension body forces in the last term on the RHS of Eq. (3.28) or the geometric information of Eq. (3.40)) is transferred to the fixed Eulerian grid by constructing an approximation of the δ-functions on the fixed grid. Eq. (3.43) presents a mathematical expression for this approximation [263, 247]:

$$\phi_{i,j,k} = \sum_l \phi_f^l w_{i,j,k}^l \frac{\Delta A}{\Delta x \Delta y \Delta z}, \tag{3.43}$$

where ΔA denotes the area of the interface element located at l. From this approximating procedure it is required that the interface quantity is conserved in the transfer process. The accuracy of such procedure is intimately related to the weighting function selected, which is typically defined as a product of one-dimensional distribution functions, as presented in Eq. (3.44):

$$w_{i,j,k}^l = d(r_x) d(r_y) d(r_z). \tag{3.44}$$

In the equation above, r_x, r_y, and r_z are the scaled distances between the front and the grid line in the x, y, and z directions, respectively. For instance, $r_x = (x_f^l/\Delta x) - i$. The expressions used in the present work for the distribution functions, $d(r)$, are those proposed by Peskin and McQueen [223], as shown in Eqs. (3.45) - (3.46), where r corresponds to r_x, r_y, or r_z:

$$d(r) = \begin{cases} d_1(r), & |r| \leq 1 \\ 1/2 - d_1(2 - |r|), & 1 < |r| < 2 \\ 0, & |r| \geq 2 \end{cases} \tag{3.45}$$

where,

$$d_1(r) = \frac{3 - 2|r| + \sqrt{1 + 4|r| - 4r^2}}{8}. \tag{3.46}$$

The above smoothing method has proven to be versatile and oftentimes more accurate than

other methods of calculating the weighting functions, such as area-based functions [290].

3.3.4.2 Solution of the Navier-Stokes equations

The following two sub-sections succinctly delineate the solution methods for the governing equations utilised in the present work in chapters 5 and 6. The Navier-Stokes equations, along with the equations governing surfactant dynamics are formulated and integrated within the LCRM framework into the CFD code BLUE, written in Fortran 2008, and parallelised via a domain decomposition strategy with message passing interface (MPI) protocols. All details pertaining this code can be found in the series of publications by its authors [263, 247, 265, 266, 267, 268].

The primary flow variables, $\mathbf{u}$ and p, are computed on the aforementioned fixed Eulerian grid via Chorin's [52] projection method in a staggered mesh. A short illustrative example of the essence of this method is presented below for a first-order temporal discretisation. As noted in the following paragraphs, the actual discretisation used in this work corresponds to a second-order method. Eq. (3.47) shows a discretised version of Eq. (3.28) employing a first-order, explicit, forward-time discretisation [290, 289, 87]:

$$\frac{\mathbf{u}^{n+1}-\mathbf{u}^{n}}{\Delta t}=\frac{1}{\rho^{n+1}}(\mathbf{A}^{n}+\mathbf{F}^{n})-\frac{1}{\rho^{n+1}}\nabla_{h}\,p. \tag{3.47}$$

In the above equation, $\mathbf{A}$ encompasses the diffusive, convective, and gravitational terms. Conversely, $\mathbf{F}$ represents the surface tension term; Δt is the size of a time-step, the subscript h implies a discretised spacial operator, and the superscripts n and $n+1$ identify the beginning and end of the step, respectively. The projection method operates on the idea that the incompressibility of the flow allows us to divide the momentum equation into two parts: a predictor step, and a projection step. These are encapsulated in Eq. (3.48) - (3.49) [263]:

$$\frac{\mathbf{u}^{*}-\mathbf{u}^{n}}{\Delta t}=\frac{1}{\rho^{n+1}}(\mathbf{A}^{n}+\mathbf{F}^{n}), \tag{3.48}$$

$$\frac{\mathbf{u}^{n+1}-\mathbf{u}^{*}}{\Delta t}=-\frac{1}{\rho^{n+1}}\nabla_{h}\,p. \tag{3.49}$$

In the predictor step, a temporary velocity, $\mathbf{u}^{*}$, is calculated by neglecting the pressure term. In the projection step, the effect of pressure is added to calculate the final velocity at the new time-step. The pressure is found by demanding that the velocity at the new time-step be divergence-free (i.e., $\nabla_{h}\cdot\mathbf{u}^{n+1}=0$). Taking the divergence of the expression in Eq. (3.49) yields Eq. (3.50), a Poisson equation for the pressure:

$$\nabla_{h}\cdot\left(\frac{1}{\rho^{n+1}}\nabla_{h}\;p\right)=\frac{\nabla_{h}\cdot\mathbf{u}^{*}}{\Delta t}. \tag{3.50}$$

Once the pressure has been found, we revert to Eq. (3.49) to find the final projected velocity at $n+1$. The discontinuous nature of the densities involved in the two-phase computations

of this work complicates the solution of the pressure's elliptic Poisson equation via traditional fast Poisson solvers [267]. The code BLUE incorporates a modified iterative multigrid solver based on the work of Kwak and Lee [156]. This implementation extends the computational reach to scenarios involving density ratios as high as $O(10^5)$. The code also integrates a standard Generalised Minimal Residual (GMRES) solver to implicitly solve for the viscous contributions to the velocity vector field. The reader is advised to refer to Shin et al. [267] for further details on this multigrid/GMRES algorithm implementation in a highly parallelised context.

Spatial discretisation, temporal discretisation, and time-stepping:

The spatial discretisation of both the Navier-Stokes equations and the bulk surfactant concentration (Eq. (3.31)) is conducted using the well-established Marker-and-Cell (MAC) method of Harlow and Welch [105] in a staggered grid. In such grid arrangement, vector variables (velocity for instance) are stored at the half-point of the cell faces whilst scalar variables and material properties, such as pressure, density and bulk surfactant concentration, are found at the cell centres. By virtue of having separate grid locations for different variables, staggered grids are endowed with tighter variable coupling, thereby reducing the risk of pressure-velocity decoupling [290]. Additionally, velocity fluxes in staggered grids are more naturally aligned with the location of velocity in the grid, leading to enhanced solution accuracy and stability compared to collocated arrangements [87].

All spatial derivatives, except for the nonlinear convective term, are approximated using a standard second-order central differences scheme. The convective terms (see the second term on the LHS of Eq. (3.28) and (3.31)) are discretised with a second-order Essentially Non-Oscillatory (ENO) scheme [267]. Additional details about the ENO scheme can be found in Shu and Oshert [269]. For temporal discretisation, the simulations in chapters 5 and 6 employ a second-order Gear method [306] for all equations, with an implicit solution for the viscous terms.

Stability of the simulations performed herein is secured by enforcing an adaptive time-step criterion involving multiple reference time-steps, as expressed in Eq. (3.51):

$$\Delta t = \min\left\{ \Delta t_{\text{cap}} = \frac{1}{2}\sqrt{\frac{(\rho_l+\rho_g)\Delta x_{\text{min}}^3}{\pi\sigma_s}},\quad \Delta t_{\text{vis}} = \frac{\rho_g \Delta x_{\text{min}}^2}{6\mu_l},\quad \Delta t_{\text{CFL}} = \frac{\Delta x_{\text{min}}}{|u_{\text{max}}|},\right.$$
$$\left. \Delta t_{\text{int}} = \frac{\Delta x_{\text{min}}}{|V_{\text{int,max}}|} \right\}, \tag{3.51}$$

where, from left to right, the time-steps relate to capillarity, viscosity, Courant-Friedrichs-Lewy condition, and interface velocity; Δx_{min} corresponds to the minimum cell size in the domain, u_{max} is the maximum fluid velocity, and $V_{\text{int,max}}$ is the maximum interface velocity; the subscripts l and g stand for the liquid and gaseous phase, respectively. The limiting time-step was found to be case-dependent in the simulations of chapters 5 and 6.

3.3.4.3 Solution of interface surfactant concentration equation

This sub-section provides an overview of the particularities revolving around the solution method for interface surfactant concentration (see Eq. (3.30)). While the most relevant details are presented here, a comprehensive description of the surfactant solution methods implemented in the code BLUE, which are partially based on the work of Muradoglu and Tryggvason [199], can be found in Shin et al. [268].

Let us begin the solution description with the LHS of Eq. (3.30), which, discretised using the Leibniz formula reads as:

$$\int_{A_e} \left[\frac{\partial \Gamma}{\partial t} + \nabla_s \cdot (\Gamma \mathbf{u}_t) \right] \mathrm{d}A \approx \frac{(\Gamma A_e)^{n+1} - (\Gamma A_e)^n}{\Delta t}. \tag{3.52}$$

Here, A_e represents the area of a triangular element e in the Lagrangian grid, where Γ resides; the n and $n+1$ superscripts represent the present and next time-steps, respectively. The second term on the LHS of the above equation does not contribute to the RHS of Eq. (3.52) given that $\int_{A_e} \nabla_s \cdot (\Gamma \mathbf{u}_t)\, \mathrm{d}A = \int_C \Gamma \mathbf{u}_t \cdot \mathbf{p}\, \mathrm{d}s$ and the tangential and binormal vectors are orthogonal. The RHS of Eq. (3.30), comprising the diffusive and source terms, is similarly discretised as:

$$\int_{A_e} (D_s \nabla_s^2\, \Gamma + S_\Gamma)\, \mathrm{d}A = \delta\Gamma^n_{D_e} + (S_\Gamma A_e)^n, \tag{3.53}$$

where $\delta\Gamma^n_D$ represents the discrete version of the diffusion term, whose definition is shown in Eq. (3.54), following Muradoglu and Tryggvason [199]'s formulation:

$$\delta\Gamma^n_{D_e} = D_s \int_{A_e} \nabla_s^2\, \Gamma\, \mathrm{d}A = D_s \int_C \nabla_s\, \Gamma \cdot \mathbf{p}\, \mathrm{d}s. \tag{3.54}$$

Similar to the schematic of figure 3.3(c) in §3.3.1.2 for a general case, C in this context represents a closed contour of an interface element and $\mathbf{p}$ is a unit vector perpendicular to the normal and tangential vectors.

The temporal integration of the aforementioned equations is straightforward for all terms, with the notable exception of the diffusion term. The challenge with this term lies in the surface gradient operator applied to Γ, $\nabla_s\Gamma$, which is highly dependent on the interface geometry, necessitating a comprehensive description of the Lagrangian interface [268]. In traditional front tracking, this operator is derived by leveraging the connectivity information between markers. Nevertheless, in LCRM, a bespoke method is required to compute the surface gradients, ensuring compatibility with both the Lagrangian and Eulerian grids. This method is elaborated upon in the following paragraphs.

Figure 3.7(a) pictures a triangular interface element with vertices ①, ②, and ③, and a normal-pointing vector $\mathbf{n}_f$ at the element's centre, where the element's Γ value is stored, Γ_f. For each edge line ($\overline{①②}$, $\overline{②③}$, $\overline{③①}$), a normal, tangential, and binormal vector is defined at

the edge's centre point, as marked in the figure in blue, green, and orange, respectively. At the mid-point of each edge, interpolated values of Γ from Γ_f are obtained, which are used to calculate the surface gradient. The diffusion line integral on the RHS of Eq. (3.54) can be approximated as the discrete sum over the three edges of the interfacial element, as illustrated in Eq. (3.55) [268]:

$$\begin{aligned} \delta\Gamma^n_{D_e} = D_s \sum_{k=1}^{3} (\nabla_s\Gamma)_k \cdot \mathbf{p}_k \ \Delta s_k = \\ D_s\{(\nabla_s\Gamma)_{12} \cdot \mathbf{p}_{12} \ \Delta s_{12} + (\nabla_s\Gamma)_{23} \cdot \mathbf{p}_{23} \ \Delta s_{23} + (\nabla_s\Gamma)_{31} \cdot \mathbf{p}_{31} \ \Delta s_{31}\} = \\ D_s\{(\nabla_s\Gamma)_{\mathbf{p},12} \ \Delta s_{12} + (\nabla_s\Gamma)_{\mathbf{p},23} \ \Delta s_{23} + (\nabla_s\Gamma)_{\mathbf{p},31} \ \Delta s_{31}\}. \end{aligned} \tag{3.55}$$

In the above, the Δs_k symbols represent the edge length of the k^{th} edge and the $(\nabla_s\Gamma)_{\mathbf{p},k}$ symbols the surface gradients in the $\mathbf{p}$ direction, which are represented in figure 3.7(b). These gradients are computed using the probing technique proposed in the work of Udaykumar et al. [294]. This technique incorporates a probing point defined at the edge's centre, from which a probing distance in the normal direction, here denoted as $\mathrm{d}l$, is constructed. The surface gradients in the binormal direction are then interpolated from the values on either side of the interface (represented by the subscripts *in* and *out*) over the probing distance, as exemplified in figure 3.7(c) for $(\nabla_s\Gamma)_{\mathbf{p},12}$; this interpolation is shown mathematically in Eq. (3.56):

$$(\nabla_s\Gamma)_{\mathbf{p},k} = \frac{\Gamma_{out} - \Gamma_{in}}{2\mathrm{d}l}, \tag{3.56}$$

where $\mathrm{d}l$ is of the order of one computational cell. As will become evident in §3.3.4.4, information about the Γ surface gradients in the tangential direction $\mathbf{t}$, $(\nabla_s\Gamma)_{\mathbf{t},k}$, are also required in order to compute the surface gradient of surface tension. These tangential gradients are interpolated in an analogous manner to their binormal counterparts, as depicted in Eq. (3.57), where the subscripts $left$ and $right$ represent the Γ values on either side of the probing point, as exemplified in figure 3.7(c) for $(\nabla_s\Gamma)_{\mathbf{t},23}$:

$$(\nabla_s\Gamma)_{\mathbf{t},k} = \frac{\Gamma_{right} - \Gamma_{left}}{2\mathrm{d}l}. \tag{3.57}$$

The above information (i.e., Γ_{left}, Γ_{right}, Γ_{in}, Γ_{out}, Γ_f) is stored in the moving Lagrangian grid. These quantities are readily transferred and distributed to the fixed Eulerian grid in the manner described in §3.3.4.1 via the immersed boundary method and by invoking Eq. (3.43). This process leverages the efficiency of parallel processing in Eulerian grids.

By collecting all discretised terms of the Γ governing equation (i.e., Eqs.(3.52) - (3.54)), one finally arrives at the updating expression for this variable, which is shown in its final form in Eq. (3.58):

$$\Gamma^{n+1} = \Gamma_n \left(\frac{A_e^n}{A_e^{n+1}} \right) + \Delta t \left[\frac{\delta\Gamma^n_{D_e}}{A_e^{n+1}} + S_\Gamma^n \right], \tag{3.58}$$

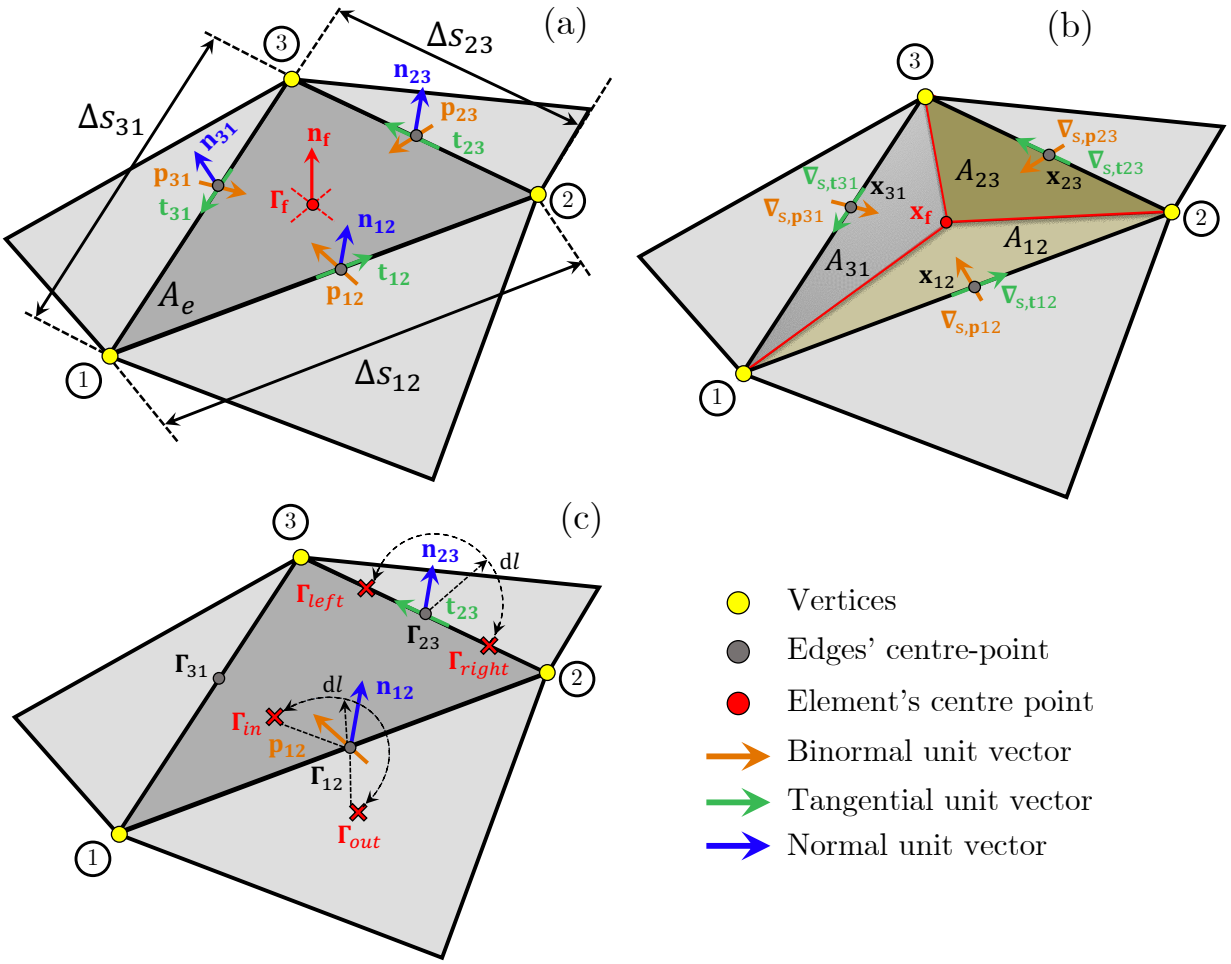

Figure 3.7: Representation of a triangular Lagrangian element of area A_e and its geometrical information: (a) interface normal, binormal, and tangential unit vectors, defined at the midpoint of each edge, element's corresponding Γ value, stored at the centre, and length of each edge; (b) surface gradient operators in the tangential and binormal directions; (c) example of probing method to approximate the tangential (utilising Γ_{left} and Γ_{right}) and binormal surface gradients (utilising Γ_{in} and Γ_{out}). Image adapted from Shin et al. [268]

where $\delta\Gamma^n_{D_e}$ is found via Eqs. (3.55) - (3.56).

3.3.4.4 Implementation of interfacial tension in the presence of surfactants

In the latest version of LCRM, the implementation of surface tension forces departs from the traditional front tracking method, where these forces are strictly calculated on the Lagrangian grid. Instead, LCRM employs a hybrid Eulerian-Lagrangian curvature formulation, which offers the significant advantage of markedly reducing the emergence of parasitic currents [247]. This formulation, expressed in Eq. (3.59), utilises a discrete curvature calculated on the Eulerian grid, κ_H, for the normal component of surface tension forces, $\mathbf{f}_{\sigma,\mathbf{n}}$ (refer to the penultimate term on

the RHS of Eq. (3.28)) [268]:

$$\mathbf{f}_{\sigma,\mathbf{n}} = \int_{A_e} \sigma\kappa\mathbf{n}\delta(\mathbf{x}-\mathbf{x}_f)\ \mathrm{d}A = \sigma\kappa_H\nabla\mathcal{H}, \tag{3.59}$$

where κ_H denotes twice the mean curvature. As previously mentioned, this curvature is computed on the moving Eulerian grid, but incorporates information from the Lagrangian grid, as depicted below in Eq. (3.60):

$$\sigma\kappa_H = \frac{\mathbf{F_L}\cdot\mathbf{G}}{\mathbf{G}\cdot\mathbf{G}}, \tag{3.60}$$

where,

$$\mathbf{F_L} = \int_{A_e} \sigma\kappa_f\mathbf{n}_f\delta(\mathbf{x}-\mathbf{x}_f)\ \mathrm{d}A, \tag{3.61}$$

κ_f and $\mathbf{n}_f$ represent twice the mean curvature and the normal vector obtained from the Lagrangian structure, respectively, and $\mathbf{G}$ was defined earlier in Eq. (3.40).

The aforementioned equations highlight the hybrid nature of the curvature formulation, where $\mathbf{F_L}$ represents the surface tension forces in a Lagrangian framework, and $\mathbf{G}$ functions a distribution mechanism. Both quantities are initially computed on the Lagrangian grid and subsequently projected onto the Eulerian grid using the immersed boundary method, as detailed in §3.3.4.1.

Attention now turns to the tangential component of the surface tension forces, denoted as $\mathbf{f}_{\sigma,s}$, defined in the final term on the RHS of Eq. (3.28) and reiterated here in Eq. (3.62). These tangential forces arise from variations in σ across the interface when surface-active materials are introduced. Since this term involves a surface gradient operator, it is advantageous to decompose it into its normal and binormal components, mirroring the approach used for the diffusion term in the Γ equation, as shown in Eq. (3.63) [268]:

$$\mathbf{f}_{\sigma,s} = \int_{A_e} \nabla_s\sigma\delta(\mathbf{x}-\mathbf{x}_f)\ \mathrm{d}A, \tag{3.62}$$

$$\nabla_s\sigma = (\nabla_s\sigma)_p\mathbf{p} + (\nabla_s\sigma)_t\mathbf{t}. \tag{3.63}$$

Following the account of how surface gradients in the tangential and binormal direction are approximated at the midpoint of the three edges of a Lagrangian element of §3.3.4.3 and associated discussion of figure 3.7, Eq. (3.64) presents a mathematical expression that permits us to compute the tangential component of surface tension forces as a weighted sum of all the edges' contributions and one third of the total element's area, A_k (see figure 3.7(b)):

$$\begin{aligned}\mathbf{f}_{\sigma,s} = {} & [(\nabla_s\sigma)_{\mathbf{p},12}\ \mathbf{p}_{12} + (\nabla_s\sigma)_{\mathbf{t},12}\ \mathbf{t}_{12}]\delta(\mathbf{x}-\mathbf{x}_{12})A_{12} + \\ & [(\nabla_s\sigma)_{\mathbf{p},23}\ \mathbf{p}_{23} + (\nabla_s\sigma)_{\mathbf{t},23}\ \mathbf{t}_{23}]\delta(\mathbf{x}-\mathbf{x}_{23})A_{23} + \\ & [(\nabla_s\sigma)_{\mathbf{p},31}\ \mathbf{p}_{31} + (\nabla_s\sigma)_{\mathbf{t},31}\ \mathbf{t}_{31}]\delta(\mathbf{x}-\mathbf{x}_{31})A_{31}.\end{aligned} \tag{3.64}$$

3.3.4.5 Sharp boundary method for bulk surfactant concentration: ghost nodes

Having thoroughly understood the solution procedure for interface surfactant concentration, as detailed in §3.3.4.3, we can now briefly delve into the solution method for the bulk surfactant concentration. As the reader may recall, Eq. (3.31) governs the transport of surfactant concentration in the bulk. This standard convection-diffusion equation is straightforward to solve, with the exception of the source term, Eqs. (3.33) - (3.34), which necessitates appropriate information exchange with Γ. In traditional formulations of surfactant-laden flows, such as those based on front tracking by Muradoglu and Tryggvason [199], the source term is incorporated into the C conservation equation using a Dirac distribution function at the interface. However, as Shin et al. [268] explains, this method demands a complex iterative approach to satisfy interface boundary conditions and is prone to under- and overshoots near the interface.

To circumvent the above mentioned challenges, the code BLUE utilises a ghost-type sharp energy method in which a number of "ghost" nodes are placed around the phase that does not contain surfactant (i.e., the gas phase in the present study, as seen in chapters 5 and 6). Consequently, the bulk concentration gradient is approximated via a first-order gradient, as expressed in Eq. (3.65):

$$\left.\frac{\partial C}{\partial \mathbf{n}}\right|_f = \frac{C_{\text{ghost}} - C_{\mathbf{x}_f}}{\mathrm{d}s_{\min}} = \frac{-S_\Gamma}{D_c}, \tag{3.65}$$

where C_{ghost} is the corresponding C value in the ghost node, $C_{\mathbf{x}_f}$ denotes surfactant concentration on the interface element, and $\mathrm{d}s_{\min}$ represents the minimum distance to the interface from the ghost node. The latter is computed during the creation of the distance function field (refer to §3.3.4). By combining Eq. (3.65) with the source term's definition in Eq. (3.33), we are finally able to derive a mathematical expression for the surfactant concentration at the ghost node, which is positioned in the vicinity of the interface;

$$C_{\text{ghost}} = C_{\mathbf{x}_f} - \frac{S_\Gamma}{D_c}\mathrm{d}s_{\min}. \tag{3.66}$$

The equation presented above concludes the overview of the high-fidelity CFD methods utilised in this investigation. It is important to emphasise that the authors of the BLUE code have rigorously benchmarked their implementation and solution of the equations governing surfactant transport. Detailed information on these benchmarking tests, which include scenarios such as an expanding drop and a stationary droplet with surfactant transport driven by diffusion [199], can be found in Shin et al. [268]. Validation tests specific to the case studies explored in this thesis are provided in each respective results chapter.

Chapter 4

Silver nanoparticles synthesis in microfluidic and well-mixed reactors: a PBM-CFD study

Contents

4.1 Motivation and overview 80

4.2 Problem formulation and summary of experimental dataset 81

4.2.1 Operating conditions in a T-junction microfluidic device 82

4.2.2 Measurements of silver ions concentration and PSD across the outlet channel in the T-junction device 83

4.2.3 Determination of the nucleation and growth constants according to the F-W two-step mechanism 84

4.3 Numerical methods and model description 85

4.3.1 Well-mixed reactor model formulation and initial code validation 85

4.3.1.1 Model implementation in open-source software and initial validation 87

4.3.2 Model extension in a T-junction microchannel 90

4.3.2.1 Governing equations 90

4.3.3 Simulation setup in a T-junction microchannel and mesh independence . 94

4.3.3.1 Boundary and initial conditions 94

4.3.3.2 Discretisation schemes 95

4.3.3.3 Mesh independence test 95

4.4 Results and discussion 99

4.4.1 Effect of pH and $[TC]_0$ on the synthesis of AgNPs in a well-mixed reactor 99

4.4.2 Parametric sweep of $k_2[A]_0/k_1$ in a well-mixed reactor 104

4.4.3 Synthesis of AgNPs in a T-junction microchannel 105

4.4.3.1 Precursor & consumption dynamics 105
4.4.3.2 Effect of hydrodynamics on the PSD of AgNPs 113
4.5 Concluding remarks 118

4.1 Motivation and overview

The literature review in §2.3 explored the state-of-the-art in AgNPs production methods, synthesis routes, applications, and mechanistic modelling. A critical conclusion from this review is that the final properties of the synthesised NPs are closely linked to the manufacturing method and its associated operating conditions. This reality often necessitates extensive experimental testing and design processes in order to synthesise AgNPs with properties tailored to specific applications. Recent review articles on AgNPs [203] conclude that the combination of microfluidics and numerical modelling is a promising approach for optimising nanoparticle production via chemical synthesis. As previously mentioned, the literature indicates that high-throughput experimental methods, such as microfluidics, offer better control over chemical reactions with fewer reagents and lower energy requirements [234]. Additionally, investigating AgNPs through computational modelling can provide valuable, often experimentally inaccessible information about the system. This approach enables comprehensive predictions of reaction outcomes while also helping to minimise the number of experiments and the consumption of materials and energy.

Numerous experimental and computational investigations have attempted to unravel the connections between operating parameters and the final properties of AgNPs for a multitude of applications. Despite these efforts, the field's understanding of the underlying phenomena that dictate a specific outcome remains incomplete and the means to reliably control the PSD in various synthesis environments elusive. For instance, and as detailed in §2.3, the mechanisms proposed in Watzky and Finke [309] (F-W two-step mechanism), Perala and Kumar [221], and Mozaffari et al. [197] to model NPs synthesis have been solely developed for batch reactors under the assumption of perfect mixing. This is completely opposed to the continuous-flow nature of microfluidics, whereby the reactants are initially segregated and mixing plays a major role in the overall process. Moreover, the available computational literature on NPs synthesis in microfluidic devices is, crucially, mainly based on precipitation and supersaturation-driven crystallisation processes [22, 21, 154, 253], which are entirely inconsistent with the reduction-based, low-saturation synthesis of AgNPs.

Motivated by the above remarks, this study proposes, for the first time, a comprehensive modelling framework based on population balance modelling and computational fluid dynamics (PBM-CFD) for extending the F-W two-step mechanism [309] (refer to figure 4.1(b)) to continuous flows in order to predict the PSD for the synthesis of AgNPs in microfluidic channels. Mixing, particles diffusion, agglomeration, and other non-negligible hydrodynamic phenomena

are all intertwined in the PBM-CFD model and directly linked to the reaction kinetics of reduction, nucleation, and growth. Through this framework—which represents a modelling novelty given that the present approach is based on a reduction-driven synthesis—, the effect of several operating conditions on the predicted particle size polydispersity is investigated. The proposed PBM-CFD model in the well-established open-source platform OpenQBMM [216]. The model was validated by an extensive set of experiments, which also provided kinetic constants for the simulations.

The synthesis process considered herein is based on a reduction protocol involving silver nitrate as precursor and a mixture of tannic acid/trisodium citrate as reducing/stabilising agents [133] in both a well-mixed batch reactor and a T-junction straight microchannel. A representation of reduction-based AgNPs production and the T-junction microchannel can be found in figure 4.1(a, c). The T-junction results suggest that the higher residence times involved in operations with lower flow rates are responsible for a cascade of kinetic/reactive and hydrodynamic events, unveiled by the simulations, that lead to higher outlet particle sizes and volume fraction of the particles in the dispersion. The simulation results also provide a characterisation of the radial heterogeneous concentration of particles and particle sizes across the channel typical of continuous-flow microfluidics. Limitations and advantages of the proposed modelling approach are discussed in the context of future lines of research.

The remainder of this chapter is organised as follows: §4.2 introduces the problem formulation and provides a concise overview of the experimental dataset used for validation. §4.3 presents a comprehensive description of the proposed model framework and formulation, including all governing equations, population balance parameters, solution methods, validation procedures, mesh resolution, and other relevant numerical considerations. The discussion of results begins in §4.4.1, focusing on the effects of pH and reactant concentration on the PSD in a well-mixed batch reactor. §4.4.3 extends this discussion to include findings from the T-junction microchannel, elucidating the impact of additional operating conditions, such as inlet flow rate, on the spatial distribution of the PSD. The chapter concludes with a summary of key findings in §4.5.

The findings of this chapter have been published in Pico et al. [224]:

Pico, P., Nathanael, K., Lavino, A.D., Kovalchuk, N.M., Simmons, M.J.H. and Matar, O.K. (2023). *"Silver nanoparticles synthesis in microfluidic and well-mixed reactors: A combined experimental and PBM-CFD study"*. Chem. Eng. J., 474, p.145692

4.2 Problem formulation and summary of experimental dataset

The following section outlines the problem formulation considered in the present investigation. Additionally, it provides a brief overview of the experimental methods employed to collect the

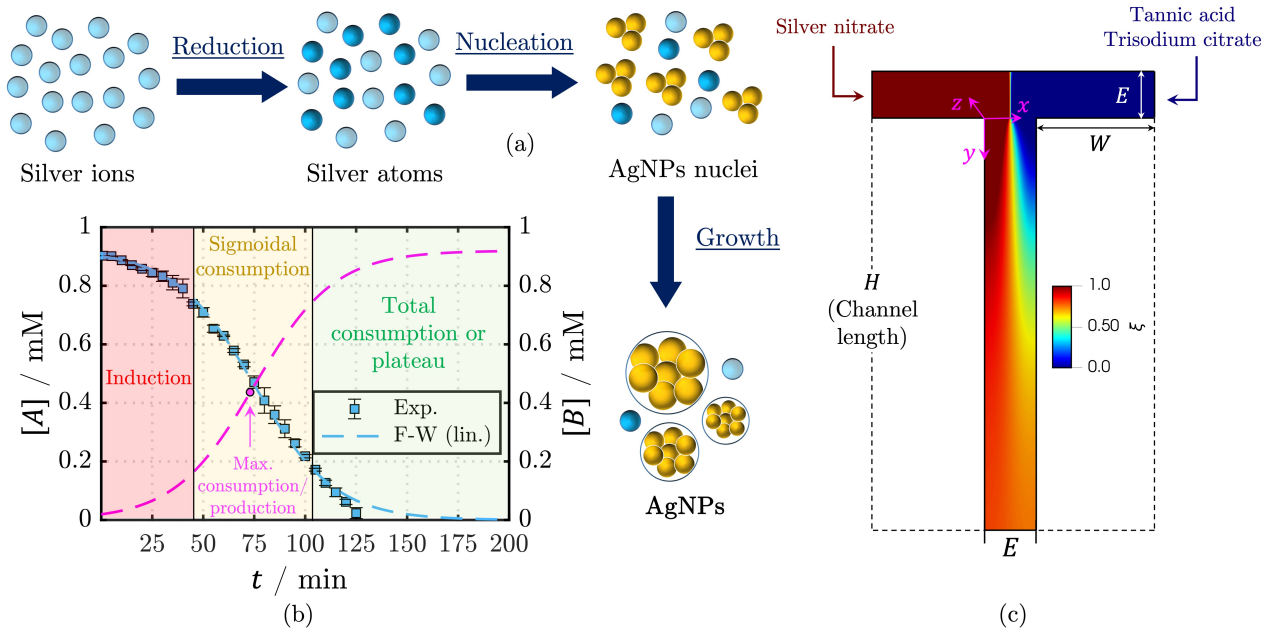

Figure 4.1: Microfluidic synthesis of AgNPs via chemical reduction: (a) simplified schematic of the reduction, nucleation, and growth steps, where the light blue spheres represent silver ions in solution, the dark blue spheres are the ions that have reduced into silver atoms, and the yellow spheres are NP nuclei that grow into AgNPs; (b) example of temporal consumption and production of silver precursor (A, left axis, blue) and AgNPs (B, right axis, magenta), respectively, in a closed and well-mixed reactor. The marks correspond to experimental measurements, as detailed in Nathanael et al. [204] and §4.2, and the dashed lines to their predicted values employing the F-W two-step mechanism in its linear form (see Eq. (2.15)). The operating conditions and kinetic constants correspond to those ascribed to the baseline case (see §4.2.3); (c) (not to scale) Schematic of the T-junction microchannel considered with a contour plot of the mixture fraction, $\xi = \frac{[SN]-[R]+[R]_0}{[SN]_0+[R]_0}$ (see Eq. (4.12)). The location of the Cartesian axis represents the outset of the geometrical domain $(x = 0, y = 0, z = 0)$

data reported throughout the manuscript and used for validation. This experimental dataset, derived from the work of Nathanael et al. [204] and Pico et al. [224], is described here solely for contextualisation purposes.

4.2.1 Operating conditions in a T-junction microfluidic device

The chemical synthesis process studied corresponds to a well-established chemical synthesis method involving silver nitrate, $AgNO_3$ (SN) as the silver precursor, with tannic acid, $C_7H_{52}O_{46}$ (TA), and trisodium citrate, $Na_3C_6H_5O_7 \cdot 2H_2O$ (TC) serving as the reducing and stabilising agents. This protocol was originally proposed in Kašpar et al. [133] and its successful application to produce monodisperse particles has been discussed in §2.3.

A continuous-flow T-junction microfluidic device (refer to figure 2.6 and associated text) has been employed, with the reactants' inlet concentrations set to 0.92 mM, 0.123 mM, and 1.91 - 3.82 mM for SN, TA, and TC, respectively. The device was operated under varying inlet flow rates

($Q = 200, 100, 67$, and 50 μL/min) and channel outlet lengths (0.1, 0.5, and 1 m). These flow rates were kept equal for both inlet channels, thus Q represents the flow rate for each individual inlet, with the total flow rate $Q_{\text{total}} = 2 \times Q$. Given that each molecule of TA can reduce up to 20 silver ions [272] and each molecule of TC can reduce 4 silver ions [241], the selected concentrations of TA and TC ensure excess conditions. To illustrate this, consider that, while the stoichiometric molar ratio of TA to SN is 0.05, this study considered an adjusted value of 0.13. A schematic representation of the T-junction device is depicted in figure 4.1(c).

In the experimental measurements shown in Pico et al. [224] and Nathanael et al. [204], the continuous-flow setup was established using a Tee tubing junction with a 0.020" thru-hole (Upchurch Scientific), a syringe pump (World Precision Instrument-AL-4000) equipped with two 5 mL syringes (Fisher), and two polytetrafluoroethylene (PTFE) tubes as inlet channels. These channels had internal diameters (ID) of $ID = 500$ μm (labelled as E in figure 4.1(c)), which were used to deliver the solutions of SN and the TA/TC mixture, respectively. An additional PTFE tube ($ID = 500$ μm and total length of 2 m, labelled as E and H in figure 4.1(c), respectively) was utilised as the reaction outlet channel.

4.2.2 Measurements of silver ions concentration and PSD across the outlet channel in the T-junction device

The numerical model proposed in this study was validated against experimental measurements of silver ion concentration and PSD in the T-junction microfluidic device. Silver ion concentration was determined using a silver electrode interfaced with a millivolt meter (Mettler Toledo-FP20). The device was calibrated using a series of standard solutions with concentrations of 0.1, 1, 5, 10, and 100 ppm, which were prepared by diluting a 1000 ppm silver standard solution from EDT direction. For concentrations above 50 ppm, 1 mL of 5 M ionic strength adjustment buffer (ISAB) was added. The calibration curve was generated by plotting millivolt values on a linear scale against the logarithmic scale of silver ion concentrations.

The PSD of the synthesised AgNPs was measured in triplicate using a Zetasizer Nano series (Malvern), with the refractive index for the AgNPs set at 0.135 [334]. These measurements were conducted under conditions similar to those used for measuring silver ion concentrations, specifically with flow rates of $Q = 200, 100$, and 50 μL/min and channel outlet lengths of 0.25, 0.5, 1, and 2 m. To prevent further reactions, the samples were immediately cooled in ice upon collection.

4.2.3 Determination of the nucleation and growth constants according to the F-W two-step mechanism

As discussed in §4.1 and comprehensively reviewed in §2.3, the foundation of the kinetic mechanism describing the synthesis of AgNPs considered herein is the F-W two-step mechanism, which is governed by the nucleation (k_1) and growth (k_2) kinetic constants. These constants, under varying conditions of pH and initial TC concentration, $[TC]_0$, were obtained from the work of our collaborators [204]. Readers interested in a detailed description of the methodology are encouraged to refer to that publication. Here, a summarised account of the most relevant details is provided.

k_1 and k_2 were determined from the absorbance intensity of AgNPs at 400 nm. The temporal evolution of the absorbance was measured every 5 minutes via a UV-vis spectrophotometer (Jenway-6300) and its equivalence to precursor concentration $[A]$ is governed by Eq. (4.1). The experimental setup for such measurements corresponded to a small well-mixed beaker with a stirring speed of 3000 rpm. This speed ensured that the production of AgNPs in the beaker was entirely kinetically-driven, neglecting any effects stemming from mass transfer. The PSD of the AgNPs produced via this method was also measured in triplicate by a Zetasizer Nano series (Malvern). From the precursor concentration measurements, k_1 and k_2 were determined by a best-fit of the integrated form of the F-W mass balances (see Eq. (2.13) and Eq. (2.15)).

$$\frac{[A]_0 - [A]}{[A]} = \frac{\alpha}{1-\alpha}. \tag{4.1}$$

In the above equation, α is equal to $A/[A_\infty]$ and A and A_∞ are the maximum absorbance at time t and at long times, respectively. By plotting $\ln(\alpha/1-\alpha)$ versus t, a straight line with a slope and intercept was obtained, see figure 4(c, d) in Nathanael et al. [204], providing values for k_1 and k_2.

For an easier discussion of the results, a "baseline" set of operating parameters and conditions is defined as follows: $Q = 200$ μL/min, $pH = 7$, $[SN]_{0,inlet} = 0.92$ mM, $[TA]_{0,inlet} = 0.123$ mM, and $[TC]_{0,inlet} = 1.91$ mM, where, for example, $[SN]_{0,inlet} = 0.92$ mM corresponds to the initial or inlet concentration of SN in the well-mixed batch reactor or in the T-junction microchannel, respectively. As seen in table 4.1 and thoroughly analysed in §4.4.1, these conditions of pH and $[TC]_0$ correspond to $k_1 = 0.0011$ min^{-1} and $k_2 = 55.51$ M^{-1}min^{-1}. Unless stated otherwise, the experimental data and simulation results are reported under these "base" conditions, from which different operating conditions are varied systematically.

4.3 Numerical methods and model description

This section details the proposed PBM-CFD numerical framework, starting with a description of the simplified formulation for systems that align with the original assumptions of the F-W two-step mechanism (i.e., well-mixed batch reactors). A validation of the implementation using open-source software is also included. The section then delves into the complexities of extending the model to capture the dynamics characteristic of continuous-flow and non-premixed systems, and outlines the proposed modifications to the well-mixed reactor model.

4.3.1 Well-mixed reactor model formulation and initial code validation

In the PBM adopted in this work the PSD is described in terms of a univariate number density function (NDF), $f(L,t)$, with particle size L as internal coordinate (i.e., $\xi = L$). The NDF, as thoroughly described in §3.2, is defined in such a way that the quantity $f(L,t)\mathrm{d}L$ corresponds to the number density of particles with size in the interval L and $L+\mathrm{d}L$ at time t. Considering this definition, the NDF is henceforth referred to as the PSD of the particle sample or both terms are used interchangeably. As detailed in §3.2, the governing population balance equation (PBE) is solved via the quadrature method of moments (QMOM) [187] in terms of the k^{th}-order moment of the distribution, $m_k(t) = \int_0^\infty f(L,t)L^k\mathrm{d}L$, as depicted in the transport equation of Eq. (4.2); for further information of these methods, the reader is referred to Marchisio et al. [187] and Passalacqua et al. [216] for the full derivation of this equation from the moment transformation of the PBE, its subsequent closure via QMOM and the NDF reconstruction, and to Yuan [328] for a review of some of the existing quadrature-based moments method (QBMM). Here, only a summary of the most noteworthy aspects.

In line with the QMOM [194], the NDF is approximated by a finite summation of Dirac delta functions as follows: $f(L,t) \approx \sum_{i=1}^{N} w_i(t)\delta(L - L_i(t))$, so that $m_k(t) \approx \sum_{i=1}^{N} w_i(t)L_i^k(t)$, where L_i and w_i are respectively the abscissas and weights of the i^{th} node of the quadrature, $\delta(L - L_i(t))$ is the Dirac delta function and N corresponds to the number of nodes of the quadrature approximation. In this approximation, the first $2N$ moments of the PSD are transported, namely $\{m_k\}$ with $k = [0,\ 2N-1]$. The weights and the abscissas of the quadrature approximation are calculated by the inverting the moments set, $\{m_k\}$, using the Wheeler algorithm [312] (see §3.2).

As discussed in §3.2, the utilisation of QBMMs to solve the PBE offers two significant advantages over alternative approaches. First, the solution process is simplified to solving transport equations for a finite number of moments of the distribution, rather than the entire distribution. Second, and particularly pertinent to the current study, each moment within the set represents a physical quantity of the system. For example, m_0 corresponds to the NP number density, m_3 is proportional to the NP volume fraction $\phi_p = k_V m_3$, where k_V is a volumetric shape factor, and the ratio m_{k+1}/m_k indicates the mean particle size (see Eqs. (3.8) - (3.10)).

From the general equations dictating the phenomenological transport of the moments set of Eq. (3.11) and Eq. (3.13), and applying the quadrature approximation (see Eq. (3.12)), a reduced PBE for the well-mixed reactor can be derived in Eq. (4.2):

$$\frac{\partial m_k(t)}{\partial t} = k \sum_{i=1}^{N} L_i^{k-1} G(L_i, y_j) w_i + J(y_j) d_{crit}^k, \tag{4.2}$$

where, from left to right, the terms represent accumulation, growth, and nucleation, respectively; $G(L_i, y_j) = dL_i(y_j)/dt$ is the growth rate, $J(y_j)$ is the nucleation rate, d_{crit} is the homogeneous NP nuclei size, and y_j represents the mass fraction of the species j in mixture. In the equation above, all spatial terms have been neglected as a consequence of the well-mixed nature of the system. In the same vein, agglomeration and breakup events have been omitted from the PBE to account for the fast mixing and the presence of a stabilising agent, which heavily opposes particle interactions (see §2.3.1.1). The expressions that define $G(L_i, y_j)$ and $J(y_j)$ are taken from the F-W-based framework introduced in Perala and Kumar [221] (see Eq. (2.11) - (2.12)):

$$J(y_j) = N_{av} \left(\frac{d_m}{d_{crit}} \right) k_1 C_A(y_j), \tag{4.3}$$

$$G(y_j, L) = \frac{1}{3} k_2 L C_A(y_j), \tag{4.4}$$

where N_{av} is the Avogadro number and d_m is the atomic diameter of silver so that d_{crit}/d_m corresponds to the number of silver atoms in a nucleus [221]. From Eqs. (4.3)-(4.4), it can be noticed that the growth and nucleation rates depend on the molar concentration of A, C_A, which itself depends on y_j (the mass fraction of species j in the mixture). For simplicity, the symbols $[j]$ and C_j are henceforth used interchangeably to denote the molar concentration of species j ($C_j = \rho_c y_j / MW_j$, wherein ρ_c is the density of the continuous phase and MW_j the molecular weight of j).

The molar concentration of species j is obtained here from the F-W expressions for A and B (Eq. (2.13)), written in the present framework as $\mathrm{d}(\rho y_j)/\mathrm{d}t = MW_j S_j$, where S_j is the mass-based source term representing the chemical reactions of nucleation and growth. Here, the expression shown in Eq. (12) of Perala and Kumar [221] has been transformed from a volume-based to a length-based NDF assuming spherical particles: $G(L, y_j) = (2/\pi) G(V, y_j)/L^2$, where $G(V, y_j)$ is a volume-based growth rate. This expression assumes that particle growth in length (diameter) is proportional to particle size. This is consistent with the aforementioned F-W assumption, in which all atoms in a NP contribute to particle growth, not just those located at the surface.

As per the assumptions of the F-W two-step mechanism, Eq. (4.2) is deployed to calculate the moment set in a well-mixed batch reactor. One major physical implication of the absence of spatial gradients and aggregation-related phenomena is the solution of the system in a "one-cell" setting, leading to space-independent outputs.

Takesue et al. [284] pursued an experimental investigation to explore the synthesis of AgNPs in the presence of TA and TC at pH = 12 and provided evidence to suggest that the process of AgNP nucleation is dominant during the first $\sim 0.59 - 0.98$ ms of operation, in which nuclei of size ~ 0.7 nm (Ag_{13} atom clusters) are predominately formed. Nevertheless, their small-angle X-ray scattering (SAXS) measurements also revealed the existence of clusters of Ag atoms of size ~ 1.2 nm (Ag_{55}). To the best of the author's knowledge, Takesue et al. [284] remains one of the few available studies that tackle the problem of estimating d_{crit} under reactive conditions similar to those examined in the present investigation. Considering this, d_{crit} is used as one of the fitting parameters of the proposed PBM-CFD model in the range $0.7 < d_{crit} < 1.35$ nm and report the value that better matched the experimental measurements in each case. This practice of tuning the PBM results using d_{crit} has previously been adopted by Perala and Kumar [221].

4.3.1.1 Model implementation in open-source software and initial validation

The mathematical framework described in this work is implemented in the C++ suite of PBM solvers *OpenQBMM* [217, 216], which itself is built upon the finite volume method package *OpenFOAM*. To this end, a new solver based on the already existing application, *pbeFoam*, was created to add the nucleation and growth models, as well as transport equations for each chemical compound in the system. For further details regarding the moment inversion algorithm, the discretisation schemes, the computation of the spatial fluxes (see next sub-section), and the general code structure, please refer to Passalacqua et al. [216]. *OpenQBMM* has been thoroughly benchmarked against experimental measurements and theoretical calculations of well-known problems involving both zero- and three-dimensional systems. Examples of these include the rigorous theoretical solutions of Vanni [296] for particle size in agglomeration-breakup scenarios in a one-cell setting and the evolution of particle size in a Taylor-Couette reactor [186, 258].

A supplementary validation is conducted herein with the objective of testing the model implementation in *OpenQBMM*. To this purpose, the numerical results reported in Perala and Kumar [221] (see figure 2 of this reference) and the experimental measurements and model of Watzky and Finke [309] (see Eq. (2.16), figure 2.5, and associated discussion) are replicated by employing the proposed PBM-CFD framework in the context of IrNPs synthesis and the original F-W two-step mechanism.

Figure 4.2(a)-(c) shows the temporal evolution of the average particle diameter, d, the standard deviation, σ^{SD}, the molar concentration of a reporter species C (proportional to the Ir precursor), and the zeroth-order moment, m_0. The chemical compound C—a particularity of the synthesis process of IrNPs—is consumed 1400 times faster than A in the growth reaction and has an initial concentration 1375 times higher than that of A; a transport equation analogous to $\mathrm{d}(\rho y_j)/\mathrm{d}t = MW_j S_j$ was added for C. The approximated PSD is reconstructed in line with the QMOM approach introduced above from a moments set $\{m_k\}$ with a number of quadrature

nodes $N = 3$, hence transporting the set $\{m_0, ..., m_5\}$, assuming a normal distribution. $N = 3$ represents a reasonable trade-off between computational cost and accuracy of the reconstructed NDF. This reconstruction is illustrated in Eq. (4.5), in line with the technique described by John et al. [124]:

$$d_{k+1,k}(t) = \frac{m_{k+1}(t)}{m_k(t)}, \qquad Cv_{k+1,k}(t) = \sqrt{\frac{m_k(t)m_{k+2}(t)}{m_{k+1}^2(t)} - 1}, \qquad \sigma_{k+1,k}^{SD}(t) = d_{k+1,k}(t)Cv_{k+1,k}(t), \tag{4.5}$$

where Cv is the coefficient of variation of the distribution.

For the case reported in figure 4.2, the reconstructed distributions have been transformed to be directly comparable with the results of Perala and Kumar [221], retrieved from a volume-based PBM. Considering the length-to-volume moment transformation $m_{k,V}(t) = k_V^k m_{3k,L}(t)$ for spherical particles [187] (the subscripts V and L represent volume- and length-based, respectively), the expression for average particle size of Perala and Kumar [221] in volume space (Eq. (4.6), $k_V = \pi/6$) becomes Eq. (4.7) in length space:

$$d_V(t) = \left(\frac{1}{k_V}\frac{m_{1,V}(t)}{m_{0,V}(t)}\right)^{1/3}, \tag{4.6}$$

$$d_L(t) = \left(\frac{m_{3,L}(t)}{m_{0,L}(t)}\right)^{1/3}. \tag{4.7}$$

It should be noted that this definition of d is only used for comparison against Perala and Kumar [221]; for comparison against the experiments from our collaborators [204], $d = m_{k+1}/m_k$ is used, as explained previously.

The virtually superposed curves of figure 4.2 suggest a correct implementation and solution of the model within our PBM-CFD framework for the operating conditions and closing parameters (k_1, k_2, d_{crit} and d_m) considered in Perala and Kumar [221]. The excellent predictions against the experiments of Watzky and Finke [309] and their derived expression (Eq. (2.16)) for d, in conjunction with the considerable discrepancies revealed when looking at σ^{SD}, are a reflection of the potential shortcomings of the original F-W two-step mechanism in fully explaining the behaviour of the PSD, as detailed in the literature review of §2.3.3 and §4.1. Nonetheless, the author of this thesis makes the brief note that part of the deviation in σ^{SD} found in Perala and Kumar [221] is likely related to the choice of representing the mean diameter by lower-order moments (refer to Appendix B for further details).

From figure 4.2(b) is should also be highlighted that, barring the outlier point at $t \approx 1.71$ h, the experimental data of σ^{SD} appear to adopt an essentially constant behaviour at $t > t_{ind}$, while both d and m_0 continue to rise well after t_{ind}. As seen in the temporal reconstructions of the PSD of figure 4.2(d), the breadth of the distribution sharply rises after t_{ind} and continues

to do so until the precursor has been fully consumed (see distributions at $t = 2 - 27$ h). The low size polydispersity of the experiments is explained by either a continuous nucleation process (as seen in the m_0 plot of figure 4.2(c)) where the nucleated particles are allowed to grow at a faster rate than larger particles to increase (decrease) the average size (standard deviation), as stated in Handwerk et al. [103], or the nucleation process promptly finishes after t_{ind}, as argued by Perala and Kumar [221]. This will be further discussed in §4.4.1 for the synthesis process under examination in this chapter (AgNPs).

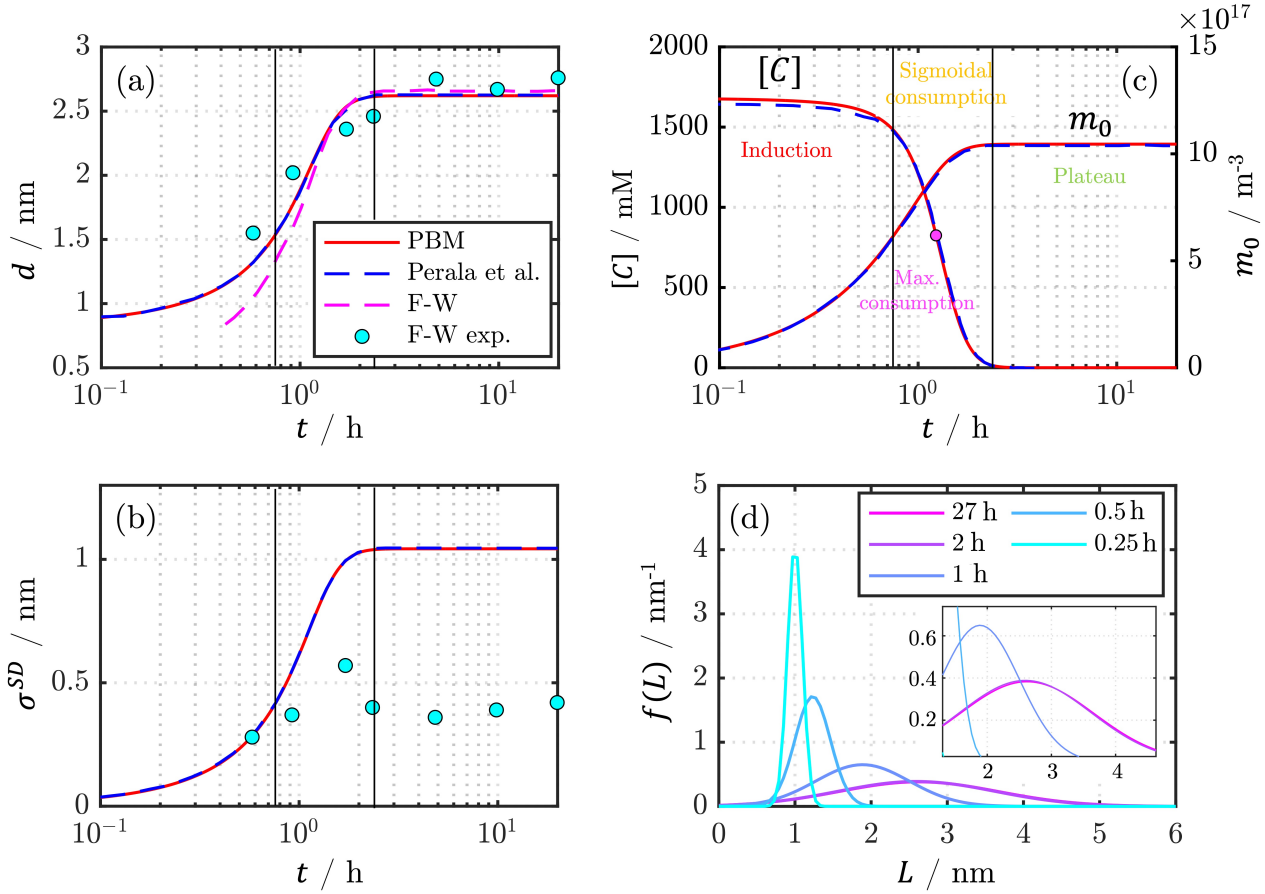

Figure 4.2: Code validation against the numerical results of Perala and Kumar [221] and the experimental data of Watzky and Finke [309] for IrNPs: Temporal evolution of (a) average particle diameter and (b) standard deviation. The marks correspond to the experimental measurements of Watzky and Finke [309] and the discontinuous magenta-coloured dashed line to the model proposed in the same reference (see Eq. (2.16)); (c) molar concentration of reporter species and zeroth-order moment and (d) evolution of normal PSD in time. The continuous vertical lines separate the stages of induction, sigmoidal consumption, and plateau. $[A]_0 = 1.2$ mM, $[B]_0 = 0.0$ mM, $[C]_0 = 1650$ mM, $k_1 = 0.0282$ h^{-1}, $k_2 = 3.379 \times 10^3$ M^{-1}h^{-1} ($[A]_0 k_2/k_1 = 159.52$), $d_{crit} = 0.83$ nm, $d_m = 0.272$ nm; $t_{\mathrm{ind,j}} = 0.89$ h, $t_{\mathrm{ind,p}} = 0.75$ h, $t_{\max} = 1.22$ h

4.3.2 Model extension in a T-junction microchannel

4.3.2.1 Governing equations

The well-mixed reactor model based on the F-W two-step mechanism previously introduced is expanded to reach the domains of continuous-flow systems by first ascribing the conditions of low particle Stokes number, $St_d << 1$, and largely diluted solid-liquid flow (particle volume fraction, $\phi_d << 1$) to the system at hand, in alignment with the approach followed in Schikarski et al. [253] for a similar system. $St_d = t_d/t_{res}$, where $t_d = \rho_d L^2/18\mu_c$ and t_{res}, defined in §4.4.3.1, refer to the characteristic relaxation time of the particles and the residence time of the flow, respectively [187] (refer to the beginning of §3.2 for further details). From experimental measurements of particle size, it can be estimated that $St_d \sim O(10^{-10})$ - $O(10^{-7})$ for the system under investigation. Consequently, a one-phase formulation is adopted in which the particles (disperse phase, denoted by d) follow the fluid flow inertia (continuous phase, c). Particle sedimentation due to gravitational effects is not considered in the present investigation given the estimated conditions of sedimentation number, $Se = U_{set}/U_a \sim O(10^{-11})$ - $O(10^{-6})$, where $U_{set} = \frac{2}{9}\frac{(\rho_d-\rho_c)gL^2}{\mu_c}$ is the Stokes settling velocity, g is the gravitational acceleration, and U_a is the average velocity of the flow, defined in §4.4.3.1.

The flow of the continuous phase, assumed to be incompressible and Newtonian, is governed by the continuity and momentum equations:

$$\begin{aligned} \nabla_{\mathbf{x}} \cdot \mathbf{u} &= 0, \\ \rho\left(\frac{\partial \mathbf{u}}{\partial t} + \mathbf{u}\cdot\nabla_{\mathbf{x}}\mathbf{u}\right) &= -\nabla_{\mathbf{x}} p + \nabla_{\mathbf{x}}\cdot\left[\mu(\nabla_{\mathbf{x}}\mathbf{u} + \nabla_{\mathbf{x}}\mathbf{u}^T)\right], \end{aligned} \tag{4.8}$$

where $\mathbf{u}$ corresponds to the fluid velocity, p is the pressure, ρ and μ are the fluid density and viscosity, respectively, under diluted conditions. A reduction reaction occurring prior to nucleation is added to account for the influence of mixing between the precursor and the reducing agent in the microreactor, in line with previous works [174, 4]. The set of chemical reactions considered for our system and their respective reaction rates read:

$$Reduction: SN + \nu_R R \xrightarrow{k_r} Ag_{(l)}; \qquad \dot{r}_r = k_r[SN][R]^{\nu_R}, \tag{4.9}$$

$$Nucleation: Ag_{(l)} \xrightarrow{k_1} Ag_{(s)}; \qquad \dot{r}_1 = k_1[Ag_{(l)}], \tag{4.10}$$

$$\begin{aligned} Growth: Ag_{(l)} + Ag_{(s)} &\xrightarrow{k_2} Ag_{(s2)}; \quad \dot{r}_2 = k_2[Ag_{(l)}][Ag_{(s)}] \\ Ag_{(l)} + Ag_{(s2)} &\xrightarrow{k_2} 2Ag_{(s2)}; \quad \dot{r}_{2'} = k_2[Ag_{(l)}][Ag_{(s2)}], \end{aligned} \tag{4.11}$$

where R corresponds to the reducing agent, $Ag_{(l)}$ to reduced silver atoms, $Ag_{(s)}$ to nuclei of nanoparticles, and $Ag_{(s2)}$ to those nuclei that have grown into AgNPs; ν is the stoichiometric coefficient of the species involved in the reduction reaction and the different k parameters cor-

respond to the reaction rate constants. To avoid any confusion, it is important to note that in the continuous-flow model, the silver precursor (silver nitrate) is denoted by SN, whereas in the well-mixed reactor model, the symbol "A" is used (refer to the previous subsection). This distinction is necessary because the addition of the reduction reaction significantly alters the temporal consumption of the precursor and its influence on the evolution of nucleation and growth, as discussed in the results section.

The mass fraction field of each chemical species in the microreactor is given by Eq. (4.12). This expression represents the conservation of the partial mass of species j, which incorporates Fick's law of diffusion and includes a source term that models species' mass exchange due to the chemical reactions. This source term is given by the elementary reactive source term of Eqs. (4.13) - (4.14):

$$\frac{\partial(\rho y_j)}{\partial t} + \nabla_{\mathbf{x}} \cdot (\rho \mathbf{u} y_j) = \nabla_{\mathbf{x}} \cdot (D_j \nabla_{\mathbf{x}} (\rho y_j)) + S_j \,, \tag{4.12}$$

$$S_j = MW_j \sum_{rxn=1}^{N_{rxn}} \hat{S}_{j,rxn} \tag{4.13}$$

$$\hat{S}_{j,rxn} = (\nu''_{j,rxn} - \nu'_{j,rxn}) \left(k_{rxn} \prod_{j=1}^{N} C_{j,rxn}^{\nu''_{j,rxn} + \nu'_{j,rxn}} \right) , \tag{4.14}$$

where D_j is the mass diffusion coefficient of species $j = (SN, R, Ag_{(l)}, Ag_{(s)}, Ag_{(s2)})$, rxn is an index denoting a specific reaction, N_{rxn} is the total number of reactions that involve species j; $\nu''_{j,rxn}$ and $\nu'_{j,rxn}$ are the stoichiometric coefficients of species j as it is produced and consumed in reaction rxn, respectively. The mass fraction of H_2O is obtained from the algebraic relationship: $y_{H_2O} = 1 - \sum_{j=1}^{N-1} y_j$.

Ranoszek-Soliwoda et al. [239] have documented the potential formation of a TA-TC complex from a solution containing these two chemical reagents, wherein the complex performs a double action as reducing and stabilising agent in the synthesis of AgNPs. These observations pose additional modelling challenges given the current uncertainty regarding the reducing strength of such complex, its transport and molecular properties, and the exact stoichiometry and kinetics of a simplified reduction reaction, such as Eq. (4.9), which are largely unexplored topics in the literature. Consequently, the framework of a generic reducing agent with transport and molecular properties equal to those of TA was adopted herein. This is because the molecular weight of this species significantly exceeds that of TC ($MW_{TA} = 1.70$ kg/mol and $MW_{TC} = 0.29$ kg/mol), thus, the transport of a potential TA-TC complex via diffusion will be greatly limited by the large-sized molecule of TA in comparison to TC ($D_{TA} \sim 2.17 \times 10^{-10}$ m^2/s and $D_{TC} \sim 1.74 \times 10^{-9}$ m^2/s [106]). In light of these uncertainties, and taking into account the comparatively much lower inlet concentration of TA with respect to TC (see §4.2.1), the effect of ν_R and k_r on the consumption of SN across the channel has been tested (see figures 4.10(b)-(f) in §4.4.3.1).

By expanding the PBE to include the effects of convection in physical space, diffusion, and particle aggregation, Eq. (4.15) is obtained [216]:

$$\begin{aligned} \frac{\partial m_k(t,\mathbf{x})}{\partial t} + \nabla_{\mathbf{x}} \cdot [\mathbf{u} m_k(t,\mathbf{x})] = k \sum_{i=1}^{N} w_i L_i^{k-1} G(L_i, y_j) \\ + \nabla_{\mathbf{x}}^2 \cdot \sum_{i=1}^{N} \left[\frac{D_0 L_0 w_i L_i^k}{L_i + L_0} \right] + \mathcal{B}(L_i)^{agg} - \mathcal{D}(L_i)^{agg} + J(y_j) d_{crit}^k. \end{aligned} \tag{4.15}$$

The expressions for nucleation and growth used correspond to those found in Eqs. (4.2) - (4.4) for the well-mixed reactor model. However, here, J and $G(L)$ are function of $C_{Ag_{(l)}}$ instead of C_A, making $C_{Ag_{(l)}}$ the driving force for nucleation and growth in the continuous-flow model; $\mathbf{u}$ is the particles' velocity (equal to the velocity of the continuous phase). All terms on the RHS of Eq. (4.15) have been closed via the QMOM introduced in §3.2.

The mass diffusion coefficient:

The mass diffusion coefficient is computed using the size-dependent Stokes-Einstein (S-E) relation, $D_L = D_0/L$, where $D_0 = \frac{k_B T}{3\pi\mu_c}$ (k_B is the Boltzmann constant and T the temperature of the system). In this study, the average particle sizes in the microreactor range from d_{crit} to 22 nm (see e.g., figure 4.12), corresponding to mass diffusion coefficients in the range 7.0×10^{-10} - 2.2×10^{-11} m^2/s. These values are entirely comparable to the experimental measurements of Ung et al. [295], which place the mass diffusion coefficient of AgNPs in an aqueous solution at $\approx 5.38 \times 10^{-11}$ - 2.56×10^{-11} m^2/s for particle sizes in the range 9.84 - 18.5 nm. Figure 4.3 provides a comparative analysis of the diffusion coefficient as calculated using the S-E relation and other commonly employed expressions.

The author of this thesis notes that the validity of the S-E expression is contingent upon its assumptions, which include fully spherical particles, low particle volume fractions, and negligible particle interactions [187, 78]. As emphasised in the experimental measurements that form the basis of this investigation [224, 204], the shape distribution of AgNPs synthesised under the studied conditions heavily lean towards spherical particles (see, for instance, figure S4 in supporting information in Pico et al. [224]). This fact, in addition to the highly diluted nature of the system ($\phi_d << 1$, discussed previously) and the accurate predictions against experimental data, provide evidence supporting the validity of the S-E equation, which has also been used to estimate the mass diffusivity of similar NPs in previous investigations [154].

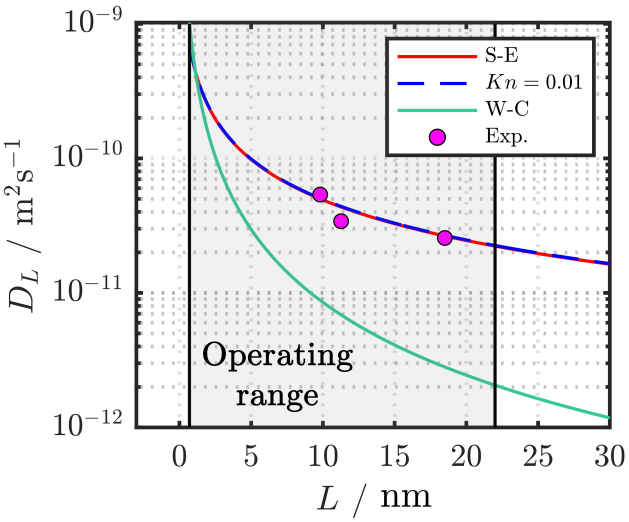

$$D_{S-E} = \frac{k_B T}{3\pi\mu_c L}$$

$$D_{Kn} = \frac{k_B T}{3\pi\mu_c L}\left[\frac{5 + 4Kn + 6Kn^2 + 18Kn^3}{5 - Kn + (8+\pi)Kn^2}\right]$$

$$D_{W-C} = \frac{5.88\,\mathrm{x}\,10^{-17}\left(\chi MW_{H_2O}\right)^{1/2} T}{\mu_c(\breve{v})^{0.6}}$$

Figure 4.3: Mass diffusion coefficient of AgNPs as a function of particle size according to the Stokes-Einstein equation (S-E), the modification considering the Knudsen number ($Kn = 0.01$) [187], and the Wilke-Chang correlation (W-C) of Wilke and Chang [314]. The magenta marks represent the experimental data of Ung et al. [295]. The vertical black lines highlight the expected ranges of diffusivity, in line with the experimental and numerical ranges of particle size ($0.7 < L < 22$ nm, see §4.4.3). Here, $T_c = 298.15$ K and $\mu_c = 0.89 \times 10^{-3}$ Pa · s were taken as the values of pure water. In the W-C correlation $\breve{v}$ is the molal volume of the NPs, defined as $\breve{v} = VN_{av}$ (V is the average volume of the particles and N_{av} Avogadro number) and $\chi = 2.6$. All variables are in international units

It is noteworthy to point out that, owing to the dependence of the diffusion coefficient on particle size, a special closure was required for the diffusion term in the moments-transport equation. This closure, showcased in the fourth term of Eq. (4.15), involves the introduction of a small non-zero term, $L_0 \sim O(10^{-12})$ m, to make $f(L)$ non-zero in the domain of the internal variable $[0, \infty)$ [187].

Agglomeration events:

In Eq. (4.15), $\mathcal{B}(L_i)^{agg}$ and $\mathcal{D}(L_i)^{agg}$ are the birth and death rate of particle size L_i due to agglomeration. These phenomena are governed by the classic expressions of Smoluchowski, which are written in their aggregate quadrature-based form in Eq. (4.16) (see Marchisio et al. [186] for the derivation from Eqs. (3.3) - (3.4)):

$$\mathcal{B}(L_i)^{agg} - \mathcal{D}(L_i)^{agg} = \frac{1}{2}\sum_{i}^{N}\sum_{l}^{N} w_i w_l \beta_{Br}(L_i, L_l)\left[(L_i^3 + L_l^3)^{k/3} - L_i^k - L_l^k\right], \tag{4.16}$$

where $\beta_{Br}(L_i, L_l)$ is the Brownian aggregation kernel stating the rate at which two particles of sizes L_i and L_l collide and aggregate due to Brownian diffusive phenomena:

$$\beta_{Br}(L_i, L_l) = \frac{2k_B T}{3\mu}\frac{(L_i + L_l)^2}{L_i L_l}. \tag{4.17}$$

This collision kernel was selected to model aggregation, in line with the laminar nature of the system, the small particle sizes involved ($<< 1$ μm) [187], and the comparatively large residence times involved in the microreactor, which allow for particle aggregation despite the presence of a stabiliser.

Similar to the well-mixed reactor model, the nucleation and growth models, in conjunction with the species transport equations and the closure of the particle diffusion model are implemented making use of *OpenQBMM* and the baseline solver *buoyantPbePimpleFoam*.

4.3.3 Simulation setup in a T-junction microchannel and mesh independence

4.3.3.1 Boundary and initial conditions

The simulation domain consists of a two-dimensional representation of the experimental T-junction channel (figure 4.1(c)) with two inlet streams of length $W = 10E$ and one outlet. Although the lengths of the inlet streams are shorter than their experimental counterparts, the simulated lengths suffice to obtain a fully developed inlet flow before mixing.

The governing equations are solved subject to the boundary conditions specified in Eq. (4.18):

$$\begin{aligned}
\mathbf{u} &= 0 \quad \text{on all walls (no-slip)},\\
\mathbf{u} &= U_a/2 \quad \text{at both inlets},\\
\frac{\partial \mathbf{u}}{\partial \mathbf{n}} &= 0 \quad \text{at the outlet (no flux)},\\
\frac{\partial p}{\partial \mathbf{n}} &= 0 \quad \text{at both inlets and on all walls (no flux)},\\
p &= p_{\text{ref}} \quad \text{at the outlet},\\
y_j &= y_{j,\text{ref}} \quad \text{at both inlets},\\
\frac{\partial y_j}{\partial \mathbf{n}} &= 0 \quad \text{at the outlet and on all walls (no flux)},\\
\frac{\partial m_k}{\partial \mathbf{n}} &= 0 \quad \text{on all boundaries (no flux)},
\end{aligned} \tag{4.18}$$

where p_{ref} and $y_{j,\text{ref}}$ represent reference pressure and reference mass fraction of species $j = (SN, R, Ag_{(l)}, Ag_{(s)}, Ag_{(s2)})$, respectively. These values correspond to the inlet concentration of each species (e.g., $y_{SN} = 0$ on the RHS inlet and $y_R = 0$ on the LHS inlet, as shown in figure 4.1(c)). All moments are initialised in zero at the channel's domain. The temperature is kept constant at 298.15 K.

A semi-uniform Cartesian mesh of cell size $\Delta\mathbf{x} = (\Delta x, \Delta y, \Delta z) = (E/50, E/40, E)$ is employed wherein the variables are solved in the $x-y$ 2-D plane with a global resolution of $\sim O(10^6)$ cells. The time-step for the simulations was set to be adaptive according to the Courant-Friedrichs-Lewy (CFL) condition: $Co = \mathbf{u}\Delta t/\Delta\mathbf{x}_{min} < 1.0$. The simulations are run until all variables have

reached a steady-state, which in most cases is attained at approximately $t = 20t_{res}$; t_{res} is the reactor's residence time, whose mathematical definition is depicted in §4.4.3.1.

4.3.3.2 Discretisation schemes

The governing equations are discretised in a finite-volume framework within a co-located mesh arrangement. The temporal terms are discretised through a first-order implicit Euler scheme, while all the divergence operators follow a first-order upwind Gaussian scheme and the Laplacian operators a second-order central-difference scheme. The pressure-velocity coupling follows the PISO (Pressure-Implicit-of-Split-Operations) [196] transient algorithm with a total of two correctors.

It is well-known [114, 218] that first-order schemes introduce numerical diffusion to the solution through the leading term of the truncation error, which takes the form of a Laplacian term (e.g., $D_{num}\frac{\partial^2 y_j}{\partial x^2}$). For a first-order scheme applied to the temporal and convective terms, the numerical diffusion coefficient—denoted as D_{num}—which modulates the importance of this fictitious diffusion, can be estimated to be proportional to $\mathbf{\Delta x}$. As a consequence of the small mass diffusion coefficients involved in the studied system ($O(10^{-11})$ - $O(10^{-9})$ m^2/s for the inlet streams and AgNPs in liquid), the error introduced by numerical diffusion is expected to be most pronounced in regions characterised by significant spatiotemporal y_j and m_k gradients. As analysed throughout the manuscript, these primarily include the regions in the vicinity of the walls and the channel centre-line in the x-direction, where the inlet reagents streams first converge and react (see figure 4.11).

Further implications of employing a first-order upwind scheme, and how an increase in the mesh resolution attenuates the above-mentioned problems are discussed with the mesh independence test results of the following sub-section. Despite their susceptibility to numerical diffusion, first-order schemes provide the benefits of yielding bounded solutions and ensuring numerical stability. These features are particularly valuable in the present application, as we are dealing with variables that have very specific limits ($0 < y_j < 1$) as well as variables whose ranges can vary over several orders of magnitude (e.g., m_0). It is worth noting that, despite the small mass diffusivity coefficients involved, first-order upwind discretisation schemes for the convective term are a common practice in the field of nanoparticle synthesis process modelling [253, 160, 174]. Similar to the present study, Schikarski et al. [253] report overestimations of mixing and nucleation/growth rates due to numerical diffusion in their supersaturation-driven synthesis process.

4.3.3.3 Mesh independence test

In order to assess the (in)dependency of the T-junction PBM-CFD simulation results on the mesh resolution, three Cartesian grids of semi-uniform size in all spatial directions have been tested

under the hydrodynamic and kinetic conditions of figure 4.11(a) for a channel length of 0.25 m. These conditions allow for a smooth solution of all variables across the y-axis of the channel while also inducing a marked variable gradient in the radial direction (see figure 4.11 and discussion). The three mesh resolutions tested correspond to $\Delta\mathbf{x} = (\Delta x, \Delta y, \Delta z) = (E/30, E/30, E)$ for M_1, $(E/40, E/50, E)$ for M_2, and $(E/60, E/60, E)$ for M_3.

In figure 4.4(a)-(d) the steady-state contour plots of $[SN]$, $[Ag_{(l)}]$, m_0, and m_3 are depicted for the three grids under consideration, whose plots are shown from top to bottom in order of increasing resolution. Figure 4.4(e)-(h) shows the steady-state surface averaged profiles of the same variables. The virtually identical contour plots and y-direction profiles of $[SN]$ and $[Ag_{(l)}]$ for all three grids suggest the attainment of a mesh-independent solution for the species mass-balances from the mesh resolution characterised by M_1 and onward. On the contrary, the contours of the PBM-related variables m_0 and m_3 show small differences at the locality of the channel walls, whereby higher concentrations of m_0 are seen for M_1. These slight differences are further evidenced by observing how the m_0 and m_3 profiles for each grid resolution begin to deviate from each other as the channel length increases, resulting, for instance, in a 2.31% decrease in m_0 going from M_1 to M_2, and a 5.55% decrease going from M_2 to M_3 at the outlet plane.

The computational times required to achieve 10 seconds of simulation using 128 CPU cores are 2.52 hours, 7.65 hours, and 36.87 hours for M_1, M_2, and M_3, respectively. Considering the substantial increase in computational time from the second highest to the highest resolution, the mesh utilsed for all simulations is based on M_2, as it offers an acceptable balance between mesh-independence and computational efficiency.

As previously discussed, the use of a first-order upwind discretisation scheme for the convective term introduces numerical diffusion to the solution. This numerical diffusion is of the form of a Laplacian term with an accompanying coefficient, D_{num}, which is estimated to be roughly equal to $\frac{1}{2}u\Delta x(1 - Co)$ under the assumptions of constant u and uniform $\Delta\mathbf{x}$ [114, 218]. In the simulations, the numerical diffusion term is likely strictly positive given that $Co \equiv \mathbf{u}\Delta t/\Delta\mathbf{x}_{min} \approx 1$ has been carefully ensured through the adaptive time-step employed. The positive nature of numerical diffusion induces an overestimation of the mixing rates of all species given their augmented diffusive transport. This, in turn, artificially increases the production of $Ag_{(l)}$ via the reduction reaction (see Eq. (4.9)), resulting in accelerated rates of nucleation and growth.

The above statements are fully consistent with the outcomes of the mesh independence test results. An examination of figure 4.4(e)-(f) uncovers a direct relationship between increased mesh resolution and increased (decreased) surface-average profiles of $[SN]$ ($[Ag_{(l)}]$) across the channel. This leads to reduced rates of nucleation/growth, which are manifested in the generally lower m_0 and m_3 profiles obtained with the highest resolution (M_3), as depicted in 4.4(g)-(h). The contour plots of m_0 and m_3 (see highlights of 4.4(c)-(d)) allow us to identify that most of

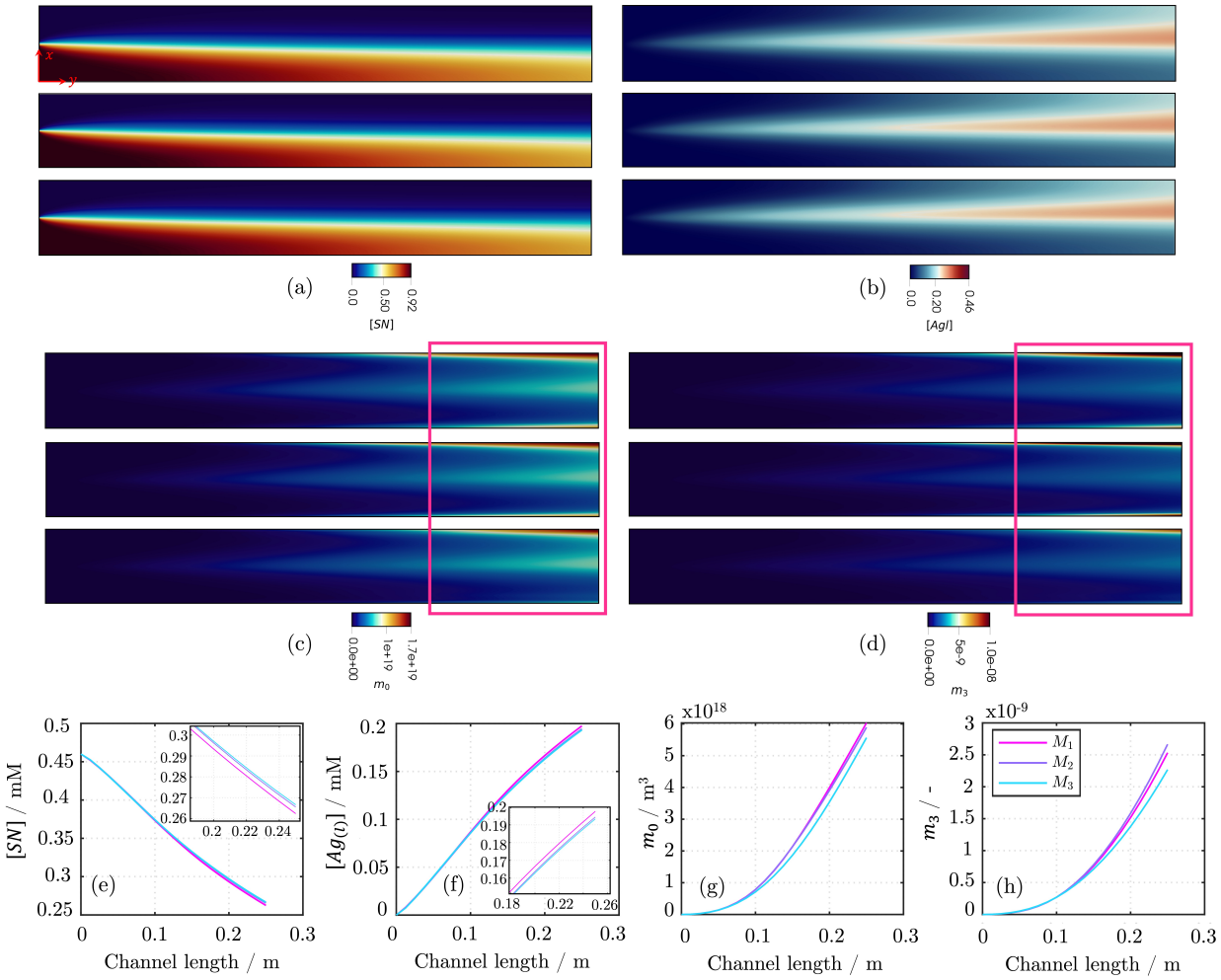

Figure 4.4: Results of mesh independence study under the operating conditions specified in figure 4.11(a) for a channel length of 0.25 m: (a)-(d) steady-state contour plots of $[SN]$, $[Ag_{(l)}]$ in mM, m_0 in m^{-3}, and m_3. From to top to bottom the results are shown for M_1, M_2, and M_3, respectively; (e)-(h) steady-state surface-averaged profiles across the channel for a first-order upwind discretisation scheme. The pink highlights in (c)-(d) represent the channel zones where slight differences are observed between mesh resolutions. For easier visualisation, the inlet streams of all contour plots have been removed and the channels have been rescaled from their original dimensions as follows: $\mathbf{x} = (7x, 0.1y, z)$.

the discrepancies obtained with different mesh resolutions can be attributed to the high-gradient regions in the vicinity of the walls, where the lowest mesh resolution appears to smear the solution.

As previously mentioned, the PBM-related variables (m_0 and m_3) seem to be more affected by the mesh resolution in comparison to those related to the mass-conservation equations of y_j. This is likely explained by the fact that the mass-diffusion coefficients of the inlet reagents (SN and R) fall within the range $O(10^{-9})$ - $O(10^{-10})$ m^2/s, whilst those of the AgNPs in water are of the order of $O(10^{-10})$ - $O(10^{-11})$ m^2/s; averaging over the different values of Δt used in each simulation, D_{num} values over the channel domain can be computed in the range $O(10^{-11})$ - $O(10^{-9})$ m^2/s for the two highest resolutions (M_2 and M_3) and $O(10^{-10})$ - $O(10^{-9})$ m^2/s for the lowest resolution (M_1).

These estimations of D_{num} for the selected mesh resolution (M_2) suggest that numerical diffusion may play a non-negligible role in specific regions of the channel, particularly along the channel walls, and for certain variables in the studied system. Notably, numerical diffusion may become a factor when considering the transport of larger-sized AgNPs across the channel. Nevertheless, given the orders of magnitude of the mass diffusion coefficients of the inlet streams and $Ag_{(l)}$, it is anticipated that numerical diffusion is not a significant concern during the stages of mixing, nucleation, and growth.

To instil confidence in the present findings, an additional test was conducted using the selected mesh resolution and a second-order upwind scheme, replicating the operating conditions of the mesh independence test. The results, illustrated in figures 4.5, indicate that although numerical diffusion may be present, its impact on the overall dynamics is minimal.

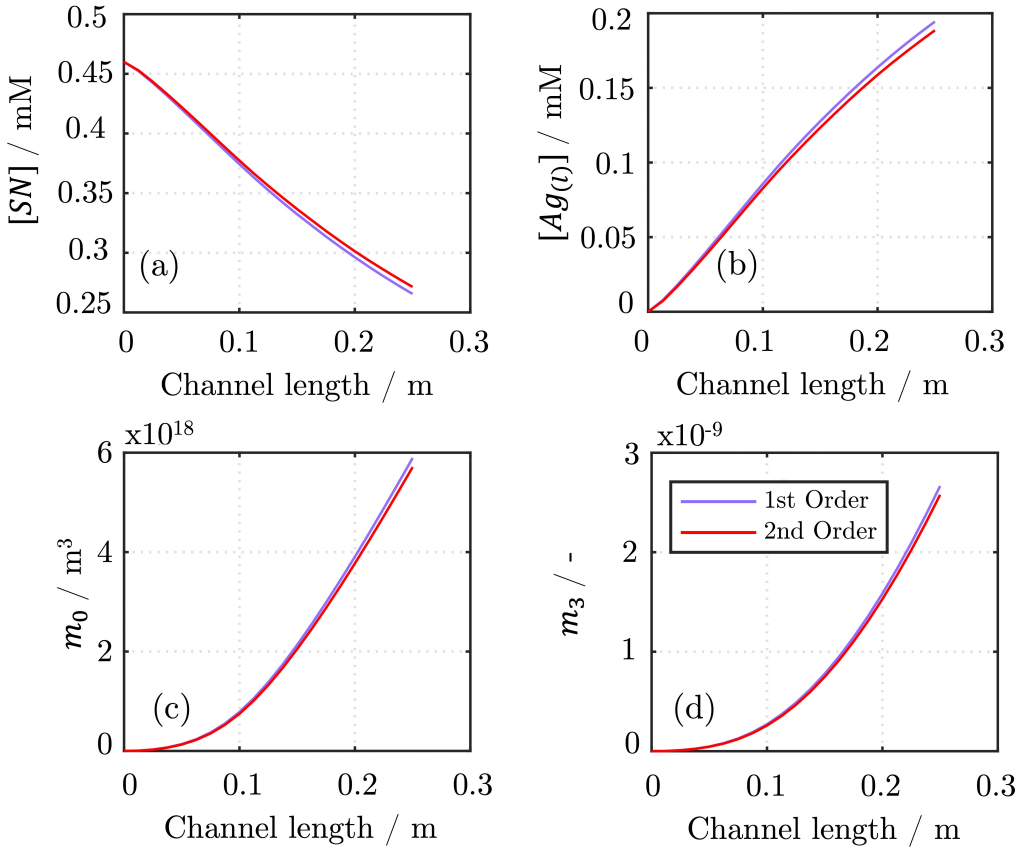

Figure 4.5: Influence of the discretisation scheme for the convective term under the operating conditions specified in figure 4.11(a) for a channel length of 0.25 m: (a)-(d) steady-state surface-averaged profiles across the channel for first- and second-order upwind discretisation schemes using M_2

To enhance the readability of the forthcoming discussions, it is relevant at this point to reiterate the extensions made to the F-W-based model for simulating synthesis in microfluidics. These extensions encompass the incorporation of a reduction reaction prior to nucleation and growth (Eq. (4.9)), adding reactive convection-diffusion equations for each species in the system

(Eqs. (4.12)-(4.14)), including the space-dependent phenomena of convection and diffusion in the PBE (Eq. (4.16)), and adding an aggregation term.

4.4 Results and discussion

4.4.1 Effect of pH and $[TC]_0$ on the synthesis of AgNPs in a well-mixed reactor

In this subsection, an examination of the original F-W two-step mechanism in the context of AgNPs synthesis in a well-mixed reactor under different operating conditions is presented. Figure 4.6(a)-(b) depicts the temporal consumption (production) of A (B) obtained by varying $[TC]_0$ experimentally (using the data from Nathanael et al. [204]) and via the present well-mixed reactor model framework at $pH = 7$. The numerical results shown in these figures were obtained by solving the F-W-based mass conservation expressions for A and B ($\mathrm{d}(\rho y_j)/\mathrm{d}t = MW_j S_j$) in conjunction with Eqs. (4.2)-(4.4) to obtain the PSD, which is discussed later on in figure 4.7 and table 4.2. Table 4.1 reports the values of k_1 and k_2 for each set of conditions, gathered from the F-W fittings described in Nathanael et al. [204], as well as the estimations of t_{ind}, t_{max}, and $t_{plateau}$ through Eqs. (2.17)-(2.20).

The kinetic curves of $pH = 7$ showcase the adoption of the typical behaviour outlined by the F-W two-step mechanism (induction, sigmoidal production/consumption, and plateau) and the excellent agreement with the proposed simulations for the three $[TC]_0$ tested. The values of the ratio $k_2[A]_0/k_1 > 1$ of table 4.1 suggest longer periods of nucleation ($t_{nuc} = 1/k_1$) compared to growth ($t_g = 1/k_2[A]_0$), at least initially, which limit the consumption of A during the induction period ($t < 40-60$ s), from which point the sigmoidal high-rate growth of B commences ($40-60 < t < 98-135$ s), rapidly decreasing the concentration of A and leading up to the plateau stage ($t > 98-135$ s).

Table 4.1: F-W two-step mechanism fitting parameters according to the experimental measurements of Nathanael et al. [204] and summarised in §4.2.3 in a well-mixed reactor for the chemical synthesis of AgNPs. $[A]_0 = 0.92$ mM, $[TA]_0 = 0.123$ mM, $[B]_0 = 0$ mM. * Baseline case conditions, as defined in §4.2.3

pH	$[TC]_0$ / mM	k_1 / min^{-1}	k_2 / M^{-1}min^{-1}	$k_2[A]_0/k_1$	$t_{ind,j}$ / min	$t_{ind,p}$ / min	t_{max} / min	$t_{plateau}$ / min
7*	1.91*	0.0011*	55.51*	46.43*	48.32*	40.16*	73.57*	98.81*
7	2.87	0.0013	37.86	26.79	62.34	52.04	99.10	135.84
7	3.82	0.0015	44.81	27.48	46.73	39.37	77.56	108.38
12	1.91	0.1000	77.97	0.72	-	-	-	5.73
12	2.87	0.0120	13.66	1.05	-	0.63	1.88	55.48
12	3.82	0.0128	26.01	1.87	-	5.82	17.03	52.89

A first look into the effect of $[TC]_0$ reveals an apparent non-monotonic response of A and B with $[TC]_0$, whereby the fastest consumption is seen for the lowest $[TC]_0$ (1.91 mM) and the

slowest for the $[TC]_0$ immediately above (2.87 mM). This sort of non-monotonic response, which is also observed in t_{ind}, t_{max}, and $t_{plateau}$ (see table 4.1), has been reported previously in the work of Sandoe et al. [248] for AgNPs synthesis in the presence of sodium citrate. The study above attributes this qualitative trend to the dual role of sodium citrate as a reducing (increasing k_1) or stabilising agent (decreasing k_1), depending on the concentration. The change in k_1 and k_2 seen in the present study by solely varying $[TC]_0$ and maintaining $[TA]_0$ constant suggests the incidence of coexisting stabilising and reducing effects of TC. Recalling the experimental observations of Ranoszek-Soliwoda et al. [239] highlighted in §4.3.2 regarding the complexing behaviour of a TA-TC mixture, the kinetic constants measured herein appear to correspond to those of a TA-TC complex with a dual role as reducing agent and stabiliser.

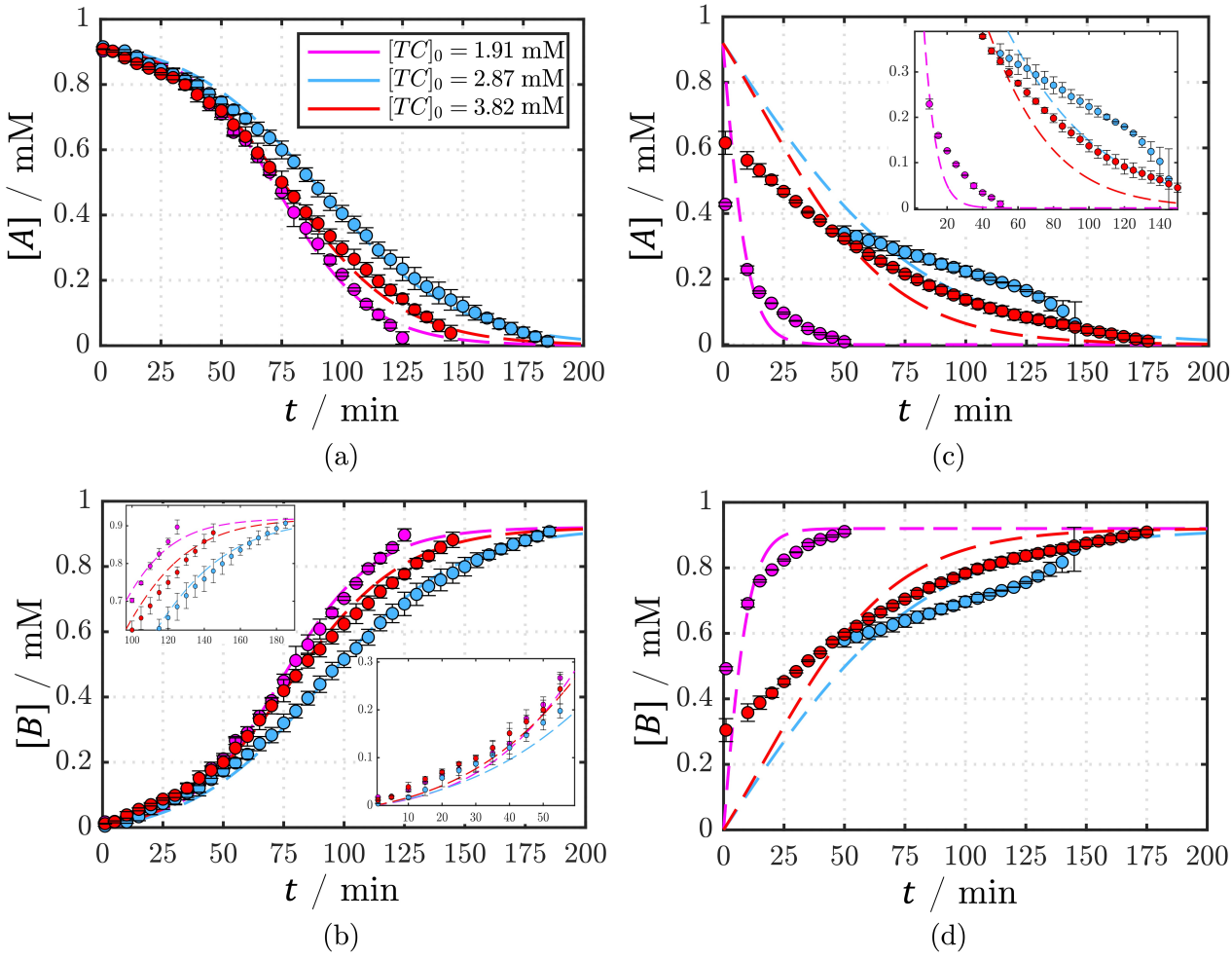

Figure 4.6: Effect of pH and $[TC]_0$ on the temporal evolution of $[A]$ and $[B]$ and comparison between the experimental measurements of Nathanael et al. [204] (marks) and F-W-based PBM predictions (dashed lines) for AgNPs in a well-mixed reactor, showing how F-W predicts well the behaviour at $pH = 7$ but not at $pH = 12$: (a)-(b) $pH = 7$; (c)-(d) $pH = 12$. $[A]_0 = 0.92$ mM, $[TA]_0 = 0.123$ mM, $[B]_0 = 0$ mM. See table 4.1 for k_1, k_2, and characterising times of induction and maximum rate of consumption/production

The experimental and well-mixed reactor PBM kinetic curves shown in figures 4.6(c)-(d) for $pH = 12$ display a distinctive behaviour that diverges substantially from that observed in

$pH = 7$. On account of the one to two orders of magnitude higher k_1 at a similar k_2 for each $[TC]_0$ (see table 4.1), the system undergoes an exceedingly fast induction period and exhibits a mode of behaviour more consistent with the decreasing and concave-up consumption of A that characterises the stages that follow the instance of maximum production of B (see $pH = 7$ curves at $t > 100$ min). In fact, the estimations of t_{ind} and t_{max} using the fittings of k_1 and k_2 lead to either negative (reported as '-' in table 4.1) or significantly smaller values than their $pH = 7$ counterparts.

The almost immediate fast-rate consumption of A seen for the high pH cases is related to the high rates of nucleation that equalise the characteristic times of nucleation and growth ($k_2[A]_0/k_1 \sim 1$). The rapid kinetics governing the consumption of A under high pH conditions, as well as the virtual absence of an induction period found here, are in complete agreement with the experimental studies of Qin et al. [232] and Dong et al. [70], which have investigated the synthesis of AgNPs in the presence of ascorbic acid-sodium citrate and sodium citrate, respectively. The reader is referred to §2.3.2 for an more in-depth review of the literature on the effect of pH on particle characteristics.

Opposite to $pH = 7$, the curves for $pH = 12$ exhibit noticeable disparities between the experimental measurements and the PBM results based on the F-W fittings for all three $[TC]_0$ tested . These discrepancies, which are especially apparent during the first ~ 50 min of operation, are an indication of the assumptions of the original F-W two-step mechanism not fully capturing the dynamics of the system. As briefly alluded to previously, the quasi-equilibration of the characteristic times of nucleation and growth ($k_2[A]_0/k_1 \sim 1$, table 4.1) indicate that a slow and continuous nucleation process does not ensue at $pH = 12$, as it is proposed in F-W. Instead, the large values of k_1 (approximately two orders of magnitude higher than in $pH = 7$), together with the aforementioned elimination of the induction period and the fast consumption of A, confirm the rapid emergence of NP nuclei within a small time span. As detailed in Nathanael et al. [204], the good F-W k_1 and k_2 fittings found for $pH = 12$ are only valid for ranges of the experimental data that exclude the measurements at early times ($t < 25$ min and $[A] > 0.6$). This fact further explains the increased deviations at those early reaction times and confirms that the assumptions of F-W are not applicable under alkaline conditions for the studied reaction system.

The PSD of the samples obtained after a total consumption of the precursor under the conditions of figure 4.6 is depicted in figure 4.7. Here, the experimental measurements, a fitting of these to a normal distribution, and the PBM predictions are plotted. These predictions take the values of $d_{4,3} = m_4/m_3$—the volume-weighted or De Brouckere mean diameter—as the basis for computing the average diameter, the coefficient of variation, and the standard deviation of the reconstructed normal distribution, in accordance with John et al. [124]'s technique (see Eq. (4.5)). The practice of using high-order moments to represent the average size of a distribution has been widely adopted in solid-liquid and solid-gas modelling applications, including granulation and precipitation [185], given their direct relationship with the larger particles of the sample.

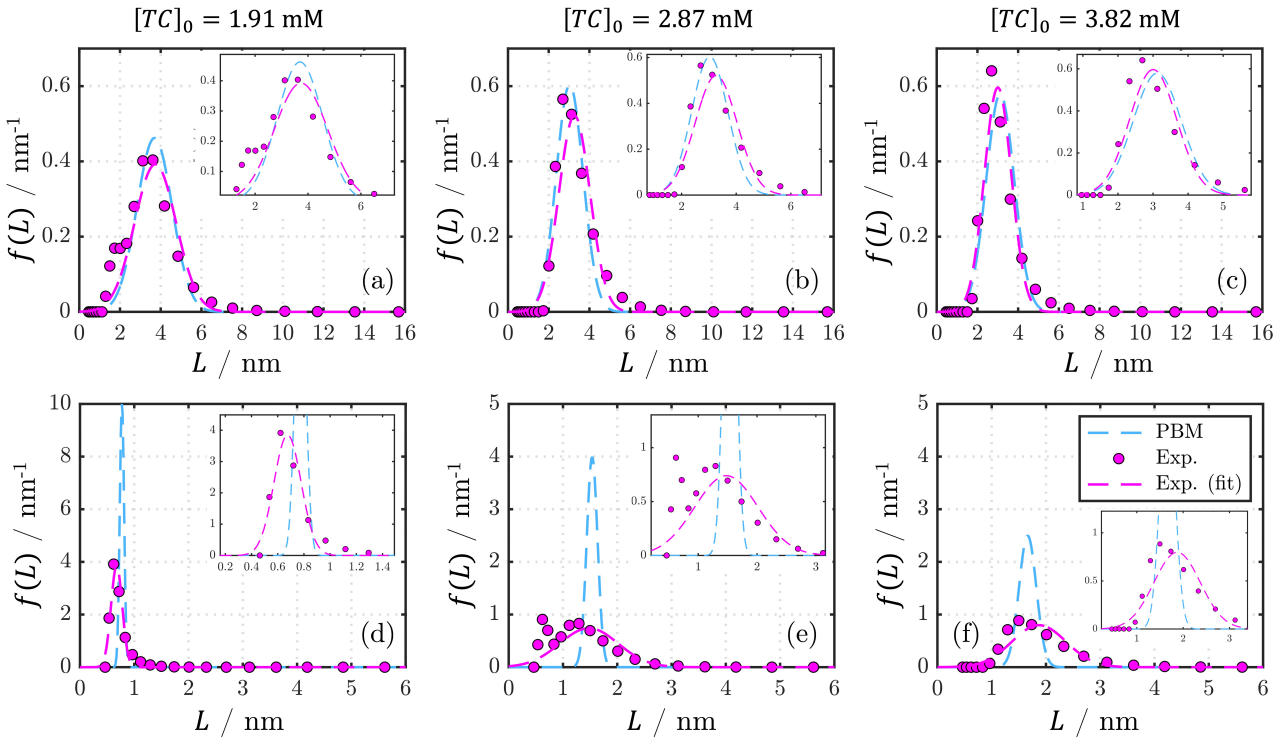

Figure 4.7: Effect of pH and $[TC]_0$ on the PSD after full precursor consumption and comparison between experimental measurements, normal distribution fitting of said measurements, and F-W-based PBM predictions for AgNPs in a well-mixed reactor, highlighting the limitations of F-W for $pH = 12$: (a)-(c) $pH = 7$; (d)-(f) $pH = 12$. Left, middle and right panels correspond to $[TC]_0 = 1.91, 2.87, 3.82$ mM, respectively. $[A]_0 = 0.92$ mM, $[TA]_0 = 0.123$ mM, $[B]_0 = 0$ mM, $d_{crit} = 1.35$ nm, $d_m = 0.344$ nm. See table 4.1 for k_1, k_2, and characterising times of induction and maximum rate of consumption/production

The average particle size, standard deviation, and $PDI = (\sigma^{SD}/d)^2$ of each case are compiled and summarised in table 4.2. These results suggest an acceptable agreement between the experimental and F-W-based PBM distributions for $pH = 7$, with maximum deviations of 10.1% and 31.2% for d and σ^{SD}, respectively (the maximum deviations against the fitted experimental data correspond to 7.2% and 13.6% for d and σ^{SD}). As stated in §2.3 and §4.1, previous investigations have reported substantial discrepancies (up to 150%) against experimental measurements when attempting to employ the original F-W two-step mechanism to describe the behaviour of the PSD, notwithstanding the model's excellent predictive capabilities in terms of precursor consumption [221, 104].

In alignment with Perala and Kumar [221], and as will become more apparent in the analysis of $pH = 12$, an amplification of these discrepancies for σ^{SD} when compared to d is observed. It is important to note, however, that the PBM simulations for all $pH = 7$ cases provide under-predictions of σ^{SD} and the opposite is reported in Perala and Kumar [221] for IrNPs (see figure 4.2(b)). Our under-predictions of σ^{SD} are likely caused by the choice of representing d by a volume-weighted average, which tends to be disproportionally influenced by the largest particles in the system, thereby resulting in slightly higher d and lower σ^{SD} than would be obtained with

lower-order moments, as calculated in Perala and Kumar [221] (see Eqs. (4.6)-(4.7)).

Table 4.2: Effect of pH and $[TC]_0$ on d, σ^{SD}, and $PDI = (\sigma^{SD}/d)^2$ after full precursor consumption and comparison between experimental measurements, normal distribution fitting of said measurements, and F-W-based PBM predictions for AgNPs in a well-mixed reactor. $[A]_0 = 0.92$ mM, $[TA]_0 = 0.123$ mM, $[B]_0 = 0$ mM, $d_{crit} = 1.35$ nm, $d_m = 0.344$ nm. * Baseline case conditions, as defined in §4.2.3. †For this case, $d_{crit} = 0.7$ nm

					$d \pm \sigma^{SD}$ / nm (PDI)		
pH	$[TC]_0$ / mM	k_1 / min^{-1}	k_2 / M^{-1}min^{-1}	$k_2[A]_0/k_1$	PBM	Exp.	Exp. (fit)
7*	1.91*	0.0011	55.51	46.43	3.60 ± 0.91 (0.064)	3.61 ± 1.30 (0.13)	3.74 ± 1.02 (0.07)
7	2.87	0.0013	37.86	26.79	3.03 ± 0.66 (0.048)	3.37 ± 0.96 (0.08)	3.26 ± 0.76 (0.05)
7	3.82	0.0015	44.81	27.48	3.12 ± 0.69 (0.049)	3.14 ± 0.94 (0.09)	3.00 ± 0.67 (0.05)
12†	1.91†	0.1000	77.97	0.72	0.77 ± 0.04 (0.003)	0.73 ± 0.18 (0.06)	0.68 ± 0.10 (0.02)
12	2.87	0.0120	13.66	1.05	1.54 ± 0.10 (0.004)	1.36 ± 0.57 (0.18)	1.48 ± 0.54 (0.13)
12	3.82	0.0128	26.01	1.87	1.66 ± 0.16 (0.009)	1.91 ± 1.10 (0.33)	1.87 ± 0.50 (0.07)

By examining the influence of $[TC]_0$ on the PSD at $pH = 7$, a similar non-monotonic behaviour mode as that seen in the consumption of A (figure 4.6) is detected for d and σ^{SD} via the experiments and PBM simulations, with the exception of σ^{SD} in the experimental data set, which exhibits a monotonically-decreasing trend with $[TC]_0$ (see table 4.2). The adherence of the system to a non-monotonic response with the concentration of the stabiliser has been outlined previously in Das et al. [64] and Henglein and Giersig [112], who have assessed the prospect of tailoring the size distribution of a sample by varying the concentration of the stabiliser. Nonetheless, a clear separation in the response of these variables can be noticed between $[TC]_0 = 1.91$ mM and the two higher concentrations, whereby the overall faster consumption of A appears to bring about higher d, σ^{SD}, and PDI.

The comparatively small particle sizes induced by the two higher $[TC]_0$, together with the above remarks in regard to the reaction kinetics and characterising times (see times in table 4.1), are likely to be signs of the stabilising activities of TC under the conditions of reactants concentration and pH considered herein. Bastús et al. [28] have described similar findings, with a decrease in the initial TA/TC concentration ratio largely associated with the synthesis of smaller-sized AgNPs.

The discussion proceeds by concentrating on the results for $pH = 12$, where an evident performance deterioration of the F-W-based PBM predictions is identified, with the deviations of σ^{SD} against the experimental measurements being particularly prominent (see figures 4.7(d)-(f)). Specifically, errors in the range 5.9 to 13.0% and 78.0 to 85.5% in terms of d and σ^{SD}, respectively, are found. As was the case for the lower pH cases, these σ^{SD} deviations correspond to under-predictions for all three $[TC]_0$, as illustrated by the PBM peaks in $f(L)$.

The source of these discrepancies in σ^{SD} appears to be associated with the fast nucleation processes that govern the synthesis at alkaline conditions ($k_2[A]_0/k_1 \sim 1$) and that manifestly conflict with the assumptions of the F-W two-step mechanism of uncoupled nucleation and growth

and that also disrupt the three well-defined stages of induction, sigmoidal growth, and plateau. Recalling previous statements concerning the equilibration of the rates of nucleation and growth, the higher values of k_1 at $pH = 12$ allow for faster creation of nuclei of size d_{crit}, which in turn decreases the average diameter of the population, as captured by the model and observed experimentally. Nonetheless, as particle growth comes into play and halts significantly earlier at high pH (see t_{max} and $t_{plateau}$ in table 4.1) due to the rapid depletion of A, the emergence of nuclei and their almost concurrent growth leads to a surge in size polydispersity that is not correctly explained by F-W.

The steep decline in d and σ^{SD} with pH uncovered by the experimental and PBM results is in agreement with multiple instances in the literature for similar processes (see Nathanael et al. [203]). The work of Alqadi et al. [8], in addition to elucidating this inverse relationship, observed a more varied distribution in terms of particle shape at lower pH conditions. The authors postulated that this variability arises at low pH as a consequence of a mismatch in the rates of nucleation and growth, suggesting a strong connection with the F-W assumption of segregated nucleation and growth. Other authors [232, 188] attribute the lower particle size at higher pH to a kinetic acceleration of the reduction reaction in particular, a statement consistent with the much marked rise in k_1 with pH than k_2 obtained here. Interestingly, the effect of $[TC]_0$ at $pH = 12$ appears to be opposite to that observed at a lower pH, with a higher concentration of TC resulting in larger-sized NPs, hinting at instances of TC promoting particle growth instead of obstructing its development and supporting the claims of "double action" as stabiliser and reducing agent.

4.4.2 Parametric sweep of $k_2[A]_0/k_1$ in a well-mixed reactor

The final discussions on the well-mixed reactor model highlight the crucial importance of the ratio $k_2[A]_0/k_1 = t_{nuc}/t_g$ in predicting the PSD within the framework of the F-W two-step mechanism. The PBM results of table 4.2 point to this ratio being a strong positive predictor of d, σ^{SD}, and PDI; in fact, the results reported in figures 4.8 and 4.9 demonstrate that it is the sole predictor of these quantities after the plateau stage has concluded in the reactor.

Figures 4.8(a)-(f) illustrate the influence of this ratio by increasing k_1 and k_2 individually and conjointly one order of magnitude from the baseline conditions reported in §4.2. In the cases labelled as $k_2[A]_0/k_1$ and $10k_2[A]_0/10k_1$, after a steady-state is reached both show a virtually identical PSD and m_0, despite the latter case exhibiting a significantly faster NP production during the first stages due to its higher k_1 and k_2 (see $[B]$, m_0, and m_3). The balance attained in terms of particle size, standard deviation, and number of particles under the same $k_2[A]_0/k_1$ conditions is explained by noticing that the fast nucleation and growth processes that characterise $10k_2[A]_0/10k_1$ trigger a swift precursor consumption that quickly finalises at $\sim$ 25 min of operation, whereby a large amount of nuclei form and grow in a limited time span. The slower processes of the case $k_2[A]_0/k_1$ allow the reactions to continue until $\sim$ 175 min, providing the

system with enough time to "catch up" in size and number of particles to $10k_2[A]_0/10k_1$.

As the quantity $k_2[A]_0/k_1$ increases (see case labelled $10k_2[A]_0/k_1$), the kinetic separation of nucleation and growth (comparatively slower nucleation) allows for the formation of enough nuclei to promote a fast NP growth step without completely consuming the precursor, leading to the large particle sizes observed for this case. In contrast, in the case labelled as $k_2[A]_0/10k_1$ the comparatively faster nucleation step brings about a large quantity of small-sized nuclei (see m_0) that do not grow at a sufficiently fast rate, which gives rise to a sample described by a low average particle size, akin to our experimental/simulation results at pH = 12. As expected, despite the highly varied temporal paths of NP formation for the four cases in figure 4.8, their equal $[A]_0$ produces very similar dispersion concentrations (see m_3, which is proportional to the volume fraction of the solid phase in liquid) after the full exhaustion of the precursor.

Additional numerical experiments were carried out to provide further evidence for these claims and to further untangle the relationship between $k_2[A]_0/k_1$ and PSD. Figure 4.9(a)-(c) showcases the d, σ^{SD}, and PDI results of a five-orders-of-magnitude sweep of the ratio $k_2[A]_0/k_1$ for three d_{crit}, achieved by varying its three constitutive parameters individually. These plots also incorporate the experimental results reported in table 4.2 for reference [224, 204]. By using d_{crit} as a scaling parameter for the d and σ^{SD} data, a clear collapse of all points into a single, monotonically increasing curve of d and σ^{SD} vs. $k_2[A]_0/k_1$ can be seen in figure 4.9(d)-(e). This curve is fitted to a two-term power-law function of the form $\sim (k_2[A]_0/k_1)^{0.40}$ for d and $\sim (k_2[A]_0/k_1)^{0.34}$ for σ^{SD}, and used to estimate the functional form of the $PDI = (\sigma^{SD}/d)^2$ in figure 4.9(f). As a cautionary note it must be mentioned that the assumptions of the F-W two-step mechanism require comparatively slower nucleation processes ($k_2[A]_0/k_1 >> 1$, highlighted by the shaded blue area in figure 4.9), which might render invalid the points collapse and power-law fitting for $k_2[A]_0/k_1 < 1$ (highlighted by the shaded grey area in figure 4.9).

The above findings from the parameter sweep can be summarised as follows: in a well-mixed reactor, longer stages of nucleation in relation to growth give rise to a population of particles defined by higher (lower) d and σ^{SD} (m_0). The aforementioned observations are broadly followed by the experimental data, as seen from table 4.2, implying that a general tuning of the NPs size can be achieved by selecting the operating conditions that allow for a particular ratio between the initial characteristic times of nucleation and growth.

4.4.3 Synthesis of AgNPs in a T-junction microchannel

4.4.3.1 Precursor & consumption dynamics

As previously remarked, the transition from a spatially-averaged well-mixed reacting system to a continuous-flow environment uncovers multiple interacting phenomena that alter the synthesis process. Following the approach of Bal and Bandyopadhyaya [22], Kumar and Ganesan

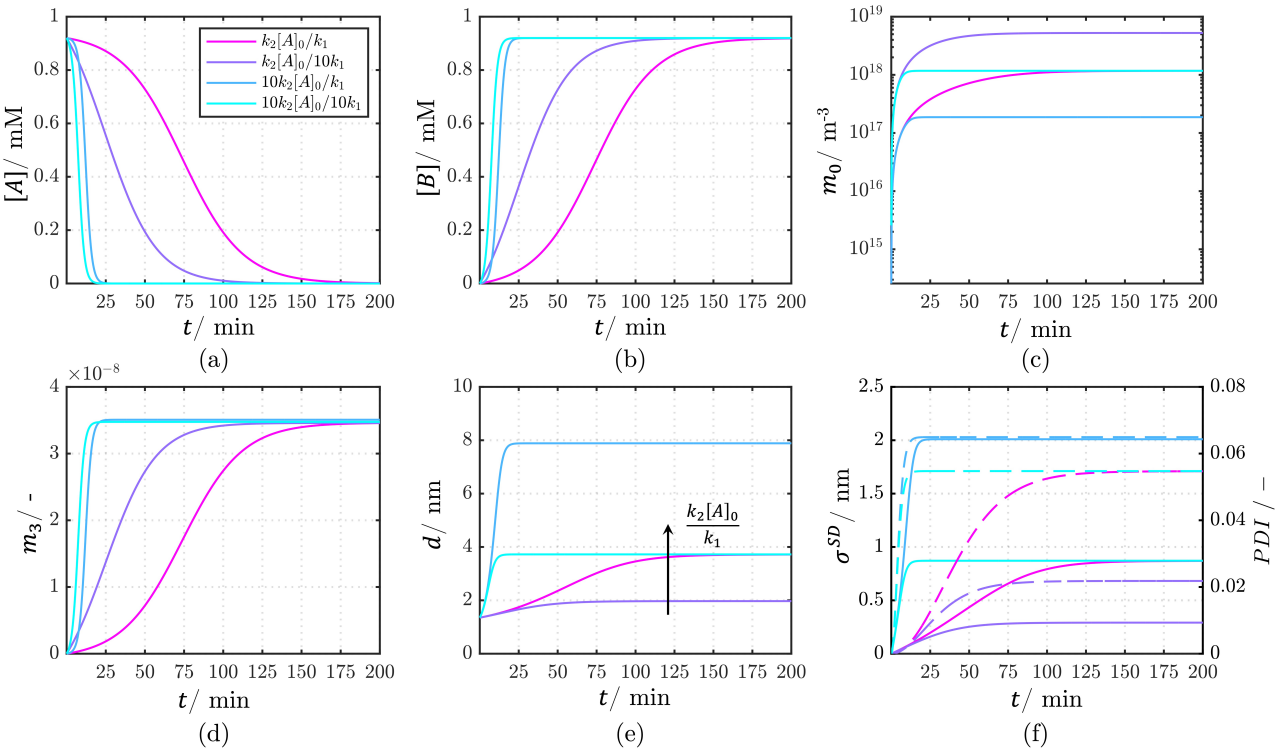

Figure 4.8: Effect of the ratio $k_2[A]_0/k_1$ on a few relevant parameters of the system in a well-mixed reactor, as predicted by the F-W two-step mechanism: (a)-(f) temporal evolution of precursor concentration, AgNPs concentration, m_0, m_3, average diameter, and standard deviation/polydispersity index, respectively. The series labelled as "$k_2[A]_0/k_1$" corresponds to the baseline case conditions, whereas the remaining denote one-order-of-magnitude increases of k_1 and k_2 individually and simultaneously. In (f), the continuous line corresponds to σ^{SD} and the dashed line to PDI. For all cases in this figure, $[A]_0 = 0.92$ mM, $[TA]_0 = 0.123$ mM, $[B]_0 = 0$ mM, $d_{crit} = 1.35$ nm, $d_m = 0.344$ nm

[154], Schikarski et al. [253], a few relevant time scales and dimensionless numbers of the process are analysed in order to elucidate the governing mechanisms driving the synthesis of AgNPs. In the proposed reduction-based PBM-CFD model, the following events are considered, each characterised by an individual time scale: i) diffusive mixing of the reactant streams, t_{mix}, ii) reduction reaction to produce silver atoms ($Ag_{(l)}$), t_r, iii) nucleation, t_{nuc}, iv) growth, t_g, v) particle diffusion, t_{diff}, and vi) particle agglomeration, t_{agg}. Taking into consideration that the driving force behind particle nucleation and growth is the concentration of $Ag_{(l)}$ (see §4.3.2), the stages of mixing and reduction that create the $Ag_{(l)}$ material and that themselves depend on the concentrations of the precursor and reducing agent (see Eqs. (4.9)-(4.11)), are particularly crucial to the process.

The following scaling is defined: $\tilde{\mathbf{x}} = \frac{\mathbf{x}}{E}$, $\tilde{\mathbf{u}} = \frac{\mathbf{u}}{U_a}$, $\tilde{t} = \frac{t}{H/U_a}$, $\tilde{\rho} = \frac{\rho}{\rho_c}$, which renders Eq. (4.12)

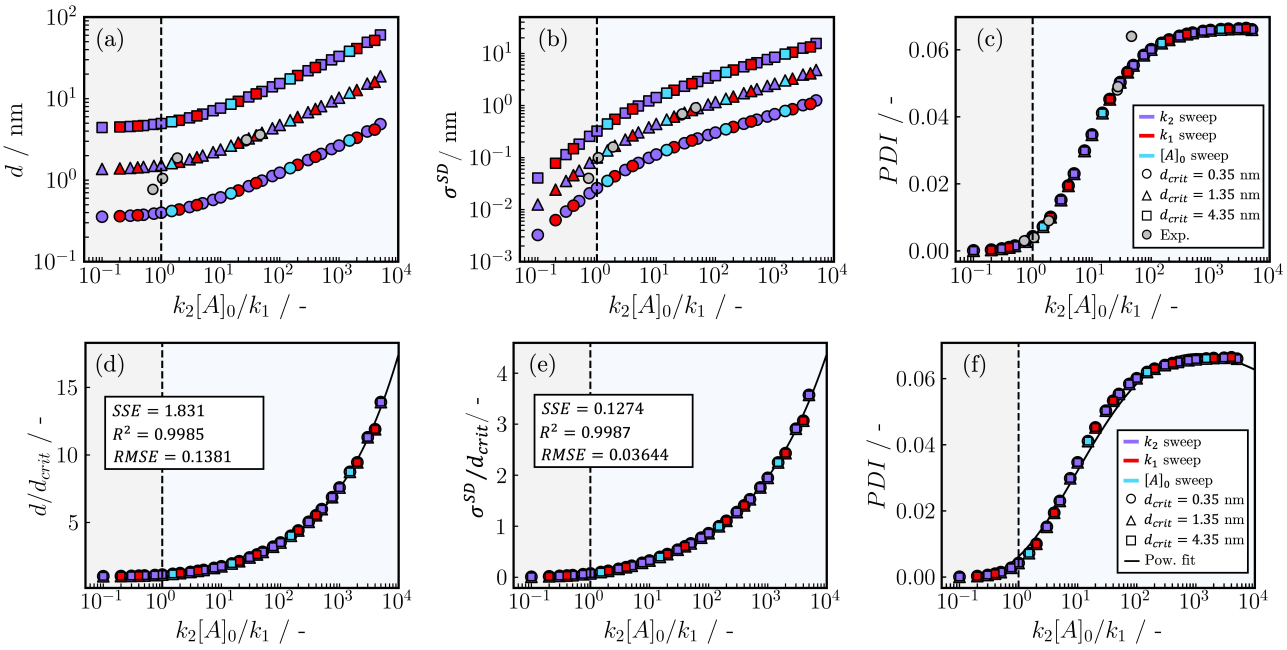

Figure 4.9: Prediction of PSD in a well-mixed reactor by using two parameters: the ratio k_2A_0/k_1 and d_{crit}, as predicted by the F-W model: (a)-(c) five-orders-of-magnitude sweep of k_2A_0/k_1 under three different conditions of d_{crit}. Experimental data measurements reported in Pico et al. [224], Nathanael et al. [204] also included for reference; (d)-(e) data point collapse of d and σ^{SD} by using d_{crit} as a scaling parameter, resulting in the power-law functions $\sim (k_2[A]_0/k_1)^{0.40}$ for d and $\sim (k_2[A]_0/k_1)^{0.34}$ for σ^{SD}. The limit $k_2[A]_0/k_1 < 1$, where F-W is typically invalid, is highlighted by the grey areas, whereas $k_2[A]_0/k_1 > 1$ is highlighted by the blue areas. Fro all cases in this figure, $[A]_0 = 0.92$ mM, $[TA]_0 = 0.123$ mM, $[B]_0 = 0$ mM

for the precursor and reducing agent dimensionless:

$$\frac{\partial(y_{SN})}{\partial\tilde{t}} + \frac{H}{E}\tilde{\nabla}_{\mathbf{x}}\cdot(\tilde{\mathbf{u}}y_{SN}) = \frac{1}{Pe_{SN}}\tilde{\nabla}_{\mathbf{x}}\cdot(\tilde{\nabla}_{\mathbf{x}}(y_{SN})) - Da_{SN,r}(y_{SN})(\tilde{\rho}y_R)^{\nu_R},$$
$$\frac{\partial(y_R)}{\partial\tilde{t}} + \frac{H}{E}\tilde{\nabla}_{\mathbf{x}}\cdot(\tilde{\mathbf{u}}y_R) = \frac{1}{Pe_R}\tilde{\nabla}_{\mathbf{x}}\cdot(\tilde{\nabla}_{\mathbf{x}}(y_R)) - Da_{R,r}(y_{SN})(\tilde{\rho}y_R)^{\nu_R}, \tag{4.19}$$

where the tildes designate dimensionless variables.

The dimensionless groups of Eq. (4.19) are defined as follows:

$$Pe_{SN} = \underbrace{\frac{U_a}{H}}_{t_{res}^{-1}}\overbrace{\frac{E^2}{D_{SN}}}^{t_{SN,mix}},\quad Da_{SN,r} = \underbrace{k_r\left(\frac{\rho_c}{MW_R}\right)^{\nu_R}}_{t_{SN,r}^{-1}}\overbrace{\frac{H}{U_a}}^{t_{res}}$$
$$Pe_R = \underbrace{\frac{U_a}{H}}_{t_{res}^{-1}}\overbrace{\frac{E^2}{D_R}}^{t_{R,mix}},\quad Da_{R,r} = \underbrace{\frac{k_r\nu_R MW_R^{1-\nu_R}\rho_c^{\nu_R}}{MW_{SN}}}_{t_{R,r}^{-1}}\overbrace{\frac{H}{U_a}}^{t_{res}}. \tag{4.20}$$

In the above, $U_a = (4/\pi)(Q/E^2)$, the average velocity across the channel, and $t_{res} = H/U_a$, the average residence time, correspond to the characteristic velocity and time scales, respectively.

In the present context, the Péclet number of species j, Pe_j, can be understood as the ratio between the characteristic time scales of diffusive mixing and flow residence time ($t_{j,mix}/t_{res}$), whereas the Damköhler number of species j, $Da_{j,r}$, provides a dimensionless measurement of the speed of consumption of species j due to the reduction reaction relative to the residence time ($t_{res}/t_{j,r}$). Consequently, a case described by $Pe_j >> 1$ and $Da_j >> 1$ is limited by the mixing of the reagents and undergoes a fast reduction process when compared to the residence time of the flow.

In addition to these dimensionless groups, it is instructive to also consider the Reynolds number of the system, $Re = \rho_c U_a E/\mu_c = 4.24 - 16.98$, and the transversal Péclet number of species j, $Pe_{trav,j} = u_x E/D_j = t_{j,mix}/t_{conv}$. This latter number establishes the relationship between the characteristic time of diffusion of j and the time associated with convective mixing, providing an estimate of the contribution of convection to the mixing process. Instead of using Ua, which is predominantly influenced by the velocity component in the y-direction, $Pe_{trav,j}$ is defined based on the transversal velocity (i.e., the velocity in the x-direction, as shown in figure 4.1(c)).

For the highest flow rate (200 μL/min) and the lowest mass-diffusion coefficient between the inlet streams (D_R), maximum values of $Pe_{trav,j}$ are estimated in the range of $\approx 10^{-1}$ to 10^{-2}. As expected, the contribution of convection to mixing in the system is negligible, and the outcomes of the process are primarily determined by diffusive mixing and its relation to t_{res}. This feature arises due to two main reasons. Firstly, the low Re ($\lessapprox 150$) fully suppress the development of asymmetric vortical structures in the channel cross-section, which are responsible for promoting mixing in microchannels, as demonstrated previously [40]. Secondly, our straight channel geometry eliminates any possibility of generating transversal flows and recirculation patterns, commonly induced by coiled reactors even at low Re [133, 318]; additional effects of employing a straight reactor geometry in the context of the PSD are discussed in §4.4.3.2.

Figure 4.10(a) portrays the experimentally-measured steady-state concentration of silver ions (silver precursor in solution) reported in the work of Pico et al. [224] across the channel length under different conditions of inlet flow rate and subject to the baseline conditions of pH and reactants concentration (see §4.2.3 and table 4.1). These experimental spatial profiles unveil the notable behavioural dissimilarities that characterise the process of precursor consumption in a well-mixed versus a continuous-flow reactor. As examined previously, the spatially-averaged concentration curves for the well-mixed reactor feature a sigmoidal-like temporal evolution that is not observed across the microchannel. In contrast, a very rapid consumption within the first ~ 0.125 m of the channel is discerned, followed by a much slower, almost linear or parabolic consumption until the 2m mark is reached, where small but non-negligible traces of precursor

are detected ($[SN] = 0.031 \pm 0.0036$ and 0.013 ± 0.0013 mM for the highest and lowest flow rates, respectively; see inset of figure 4.10(a)). The rapid precursor consumption seen across the channel displays an inverse response against the inlet flow rate. Lower flow rates give rise to higher residence times whose influence is materialised in higher (lower) $Da_{j,r}$ (Pe_j), promoting the consumption of both SN and R via the reduction reaction, as well as their diffusive transport (see Eq. (4.19)).

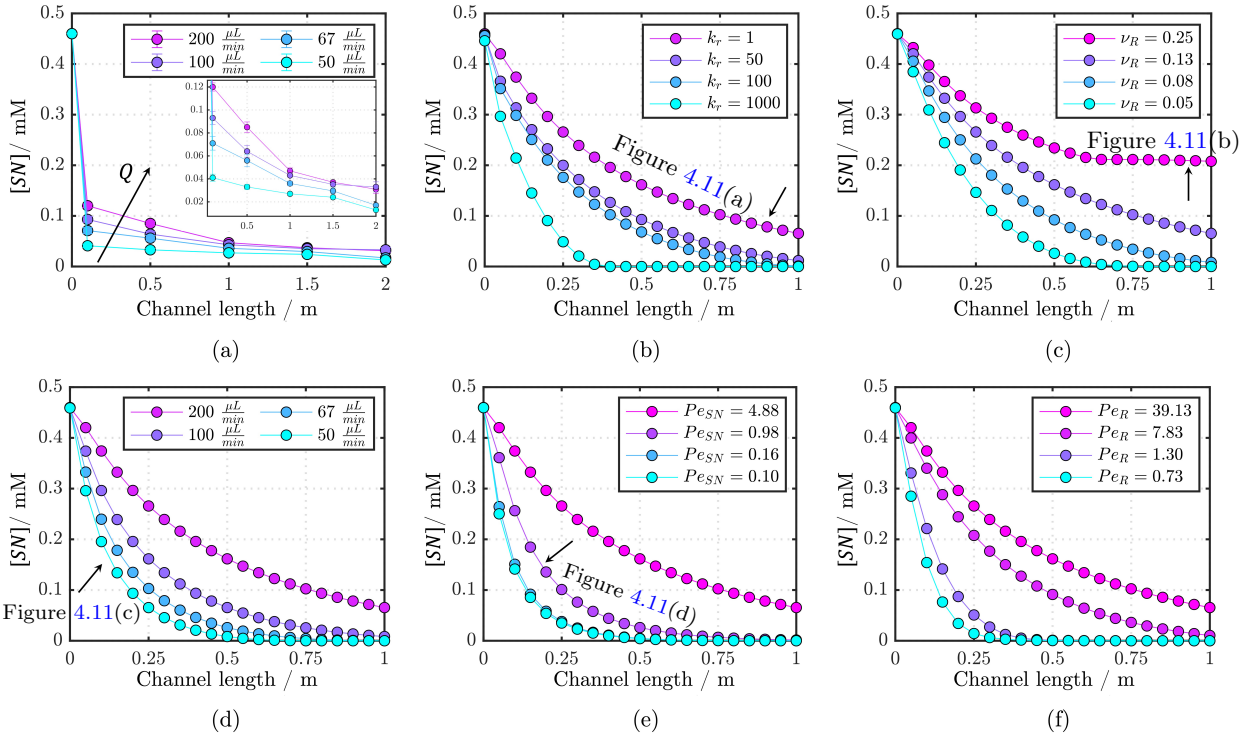

Figure 4.10: Influence of hydrodynamic parameters on the steady-state concentration of AgNPs precursor (or silver ions) along the T-junction microchannel: (a) experimental data reported in the work of Pico et al. [224] measured under different conditions of Q; (b) effect of k_r (varying $Da_{j,r}$); (c) effect of ν_R (varying $Da_{j,r}$); (d) effect of Q (varying $Da_{j,r}$ and Pe_j simultaneously); (e) effect of Pe_{SN}; (f) effect of Pe_R. The data points from the simulations correspond to the cell averages over different cross-section planes normal to the y-direction (channel length). The black arrows indicate simulations under the same conditions as depicted in figure 4.11. All other operating parameters remain unchanged from those specified in §4.2.3 for the base case and the kinetic/dimensionless parameters not mentioned explicitly in the labels of each plot correspond to $k_r = 1$ $\mathrm{m}^{3\nu_\mathrm{R}}\mathrm{s}^{-1}\mathrm{mol}^{-\nu_\mathrm{R}}$, $\nu_R = 0.13$, $Pe_{SN} = 4.88$, and $Pe_R = 39.13$

The relationship between precursor consumption and inlet flow rate found experimentally in [224] is reproduced via the numerical simulations, as depicted in figure 4.10(d). It should be noted that all simulation results shown in this set of plots, in conjunction with those of figure 4.11, were run for a total channel length of 1 m due to the extensive computational resources required to capture the entire 2 m domain; as seen from the experimental profiles, the zones where most phenomena of interest take place are well within the first 1m of the channel. The intensification of precursor consumption per channel length seen at lower flow rates triggers a similar effect on the formation of silver atoms ($Ag_{(l)}$) available for nucleation and growth, which,

as will become apparent in the following discussions, have major consequences on the PSD and its spatial distribution within the channel.

Yoo et al. [326] and Iwamoto et al. [118] have suggested that variations in the rate of the reduction reaction in particular bring about prominent changes to the evolution of the subsequent reactions and the final PSD for AuNPs. Accordingly, figure 4.10(b) illustrates the effect of the reduction kinetic constant for the studied system using the stoichiometric conditions and transport properties that correspond to those of TA for the reducing agent, as stipulated in §4.3.2. Expectedly, increasing k_r under the concentration conditions of the reducing agent ($\nu_R = 0.133$ and $[R]_{inlet} = 0.123$ mM) increases the rate of SN consumption across the channel (increased $Da_{j,r}$) until a virtually total consumption before 1m is seen at $k_r > 100$ $\mathrm{m}^{3\nu_\mathrm{R}}\mathrm{s}^{-1}\mathrm{mol}^{-\nu_\mathrm{R}}$.

Figure 4.10(c) shows that precursor consumption is also heavily linked to the stoichiometric conditions of the reduction reaction between SN and a potential TA-TC complex. It is observed that ν_R inversely generates higher rates of SN consumption per reactor length, explained by the accentuation of the "excess" effects concerning the concentration of the reducing agent (0.123 mM) and its imbalance against that of SN (0.92 mM). Therefore, as ν_R increases to reach a critical value located in the range $0.133 - 0.25$, R begins to be consumed at a decidedly faster rate than SN, as evidenced by the non-zero constant profile of $[SN]$ beyond 0.6m from the inlet at $\nu_R = 0.25$, indicating now an excess concentration of SN.

To conclude this segment of the discussion, figure 4.10(e)-(f) presents several plots depicting the profiles of precursor concentration under varying Pe_j, while keeping all other dimensionless numbers and reaction parameters consistent with those specified in the figure's caption. The variations of Pe_j were made by altering the values of the mass diffusion coefficients of species $j = SN, R$. This set of results clearly exemplifies the coupled and interdependent effects of flow hydrodynamics and reaction kinetics that govern the synthesis of AgNPs. As Pe_j decreases (D_j increases), a much higher consumption of SN per reactor length is found given the faster mixing of the reactants and its concomitant accelerated reduction kinetics within the region 0-0.25 m (see last term on the RHS of Eq. (4.19)).

The parametric sweep examined above has demonstrated the strong influence of flow hydrodynamics on the evolution of the chemical reactions involved in the system. These concepts are expanded upon through figure 4.11, where the steady-state contour plots of a few relevant variables across the T-junction microchannel are displayed. From top to bottom, these variables are: $[SN]$, $[R]$, ξ, $\dot{r}_{Ag_{(l)},r}$, $[Ag_{(l)}]$, and $[Ag_{(s)}] + [Ag_{(s2)}]$. In this context, $\xi = \frac{[SN]-[R]+[R]_{inlet}}{[SN]_{inlet}+[R]_{inlet}}$ corresponds to the mixture fraction, which provides a quantitative measure of the degree of mixing of two flow streams ($\xi = 1$ for pure SN, $\xi = 0$ for pure R, and $\xi = 0.5$ for a well-mixed and non-reacted feed) [185]; $\dot{r}_{Ag_{(l)},r} = k_r[SN][R]^{\nu_R}$ is the rate of $Ag_{(l)}$ production (in mM) due to the reduction reaction (see Eq.(4.9)). The dashed white line on each contour marks the channel centre-line normal to the x-direction ($x/E = 0.5$, see the location of Cartesian axis)

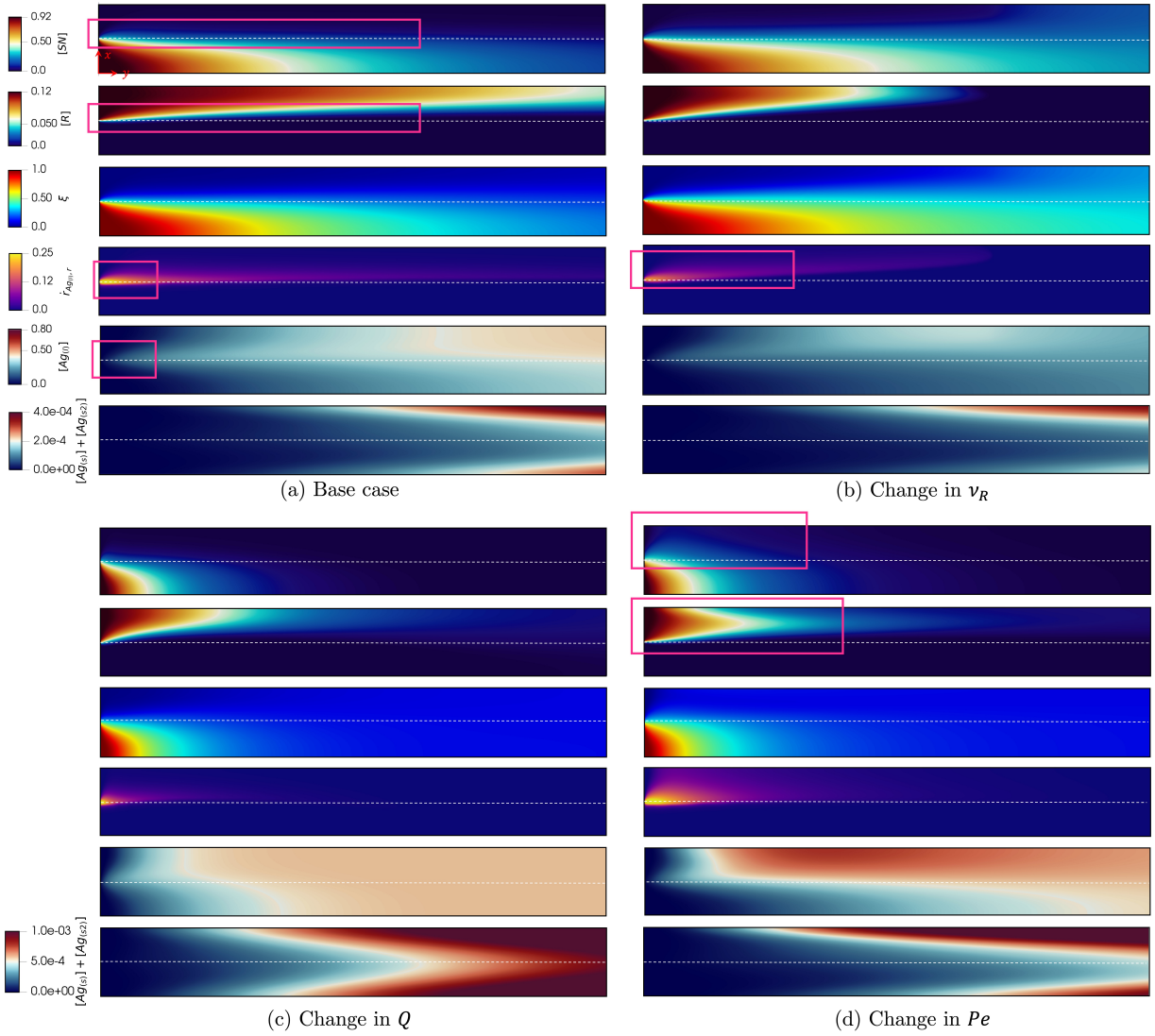

(a) Base case

(b) Change in ν_R

(c) Change in Q

(d) Change in Pe

Figure 4.11: Steady-state simulation contour profiles in the T-junction microchannel for $[SN]$ in mM, $[R]$ in mM, ξ, $\dot{r}_{Ag_{(l)},r}$ in mMs^{-1}, $[Ag_{(l)}]$ in mM, and $[Ag_{(s)}]+[Ag_{(s2)}]$ in mM (top to bottom, respectively): (a) $k_r = 1$ m$^{3\nu_R}$s^{-1}mol$^{-\nu_R}$, $\nu_R = 0.133$, and $Q = 200$ μL/min ($Da_{j,r} = 68.78, 91.60$ and $Pe_j = 4.88, 39.13$ for SN and R, respectively); (b) $\nu_R = 0.25$ ($Da_{j,r} = 2.55\times10^4, 3.63\times10^2$ for SN and R, respectively); (c) $Q = 50$ μL/min ($Da_{j,r} = 2.75\times10^2, 3.66\times10^2$ and $Pe_j = 1.22, 9.78$ for SN and R, respectively); (d) $Pe_{SN} = 0.98$. All other operating parameters remain unchanged from those specified in §4.2.3 for the base case and all kinetic/dimensionless parameters not mentioned in the captions of each figure correspond to those of (a). For easier visualisation, the inlet streams of all contour plots have been removed and the channels have been rescaled from their original dimensions as follows: $\mathbf{x} = (25x, 0.1y, z)$

The case shown in figure 4.11(a), whose $[SN]$ profile is labelled in figure 4.10(b), exemplifies the comparatively faster consumption of SN obtained as a result of the reaction stoichiometry ($\nu_R = 0.133$ and $7.5:1$ $[SN]_{inlet}:[R]_{inlet}$), whereby SN shows a steep concentration decline before reaching the channel centre in the length-wise direction ($y/H \sim 0.5$ m) whilst, for the most part, $[R] > 0.05$ mM on its side of the channel ($x/E > 0.5$) throughout the entire length domain. Although not explicitly shown in the figures, it is reported for this case that around 7.12% of the inlet concentration of SN is left at the outlet, compared to the 13.32% of its R counterpart.

This unbalanced consumption of the two main reagents notably limits the production of $Ag_{(l)}$, the size of the particles, and the outlet sample's concentration of AgNPs, as explained in the following subsection. The contours of ξ, $\dot{r}_{Ag_{(l)},r}$, $[Ag_{(l)}]$, and $[Ag_{(s)}] + [Ag_{(s2)}]$ for this case reveal the existence of small localised regions of perfect mixing ($\xi = 0.50$) in the vicinity of $x/E = 0.50$ and close to the T-junction in the y-direction, where $\dot{r}_{Ag_{(l)},r}$ reaches its maximum value (see highlighted zone). Downstream from this region, the fast consumption of SN induces a rapid drop in $\dot{r}_{Ag_{(l)},r}$ and an appreciable distortion of the zones described by $\xi = 0.50$.

In figure 4.11(a) a stark difference in the location of the accumulation zones of $Ag_{(l)}$ (channel centre in x and towards the outlet) versus those of Ag_s and Ag_{s2} (near the channel walls) is detected. This observation is a clear indication of the timescale disparity related to the phenomena of reduction and nucleation/growth and how each one compares to t_{res}. For this case, $t_{res} \sim 29$ s, $t_r \sim 0.30 - 0.40$ s, $t_{nuc} = 1/k_1 = 5.45 \times 10^4$ s, and $t_g = 1/k_2[Ag_{(l)}]_{max} = 1.18 \times 10^3$ s (i.e., $t_r < t_{res} < t_g < t_{nuc}$). The fast reduction step induces an almost immediate formation of $Ag_{(l)}$ at the centre of the channel (where $\xi = 0.5$), as seen in the highlighted section of the $[Ag_{(l)}]$ contour, that leads to an eventual $[Ag_{(l)}]$ accumulation in the areas surrounding the outlet. In contrast, the much slower nucleation and growth steps restrict the formation of $Ag_{(s)}$ and Ag_{s2} to the regions where the local residence time is large enough for those processes to take place (near the channel walls) and where the concentration of $Ag_{(l)}$ is sufficiently high (the channel outlet).

By exploring the concentration of SN and R beyond the side of their individual inlet in the x-direction (i.e., exploring $x/E > 0.5$ for SN and $x/E < 0.5$ for R), one can discern a higher SN "crossover" to the side of R, as highlighted in the contour plots. These findings can be rationalised by linking them to the mass diffusivity coefficients of SN and R (and Pe_j). The higher diffusivity of SN (lower Pe) allows it to cross the centre-line at a faster rate than R, providing an explanation for the residual SN at $x/E > 0.5$ and the preferential formation of $Ag_{(l)}$ towards those regions in the channel.

The repercussions of $D_{SN} > D_R$ become particularly noticeable as ν_R is increased to reach the domains of excess SN (total exhaustion of R), as depicted in figure 4.11(b), where it is seen that the presence of SN extends over the entire channel diameter as we approach the channel outlet. This mass diffusivity disparity between SN and R is also responsible for the spatially uneven development of the high $\dot{r}_{Ag_{(l)},r}$ trail that emerges from the hot spot close to the T-junction (see figure highlight).

As previously remarked, the longer flow residence that characterises an operation with lower flow rates promotes the consumption of both SN and R due to an increased (decreased) $Da_{j,R}$ (Pe_j). These effects can be appreciated in the contour plots of figure 4.11(c) for $Q = 50$ μL/min, where both species are nearly consumed before reaching the channel half point. The rapid consumption of both reagents, in addition, increases the overall production of $Ag_{(l)}$ per channel length and thus that of $Ag_{(s)}$ and $Ag_{(s2)}$ (notice the colour bar scale of the latter two species in

comparison to that of figure 4.11(a)-(b)). These higher residence times are also responsible for the effectively homogeneous distribution of $[Ag_{(l)}]$ after $y/H \sim 0.5$.

Figure 4.11(d) describes how a reduction in Pe_{SN} from a rise in D_{SN}, in addition to accentuating the radial disparity in the concentration profiles of SN and R (see highlights), considerably increases $\dot{r}_{Ag_{(l)},r}$, $[Ag_{(l)}]$, and $[Ag_{(s)}]$ compared to, for example, figure 4.11(a). This is due to a higher SN crossover to the realms of $x/E > 0.5$, which consequently triggers higher mixing and reaction rates. The steady-state profiles of SN along the channel that correspond to the cases of figure 4.11(c) and (d) (figure 4.10(d) and (e), respectively) suggest similar overall amounts of SN consumed and $Ag_{(l)}$ produced (not shown explicitly here). However, the $[Ag_{(l)}]$ contour of figure 4.11(d) depicts a notably more uneven spatial distribution of this species, an observation likely caused by the larger D_{SN}/D_R ratio of this case compared to that of figure 4.11(c).

4.4.3.2 Effect of hydrodynamics on the PSD of AgNPs

The previous subsection provided a detailed illustration of the underlying phenomena governing the synthesis of AgNPs from the perspective of hydrodynamic and kinetic time-scale competitions and their notable influence on the consumption of reactants/production of nanoparticles. This subsection links these experimental and simulation findings to the PSD of the samples in the T-junction microchannel and thoroughly describes the spatial distribution of the variables involved in the process along the channel.

Figures 4.12(a)-(c) present the experimentally-measured steady-state PSD across different channel lengths and for different inlet flow rates reported in Pico et al. [224], with the summarised results reported in the table insets of each figure; as is the case throughout this investigation, the remaining operating conditions are those assigned to the base case.

These figures elucidate the strong connections between flow hydrodynamics and PSD, whereby for all channel lengths the average particle size and its standard deviation undergo a monotonic decrease with an increase of inlet flow rate. Barring the outlier measurements at 1m and $Q = 200$ μL/min, both d and σ^{SD} appear to follow an almost-linear trend against channel length; the slopes of these functions also exhibit a negative response to the flow rate (d slope $\sim 5.38, 5.33, 5.04$ and σ^{SD} slope $\sim 2.11, 1.79, 1.53$ nm/m for $Q = 50, 100, 200$ μL/min, respectively). Interestingly, the PDI does not appear to show a clear monotonic response against either channel length or flow rate, but in all cases (except for $Q = 50$ μL/min at 2 m) is within an acceptable range for a monodispersed sample ($PDI \lessapprox 0.10$) [53]. The simulation results of figures 4.12(d)-(f) adhere to the same inverse relationship between flow rates and PSD and depict a similar semi-linear evolution of d and σ^{SD} across the channel domain as the experiments. We note that these simulation results are reported for a shorter channel length (0.25 m) due to the prohibitively large computational resources needed to resolve the dynamics of the full channel, which is left for future work

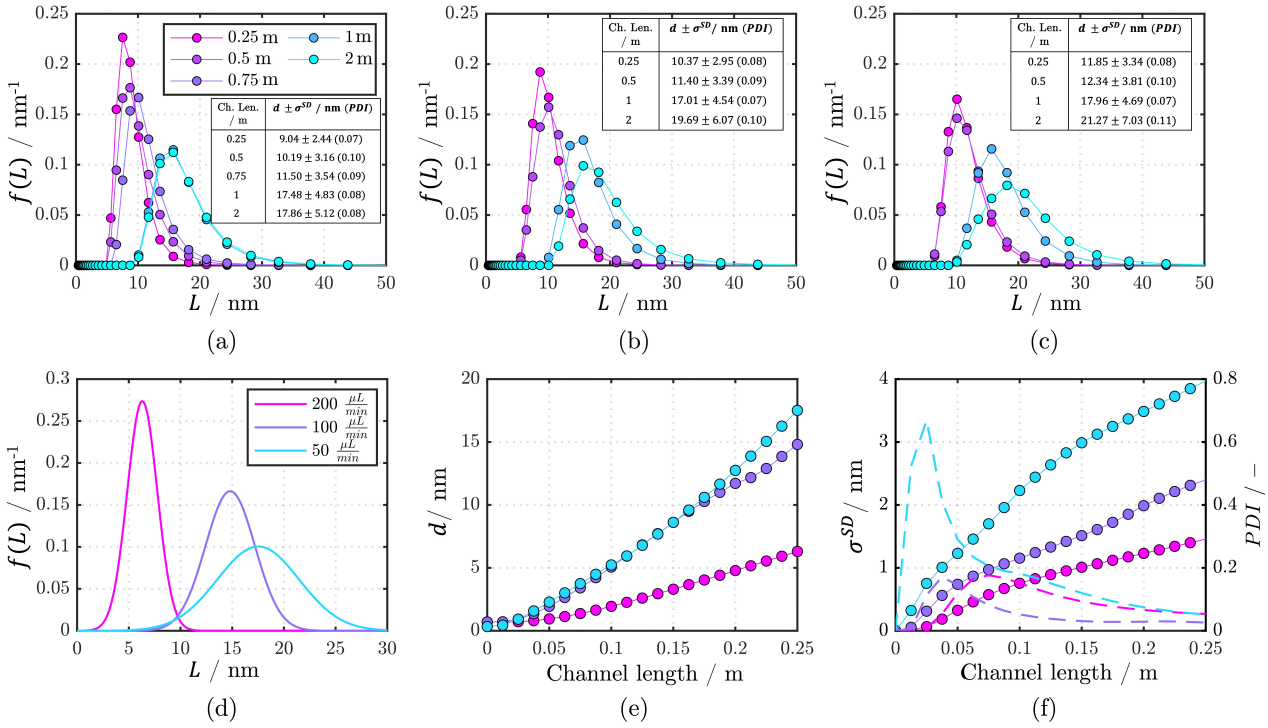

Figure 4.12: Influence of inlet flow rate on the PSD along the T-junction microchannel: (a)-(c) experimental data measured at different outlet channel lengths for (a) $Q = 200$ μL/min, (b) $Q = 100$ μL/min, and (c) $Q = 50$ μL/min, as reported in Pico et al. [224]; (d) steady-state PBM-CFD PSD obtained at an outlet length of 0.25 m; (e) steady-state PBM-CFD average diameter along the channel length; (f) steady-state PBM-CFD standard deviation (left axis, marks) and PDI (right axis, dashed line) along the channel length. The data points in (e) and (f) correspond to the cell averages over different cross-section planes normal to the y-direction. All other operating parameters remain unchanged from those specified in §4.2.3 for the base case. For these cases, $k_r = 1000$ m$^{3\nu_R}$s^{-1}mol$^{-\nu_R}$, $\nu_R = 0.05$, $d_{crit} = 0.7$ nm, and $d_m = 0.344$ nm. These reacting parameters have been selected as they better adhere to the excess conditions of the reducing agent in the experiments, as well as the reduction time ($\sim 3.9 \times 10^{-4}$ s) suggested in the literature [284]. The dimensionless numbers and characteristic times that describe these cases, in order of decreasing Q, are: $t_{res} \sim 7.36, 14.72, 29.45$ s, $Da_{SN,r} = 1.01 \times 10^4, 2.03 \times 10^4, 4.05 \times 10^4$, $Da_{R,r} = 5.07 \times 10^3, 1.01 \times 10^4, 2.03 \times 10^4$, $Pe_{SN} = 1.95 \times 10^1, 9.76, 4.88$, $Pe_R = 1.57 \times 10^2, 7.88 \times 10^1, 3.91 \times 10^1$. For all three cases, $t_{SN,r} \sim 7.27 \times 10^{-4}$ s, $t_{R,r} \sim 1.45 \times 10^{-3}$ s, $t_{SN,mix} \sim 1.43 \times 10^2$ s, $t_{R,mix} \sim 1.15 \times 10^3$ s, $t_{nuc} \sim 5.45 \times 10^4$ s and $t_g \sim 1.18 \times 10^3$ s

The above results are entirely consistent with previous investigations of similar systems, where experiments have demonstrated that the hydrodynamic conditions of laminar microreactors exert a major influence over the PSD [137, 143]. The variation in residence time brought about by modifying, for instance, the operating flow rate has been determined to be one of the main factors that alter the PSD and the shape of the NPs. Ling et al. [172] and Aljarrah et al. [6] have examined the effect of residence time on the morphology of silica and gold NPs, respectively, and have reported that shorter residences times lead to smaller size distributions. From the current findings regarding figures 4.10-4.11, it can be suggested that it is the narrowing of the discrepancy between the comparatively short residence time and the long characteristic times of nucleation/growth that gives rise to larger particles at lower flow rates. Besides these components, within the

framework of the proposed model, it is observed that lower flow rates are also responsible for a higher consumption of the precursor per reactor length, which subsequently leads to a higher concentration of $Ag_{(l)}$ available for nucleation and growth (see Eq. (4.10)-(4.11)).

The crucial differences in the dynamics that transpire going from a well-mixed reactor to a continuous-flow microchannel are evident when comparing the sizes reported in figure 4.12 to those in figure 4.7(a) (and table 4.2) under the same conditions of pH and $[TC]_0$. The approximately tenfold increase in both d and σ^{SD} seen by synthesising AgNPs in a microreactor is a clear depiction of how hydrodynamics, kinetics, and PSD are closely intertwined. Herein, the explicit interrelations between these phenomena are elucidated and contextualised in terms of the differences between the F-W mechanism for well-mixed reactors and the proposed extension for microfluidics.

In a well-mixed reactor, the attainable particle sizes are strictly constrained by both the availability of precursor A for direct conversion into B (see Eqs. (2.11) - (2.12)) and the interplay between nucleation and growth. This constraint arises from the fact that the F-W expressions employed to simulate these phenomena (Eqs. (4.3) - (4.4)) are direct functions of $[A]$ and are mediated by the relation between nucleation and growth (as demonstrated in figure 4.8). In a well-mixed system the consumption process of A proceeds continuously and without delays caused by transport phenomena. Consequently, the "fast" and "direct" consumption of A into B limits the particle sizes that can be reached.

In contrast to the above, reactions in microchannels are governed by the very slow convective/diffusive dynamics ($Re = 4.24 - 16.98$ in our system) responsible for mixing the initially-separated reactants streams. These slow and controlled processes, in addition to delaying precursor consumption, facilitate particle agglomeration events that lead to larger particles. From these remarks, it is possible to envision the well-mixed reactor as the limit where the onset of precursor consumption occurs almost immediately after the start of the operation (i.e., no reaction delays stemming from mixing) and where particles do not have enough time to aggregate in the reactor.

The above discussion serves as an additional explanation of the inverse relationship observed between outlet particle sizes and inlet flow rates. As the flow residence time decreases with an increase in the flow rate, both the simulations and the experiments suggest a reduction in the consumption of the precursor per reactor length (see the discussion of figures 4.10 - 4.11). This in turn critically diminishes the production of $Ag_{(l)}$, the driving force for nucleation and growth (see Eqs. (4.10) - (4.11)). The combination of an overall lower concentration of $Ag_{(l)}$ available for nucleation and growth, along with a shorter time for agglomeration, explains the smaller particle sizes observed at higher flow rates.

In the studied system, the use of microfluidics permits the synthesis of larger-sized NPs with equal or even higher-size monodispersity, as seen from the PDI values. The work of Wu et al. [318] has established similar connections between mixing rates and residence times with

the PSD by analysing different microreactor geometries. A key finding from that work is the significant reduction in particle size obtained via operations with helical microreactors, whose curved domains allow for the development of secondary transversal flows that aid in the mixing of the reagents, reducing the radial-wise variability in species concentration and promoting a rapid consumption of the precursor and NP nucleation. Considering the above remarks, the well-mixed reactor can be envisioned as the limit where the onset of precursor consumption occurs almost immediately after the start of the operation (i.e., no reaction delays stemming from mixing), leading to a faster birth and growth of NP nuclei within a much lower time-span, restricting the particle size.

The discussion now proceeds to analyse the spatial distributions of a few relevant PBM-related variables within the T-junction microchannel; these distributions clearly encapsulate and summarise the connections between hydrodynamics, reaction kinetics, and PSD. Figures 4.13(a)-(c) portray the steady-state snapshots of m_0, m_3, and d for the three flow rates tested. These contours are complemented with the plots of figures 4.13(d)-(i), which depict the radial-wise profile of each variable at the outlet plane of the channel (normal to the y-direction).

As expected from previous findings related to $[Ag_s + Ag_{s2}]$ in figure 4.11, the volume fraction of the dispersed phase ($\phi_d \sim m_3$) preferentially accumulates at the vicinity of the walls, where, on average, the particles are also much larger than at the centre-line. Recalling previous statements about the critical effects associated with the residence time in the channel, it is unsurprising that the largest-sized particles tend to gather near the channel walls, where the lowest flow velocities are found (figure 4.13(d)) and, consequently, the particles have a longer time to grow from nuclei, agglomerate, and deposit, leading to a higher ϕ_c.

As seen from the contour plots and the outlet profiles, these outcomes are heightened by operations with lower flow rates, whereby a cascade of coupled kinetic and hydrodynamic events, driven by higher residence times, give rise to larger AgNPs and higher NPs volume fractions. Namely, longer residence times initially lead to an accelerated precursor consumption per reactor length (see $[SN]$ outlet profile, figure 4.13(h)), which promotes the production of $Ag_{(l)}$ close to the inlets and therefore the generation and growth of small-sized nuclei. The increased time span in which nucleation and growth are allowed to take place eventually generates high rates of $Ag_{(l)}$ consumption at low Q, which virtually equalise the average $[Ag_{(l)}]$ at the outlet plane between the highest and lowest Q (figure 4.13(i)). These events, in conjunction with inter-particle agglomeration instances (which are boosted by particle size, see Eq. (4.17)) finally bring about the noteworthy differences in particle size observed between varying flow rates.

The effects of flow residence time on the balance between nucleation, agglomeration, and particle diffusion are manifested in the appreciably more homogeneous m_0 (number of particles density) outlet radial profiles at lower flow rates, despite similar surface-averaged values over this plane ($1.81, 2.28, 2.52 \times 10^{19}$ m^{-3} for $Q = 200, 100, 50$ μL/min, respectively). Under high Q

conditions, the particles tend to accumulate close to the walls and disproportionately towards one side of the channel given the uneven radial distribution of $[Ag_{(l)}]$ (refer to the analysis of §4.4.3.1 and figure 4.13(i)). These axial heterogeneities diminish at lower flow rates via diffusive transport of $Ag_{(l)}$, the nuclei, and the AgNPs themselves.

Interestingly, figures 4.13(a,e) show that the preferred zones of m_0 accumulation in the radial direction do not correspond to the vicinity of the walls, as it is the case of d and m_3 (figures 4.13(f-g)); instead, the particle accumulation areas are shifted toward the channel centre. This suggests instances of dominant agglomeration over nucleation events at the locality of the walls, whereby the rapid rates of nucleation induced by high $[Ag_{(l)}]$ are not sufficient to overcome the rates of agglomeration, resulting in lower m_0. Looking at the overall picture, a similar but opposite remark can be made about the influence of the flow rate on m_0, where the surface-averaged values over the outlet plane slightly increase with a Q decrease. Considering the higher rates of both nucleation and agglomeration per channel length at $Q = 50$ μL/min, the fact that m_0 is still higher on average than at $Q = 200$ μL/min appears to be an indication of dominant particle-creation nucleation events over m_0-destructive agglomeration instances.

At this point, attention is drawn to the fact that the proposed F-W-based PBM-CFD simulations provide useful and acceptable quantitative predictions of d and σ^{SD} in the microreactor and, as mentioned before, are able to correctly capture the overall phenomena involved in the reacting system, especially in terms of operation-driven variations in d and σ^{SD} and their distributions as the flow evolves along the channel. The quantitative deviations from the experiments of Pico et al. [224] are attributed to three main limitations of the model. The first one corresponds to the uncertainty regarding the reduction reaction and the role/properties of the TA-TC complex, both of which influence the rate of precursor consumption and thus the PSD of the sample in a pronounced manner, as seen in figures 4.10(b)-(c).

The second factor is related to using the F-W two-step mechanism—originally designed for a well-mixed system—as the basis for modelling the continuous-flow microreactor. Even though the proposed model extensions take into account the diffusive and convective mixing effects not explicitly accounted for in the F-W mechanism, certain incompatibilities between the two systems may exist. For instance, notice that the kinetic constant k_1 describing nucleation, as it is proposed, already takes into account every step leading up to nucleation, including the reduction reaction, which are modelled separately. In addition, it should be highlighted that the numerical results at the lower flow rates feature apparent over-predictions of particle size in the range $30-40\%$, whilst the data points at $Q = 200$ μL/min correspond to under-predictions. From the above observation, it can be inferred that the simulations overestimate the effects of higher residence times, which likely stems from overly-magnified agglomeration events, which were modelled through a purely hydrodynamic agglomeration kernel (Eq. (4.17)). As an avenue for future work, it is proposed to add an agglomeration efficiency term to the PBE (see Eqs. (4.16)-(4.17)) that explicitly correlates inter-particle and particle-stabiliser interactions [70] at the molecular level to an agglomeration

efficiency per collision event, similar to that employed in Bal and Bandyopadhyaya [22].

The third factor corresponds to the deviations inherent to the F-W two-step mechanism in predicting the system's temporal evolution in well-mixed environments, as mentioned in the literature review of §2.3 and discussed in §4.4.1, whose deviations are presumably carried over to the T-junction simulations. It should also be highlighted that, as opposed to the circular cross-section geometry of the channel in the experimental setting, the simulation domain corresponds to a simplified 2-D version of the channel. This feature might trigger small but non-negligible differences in the mixing process, which, as seen throughout the manuscript, have a direct influence over the PSD and may contribute to the deviations found. A final restriction of the proposed model worth mentioning corresponds to its current limitation to continuous-flow microfluidic operations, which represent highly-diluted reactive single-phase flows. Adapting the computational model to cover droplet-based synthesis in microfluidics introduces additional complexity, necessitating a robust framework to capture the intricate interfacial phenomena that characterise reactive liquid-liquid flows; this topic is also suggested for future work as interesting comparisons could be made between the performance of droplet-based microfluidics and that of continuous-flow systems with coiled reactors.

4.5 Concluding remarks

This work presents an exhaustive examination of the underlying phenomena dictating the chemical synthesis of AgNPs in a continuous-flow microchannel and a well-mixed batch reactor via a numerical approach. A coupled PBM-CFD framework is proposed to extend the reach of spatially-averaged, time-dependent models, such as the well-established Finke-Watzky (F-W) two-step mechanism [309], to cover the highly interdependent dynamics inherent to continuous-flow and non-premixed reacting environments, such as microfluidic channels. The proposed framework takes into consideration diffusive and convective mixing phenomena associated with the main reactants, their limiting role in the subsequent steps of the process, their interplay with particle nucleation, growth, and agglomeration, and their fundamental role in determining the final PSD of the sample.

The synthesis of Ag and similar NPs poses significant challenges from a modelling perspective given its incompatibility with the much better understood crystallisation- and precipitation-based production of other types of NPs, which typically involves fast supersaturation-driven nucleation events and diffusion-limited growth models (see Schikarski et al. [253], Bal and Bandyopadhyaya [22] for example). Contrastingly, the synthesis of AgNPs is a multi-step interacting process based on the reduction of a silver precursor into Ag atoms, whose concentration serves as the driving force behind a controlled nucleation process and a rapid growth step. To the best of the author's knowledge, this is the first implementation in open-source code of the coupling between the hydrodynamic and reactive aspects of the system with a population balance model to predict

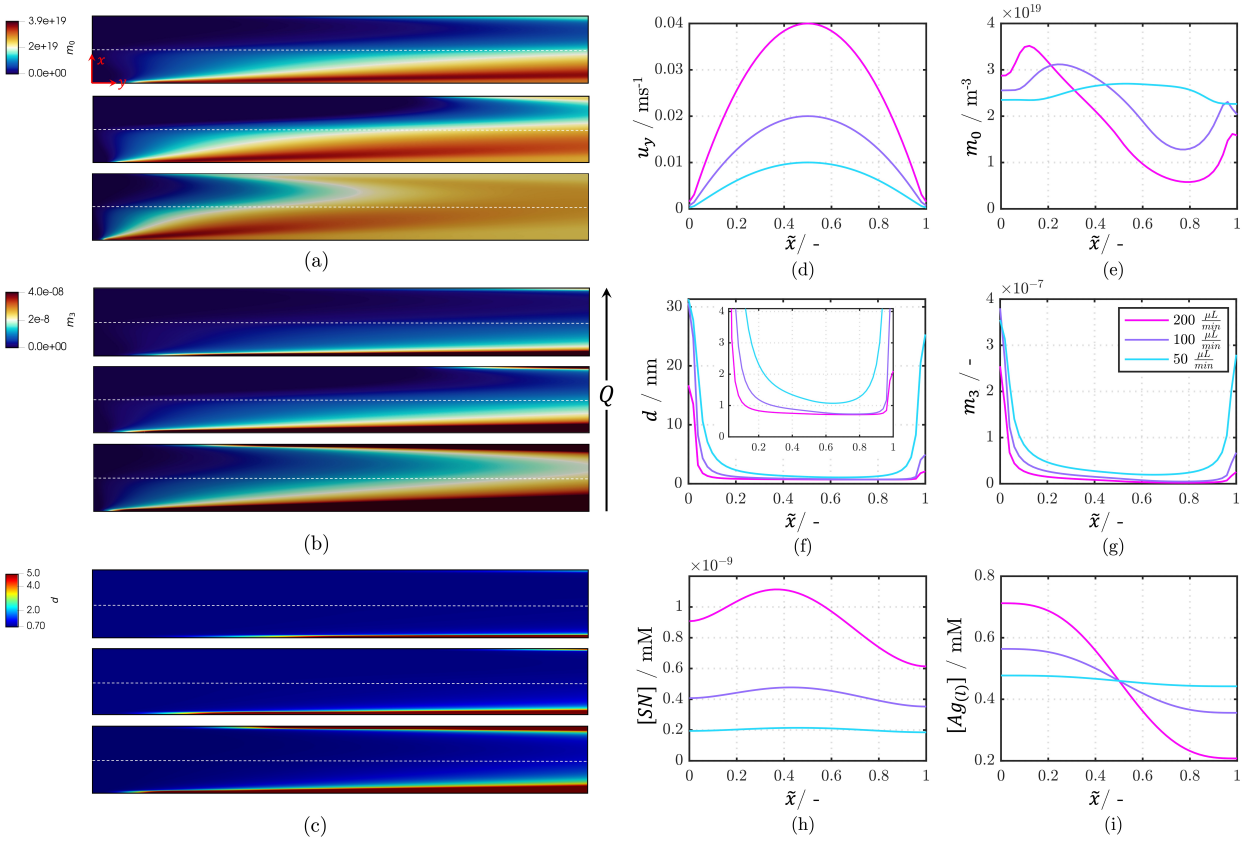

Figure 4.13: Influence of inlet flow rate on the spatial distribution of AgNPs in the T-junction microchannel: (a)-(c) steady-state contour plots of m_0 in m^{-3}, m_3, and d in nm, respectively. From top to bottom: $Q = 200, 100, 50$ μL/min; (d)-(i) steady-state radial distributions of the variables at the outlet plane for a channel length of 0.25 m. All other operating parameters remain unchanged from those specified in §4.2.3 for the base case. For these cases, $k_r = 1000$ $\mathrm{m}^{3\nu_R}\mathrm{s}^{-1}\mathrm{mol}^{-\nu_R}$, $\nu_R = 0.05$, $d_{crit} = 0.7$ nm, and $d_m = 0.344$ nm. See the caption of figure 4.12 for the characteristic times and dimensionless numbers for each flow rate case. The scale colour bar of d is set from d_{crit} to 5 nm for a clearer depiction of the profiles, refer to (f) for the real values. For easier visualisation, the inlet streams of all contour plots have been removed and the channels have been rescaled from their original dimensions as follows: $\mathbf{x} = (7x, 0.1y, z)$

the size distribution of the NPs, elucidate the mechanisms by which the operating conditions influence it, and compare the dynamic events governing microfluidic production to those of well-mixed batch reactors.

The exploration of the system's behaviour in the well-mixed batch reactor revealed the critical importance of the kinetic separation between nucleation and growth in correctly predicting the experimental temporal evolution of precursor consumption and the PSD based on the F-W two-step mechanism. Under the synthesis protocol followed [133], an operation at pH = 7 with initial stabiliser concentration (trisodium citrate) in the range $1.91 - 3.82$ mM allowed for a slow generation of nuclei and a comparatively fast NP growth ($t_n > t_g$), for which cases the F-W two-step mechanism provided a faithful capturing of both the temporal consumption of the precursor and the final PSD of the samples. Alkaline conditions (pH = 12), on the other hand, were found to induce accelerating phenomena on the rates of nucleation, negating the above-

mentioned separation between nucleation and growth ($t_{nuc} \approx t_g$) and thus leading to significant discrepancies against experimental data.

Despite these deviations, the F-W model is able to reproduce in an excellent manner the overall dynamics and qualitative experimental trends regarding pH, stabiliser concentration, and average particle size. In fact, the F-W-based simulations allowed us to summarise the influence of pH and initial stabiliser concentration on the size distribution by way of a unique parameter that decisively determines the final average particle size, the standard deviation of the distribution and consequently, the polydispersity index. This parameter corresponds to the ratio between the initial time-scales of nucleation and growth, expressed in terms of kinetic constants as $k_2[A]_0/k_1 = t_n/t_g$ [309], whose value can be directly correlated to the size of the particles through a power-law functional form (see figure 4.8). As such, the notably smaller AgNPs obtained at high pH can be understood as simply the product of a promoted nucleation process ($k_2[A]_0/k_1 < 1$) that utilises the available precursor concentration to generate a large number of small nuclei instead of increasing their size via growth events, leading to a fast exhaustion of the precursor, severely restricted growth, and small particle sizes; opposite arguments can be given for cases characterised by $k_2[A]_0/k_1 > 1$.

The simulation results for the continuous-flow microchannel unveiled a strong coupling between the system's hydrodynamics, multi-reaction kinetics, and the number and size of the particles. Through dimensionless and time-scales analyses, it has been showcased how differences in the operating conditions, particularly on the inlet flow rates, in conjunction with the transport properties of the reactants, give rise to varied rates of precursor consumption per reactor length due to alterations in the time-scale ratios between flow residence, reactants mixing, and the reduction reaction. The effects of these varied rates of precursor consumption are carried over to the outlet PSD of the samples through a series of complex steps involving the balance between the creation of Ag atoms and their consumption in nucleation/growth, and between the surge in the number of particles density through nucleation and their decline by means of agglomeration and diffusion.

Despite the critical role the T-junction PBM-CFD simulations played in elucidating the experimental trends observed, it is important to highlight the discrepancies between the experimentally measured values and the model's predictions of average particle size, which tend to overestimate the effects of reduced inlet flow rates. Consequently, future research should focus on the implementation of an agglomeration efficiency kernel to modulate the number of successful collisions based on molecular interactions between the nanoparticles. Additionally, further examination of the role of the tannic acid-trisodium citrate complex in the reduction of silver nitrate is warranted.

Moreover, it is crucial to underscore that the PBM-CFD framework, which builds upon the well-established F-W mechanism and incorporates extensions for microfluidic channels, shows significant potential in modelling reduction-based synthesis processes, including those for iridium

nanoparticles (IrNPs) and gold nanoparticles (AuNPs). However, it is imperative to conduct further testing to verify the applicability and reliability of the presented computational framework and to validate the findings of this study. As an immediate next step, it is proposed to test the model using an alternative chemical synthesis protocol for silver nanoparticles (AgNPs) in both well-mixed and microfluidic channels.

Chapter 5

Drop encapsulation and bubble bursting in surfactant-laden flows in capillary channels

Contents

5.1 Motivation and overview 123

5.2 Numerical methods and problem formulation 124

5.2.1 Numerical modelling and non-dimensionalisation 124

5.2.2 Simulation setup 127

5.3 Mesh independence 129

5.3.1 Global variables 129

5.3.2 Pinch-off locality 132

5.4 Validation in square capillaries 134

5.5 Results and discussion 136

5.5.1 Bubble dynamics in surfactant-free cases: tail undulations, curvature disruptions, and encapsulations 136

5.5.2 Influence of surfactant parameters on re-entrant liquid jet formation and encapsulation dynamics 141

5.5.2.1 Focus on the pinch-off dynamics for surfactant-free and surfactant-laden cases 141

5.5.2.2 Marangoni stresses, surface elasticity, and Biot number 144

5.5.2.3 Effect of surfactant adsorption/desorption kinetics (Da and k) and the Reynolds number (Re) 152

5.5.3 Bubble bursting, back deformations, and regime maps 156

5.6 Concluding remarks 159

5.1 Motivation and overview

The fluid mechanics problem of elongated bubbles travelling through small-scale channels was described and contextualised according to the current state-of-the-art in chapter 2 (§2.4). This literature review has highlighted several knowledge gaps in the field, primarily concerning the behaviour of the bubble-liquid interface when the system deviates from ideal conditions. These ideal conditions include perfectly circular channels, low Capillary and Weber numbers (indicating negligible inertia), and the absence of contaminants. Notably, there is also a scarcity of studies addressing the intriguing phenomena of bubble rear curvature inversion and liquid infiltration into the bubble domain under conditions where the system's capillary forces are weakened either naturally or due to the incorporation of surface-active material [17].

As introduced in chapter 1 (see figure 1.1), the upcoming chapter presents a systematic parametric study of the unsteady phenomena associated with the flow of elongated gas bubbles travelling through liquid-filled square capillaries under the less studied conditions of high Weber and Capillary numbers and non-circular geometries. Some of this conditions specifically induce the formation of an indentation at the back of the bubble that commonly gives way to a deep re-entrant liquid jet penetrating the bubble. Subsequent steps include pinch-off events in the penetrating liquid to generate one or multiple encapsulated drops which may coalesce, in conjunction with the bursting of the bubble-liquid interface by either the liquid jet or the drops. Some of these interfacial instabilities have previously been reported experimentally [212, 211] an numerically [120] for liquid-liquid flow in microchannels. Direct numerical simulations are carried out based on the LCRM, proposed by Shin and Juric [264] and collaborators, which is a hybrid interface-tracking/level-set method capable of accounting for the presence and dynamic exchange of surfactants between the liquid bulk phase and the liquid-gas interface. Further details about this method can be found in §3.3.4.

The results presented indicate that the delicate interplay among inertia, capillarity, viscosity, surfactant adsorption/desorption kinetics, and Marangoni stresses has a dramatic influence over the nonaxisymmetric morphological structures of the encapsulated drops-elongated bubble. This strong coupling also influences the pinch-off time, penetration depth of the liquid, and number, size, and velocity of the encapsulated drops across the bubble. The observed phenomena are comprehensively summarised and discussed in detail within three principal morphological regimes, categorised based on surfactant-related parameters and dimensionless groups.

The remainder of this chapter is structured as follows: §5.2 delineates the problem formulation, computational setup, and numerical approach. §5.3 presents and discusses the multiple tests performed to ensure mesh-independent results, while §5.4 provides a validation of the numerical results for square channels. §5.5 offers a discussion of the results, emphasising encapsulation phenomena in clean interfaces, followed by an analysis of surfactant-laden systems. Finally, concluding remarks are presented in §5.6.

The findings of this chapter have been published in Pico et al. [225]:

Pico, P., Kahouadji, L., Shin, S., Chergui, J., Juric, D. and Matar, O.K. (2024). *"Drop encapsulation and bubble bursting in surfactant-laden flows in capillary channels"*. Phys. Rev. Fluids., 9, p.034001

5.2 Numerical methods and problem formulation

5.2.1 Numerical modelling and non-dimensionalisation

A horizontal liquid-filled square capillary of width and height D in a Cartesian three-dimensional domain, $\mathbf{x} = (x, y, z)$, with an elongated gas bubble propagating through its interior (see figure 5.1) is considered. Assuming incompressible flow, Newtonian fluids, and negligible gravitational effects, direct numerical simulations (DNS) are performed based on the two-phase Navier-Stokes equations and a hybrid front-tracking/level-set method to handle the interface and surface tension forces. This method, as formulated and implemented in Shin and Juric [263], is coupled with the resolution of surfactant transport and exchange between the interface and the liquid phase bulk, as described in Shin et al. [268]. A detailed account of this method can be found in §3.3.4.

The relevant variables involved in the system have been rendered dimensionless (denoted by tildes) by using the scalings depicted in Eq. (5.1),

$$\tilde{\mathbf{x}} = \frac{\mathbf{x}}{D},\ \tilde{\mathbf{u}} = \frac{\mathbf{u}}{U_a},\ \tilde{t} = \frac{t}{D/U_a},\ \tilde{p} = \frac{p}{\rho_l U_a^2},\ \tilde{\sigma} = \frac{\sigma}{\sigma_s},\ \tilde{\Gamma} = \frac{\Gamma}{\Gamma_\infty},\ \tilde{C} = \frac{C}{C_\infty},\ \tilde{C}_s = \frac{C_s}{C_\infty}, \tag{5.1}$$

where $\mathbf{u}$, t, p, σ, Γ, C, and C_s represent velocity, time, pressure, surface tension, interfacial surfactant concentration, bulk surfactant concentration, and bulk surfactant concentration in the vicinity of the interface, respectively. The physical parameters included in the scaling correspond to the width of the channel, D, the average inlet velocity of the liquid, U_a, the density of the liquid phase, ρ_l, the surface tension in a surfactant-free interface, σ_s, the saturation interfacial concentration, Γ_∞, and the initial bulk surfactant concentration, C_∞, in line with the scaling proposed by Batchvarov et al. [31] for a similar system. In what follows, each variable is referred to by its name to signify its dimensionless version, unless stated otherwise and add the subscript b to signify that the variable is reported at the bubble nose.

The mass and momentum equations are written in dimensionless form and according to a 'one-fluid' formulation (see Eq. (3.28)) to obtain Eqs. (5.2) - (5.3):

$$\begin{aligned} \nabla \cdot \tilde{\mathbf{u}} &= 0, \\ \tilde{\rho}\left(\frac{\partial \tilde{\mathbf{u}}}{\partial \tilde{t}} + \tilde{\mathbf{u}} \cdot \nabla \tilde{\mathbf{u}}\right) &= -\nabla \tilde{p} + \frac{1}{Re}\nabla \cdot \left[\tilde{\mu}(\nabla \tilde{\mathbf{u}} + \nabla \tilde{\mathbf{u}}^T)\right] + \frac{1}{ReCa}\int_{\tilde{A}(\tilde{t})} \left(\tilde{\sigma}\tilde{\kappa}\mathbf{n} + \nabla_s \tilde{\sigma}\right) \delta\left(\tilde{\mathbf{x}} - \tilde{\mathbf{x}}_f\right) d\tilde{A}, \end{aligned} \tag{5.2}$$

$$\begin{aligned}\tilde{\rho}\left(\mathbf{x},t\right) &= \rho_g + (\rho_l - \rho_g)\mathcal{H}\left(\mathbf{x},t\right), \\ \tilde{\mu}\left(\mathbf{x},t\right) &= \mu_g + (\mu_l - \mu_g)\mathcal{H}\left(\mathbf{x},t\right),\end{aligned} \tag{5.3}$$

where $\mathcal{H}\left(\mathbf{x},t\right)$ is a smoothed Heaviside function that adopts the value of zero in the gas phase and unity in the liquid phase, ρ is the density and μ the viscosity of the fluids. Here, we denote the liquid and gas phases with the subscripts l and g, respectively. The normal and tangential components of the surface tension forces are represented by the last two terms on the right-hand-side (RHS) of Eq. (5.2), wherein $\tilde{\kappa}$ corresponds to twice the mean interface curvature, $\mathbf{n}$ to a unit normal to the interface, $\delta\left(\tilde{\mathbf{x}} - \tilde{\mathbf{x}}_f\right)$ to a Dirac delta function that is zero everywhere except for the interface (located at $\tilde{\mathbf{x}} = \tilde{\mathbf{x}_f}$), $\tilde{A}(\tilde{t})$ to the time-dependent interface area, and ∇_s to the surface gradient operator [265, 267].

The convention that positive $\mathbf{n}$ vectors point outwards from the interface towards the liquid phase is adopted. Accordingly, positive values of $\tilde{\kappa}$ describe a convex interface, as exemplified in figure 5.1. As is typical in front-tracking, the Lagrangian interface is advected by integrating $d\mathbf{x}_f/dt = \mathbf{V_f}$, where the vertices of the Lagrangian triangular mesh discretising the interface, $\mathbf{x_f}$, are displaced in time by the fluid velocity, $\mathbf{V_f}$, at those vertices.

Note that the gas phase dynamics are not neglected within this one-fluid formulation and are resolved along with that of the liquid via solution of Eqs. (5.2)-(5.3) with the density and viscosity defined by Eq. (5.3). Consequently, the tangential component of the interfacial stress is finite with further contributions to it arising from the surface tension gradients; the latter owe their existence to the interfacial surfactant concentration gradients, as will be discussed below.

The mass conservation of surfactant species at the interface and bulk are given by Eq. (5.4) - (5.5), which correspond to the dimensionless versions of the equations described in §2.2 and §3.3.2 (Eqs. (3.30) - (3.35)). The source term representing surfactant exchange between the interface and the bulk region immediately adjacent is given by Eq. (5.6):

$$\frac{\partial\tilde{\Gamma}}{\partial\tilde{t}} + \nabla_s\cdot(\tilde{\Gamma}\tilde{\mathbf{u}}_t) = \frac{1}{Pe_s}\nabla_s^2\tilde{\Gamma} + Bi\left(k\tilde{C}_s(1-\tilde{\Gamma}) - \tilde{\Gamma}\right), \tag{5.4}$$

$$\frac{\partial\tilde{C}}{\partial\tilde{t}} + \tilde{\mathbf{u}}\cdot\nabla\tilde{C} = \frac{1}{Pe_c}\nabla\cdot(\nabla\tilde{C}), \tag{5.5}$$

$$\mathbf{n}\cdot\nabla\tilde{C}|_{interface} = -Pe_cDaBi\left(k\tilde{C}_s(1-\tilde{\Gamma}) - \tilde{\Gamma}\right), \tag{5.6}$$

where $\tilde{\mathbf{u}}_t = (\tilde{\mathbf{u}}_s\cdot\mathbf{t})\mathbf{t}$ is the projection of the interface velocity vector, $\tilde{\mathbf{u}}_s$, on the interface unit tangent, $\mathbf{t}$. The dependence of surface tension on local interface surfactant concentration is represented by a non-linear equation of state derived from Langmuir adsorption isotherm [184, 213, 199], as expressed in Eq. (5.7):

$$\tilde{\sigma} = \max\left(\epsilon_\sigma, 1 + \beta_s\ln\left(1-\tilde{\Gamma}\right)\right), \tag{5.7}$$

where $\beta_s = \mathcal{R}T\Gamma_\infty/\sigma_s$ is the surfactant elasticity number; $\mathcal{R}$ and T are the thermodynamic ideal gas constant and temperature, respectively. The non-linear equation of state described above is valid for very dilute systems in which $\Gamma << \Gamma_\infty$. As Γ increases, the equation of state yields unphysical negative values of surface tension. To circumvent this, a limiting value for $\tilde{\sigma}$, $\epsilon_\sigma = 0.05$, has been introduced, in accordance with Muradoglu and Tryggvason [199] and Shin et al. [268].

The tangential surface stresses or tangential Marangoni stresses, heavily discussed throughout this chapter, are calculated via Eq. (5.8), obtained by non-dimensionalising Eq. (2.7) and projecting it onto the tangential direction:

$$\tilde{\tau}_m \equiv \nabla_s\tilde{\sigma}\cdot\mathbf{t} = -\beta_s\frac{1}{1-\tilde{\Gamma}}\nabla_s\tilde{\Gamma}\cdot\mathbf{t}, \tag{5.8}$$

A summary of the definitions of the dimensionless groups that characterise the system is as follows:

$$\begin{gathered} Re = \frac{\rho_l U_a D}{\mu_l},\ Ca = \frac{\mu_l U_a}{\sigma_s},\ We = \frac{\rho_l U_a^2 D}{\sigma_s},\ Bo = \frac{(\rho_l-\rho_g)gD^2}{\sigma_s},\ \frac{L}{D}, \\ Pe_{c,s} = \frac{U_a D}{D_{c,s}},\ Bi = \frac{k_d D}{U_a},\ Da = \frac{\Gamma_\infty}{DC_\infty},\ k = \frac{k_a C_\infty}{k_d},\ \beta_s = \frac{\mathcal{R}T\Gamma_\infty}{\sigma_s},\ Ma = \frac{\beta_s\sigma_s}{\mu_l U_a}, \end{gathered} \tag{5.9}$$

where Re, Ca, We, and Bo are the Reynolds, Capillary, Weber, and Bond numbers, respectively ($Oh = \sqrt{Ca/Re}$). $L/D = 27$ is the ratio between channel length and diameter. Pe_c and Pe_s are the bulk and interfacial Péclet numbers, which provide a measure of the importance of inertia relative to surfactant mass diffusion across the interface (modulated by a diffusivity D_c) or the bulk (modulated by a diffusivity D_s), respectively; Bi represents the Biot number, describing the competition between convective, $t_{conv} = D/U_a$, and interface surfactant desorption, $t_d = k_d^{-1}$, time scales. The Damköhler number, Da, provides a dimensionless measure of the initial interface saturation, and the number k reflects the interplay between the characteristic time scales of interface surfactant adsorption, $t_a = (k_a C_\infty)^{-1}$, and desorption. Gravitational effects have not been taken into account in this study. Hence, all simulations are run under vanishing Bond number conditions, $Bo = 0$.

A Marangoni number is defined here and in Chapter 6 as the ratio between characteristic Marangoni and viscous stresses ($\tau_{m,ch}$ and $\tau_{vis,ch}$, respectively [213, 184]). This definition has been used in previous investigations (see Eq. (3.91) of Manikantan and Squires [184]) and is similar to the definition discussed in §2.2. For the estimation of characteristic Marangoni stresses, the initial surfactant concentration, Γ_0, has been employed as a characteristic state. The definition of Ma for the present system is shown in Eq. (5.10):

$$Ma = \frac{\tau_{m,ch}}{\tau_{vis,ch}} = \frac{\beta_s\sigma_s}{\mu_l u_c}. \tag{5.10}$$

As demonstrated by the above equation, larger β_s values directly lead to higher Ma, indicating an increased significance of Marangoni stresses relative to viscous stresses.

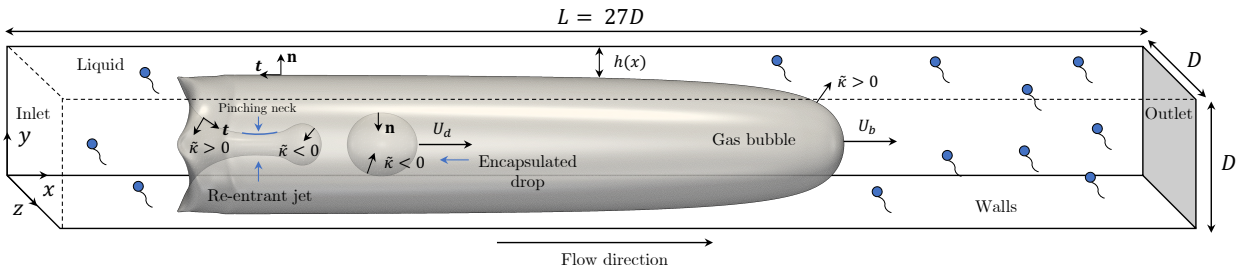

Figure 5.1: (not to scale) Schematic of simulation setup, re-entrant liquid jet penetrating the bubble, and encapsulated drop. The direction of outwards pointing normal vectors, liquid film thickness, $h(x)$, and curvature sign according to the adopted convention, are also highlighted. The location of the Cartesian axis represents the outset of the geometrical domain ($x = 0, y = 0, z = 0$)

For an exhaustive description of the discretisation schemes and numerical framework employed for solving the above mentioned governing equations, the reader is referred to the original publications by Shin et al. [268, 267], and to Shin and Juric [265] for a comprehensive account of the hybrid front-tracking/level-set method, also called Level Contour Reconstruction Method (LCRM), which has also been described in §3.3.4. Here, only short summary of the most relevant aspects is presented. The LCRM considers the combination of a fixed structured Eulerian grid for the resolution of field equations and a moving and deforming Lagrangian grid for the interface, discretised via an unstructured triangular mesh. These interface elements are consequently advected through the integration of the Lagrangian equation $\mathrm{d}\mathbf{x}_f/\mathrm{d}t = \mathbf{v}$, where $\mathbf{v}$ corresponds to the interface velocity, which is interpolated from the Eulerian grid.

The integration of the above Lagrangian equation is carried out with a second-order Runge-Kutta method. The spatial derivatives of the fields in the Eulerian grid are discretised through a standard cell-centred scheme for all terms, with the exception of the non-linear convective terms, for which a second-order essentially non-oscillatory (ENO) procedure is used [269, 281]. For the viscous term in the momentum equation, a second-order centred difference scheme is employed. A second-order Gear method [306] is adopted for the temporal terms, with an implicit time integration for the viscous terms. The time step is set to be adaptive, according to the following criterion: $\Delta t = \min\{\Delta t_{\mathrm{cap}} = \frac{1}{2}\sqrt{\frac{(\rho_l+\rho_g)\Delta x^3}{\pi\sigma_s}}, \Delta t_{\mathrm{vis}} = \frac{\rho_g \Delta x^2}{6\mu_l}, \Delta t_{\mathrm{CFL}} = \frac{\Delta x}{|u_{max}|}, \Delta t_{\mathrm{int}} = \frac{\Delta x}{|V_{int}|}\}$, where the time steps relate to viscosity, capillarity, Courant-Friedrichs-Lewy condition, and interface, respectively; Δx is the minimum cell size, u_{max} is the maximum fluid velocity, and V_{int} is the maximum interface velocity. The time-step related to the interface was found to be the limiting time-step in all simulations ($\Delta t_{\mathrm{int}} \sim O(10^{-7})$ s).

5.2.2 Simulation setup

As depicted in figure 5.1, the simulation domain consists of a three-dimensional rectangular box of dimensions $27D \times D \times D$, corresponding to the x (channel length), y (channel height), and z (channel width)-directions, respectively. The value of the channel length was selected to

ensure the attainment of a steady-state bubble propagation for $We < 10$, following the results of Batchvarov et al. [31] and Magnini and Matar [179]. Under conditions of $We > 10$, highly unsteady encapsulation/bursting phenomena are detected in the system, as explored in §2.4.2. The channel length chosen allowed for the observation of all relevant phenomena, including the formation of the re-entrant jet, drop encapsulations and coalescence events, and bubble bursting, for all conditions tested.

The elongated bubble was initialised in quiescent conditions close to the channel inlet and at the centre-line of the y and z-directions as a horizontal cylinder of length $3.12D$ with two hemispherical caps of diameter $0.94D$ on each end. The boundary conditions associated with Eqs. (5.2)-(5.5) are written in Eq. (5.11)

$$\begin{aligned}
\mathbf{u} &= 0 \quad \text{on all walls (no-slip)},\\
\mathbf{u} &= u(y,z) \quad \text{at the inlet (laminar profile)},\\
\frac{\partial \mathbf{u}}{\partial \mathbf{n}} &= 0 \quad \text{at the outlet (no flux)},\\
\frac{\partial p}{\partial \mathbf{n}} &= 0 \quad \text{at the inlet and on all walls (no flux)},\\
p &= p_{\text{ref}} \quad \text{at the outlet},\\
\frac{\partial C}{\partial \mathbf{n}} &= 0 \quad \text{on all boundaries (no flux)},\\
\mathbf{n}\cdot\nabla\tilde{C}|_{interface} &= -Pe_c DaBi\left(k\tilde{C}_s(1-\tilde{\Gamma})-\tilde{\Gamma}\right) \quad \text{at the interface},
\end{aligned} \tag{5.11}$$

where $u(y,z)$ is a developed laminar velocity profile and p_{ref} is a reference pressure. The bubble-liquid interface was initially covered with surfactant of uniform concentration Γ_0, determined from an initial equilibrium between surfactant adsorption and desorption (last term on the RHS of Eq. (5.4) equal to zero), which, assuming $C_s = C_\infty$ initially, reads:

$$\Gamma_0 = \frac{k}{k+1}\Gamma_\infty. \tag{5.12}$$

This set-up closely resembles the approaches followed in previous numerical investigations for similar systems [17, 202, 178].

The effects of the dimensionless numbers and flow parameters that characterise the system (see Eq. (5.9)) are explored considering the following ranges: $Ca = 0.0089 - 0.0693$, $Re = 100 - 443$, $We = 3.94 - 30.70$ ($Oh = 4.48\times10^{-3} - 1.25\times10^{-2}$), $Pe_{c,s} = 100$, $Bi = 0.025 - 5$, $Da = 0.01 - 1$, $k = 0.10 - 10.00$, $\beta_s = 0.1 - 1$, and $Ma = 1.44 - 14.43$. For all cases simulated, the viscosity and density ratio between the phases is kept constant and in line with representative values for water and air: $\rho_l/\rho_g = 1000$ and $\mu_l/\mu_g = 100$. As previously mentioned, the ratio between channel length and diameter is kept constant at $L/D = 27$.

A "base" case from which the parametric sweep was carried out is defined with the following

conditions: $Re = 443$, $Ca = 0.0693$, $We = 30.7$, $Pe_{c,s} = 100$, $Bi = 0.10$, $Da = 1$, $k = 0.10$, $\beta_s = 0.50$, and $Ma = 7.22$. Unless stated otherwise, all results correspond to simulations under these conditions. The selection of the testing ranges was based on common values encountered in bubbly flow systems in the presence of surfactants, as reported in Atasi et al. [17], as well as values of We that would allow a significant disruption of the bubble back to generate the aforementioned penetrating liquid and consequent drop encapsulation [96, 13].

For typical ionic and non-ionic surfactants in water, such as sodium dodecyl sulphate (SDS), N-dodecyl-N,N-dimethylammonio-3-propane sulfonate, and Triton X-100 (TX100), the value of Γ_∞ ranges between $O(10^{-6} - 10^{-5})$ mol/m^2 and D_s between $O(10^{-12} - 10^{-9})$ m^2/s, which results in $Pe_s = O(10^3 - 10^6)$ [127, 55, 129]. As noted previously in Constante-Amores et al. [58] and Batchvarov et al. [31], saturation of the system's dynamics is reached above $Pe_s \sim 100$. Pe_c was set to be equal to Pe_s, following the study of Agrawal and Neuman [3].

Based on Kamat et al. [130], Constante-Amores et al. [58] and our range of characterising Oh, we define an inertial-capillary or Rayleigh time scale as $t_c = \sqrt{\rho_l D^3/\sigma_s}$ for $Oh << 1$ and a Marangoni time scale as $t_\mathrm{m} = \sqrt{(\mu_l D)/\Delta\sigma}$, where $\Delta\sigma = \sigma_s - 0.05\sigma_s$ is a measurement of the surface tension gradients. The ranges for the characteristic time scales of the system are estimated to be: $t_a \sim O(10^{-4} - 10^{0})$ s, $t_d \sim O(10^{-3} - 10^{-1})$ s, $t_c \sim O(10^{-3} - 10^{-2})$ s, $t_{conv} \sim O(10^{-3} - 10^{-2})$ s, and $t_m \sim O(10^{-4})$ s (for surfactant-laden cases). These time scales ensure that adsorptive/desorptive, inertial, capillary, and Marangoni phenomena will play an important role in the dynamics of the system.

5.3 Mesh independence

Following numerous studies making use of the numerical methods described above for inertial and capillary phenomena (see Constante-Amores et al. [59], Batchvarov et al. [31], Constante-Amores et al. [54]), this work employs a fully-structured and uniform Cartesian grid divided into $54 \times 4 \times 4$ sub-domains, further divided into $64 \times 32 \times 32$ cells per sub-domain, rendering a global resolution equal to $3456 \times 128 \times 128$ cells. On account of ensuring this resolution produces mesh-independent results on a global and localised basis, a mesh analysis in surfactant-free and surfactant-laden conditions has been performed.

5.3.1 Global variables

For the assessment of the results' (in)dependency on the mesh, two uniform Cartesian grids with varying resolutions have been tested on both surfactant-free and surfactant-laden cases. The operating conditions for all testing cases are those that allow the development of the liquid jet and drop encapsulation phenomenon, thus evaluating the resolution on small velocity and time

scales.

Figure 5.2 depicts the temporal evolution of the kinetic energy, $E_k = \int_V (\rho \mathbf{u}^2)/2 \, dV$, the interfacial area, and the position of the bubble nose, $\tilde{x}_b$, the former two being normalised by their values at $\tilde{t} = 0$. The tested mesh resolutions correspond to $M_1 = 3456 \times 128 \times 128$ and $M_2 = 6912 \times 256 \times 256$, and the cases to surfactant-free for "Case 0" and surfactant-laden with $Da = 1$, $k = 0.1$ for "Case 1" and $Da = 0.1$, $k = 1$ for "Case 2". All other parameters remain unchanged from those specified in §5.2.2. Table 5.1 reports a few additional features of the tested mesh resolutions, including the minimum cell size, Δx_{min}, the maximum relative variation of the gas phase volume, $\Delta V_g = (V_g - V_{g0})/V_{g0}$, and that of the liquid phase, $\Delta V_l = (V_l - V_{l0})/V_{l0}$. Considering the adaptive nature of the time-step treatment (see §5.2.1), it is relevant to highlight that modifying the mesh resolution alters the simulation time-step in accordance to the cell size. For Case 1, $\Delta t \approx 8 \times 10^{-7}$ s and $\Delta t \approx 4 \times 10^{-7}$ s for M_1 and M_2, respectively.

The almost complete overlapping of the plots displayed in figure 5.2 for the grids considered and the three sets of operating conditions suggests that increasing the resolution by twofold on each direction does not lead to the development of significantly different dynamics. Unless stated otherwise, all simulations have been run with M_1 given that it provides enough resolution to ensure mesh-independent results, while also requiring substantially less computational resources, as seen in table 5.1. This table also indicates that M_1 allows us to achieve volume conservation for both phases with a deviation of 8×10^{-3} % or lower from the onset of the simulations.

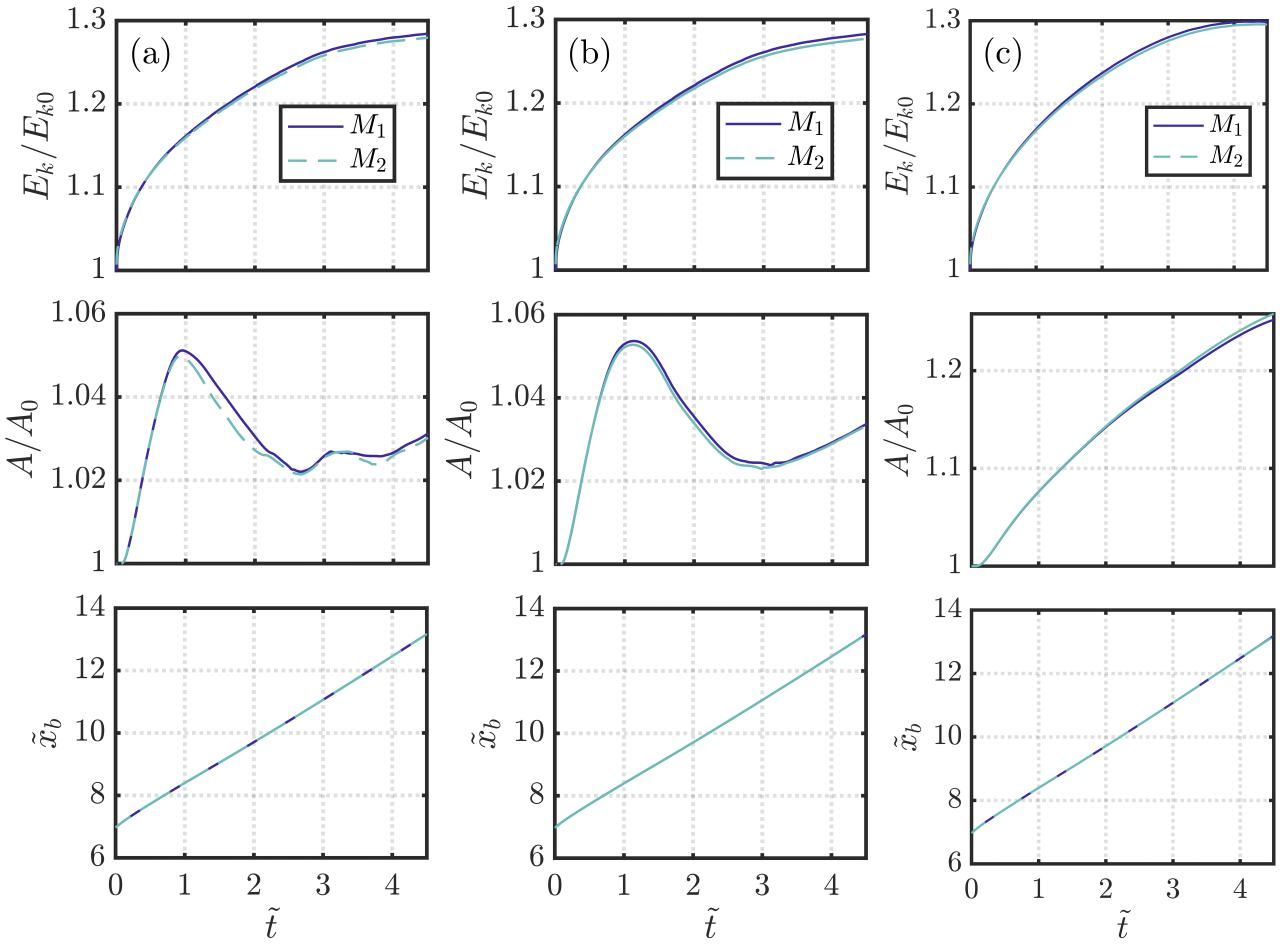

Figure 5.2: Results of mesh independence study for surfactant-free and surfactant-laden elongated bubbles, showcasing from top to bottom the temporal evolution of dimensionless kinetic energy, interfacial area normalised by its initial value, and dimensionless axial location of the bubble nose: (a) Case 0 (surfactant-free); (b) Case 1; (c) Case 2

Table 5.1: Additional features of the mesh resolutions tested in surfactant-free and surfactant-laden elongated bubbles, including computing time, minimum cell size, and maximum volume variation in both the gas and liquid phases

Case name	Mesh	Computing time per CPU to reach 10 ms / h	Δx_{min} / μm	max(ΔV_g) / %	max(ΔV_l) / %
Case 0	M_1	0.60	7.81	7.70×10^{-3}	1.04×10^{-3}
	M_2	8.46	3.91	-6.13×10^{-3}	8.27×10^{-4}
Case 1	M_1	0.78	7.81	7.65×10^{-3}	3.02×10^{-4}
	M_2	12.71	3.91	3.84×10^{-3}	5.19×10^{-4}
Case 2	M_1	2.21	7.81	8.00×10^{-3}	2.61×10^{-4}
	M_2	7.34	3.91	7.28×10^{-3}	9.83×10^{-4}

5.3.2 Pinch-off locality

An additional mesh independence test was carried out to specifically evaluate the pinch-off dynamics' sensitivity to the mesh resolution. For this test, the time taken to reach the curvature inversion, t_{inv} (described in §5.5.1), and the back and interior pinch-off times, $\tilde{t}_{p-o,bk}$ and $\tilde{t}_{p-o,int}$, respectively, were contrasted for Case 0 and Case 1. The difference between these two pinch-off events is schematically highlighted in figure 5.9(c) and analysed in more detail in §5.5.1. Table 5.2 depicts these values for the two mesh resolutions considered. Notice that both $\tilde{t}_{p-o}$ are reported with $\tilde{t}_{inv}$ as the reference frame. As a complement to the pinch-off times, table 5.3 compares the size of the entrapped drops at selected times after the pinch-off event and before their stabilisation (see figures 5.10-5.11(b)). These results indicate that increasing the mesh resolution by a factor of 8 does not alter the dynamics at the locality of the pinch-off more than 3.5% for surfactant-free and surfactant-laden cases.

Table 5.2: Recorded $\tilde{t}_{inv}$, $\tilde{t}_{p-o,bk}$, and $\tilde{t}_{p-o,int}$ for the two mesh resolutions tested in surfactant-free and surfactant-laden elongated bubbles. The values of $\Delta\tilde{t}$ represent the percent change of $\tilde{t}$ going from M_1 to M_2

	$\tilde{t}_{inv}$			$\tilde{t}_{p-o,bk}$			$\tilde{t}_{p-o,int}$		
	M_1	M_2	$\Delta\tilde{t}_{inv}$	M_1	M_2	$\Delta\tilde{t}_{p-o,bk}$	M_1	M_2	$\Delta\tilde{t}_{p-o,int}$
Case 0	0.122	0.120	−1.964%	2.158	2.098	−2.762%	2.328	2.265	−2.696%
Case 1	0.117	0.120	2.389%	2.904	2.829	−2.593%	2.647	2.563	−3.129%

Table 5.3: Interfacial area (A_d in mm^2) of encapsulated drop post pinch-off. The values of ΔA_d represent the percent change of A_d going from M_1 to M_2

	Case 0				Case 1			
$\tilde{t}$	2.979	3.422	3.865	4.308	2.984	3.427	3.870	4.313
A_d M_1	0.800	0.762	0.755	0.754	0.713	0.709	0.709	0.709
A_d M_2	0.777	0.747	0.739	0.741	0.693	0.693	0.697	0.694
ΔA_d	−2.943%	−1.898%	−2.242%	−1.714%	−2.805%	−2.257%	−1.693%	−2.116%

The final evaluation of the selected mesh resolution concentrates on the evolution of the system's interfacial profiles in the vicinity of the pinch-off event, denoted by the general time t_{p-o}. Figure 5.3 illustrates the temporal evolution of the bubble-liquid interface at equal distances from breakup for Case 0, utilising mesh resolutions M_1, M_2, and a medium resolution $M_{1.5}$ characterised by $M_{1.5} = 5376 \times 192 \times 192$. These depictions reveal that during the initial stages of the encapsulation process, specifically during curvature inversion and re-entrant jet formation, all three resolutions yield nearly identical results. Only minor differences become evident as the system approaches pinch-off, at $\tilde{t}_{p-o} - \tilde{t} < 2.3 \times 10^{-2}$. A more in-depth analysis of the pinch-off dynamics can be found in §5.5.2.1.

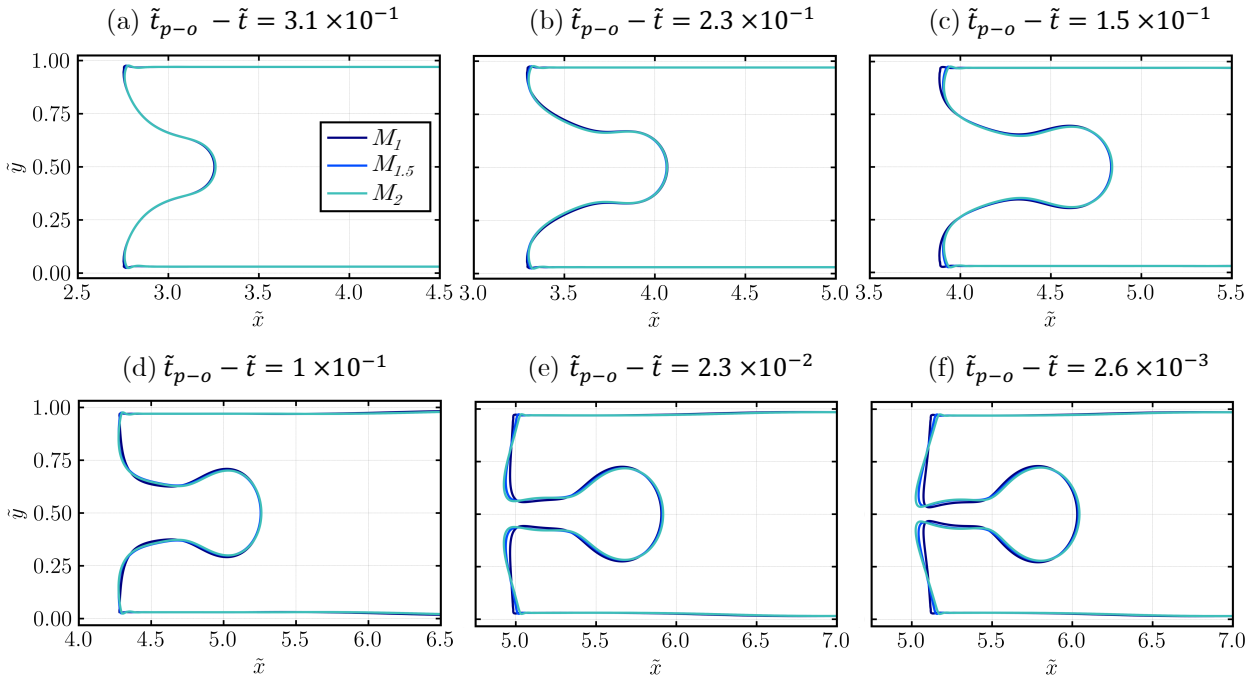

Figure 5.3: Elongated bubble-liquid interfacial profiles across time in the vicinity of a pinch-off event denoted by $\tilde{t}_{p-o}$ and comparison between different mesh resolutions for Case 0

Before concluding this section, it is important to note that the mesh size selected also allowed to capture accurately the thin liquid film surrounding the bubble, which, according to Gupta et al. [101], Magnini and Matar [179], requires a minimum of 5-10 computational cells covering its domain for a correct development of the liquid velocity profile. In the simulations, the placement of at least 5-6 cells in the liquid film section has been ensured for the cases that exhibit encapsulation ($We \sim 30$), for which $h(x)/D \sim 5^{-2}$ (see figure 11 of Magnini and Matar [179]). This condition is further achieved in the surfactant-laden simulations, which develop a thicker liquid film. The author of this thesis makes the note, however, that the size of the entire domain, as well as the comprehensive sweep over dimensionless numbers presented, make it prohibitively expensive in terms of computation to achieve the refinement levels reported in works such as Castrejón-Pita et al. [46], Li and Sprittles [166] to fully capture all regime transitions leading to the interfacial singularities of an isolated pinch-off event.

In addition, the selected mesh size ensured accurate capturing of the surfactant diffusion boundary layer. To estimate the thickness of this concentration boundary layer, Classic Boundary Layer Theory in a flat plate was utilised as an approximation, given the low to moderate values of the Schmidt number considered in this study, $Sc = \mu_l/(\rho_l D_c) = 0.22 - 1$. This led to a boundary layer thickness along the channel of $\delta_c(x) \approx 5xPe_x^{-1/2}$ [67], where $Pe_x = U_a x/D_c$ and x is the distance from the channel's inlet along the main flow axis. Under the studied conditions, the ratio $\delta_c(x)/\Delta x_{min}$ varied from 6 to 326 for distances from the inlet of $x/D = 0.01$ to the channel outlet ($x/D = 27$, see figure 5.1). This analysis indicates that the mesh resolution is sufficient to place at least 6 computational cells in the concentration boundary layer along the channel.

5.4 Validation in square capillaries

The numerical framework and simulation setup presented herein have previously been carefully validated in the context of elongated bubbles in circular capillary channels. For this validation, the reader is referred to the work of Batchvarov et al. [31], in which the code was benchmarked against the well-known correlation of Han and Shikazono [102] for steady-state liquid film thickness in conditions of non-negligible inertia (see Eq. (2.24) and associated discussion in §2.4.1). For $Ca \sim O(10^{-2})$ and $Re \sim O(10^{2})$, deviations of up to 10% were reported, which are within the uncertainty of the correlation. A complementary validation is reported in the following paragraphs to demonstrate the faithful capturing of the bubble's main morphological regimes in square capillary channels, as proposed by Magnini and Matar [179].

This supplementary validation for square capillary channels is conducted using the numerical data and conditions described in Magnini and Matar [179] for surfactant-free scenarios under non-negligible inertia. Satisfactory quantitative agreement between the present results and those of Magnini and Matar [179] is achieved in terms of bubble-to-liquid velocity ratio, U_b/U_l, and gas area fraction, ϵ (see figure 5.4(a)-(b)), with maximum deviations of 2.7% and 3.1%, respectively. The cases that do not have a direct counterpart from the above mentioned reference (i.e., $Ca = 0.0089$, $Ca = 0.0377$, and $Ca = 0.068$ for $Re = 443$) adequately follow the qualitative trend of increasing U_b/U_l and decreasing ϵ with Ca and Re.

Figure 5.4(c)-(d) exemplifies the well-known bubble morphological regimes found in non-circular channels, as well as the present model's correct capturing of the non-axisymmetric bubble shapes that arise below a threshold Ca [145, 108, 49] (see figure 2.8 and associated discussion in §2.4.2). In accordance with Ferrari et al. [86], the corner flow effects exhibited in $Ca \lessapprox 0.01$ promote the development of a saddle-shaped interface nearby the channel centre lines (see outermost series in figures 5.4(c)-(d)), which brings about the formation of four lobes projecting towards the channel corners. As portrayed in figure 5.4(c), these lobes are located furthest away from the channel centre-point (highest r/R_h) and will continue to grow as the saddle deepens ($r_d > r_c$) with decreasing Ca. The presence of the saddle shifts the minimum liquid film thickness, h_{min}, from the centre-line of the channel to a position, l_y, that varies as a function of Ca. For the case highlighted in the figure, $l_y/R_h = 0.2$ is computed, which matches remarkably well with the value reported by Magnini and Matar [179] for $We << 1$ ($l_y/R_h \approx 0.195$, see figure 7(b) of the reference). The high pressure zones at the saddles showcased in figure 5.4(d) are evidence of significant capillary flow drainage away from the thin-liquid film region, as reported in Magnini and Matar [179].

The other morphological regimes represented in figure 5.4(c)-(d) correspond to an additional non-axisymmetric cross-section regime for $0.01 \lessapprox Ca \lessapprox 0.05$, characterised by $r_d > r_c$ and the absence of the saddle ($l_y = 0$, see $Ca = 0.02$ in the figure), and a fully symmetric bubble topology ($r_d = r_c$, see $Ca = 0.1$ in the figure) for the final regime. It is important to draw attention to

the almost perfect alignment of these regimes and the ranges of Ca in which they occur between the present numerical predictions and those of the literature, notwithstanding that the regimes documented in the literature were observed under conditions of vanishing inertia.

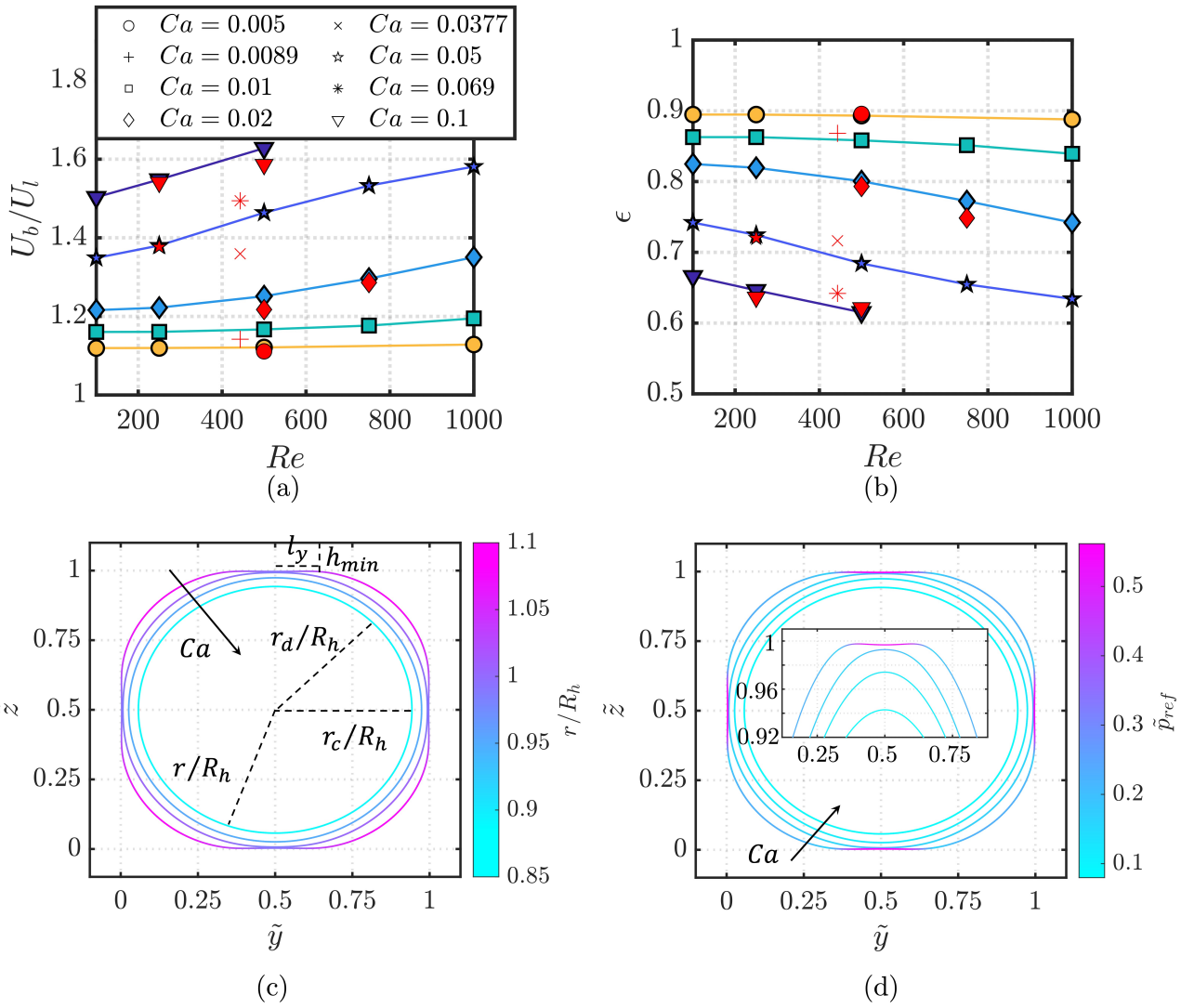

Figure 5.4: Validation elongated bubbles travelling in square capillary channels and under $We > 1$ conditions in terms of (a) bubble nose velocity relative to average liquid phase velocity, and (b) gas phase area fraction. Each marker corresponds to a different Ca (as seen from the legend). The colour red represents the numerical results and the remaining colours Magnini and Matar [179]'s results; (c)-(d) replication of the bubble morphological structures proposed in the same reference with the present numerical simulations in terms of (c) distance from channel centre to any point of the interface normalised by the channel's hydraulic radius, R_h, and (d) normalised relative pressure, $\tilde{p}_{ref} = (p - p_b)/\rho_l U_a^2$. From outermost to innermost series, the results are shown for: $Ca = 0.0089$, $Ca = 0.02$, $Ca = 0.0377$, and $Ca = 0.1$ at $Re = 443 - 500$. Results in (b)-(d) are measured at a cross-sectional plane normal to the stream-wise direction located at a distance of $5.5D$ behind the bubble nose, as reported in Magnini and Matar [179]

To attach a physically-relevant meaning to the dimensionless times referenced and the comparisons made throughout this chapter, all times are henceforth reported from $\tilde{t} = 0.0$, corresponding to the moment of the bubble rear's curvature inversion (discussed in §2.4 and illustrated in figure

5.6) for each set of conditions. For the surfactant-free and low Ca cases which did not exhibit curvature inversion (see figure 5.5 for $Ca = 0.0089, 0.0377$), $\tilde{t} = 0.0$ is defined as the inversion time of the surfactant-free case that underwent this process (see §5.5.1).

5.5 Results and discussion

The results of the present investigation are presented in three parts. The first, §5.5.1, introduces the phenomenon of drop encapsulation by contrasting the behaviour of three surfactant-free cases of varying Ca and exposed to non-negligible inertial effects ($Re = 443$, figure 5.5). The second part of the results, §5.5.2, analyses selected cases from the surfactant-related parameter sweep (β_s, Bi, k, Da, and Re) and quantifies their influence on drop encapsulation. The final set of results, §5.5.3, summarises all encapsulation behaviours observed in two regime maps in the $\beta_s - k$ and $Bi - k$ spaces (figure 5.15).

5.5.1 Bubble dynamics in surfactant-free cases: tail undulations, curvature disruptions, and encapsulations

This discussion section begins by showcasing the bubble topology at a two-dimensional projection in the (x,y) plane at the channel centre-line ($\tilde{z} = 0.5$), as well as the normalised mean curvature, $\tilde{\kappa}$, and the normal, $\tilde{\tau}_n$, and tangential, $\tilde{\tau}_t$, components of the viscous stress along the interface (see figures 5.5(a)-(b)). Here, these quantities are defined as $\tilde{\kappa} = \kappa/\kappa_c$, $\tilde{\tau}_n = \tau_n/(D/U_a)$, and $\tilde{\tau}_t = \tau_t/(D/U_a)$, respectively, where $\tau_n = (\mathbf{D}\cdot\mathbf{n})\cdot\mathbf{n}$, $\tau_t = (\mathbf{D}\cdot\mathbf{n})\cdot\mathbf{t}$, $\mathbf{D} = (\nabla\mathbf{u} + \nabla\mathbf{u}^T)/2$ (rate of deformation tensor), and κ_c corresponds to the curvature of a sphere with a volume equal to the initial bubble volume. Under the sign conventions adopted, $\tilde{\tau}_n > 0$ denotes stresses exerted on the interface towards the liquid phase.

Conforming to previous observations [283, 96, 251, 2], the plots reveal a loss of sphericity (typical of fully dominant capillary forces) at the bubble front and back with increasing Ca, in conjunction with an overall axial bubble elongation. The interface at the bubble front sharpens and expands, whilst the bubble back becomes progressively flattened with Ca, adopting a "bullet-like" shape ($\tilde{\kappa}_{front} > \tilde{\kappa}_{back}$). This process continues until a curvature inversion emerging from $\tilde{y} = 0.5$ is detected for $Ca = 0.0693$, which eventually leads to a drop encapsulation. As mentioned in §2.4, this type of curvature sign inversion is triggered by a combination of large Ca and Re. From the surfactant-free results shown in figure 5.5(a) at $Re = 443$, as well as those reported in §5.4, which encompass various Ca and Re values ($We = 2.5 - 50$), the threshold value for curvature inversion is placed in the range $17 < We < 20$. This range is fully consistent with that previously found in Giavedoni and Saita [96] ($We \approx 20$ for $Re \sim O(10^1)$) in circular channels.

The bubble shapes presented in figure 5.5(a) correspond to the systems' initial stages of

development in terms of the re-entrant jet and the front/rear menisci ($\tilde{t} = 0.76$). During these early stages, the systems are still distant from equilibrium, which is typically achieved at $\tilde{t} \approx 6$ for the non-encapsulated cases $Ca = 0.0089, 0.0377$ (and notably not attained for the encapsulated case, as demonstrated in both the present study and prior research, see §2.4). Consequently, the well-established direct relationship between liquid film thickness, $h(x)$, and Ca [179, 102, 43] has not materialised fully in the systems at this early stage, explaining the apparent absence of differences in $h(x)$ for varying Ca. A further discussion of the effects of Ca on $h(x)$ was provided in §5.4, where the cross-section bubble shapes of the systems depicted in figure 5.5(a) were displayed and analysed at a later time (see figure 5.4). Detailing the behaviour of $\tilde{\kappa}$ for $Ca = 0.0693$ along the interface path going from the re-entrant liquid jet vertex to the bubble nose, a zone of negative curvature is first observed at $3.8 \lessapprox \tilde{x} \lessapprox 4.1$, followed by a positive curvature meniscus at $3.3 \lessapprox \tilde{x} \lessapprox 3.8$. This particular curvature sign inversion is a manifestation of the early stages that precede pinch-off and drop encapsulation. This process, and its connection to other well-known systems that exhibit capillary instabilities, are examined further along in this chapter. Exiting the interior of the liquid jet towards the region adjacent to the liquid film ($3.3 \lessapprox \tilde{x} \lessapprox 7.0$), a non-uniform low curvature zone that encompasses the majority of the bubble is identified, later culminating in the high-curvature bubble nose seen for $\tilde{x} > 7.0$. Contrasting this evolution to that of the two lowest Ca, it can be noticed that the spatial location that marks the beginning of the bubble nose (sudden curvature rise from the thin-liquid film region, highlighted in grey in figure 5.5(a)) shifts to lower $\tilde{x}$ for decreasing Ca. Notable curvature inversions at the bubble tail are also identified for the low Ca cases, expressed in the undulatory structures emphasised in figure 5.5(b). These interfacial waves, previously reported in Magnini et al. [180], Edvinsson and Irandoust [77], Giavedoni and Saita [96], moderately diminish in frequency and amplitude with Ca at the same Re, as illustrated in the figure.

The dynamics of the bubble-liquid interface and its curvature gradients are readily mapped onto the $\tilde{\tau}_{n,t}$ spatial profiles of figure 5.5. Pertaining to the trailing undulatory structures (highlighted in yellow and green for $Ca = 0.0089$ and $Ca = 0.0377$, respectively), it is found that these are first characterised by a sudden surge in $\tilde{\tau}_n$ that terminates in a local maximum, which pushes the interface towards the channel walls and thus creates the crests of the interfacial waves. These peaks are promptly followed by a rapid $\tilde{\tau}_n$ decrease approaching a local minimum that contributes to the formation of the wave troughs by pulling the interface back towards the bubble. Concurrently, the tangential stresses feature similar inverse patterns of local maxima/minima that promote the sharpening of the crests/troughs. A substantial drop in $\tilde{\tau}_{n,t}$, mirrored by $\tilde{\kappa}$, is observed by departing from the rear undulatory region to the high-pressure central section of the bubble. $\tilde{\tau}_{n,t}$ remain quasi-constant and close to zero throughout this section until the reappearance of local maxima/minima marks the onset of the bubble nose. Note the generally higher $|\tilde{\tau}_t|$ exerted on the bubble nose at $\tilde{y} = 0.5$ for decreasing Ca, partly contributing to a lower curvature (more spherical) bubble front. Similar remarks about the close relationship between curvature, capillarity, and interfacial stresses have been made by Atasi et al. [17].

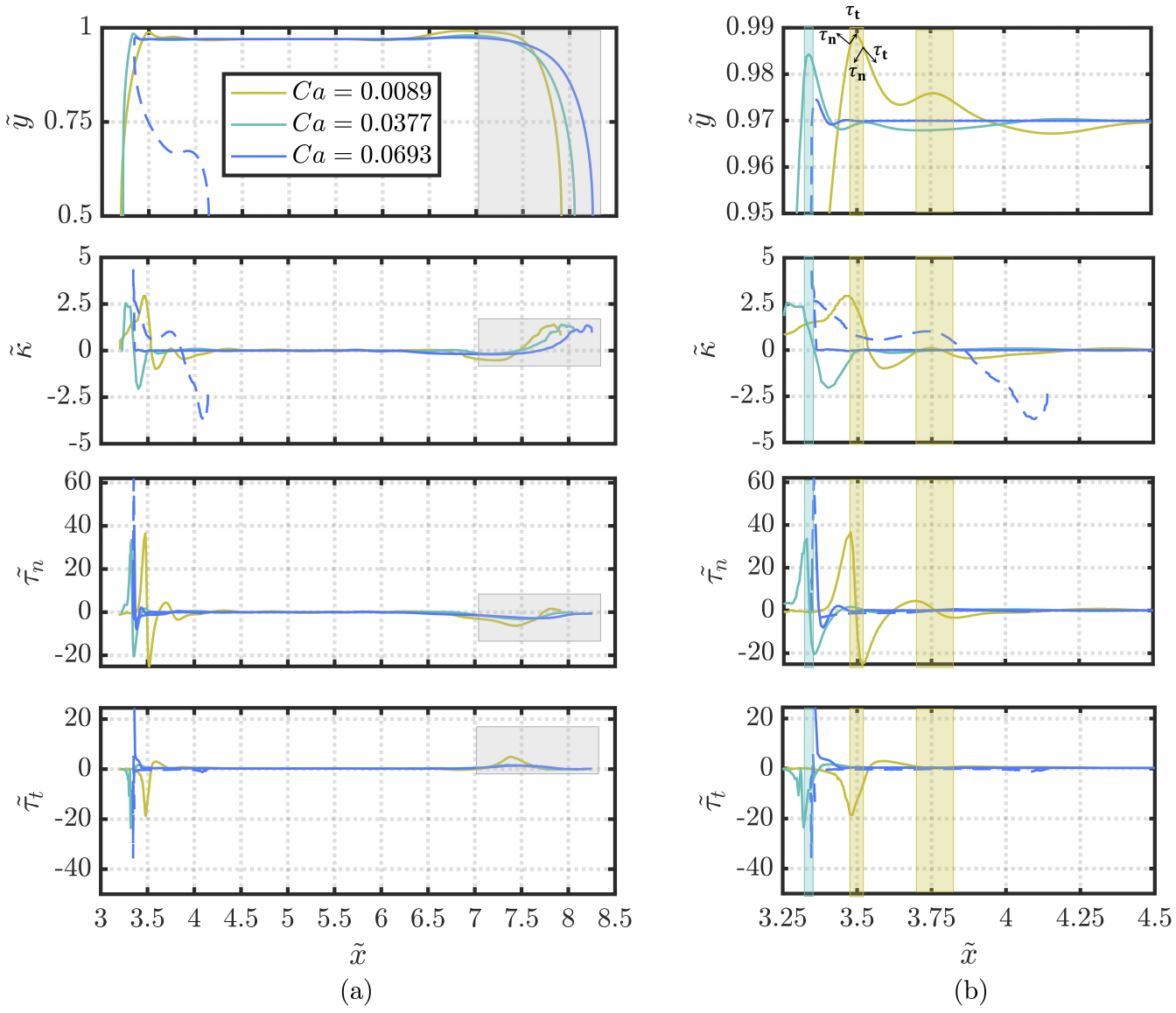

Figure 5.5: Effect of Ca on bubble dimensionless characteristics for surfactant-free cases at $\tilde{t} = 0.76$. From top to bottom, the panels showcase bubble shape, curvature, normal viscous stresses, and tangential viscous stresses. (a) Full bubble length in the axial direction; (b) zoom over the trailing undulatory structures at low Ca ($3.25 < \tilde{x} < 4.5$). From top to bottom the plots correspond to bubble-liquid interface shape, normalised mean curvature, $\tilde{k}$, normalised normal component of viscous stress on the interface, $\tilde{\tau}_n$, and normalised tangential component of viscous stress on the interface, $\tilde{\tau}_t$, respectively. Dotted line for $Ca = 0.0693$ highlights the re-entrant liquid jet. All other parameters remain unchanged from those specified in §5.2.2 for the base case. The highlighted zones in (b) represent the areas bounded by $\tilde{\tau}_n$ local maxima and minima their projections in the $\tilde{y}$, $\tilde{\kappa}$, and $\tilde{\tau}_t$ profiles

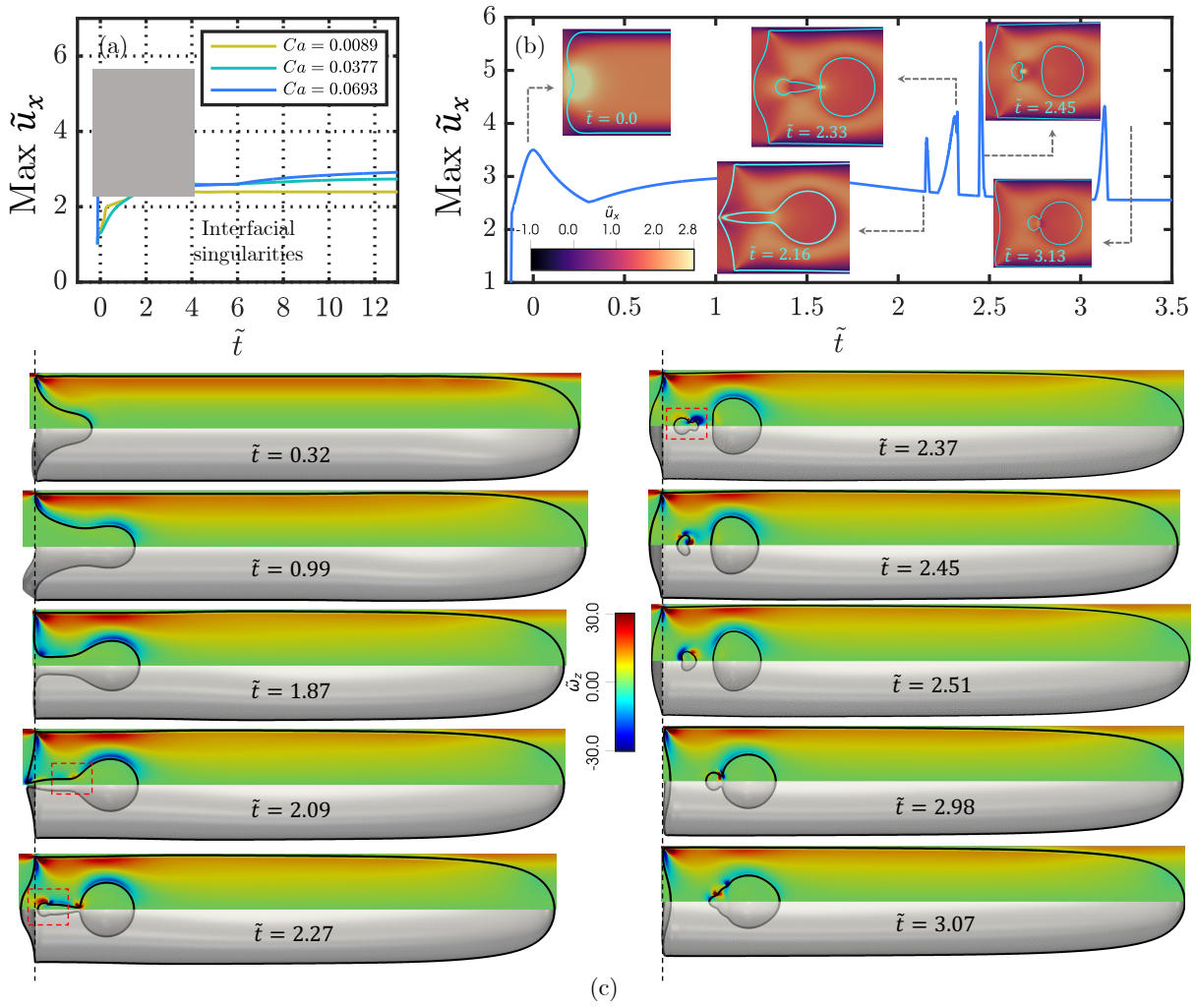

Figure 5.6: Temporal evolution of interface characteristics in surfactant-free cases: (a) maximum dimensionless velocity in x-direction; (b) zoom on interfacial singularities found for $Ca = 0.0693$; (c) detailed evolution of encapsulation process for $Ca = 0.0693$. Contour plots of normalised azimuthal vorticity, $\tilde{\omega}_z = \omega_z/(D/U_a)$ (top) and three-dimensional bubble shape (bottom). The interfaces of these contour plots have been translated in the x-direction to have a common point of reference (marked by the black dotted line)

The discussion now proceeds to detail the encapsulation process by first illustrating the numerous flow singularities produced by high Ca conditions in uncontaminated interfaces. In figure 5.6(a) the temporal evolution of the maximum normalised velocity in x-direction, Max $\tilde{u}_x$, is plotted. This evolution reveals five major local peaks in $Ca = 0.0693$ in the interval $0 < \tilde{t} < 3.5$, which materialise in (i) the previously analysed curvature inversion at the bubble back, (ii)-(iii) two pinch-offs that give rise to a "satellite" and a primary drop, (iv) an abrupt retraction and subsequent expansion of the former, and (v) a coalescence event between the two drops (see figure 5.6(b)).

A first description of the mechanisms by which these interfacial singularities come about is shown in figure 5.6(c), where a liquid infiltration deepening in the positive x-direction takes place at $0.32 < \tilde{t} < 0.99$. The fate of this liquid structure can be understood through the hybrid lens of

the well-known problems of liquid filament breakup surrounded by a gas phase [80, 45] and liquid dripping faucets [10]. The liquid jet at $\tilde{t} < 0.99$ can be thought of as a quasi-cylindrical liquid filament ($Oh \approx 0.0125$) with a low ratio between its length, $2L_{\text{jet}}$, and radius, R_{jet} undergoing end-pinching.

At around $\tilde{t} = 0.99$ in figure 5.6(c), a halt in jet axial growth is observed as capillary pressure builds at the bubble rear, inducing a vertical expansion towards the channel centre-line ($\tilde{y} = 0.5$), creating an essentially flat bubble back at $\tilde{t} = 1.87$ and a nascent pinching neck characterised by a high $|\tilde{\omega}_z|$ ring. The interface areas covered by the ring are further pulled in the counter-flow direction, prompting an additional curvature inversion at the bubble rear and the first pinch-off thereupon (see $\tilde{t} = 2.09$). This capillary singularity promotes a swift and opposite-direction recoil of the bubble back and the newly-entrapped liquid structure, thus forming the globoid-shaped bubble rear observed in $\tilde{t} = 2.27 - 2.51$. The rapidly forming rear pinching neck witnesses the incipience of an additional capillary neck at the interior of the bubble (see highlight and high $\tilde{\omega}_z$ ring in $\tilde{t} > 2.09$). This concludes in a second pinch-off and a precipitous recoil into a satellite drop (see $\tilde{t} = 2.37$). Henceforth, the first of these pinch-off events will be referred to as "back pinch-off" and the second as "interior pinch-off"; the times for these events are denoted as $\tilde{t}_{p-o,bk}$ and $\tilde{t}_{p-o,int}$, respectively. These phenomena of successive back and interior pinch-offs in surfactant-free cases are in agreement with previous numerical observations [13].

The post second pinch-off dynamics are driven by rich rotation mechanisms around both the satellite and primary drops. The two pinch-off events create a small contracting liquid filament, characterised by local $Oh \sim 0.05$ and $L_{\text{ligament}}/R_{\text{ligament}} \sim 2.62$ and similar to those studied previously [210, 72]. This small aspect ratio, in conjunction with the strong contracting kinetic energy derived from the second pinch-off, overcome capillary pressure forces to avoid an additional pinch-off instance in the small ligament. Observing the vorticity contours and the highlights at $\tilde{t} = 2.27 - 2.37$, an example of a vortex ring detachment can be noticed at the forming neck of the filament, where the vorticity boundary layer detaches and advects towards the centre of the bulbous region, pushing flow away from the neck and promoting the escape from pinch-off [115, 303, 54]. As seen in $\tilde{t} = 2.45$, succeeding the small liquid filament retraction in the counter-flow direction ($\tilde{t} = 2.37$) a counter expansion is spotted (see positive $\tilde{\omega}_z$ at $\tilde{t} = 2.45$). This generates the bullet-like satellite drop depicted at $\tilde{t} = 2.51$ and that eventually coalesces with the primary drop. The process of incorporation of the satellite into the primary drop exhibits the progressive growth of the finite liquid bridge [81], driven by the two opposite-signed high $|\tilde{\omega}_x|$ rings in its vicinity (see $\tilde{t} = 2.98$) as well as complex dynamics of interfacial waves across the newly-formed drop (see $\tilde{t} = 3.07$).

5.5.2 Influence of surfactant parameters on re-entrant liquid jet formation and encapsulation dynamics

Having examined in detail the various encapsulation phenomena observed at high Ca in surfactant-free interfaces, the analysis proceeds to explore the influence of key surfactant dimensionless groups. The analysis begins by investigating the locality of the pinch-off in both surfactant-free and surfactant-laden cases. This is followed by an examination of the influence of Marangoni stresses on the shape of the infiltration liquid, and a discussion on the relative effects of β_s and Bi. Subsequently, the competition between the rates of interface surfactant adsorption and desorption, represented by k and Da, respectively, is analysed.

5.5.2.1 Focus on the pinch-off dynamics for surfactant-free and surfactant-laden cases

This subsection examines the locality of the re-entrant jet breakup in the simulations and contrasts the neck thinning behaviour to that of the well-established theoretical scalings of Eggers [79] and Day et al. [65] for the minimum neck radius, r_{min}, and its evolution over time, $t_{p-o} - t$, where t_{p-o} is the breakup or pinch-off time. The focus is first on the observed breakup singularity for the surfactant-free case, which corresponds to a "back pinch-off" event, as defined in §5.5.1 and figure 5.6(a,c) at $\tilde{t} = 0.99 - 2.16$. Figure 5.7(a) contrasts the thinning progression of the pinching necks using the three mesh resolutions extensively tested in §5.3 (M_1, $M_{1.5}$, and M_2). Figure 5.7(b) depicts zoomed-in snapshots, colour-coded by $\tilde{\omega}_z$, of the liquid jet as it approaches the singularity.

An inspection of this figure provides further evidence of the nearly complete independence of the obtained results on the mesh resolution from M_1 and beyond, as well as the robustness of the adopted numerical approach, which is able to correctly capture the system's universal dynamics at the scale of the pinch-off in terms of both thinning rate and scaling exponents. Reassuringly, an almost complete overlap of the curves for the three resolutions is observed as $r_{min}(t) \to 0$ ($\tilde{t}_{p-o} - \tilde{t} \lessapprox 4 \times 10^{-3}$), where the universal scaling for the inertial-viscous (IV) regime of Eggers [79] ($r_{min} \sim (t_{p-o} - t)$) is correctly recovered. At early thinning stages ($\tilde{t}_{p-o} - \tilde{t} \approx 2 \times 10^{-1} - 6 \times 10^{-2}$ in the present systems), the competition between fluid inertia the opposing capillary forces yields the inertial-capillary regime (IC [65], dictated by $r_{min} \sim (t_{p-o} - t)^{2/3}$ and highlighted in red) for the liquid thread, which later transits into intermediate regimes, as predicted in Castrejón-Pita et al. [46].

It is important to note that although the obtained solution approximates the inertial-capillary (IC) regime, it does not precisely match the theoretical pre-exponent of ≈ 0.7 [80] or the 2/3 exponent proposed by Day et al. [65]. For reference, the closest matches to the scaling were found to be $\tilde{r}_{min} \approx 0.67(\tilde{t}_{p-o} - \tilde{t})^{2/3}$, $\tilde{r}_{min} \approx 0.6(\tilde{t}_{p-o} - \tilde{t})^{0.62}$, and $\tilde{r}_{min} \approx 0.55(\tilde{t}_{p-o} - \tilde{t})^{0.56}$ for M_1, $M_{1.5}$,

and M_2, respectively. Furthermore, it is observed that the intermediate stages in the plot appear to be moderately sensitive to the resolution.

The above mentioned deviations from the theoretical scalings can be attributed to the dissimilarities between the present system and those those studied in Eggers [79], Day et al. [65]. The studied system consists of a three-dimensional confined capillary channel wherein inertial effects are non-negligible, the pinching thread grows axially due to the action of the main flow, and the pinching domain remains in motion across the channel. These intricate dynamics are not accounted for in the theoretical scalings, which were initially proposed in an axisymmetric context under free-flow conditions. It is these dissimilarities between our system and the theoretical framework that likely contribute to the observed discrepancy between the obtained solution and the IC regime.

As mentioned in previous work using the same numerical approach [59, 54], the nature of this type of 3-D simulations makes it prohibitively difficult to capture the dynamic intermediate regimes reported in Castrejón-Pita et al. [46], a fact that likely explains the deviations found between mesh resolutions at intermediate times.

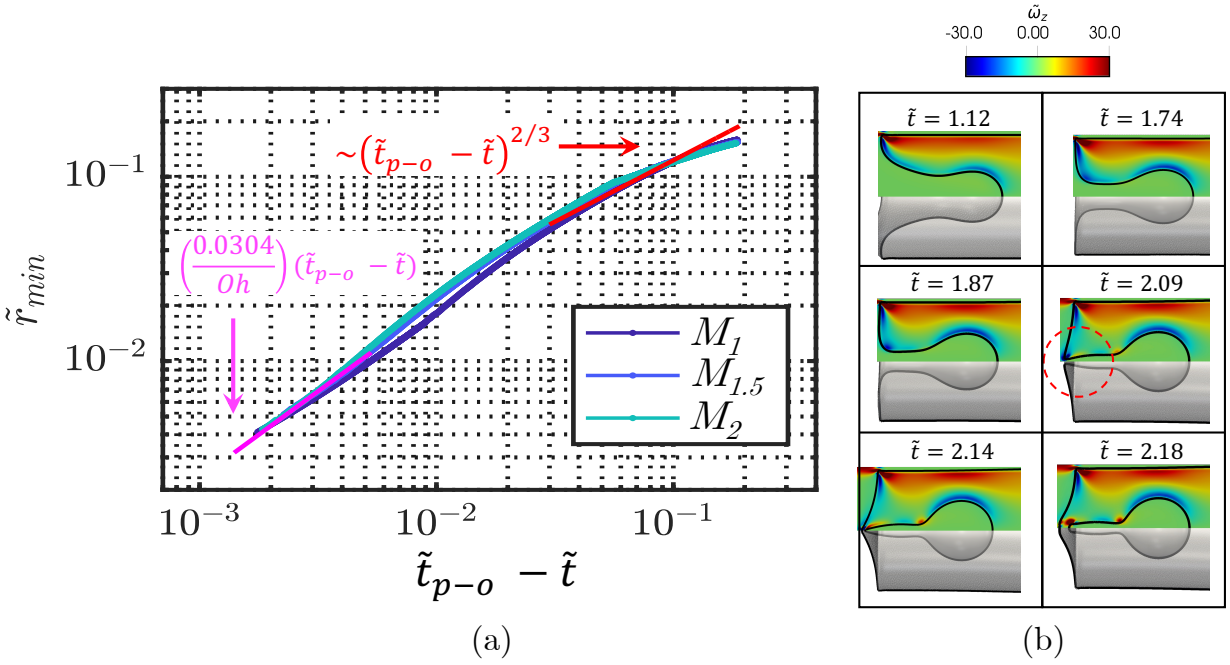

Figure 5.7: Neck thinning analysis for the "back pinch-off" event of a surfactant-free interface: (a) plot of the minimum neck radius, r_{min}, vs. the time before pinch-off, $t_{p-o} - t$, depicting how the simulations correctly retrieve the well-known inertial-viscous (pink line) pinching regime of Eggers [79] and approximate the inertial-capillary regime predicted by Day et al. [65]. Here, the time has been scaled by the inertial-capillary time scale, $t_c = \sqrt{\rho_l D^3/\sigma_s}$; (b) zoomed-in $\tilde{\omega}_z$ contour plots of the pinch-off. All other parameters remain unchanged from those specified in §5.2.2 for the base case.

The pinching phenomenon of the system is further investigated by tracking the re-entrant jet

breakup process in the presence of surfactants. To do so, the first "interior pinch-off" event of a simulation run characterised by $k = 0.25$ ($Da = 0.4$) is taken as a case-study, with the remaining parameters kept constant from those ascribed to the base case in §5.2.2. The results from this analysis are summarised in figure 5.8. Remarkably, these results are in agreement with the existing literature on surfactant-covered liquid thread breakup surrounded by a static gas phase (see for example Liao et al. [167], Kamat et al. [130], Xu et al. [322], Craster et al. [60], Wee et al. [310]); the present surfactant-laden system, which is characterised by a moving liquid jet in confined flow with non-negligible inertia, adheres to a breakup mode in the inertial-viscous regime of Eggers [79] as $r_{min}(t) \to 0$ and to the inertial-capillary regime in the early thinning stages, akin to the observations for the surfactant-free case.

As well documented in the references provided above, at the locality of the pinch-off, the competing inertial, viscous, capillary, and Marangoni-related forces balance in such a manner that the thinning neck evolves as if no surfactants were present, even when significant Marangoni stresses arise near the pinching point to re-open the neck [130]. However, the intermediary dynamics in-between the $(\tilde{t}_{p-o} - \tilde{t})^{2/3}$ and $(\tilde{t}_{p-o} - \tilde{t})$ scalings are influenced by the presence of surfactant. The existence of intermediary scalings that eventually lead to the inertial-viscous regime has been previously reported by Xu et al. [322] for small Pe and observed by Wee et al. [310] and Kamat et al. [130] for $Pe \to \infty$ (see figure 5 of the first reference). This is illustrated in figure 5.8(b), where the lower half of the jet is coloured by interfacial surfactant concentration, $\tilde{\Gamma}$. Due to the confinement effects present in the system, the bulk flow in the axial direction drags surfactants from their accumulation zones at the bubble's rear and distributes them along the liquid jet. In the present system, this action appears to counteract the surfactant depletion process at the pinching point typically reported in surfactant-covered capillary breakup [60, 310].

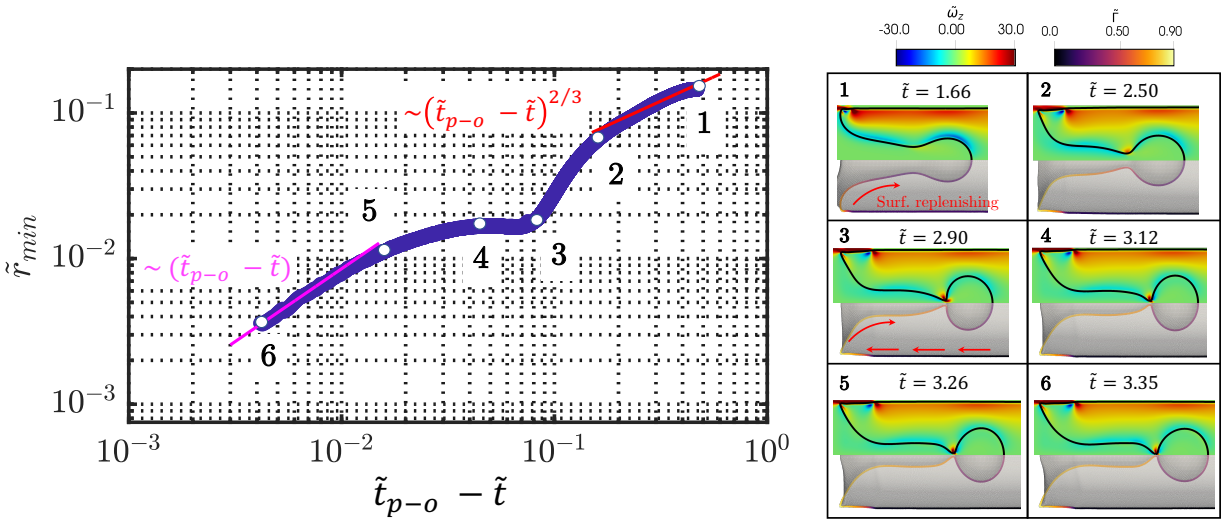

(a) (b)

Figure 5.8: Neck thinning analysis for the "interior pinch-off" event of a surfactant-laden case characterised by $k = 0.25$ ($Da = 0.4$): (a) plot of the minimum neck radius, r_{min}, vs. the time before pinch-off, $t_{p-o} - t$, depicting how the simulations correctly retrieve the well-known inertial-capillary (red line) and inertial-viscous (pink line) pinching regimes predicted by Eggers [79] and Day et al. [65], and the occurrence of three intermediary regimes. Here, the time has been scaled by the inertial-capillary time scale, $t_c = \sqrt{\rho_l D^3/\sigma_s}$; (b) zoomed-in $\tilde{\omega}_z$ (top) and $\tilde{\Gamma}$ (bottom) contour plots of the pinch-off. All other parameters remain unchanged from those specified in §5.2.2 for the base case.

5.5.2.2 Marangoni stresses, surface elasticity, and Biot number

Herein, the behaviour of a surfactant-laden system under the conditions ascribed to the "base" case (refer to §5.2.2) is elucidated and compared to that of clean interfaces. To isolate the effects of lower surface tension from those arising due to Marangoni stresses on the encapsulation dynamics, an additional case, denoted by $|\tilde{\tau}_m| = 0$, has been set up. In this case, the last term on the RHS of Eq. (5.2) has been suppressed to inhibit Marangoni stresses while simultaneously allowing the reduction of surface tension (i.e., $\nabla_s \tilde{\sigma} = 0$).

Figure 5.9(a)-(b) shows the shape of the liquid jet and a few other characteristics along its interface at $\tilde{t} = 2.09 - 2.11$. The plots of interfacial shape have been duplicated on both column panels for clarity. Examination of the plots uncovers an almost surfactant-free interface at the liquid jet for $|\tilde{\tau}_m| = 0$, which exhibits a significant drop in $\tilde{\Gamma}$ going from the edge to the interior of the re-entrant jet in the stream-wise direction and a slight surge after surpassing the incipient pinching neck. This rapid loss of surfactant for $|\tilde{\tau}_m| = 0$, as opposed to the Marangoni-supported case, $|\tilde{\tau}_m| > 0$, is explained by noticing that the base case's operating conditions promote surfactant desorption (large Da and small k) as $\tilde{\Gamma} \to 1$ (see Eq. (5.6)) as well as slow interface surfactant diffusion (large Pe_s).

Reverting back to the remarks by Batchvarov et al. [31] and Atasi et al. [17], as well as the literature review on surfactants of §2.2, the motion of the bubble prompts surfactant accumulation at the back due to drag forces from the liquid phase, partially counteracted by Marangoni stresses in the opposite direction for $|\tilde{\tau}_m| > 0$ (see schematic of figure 2.2(a)-(b)). The absence of Marangoni stresses in the $|\tilde{\tau}_m| = 0$ case leads to a continuous process of local surfactant accumulation at the back and desorption into the bulk, depleting the interface of surfactants.

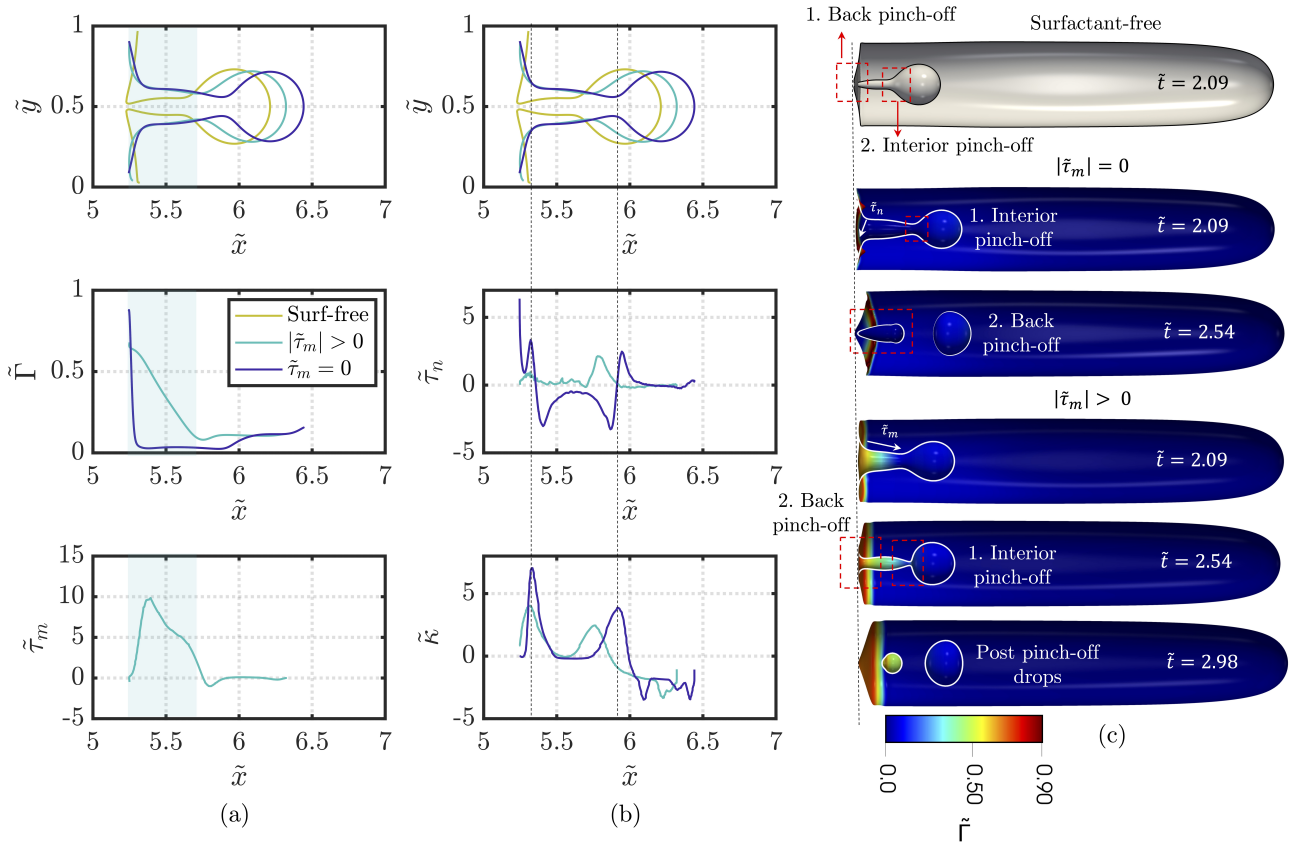

Figure 5.9: Effect of Marangoni stresses on re-entrant liquid jet formation and encapsulation. (a) Liquid-filled jet shape (top panel), surfactant interfacial concentration (middle panel), and Marangoni stresses (bottom panel); (b) Liquid jet shape (top panel), normal stresses (middle panel), and interface curvature (bottom panel). $|\tilde{\tau}_m| > 0$ corresponds to Marangoni-supported, while $|\tilde{\tau}_m| = 0$ to Marangoni-free. Plots on two-dimensional projection in x-y plane ($\tilde{z} = 0.5$) and at $\tilde{t} = 2.09, 2.10, 2.11$ for surfactant-free, $|\tilde{\tau}_m| = 0$, and $|\tilde{\tau}_m| > 0$, respectively; (c) 3-D schematic of pinch-off mechanisms. The interfaces of these images have been slightly translated in the x-direction to have a common point of reference (marked by the black dotted line); for their real location in the channel, refer to (a, top). $\tilde{t}_{p-o,bk} = 2.16, 2.55, 2.90$ and $\tilde{t}_{p-o,int} = 2.33, 2.37, 2.62$ for surfactant-free, $|\tilde{\tau}_m| = 0$, and $|\tilde{\tau}_m| > 0$, respectively. All other parameters remain unchanged from those specified in §5.2.2 for the base case.

Figure 5.9(c) portrays a key difference in the encapsulation behaviour between the three cases, where the succession of back pinch-off first and interior pinch-off second observed for clean interfaces is reversed in the presence of surfactants and the overall pinch-off dynamics are delayed (see the figure caption for the pinch-off times). This delay is accentuated for $|\tilde{\tau}_m| > 0$, as can be observed from the local peaks in $\tilde{\kappa}$ and $\tilde{\tau}_n$ of figure 5.9(b), which, in the case of $|\tilde{\tau}_m| = 0$, are

already pulling the interface towards the channel centre, signalling the onset of capillary neck closure.

Part of the role of Marangoni stresses can be seen in the green-shaded region of figure 5.9(a), where these tangential stresses counteract capillary forces at both the back and interior pinch-off regions. These observations are in complete agreement with Kamat et al. [131, 130], Constante-Amores et al. [54] for liquid threads, although it should be noted that in the present system the Marangoni forces exerted on the interface are not sufficient to escape pinch-off completely. The inversion of back and interior pinch-off times in contaminated interfaces can be attributed to the noticeably non-uniform surfactant distribution along the liquid jet, which displays its highest values in the regions neighbouring the capillary neck at the back of the jet, lowering surface tension and providing additional disruption to neck closure in comparison to the interior neck.

The effect of the surfactant-induced interior and back pinch-off delays can be further described through the evolution of the satellite drop, illustrated in figure 5.9(c) for $|\tilde{\tau}_m| > 0$. Unlike its surfactant-free counterpart (see figure 5.6(c), $\tilde{t} = 2.37 - 2.98$), this satellite drop does not re-coalesce with the main drop before the bubble reaches the end of the channel domain in our simulations. Nevertheless, notice that the satellite drop's average velocity exceeds that of the main drop by about 30% under the conditions displayed in figure 5.9(c), suggesting an eventual drop coalescence in an extended channel. In surfactant-laden scenarios, the delayed coalescence of drops is attributed to the re-entrant jet's lower surface tension, allowing faster infiltration into the bubble due to reduced resistance to liquid flow. This, in combination with Marangoni stresses opposing the jet's breakup, causes a delay in the back and interior pinch-off events and increases the spatial separation between the main and satellite drop. Measurements at $\tilde{t} = 2.66$ reveal a dimensionless distance ($\tilde{d}_{main,sat}$) of 0.13 for surfactant-free cases and 0.31 for the surfactant-laden case depicted in figure 5.9(c). It is relevant to note that the formation of the satellite drop is confined to surfactant-laden cases with highly desorptive characteristics, as explained in §5.5.3.

For the first part of the parametric investigation, the effect of β_s on encapsulation and the post pinch-off dynamics is studied. As figure 5.10(a) depicts, and in line with previous studies in the context of ink-jet printing [16], increasing surfactant strength gradually increases the speed of liquid infiltration and decreases the rate of neck thinning at both the back and interior of the re-entrant jet (see locations of jet nose in figure 5.10(a) and pinch-off times in the figure caption). This delay is materialised in the larger $|\tilde{\kappa}|$ peaks seen for $\beta_s = 0.25$ at the incipient pinching necks, as well as the higher $|\tilde{\tau}_m|$ that arise at their vicinity, seeking to counteract capillary draining [9].

Figure 5.10(b) illustrates the progression of the primary encapsulated drop as it travels across the bubble's domain in the form of its volume-averaged x-velocity, $u_{x,d}$, normalised by U_b (top), interfacial area, A_d, normalised by its area after pinch-off, $A_{d,0}$ (middle), and ratio between drop length in the x and y-directions, a/b (bottom). The encapsulated drops exhibit three common characteristics irrespective of the presence of surfactants; namely, a higher stream-wise velocity

than the bubble nose, highlighting the potential for a scenario in which the bubble nose interface is ruptured by the drop, an overall decrease in interfacial area, and dampening a/b oscillations in time, which culminate in virtually spherical drops. This bubble nose rupture is further analysed in §5.5.3. Under the conditions considered, the addition of a strong surfactant ($\beta_s = 1$) decreases the rate of surface area reduction and significantly increases drop velocity relative to the bubble nose. The non-monotonic behaviour of $u_{x,d}/U_b$ with regard to a clean interface and weak surfactants ($\beta_s = 0.25 - 0.50$) can be explained by observing in figure 5.10(c) the spatial distribution of $\tilde{\Gamma}$, $\tilde{\sigma}$ and $\tilde{\tau}_m$ in the encapsulated drop at $\tilde{t} = 7.70$. Despite the largest $|\tilde{\tau_m}|$ opposing drop propagation in the stream-wise direction for the strongest surfactant, it is seen that these effects are fully countered by the lower surface tension across the drop's domain, yielding a higher drop velocity than the surfactant-free case. In contrast, the weak surfactant cases feature an almost clean interface with surface tension values very close to the clean case, but with non-zero Marangoni effects that induce a delay in drop propagation.

The morphological deformations that characterise drop behaviour after pinch-off, as depicted in figure 5.10(b)(bottom), demonstrate the presence of a semi-periodic oscillating pattern monotonically influenced by surface elasticity. In the inset of this figure, a higher deviation from a fully spherical drop can be appreciated for the surfactant-free case in both the major crests and troughs of the oscillatory structures. Considering these results, parallels can be drawn with the study of Wang et al. [305] in an ink-jet system, whose main results suggest that the extent of deformation decreases with Ca (after a critical Ca has been reached), in line with the present numerical observations for increasing β_s. Estimating the frequency of a/b oscillations through the classic expression of Rayleigh [242] ($f \sim \sqrt{\sigma/\rho_c r_d^3}$, where r_d is the drop's spherical equivalent radius) at the latest time recorded ($\tilde{t} \approx 13.17$), $\tilde{f} \sim 1.49, 1.55, 1.55, 1.57$ is obtained for surfactant-free and $\beta_s = 0.25, 0.50, 1$, respectively, implying a dominating effect of lower drop radius over lower surface tension on the frequency of deformation cycles for increasing β_s.

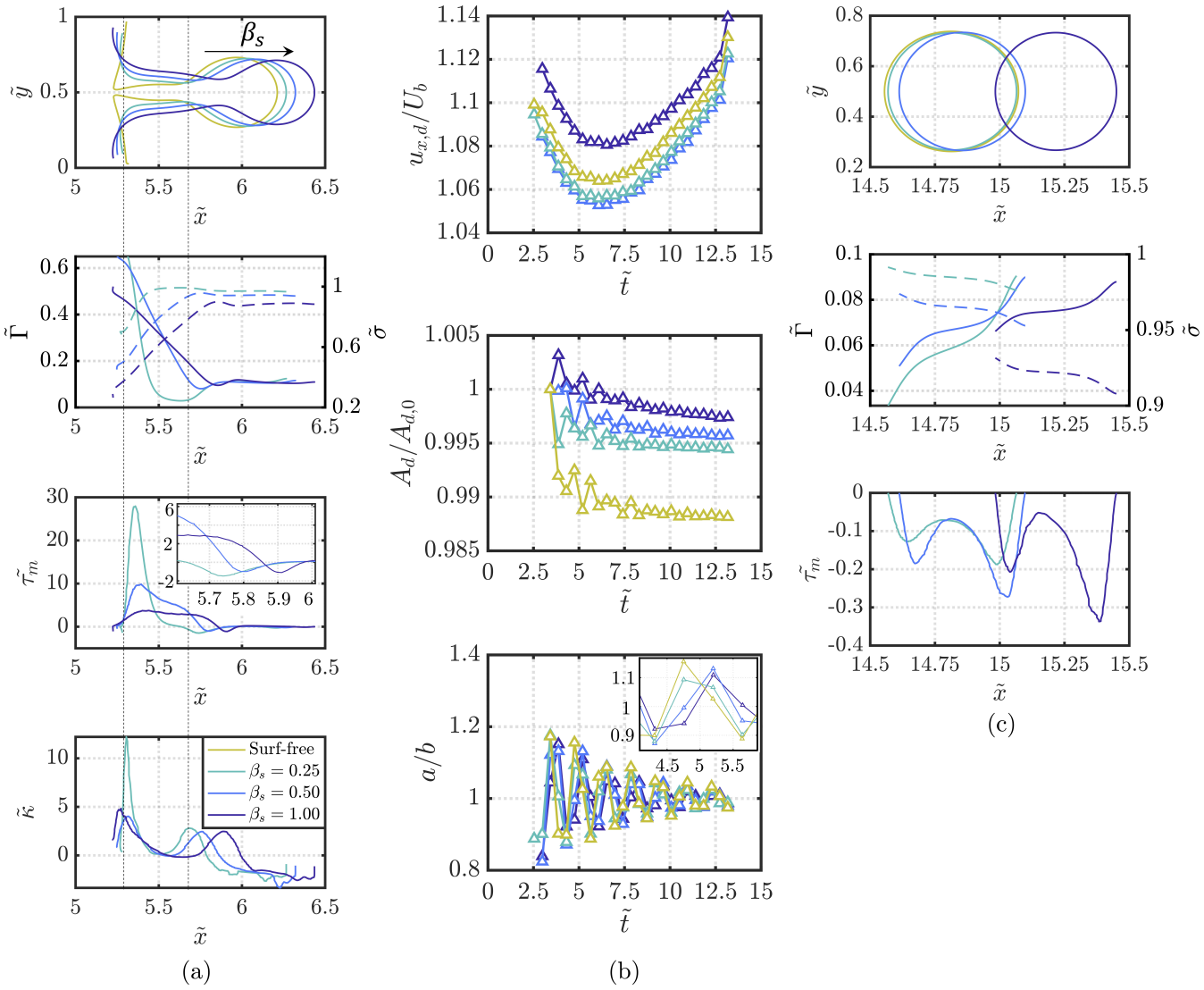

Figure 5.10: Effect of β_s on re-entrant liquid jet formation and encapsulation: (a) from top to bottom: liquid jet shape, surfactant interfacial concentration (left axis, continuous line) and surface tension (right axis, dotted line), Marangoni stresses, and interface curvature at $\tilde{t} = 2.09, 2.10, 2.10, 2.09$ for surfactant-free, and $\beta_s = 0.25, 0.50, 1$ ($Ma = 3.6 - 14.43$), respectively; (b) from top to bottom: temporal evolution of primary encapsulated drop velocity normalised by bubble velocity, primary drop interfacial area normalised by area after pinch-off, and ratio between drop length in the x and y directions. Data points computed for all cases every 10^{-3} s; (c) from top to bottom: primary encapsulated drop shape, surfactant interfacial concentration (left axis, continuous line), and surface tension (right axis, dotted line) and Marangoni stresses at $\tilde{t} = 7.70$. Plots on two-dimensional projection in x-y plane ($\tilde{z} = 0.5$) for (a, c). $\tilde{t}_{p-o,bk} = 2.16, 2.52, 2.90, 3.83$ and $\tilde{t}_{p-o,int} = 2.33, 2.40, 2.62, 2.77$ for surfactant-free, and $\beta_s = 0.25, 0.50, 1$, respectively. All other parameters remain unchanged from those specified in §5.2.2 for the base case

The effects arising from altering Bi in the range $0.01 - 1$ are depicted in the plots of figure 5.11. An interface covered by a highly soluble surfactant (i.e., high Bi) undergoes rapid rates of mass exchange between the interface and bulk as a result of its comparatively low (high) characteristic desorptive (inertial) time. This is demonstrated by noticing the significantly lower

$\tilde{\Gamma}$ distributed along the liquid jet for the highest Bi considered, which, barring the surfactant-free case ($Bi \to \infty$), exhibits the slowest rate of jet formation and the fastest pinch-off events (see location of jet nose in figure 5.11(a)(top) and figure caption for the pinch-off times). Similar to previous remarks, the signature $|\tilde{\tau}_m|$, $|\tilde{\kappa}|$, and capillary pressure peaks (not shown) that signal the onset of capillary neck closure and the advent of pinch-off are already developing in a noticeable manner for $Bi = 1$, in contrast to $Bi = 0.01 - 0.10$.

The post pinch-off temporal evolution of the primary drop, as depicted in figure 5.11(b), reveals similar trends to those referenced in the above analysis of β_s in terms of drop shrinkage, its attenuation in surfactant-laden cases, and semi-periodic drop size oscillations. Figure 5.12 elucidates the functional relationships that interlink β_s and Bi to key outcomes characterising the encapsulating system. These outcomes encompass the first pinch-off event ($\tilde{t}_{p-o,1}$), the post-detachment volume-averaged drop velocity ($\tilde{u}_{x,d}$), the first encapsulated drop's volume (normalised by the bubble's initial volume, V_d/V_0), and the drop's interface surfactant concentration (normalised by the initial concentration, Γ_d/Γ_0). The figure incorporates best-fit curves for each variable for reference. An examination of the relationships pertaining to β_s in figure 5.12(a) unveils a distinct divergence between behavioural modes for $\beta_s < 0.4$ (highlighted in blue) and $\beta_s \geq 0.4$ (highlighted in green). This divergence is particularly evident for $\tilde{t}_{p-o,1}$ and $\tilde{u}_{x,d}$. In the latter β_s range, well-established surfactant-induced effects, discussed in this chapter and widely reported in the literature, come to the forefront. These include the concurrent impact of stabilising Marangoni stresses and reduced local surface tension (i.e., increase in local Oh) contributing to thwart/delay capillary breakup and reduce drop size, as previously reported in Kamat et al. [130, 131], Kalli et al. [128].

The simulation results reveal that a surface elasticity surge (maintaining all other dimensionless groups unchanged) brings about the generation of encapsulated drops of increasing surfactant concentration and smaller size (see plots of Γ_d/Γ_0 and V_d/V_0). A larger Γ/Γ_0, in tandem with an augmented sensitivity of $\tilde{\sigma}$ to $\tilde{\Gamma}$ for increased β_s (indicated by the Langmuir relation in Eq. (5.7)) point to lower $\tilde{\sigma}$ during the re-entrant jet infiltration and pinch-off events. In fact, applying the Langmuir relation to the Γ_d/Γ_0 data of figure 5.12(a), it is found that $\tilde{\sigma}$ ranges from 1 to 0.869 for $\beta_s = 0$ and $\beta_s = 1$, respectively. Coupling this analysis with the understanding that $|\tau_m| \sim \beta_s$ (see §5.2.1), it is possible to rationalise the direct relationship between $\tilde{t}_{p-o,1}$ and β_s by invoking the above mentioned compounded action of larger Marangoni stresses and lower surface tension to resist capillary breakup for larger values of β_s.

The direct relationship registered between $\tilde{u}_{x,d}$ and β_s for $\beta_s \geq 0.4$, featuring a linear growth under our studied conditions, owes its behaviour to the diminished capillary resistance to liquid infiltration into the bubble's domain, as mentioned previously in §2.4. This directly proportional response of $\tilde{u}_{x,d}$ to β_s is akin to the well-established links between velocity of drops formed depicts, and in line with previous studies in the context of ink-jet printing through end-pinching and Oh ($\sim \sigma^{-1/2}$, precipitated by larger β_s in our simulations, as previously explained) in the problem of

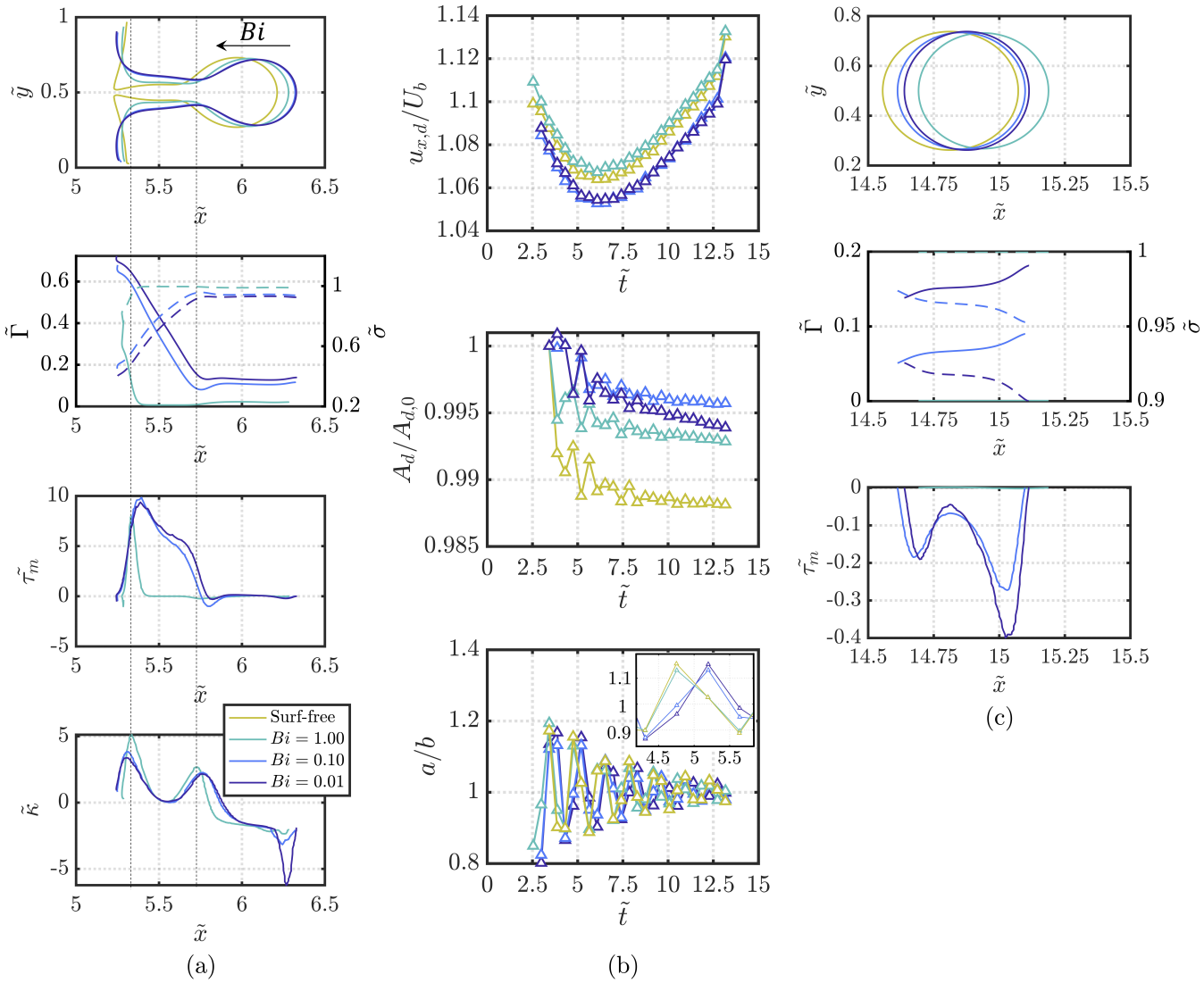

Figure 5.11: Effect of Bi on re-entrant liquid jet formation and encapsulation: (a) from top to bottom: liquid jet shape, surfactant interfacial concentration (left axis, continuous line) and surface tension (right axis, dashed line), Marangoni stresses, and interface curvature at $\tilde{t} = 2.09, 2.10, 2.10, 2.10$ for surfactant-free and $Bi = 1, 0.10, 0.01$, respectively; (b) from top to bottom: temporal evolution of primary encapsulated drop velocity normalised by bubble velocity, primary drop interfacial area normalised by area after pinch-off, and ratio between drop length in the x and y directions. Data points computed for all cases every 10^{-3} s; (c) from top to bottom: primary encapsulated drop shape, surfactant interfacial concentration (left axis, continuous line), surface tension (right axis, dashed line), and Marangoni stresses at $\tilde{t} = 7.70$. Plots on two-dimensional projection in $x - y$ plane ($\tilde{z} = 0.5$) for (a,c). $\tilde{t}_{p-o,bk} = 2.16, 2.63, 2.90, 3.09$ and $\tilde{t}_{p-o,int} = 2.33, 2.37, 2.62, 2.68$ for surfactant-free and $Bi = 1, 0.10, 0.01$, respectively. All other parameters remain unchanged from those specified in §5.2.2 for the base case

jet droplets released to the atmosphere through bursting bubbles [100]. The inversely monotonic $\tilde{u}_{x,d}$ vs. β_s relationship, evident for $\beta_s < 0.4$, embodies the nuanced effects of surface tension and Marangoni stresses, as briefly discussed in our analysis of figure 5.10. The uneven distribution of surfactant across encapsulated drops (larger concentration at the drop's nose, refer to figure 5.10(c, bottom)) instigates counter-flow Marangoni stresses ($\tilde{\tau}_{m,x} < 0$), hindering the motion of

the drop. These Marangoni stresses, though small, are non-negligible, constituting approximately 10% of the Marangoni forces exerted on the infiltrating jet prior to pinch-off (see figure 5.10). For instances where $\beta_s < 0.4$, the anticipated acceleration of the drop due to reduced surface tension is offset by these Marangoni stresses, thereby resulting in a slightly decreased drop velocity with increased surfactant strength.

The parameter sweep of surfactant solubility elucidated in figure 5.12(b) mirrors that of β_s in the discernible emergence of dual behavioural modes, this time noticeable for $\tilde{u}_{x,d}$ and V_d/V_0 and clearly separated by $Bi \approx 0.30$. Before understanding this duality (highlighted in gray and magenta), we examine the expected behaviour detected for $\tilde{t}_{p-o,1}$ and Γ_d/Γ_0. Both variables conform to a conspicuous exponential decline with increased Bi. This signals that elevated rates of mass transfer between the interface and the bulk compared to convection—indicative of enhanced solubility or larger Bi—predominantly deplete the interface of surfactant and concurrently accelerate capillary breakup with respect to lower Bi. Notice that these cases correspond to $k = t_d/t_a = 0.1$, stipulating that surfactant desorption is heavily promoted over adsorption, leading to the high-rate plummeting of $\tilde{\Gamma}/\tilde{\Gamma}_0$ with Bi and the roughly surfactant-free drops observed for $Bi > 1$ ($\tilde{\sigma} \approx 1 - 0.08e^{-3.81Bi}$, not shown in the plot). The inverse exponential dependence recovered for $\tilde{t}_{p-o,1}$ and Γ_d/Γ_0 imposes explicit bounds for these values between the two limiting cases: surfactant-free ($Bi \to \infty$, $\tilde{t}_{p-o,1} = 2.48$ and $\Gamma/\Gamma_0 = 0$) and insoluble surfactant ($Bi = 0$, $\tilde{t}_{p-o,1} = 2.81$ and $\Gamma/\Gamma_0 = 1.87$). The approximately two-fold increase in drop surfactant concentration with respect to initial surfactant coverage as the insoluble limit is approached is consistent with other applications. For instance, in the context of jet drops formed via bursting bubbles, Constante-Amores et al. [55] reports a 1.6 times increase in $\tilde{\Gamma}$ of the released drops with respect to that of the equilibrated bubble interface before bursting.

Focusing on the behavioural divergence obtained for $Bi \approx 0.3$, an inverse relation between V_d/V_0 and Bi is recovered for $Bi > 0.3$. In a similar fashion to the trends elucidated for surface elasticity, the diminished $\tilde{\sigma}$ associated with augmented surfactant coverage as Bi decreases generates smaller encapsulated drops. As we venture into the $Bi \lessapprox 0.3$ territory, a pronounced plunge in the sensitivity of V_d/V_d to Bi is identified with respect to that of $Bi > 0.3$. The $Bi < 0.3$ range adheres to $|d(V_0/V_d)/dBi| = -0.0125Bi^{-3/4}$, whereas $Bi > 0.3$ is driven by $|d(V_0/V_d)/dBi| = 0.105Bi^{-1.35}$ (1-2 orders of magnitude larger $|d(V_0/V_d)/dBi|$ for $Bi > 0.3$ within the entire Bi range studied). This analysis hints to a saturation of surfactant effects for increasingly insoluble contaminants. To finalise the present discussion of figure 5.12, we bring attention to the similar behaviour of $\tilde{u}_{d,x}$ in $Bi > 0.3$ as that in $\beta_s < 0.4$. That is, a neutralisation of the drop acceleration effects introduced by lower surface tension (prompted by larger β_s or smaller Bi) by counter-flow Marangoni stresses ($\tilde{\tau}_{m,x} < 0$).

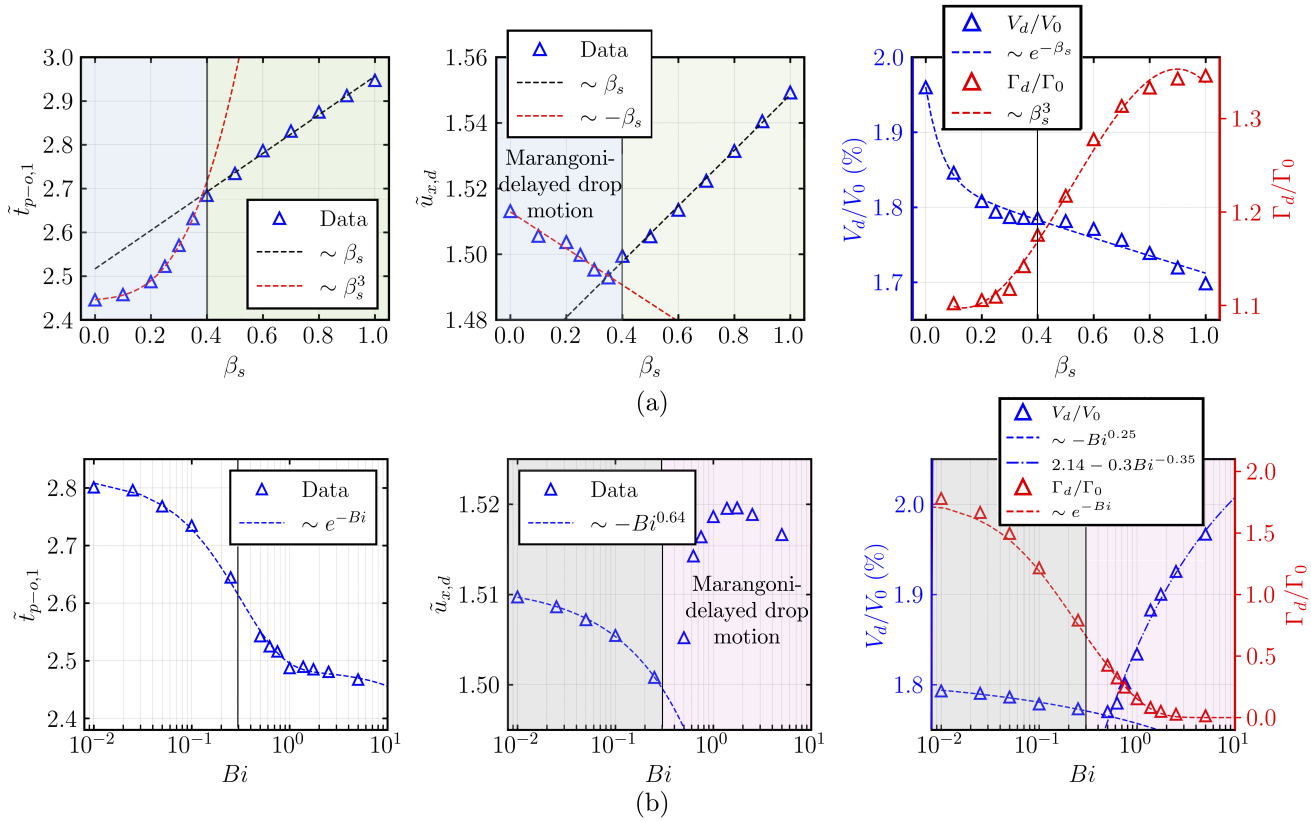

Figure 5.12: Impact of surfactant parameters on pinch-off dynamics and evolution of first encapsulated drop for a highly desorptive surfactant ($k = 0.1$): (a) Effect of β_s at $Bi = 0.1$; (b) Effect of Bi at $\beta_s = 0.5$. In (a)-(b), the panels show, from left to right, the time of the first recorded pinch-off event, post-detachment volume-averaged drop velocity, and the first encapsulated drop's volume (normalised by the bubble's initial volume, V_d/V_0). All other parameters remain unchanged from those specified in §5.2.2 for the base case

5.5.2.3 Effect of surfactant adsorption/desorption kinetics (Da and k) and the Reynolds number (Re)

The discussion now proceeds to examine the influence of directly contrasting the characteristic times of adsorption and desorption, along with the initial interface saturation through varying k and Da simultaneously. This concurrent variation allows us to maintain all other parameters constant. Figure 5.13(a) portrays a monotonic response of the liquid infiltration depth and $\tilde{\Gamma}$ with k and Da, where the rapid rates of surfactant adsorption inherent to the high k (low Da) cases are materialised in the relatively large and comparatively constant $\tilde{\Gamma}$ distributions along the re-entrant jet. In line with previous results shown in this chapter, general reductions in local surface tension at the bubble rear, brought about by higher k or β_s and lower Bi conditions, promote a faster and deeper infiltration of liquid into the bubble domain.

In figure 5.13(b) the time until the first pinch-off instance at the bubble interior is recorded as a function of k for the entire parameter space explored. A retardation of the capillary instabilities that lead to end-pinching is seen as k is increased in the range 0 (surfactant-free) $< k < 1$,

consistent with previous remarks about the combined effect of $\tilde{\sigma}$ and Marangoni stresses on opposing drop encapsulation. This behaviour is mirrored by the $\tilde{\tau}_m$ and $\tilde{\kappa}$ peaks exposed near the nascent pinching necks for the lowest k cases displayed in figure 5.13(a) ($k = 0.1 - 1.0$), while the oscillations seen for $k = 10$ correspond to capillary waves in the infiltrating liquid, reported by Constante-Amores et al. [54] for long liquid ligaments.

Similar to previous analyses on β_s, Bi, and Marangoni-free case for $k = 0.10$, it is found that increasing k in the range $k < 0.10$ results in a sequence inversion of the two main pinch-off events ($\tilde{t}_{p-o,bk} > \tilde{t}_{p-o,int}$) identified in clean interfaces ($\tilde{t}_{p-o,bk} < \tilde{t}_{p-o,int}$, see caption of figure 5.13). Interestingly, it is also found that for all cases above $k = 0.25$, the large accumulation of surfactants nearby the bubble rear provides a strong resistance to capillary pressure buildup in those regions, resulting in the partial elimination of the "back pinch-off" event until bubble bursting events occur. This will be further discussed in the following section.

Another notable feature to highlight from figure 5.13(b) is the sharp decrease in $\tilde{t}_{p-o,int}$ above the critical value of $k = 1$. This discontinuity in the function $\tilde{t}_{p-o,int}$ vs. k, in conjunction with our observations about the elimination of the back pinch-off suggest a partition of the encapsulation dynamics into two major regions according to the rates of adsorption/desorption: i) the above described region for $k < 1$, in which the presence of surfactants exerts a stabilising effect, leading to a delay in neck thinning in relation to a fully clean interface; and, ii) a region of rapid Liquid jet formation in the axial direction alongside a significant acceleration of the first interior pinch-off event for $k > 1$. The first region is further segregated by the occurrence ($k < 0.25$, region i.a) or elimination ($k > 0.25$, region i.b) of the back pinch-off. An explanation for the marked transition from the first to the second region in terms of thinning rates is as follows. A general increase of surfactant coverage due to high rates of adsorption introduces high rates of viscous and inertial deformation to the interface, as noted by Bazhlekov et al. [32], hence, increasing the axial velocity of the infiltrating liquid and its aspect ratio. Recalling the observations of Wang et al. [303] and Ambravaneswaran and Basaran [9] in contracting/expanding liquid filaments, figure 5.13(c) shows how, in cases above the critical k, L_{jet}/R_{jet} surpasses a given threshold value to enter the breakup regime and accelerate end-pinching, even if the local values of surface tension are lower than those of smaller k conditions.

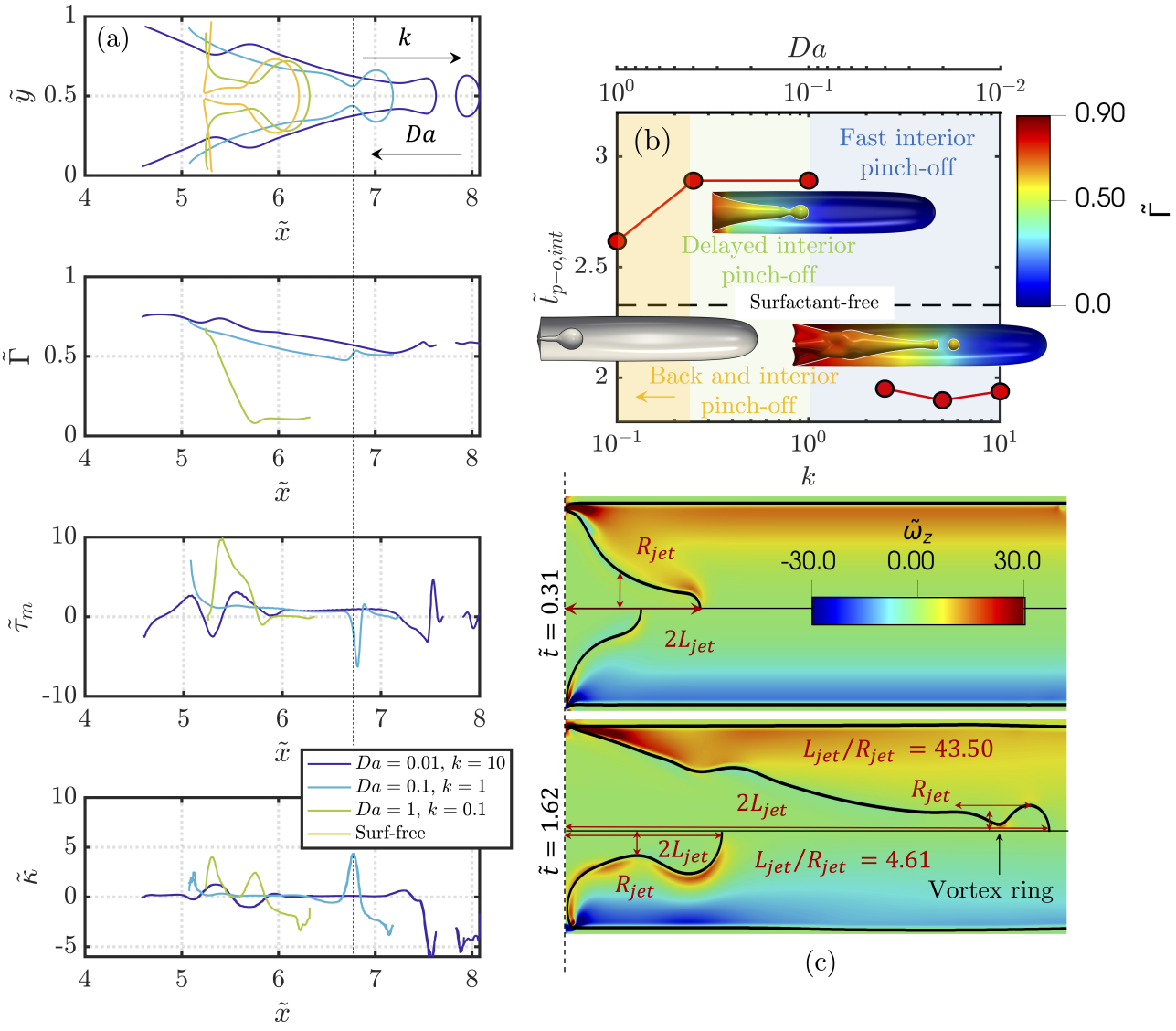

Figure 5.13: Effect of k and Da on re-entrant liquid jet formation and encapsulation: (a) from top to bottom: liquid jet shape, surfactant interfacial concentration, Marangoni stresses, and interface curvature at $\tilde{t} = 2.09, 2.10, 2.09, 2.09$ for surfactant-free and $k = 0.1, 1, 10$, respectively; (b) interior pinch-off time vs. k and Da, and schematic of the three regions that divide thinning behaviour; (c) contour plots of normalised vorticity in z-direction and comparison of infiltrating liquid shape for $k = 10.0, Da = 0.01$ (top) and $k = 0.1, Da = 1.0$ (bottom). The interfaces of these contour plots have been translated in the x-direction to have a common point of reference (marked by the black dotted line). Plots on two-dimensional projection in x-y plane ($\tilde{z} = 0.5$). All other parameters remain unchanged from those specified in §5.2.2 for the base case

Moving on to the final exploration of the dimensionless space of the system, the influence of varying Re in the range $100 - 443$ ($We = 6.93 - 30.70$) and maintaining all other characterising dimensionless numbers constant, $Ca = 0.0693$, $Pe_{c,s} = 100$, $Bi = 0.1$, $Da = 0.1$, $k = 1$, and $\beta_s = 0.5$, is tested. Figure 5.14 demonstrates the pronounced effects of Re on cavity formation and the overall surfactant dynamics, where the presence of comparatively lower inertial forces of reduced Re and constant Ca (lower We) appears to oppose the complete development of the liquid cavity and the process of drop entertainment, whilst still allowing the rear curvature

inversion described for large Ca (see §5.5.1). The spatial profiles of $\tilde{\Gamma}$ show a cavity largely covered in a uniform manner by surfactants for $Re = 100$, manifested in the very low $\tilde{\tau}_m$ exerted and the virtually planar $\tilde{\kappa}$ of a significant portion of its cavity. This contrasting behaviour against the highly non-uniform and smaller $\tilde{\Gamma}$ describing high Re provides evidence for arguing that, in the locality of the cavity, inertio-capillary forces are greatly overcome by viscous-related forces, strongly opposing liquid infiltration, necking, and ultimately pinching. The combined influence of both Ca and Re on the successful entrapment of liquid drops within the bubble domain is underscored. This process necessitates an initial inversion of the bubble rear, a sufficiently rapid cavity development, and the occurrence of capillary pressure buildup that leads to pinch-off.

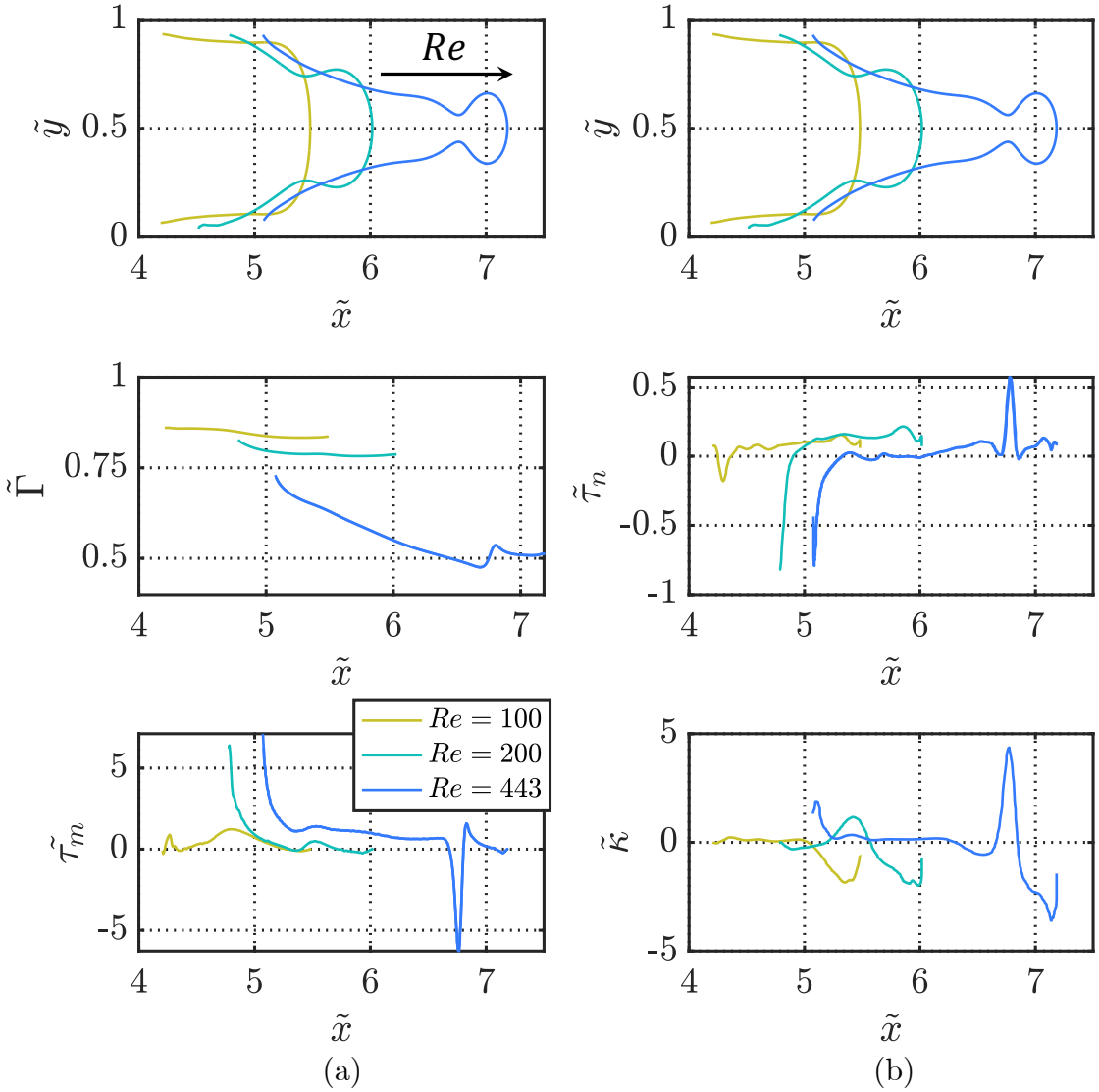

Figure 5.14: Effect of Re on re-entrant liquid jet formation and encapsulation: (a) from top to bottom: liquid jet shape, surfactant interfacial concentration, and Marangoni stresses; (b) from top to bottom liquid jet shape, normal stresses, and interface curvature. Plots on two-dimensional projection in x-y plane ($\tilde{z} = 0.5$) and at $\tilde{t} = 2.22$. For the three cases shown, $Ca = 0.0693$, $Pe_{c,s} = 100$, $Bi = 0.10$, $Da = 0.10$, $k = 1$, and $\beta_s = 0.50$. Pinch-off not observed for $Re = 100 - 200$. For this set of results, $Da = 0.10$ and $k = 1$. All other parameters remain unchanged from those specified in §5.2.2 for the base case.

5.5.3 Bubble bursting, back deformations, and regime maps

This section provides a more detailed account of the post pinch-off dynamics, focusing specifically on the process of bubble bursting via the liquid jet/entrapped drops and the temporal fate of the bubble back and accompanying trailing structures.

In figure 5.15(a)-(b), the three main bursting behaviours observed in the β_s-k and Bi-k (Da) spaces are summarised, leaving all other conditions specified in the baseline case unchanged. As captured in the figure, a first regime (I), distinctly bounded by a surfactant-free interface and k below the critical value defined in the previous section, is identified for all β_s and Bi tested. This regime adheres to a behaviour mode of slow infiltration of liquid, monotonic delay of the first interior pinch-off event with increasing (decreasing) β_s (Bi) (see figure 5.12), and most importantly, eventual restoration of the interfacial morphology of the bubble back, depicted in figure 5.15(c, top). This restoration ensures a pseudo-stable entrapment of one or multiple drops of varying size and $\tilde{\Gamma}$ within the bubble domain, only disrupted by a potential rupture of the bubble nose by the first drop. It must be noted that this rupture was not observed for any of the cases encompassed within (I) given the channel length employed in the simulations and the significant elongation of the bubble across the channel. The stability of the encapsulated drops-bubble compound in regime I poses a potential avenue for future research, as remarked in §5.6.

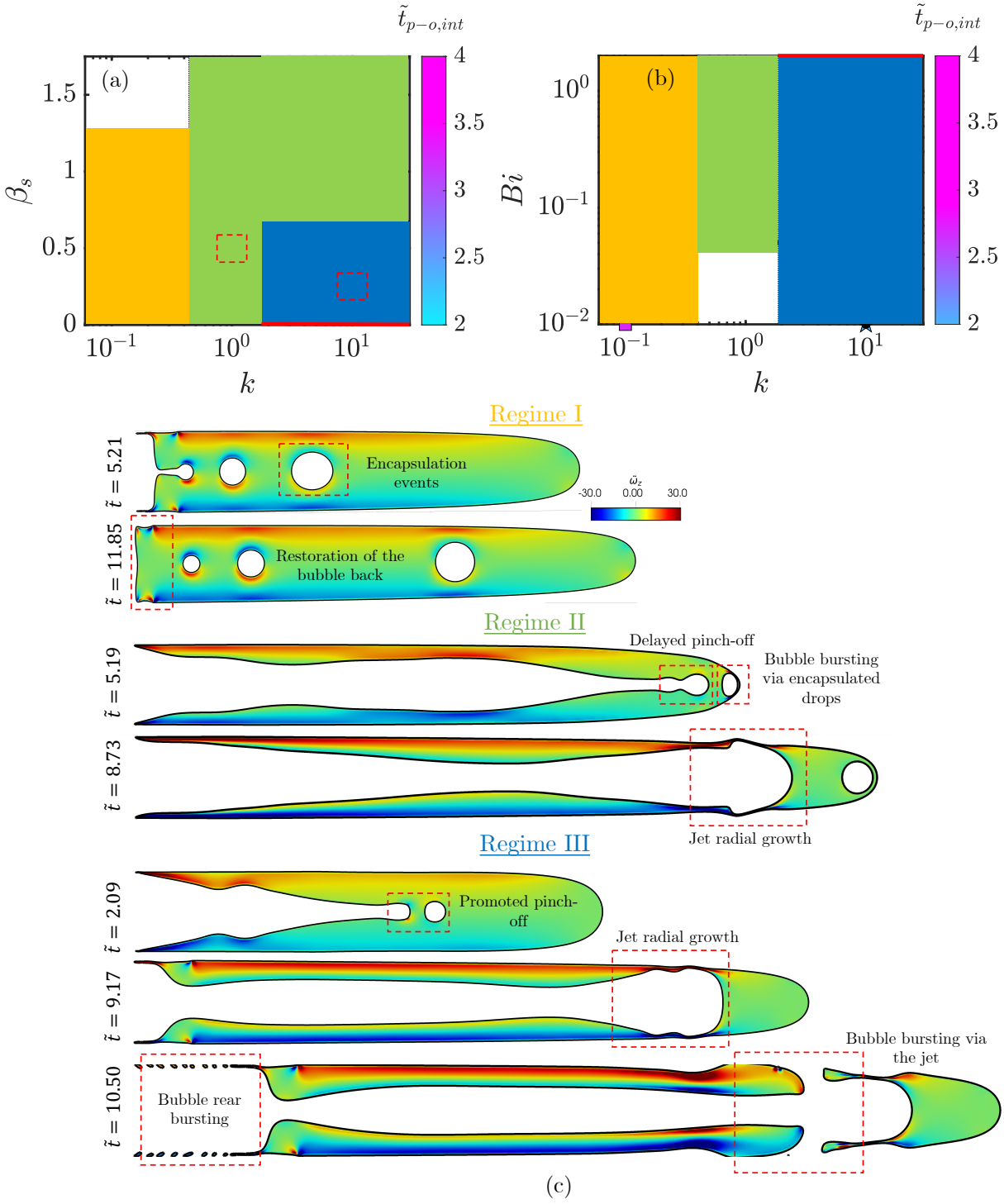

Figure 5.15: Encapsulation and bursting regime maps in the (a) β_s-k and (b) Bi-k spaces. $Bi = 0.10$ for (a) and $\beta_s = 0.50$ for (b). The results of the present work, shown as markers coloured by the first interior pinch-off event, reveal three distinct regimes: I (squares), II (circles), and III (stars). The black markers correspond to the data set of Atasi et al. [17], which does not differentiate regime II from III; (c) schematic contour plots of normalised vorticity in z-direction and comparison for the three regimes identified. All other parameters remain unchanged from those specified in §5.2.2 for the base case. Regime maps developed for $Bo \to 0$

A second regime (II) emerges as k approaches the critical value, where a much faster and

deeper liquid jet develops across the bubble and, ensuing from diminished capillary forces, further delays to pinch-off are recorded. These delays lead to the entrapment of the first drop in regions approaching the bubble nose in the axial direction, promptly leading to its rupture, as illustrated at $\tilde{t} = 5.19$ in figure 5.15(c, middle). Following a series of end-pinching events, the liquid jet undergoes several instances of escapes of pinch-off, in conjunction with a surge of surface capillary waves across its domain, and a radial growth that gives rise to a large bulbous end (see $\tilde{t} = 8.73$). These mechanisms are closely related to the intricate phenomena stemming from retracting liquid filaments, as addressed in Anthony et al. [15], Constante-Amores et al. [54]. This substantial growth causes the liquid jet to burst the interface near the channel walls, thereby fully separating the original bubble into two individual entities.

The third regime (III) is confined to regions of above critical k with moderate β_s and $0.01 < Bi < 1$ and closely resembles the mechanisms of II, with the pinch-off times being the key differentiating characteristic. In III, the fast expansion of the liquid jet expedites the first pinch-off with respect to the surfactant-free case (see previous sub-section). Although the location of the first entrapment is much farther away from the bubble nose than in II, the encapsulated drops exhibit a comparatively faster velocity (e.g., $u_{x,d}/U_b = 1.27$ and $u_{x,d}/U_b = 1.47$ at $\tilde{t} = 4.75$ for the cases in II and III emphasised in figure 5.15(a), respectively), also leading to bubble nose ruptures by the drops and the consequent radial rupture by the bulbous end of the liquid jet mentioned above (see $\tilde{t} = 10.50$).

Figure 5.15 also displays the numerical data derived from the regime maps proposed in Atasi et al. [17] for surfactant-laden systems (see figure 2.11 and associated discussion). A qualitative comparison is drawn between the bubble rear bursting phenomena characteristic of regime III (see $\tilde{t} = 10.50$ in figure 5.15(c)) and the observations of Nath et al. [202] for liquid-liquid flow in clean interfaces (see figure 15 of this reference). As depicted in the figure, the proposed transition from regime I (curvature inversion without bursting) to regimes II and III (bubble bursting) at $k \approx 0.45$ for varying β_s and Bi aligns remarkably well with that found in Atasi et al. [17] for $Ca \to 1$ (see figure 16 of this reference). Notice that Atasi et al. [17] does not dive into the pinch-off dynamics of the system, precluding us from making a direct classification of their bubble bursting cases into regimes II and III.

A few caveats should be noted concerning these comparisons with previous investigations. While the proposed regimes and observations of the bubble's behaviour align with previous results, it is pertinent to emphasise that the operating conditions considered herein differ significantly from those of Atasi et al. [17] and Nath et al. [202]. The former reference examines a system characterised by negligible inertia, a nearly spherical bubble, and a circular cross-sectional channel. The latter reference, as previously mentioned, involves the motion of a droplet in the absence of surfactant material. These differences elucidate why their encapsulation phenomena occur at Ca values much larger than those observed here ($Ca \sim O(10^0)$ compared to $Ca = 0.0693$) and why it is not feasible to map the exact operating conditions of Nath et al. [202] onto those

explored in this investigation.

To finalise this analysis, the author of this thesis wishes to highlight the limitations of the proposed encapsulation regime maps. As briefly mentioned in §5.2.1, gravitational forces are neglected in the simulations ($Bo = 0$) as their effects typically become significant only in channels larger than 1 mm [181], given the prevailing influence of capillary forces at the microscale. The primary focus of this study was to characterise encapsulation mechanisms within scenarios involving inertia, non-circular geometries, and the presence of contaminants. Hence, isolating these influences from other non-idealities, including gravitational effects, was essential for the present objectives. It is crucial to recognise, however, that the diminished influence of capillary forces—an essential condition for encapsulation, accentuated by surfactants—could potentially magnify the importance of gravitational forces, consequently impacting encapsulation dynamics.

The potential impact of gravity has been assessed by comparing characteristic time scales within the system to the free-falling time of an encapsulated drop. Adopting $Bo = 0.15$, a moderate value of Bo that still induces noticeable gravitational effects on gas-liquid systems [195]), it is found that the falling time of encapsulated drops ($\approx 4.5 \times 10^{-2}$ s) largely exceeds the re-entrant jet's pinch-off times under the tested conditions ($\approx 5-7 \times 10^{-3}$ s) but is comparable to the total travel time of the bubble across the channel domain ($\approx 3-6 \times 10^{-2}$ s). This suggests that gravitational effects are unlikely to significantly influence the curvature inversion, jet infiltration, and breakup processes elucidated in this study, or the impact of surfactants. Nevertheless, gravity is certain to disrupt the trajectory, velocity of entrapped drops, and thus the proposed regime maps illustrated in figure 5.15.

5.6 Concluding remarks

This work presents an in-depth characterisation of the unsteady mechanisms describing elongated bubbles flowing across liquid-filled channels via numerical simulations under negligible gravitational effects. These mechanisms arise in opposition to the well-known steady-state phenomena of Taylor bubbles under the traditional assumptions of negligible inertial/viscous effects, symmetric cross-section channels, and the absence of interfacial contaminants. As reported in limited instances (see Atasi et al. [17] and Sauzade and Cubaud [251]) and confirmed here, interesting dynamics emerge as $We \to O(10)$. Notably, the concomitant reduced capillary effects of high Ca (and We) induce a loss of sphericity at the bubble's front and back, triggering an elongation in the flow direction of the former and a flattening and subsequent curvature inversion of the latter. The underlying mechanisms by which this curvature inversion evolves into a re-entrant liquid jet infiltrating the bubble, how this liquid structure collapses into small liquid drops entrapped in the bubble domain, and the overall role of surfactants in these processes have been analysed in detail. The multiple parallels between the various interfacial features and singularities observed in this study and those occurring in other well-known systems involving capillary liquid breakup, such

as inkjet printing, two-phase microfluidics, contracting liquid filaments, and sheet cavitation, are readily emphasised.

By performing a systematic sweep of a number of surfactant parameters and characterising dimensionless groups, the coupled effect of lower surface tension and Marangoni stresses and their interactions with inertia and viscosity have been elucidated. Two distinct modes of liquid jet breakup/drop encapsulation were found for comparatively low rates of surfactant adsorption (low k): one closure of the liquid jet at the bubble's rear and one end-pinching breakup mode at the interior of the jet. The simulations have shown that the combined and individual effects of both surface tension and Marangoni stresses induce a delayed response in terms of pinch-off times, as well as an inversion of the sequence of breakup modes with respect to clean interfaces. Provided that k is low enough, these effects are maintained for increasingly strong (large β_s) and less soluble (small Bi) surfactants. Under the baseline conditions considered, a critical value of $k = 1$ represents a phenomenological limit from which an increase of k represents an acceleration of the second mode of jet breakup when compared to an uncontaminated interface. This is due to the fast and deep liquid infiltration in the bubble at high k, which promotes capillary breakup.

A summarising map with three regimes of behaviour was constructed in the β_s-k and Bi-k (Da) spaces, where regime I, limited by the critical k, allows for a semi-stable drop entrapment due to the eventual closure and restoration of the bubble back in the aftermath of pinch-off. Conversely, in regimes II (delayed pinch-off) and III (expedited pinch-off), the deep infiltration of the liquid jet that precedes end-pinching, together with the high relative velocity of the entrapped drops are responsible for the subsequent bursting of the bubble nose. These two regimes, in addition, display a multitude of rich interfacial events following the liquid jet end-pinching, including escapes from pinch-off, radial growth, and an eventual bubble bursting in the vicinity of the channel walls.

To the best of the author's knowledge, this is the first thorough and detailed characterisation of the phenomenon of drop encapsulation in moving bubbles in the presence of surfactants. There are, however, a few avenues worthy of further pursuit in this topic. First, the author recommends an examination of the validity of the results, including the proposed encapsulation regime maps and the observed bursting behaviours, in a circular channel geometry, either via numerical simulations or experimentation. Given that the rear curvature inversion and encapsulation events were found to be prompted by low Ca and We, which exert a thickening effect on the liquid film surrounding the bubble (see figure 2.7(b)-(c) and Eqs. (2.24) - (2.26)), it is likely that these phenomena will be largely unaffected by the channel geometry. Nevertheless, further investigation is necessary to confirm this.

In addition to the above, an examination of the influence of surfactant parameters, β_s for example, on the critical k value. Based on the numerical results, it is likely that this critical k will decrease with increasing β_s, but additional evidence is required. A deeper exploration

of the stability of the encapsulated drops in regime I may also be of interest to determine if there exists a set of conditions that allow for a perpetual entrapment of these drops, and the potential applications of such systems in the context of emulsification. Finally, an expansion of the proposed regime maps to include the effects of gravitational forces represents an interesting avenue for further research.

Chapter 6

Surfactant-laden bubble bursting: dynamics of capillary waves and Worthington jet at large Bond number

Contents

6.1 Motivation and overview . . . 163

6.2 Formulation and problem statement . . . 164

6.2.1 Governing equations and dimensionless numbers . . . 164

6.2.2 Numerical method . . . 167

6.2.3 Simulation setup and timescales . . . 168

6.2.3.1 Computational domain, initial conditions, and boundary conditions . . . 168

6.2.3.2 Selection of operating conditions and their equivalence with previous studies . . . 170

6.3 Bursting bubble validation and drop size/velocity in the presence of surfactant . . . 172

6.4 Results and discussion . . . 174

6.4.1 Uncontaminated interfaces: buoyancy effects on capillary wave velocity and Worthington jet . . . 174

6.4.2 Contaminated interfaces: phenomenology of bubble collapse . . . 180

6.4.2.1 Surfactant-induced wave retardation and break of linearity . . . 180

6.4.2.2 Effect of surfactant solubility and Marangoni stresses transition 184

6.4.2.3 Effect of surfactant elasticity and capillary wave velocity compilation . . . 186

6.4.3 Contaminated interfaces: jet drops and aerosol release . . . 190

6.4.3.1 Cap retraction and its effects on ejected jets 194
6.5 Concluding remarks 195

6.1 Motivation and overview

The final results chapter of this thesis explores the well-known phenomenon of bubble bursting through liquid-gas interfaces. As reviewed in chapter 2 (§2.5), the small liquid drops released from these events are highly relevant not only to environmental/atmospheric sciences and advanced technologies but also to everyday life [93, 298, 257]. The release of these drops encompasses a wealth of fascinating fluid mechanics phenomena. This process involves the ascent and contamination of bubbles in a liquid medium [73, 122], the collapse of the thin film separating the bubble from the atmosphere through cap retraction dynamics akin to Taylor–Culick flows, or via the Rayleigh–Taylor instability, resulting in the release of "film drops" [299]. Additionally, it includes the generation of capillary waves that converge at the bubble's base [100], leading to the generation of a Worthington jet and its subsequent breakup through the Rayleigh–Plateau instability [34, 68].

This chapter specifically focuses on the main sub-stages following bubble ascension and cap collapse: the propagation of capillary waves along the bubble, their convergence at the bubble's apex, the rapid rise of a Worthington jet, and its breakup to release liquid drops. The key concluding remarks of the literature review highlight the need to address two crucial yet often overlooked aspects of these sub-stages: the presence of surface-active agents and the dynamics influenced by non-negligible gravitational effects, quantified by the Bond number. As explained in §2.5, the large bulk of available knowledge on bursting bubbles corresponds to situations devoid of contamination and featuring negligible gravitational effects ($Bo \sim O(10^{-3})$). Only a handful of recent experimental [227, 297] and numerical [55] investigations have begun examining the influence of surfactant material on the bursting phenomenon and the Worthington jet.

Through high-fidelity 3-D simulations, the presented findings propose, for the first time, a mechanism explaining capillary wave retardation in the presence of surfactants. This mechanism involves the transition from bi-directional to uni-directional Marangoni stresses, which pull the interface upwards, counteracting the motion of the waves. Additionally, this work quantitatively elucidates the variable nature of wave velocity under different surfactant parameters, including surfactant solubility and elasticity, marking a departure from the constant behaviour documented in clean interfaces. Finally, this study reports on the dual effects of surfactants on jet ejection velocity and the velocity of the ejected drops.

The rest of this chapter is organised as follows: §6.2 introduces the system considered, the numerical approach, and related dimensionless parameters. §6.3 is devoted to providing a thorough validation of the numerical setup against experimental measurements from various sources and

involving multiple variables. §6.4 presents a discussion of the results, focusing first on surfactant-free interfaces at large Bo, and then inspecting the striking influence of surfactants in terms of capillary wave propagation and Worthington jet ejection. Concluding remarks are provided in §6.5.

The findings of this chapter have been published in Pico et al. [226]:

Pico, P., Kahouadji, L., Shin, S., Chergui, J., Juric, D. and Matar, O.K. *"Surfactant-laden bubble bursting: dynamics of capillary waves and Worthington jet at large Bond number"*. Phys. Rev. Fluids., 9, p.83606

6.2 Formulation and problem statement

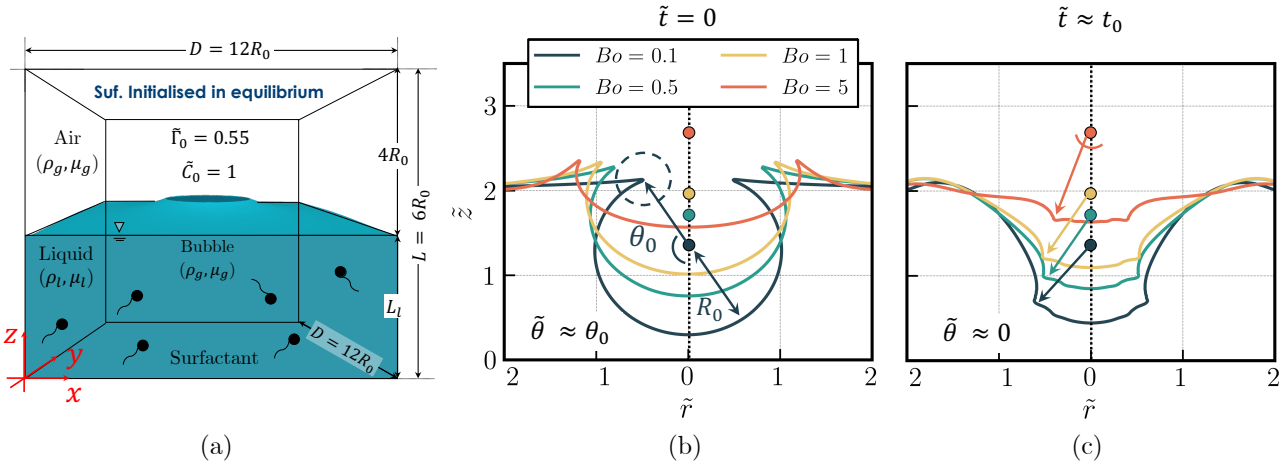

Figure 6.1: 3-D computational domain in a Cartesian coordinate system $\mathbf{x} = (x, y, z)$ and initial bubble shapes. A radial coordinate is defined as $r = \sqrt{(x - x_0)^2 + (y - y_0)^2}$, where x_0 and y_0 correspond to the domain's centre point: (a) Schematic representation of the simulated domain, showcasing an equilibrated initial bubble immersed in a liquid pool with initial surfactant concentration $\tilde{C}_0$ and interfacial concentration $\tilde{\Gamma}_0$ (not to scale); (b) 2-D projection in a $x - z$ plane of initial ($\tilde{t} = 0$) bubble shape for different Bo; (c) Representation of an instant approaching cavity collapse ($\tilde{t} \approx t_0$) at the bubble apex, where $\tilde{\theta} \approx 0$. The points located at $\tilde{r} = 0$ in (b,c) mark the centre of each bubble, from which the angle of the dominant capillary wave is measured [100]. The dashed circle highlights the high-curvature region connecting the cavity to the liquid pool

6.2.1 Governing equations and dimensionless numbers

Two-phase direct numerical simulations are conducted to investigate the dynamics of an isolated bursting bubble event immersed in a three-dimensional (3-D) Cartesian domain denoted by $\mathbf{x} = (x, y, z)$ (refer to figure 6.1(a)). The simulations incorporate surface-active material, and the equations presented in this chapter are formulated within the framework of Level Contour Reconstruction Method (LCRM). This method is employed to handle surface tension forces, the interface, and their coupling with surfactant transport. Details of this approach can be found

in Shin and Juric [265], Shin et al. [267, 268] and §3.3.4. All variables and physical parameters involved in the system are rendered dimensionless via the scalings expressed by Eq. (6.1), which are consistent with previous work on bursting bubbles [55, 100]:

$$\tilde{\mathbf{x}} = \frac{\mathbf{x}}{R_0}, \quad \tilde{t} = \frac{t}{t_c}, \quad \tilde{\mathbf{u}} = \frac{\mathbf{u}}{u_c}, \quad \tilde{p} = \frac{p}{\rho u_c^2}, \quad \tilde{\mu} = \frac{\mu}{\mu_l}, \quad \tilde{\rho} = \frac{\rho}{\rho_l}, \quad \tilde{\sigma} = \frac{\sigma}{\sigma_s}, \\ \tilde{\Gamma} = \frac{\Gamma}{\Gamma_\infty}, \quad \tilde{C} = \frac{C}{C_\infty}, \quad \tilde{C}_s = \frac{C_s}{C_\infty}, \tag{6.1}$$

where $\tilde{t}$, $\tilde{\mathbf{u}}$, $\tilde{p}$, $\tilde{\mu}$, $\tilde{\rho}$, and $\tilde{\sigma}$ represent time, velocity vector, pressure, and local viscosity, density, and surface tension, respectively; $\tilde{\Gamma}$, $\tilde{C}$, and $\tilde{C}_s$ are surfactant concentration at the interface, bulk, and bulk region in the vicinity of the interface, respectively. Hereinafter, tildes represent dimensionless variables, and the subscripts l and g distinguish between the liquid and gas phases.

In the above equations, R_0 is the bubble size, $u_c = \sqrt{\sigma_s/(\rho_l R_0)}$ is the velocity time-scale, $t_c = R_0/u_c = \sqrt{\rho_l R_0^3/\sigma_s}$ is the capillary time-scale, and σ_s is the surface tension in a surfactant-free interface. Surfactant-related variables are scaled on the saturation interface surfactant concentration or maximum packing, Γ_∞, and the initial bulk surfactant concentration, C_∞. In what follows, all variables are referred to by their name to refer to their dimensionless version, unless stated otherwise.

The equations governing the simulation, presented herein, are expressed in dimensionless form under the assumptions of Newtonian fluids, immiscible phases, and incompressible flow. The continuity and momentum equations, written within a one-fluid formulation, are provided in Eqs. (6.2)-(6.4),

$$\nabla \cdot \tilde{\mathbf{u}} = 0, \tag{6.2}$$

$$\tilde{\rho}\left(\frac{\partial \tilde{\mathbf{u}}}{\partial \tilde{t}} + \tilde{\mathbf{u}} \cdot \nabla \tilde{\mathbf{u}}\right) + \nabla \tilde{p} = -Bo\mathbf{i}_z + Oh\ \nabla \cdot \left[\tilde{\mu}(\nabla \tilde{\mathbf{u}} + \nabla \tilde{\mathbf{u}}^T)\right] + \\ \int_{\tilde{A}(\tilde{t})} (\tilde{\sigma}\tilde{\kappa}\mathbf{n} + \nabla_s \tilde{\sigma})\delta\left(\tilde{\mathbf{x}} - \tilde{\mathbf{x}}_f\right) \mathrm{d}\tilde{A}, \tag{6.3}$$

$$\tilde{\rho}\left(\mathbf{x}, t\right) = \rho_g/\rho_l + (1 - \rho_g/\rho_l)\mathcal{H}(\tilde{\mathbf{x}}, \tilde{t}), \\ \tilde{\mu}\left(\mathbf{x}, t\right) = \mu_g/\mu_l + (1 - \mu_g/\mu_l)\mathcal{H}(\tilde{\mathbf{x}}, \tilde{t}), \tag{6.4}$$

where $\mathcal{H}$ is a smoothed Heaviside function that adopts the value of zero in the gas phase and unity in the liquid phase. This function is computed directly from the interface and solved numerically with a smooth transition across three or four cells [265, 267].

As introduced in the review of the literature of §2.5, Bo denotes the Bond number, and Oh is the Ohnesorge number (see Eq. (6.9) for their definitions). In Eq. (6.3), the last two terms on the RHS account for the normal and tangential components of the surface tension forces, $\tilde{\mathbf{f}}_\sigma$. The normal component arises from the average localised surface tension, while the tangential component, or Marangoni stresses, acts on the interface due to surfactant-induced surface tension variations across the interface (refer to §2.2 for a more in-depth discussion of Marangoni stresses

and Marangoni flows). In these definitions, $\tilde{\kappa}$ is twice the mean interface curvature, $\mathbf{n}$ represents a unit vector normal to the interface pointing towards the liquid phase, $\tilde{A}(\tilde{t})$ denotes the time-dependent interface area, and $\delta(\tilde{\mathbf{x}} - \tilde{\mathbf{x}}_f)$ is a Dirac delta function. This delta function vanishes everywhere except for the interface (located at $\tilde{\mathbf{x}} = \tilde{\mathbf{x}}_f$); $\nabla_s = (I - \mathbf{nn}) \cdot \nabla$ signifies the surface gradient operator (refer to 3.3).

Surfactant transport is resolved in both the liquid bulk phase and at the interface via the non-passive convection-diffusion expressions of Eqs. (6.5) - (6.6), according to the well-established formulation by Eggleton and Stebe [82], Muradoglu and Tryggvason [199] (and references therein):

$$\frac{\partial \tilde{\Gamma}}{\partial \tilde{t}} + \nabla_s \cdot (\tilde{\Gamma} \tilde{\mathbf{u}}_\mathrm{t}) = \frac{1}{Pe_s} \nabla_s^2 \tilde{\Gamma} + Bi \left(k \tilde{C}_s (1 - \tilde{\Gamma}) - \tilde{\Gamma} \right), \tag{6.5}$$

$$\frac{\partial \tilde{C}}{\partial \tilde{t}} + \tilde{\mathbf{u}} \cdot \nabla \tilde{C} = \frac{1}{Pe_c} \nabla^2 \tilde{C}, \tag{6.6}$$

$$\mathbf{n} \cdot \nabla \tilde{C}|_{interface} = -Pe_c Da Bi \left(k \tilde{C}_s (1 - \tilde{\Gamma}) - \tilde{\Gamma} \right), \tag{6.7}$$

where $\tilde{\mathbf{u}}_\mathrm{t} = (\tilde{\mathbf{u}}_\mathrm{s} \cdot \mathbf{t})\mathbf{t}$ is the tangential projection of the surface velocity vector, $\tilde{\mathbf{u}}_\mathrm{s}$. Within this formulation, surfactant is exchanged between the interface and the bulk region immediately adjacent via the source term written in Eq. (6.7). The dependence of surface tension on variations in $\tilde{\Gamma}$ is computed via the nonlinear Langmuir equation of state, which assumes that non-interacting surfactant molecules occupy finite-sized sites on a lattice [184]. This expression reads

$$\tilde{\sigma} = \max \left(\epsilon_\sigma, 1 + \beta_s \ln \left(1 - \tilde{\Gamma} \right) \right), \tag{6.8}$$

with $\beta_s = \mathcal{R}T\Gamma_\infty / \sigma_s$ representing surfactant elasticity or surfactant "strength", as defined in previous investigations [199, 213], and $\epsilon_\sigma = 0.05$. Here, $\mathcal{R}$ is the ideal gas constant and T the system's absolute temperature. The ϵ_σ parameter corresponds to a limit placed on $\tilde{\sigma}$ and introduced in the formulation to circumvent the issue of unphysical negative surface tensions predicted by the Langmuir expression in non-dilute systems where surfactant concentration approaches the maximum packing ($\tilde{\Gamma} \to 1$) [199, 268]. The dimensionless groups that govern the system are defined here as

$$\begin{gathered} Bo = \frac{\rho_l g R_0^2}{\sigma_s}, \quad La = Oh^{-2} = \frac{\rho_l \sigma_s R_0}{\mu_l^2}, \quad \frac{L}{D}, \quad \frac{L}{L_l}, \quad Bi = \frac{k_d R_0}{u_c}, \quad k = \frac{k_a C_\infty}{k_d}, \\ Da = \frac{\Gamma_\infty}{R_0 C_\infty}, \quad Pe_{s,c} = \frac{u_c R_0}{D_{s,c}}, \quad \beta_s = \frac{\mathcal{R}T\Gamma_\infty}{\sigma_s}, \quad Ma = \frac{\beta_s \sigma_s}{\mu_l u_c}, \end{gathered} \tag{6.9}$$

where Bo characterises the interplay between gravitational and capillary forces, while La quantifies the relative significance of viscous to capillary forces; The Biot number, Bi, serves as a metric for surfactant solubility, comparing the capillary and desorptive, $t_d = k_d^{-1}$, timescales. The parameter k directly influences the balance between surfactant adsorption, $t_a = (k_a C_\infty)^{-1}$, and desorption time-scales. The Damköhler number, Da, provides insight into the initial surfactant saturation, while $Pe_{s,c}$ denotes the Péclet numbers associated with the significance of

surfactant diffusive effects on both the interface (modulated by diffusivity D_s) and the liquid bulk (modulated by diffusivity D_c) with respect to the characteristic timescale of the system, t_c. The geometrical parameters L/D and L/L_l correspond to the ratios between the height and width of the simulation domain and the height of the liquid pool, respectively, as shown in figure 6.1(a).

In the present study, the dimensionless Marangoni stresses, $\tilde{\tau}_m$, are computed by using Eq. (6.10):

$$\tilde{\tau}_m \equiv \nabla_s \tilde{\sigma} \cdot \mathbf{t} = -\frac{\beta_s}{1-\tilde{\Gamma}} \nabla_s \tilde{\Gamma} \cdot \mathbf{t}. \tag{6.10}$$

In addition to modulating surface pressure ($\Pi = -\beta_s \sigma_s \ln(1 - \frac{\Gamma}{\Gamma_\infty})$) and Marangoni stresses, β_s acts as a direct regulator of various thermodynamic concepts within the Langmuir isotherm framework, including the Gibbs-Marangoni moduli and the Marangoni number, represented here as Ma. The standard expression for the Marangoni modulus, E_0, for the Langmuir isotherm, can be rearranged in terms of β_s as $E_0 \equiv \Gamma \frac{\partial \Pi}{\partial \Gamma}\Big|_N = \frac{\beta_s \sigma_s \Gamma}{\Gamma_\infty (1-\Gamma/\Gamma_\infty)}$ (with N being the number of moles), underscoring the direct influence of β_s on this parameter [184]. For the same values of Γ, higher β_s values result in stronger resistances to interfacial compression, leading to increased interfacial "rigidification" or "immobilisation". E_0 can also be interpreted as the work done by the process of "squeezing" surfactant molecules together [184]. An more in-depth discussion of these surfactant concepts can be found in §2.2 and §3.3.2.

As mentioned in Chapter 5, this investigation defines a Marangoni number based on the ratio between characteristic Marangoni and viscous stresses [184].

6.2.2 Numerical method

For the calculations, the code BLUE is employed, which is based on the LCRM method. This method and code have been successful in reproducing both experimental and numerical data in a plethora of applications involving complex interfacial flow instabilities with contaminants, including bursting bubbles for very small Bond number [55]. This sub-section presents a brief summary of the most relevant aspects of the method and refer the reader to Shin and Juric [265], Shin et al. [267, 268] and §3.3.4 for further details.

The field equations presented above are resolved by utilising a finite-difference method with a fixed Eulerian grid. Spatial derivatives of the Eulerian grid fields are discretised through a standard cell-centred scheme for most terms, except for the nonlinear convective terms, which employ a second-order essentially non-oscillatory (ENO) procedure [269] on staggered grid. The viscous term in the momentum equation is discretised using a second-order centred difference scheme. Temporal terms are handled with a second-order Gear method [306], incorporating implicit time integration for the viscous terms.

The interface is tracked with a front-tracking method and reconstructed using a level-set approach [263, 265]. The connection between Lagrangian and Eulerian grid is achieved through Peskin [222]'s well-known immersed boundary method. The front-tracking utilises a deformable grid with Lagrangian elements discretised using a triangular mesh. These Lagrangian elements are advected by integrating equation $\mathrm{d}\mathbf{x}_f/\mathrm{d}t = \mathbf{V}_f$, where $\mathbf{V}_f$ represents the interface fluid velocity, which displaces the vertices of the Lagrangian triangular mesh, $\mathbf{x}_f$. This integration is performed using a second-order Runge-Kutta method.

6.2.3 Simulation setup and timescales

6.2.3.1 Computational domain, initial conditions, and boundary conditions

The computational domain for most simulations consists of a rectangular box of size $12R_0 \times 12R_0 \times 6R_0$, where the latter dimension corresponds to the domain's height (see figure 6.1(a)). It should be highlighted that this height is smaller than that of previous numerical studies, such as the $15R_0$ used in Constante-Amores et al. [55] or the $8R_0$ used in Sanjay et al. [249] as the focus is specifically on the large Bond ($Bo = 0.5 - 5$) regime. In this regime, the system exhibits a significant reduction in the velocity and length of the jet [68, 34]. During testing, this domain size was found to be appropriate to render radially- and height-related boundary effects negligible. For the simulations characterised by $Bo = 0.1$, the domain size was increased to $(12R_0)^3$.

The system is initiated with a static equilibrated bubble positioned beneath the liquid-gas interface, shaped according to the Young-Laplace equation. This equation dictates the bubble's morphology based on a static quasi-equilibrium between surface tension and gravity, directly influenced by the choice of Bo [163, 331]. A cross-section of the initial bubble shapes for the four tested Bo values is depicted in figure 6.1(b), where the initial angular location of the dominant capillary wave, $\tilde{\theta}_0$, is highlighted, alongside its value at the moment of collapse. Notice that, as Bo increases, there is a clear departure from sphericity, accompanied by reduced immersion in the liquid bulk. Further details on this solution and the effect of Bo on initial bubble shape can be found in §2.5.

In adherence to the common approach in numerical investigations of bursting bubbles, even at $Bo > 1$ [302], the simulations commence at the point when the liquid cap completes its draining process. This simplification, enabling the exclusion of the liquid cap, is justified by the markedly larger Taylor-Culick velocity associated with cap retraction time, u_{TC}, in comparison to the system's main phenomena. Under the studied conditions, u_{TC} is larger than the characteristic velocity scale u_c by three to two orders of magnitude. The implications of neglecting the cap dynamics at large Bo and the caveats of our results are discussed at the end of §6.4.1 and §6.4.3.1.

A structured uniform grid of resolution $(768)^2 \times 384$ ($(768)^3$ for $Bo = 0.1$) is employed, ensuring converged and mesh-independent results during testing for both the present study and

prior work on bursting bubbles using the same numerical approach [55]. This grid resolution proves crucial, particularly at the instants of jet ejection and breakup, where large velocities are involved. For a comprehensive validation of the code used, extending beyond prior work on bursting bubbles using the LCRM [55], please refer to §6.3.

Solutions to the governing equation are sought subject to free-slip conditions at the lateral boundaries and no-slip conditions at the bottom boundary for velocity ($\mathbf{u} = (u_x, u_y, u_z)$), pressure, and surfactant concentration. An outflow condition is utilised for the top boundary to ensure the ejected drops from the Worthington jet do not bounce off the boundary [249]. A summary of all boundary conditions can be found in Eq. (6.11) (refer to figure 6.1(a) for reference on the location of each plane):

$$\begin{aligned}
u_x &= 0 \quad \text{on boundaries normal to the } (y-z) \text{ plane,} \\
\frac{\partial u_x}{\partial \mathbf{n}} &= 0 \quad \text{on boundaries normal to the } (x-z) \text{ plane,} \\
u_y &= 0 \quad \text{on boundaries normal to the } (x-z) \text{ plane,} \\
\frac{\partial u_y}{\partial \mathbf{n}} &= 0 \quad \text{on boundaries normal to the } (y-z) \text{ plane,} \\
\frac{\partial u_z}{\partial \mathbf{n}} &= 0 \quad \text{on boundaries normal to the } (x-z) \text{ and } (y-z) \text{ planes,} \\
\mathbf{u} &= 0 \quad \text{on bottom boundary (no-slip),} \\
\frac{\partial \mathbf{u}}{\partial \mathbf{n}} &= 0 \quad \text{on top boundary (no flux),} \\
\frac{\partial p}{\partial \mathbf{n}} &= 0 \quad \text{on all boundaries (no flux),} \\
\frac{\partial C}{\partial \mathbf{n}} &= 0 \quad \text{on all boundaries (no flux),} \\
\mathbf{n} \cdot \nabla \tilde{C}|_{interface} &= -Pe_c Da Bi \left(k\tilde{C}_s(1-\tilde{\Gamma}) - \tilde{\Gamma} \right) \quad \text{at the interface.}
\end{aligned} \tag{6.11}$$

Surfactant material is initialised with an equilibrium condition between the bulk and interface. By equating the last term on the RHS of Eq. (6.5) to zero and considering $\tilde{C} = 1 = \tilde{C}_s$, the initial interface surfactant concentration is set to $\tilde{\Gamma}(\mathbf{x}, t = 0) = \tilde{\Gamma}_0 = k/(k+1) = 0.55$. This concentration is kept constant in all simulations to isolate the "pure" effects of other, less understood surfactant parameters, such as solubility and surface elasticity. This approach also allows for a clearer analysis of the relationship between these parameters and Marangoni stresses.

The impact of surfactant solubility is examined within the range $Bi = 0 - 10$ and surfactant strength within the range $\beta_s = 0.05 - 1$, equivalent to $Ma = 15 - 311$, which is in line with previously reported Ma for common surfactants ($Ma \sim O(10^1)$ [277]). As implied in Eq. (6.9), the present formulation specifies that $Bi = 0$ denotes an insoluble surfactant (i.e., no surfactant desorption), while the limit $Bi \to \infty$ corresponds to a surfactant-free interface. The additional dimensionless parameters associated with surfactant remain constant at $k = 1.22$, $Pe_{s,c} = 100$, and $Da = 1$. Along with the above parameters, both Bo and La are varied in the ranges

$0.1 < Bo < 5$ and $10^4 < La < 10^6$ ($10^{-2} > Oh > 10^{-3}$). These La conditions are well above the "optimal" value of $La \approx 1000$, where the system approaches a singularity at the instant of collapse and the maximum (minimum) jet velocity (drop size) is attained for $Bo \to 0$ [34, 100].

6.2.3.2 Selection of operating conditions and their equivalence with previous studies

As also analysed in §5.2.2, the selection of dimensionless parameter values is informed by the characteristics of commonly employed commercial surfactants in bursting bubble applications, such as sodium dodecyl sulfate (SDS) and Triton X-100 (TX100) [227, 297]. These surfactants exhibit diffusivities in the range of $D_{s,c} = O(10^{-10} - 10^{-9})$ $\mathrm{m^2 s^{-1}}$, resulting in corresponding Péclet numbers of $Pe_{s,c} = O(10^3 - 10^6)$. This indicates that surfactant transport and rearrangement events across the interface are unlikely to be dominated by interfacial surfactant diffusion. The chosen conditions also ensure the significant involvement of Marangoni stresses in tye system, given the comparable nature of the Marangoni time-scale, $t_m = \mu_l R_0/(\Delta\sigma) = O(10^{-2})$ s, with those associated with sorption kinetics, $O(10^{-2}) - O(10^{-1})$ s [192]. Furthermore, the current operation is at sufficiently low bulk surfactant concentrations to neglect the micelle formation and its potential effects on the system.

In selecting the operating conditions for the simulations, the objective was to explore an interesting and previously unexplored parameter space, such as varying Bi and β_s while keeping all other parameters constant, alongside conditions grounded in reality and previous research. To the best of the author's knowledge, Pierre et al. [227] and Vega and Montanero [297] are the only published experimental studies providing data on surfactant-laden bubble collapse times without surface rheological effects. Despite using the same surfactant (SDS) and similar Bo and Oh values for their bursting bubble investigations, these studies differ in their C/CMC ranges: Pierre et al. [227] spans $C/CMC \approx [0.25, 5]$, while Vega and Montanero [297] covers $C/CMC \approx [0.1, 4]$. The comparisons made in this chapter highlight the most comparable points among Pierre et al. [227], Vega and Montanero [297], and the present operating conditions in terms of β_s, Bo, Oh, and initial surfactant concentration.

By using Vega and Montanero [297]'s SDS data of equilibrium surface tension vs. surfactant concentration (see figure 2(c) of that reference), non-dimensionalising by the clean surface tension, $\sigma_s \approx 72$ $\mathrm{mN \cdot m^{-1}}$, and maximum packing, $\Gamma_\infty \approx 3.2$ $\mu\mathrm{mol \cdot m^{-2}}$, and fitting the data to the Langmuir expression of Eq. (6.8), figure 6.2(a)-(b) is obtained. This figure suggests that a good fit for this particular surfactant is obtained for $\beta_s \approx 0.1$. This is the reason why, as shall be seen in figure 6.13, Pierre et al. [227]'s and Vega and Montanero [297]'s surfactant data points have been placed at $\beta_s = 0.1$.

Given that the data points of the above mentioned references are reported under varying initial surfactant concentrations, an equivalence to the present operating conditions was also required. As mentioned in the previous sub-section, all simulations were conducted with a constant initial

surfactant concentration of $\tilde{\Gamma}_0 = \Gamma_0/\Gamma_\infty = 0.55$. Based on published data on Γ vs. C/CMC for SDS (see figure 2(b) of Vega and Montanero [297]), it was found that an initial $\tilde{\Gamma}_0 = 0.55$ corresponds to $C/CMC \approx 0.125$. While Vega and Montanero [297] provides bursting bubble data at this concentration (red lines in figure 6.2(c)), the lowest C/CMC tested in Pierre et al. [227] is approximately 0.25, corresponding to $\tilde{\Gamma}_0 \approx 0.81$ (blue lines in figure 6.2(c)).

Considering the aforementioned points, it was decided to report the data from Vega and Montanero [297] at $C/CMC \approx 0.25$ instead of $C/CMC \approx 0.125$ in figure 6.13. Although the initial conditions established in the present study are more accurately represented by $C/CMC \approx 0.125$, the choice of $C/CMC \approx 0.25$ was made to ensure uniformity and compatibility with the data from Pierre et al. [227]. It should be noted that the collapse time data at these two C/CMC values does not vary significantly, as both are well below the CMC. This is supported by Vega and Montanero [297]'s figure 12.

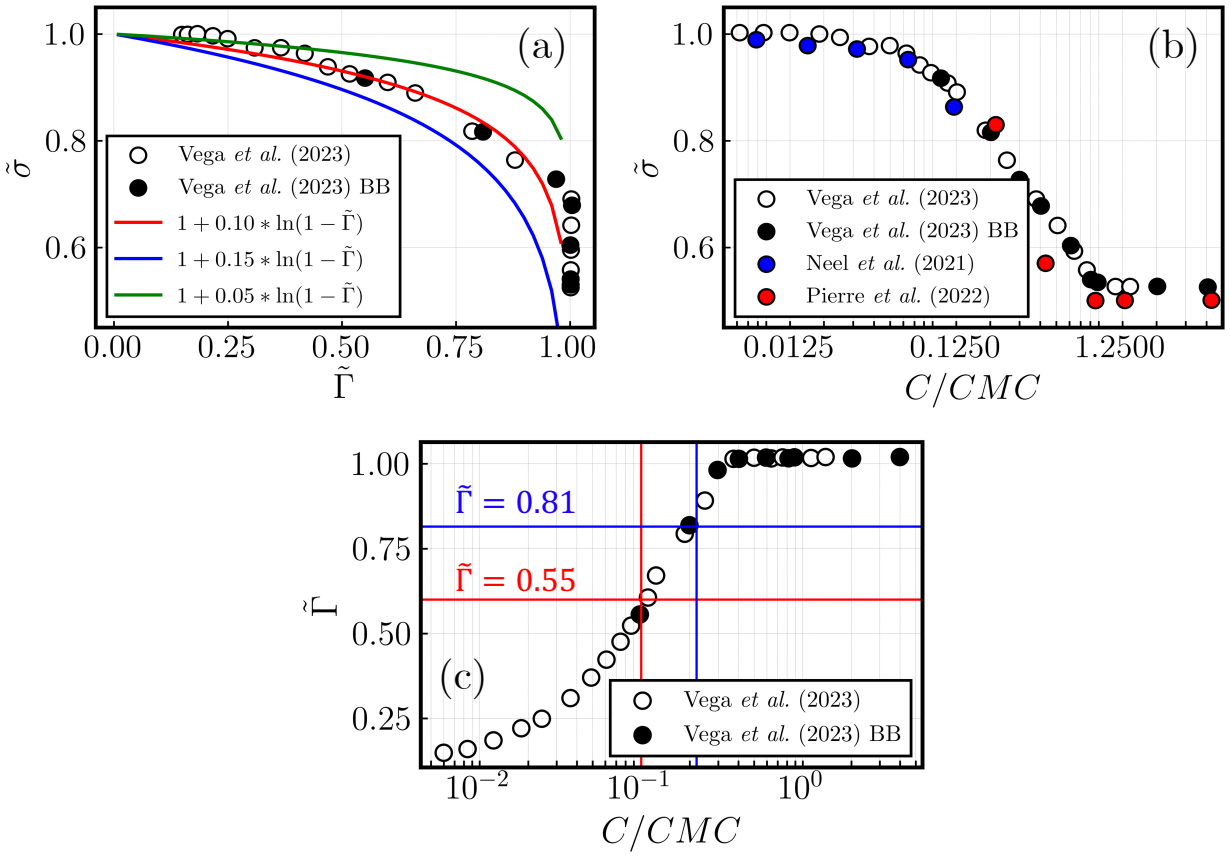

Figure 6.2: Interfacial tension isotherm and equilibrium interfacial concentration as a function of bulk surfactant concentration for SDS surfactant, as measured experimentally in Vega and Montanero [297], Pierre et al. [227], Néel and Deike [206]: (a)-(b) interfacial tension as a function of surfactant concentration; (c) relationship between interfacial and bulk surfactant concentration. In (a)-(b), the white dots represent the surface tension data measured by Vega and Montanero [297], whereas the black dots represent the testing points in the bursting bubble (BB) system. Published data points from Néel and Deike [206] (figure 2) and Pierre et al. [227] (figure 2(a)) have also been included for reference. The red lines in (c) showcase the point $\tilde{\Gamma} \approx 0.55$ and $C/CMC \approx 0.125$, while the blue lines showcase the point $\tilde{\Gamma} \approx 0.81$ and $C/CMC \approx 0.25$

6.3 Bursting bubble validation and drop size/velocity in the presence of surfactant

Due to the inherent complexity of bursting bubbles and their associated features, it is crucial to ensure that the numerical method and setup employed correctly recover the well-documented bursting behaviour at different stages (refer to §2.5 for further details). In figure 6.3, the surfactant-free numerical results are presented across different Bo and La conditions, comparing them with the scaling laws proposed by Lai et al. [158] for two key parameters: jet length before first drop detachment, L_{jet}, and the temporal interval between first detachment, t_{d1}, and bubble collapse, t_0. These variables are made dimensionless by the viscous length- and time-scales (l_{vis} and $t_{vis} \equiv l_{vis}/u_{vis}$, respectively); the x-axis variable, ϕ, is defined in Eq. (6.12):

$$t_{vis} = \frac{\mu_l^3}{\rho_l \sigma_s^2}, \quad l_{vis} = \frac{\mu_l^2}{\rho_l \sigma_s}, \quad u_{vis} = \frac{\sigma_s}{\mu_l}, \quad \phi = La(La_*^{-1/2} - La^{-1/2}) = Oh^{-2}(Oh_* - Oh). \tag{6.12}$$

In the above, $La_* \approx 500$ denotes the critical value below which no drop detachment is observed as $Bo \to 0$. ϕ represents a scaling variable proposed in Gañán-Calvo [90] to collapse various measurements of first ejected drop size and velocity, as well as jet length; ϕ is proportional to La. As depicted in figure 6.3, the simulation results exhibit favourable agreement with prior numerical and theoretical investigations. The minor deviations observed in terms of L_{jet} with increasing Bo indicate the presence of subtle but non-negligible gravitational effects beyond $Bo \approx 1$, impeding jet growth before the first detachment. In §6.4.1, the implications of these small effects, which become increasingly pronounced following initial detachment, are analysed.

This validation is complemented by examining the size, R_{d1}, and velocity, u_{d1}, of the first ejected drop in surfactant-free interfaces in figure 6.4(b)-(c). Drop sizes are compared against the scaling proposed by Gañán-Calvo [90], while velocities are assessed against Deike et al. [68]'s extension of Gañán-Calvo [90]'s original law to include the effects of Bo. A few numerical and experimental results from previous investigations are also incorporated in the figures. Particularly, the experimental measurements of R_{d1} by Brasz et al. [42] at $Bo = 0 - 1$ and the numerical results reported in Berny et al. [34] at $Bo = 1$, are included. For u_{d1}, the results of Gordillo and Rodríguez-Rodríguez [100] at $Bo = 5 \times 10^{-1}$, those of Deike et al. [68] at $Bo = 10^{-3} - 0.5$, and those of Berny et al. [34] at $Bo = 1$, are displayed. As heavily discussed in §6.4.1, R_{d1} and u_{d1} have been extensively investigated, resulting in a substantial body of numerical and experimental data validating the proposed scalings. The figure includes a select set of datasets under conditions similar to the present study for reference, but readers are encouraged to consult [38, 93, 74, 257, 275, 276, 152] for additional data points.

Ejected drop and Worthington jet velocities have been a subject of considerable debate, primarily due to measurement inconsistencies across different studies. In Deike et al. [68], velocities are measured at the instant before jet breakup, when the jet has stabilised at a constant verti-

cal velocity. This definition deviates from the approach of Gordillo and Blanco-Rodríguez [99] and collaborators, where the jet's velocity at its very inception is the variable considered and related to La. Others [93], perform their measurements at the moment the jet crosses the liquid pool-atmosphere interface. These inconsistencies explain why, for instance, Gordillo and Rodríguez-Rodríguez [100]'s velocities in the plot of figure 6.4(b) are generally larger than Deike et al. [68]'s, even at similar Bo. By adhering to the latter reference's definition, it is demonstrated how the simulations align well with the scalings observed in previous work. The point corresponding to $La = 10^4$ (shown as $La(1 + \alpha_{Deike}Bo) = 3.1 \times 10^4$) and $Bo = 1$ appears to be an outlier as our prediction for this points deviates significantly more than the rest, but remains within the same deviation order as the points of Berny et al. [34] at $Bo = 1$.

To conclude this sub-section, a comparison of the first ejected drop size and velocity in surfactant-laden cases is presented in parts (d) and (e) of figure 6.4. The numerical results of the present work are compared with experimental data from Pierre et al. [227], Vega and Montanero [297], Néel and Deike [206] for SDS surfactant across various ranges of Bo, Oh, and C/CMC. In these plots, sizes and velocities are non-dimensionalised by the effective viscous length and velocity ($l_{vis,eff}$ and $u_{vis,eff}$, respectively), calculated using Eq. (6.12) with the system's surface tension at the initial surfactant concentration. ϕ_{eff} and La_{eff} are similarly computed. As evidenced in other applications involving surfactants, the presence of these contaminants typically results in reduced droplet sizes in liquid-air and liquid-liquid systems, as seen in chapter 5 [225]. This is clearly illustrated in figure 6.4(d), where the dimensionless drop sizes from all referenced studies, including the present numerical analysis, fall well below the scaling laws for uncontaminated systems, with only a few exceptions observed in Vega and Montanero [297]. It is important to note that the computational points displayed correspond to those cases where the full post-collapse dynamics were simulated and jet pinch-off was observed.

Figure 6.4(e) compares the reported values of the first detached drop velocity from the aforementioned references with those from the present study, as well as with Deike et al. [68]'s scaling for clean interfaces. The obtained data is presented both in terms of the velocity at the instant preceding detachment and the jet ejection velocity, in accordance with Gordillo and Rodríguez-Rodríguez [100] (see inverted triangles and triangles, respectively, in the figure). Considering the results and discussion in §6.4.3 (figure 6.14), the obtained data in figure 6.4 suggest that the jet ejection velocity in surfactant-laden systems exceeds the clean interface scaling and its associated uncertainty (approximately 20%). Interestingly, the opposite trend is observed for drop detachment velocity, indicating significant Marangoni-driven effects that oppose jet growth, as thoroughly analysed in Constante-Amores et al. [55].

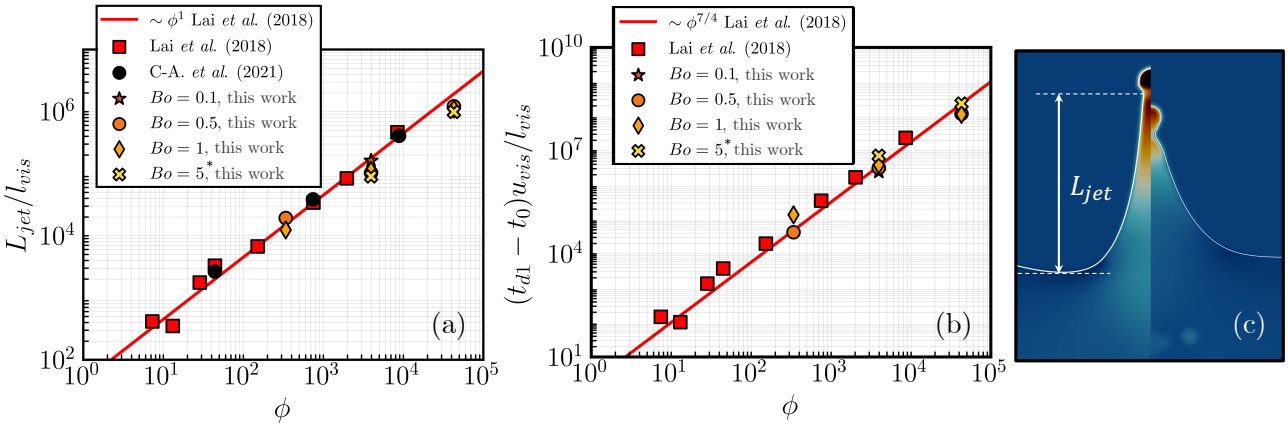

Figure 6.3: Comparison of surfactant-free simulations results for varying Bo and La against the scaling (red lines) and numerical simulations (red squares) of Lai et al. [158] and the numerical data of Constante-Amores et al. [55] at $Bo \sim O(10^{-3})$ (black circles) using the same numerical approach employed here: (a) dimensionless jet length before first drop detachment, L_{jet}/l_{vis}; (b) dimensionless temporal distance between cavity collapse and first detachment, $(t_{d1} - t_0)u_{vis}/l_{vis}$; (c) schematic representation of how L_{jet}/l_{vis} is measured. *Measurements at the point of largest L_{jet} attained for $Bo = 5$ given the complete escape from pinch-off.

6.4 Results and discussion

6.4.1 Uncontaminated interfaces: buoyancy effects on capillary wave velocity and Worthington jet

Let us begin the discussion by analysing the influence of gravitational effects in surfactant-free interfaces. Figure 6.5 offers a qualitative comparison of the system's behaviour pre- (a)-(d) and post- (e)-(h) bubble collapse for $Bo = 0.5$ and $Bo = 5$ in a representative case at $Oh = 3.21 \times 10^{-3}$. In order to make temporal one-to-one comparisons between different cases and bursting stages, a comparative time is defined, $T = (\tilde{t} - \tilde{t}_0)/\tilde{t}_0$, which takes the bubble collapse time, t_0, as a reference and compares the system's dynamics at the same temporal distance from collapse. Thus, $T < 0$ ($T > 0$) designates the pre-collapse (post-collapse, or jetting) stages. The pressure fields depicted in the figures are presented in relation to the pressure at the pool-atmosphere interface. As detailed in the review of the literature of §2.5, the process of liquid cap retraction concludes in the outset of capillary wave motion away and down the cavity. The latter set of waves ultimately converges at the bubble's bottom, giving rise to the Worthington jet. The dominant capillary waves (i.e., those characterised by the largest curvature [100]) are clearly seen at the low-pressure locations marked by white arrows.

During the early and middle bursting stages ($T < -0.25$), the high-pressure regions immediately upstream of the bubble's dominant wave create a negative pressure gradient, directing the flow downward in the z-direction and facilitating capillary wave motion towards the bottom of the cavity, as depicted in red in the figure. In the case of $Bo = 5$, this negative pressure gradient competes with the upward pressure gradient between the high-pressure liquid bulk and

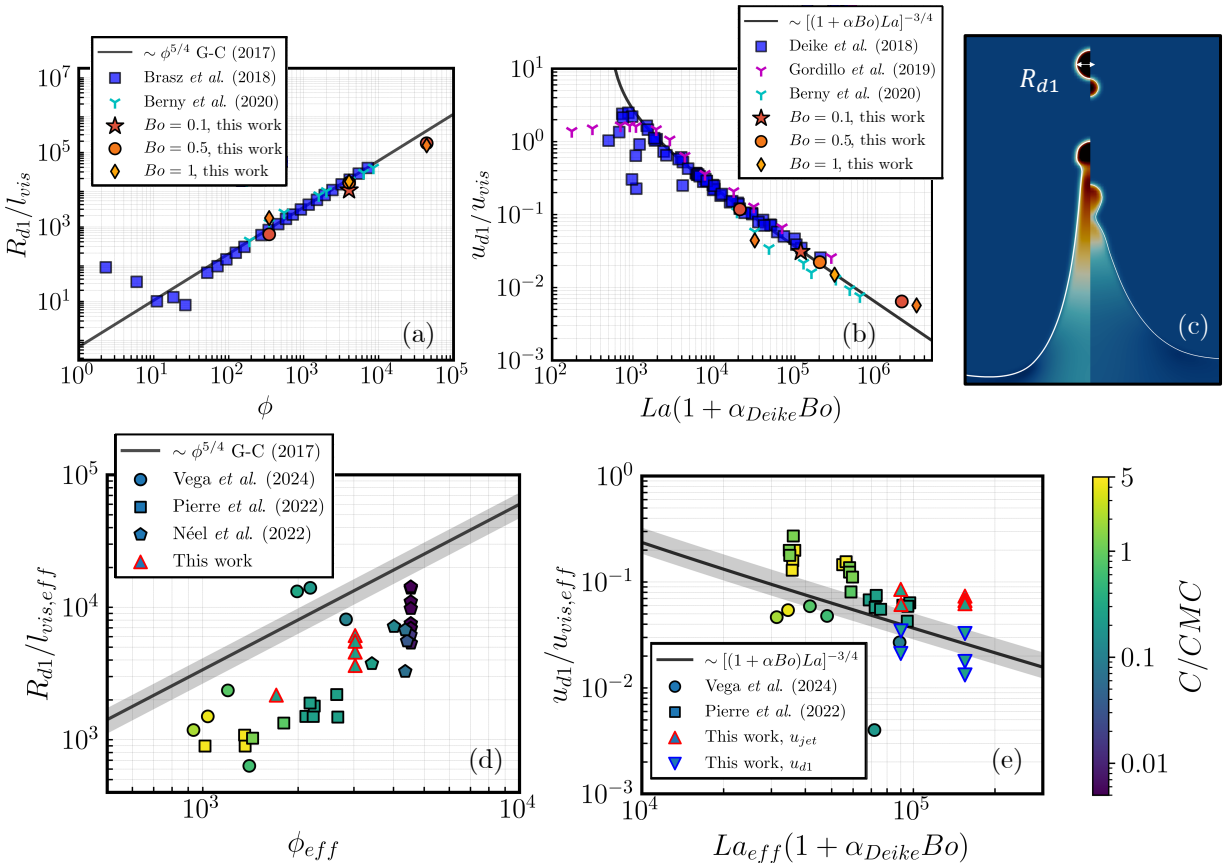

Figure 6.4: Comparison of the dynamics of the first released drop obtained with surfactant-free (a,b) and surfactant-laden (d,e) simulations against previous work: (a) scaling for dimensionless drop size, R_{d1}/l_{vis}, proposed by Gañán-Calvo [90] (black line); (b) Bo-dependent scaling for dimensionless drop velocity, u_{d1}/u_{vis}, proposed by Deike et al. [68] (black line). Here, $\alpha_{Deike} = 2.2$; (c) schematic representation of R_{d1}; (d-e) first released drop size and velocity in surfactant systems against SDS literature under varying C/CMC conditions. The shaded grey area portrays the dispersion of experimental data in surfactant-free systems, amounting to $\approx 20\%$. The points from Vega and Montanero [297] are at $Bo \approx 0.13 - 0.16$, Pierre et al. [227] at $Bo \approx 0.1 - 0.4$, and Néel et al. [207] at $Bo \approx 0.4$. The points represented by triangles in (e) denote jet ejection velocity, whereas inverted triangles denote first ejection velocity. The surfactant conditions shown in the plot are $Bo = 0.1, 0.5$, $Bi = 0, 5$, and $\beta_s = 0.3, 0.7$.

the low-pressure region beneath the bubble's bottom. The discussion of subsequent figures will elucidate how this competition between pressure gradients is accountable for delaying capillary wave motion, resulting in a lower average motion velocity above $Bo = 1$. Furthermore, it will be explored how these retarding gravitational effects do not impact the linearity of the motion, in contrast to the effects induced by surfactant.

The post-collapse phenomena of figure 6.5(e)-(h) underscore the anticipated stabilising influence of gravity on capillary breakup and jet growth, resulting in complete avoidance of pinch-off and notably smaller jets for $Bo = 5$ across all tested La values (refer to previous sub-section, §6.3 for a compilation of the effects of La and Bo on jet length and velocity at the instant before the first pinch-off, as well as the size of the first ejected drop). As is evident from the interfacial shapes in figure 6.5, the deceleration of the jet due to gravitational forces continues to shape the

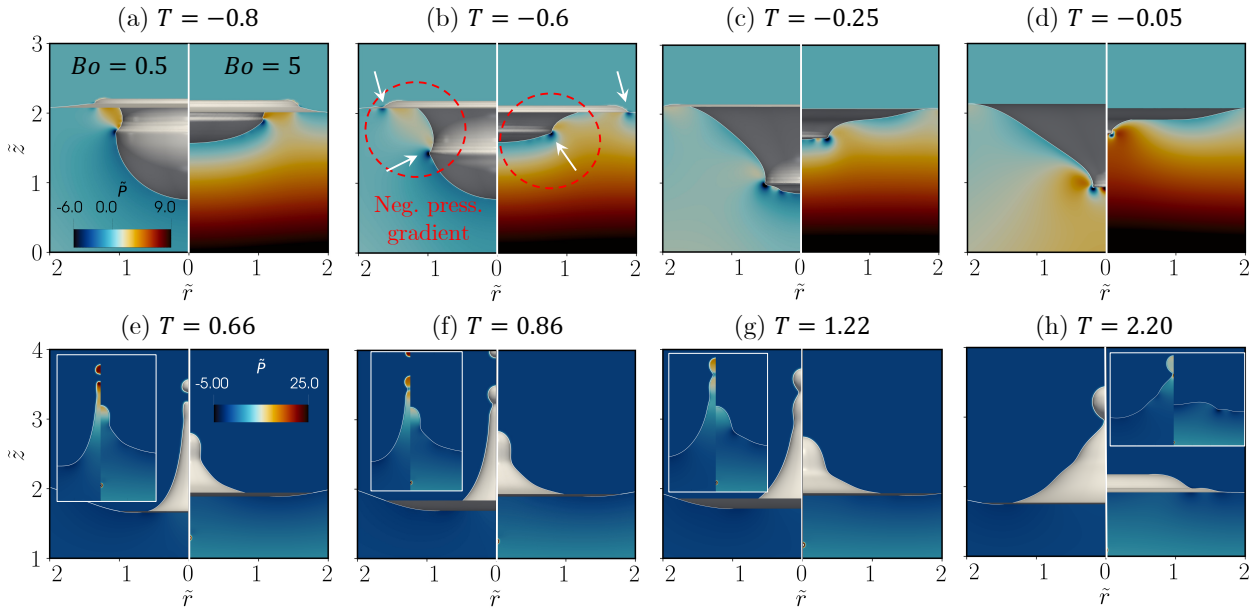

Figure 6.5: Bubble bursting dynamics in surfactant-free interfaces: comparison of pressure fields and interface shape at the same T for a moderate $Bo = 0.5$ on the left half and a large $Bo = 5$ on the right half: (a)-(d) pre-collapse dynamics; (e)-(h) Worthington jet motion and drop detachment. The insets in (e)-(h) focus on the emerging jet's pressure fields, the white arrows point to the location of the dominant capillary wave, and the dashed red circles highlight the negative pressure gradients. For all cases in this figure, $Oh = 3.21 \times 10^{-3}$ ($La = 9.7 \times 10^{4}$).

jet's dynamics following the initial pinch-off event for $Bo = 0.5$. Notably, it is observed that the maximum dimensionless jet length achieved, irrespective of pinch-off occurrences, exhibits a relationship with Bo given approximately by $(L_{jet}/l_{vis})_{\text{Max}} \sim Bo^{-0.36}$ across all three considered La values, in contrast to the moment of the first pinch-off where $(L_{jet}/l_{vis}) \sim Bo^{-0.16}$. Here, l_{vis} denotes the viscous length scale, defined in Eq. (6.12). This inverse relationship between jet length and Bo is in agreement with the observations of Walls et al. [302]. It should be highlighted that the threshold for jet drop production in the present simulations also aligns completely with the $Oh - Bo$ maps indicating production/no production from the same reference (see figure 4 in that reference).

In figure 6.6, the measurements of angular location of the dominant (or "strongest", as referred to in other works [249]) capillary wave, $\tilde{\theta}$, as it transverses down the bubble's domain are plotted. This dominant wave corresponds to the sharpest (of lowest wavelength) wave not fully dampened by viscous dissipation [99, 100]. The present $\tilde{\theta}$ numerical observations align with the methodology outlined by Gordillo and Rodríguez-Rodríguez [100], where the angle for each Bo is measured from the bubble's initial centre-point, as illustrated in figure 6.1(b)-(c). In Part (a) of figure 6.6, a nearly complete marker superposition in the $\tilde{\theta}$ vs. $\tilde{t}$ data is observed for all Oh tested under the same Bo. This alignment not only reaffirms prior findings indicating a negligible influence of Oh on capillary wave velocity up to $Bo = 0.7$, as demonstrated by previous researchers (see supplementary information in Blanco-Rodríguez and Gordillo [38]), but also extends this observation to higher Bond numbers ($Bo < 5$). It is essential to note that the downward shift of

the data for increasing Bo values is attributed to variations in the initial angle, $\tilde{\theta}_0$, which itself results from differences in the initial submersion degrees of the bubbles for different Bo.

It is also noteworthy that, akin to prior studies utilising other numerical methods, the emergence of high velocities and pressures as collapse is approached impedes the unambiguous tracking of $\tilde{\theta}$ as $\tilde{t} \to \tilde{t}_0$. Consequently, the measurements presented herein do not precisely terminate at $\tilde{\theta} = 0$. The calculated slope values from the available data (normalised by u_c), denoted as $\tilde{u}_\theta = u_c^{-1}(\theta_f - \theta_0)/t_f$, are compiled in figure 6.6(c). Inspection of these values reveals a transition from $|\tilde{u}_\theta| \approx 5$ (fully consistent with Blanco-Rodríguez and Gordillo [38], Gordillo and Rodríguez-Rodríguez [100]) at $Bo = 0.1, 0.5, 1$ to $|\tilde{u}_\theta| \approx 4.35$ at $Bo = 5$. Although small, this velocity decrease is found to persist for all Oh tested, suggesting an approximate relation of the form $|\tilde{u}_\theta| \sim -Bo$, as seen by the curve displayed in the figure for reference. Figure 6.6(b), along with the R^2 values of a linear fit (ranging from 0.998 to 0.999 in all cases) clearly illustrate the constant nature of the capillary wave velocity in surfactant-free interfaces, even at large Bo. The linearity of $\tilde{\theta}$ vs. $\tilde{t}$ enables the collapse of all data points using the comparative time, $T = (\tilde{t} - \tilde{t}_0)/\tilde{t}_0$, and the initial location of the capillary wave.

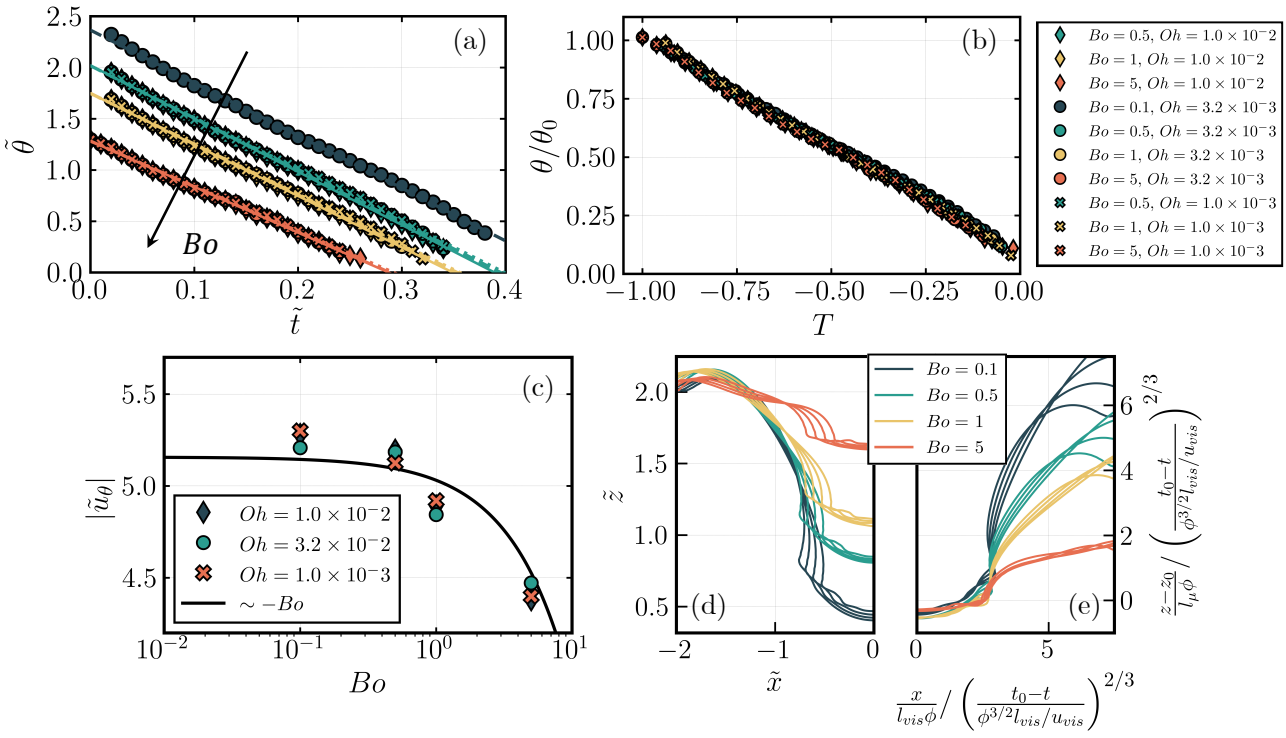

Figure 6.6: Dynamics of capillary wave velocity and interfacial shape in surfactant-free interfaces: effect of Bo and Oh; (a) temporal evolution of $\tilde{\theta}$. The markers represent the simulation data (taken every $\Delta\tilde{t} = 0.01$) and the line corresponds to a linear fit of the data; (b) data scaled by θ_0 and $\tilde{t}_0$, showcasing the constant nature of the capillary wave velocity, even at the largest Bo tested, $Bo = 5$; (c) compilation of $|\tilde{u}_\theta|$ vs. Bo data, wherein $-0.126Bo$ with $R^2_{pow} = 0.9833$; (d)-(e) interfacial shapes for varying Bo across four different times in the range $t_0 - t \approx 6t_{pre} - 10t_{pre}$ in the standard Cartesian space and in the rescaled spaced proposed in [158]; z_0 represents the point in the vertical coordinate where jet ejection occurred. For these cases, $Oh = 3.21 \times 10^{-3}$.

This $\tilde{\theta}$ collapse can be related to the well-known interfacial shape self-similar behaviour featured in uncontaminated interfaces. This self-similarity has been shown to underpin the dynamics of collapsing structures that lead to jetting, such as bursting bubbles and interfacial waves [158, 74, 94, 330]. An inviscid and incompressible balance of inertia and capillarity in scenarios neglecting gravity leads to an interface shape scaling that obeys $h(r,t) \sim |t_0 - t|^{2/3}$. The work of Lai et al. [158] has demonstrated that this scaling is valid before and after bubble collapse in a specific range of temporal distances from collapse. During the pre-collapse period, this range corresponds to $t_0 - t \approx 6t_{pre} - 10t_{pre}$, where $t_{pre} = \phi^{3/2} l_{vis}/u_{vis}$ is the characteristic time of the capillary wave; ϕ, l_{vis}, and u_{vis} are defined in Eq. 6.12. As $t_0 - t \to 0$ and the curvature inversion that leads to the nascent jet takes place, this self-similarity is disrupted (refer to §2.5 for further details).

Based on the above, the computed interfacial shapes for different Bo and for $Oh = 3.21 \times 10^{-3}$ ($La = 97000$) are plotted in the standard Cartesian space and in the rescaled space proposed in Lai et al. [158] in figure 6.6(d)-(e). Lines of the same colour correspond to the same Bo at four different times falling approximately within the $t_0 - t \approx 6t_{pre} - 10t_{pre}$ window. Reasonable interfacial collapse is observed in the region surrounding the bottom of the cavity, both across varying times for individual cases and between different Bo values. Although reasonable, the fact that the rescaled profiles do not exactly fall within a single universal line is a testament of the non-negligible gravitational effects present at large Bo. Attention should be drawn to the fact that this scaling was originally reported to be valid only for $La \approx 1000 - 5000$ during pre-collapse, further explaining the incomplete collapse of the curves.

The influence discussed previously of gravity on both the dominant capillary wave's motion and jet growth/breakup is further illustrated in figure 6.7. This figure presents the temporal evolution of kinetic energy, denoted as $E_k = \int_V (\rho \mathbf{u}^2)\, \mathrm{d}V$, interfacial area normalised by the initial value, $A_{s,0}$, viscous dissipation energy, $E_\mu = \int_t (\epsilon_\mu) \mathrm{d}t$ [236], and maximal vertical interface location, $\tilde{z}_{\max}$, for various Bo; ϵ_μ is calculated as $\epsilon_\mu = \int_V (2\mu |\mathbf{D}|^2) \mathrm{d}V$, where $|\mathbf{D}|$ is the second invariant of the deformation tensor. Here, E_k and E_μ are normalised by $\sigma_s R_0^2$, and a flat liquid pool is taken as a reference state to calculate A_s. The notably faster interfacial energy loss with respect to the system's initial energy (i.e., $A_{s,0}$) for larger Bo, combined with their lower energy dissipated by viscous forces at the same Oh, and their lower maximal and asymptotic $\tilde{E}_k$ values, suggest a heightened presence of gravitational potential energy (with the liquid pool-atmosphere interface as the reference position), influencing the system and retarding motion ($E_p \sim Bo$). As previously elucidated, these effects are present during the rise of the Worthington jet (see figure 6.7(d)), bringing about significantly shorter jets and entirely precluding pinch-off for $Bo = 5$.

Before transitioning into the effects of surfactants, it is imperative to discuss a few implications of the computational setup employed. Specifically, the ramifications of neglecting the dynamics of the retracting liquid cap at large Bo must be addressed. While this approach is common in computational studies, even up to $Bo \approx 5$ [302], several experimental works have hinted at the

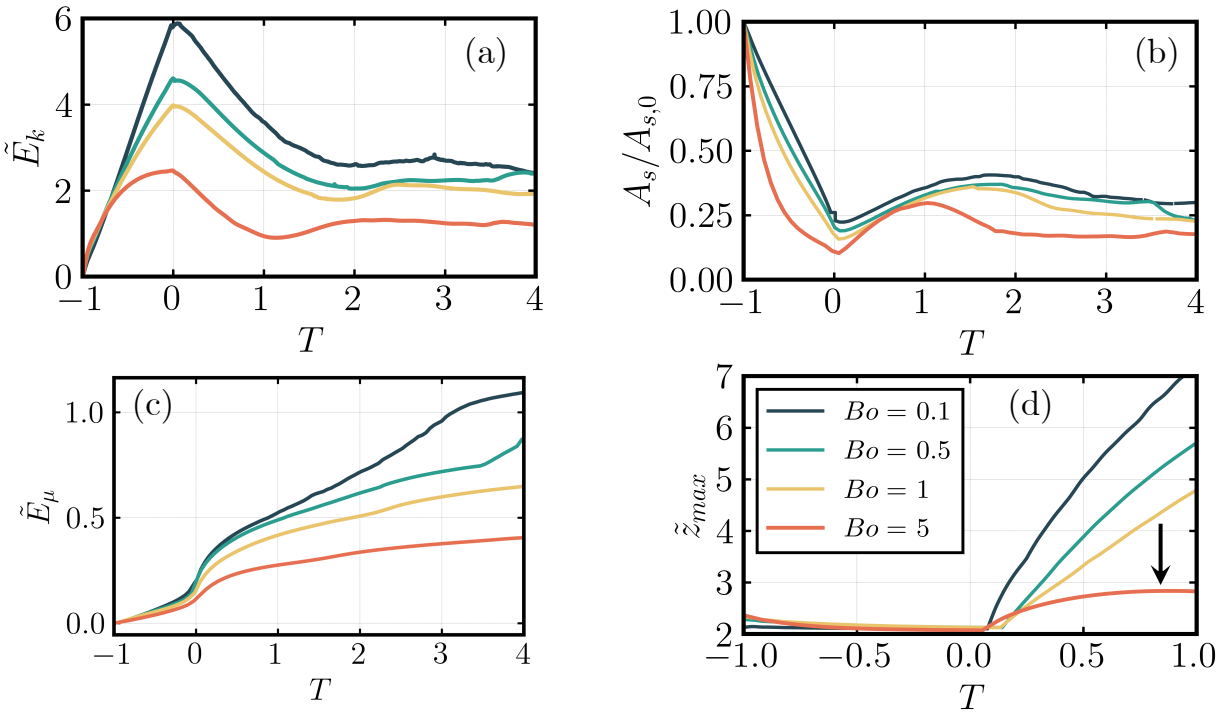

Figure 6.7: Temporal evolution of (a) kinetic energy, (b) interfacial area, (c) viscous dissipation energy, and (d) maximal vertical location of the interface in surfactant-free cases (i.e., vertical position of the Worthington jet/released drops for $(\tilde{t} - \tilde{t}_0)/\tilde{t}_0 > 0$). The jet characterised by $Bo = 5$ did not produce drops, as indicated by the black arrow. For all cases in this figure, $Oh = 3.21 \times 10^{-3}$

emergence of markedly different jets as Bo increases (see, for instance, figure 1 in Walls et al. [302] or figure 6 in Vega and Montanero [297]).

As dictated by the Young-Laplace expression, instances characterised by larger Bo entail reduced submersion of the bubble into the liquid pool, leading to a liquid film with much greater surface area exposed to the atmosphere. Consequently, the likelihood of the first cap hole appearing precisely at the flow origin (i.e., at $\tilde{r} = 0$ or $\tilde{x} = 6$ in radial and Cartesian coordinates, respectively), from which fully symmetric cap retraction, capillary wave motion, and jet ejection phenomena unfold, is greatly diminished. The appearance of a liquid cap hole shifted from the axis centre triggers an imbalanced capillary wave motion and a wave convergence point shifted away from $\tilde{x} = 6$, which, in turn, leads to the ejection of non-symmetrical jets. A schematic illustrating this mechanism can be found in figure 6.15 of §6.4.3.1.

The nucleated hole at $\tilde{x} > 6$ elicits a temporal delay in the dynamics at $\tilde{x} < 6$, approximated by the cap retraction time, $t_{TC} \sim E/u_{TC} = (R_0^3/l_c^{3/2})((\rho_l)/(2\sigma_s\omega))^{1/2}$, where $E \sim R_0^2/l_c$ represents the liquid cap's extent, $l_c = \sqrt{2\sigma_s/(\rho_l g)}$ is the capillary length scale, and $\omega = 10^3$ [299, 327]. Thus, capillary waves travelling at the $\tilde{x} > 6$ side at a velocity equal to ≈ 4 to $5u_c$ meet their counterparts not at $\tilde{x} = 6$, but at $\tilde{x} < 6$, leading to complex wave interactions and non-symmetric jet formation. As this retardation time increases with gravity and R_0, one can envision a scenario where it becomes comparable to the characteristic time of the problem, t_c. A comprehensive

investigation into this phenomenon of non-symmetric jets and unbalanced capillary wave motion is deferred to future studies.

6.4.2 Contaminated interfaces: phenomenology of bubble collapse

6.4.2.1 Surfactant-induced wave retardation and break of linearity

The focus is now directed towards the intriguing and notably distinct dynamics that emerge with the introduction of surface-active contaminants into the system. In figure 6.8, a qualitative comparison of wave evolution is presented for two scenarios: a clean case (left half, denoted as "Clean") and a case with insoluble surfactant characterised by $\beta_s = 0.3$ (right half, denoted as "$|\tilde{\tau}_m| > 0$", whose interface is coloured by $\tilde{\Gamma}$), $Bo = 0.5$, and $Oh = 3.21 \times 10^{-3}$. The values for the remaining surfactant-related dimensionless groups are set out in §6.2.3. Each column in the figure corresponds to a distinct dimensionless time, and the background contour plots depict pressure (panels a-d) and velocity magnitude (panels e-h). It is important to note that the comparative time, T, is not utilised in this figure. This decision is due to the fact that both scenarios have the same Bo, and the specific focus here is on analysing the pre-collapse dynamics from the start of the simulation.

A first inspection of figure 6.8 reveals a noticeable delay in the motion of the dominant capillary wave, whose effects are accentuated in time, as demonstrated in the upcoming discussions. This delay has been reported in a few experimental and numerical studies involving various contaminants, including surfactants [227, 297, 122, 123]. Surfactant-driven delays in bubble collapse time range from 35 to 70%, depending on the initial surfactant concentration, aligning well with the numerical results obtained in this investigation. The similarities between the surfactant-laden and surfactant-free pressure contour plots in figure 6.8 indicate that surfactant-induced retardation does not completely prevent wave convergence and jet formation for the current parameters. This contrasts with observations in non-Newtonian liquids at high plastocapillary numbers [249], where capillary wave focusing motion is fully dampened, and the cavity remains open.

In the case of surfactants, the initially imposed homogeneity of interface surfactant concentration ($\tilde{\Gamma}_0 = 0.55$) is promptly destabilised by the substantial capillary pressure stemming from the high-curvature ($|\tilde{\kappa}| \sim O(10)$ at $Oh = 3.21 \times 10^{-3}$) region connecting the bubble and the liquid pool-atmosphere interface (see highlighted region in figure 6.1). As the dominant wave traverses down the bubble, propelled by the negative pressure gradient, a high $\tilde{\Gamma}$ toroidal structure is formed in the vicinity of the dominant wave, from which Marangoni stresses arise (refer to figure 6.9(j) for the temporal evolution of $\tilde{\Gamma}$ evaluated at the location of the dominant capillary wave location, denoted as $\tilde{\Gamma}|_{\tilde{\theta}}$). The action of these Marangoni stresses ultimately brings about a consistent reduction in capillary wave velocity, as seen next in the analysis of figure 6.9 and discussed extensively in §6.4.2.2. It also causes a generalised flow stabilisation, as evidenced by

the noticeably lower flow velocities in surfactant cases shown in figure 6.8(e)-(h) and the kinetic energy analyses of Constante-Amores et al. [55] (see figure 6(a) of this reference).

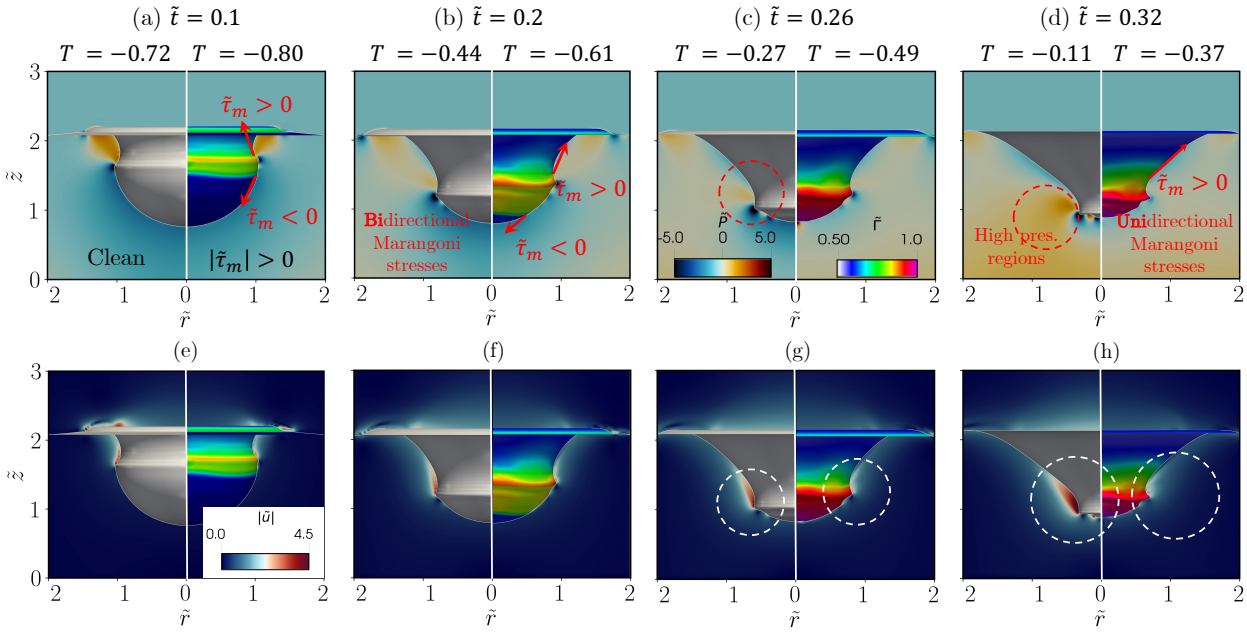

Figure 6.8: Surfactant-driven capillary wave motion delay: comparison of temporal evolution (at the same $\tilde{t}$) of pre-collapse bubble for surfactant-free interfaces on the left half and insoluble surfactant ($Bi = 0$, $\beta_s = 0.3, Ma = 93.43$) on the right half. For reference, the corresponding values of T are reported for each case; (a)-(d) pressure fields; (e)-(h) velocity magnitude fields. The red arrows schematically indicate the primary direction of Marangoni stresses, suggesting an eventual dominance of motion-delaying positive Marangoni stresses. The red dashed circles highlight the significantly larger negative pressure gradient in clean cases [55], while the white dashed circles illustrate the stabilising effect of surfactant on flow velocity. For all cases in this figure, $Bo = 0.5$, and $Oh = 3.21 \times 10^{-3}$

In figure 6.9(a)-(d), temporal evolution of the dominant capillary wave angular location is presented from the insoluble surfactant simulations across varying Bo values, juxtaposed with their surfactant-free counterparts. A consistent pattern of wave retardation is observed across all Bo values, as discussed before in figure 6.8. It is worth noting that the surfactant plots show the last recoverable $\tilde{\theta}$ value before the singularity occurred in the simulations. This limitation arises due to the high pressures and velocities near and at the moment of jet ejection, complicating the accurate determination of $\tilde{\theta}$. These challenges are more pronounced in surfactant cases due to significantly larger local Oh, resulting from the high $\tilde{\Gamma}$ at the wave focusing point ($T \approx 0$, refer to figure 6.8(d,h) and figure 6.9(j)).

In addition to wave retardation, figure 6.9(a)-(d) showcases a non-linear trend in the $\tilde{\theta}$ vs. $\tilde{t}$ data (black dashed lines and corresponding R^2_{lin} values of a linear fit in table 6.1). Further reinforcing this nonlinearity, figure 6.9(i) and the last two columns of table 6.1 demonstrate that $\tilde{\theta}$ evolves in close agreement with a power-law $\tilde{\theta} \sim \tilde{t}^{\alpha}$, where α generally increases with Bo, hinting at weakened surfactant effects with increased buoyancy. Figure 6.9(e)-(h) highlights a critical feature of bursting bubbles with surfactants. The nonlinear nature of $\tilde{\theta}$ vs. $\tilde{t}$ in surfactant

cases prevents data collapse using T and $\tilde{\theta}_0$, unlike the clean cases for all Bo and Oh (see figure 6.6(b)). This non-collapsing behaviour between surfactant-free and surfactant-laden cases aligns with findings of Pierre et al. [227], where bubble collapse times with surfactant could not be rescaled using t_c to match those in clean interfaces (see figure 2 of this reference). These observations, along with insights from Constante-Amores et al. [55] and the negligible influence of Oh on wave velocity (figure 6.6(a)), collectively suggest that Marangoni stresses—rather than lower overall surface tension—are the primary cause of delays and nonlinearity in capillary wave motion.

To conclude this subsection, it is pertinent to comment on the moments nearing the collapse singularity in surfactant-laden cases. In figure 6.9(k)-(l), the computed interfacial shapes for cases with insoluble surfactants across varying Bo are presented, along with their scaled counterparts based on the self-similarity proposed in Lai et al. [158] ($h(r,t) \sim |t_0 - t|^{2/3}$, as discussed earlier in figure 6.6(d)-(e) for clean cases). Interestingly, even in the presence of surfactant, an almost perfect data collapse across time is observed for each case below $Bo = 5$. This behaviour can be explained as follows: the times displayed in the plots align with the valid temporal ranges reported in Lai et al. [158], corresponding to $T \gtrapprox -0.1$. As can be seen in figure 6.9(j), the systems reach surfactant saturation at these comparative times, suggesting a local reduction (increase) in Oh (La) and bringing them much closer to the collapsing La range (1000 - 5000) reported in Lai et al. [158] compared to the clean cases.

Although the power-law fits offer a good representation of the $\tilde{\theta}$ data, it should be emphasised that the complex dynamics in the collapse vicinity preclude us from tracking the dominant capillary wave all the way to $\tilde{\theta} = 0$, complicating the examination of the final stages. As previously mentioned, the curvature reversal at the instant of jet ejection disrupts the system's self-similar behaviour in clean cases as proposed in earlier works [158, 74, 330, 94]. In surfactant-laden cases, major disruptions to the proposed power-law $\tilde{\theta}$ behaviour are expected as collapse is approached. In fact, a transition to a different regime, distinct from the power-law behaviour, can be inferred at $T \gtrapprox -0.12$, given that the projections of the power-law fits to $\tilde{\theta} = 0$ do not match the recorded collapsing times in the simulations. For all cases, the recorded times fall behind those of the power-law projections, suggesting an acceleration of the dynamics. The author recommends a thorough investigation of the moments very close to wave focusing and jet ejection ($\theta \approx 0$) in the presence of surfactants as an avenue for future research. Specifically, a focus on the "Axe" shape adopted by the cavity as $\tilde{\theta} = 0$ is approached in the presence of surfactants is recommended, as seen previously in Pierre et al. [227], Ji et al. [123].

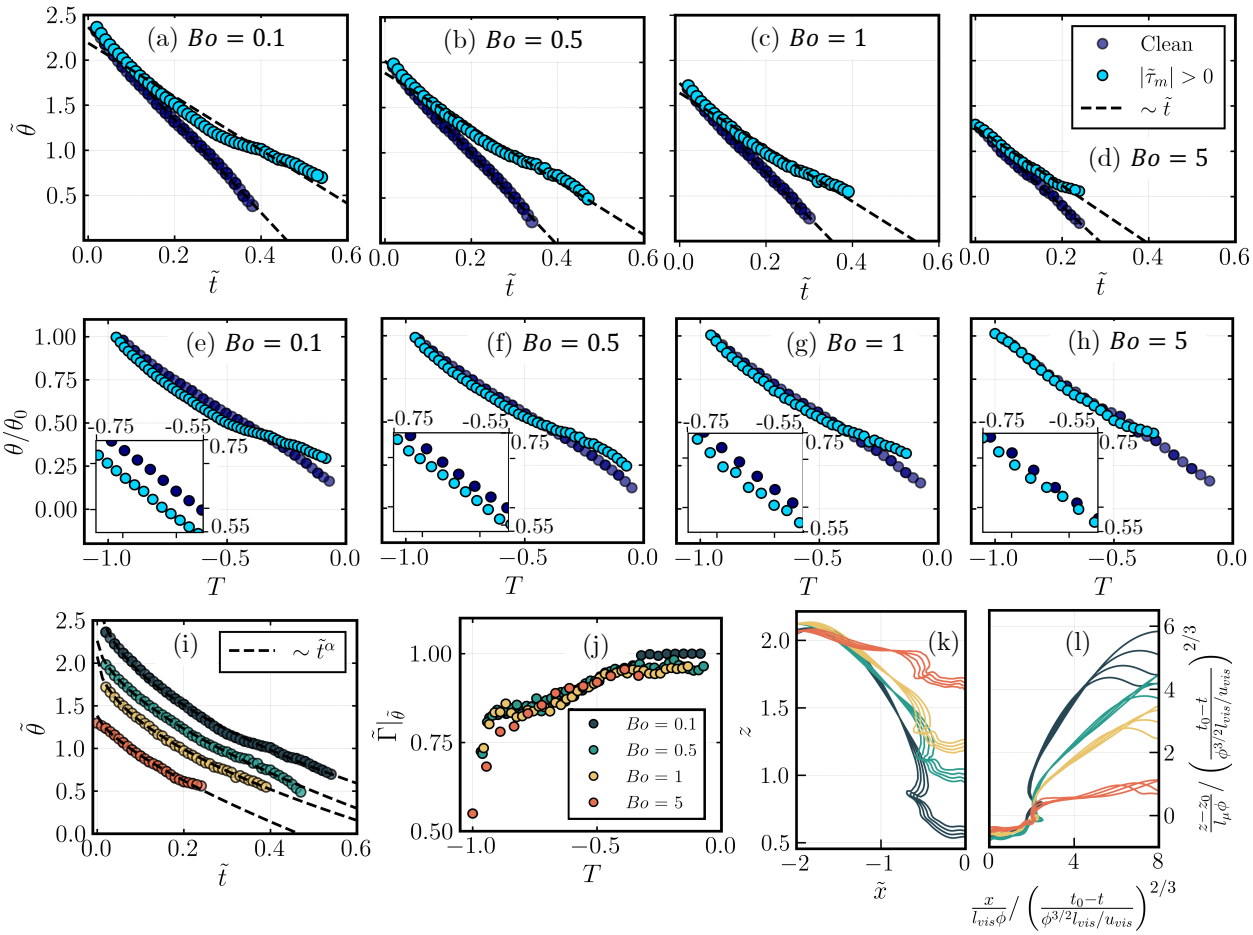

Figure 6.9: Effect of insoluble surfactant ($Bi = 0$, $\beta_s = 0.3, Ma = 93.43$) on the dynamics of the capillary wave velocity: (a)-(d) temporal evolution of $\tilde{\theta}$; (e)-(h) data scaled by θ_0 and $\tilde{t}_0$, showcasing the break of linearity and non-collapsed solutions of contaminated interfaces vs. surfactant-free interfaces; (i) direct comparison of capillary wave dynamics in surfactant-laden cases for varying Bo: the markers represent the simulation data (taken every $\Delta\tilde{t} = 0.01$), the lines correspond to linear or power-law fits of the data, and the values of the exponent α for each Bo are found in table 6.1; (j) interface surfactant concentration evaluated at the location of the dominant capillary wave; (k)-(l) interfacial shapes for varying Bo across four different times in the range $t_0 - t \approx 6t_{pre} - 10t_{pre}$ in the standard Cartesian space and in the rescaled spaced proposed in [158]; z_0 represents the point in the vertical coordinate where jet ejection occurred. For all the cases in this figure, $Oh = 3.21 \times 10^{-3}$.

Table 6.1: Comparison of capillary wave velocity in clean interfaces and in the presence of insoluble surfactant ($Bi = 0$, $\beta_s = 0.3, Ma = 93.43$). R^2_{lin} represents the coefficient of determination of the linear fits shown in figure 6.9(a-d) and R^2_{pow} those of the power-law fits for the surfactant cases, shown in figure 6.9(i). These fits are of the form $\tilde{\theta} \sim \tilde{t}^{\alpha}$, where α is the best-fit exponent

	Clean			$\lvert\tilde{\tau}_m\rvert > 0$				
Bo	$\lvert\tilde{u}_\theta\rvert$	$\lvert\tilde{u}_{\theta,lin}\rvert$	R^2_{lin}	$\lvert\tilde{u}_\theta\rvert$	$\lvert\tilde{u}_{\theta,lin}\rvert$	R^2_{lin}	α	R^2_{pow}
0.1	5.228	5.145	0.998	3.202	2.967	0.961	0.456	0.997
0.5	5.185	5.108	0.998	3.315	2.987	0.980	0.587	0.998
1	4.844	4.951	0.999	3.125	3.003	0.975	0.517	0.998
5	4.472	4.450	0.998	3.068	3.216	0.983	0.707	0.996

6.4.2.2 Effect of surfactant solubility and Marangoni stresses transition

Having dived into the general effects of surfactant addition, the discussion now proceeds to elucidate the effects of surfactant solubility and unveil the specific effects of Marangoni stresses on wave propagation. Figure 6.10(a)-(l) presents a few snapshots of interface shape, $\tilde{\Gamma}$ profiles, and Marangoni stresses profiles in the z-direction, $\tilde{\tau}_m$, calculated via Eq. (6.10) for various Bi. Rows 1-4 in this series of plots represent different dimensionless times and columns 1-3 display projections of $\tilde{r}$, $\tilde{\Gamma}$, and $\tilde{\tau}_m$ (shown in the $x-$axis) across the vertical axis, $\tilde{z}$ (shown in the $y-$axis). It is relevant to reiterate here that under the employed formulation, an increase in Bi signifies a higher likelihood of surfactant desorption into the bulk phase due to the smaller desorptive time-scale compared to that of convection. Consequently, the Bi range is confined between a surfactant-free case ($Bi \to \infty$) and a fully insoluble surfactant ($Bi = 0$).

A clear monotonic trend regarding wave retardation and surfactant solubility is revealed, whereby lower Bi (lower solubility) cases consistently exhibit more pronounced delays in capillary wave motion in both the train evolving down the cavity and the one departing from it. A comparison of interfacial shapes at early ($\tilde{t} = 0.1$) and later ($\tilde{t} = 0.32$) bursting stages suggests that these delays intensify in time and that a distinct separation between surfactant and clean cases emerges over time. This observation is consistent with those of Vega and Montanero [297], where even small surfactant concentrations ($C/CMC = 0.1$) were sufficient to actively alter the bursting dynamics.

A measure of these delays is illustrated in figure 6.10(m), where progressively larger deviations from the linear behaviour of the clean case arise as solubility is decreased. Similar to the insoluble cases at different Bo presented in §6.4.2.1, surfactant cases display non-collapsing dynamics against surfactant-free interfaces, as evidenced in figure 6.10(n). Despite the higher rates of surfactant desorption in larger Bi cases, reflected in the lower $\tilde{\Gamma}$ of the dominant wave at early and middle stages (figure 6.10(o), $T < -0.25$), it is interesting to note that all cases reach surfactant saturation near collapse ($\tilde{\Gamma} \to 1$). This is attributed to the much smaller interfacial areas involved in the temporal vicinity of collapse (see for example figure 6.7(b) at $T = 0$).

It is instructive to inspect the evolution of Marangoni stresses and surfactant concentration across the bubble's domain in the z-direction. The $\tilde{\Gamma}$ peaks at early stages ($\tilde{t} = 0.1 - 0.2$, figure 6.10(b,e)), besides highlighting the location of the dominant wave, act as an important source of Marangoni stresses due to the generation of surface tension gradients (see Eq. (6.10)). In the present formulation, positive-signed Marangoni stresses projected onto the z-direction ($\tilde{\tau}_m > 0$, denoted as $\tilde{\tau}_m^+$) are exerted in the positive z-direction, diverting flow away from the bottom of the bubble and wave focusing point. In contrast, negative Marangoni stresses ($\tilde{\tau}_m < 0$, denoted as $\tilde{\tau}_m^-$) tend to pull the interface towards the focusing point at $\tilde{r} = 0$.

Armed with the above definitions, it is clear that the high $\tilde{\Gamma}$ toroidal structure surrounding

the dominant capillary wave engenders a complex interplay between positive and negative $\tilde{\tau}_m$, which retard and promote wave motion down the cavity, respectively. This is illustrated in figure 6.10(c,f,i), in which two primary competing $\tilde{\tau}_m$ peaks are displayed. The present work henceforth refers to interfaces in this situation as subjected to "bi-directional" Marangoni stresses. As the system advances towards surfactant saturation in the region surrounding the collapsing point ($\tilde{t} = 0.32$, figure 6.10(j,k,l)), the motion-promoting negative Marangoni stresses nearly vanish, leaving the interface exposed to strong motion-delaying positive Marangoni stresses (note the x-axis scale difference in the $\tilde{z}$ vs. $\tilde{\tau}_m$ plots between $\tilde{t} = 0.32$ and the preceding times).

The emergence of bi-directional Marangoni stresses in the regions surrounding a capillary wave has also been observed in the context of surfactant-laden plunging breakers. As shown in figure 5(a) of Erinin et al. [83], there is a leap from low $\Delta\sigma/\Delta A$ ($|\tilde{\tau}m| = 0$) to high $\Delta\sigma/\Delta A$ ($|\tilde{\tau}m| > 0$) near the point of maximum curvature, and back to low $\Delta\sigma/\Delta A$ (see figure 6.10(c)).

The mechanism outlined above elucidates what the author defines as a transition from bi-directional to uni-directional Marangoni stresses, a pivotal factor in the observed retardation of capillary waves on surfactant-laden bursting bubbles, as documented in this and prior studies. A visual depiction of this transition is provided in figure 6.8(a)-(d). As shown in figure 6.10(m), the magnitude of motion-delaying positive Marangoni stresses appears to overcome that of motion-promoting negative stresses within the time interval of $\tilde{t} = 0.20 - 0.26$. This critical period is demarcated by the corresponding vertical dashed lines in figure 6.10(n), marking the juncture where the $\tilde{\theta}$ versus $\tilde{t}$ data for $Bi = 0$ begin to diverge markedly from the behaviour observed in surfactant-free cases. In the scaled space outlined by θ/θ_0 and T in figure 6.10(n), these times correspond to $T \approx [-0.60, -0.50]$ for $Bi = 0$, also coinciding with the onset of significant non-collapsing behaviour.

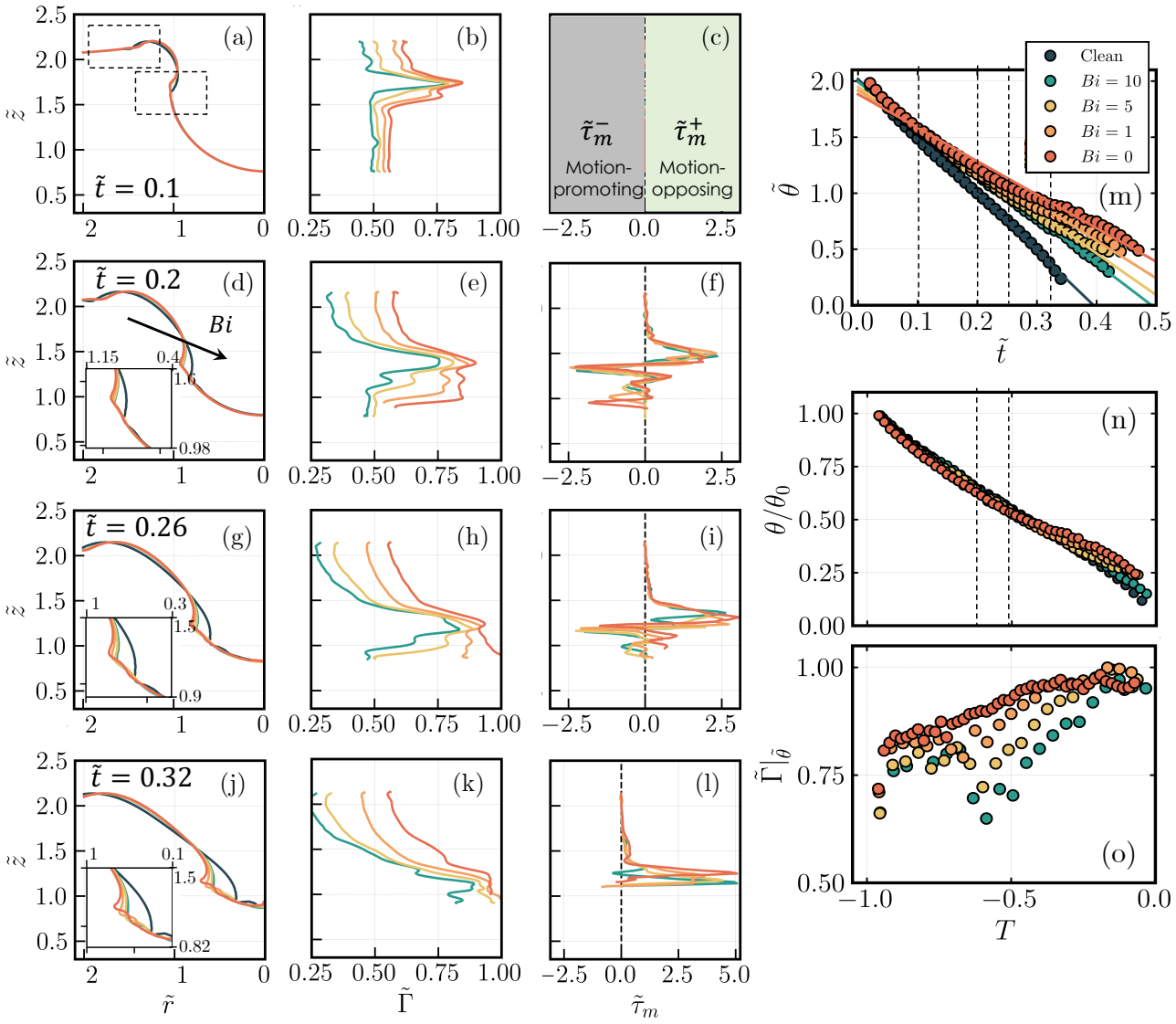

Figure 6.10: Effect of surfactant solubility at $\beta_s = 0.3$ ($Ma = 93.43$) on capillary wave dynamics: (a,d,g,j) interface shape; (b,e,h,k) surfactant concentration along the interface; (c,f,i,l) Marangoni stresses along the interface. In (a-l), the abscissa represent the values of $\tilde{r}$, $\tilde{\Gamma}$, and $\tilde{\tau}_m$, shared across each column, and the ordinate represent the vertical coordinate, $\tilde{z}$, shared across all plots; (m) temporal evolution of $\tilde{\theta}$ wherein the vertical dashed lines correspond to the times depicted in (a-l); (n) data scaled by θ_0 and $\tilde{t}_0$; (o) interface surfactant concentration evaluated at the location of the dominant capillary wave. The markers represent the simulation data (taken every $\Delta\tilde{t} = 0.01$) and the lines correspond to a linear fit of the data for reference. For all cases in this figure, $Bo = 0.5$ and $Oh = 3.21 \times 10^{-3}$

6.4.2.3 Effect of surfactant elasticity and capillary wave velocity compilation

In this subsection, the impact of surface elasticity, denoted by β_s, on wave propagation is illustrated. Additionally, an analysis of the combined effects of Bi and β_s on average capillary wave velocity, $|\tilde{u}_\theta|$, across varying Bo values is presented. As explained in §6.2.1, β_s characterises the sensitivity of surface tension to surfactant concentration, as expressed in Eq. (6.8). It also quantifies the strength of Marangoni stresses, as shown in Eq. (6.10), the Marangoni modulus

[184], and the Marangoni number Ma, as seen in Eq. (5.10). Ma provides a dimensional measure of the significance of Marangoni stresses relative to viscous stresses. Figure 6.11(a) provides a comparison of the temporal evolution of $\tilde{\theta}$ for different values of β_s, with the surfactant-free case denoted as $\beta_s = 0$. Sample snapshots of the interface shape are also shown in figure 6.11(d,g). As anticipated, an increment in β_s yields a positive, monotonic response in terms of wave motion retardation. Similar delays in capillary-related events with increased surfactant elasticity have been documented in previous studies concerning liquid thread retraction/breakup [54, 60], ink-jet printing [16], and drop impact [57].

It is interesting to note that the condition with the most pronounced wave delay (i.e., $\beta_s = 0.7$, $Ma = 218$) does not align with the one exhibiting the highest $\tilde{\Gamma}$ at the dominant wave location at the same comparative time (refer to figure 6.11(b)). Similarly, it does not correspond to the largest $\tilde{\Gamma}$ in the toroidal region formed in the vicinity of the dominant wave, as seen in figure 6.11(e,h). This contrasts with the dynamics explored in our examination of Bi, where the case yielding the greatest delays ($Bi = 0$, insoluble surfactant) always corresponded to the highest $\tilde{\Gamma}$ at the dominant wave and its surrounding regions (refer to figure 6.10(o) and (b,e,h,k)). This is easily explained by recalling the fact that an increase in β_s is accompanied by an increase in Marangoni stresses strength relative to viscous stresses (larger Ma). These stresses promptly redistribute $\tilde{\Gamma}$ across the interface, forming a larger surfactant "spread" near the dominant wave, leading to localised lower $\tilde{\Gamma}$ at larger β_s.

Increased β_s values lead to greater interfacial resistance to compression, as demonstrated by the consistently larger Marangoni elasticity E_0 profiles in figure 6.11(f)-(i) (see the end of §6.2.1 for the definition of E_0). This resistance, due to surface-active contaminants, is well known to be associated with interface rigidification and reduced interfacial velocity, as previously demonstrated in bursting bubbles [55] and other scenarios [30, 31]. This phenomenon further elucidates the observed bubble collapse retardation at higher β_s values (higher Ma).

The preceding discussion offers a direct link to why larger values of β_s precipitate lower wave propagation velocities. Illustrated in figure 6.11(c) are the computations of the magnitude difference between the peaks of positive (motion-opposing) and negative (motion-promoting) Marangoni stresses in the z-direction at the beginning and end of the high $\tilde{\Gamma}$ toroidal structure, denoted as $\tilde{\tau}_{m,d} = |\tilde{\tau}_m^+| - |\tilde{\tau}_m^-|$. This parameter serves as a measure of the collective influence of Marangoni stresses within the system, with positive $\tilde{\tau}_{m,d}$ instigating overall wave motion retardation down the cavity. As depicted in figure 6.11(c), the time interval $T \approx [-0.75, -0.60]$ marks the juncture where motion-delaying stresses prevail over their motion-promoting counterparts as a whole. In this figure one can also see that the largest β_s case consistently experiences the largest $\tilde{\tau}_{m,d}$ after $T \approx [-0.75, -0.60]$, confirming the presence of overall stronger motion-delaying Marangoni stresses and explaining the lower average wave velocities obtained for larger β_s and their more pronounced departures from linearity.

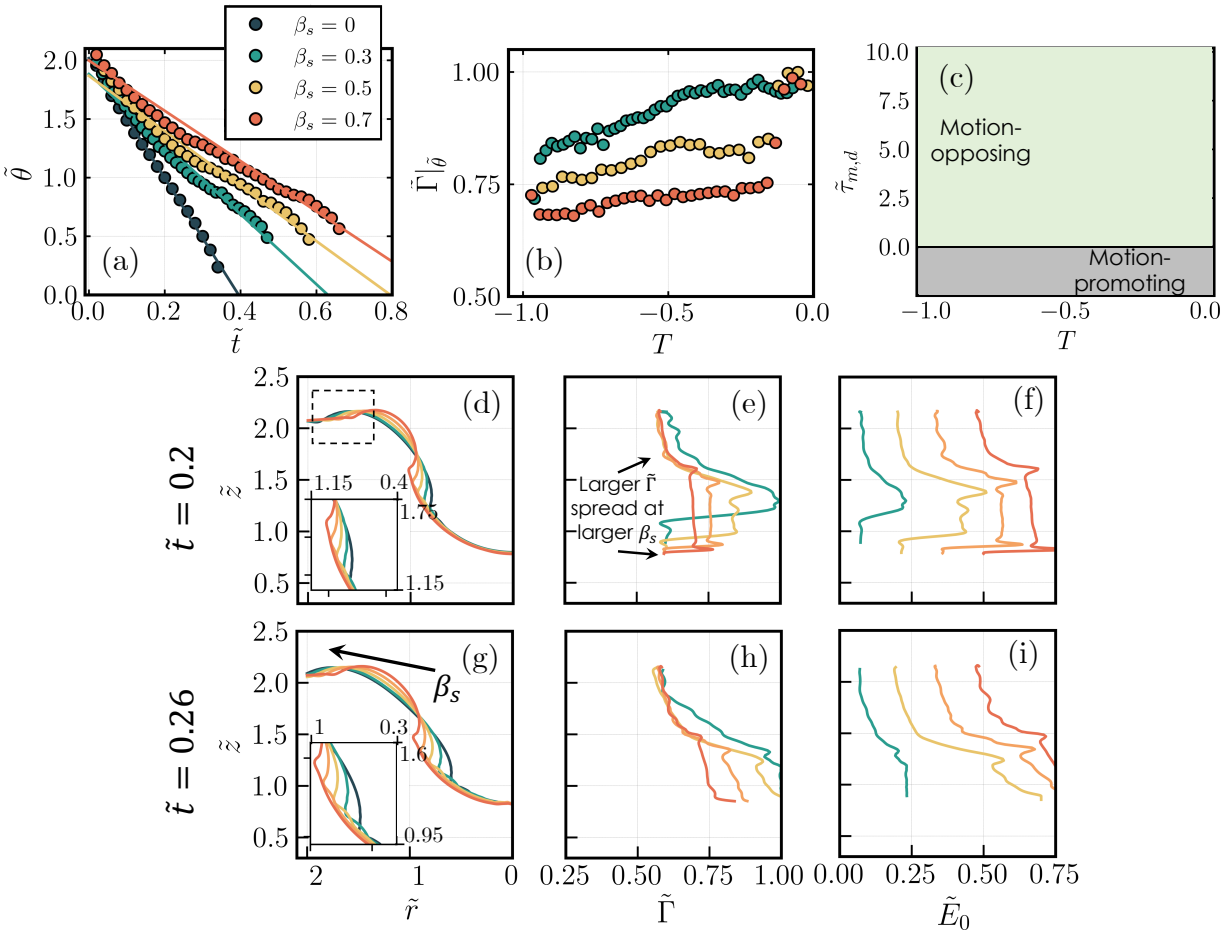

Figure 6.11: Effect of surfactant elasticity at $Bi = 0$ in the range $\beta_s = 0.3 - 0.7$ ($Ma = 93.43 - 218.01$) on capillary wave dynamics: (a) temporal evolution of $\tilde{\theta}$; (b) interface surfactant concentration evaluated at the location of the dominant capillary wave, scaled temporarily by the comparative time; (c) magnitude difference of positive (motion-opposing) and negative (motion-promoting) Marangoni stresses peaks across the interface. The markers represent the simulation data (taken every $\Delta\tilde{t} = 0.02$) and the lines correspond to a linear fit of the data for reference; (d-i) sample interface shapes, surfactant concentrations, and Marangoni moduli along the interface at $\tilde{t} = 0.2$ for (d-f) and $\tilde{t} = 0.26$ for (g-i)). In (d-i), the abscissa represent the values of $\tilde{r}$, $\tilde{\Gamma}$, and $\tilde{E}_0 = E_0/\sigma_s$ and the ordinate represent the vertical coordinate, $\tilde{z}$, shared across all plots. For all cases in this figure, $Bo = 0.5$ and $Oh = 3.21 \times 10^{-3}$

Figure 6.12 illustrates the effects of Bi and β_s at constant $Bo = 5$ and $Oh = 3.21 \times 10^{-3}$ on the universal interfacial shape profiles proposed in Lai et al. [158]. As discussed in figures 6.6(d)-(e) and 6.9(k)-(l), a significant distinction is observed between the uncontaminated case (dark green) and the surfactant cases. This disparity is particularly noticeable in the β_s plot in rescaled space, where the profiles for $\beta_s = 0.3 - 0.7$ collapse reasonably well over time and among themselves, contrasting sharply with the clean case which stands out as an outlier. As previously noted, the regions surrounding the bottom of the cavity in surfactant cases exhibit much larger Oh values due to reduced surface tension, bringing the system closer to bursting conditions for which the scaling of Lai et al. [158] was originally proposed. As demonstrated in figures 6.10(a)-(l) and 6.11(d)-(i), Marangoni stresses, though significant in magnitude at these time points (see figure

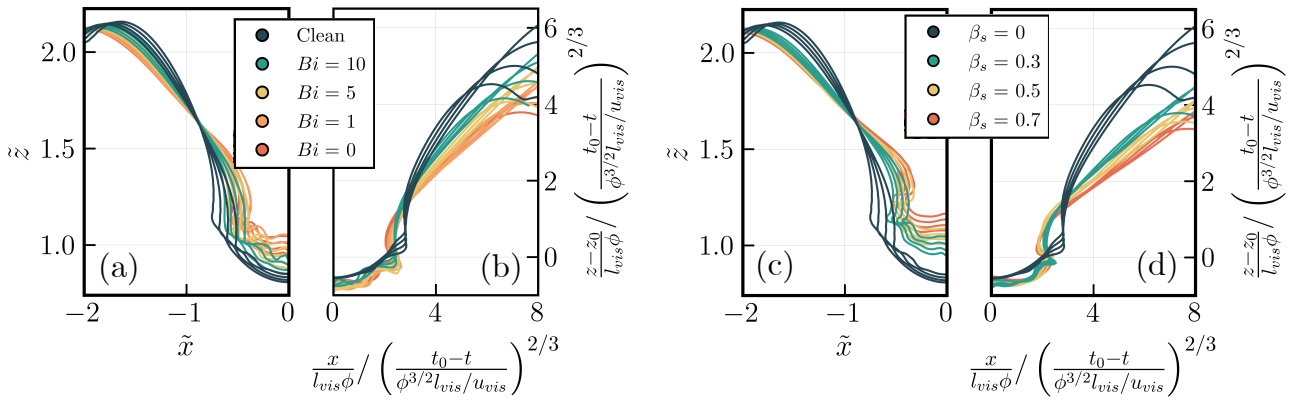

Figure 6.12: Interface collapse under varying Bi and β_s conditions according to the scaling proposed in Lai et al. [158] in the range $t_0 - t \approx 6t_{pre} - 10t_{pre}$; z_0 represents the point in the vertical coordinate where jet ejection occurred; (a)-(b) effect of Bi at constant $\beta_s = 0.3$ ($Ma = 93.43$); (c)-(d) effect of β_s in the range $\beta_s = 0.3 - 0.7$ ($Ma = 93.43 - 218.01$) at constant $Bi = 0$. The clean case in (c)-(d) is denoted by $\beta_s = 0$. For these cases, $Oh = 3.21 \times 10^{-3}$ and $Bo = 0.5$

6.11(c) for $T > -0.1$), primarily manifest upstream from the bubble's dominant wave, suggesting a Marangoni-free zone at the cavity's bottom and elucidating the better collapse observed in surfactant cases. It should be noted here that the semi-collapsed interface profiles shown in figure 6.12 correspond to times close to the bubble collapse singularity ($T > -0.1$), whose dynamics differ from the behaviour of $\tilde{\theta}$ vs. $\tilde{t}$ discussed earlier.

The aforementioned non-linearity in the propagation of the dominant capillary wave in surfactant cases, across various Bi values (see figure 6.10(m)) and β_s values (see figure 6.11(a)), is further elucidated in table 6.2. Upon examining this and table 6.1, which illustrates the influence of Bo on the exponent of the power-law fit $\tilde{\theta} \sim \tilde{t}^{\alpha}$, it is evident that α increases with Bo, which signifies a closer behaviour to that of clean interfaces for larger, more deformable bubbles. In the case of increasing β_s, the value of α reduces to that associated with weakly-deformable bubbles characterised by vanishingly small Bi (insoluble cases). This is consistent with the fact that surfactant-induced Marangoni stresses counter-act the propagation of the waves and act to rigidify the interface.

We conclude the exploration of the pre-collapse dynamics by presenting an extended sweep of Bi and β_s in figure 6.13(a)-(b), which illustrates the intertwined influence of these surfactant parameters on the average wave velocity, $|\tilde{u}_\theta|$, across varying Bo conditions. It is relevant to reiterate that $|\tilde{u}_\theta|$ represents the *average* velocity computed over time for each case, acknowledging the previously discussed nonlinear nature of $\tilde{\theta}$ vs. $\tilde{t}$ in surfactant-laden cases. The extended parametric sweep confirms that the distinct monotonic effects of Bi and β_s elucidated previously persist up to the highest Bo tested ($Bo = 5$). Specifically, it is observed that $|\tilde{u}_\theta|$ exhibits a negative response (i.e., motion retardation) to a decrease in Bi (less soluble surfactant) or an increase in βs ("stronger" surfactant) for all Bo.

Table 6.2: Effect of Bi (at constant $\beta_s = 0.3$) and β_s (at constant $Bi = 0$) on the exponent of a power-law fit of the form $\tilde{\theta} \sim \tilde{t}^{\alpha}$ of the $\tilde{\theta}$ vs. $\tilde{t}$ data (see figures 6.10(m) and 6.11(a)). For all cases displayed in the table, $Bo = 0.5$ and $Oh = 3.21 \times 10^{-3}$

Bi	$\lvert\tilde{u}_\theta\rvert$	$\lvert\tilde{u}_{\theta,lin}\rvert$	α	β_s (Ma)	$\lvert\tilde{u}_\theta\rvert$	$\lvert\tilde{u}_{\theta,lin}\rvert$	α
10	3.866	4.047	0.868	0.1 (31.15)	3.774	3.585	0.6
5	3.747	3.716	0.729	0.3 (93.43)	3.315	2.987	0.587
1	3.499	3.354	0.637	0.5 (155.76)	2.837	2.348	0.5936
0	3.315	2.987	0.587	0.7 (218.07)	2.433	2.143	0.559

As previously discussed, the dependence of $|\tilde{u}_\theta|$ on Bi and β_s can be attributed to the significant increase in motion-delaying Marangoni stresses observed with decreasing Bi or increasing β_s (see, for example, figure 6.11(c)). It must be highlighted, however, that these heightened stresses, which directly correlate with $\nabla_s\tilde{\Gamma}$ and β_s (refer to Eq.(6.10)), are manifested differently for Bi and β_s. In cases of decreased Bi, the higher $\nabla_s\tilde{\Gamma}$ at the start and end of the toroidal structure carrying the dominant wave induces the generation of larger Marangoni stresses compared to cases with larger Bi (see figure 6.10(k)). Conversely, as β_s increases, it is the greater magnitude of β_s itself, rather than larger surface tension gradients at the toroidal structure, $\nabla_s\tilde{\Gamma}$, that leads to larger Marangoni stresses.

As illustrated by the identical ordinate range of the plots in figure 6.13(a)-(b), $|\tilde{u}_\theta|$ appears to be consistently more sensitive to variations in Bo across the tested range of Bi compared to β_s. This trend suggests that the influence of β_s overwhelmingly dominates that of Bo. The non-negligible Bo effects across the studied Bi range align with the initial surfactant concentration effects on collapse time revealed experimentally by Vega and Montanero [297].

Figure 6.13(c) compares the obtained dimensionless collapse times with experimental data from Pierre et al. [227], Vega and Montanero [297], demonstrating that the present results align well within the ranges reported in these studies for both surfactant-free (shown as $\beta_s = 0$) and surfactant-laden cases (shown as $\beta_s = 0.1$) under similar conditions of Oh and Bo. Both referenced studies utilise sodium dodecyl sulfate (SDS), an insoluble surfactant, and provide data at varying initial surfactant concentrations.

6.4.3 Contaminated interfaces: jet drops and aerosol release

The focus now turns briefly on the Worthington jet and the process of surfactant enrichment during collapse and jet breakup. As remarked in the literature review of §2.5, recent works by Gordillo and Blanco-Rodríguez [99], Gordillo and Rodríguez-Rodríguez [100] have proposed that

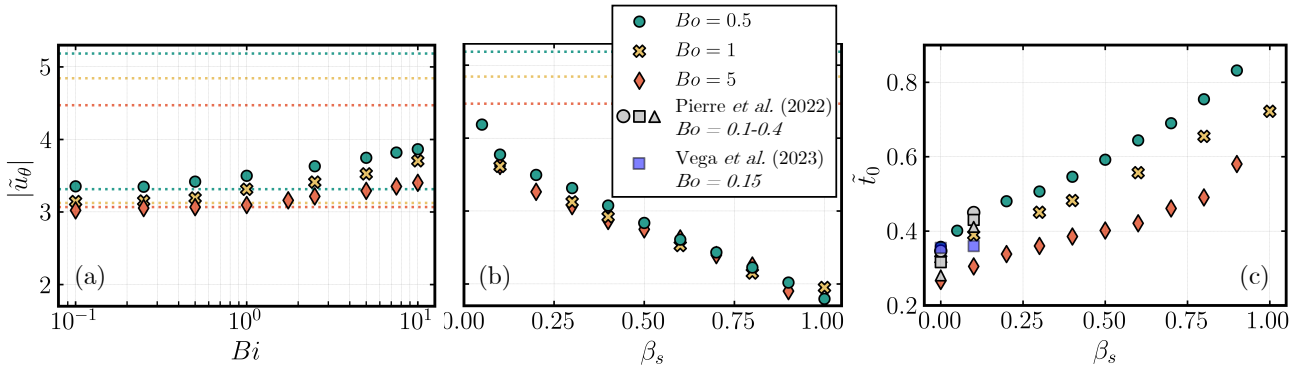

Figure 6.13: Compilation of Bi and β_s effects on average dominant capillary wave velocity and collapse time under varying Bo conditions: (a) effect of Bi on $|\tilde{u}_\theta|$ at constant $\beta_s = 0.3$ ($Ma = 93.43$); (b) effect of β_s on $|\tilde{u}_\theta|$ at constant $Bi = 0$. The dotted lines in (a) represent the average velocity of each Bo for the clean case (top lines, $Bi \to \infty$) and insoluble surfactant (bottom lines, $Bi = 0$). The dotted lines in (b) represent the average velocity of each Bo for the clean case ($\beta_s = 0$). For all cases in (a)-(b), $Oh = 3.21 \times 10^{-3}$; (c) effect of β_s in the range $\beta_s = 0.05 - 1$ ($Ma = 15 - 311$) at constant $Bi = 0$ on collapse time and comparison against the experimental measurements of Pierre et al. [227], Vega and Montanero [297] ($Oh \sim O(10^{-3})$) at an equivalent equilibrium concentration $C/CMC \approx 0.25$. The markers representing Pierre et al. [227]'s data correspond to circles for $Bo \approx 0.1$, squares for $Bo \approx 0.17$, and triangles for $Bo \approx 0.40$

the jet ejection phenomenon following cavity collapse is primarily driven by inertia, with viscosity playing a modulating role, rather than by an inertio-capillary mechanism.

Figure 6.14(a)-(h) presents a few snapshots of post-collapse interfacial shape and pressure contours for a surfactant-free (left half) and an insoluble surfactant case (right half). The parameters for these cases are identical to those in figure 6.8. It should be noted that these snapshots are taken at the same temporal distance from collapse and hence the visualisations represent the true differences between cases at the same stages of development. To complement these visualisations, plots of maximal interface location in the z-direction as a function of the comparative time are presented for multiple Bo and β_s in figure 6.14(i)-(l). As mentioned in the discussion of figure 6.7(d), $\tilde{z}_{max}$ serves as a proxy for the location of the jet or first released drop.

Building upon the insights from §6.4.2, the observations from figure 6.10(o) and figure 6.11(b), alongside previous work [55], demonstrate that surfactant concentration approaches saturation close to the moment of cavity collapse under the studied set of Bi, β_s, and Bo. This critical observation lays the foundation for the emergence of Worthington jets in areas marked by high $\tilde{\Gamma}$, which, as a result, exhibit significantly larger local Oh compared to cases devoid of surfactant contamination. Invoking the jet ejection velocity scalings proposed and validated by Refs. [99, 100], $\tilde{u}_{jet} \sim Oh^{1/2}$ for $Oh < 0.043$, or those of Ref. [90], $\tilde{u}_{jet} \sim Oh^{1/2}(Oh_* - Oh)^{-3/4}$ ($Oh_* = 0.043$), it is therefore expected that the addition of surfactant increases the dimensionless jet ejection velocity.

The above is evidenced qualitatively during the first few post-collapse stages in figure 6.14(a)-(c) ($T < 0.18$), where the tip of the surfactant-covered jet consistently exceeds the vertical location

of the surfactant-free jet. Examining the insets of figure 6.14(i)-(k), with the horizontal dashed line representing the location of the liquid pool-atmosphere interface ($\tilde{z} = 2$) and the vertical line the bubble collapse time, it is clear that between the surfactant-free and surfactant-covered jet, it is the latter that first surpasses $\tilde{z} = 2$, suggesting a larger ejection velocity. Additional discussions on how jet and first detached drop velocities in contaminated scenarios compare to uncontaminated systems can be found in 6.3 (figure 6.4 (e)).

The authors of Pierre et al. [227] have documented much larger jet velocities generated by surfactant-laden bursting bubbles prior to the first pinch-off event. Interestingly, the present results after these first ejection stages ($T > 0.18$, figure 6.14(d)-(h)) uncover a complete trend reversal in terms of jet velocity and shape. While the surfactant-free jet continues to grow and undergo pinch-off events up until $T \approx 1.22$, the contaminated jet quickly reaches its maximum length at $T \approx 0.40$ and proceeds to drain out, leading to the thick, interfacially rigid structure shown at $T = 2.20$. These findings can be rationalised by incorporating the effects of Marangoni stresses into the analysis. As the jet grows in size and interfacial area surges after t_0 (see figure 6.7(b)), surface tension gradients arise across the jet's domain, resisting the positive pressure gradient pushing the jet upwards and prompting interfacial stabilisation. This is schematically shown by the red arrows in the contour plots.

An in-depth showcase of the Marangoni stresses profile along the Worthington jet can be found in the work of Constante-Amores et al. [55]. While this manuscript attributes the lower jet velocity at later times to Marangoni stresses opposing the direction of growth, it is important to note that surfactant-laden systems in real-life scenarios may also exhibit additional rigidification and viscosity-related effects due to surface viscoelasticity [184]. Considering these additional dynamics alongside purely Marangoni effects may help reconcile measurements in surfactant-laden cases with those of clean interfaces; this topic is suggested as an avenue for future research.

The variations in $\tilde{z}_{max}$ resulting from changes in β_s (figure 6.14(l)) are a testament of the complex dynamics underpinning surfactant-laden bursting bubbles. In the case of $\beta_s = 0.1$, not only does the jet ejection velocity surpass that of the surfactant-free case, but its first ejected drop maintains this higher velocity throughout the entire temporal span. The above suggests that there exist situations in which Marangoni stresses originated from very weak surfactants cannot override the lowered capillary resistance to jet growth/breakup (larger local Oh) caused by the surfactant presence. Similar intricate surfactant behaviours were observed in chapter 5 [225].

In addition to jet velocity and size, surfactant contamination severely disrupts the capillary breakup dynamics of the Worthington jets. As is well-known in the literature across a wide array of fluid mechanics problems (see, for instance, [60, 131, 130, 167, 9, 54, 147, 128, 193]), Marangoni stresses, rather than reduced local surface tension, play a primary role in seeking to reopen the capillary neck, thereby resisting end-pinching. In the context of bursting bubbles, this either dramatically reduces the number of ejected drops or completely inhibits the capillary

singularity, as highlighted by the black arrows in figure 6.14(j)-(l). In these cases, the combination of Marangoni-driven end-pinching resistance and the stabilising action of gravitational forces discussed in §6.4.1 completely preclude the jet from pinching. The aforementioned Marangoni-driven phenomenon can be related to the "escape from pinch-off" mechanism in isolated liquid threads described by Kamat et al. [131], Constante-Amores et al. [54], wherein neck re-opening is attributed to the detachment and advection of a vortex ring towards the bulk of the forming bulbous tip.

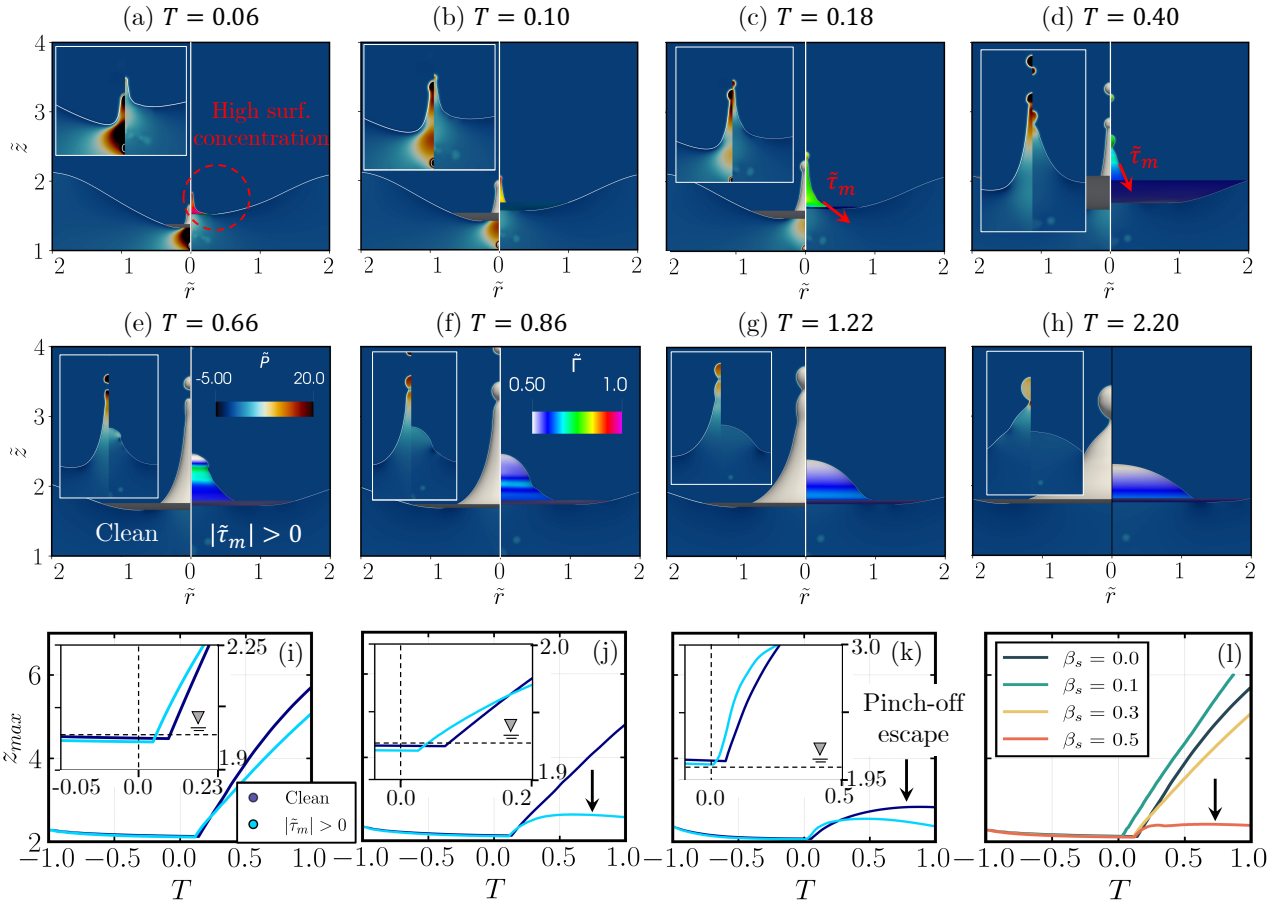

Figure 6.14: Effect of insoluble ($Bi = 0$) surfactant on Worthington jet dynamics: (a)-(h) comparison of temporal evolution (at the same T) of interface shape and pressure fields for surfactant-free interfaces on the left half and insoluble surfactant on the right half; the operating conditions for both the clean and surfactant case are identical to those in figure 6.8. The insets focus on the emerging jet's pressure fields, while the dashed red circle focuses of the jet's near surfactant saturation at early jetting stages. The red arrows schematically indicate the primary direction of Marangoni stresses; (i)-(k) temporal evolution of maximal vertical location of the interface for $Bo = 0.5, 1, 5$, respectively; (l) effect of β_s at $Bo = 0.5$. The black arrows point to instances of pinch-off escape

This discussion concludes by delving into the process of contamination enrichment of aerosol drops. As demonstrated in previous investigations [73], any type of contamination in the liquid bulk can have highly problematic consequences due to the accumulation of these contaminants—oftentimes environmentally harmful—in the drops released to the atmosphere. Although the focus of this study comprised situations in which drop release is heavily suppressed, a few

insights can be gathered from the simulations. Taking the base surfactant-free case, characterised by $Oh = 3.21 \times 10^{-3}$ and $Bo = 0.5$, a total of three ejected drops were obtained, with their radii relative to the bubble radius being $R_{d,i}/R_0 = 7.7\%$, 9.42%, and 21.3%, respectively (i denotes the order of ejection).

It should be noted that the size of the first ejected drop agrees well with the reports by Blanchard and Syzdek [37] ($R_{d,1}/R_0 \approx 6\%$). In contrast, the sole drop produced by an insoluble surfactant at the same Bo and a moderate $\beta_s = 0.3$ exhibited a size of $R_{d,1}/R_0 = 4.9\%$ and showed significant enrichment in terms of both interface and bulk surfactant concentration. Specifically, taking the surface average of Γ and the volume average of C within the drop, $\Gamma_{d,1}/\Gamma_0 = 145.4\%$ and $C_{d,1}/C_\infty = 774.4\%$ are obtained. This striking surfactant enrichment ($\approx 1.5 - 8$ times the initial values) is within the range of experimental enrichment factors of particulate and bacterial contaminants reported in Blanchard and Syzdek [37], Bezdek and Carlucci [35], Ji et al. [122].

6.4.3.1 Cap retraction and its effects on ejected jets

As briefly mentioned at the end of §6.4.1, cap retraction dynamics are increasingly relevant as Bo grows due to the comparable time-scales associated with cap retraction and bubble collapse. In all simulations, it was opted for neglecting the effects of the cap given that the time associated with its retraction is typically at least 2-3 orders of magnitude lower than those of cavity collapse. Nevertheless, it is crucial to highlight here that an asymmetric puncture in the cap can have enormous consequences in the pre- and post-collapse dynamics. As depicted in figure 6.15(a)-(b), a hole opening in the $\tilde{x} > 6$ region brings about the generation of an oblique jet due to the dominant capillary waves focusing at a point shifted away from $\tilde{x} = 6$. These phenomena have been observed experimentally in the work of Ghabache [92], showcased in figure 6.15(c).

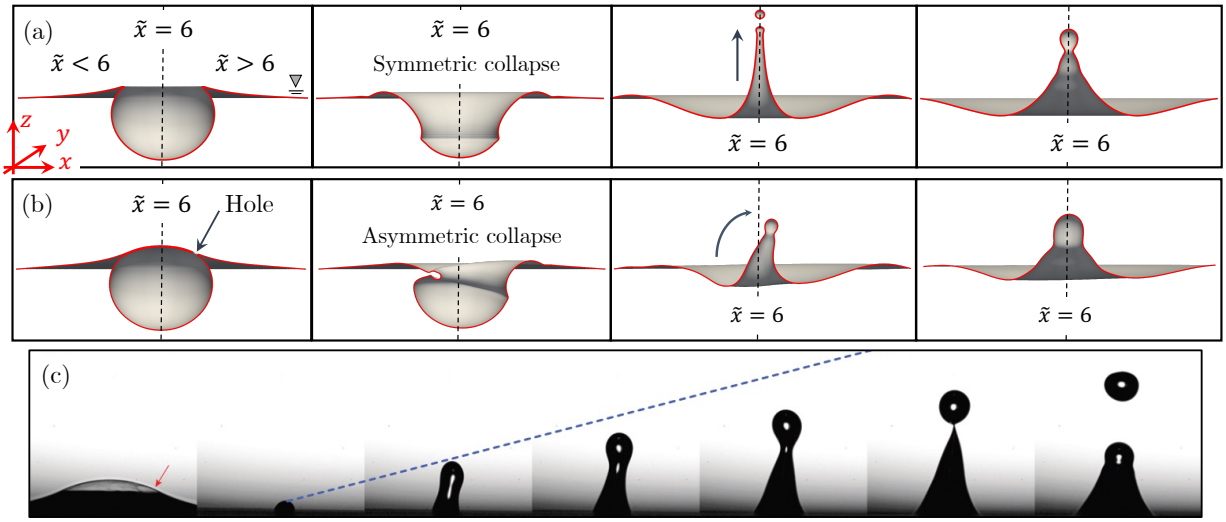

Figure 6.15: Influence of bubble cap and hole opening location on Worthington jet: (a) schematic of cap-less bursting, inducing a symmetric train of capillary waves along the bubble and generating a symmetric Worthington jet; (b) schematic of asymmetric bursting, generating an oblique jet. The simulation conditions of (a)-(b) correspond to $Bo = 0.5$ and $Oh = 1 \times 10^{-2}$ with cap thickness $\delta = 0.05 R_0$; (c) experimental images of asymmetric bursting taken and adapted from Ghabache [92]

6.5 Concluding remarks

This work has dived into the classic phenomenon of bubbles bursting through a liquid-gas interface via numerical simulations, exploring two scenarios that, despite their practical significance, have only recently garnered attention: surface-active contamination and non-negligible gravitational forces compared to capillary forces, characterised by large Bond numbers, $Bo >> 10^{-3}$.

Building upon the recent experimental [123, 297, 227] and numerical [55] work centred around surfactant effects on bursting bubble dynamics, the simulations conducted have allowed us to provide detailed quantitative insights about the system. These include the temporal evolution of the dominant capillary wave angular location as it traverses down the cavity before collapse ($\tilde{\theta}$ vs. $\tilde{t}$), an exploration of the self-similarity of interfacial shape, Worthington jet growth, surfactant concentration and Marangoni stresses profiles along the interface, and the collective impact of surfactant parameters on these variables. This information is notably challenging to access experimentally. Herein, it has also been proposed, for the first time, a phenomenological mechanism that explains the capillary wave retardation reported experimentally and numerically in surfactant-laden bursting bubbles.

Gravitational effects were found to be relevant in uncontaminated interfaces in terms of average velocity of the capillary wave, $|\tilde{u}_\theta|$, at large Bo. Prior investigations [38] had reported insignificant variations in $|\tilde{u}_\theta|$ with Bo for $Bo < 0.7$. Nonetheless, this study, which extended the examined Bond number range up to $Bo = 5$, reveals small but non-negligible decreases in

$|\tilde{u}_\theta|$ with Bo for the Oh range considered, $1 \times 10^{-3} < Oh < 1 \times 10^{-2}$, suggesting a power-law fitting of the form $|\tilde{u}_\theta| \sim -Bo$. The negative response of $|\tilde{u}_\theta|$ to Bo has been attributed to the much larger pressure gradients between the depths of the liquid pool and the areas surrounding the bubble at larger Bo, which compete with capillary wave motion and stabilise the system. In line with previous work for $Bo \to O(10^{-3})$ [99, 100], the extended Bo range has confirmed that alterations in Oh do not produce variations in $|\tilde{u}_\theta|$, even at $Bo = 5$.

An important conclusion that can be drawn from this investigation corresponds to the substantially different pre-bubble collapse phenomena that emerge as surfactant is introduced to the system. Previous investigations, alongside the present research, have demonstrated that $\tilde{\theta}$ vs. $\tilde{t}$ behaves linearly in interfaces devoid of surfactant, implying constant $|\tilde{u}_\theta|$. The simulations conducted have revealed that Marangoni stresses, generated by non-homogeneous surface tension distributions, not only delay wave motion by about $30 - 70\%$, but also completely disrupt the linearity of $\tilde{\theta}$ vs. $\tilde{t}$. For insoluble surfactants, dominant capillary wave motion was found to lean closer to $\tilde{\theta} \sim \tilde{t}^{\alpha}$, with $\alpha = 0.45 - 0.70$, depending on Bo. It should be noted, however, that the dominant capillary wave undergoes a behavioural transition close to the instant of collapse, briefly exhibiting motion acceleration. A comprehensive examination of the moments leading up to bubble collapse is left for future work.

Throughout this investigation a mechanism that rationalises the delays in wave motion induced by surfactants has been introduced, involving the transition from primarily "bi-directional" to primarily "uni-directional" Marangoni stresses. This mechanism can be summarised as follows. The large curvature that accompanies the surrounding areas of the dominant wave generates a toroidal region covered with surfactant (see figure 6.8(a)) from which "downwards" ($\tilde{\tau}_m < 0$, motion-promoting) and "upwards" ($\tilde{\tau}_m > 0$, motion-opposing) Marangoni stresses emerge. As collapse is approached, surfactant saturation at the bottom of the bubble (see figure 6.8(c)) eliminates $\tilde{\tau}_m < 0$, subjecting the interface to strong, uni-directional stresses heavily opposing wave motion across the cavity. This work has also presented a parametric sweep of two dimensionless groups relevant to various types of surfactants: surfactant solubility, given by Bi, and surfactant strength, given β_s. The former quantifies the rate at which surfactant desorbs into the liquid bulk phase while the latter is a proxy for the strength of Marangoni stresses. More pronounced reductions in capillary wave velocity were found for surfactants featuring weaker solubility (lower Bi) and larger β_s. This trend is explained by larger Marangoni stresses prompted by smaller Bi and larger β_s.

Finally, this study has complemented the numerical observations of Constante-Amores et al. [55], Pierre et al. [227] regarding surfactant effects on the Worthington jet. The unequivocally larger local Oh close to the bubble collapse point brings about larger jet ejection velocities in surfactant cases, in line with the well-established scalings proposed in previous works for clean interfaces [90, 100]. Nevertheless, jet expansion and growth force the emergence of strong Marangoni stresses that resist interfacial elongation and jet breakup via the Rayleigh–Plateau instability,

ultimately leading to low-velocity jets and a significantly reduced number of ejected drops.

This investigation provides additional evidence to underscore the profound impact of surface-active contaminants, which are ubiquitous in nature, on the dynamics of bursting bubbles throughout the pre- and post-collapse stages. These effects extend beyond the mere retardation of bubble collapse, influencing the size distribution and degree of contamination of aerosol drops. For future research, the author recommends an in-depth numerical and experimental exploration of surface rheological effects with surfactants, which are believed to significantly influence bursting bubbles, as indicated by the experiments of Ji et al. [123]. Of particular interest is the behaviour of the jet, from ejection to drop detachment, and the isolation of Marangoni-driven mechanisms from those emerging due to surface rheology.

Chapter 7

Conclusions and future outlooks

7.1 Conclusions and main contributions

This thesis has been an exploration of the inherently complex nature of general multiphase flows, with particular focus on complex interfacial systems with surfactants, microfluidics, and polydisperse multiphase flows. The phenomenological complexity of such flows manifests in the form of interfacial singularities, intricate interactions between inertia, gravity, viscosity, and surface tension, coupled multiscale dynamics, multi-physics processes—including chemical reactions—and non-monotonic responses to perturbations. Elucidating these complex behaviours from a fundamental perspective gives way to a more thorough understanding of the underlying dynamics that dictate how a system will behave under operating conditions relevant to a multitude of engineering applications. This, in turn, results in an overall process design improvement, enhanced control over the properties of the final products, and increased efficiency and reliability across industrial processes.

The above mentioned complexities demand for the careful formulation, implementation, and selection of appropriate mechanistic models and computational frameworks, enabling the exploration of uncharted scenarios, the discovery of previously unknown behaviours, and the support and guidance of present and future experimental efforts. This work has focused on the investigation of multiphase flows through the lens of three case-studies that serve as examples of the intricate and intriguing behaviours exhibited by multiphase flows and that hold significant academic, environmental, and industrial relevance. These case-studies—the synthesis of AgNPs, the motion of elongated bubbles in small-scale channels, and the bursting of bubbles through liquid-gas interfaces—have been investigated through computations of varying modelling scales and fidelities in accordance to their specific requirements in terms of spatio-temporal resolution and specific application. On the one hand, a hybrid meso- and macroscale approach, integrating population balance modelling with computational fluid dynamics (PBM-CFD), was employed to track the temporal and spatial evolution of AgNPs and their interactions with the continuous

phase. As opposed to a purely Lagrangian tracking of each particle, population balances grant access to the particles behaviour via the computation of quantities pertaining to the population, such as the distribution of particle properties, all while avoiding substantial computational costs. On the other hand, a state-of-the-art high-fidelity method for treating two-phase flows in the presence of surfactants, the level contour reconstruction method (LCRM) [264], was the modelling choice for the second and third case-studies as it provides the necessary features to track complex interfacial behaviours, such as highly deformed interfaces and capillary breakup.

The literature review conducted for each case-study has brought to light the extensive body of experimental, theoretical, and computational work that has preceded this investigation and has served as a stepping stone for the contributions of this thesis. While the case-studies considered herein may initially appear disparate, the review has revealed underlying similarities in their knowledge gaps. These gaps predominantly pertain to the significantly under-explored operating conditions and regimes, resulting in a limited understanding, documentation, and quantification of specific system behaviours, as well as a marked deficiency in the development of robust and realistic models for capturing the unique dynamics of these systems.

This latter deficiency was particularly evident in the field of NP synthesis, where, despite significant efforts [309, 253, 221], the scientific community had yet to establish a unified modelling framework capable of addressing both well-mixed and open-flow microchannels under supersaturation-driven synthesis scenarios, such as those encountered in the production of AgNPs. Similarly, the topics of bubble motion in small-scale channels and bubble bursting had been insufficiently explored beyond a narrow set of idealised conditions [43, 102, 18], thereby limiting the discovery of valuable phenomena with further applications. Specifically, the investigation into bubble motion through small channels necessitated an in-depth examination of events such as bubble back curvature inversion, re-entrant jet formation, and droplet encapsulation, which occur as the dominance of capillary forces diminishes. While the effects of the Ohnesorge (or Laplace) number on ejected drop size and velocity during bubble bursting events are well-understood [68, 94, 34, 100, 90], this process had not been extensively examined under more realistic conditions, including the presence of surface-active contaminants and non-negligible gravitational forces.

The following paragraphs will present specific concluding remarks for each case-study examined in this thesis. Regarding the synthesis of AgNPs, the proposed PBM-CFD modelling framework, based on the well-established Finke-Watzky two-step mechanism (F-W), was rigorously validated against experimental data from the literature [221] and measurements obtained by our collaborators [204, 224] in both a batch-style reactor with high mixing rates ("well-mixed" reactor) and a T-junction continuous-flow microchannel. These validations, coupled with additional testing of mesh resolution and the robustness of the numerical methods, confirmed the reliability of the model's implementation in open-source code using the suite of solvers *OpenQBMM*. The results also demonstrated the model's strong predictive capabilities in well-mixed

reactors under conditions that maintain a kinetic separation between nucleation and growth (with the rate of growth exceeding that of nucleation), particularly at low pH and high concentrations of the stabilising agent. However, the model's performance was observed to decline under operating conditions where nucleation rates significantly exceed growth rates, such as in alkaline environments. In these scenarios, the rapid nucleation consumes the majority of the silver precursor, resulting in the formation of small-sized nanoparticles that exhibit slow growth, thereby producing particle size distributions that are significantly biased towards smaller sizes.

Despite the observed deviations from the well-mixed experimental data—which did not exceed 15% in terms of average particle size across all tested scenarios—the proposed model successfully captured and reproduced the overall system dynamics and qualitative experimental trends. Through the well-mixed model, it was determined that the variability in PSD under different operating conditions could be largely attributed to variations in a single kinetic parameter, $k_2[A]_0/k_1 = t_n/t_g$ (where t_n and t_g represent the characteristic times for nucleation and growth, respectively), and the critical nucleation radius, d_{crit}. Empirical power-law relationships, expressed as $d \sim (k_2[A]_0/k_1)^{0.40}$ for average particle size and $\sigma^{SD} \sim (k_2[A]_0/k_1)^{0.34}$ for standard deviation, were identified, effectively collapsing all simulation data points across several decades of $k_2[A]_0/k_1$ values and various d_{crit} values.

The extensions proposed to adapt the model to the dynamics of microfluidics revealed a strong coupling between hydrodynamics, multi-reaction kinetics, and the distribution of particle number, size, and volume fraction across the microchannel. Through time-scale analyses and the use of dimensionless parameters, the effects of operating conditions—such as inlet flow rates, reactor length, and reagent transport properties—were rationalised as alterations in the ratios between flow residence time, diffusive mixing, and reduction reactions. These alterations lead to varying rates of precursor consumption per unit reactor length, which subsequently cascade through a complex sequence of kinetic and hydrodynamic events, including the creation of silver atoms via reduction and their consumption via nucleation and growth, and ultimately result in different outlet PSDs. Additionally, significant heterogeneities in the radial distribution of variables across the channel were observed, particularly under conditions that induce extended reactor residence times (low flow rates). These heterogeneities were mainly explained by the lack of secondary vortical structures inherent to straight-channel geometries.

On the topic of elongated bubbles flowing across liquid-filled channels, the present work set out to explore the mechanisms underlying the highly unsteady phenomena of curvature inversion, re-entrant jet penetration, and drop encapsulation. These phenomena sharply contrast with the steady dynamics observed under conditions of dominant capillarity, negligible inertia, symmetric channel cross-sections, and the absence of contaminants. As also reported in previous investigations [179], non-axisymmetric bubble topologies were found to emerge at the channel's cross section when the channel deviates from a fully circular geometry. These non-axisymmetric structures were found to become more prominent as Ca decreases, leading to a thinning effect on the

liquid film thickness.

The high-fidelity simulations conducted in this investigation under larger Ca and We conditions have elucidated the intricate interplay among surfactant parameters, Marangoni stresses, inertia, viscosity, and surface tension in governing the aforementioned encapsulation processes. A critical Weber number of $We \approx 20$, at a Reynolds number of $Re \sim O(10^1)$, was identified as the threshold beyond which capillary forces fail to maintain a purely hemispherical shape at the bubble's front and rear menisci, leading to interface distortion driven by the flow of the continuous phase. This distortion is evidenced in an overall bubble axial elongation and a curvature inversion at the rear meniscus from which encapsulation events take place. Numerous similarities between the interfacial features and singularities observed in this study and those found in other well-known systems involving capillary-driven liquid breakup—such as inkjet printing, two-phase microfluidics, contracting liquid filaments, and sheet cavitation—were identified and described.

Through a systematic exploration of various surfactant parameters, including the rates of adsorption/desorption and surfactant elasticity, two distinct modes of jet breakup and encapsulation were identified. The first mode, referred to here as "back pinch-off," involves the closure of the bubble's rear. The second mode, termed "interior pinch-off," corresponds to the capillary breakup of the re-entrant jet within the interior of the bubble domain. In the presence of surfactants, when the rates of desorption exceed those of adsorption (characterised by reduced values of the dimensionless number k), the combined and isolated effects of reduced surface tension and Marangoni stresses were observed to delay both pinch-off modes. Similar delays were also noted in cases involving low solubility (low Bi) and highly elastic (large β_s) surfactants. Interestingly, when k exceeds a critical value of approximately 1, an acceleration of the back pinch-off mode relative to clean interfaces was recorded. This acceleration was attributed to capillary breakup dynamics typically observed in liquid filaments [131, 54].

The observed encapsulation behaviours were systematically categorised into a regime map within the $\beta_s - k$ and $Bi - k$ parameter spaces, delineating three distinct behavioural regimes. Regime I encompasses all systems below the critical threshold of $k = 1$, where stable encapsulation of liquid drops was observed, driven by back pinch-off events that promote stabilisation and closure of the bubble's rear. In contrast, regimes II (delayed pinch-off) and III (expedited pinch-off) are characterised by the deep penetration of the liquid jet prior to end-pinching, which, together with the high relative velocity of the entrapped drops, results in the subsequent bursting of the bubble's front. These two regimes also display a range of complex interfacial phenomena following the liquid jet's end-pinching, including escapes from pinch-off, radial expansion, and eventual bubble rupture near the channel walls.

The final case study concentrated on delivering comprehensive and detailed quantitative insights into the behaviour of bursting bubbles, informed by recent experimental [227, 297] and numerical investigations [55] involving both surfactant-laden and clean interfaces. Gravitational

effects, quantified by the Bond number, Bo, were found to exert sufficient influence to alter the magnitude of the average wave propagation velocity, $|\tilde{u}_\theta|$, for $Bo = 1$ and beyond across all tested values of the Ohnesorge number ($1 \times 10^{-3} < Oh < 1 \times 10^{-2}$). Despite these variations in magnitude, the previously reported linear relationship between the angular position of the dominant capillary wave and time ($\tilde{\theta}$ vs. $\tilde{t}$ [100, 38]) was observed to persist even at the higher Bond number tested, $Bo = 5$. The reductions in capillary wave velocity under increased gravitational forces were attributed to heightened pressure gradients between the liquid pool and the areas surrounding the bubble, which serve to stabilise the system and counteract wave propagation.

Upon the introduction of surfactants into the system, and the subsequent development of Marangoni stresses due to heterogeneous interfacial surfactant concentration distributions along the bubble, wave motion retardations were observed, resulting in a 30% to 70% decrease in average wave velocity compared to clean interface cases. Detailed tracking of the dominant capillary wave's evolution through simulations revealed significant deviations from the linearity of the $\tilde{\theta}$ vs. $\tilde{t}$ relationship. For insoluble surfactants, the system exhibited behaviours closer to $\tilde{\theta} \sim \tilde{t}^{\alpha}$, where α ranged from 0.45 to 0.70, depending on Bo. A parametric sweep over surfactant solubility and elasticity (characterised by Bi and β_s, respectively) revealed monotonic decreases in average wave velocities with increasing β_s and decreasing Bi. A phenomenological mechanism has been proposed to explain the observed surfactant-induced wave retardations, centred on the transition from bi-directional to uni-directional Marangoni stresses. In the bi-directional stage, the system experiences both wave motion-promoting and motion-opposing Marangoni stresses. As the system transitions to the uni-directional stage, the motion-promoting stresses are effectively neutralised by the opposing forces, resulting in a net delay in wave propagation.

Finally, the influence of surfactants on the ejection and breakup of the Worthington jet was analysed. Consistent with scaling laws that relate jet ejection velocity to Oh for clean interfaces [99, 68, 90], cases involving surfactants demonstrated a significantly higher ejection velocity. This increase is attributed to the substantially elevated local Oh at the ejection point, resulting from the considerable accumulation of surfactants in that region. Conversely, the velocity of the first ejected drop in surfactant cases was observed to be lower than that in clean cases, a phenomenon ascribed to the heightened influence of Marangoni stresses as the jet undergoes axial growth.

7.2 Future outlooks

This study has tackled numerous challenges in the fields of polydisperse multiphase flows and complex interfacial dynamics involving surfactants. The following sections outline several recommendations and proposed directions for future research.

Along the lines of the first case-study, a logical subsequent step would be to apply the proposed PBM-CFD framework to model the synthesis of AgNPs using an alternative synthesis protocol to

evaluate its validity and performance. A key area of interest would be to assess the reproducibility of the previously observed relationship between the ratio $k_2[A]_0/k_1$ and particle size in a well-mixed reactor, as depicted in figures 4.8 and 4.9, employing different reducing and stabilising agents. To initiate this exploration, it is suggested to test a synthesis protocol incorporating a reducing agent with enhanced reducing power, such as dimethylborane (DMAB), in conjunction with a commonly used anionic surfactant, such as sodium dodecyl sulfate (SDS), as the stabilising agent. Although the literature provides numerous examples of the use of DMAB [244, 250, 316, 20] and SDS [200], the simultaneous application of both reagents in the synthesis process has not been previously investigated. Moreover, the potent reducing capabilities of DMAB are expected to drive the system into the low $k_2[A]_0/k_1$ regime (larger rates of nucleation compared to growth), where deviations from experimental observations were found in the present study.

Regarding the PBM-CFD model itself, several opportunities for refinement have been identified. Most notably, comparisons with experimental data from the T-junction microchannel indicate a tendency of the model to overestimate the impact of reduced inlet flow rates, as evidenced by the over-prediction of outlet particle sizes. This discrepancy is likely attributable to the omission of an aggregation efficiency term within the agglomeration kernel. Such a term can be crucial as it modulates the number of collisions that successfully result in particle aggregation, factoring in the molecular interactions between the particles and the stabilising agent. Given the diversity of stabilising agents employed in the chemical synthesis of AgNPs (as detailed in table 2.1), the formulation of an all-encompassing aggregation efficiency term is a non-trivial endeavour. This challenge will likely necessitate a synergistic approach, combining experimental data with simulations at the molecular level, such as molecular dynamics simulations.

In addition to the above, an investigation of alternatives to the straight T-junction microchannel geometry considered in this work is imperative to further our understanding of microfluidic synthesis. As a staring point, an exploration of coiled and curved microchannels through experiments and simulations is recommended as these types of geometries have been shown to promote radial mass transfer due to the formation of Dean vortices [318]. This, in addition to significantly improving radial mixing, could markedly affect the resulting PSD.

Regarding the second case study, the author strongly underscores the importance of conducting systematic experimental investigations within the $We > 20$ regime to further substantiate the numerical findings presented in this work. This is particularly critical with respect to the proposed regime maps, which, while in remarkable agreement with previous studies [17, 202], have ventured into uncharted territory that demands rigorous experimental verification. As highlighted earlier, experimental research has predominantly focused on the low Ca and We regimes, leaving the high Ca and We domains significantly underexplored, even in surfactant-free interfaces. Notably, the most recent peer-reviewed experimental studies on encapsulation dynamics date back to the 1990s [212, 211].

Another promising area for future research related to the second case-study involves exploring the effects of gravitational forces on pre- and post-encapsulation dynamics. Although on this occasion gravitational forces have been neglected ($Bo \equiv (\rho_l - \rho_g) g D^2/\sigma_s = 0$), it should be highlighted that the reduction in dominance of capillary forces-an essential condition for the encapsulation process, accentuated by surfactants-could potentially amplify the relative significance of gravitational forces, thereby affecting the trajectory of the encapsulated drops. Preliminary assessments have estimated the effect of gravity by comparing the characteristic time scales within the system to the predicted falling time of an encapsulated drop. Operating conditions from Moran et al. [195] were referenced, specifically investigating buoyancy effects ($0.11 \leq Bo \leq 3.5$) in a similar system ($Re \sim O(10^2)$). For a moderate value of $Bo = 0.15$, the falling time of encapsulated drops was found to be $t_{\text{fall}} = 4.5 \times 10^{-2}$ s, significantly longer than the re-entrant jet's pinch-off times under the tested conditions ($5 - 7 \times 10^{-3}$ s) but comparable to the bubble's total travel time across the channel domain ($3 - 6 \times 10^{-2}$ s). This suggests that gravitational effects are unlikely to significantly impact curvature inversion phenomena, jet infiltration and breakup processes, or surfactant influence on these mechanisms. However, gravity may affect the trajectory and velocity of entrapped drops, as well as the liquid film thickness around the bubble, as observed in Moran et al. [195], and potentially alter the regime maps in figure 5.15. An additional simulation with $Ca = 0.0693$ and $Bo = 0.15$ confirmed that curvature inversion and pinch-off dynamics remain unaffected by gravity, though the trajectory of the entrapped drop is altered compared to the $Bo = 0$ scenario (see figure 7.1).

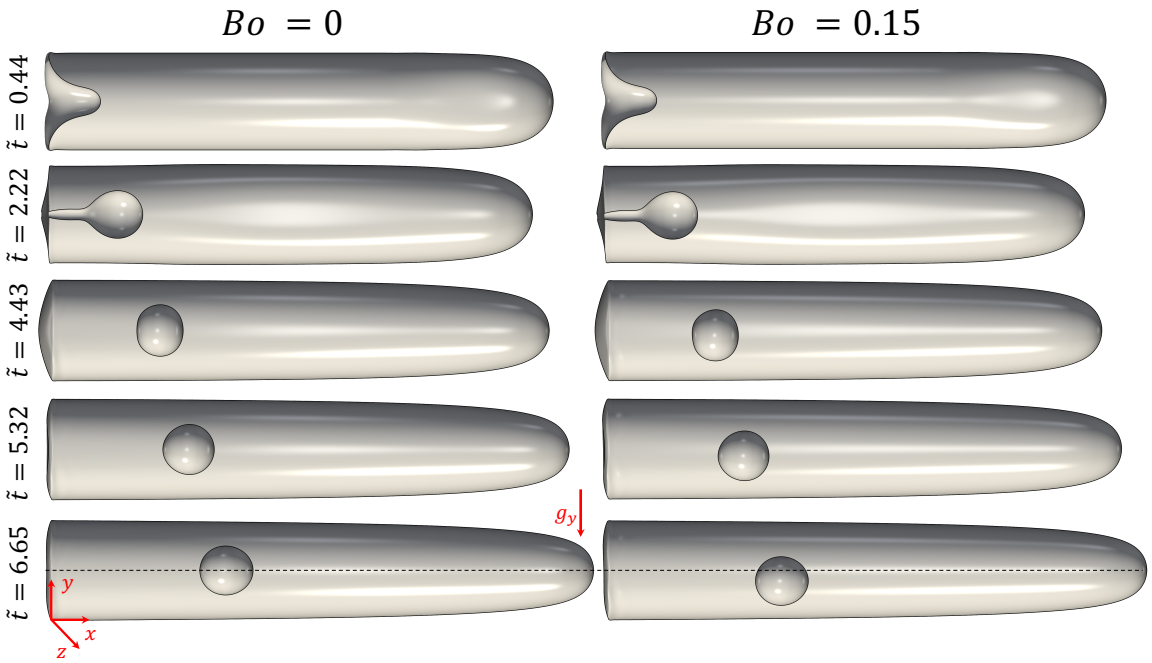

Figure 7.1: Effect of gravity on encapsulation dynamics for a surfactant-free case under the same operating conditions as figure 5.5 ($Ca = 0.0693$)

Lastly, the bursting bubbles findings pave the way for future research endeavours on two main areas. The first is inspired by the works of Dubitsky et al. [73] and Ji et al. [122] on

bubble enrichment by particle scavenging during the bubble's rise to the surface. This and other studies of a similar nature have provided the fluid mechanics community with a general understanding of how these contaminant particles are transported to the atmosphere via the Worthington jet, mostly through numerical simulations with passive scalar fields to represent the scavenged particles. Nevertheless, the small-scale dynamics that occur during bursting bubbles, specially near the moment of bubble collapse, call for the direct consideration of the interactions between individual particles and the bubble-liquid interface. For this, high-fidelity simulations similar to those presented in this thesis, but with the inclusion of several particles, tracked through Lagrangian equations of motion, are suggested. Preliminary tests, as shown in figure 7.2, indicate that the presence of particles can significantly disrupt the bubble bursting process, even to the extent of preventing the formation of the Worthington jet.

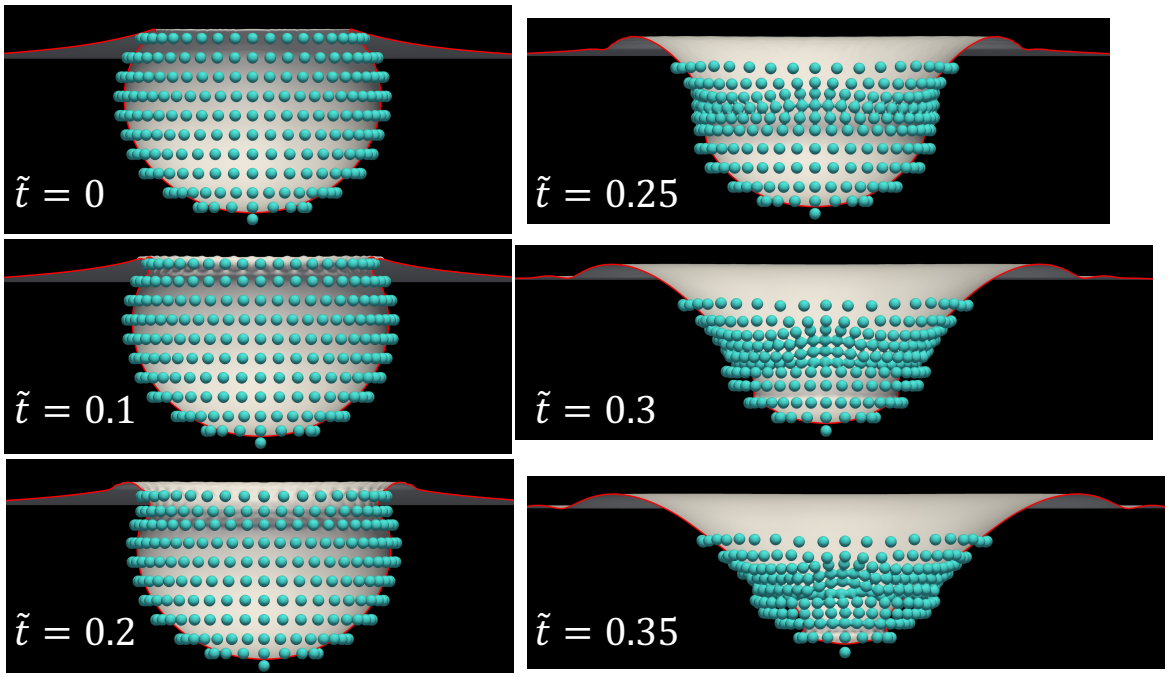

Figure 7.2: Effect of Lagrangian particles on bubble collapse under conditions of $Bo = 0.5$ and $Oh = 3.21 \times 10^{-3}$ ($La = 9.7 \times 10^{4}$)

The final area of focus for the third case study pertains to the incorporation of surface rheological effects, such as viscoelasticity, into the simulations. Surface rheology is an important and active area of research within the interfacial mechanics community and has shown great potential in providing further insights on a multitude of interfacial systems. In the context of bursting bubbles, viscoelasticity may result from the interactions between the bubble-liquid interface and macromolecules, such as microorganisms present in aquatic environments [123]. The recent experimental campaign of Ji et al. [123] has demonstrated that surface rheological effects are uniquely responsible for secondary bubble entertainment phenomena during bursting bubble events. However, distinguishing the contributions of dilatational stresses from those of shear stresses presents a substantial experimental challenge, which could be effectively addressed through numerical simulations.

7.2.1 Explorations of data-driven approaches

A central theme of this thesis has been the integration of multi-scale and multi-fidelity modelling and simulation approaches to tackle some of the challenges inherent to multiphase flows. The final recommendation for future research involves the exploration of low-fidelity, data-driven approaches, such as Machine learning (ML) and Deep learning (DL), to advance the study of interfacial phenomena. As an example of such approach, presented herein are preliminary, proof-of-concept results on regression models to predict the unsteady behaviour of interfacial oscillations. Interfacial oscillations are another classic problem in fluid mechanics with multiple parallels to the dynamics of bursting bubbles, as will be explored in the following paragraphs. The setup for this system has been heavily inspired by the theoretical and CFD work of Farsoiya et al. [85], Basak et al. [26], Kayal et al. [136], and collaborators.

Let us consider a system characterised by an initial state, as depicted in figure 7.3(a)-(b), where a liquid pool with viscosity μ_l and density ρ_l is perturbed according to a zeroth-order Bessel function of the first kind. This liquid pool is situated beneath a gaseous phase with viscosity μ_g and density ρ_g, and the surface tension coefficient between these two phases is denoted by σ_s. Given the coordinate system defined in figure 7.3(a)-(b), the initial wavy structure is described by

$$\eta(r, t = 0) = (z - z_0) + a_{k0}(t = 0)\mathrm{J}_0(rk), \tag{7.1}$$

where $r = \sqrt{x^2 + y^2}$ represents the radial coordinate, a_{k0} denotes the perturbation amplitude, k is the wave number, and J_0 is the zero$^{\text{th}}$-order Bessel function of the first kind. The typical behaviour of this system involves the gradual damping of the wavy structure due to viscous forces. However, under certain conditions, including the imposition of a large-amplitude initial perturbation, the formation of a Worthington-style jet, capable of releasing small droplets similar to the phenomena observed in bursting bubbles, has been reported. The temporal evolution of a_{k0} at the centre of the domain under these two scenarios is illustrated in figure 7.3(c).

While previous theoretical models have successfully reproduced the temporal profiles of a_{k0} with a high degree of accuracy under conditions leading to complete viscous damping of the initial perturbation [85, 26, 136], these approaches have largely been unsuccessful in precisely identifying the threshold value of $a_{k0}(t = 0)$ above which jetting and capillary breakup occur. Additionally, the influence of other factors, such as viscosity and density ratios, as well as the effects of gravity, have not been fully explored. This context presents an opportunity for alternative data-driven approaches, which enable a more extensive and rapid exploration of the parameter space compared to high-fidelity CFD simulations.

To accomplish this, a comprehensive dataset for model training, testing, and validation was generated using high-fidelity CFD simulations based on the LCRM (see §3.3.4). The parameter space explored encompassed multiple orders of magnitude of the dimensionless numbers charac-

terising the system, as defined in Eq. (7.2) [85].

$$\epsilon = a_{k0}(t=0)k, \quad \rho_r = \frac{\rho_l}{\rho_g}, \quad \mu_r = \frac{\mu_l}{\mu_g}, \quad La = \frac{\sigma_s \rho_l}{\mu_l^2 k}, \quad Bo = \frac{\rho_l g}{\sigma_s k^2}, \tag{7.2}$$

where ϵ is the dimensionless initial perturbation amplitude, ρ_r and μ_r are, respectively, the density and viscosity ratios, La is the Laplace number, and Bo denotes the Bond number. The ranges of exploration of these variables are showcased in table 7.1.

Table 7.1: Model input features and their corresponding ranges used for training, testing, and validation

Input features	Ranges
ϵ	$[1 \times 10^{-1}, 3 \times 10^{0}]$
ρ_r	$[1 \times 10^{0}, 1.025 \times 10^{3}]$
μ_r	$[1 \times 10^{0}, 2.732 \times 10^{3}]$
La	$[2.045 \times 10^{1}, 3.78 \times 10^{5}]$
Bo	$[0, 1 \times 10^{2}]$

A total of 152 simulations were conducted, during which the location of the interface at the radial midpoint (i.e., a_{k0}) and cross-sectional images of the interface were tracked over time. For each simulation, this information was recorded 101 times, at intervals of $T_0/20$, resulting in a comprehensive dataset comprising 15,352 data points for training, testing, and validation. Here, $T_0 \equiv 2\pi/\omega_0$ represents the wave oscillation period, with ω_0 determined by the dispersion relation for capillary-gravity waves:

$$\omega_0 = gk\left(\frac{\rho_l - \rho_g}{\rho_l + \rho_g}\right) + \frac{\sigma_s k^3}{\rho_l + \rho_g}. \tag{7.3}$$

All simulations were run on a fully structured Cartesian grid with a global resolution of $(257)^3$. Validation of the simulation outcomes is presented in figure 7.3(d)-(k), demonstrating excellent agreement with the CFD data reported by Farsoiya et al. [85].

7.2.1.1 Single-variable predictions of a_{k0} through ensemble and deep learning regressions

In this subsection, single-variable predictions of the dimensionless interface location at the domain's midpoint, $\tilde{a}_{k0} = a_{k0}/a_{k0}(t=0)$, are analysed based on six features—namely, the five dimensionless parameters outlined in table 7.1 and the dimensionless time $\tilde{t} = t\omega_0$—using three regression techniques.

The regression methods employed include eXtreme Gradient Boosting (XGBoost), random forest (RF), and a multilayer perceptron neural network (MLP) [51], implemented with the Python libraries scikit-learn and Keras. A 75%-25% training-testing split was applied across

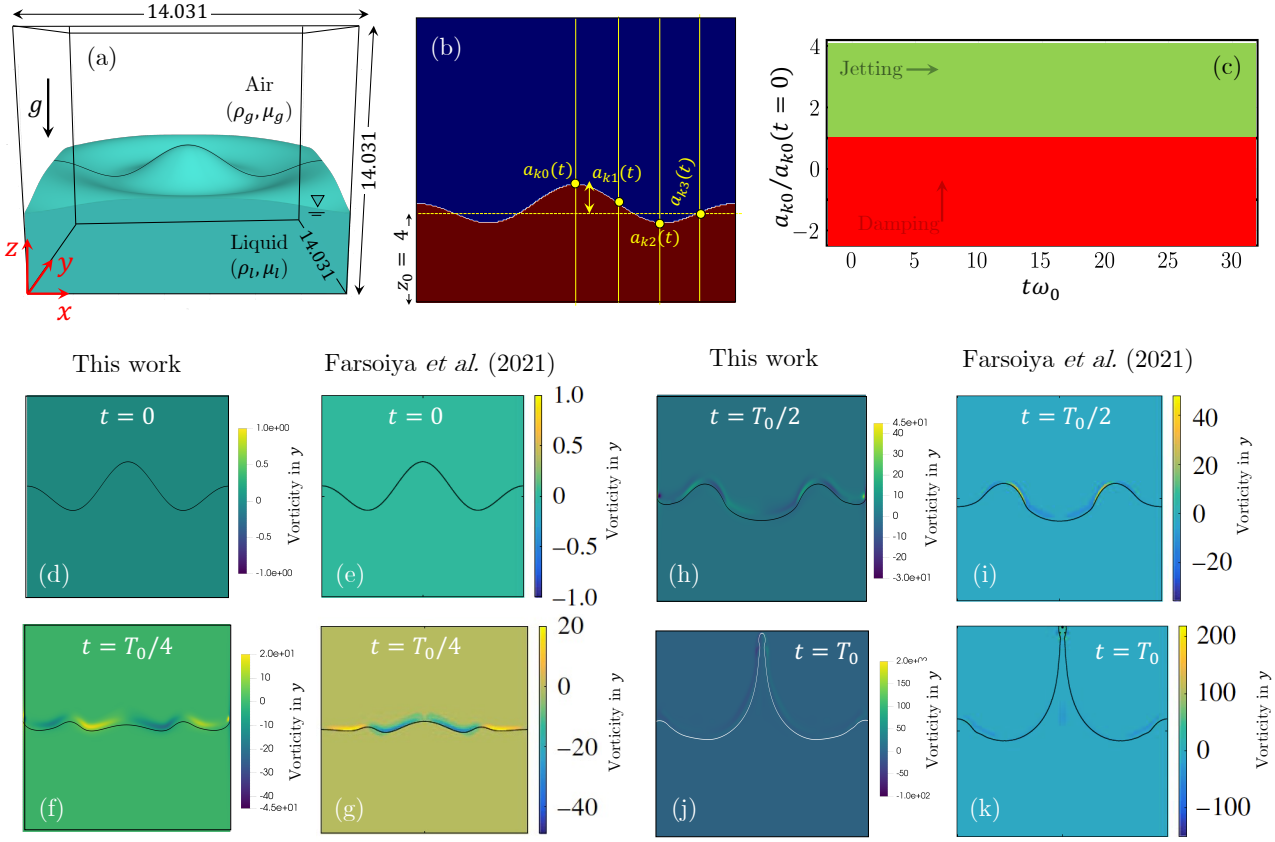

Figure 7.3: Setup of the interfacial oscillations system and validation against the simulations of Farsoiya et al. [85]: (a) CFD simulation domain, illustrating the system's initial configuration and all pertinent measurements in centimetres; (b) cross-sectional view of the initial interface, detailing various interface positions, including the radial midpoint, a_{k0}; (c) sample temporal evolution of a_{k0}, displaying cases where jet formation was observed ($a_{k0}/a_{k0}(t=0) \geq 1$) and cases where wave damping occurred ($a_{k0}/a_{k0}(t=0) < 1$); (d)-(k) comparative analysis of multiple snapshots of the vorticity field in the y-direction (made non-dimensional by using ω_0) and the corresponding interface shape

all methods, with an additional 20% of the training data allocated for validation during the MLP training process. The constructed MLP architecture comprised five hidden layers, containing 256, 128, 34, 32, and 16 neurons, respectively. An early stopping criterion was implemented to monitor the validation loss (R^2), ensuring a consistent decrease and mitigating the risk of overfitting. Each regression technique underwent extensive hyperparameter tuning, incorporating 5-fold cross-validation. The optimal parameter ranges and the corresponding performance metrics for each model are summarised in table 7.2.

Figure 7.4 presents a graphical comparison of the true data versus the predicted values for all three models. These plots, along with the performance metrics detailed in table 7.2, highlight the robust predictive capabilities of each model, with XGBoost demonstrating the highest performance. Although there are indications of potential overfitting in the XGBoost model, as shown in figure 7.4(a), the model still exhibits satisfactory generalisation beyond the training data, as evidenced by figure 7.4(b) and the associated R^2 values. The comparison plots also suggest that the predictions remain accurate across both jetting ($\tilde{a}_{k0} \geq 1$) and non-jetting ($\tilde{a}_{k0} < 1$) scenar-

ios. This indicates that these models are powerful tools for accurately predicting the complex, non-steady, and non-linear dynamics associated with jetting from interfacial oscillations.

Table 7.2: Hyperparameter search space, best configuration, and performance metrics in testing dataset, where MAE stands to mean absolute error, and MSE for mean squared error

Model	Hyperparameters	Ranges	Best configuration	Metrics in test. set
XGBoost	n_estimators	50,54,58,...,198	190	$R^2 = 0.976$
	max_depth	1,2,3,...,28,29	9	$MAE = 0.06747$
	eta	[0.01, 0.1, 0.3]	0.3	$MSE = 0.01229$
RF	n_estimators	[200,300,400]	200	$R^2 = 0.939$ $MAE = 0.11233$ $MSE = 0.03133$
	max_features	['auto', 'sqrt']	'sqrt'	
	max_depth	20,25,30,...,120	120	
	min_samples_split	[2, 6, 10]	10	
	min_samples_leaf	[1, 3, 4]	4	
	bootstrap_range	[True, False]	True	
MLP	activation_functions	['relu','tanh','sigmoid']	'relu'	$R^2 = 0.920$ $MAE = 0.12931$ $MSE = 0.03959$
	optimizers	[Adam,SGD,RMSprop]	RMSprop	
	learning_rates	[0.001, 0.01]	0.001	
	l2_rates	[0, 0.0001, 0.001]	0	

7.2.1.2 Image predictions through dimensionality reduction

The previous subsection highlighted the potential of data-driven approaches to unravel complex interfacial phenomena within fluid mechanics. This subsection advances this analysis by offering predictions of the temporal evolution of cross-sectional images of the interface, similar to the one depicted in figure 7.3(b). These predictions provide a more detailed understanding of the system's dynamics, complementing the earlier predictions of $\tilde{a}_{k0}$. While the $\tilde{a}_{k0}$ parameter is valuable for identifying jetting behaviour or pure damping, it alone is insufficient to fully capture intricate phenomena such as jet capillary break-up. The cross-sectional predictions, therefore, offer a more comprehensive depiction of the events unfolding within the system.

As previously discussed, each simulation involved 101 recordings of $\tilde{a}_{k0}$ accompanied by 101 cross-sectional images of the system (normal to the y-direction, as depicted in figure 7.3(a)). These images represent the Heaviside function field, $\mathcal{H}(\mathbf{x}, t)$ (see §3.3), which takes a value of 1 in the liquid phase and 0 in the gas phase. Each image, comprising 257×257 pixels, resulted in a total of 66,049 pixels per image requiring prediction. Given the high dimensionality of these images, principal component analysis (PCA) [51] was employed as a dimensionality reduction technique to streamline the problem. This approach enabled the regression task to focus on predicting the first few principal components using six features ($\tilde{t}$, ϵ, ρ_r, μ_r, La, and Bo). The predicted principal components were subsequently transformed back into the original image space via inverse PCA, thereby reconstructing the images.

During testing, it was found that 50 principal components were sufficient to explain well over 95% of the cumulative variance by component in the training dataset. A comparison between the

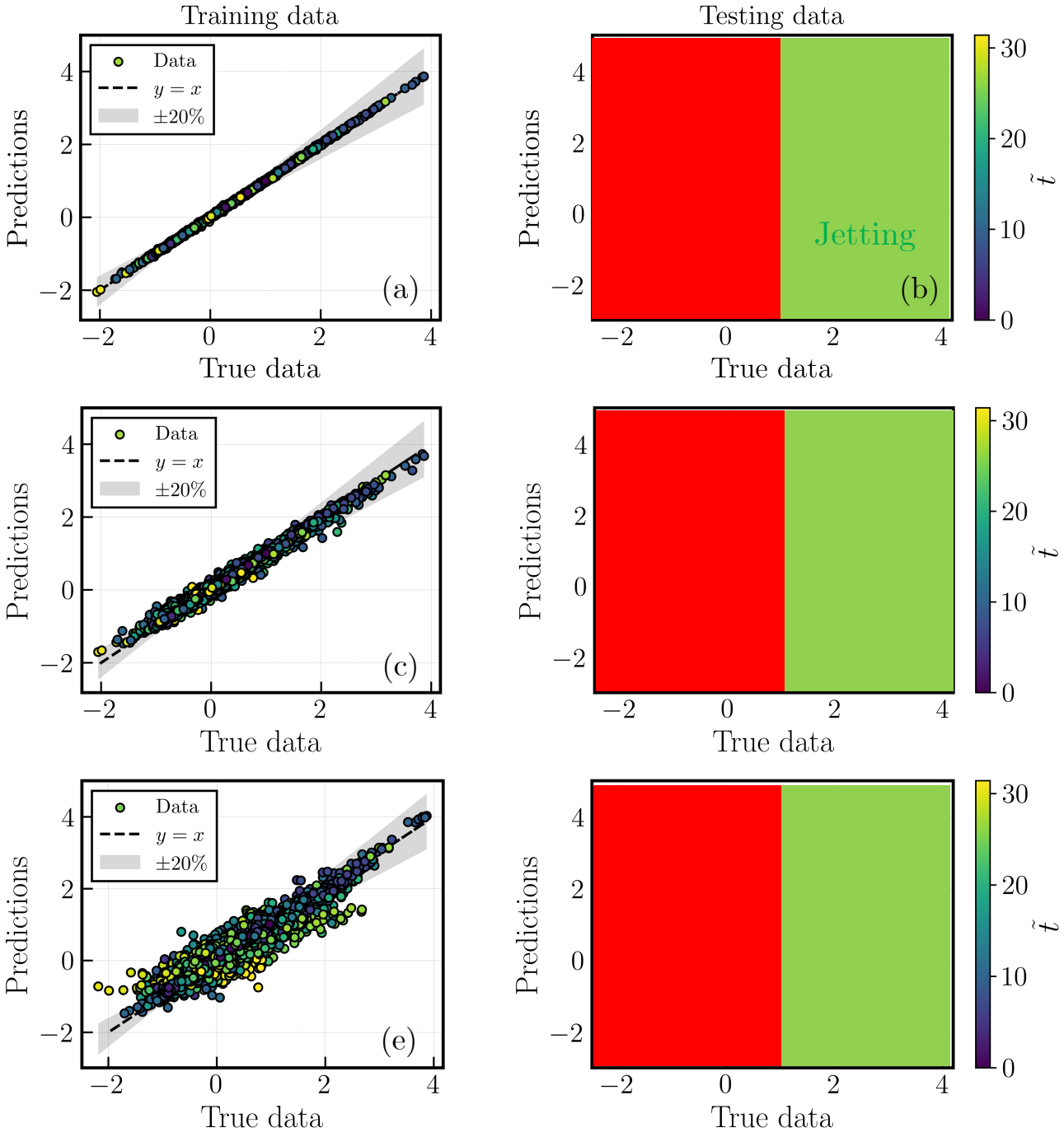

Figure 7.4: Comparison between true and predicted $\tilde{a}_{k0}$ data, segregated by their corresponding dimensionless time $\tilde{t}$ and error dispersion for training (left columns) and testing (right columns) sets; (a)-(b) XGBoost; (c)-(d) RF; (e)-(f) MLP. The areas shaded in light grey correspond to a ±20% dispersion of the data

original training images and the reduced and later reconstructed ones yielded an average structural similarity index measure (SSIM) [307] of 0.9982 over all training images. The calculation of SSIM was achieved using the scikit-image library. It should be mentioned that a post-processing step was applied to the reconstructed images to ensure that the image values of the Heaviside function adopt only binary values of 0 and 1. This post-processing step is shown in Eq. (7.4), where

$\mathbf{Y}^{(i)}_{\text{recons}}$ denotes the i^{th} pixel of a reconstructed image.

$$\mathbf{Y}^{(i)}_{\text{recons}} = \begin{cases} 1 & \mathbf{Y}^{(i)}_{\text{recons}} > 0.5 \\ 0 & \mathbf{Y}^{(i)}_{\text{recons}} \leq 0.5. \end{cases} \tag{7.4}$$

XGBoost was selected as the preferred method for predicting the first 50 principal components. A reduced hyperparameter search was conducted, focusing on the following ranges: `n_estimators` = [10, 100, **150**], `max_depth` = [10, **20**, 50], and `eta` = [0.01, **0.1**, 0.3], with the values highlighted in bold yielding the best performance. The model's performance was excellent, given the complexity of the regression task. On the training dataset, the model achieved $R^2 = 0.91540$, $MAE = 0.00065$, and $MSE = 0.00065$, while on the testing dataset, it attained $R^2 = 0.91535$, $MAE = 0.00150$, and $MSE = 0.00150$. These performance metrics were calculated by comparing the original images with the predicted and reconstructed images in the expanded space.

Figures 7.5 through 7.7 present temporal comparisons between the original and predicted images for several sample cases, which serve as representative indicators of the model's overall performance. As illustrated in figure 7.5, the model demonstrates excellent accuracy in cases where the operating conditions preclude jet formation, resulting in fully damped waves, with only minor localised deviations near the interface. This high level of performance persists in jet-forming scenarios that do not exhibit complex interfacial dynamics, such as capillary breakup, as demonstrated by the case shown in figure 7.6. However, noticeable declines in the model's accuracy become apparent under conditions that induce jet formation and significant alterations in the interface's topology. For example, figure 7.7 illustrates the model's inability to accurately capture the small bulbous structure forming at the jet's tip before pinching (see $\tilde{t} = 6.91$ and $\tilde{t} = 10.37$), as well as its failure to detect the small entrapped bubble at $\tilde{t} = 13.82$.

Despite the limitations noted above, the preliminary results presented in this section underscore the significant potential of complementing purely physics-driven, high-fidelity simulations with lower-fidelity data-driven approaches in the study of fluid mechanics systems. As a direction for future research, the author of this thesis recommends a more in-depth investigation of the relative influence of each dimensionless parameter ($\tilde{t}$, ϵ, ρ_r, μ_r, La, and Bo) on the predicted $\tilde{a}_{k0}$ values through the application of explainable machine learning models, such as SHAP (SHapley Additive exPlanations) values. Another promising research avenue, inspired by the preliminary results presented here, involves the development of an inverse model. In this model, an image displaying a particular interfacial behaviour (e.g., damping, jet ejection, drop aerosol release) would be input into the model, and the corresponding output would be the set of dimensionless parameters that produced the given image.

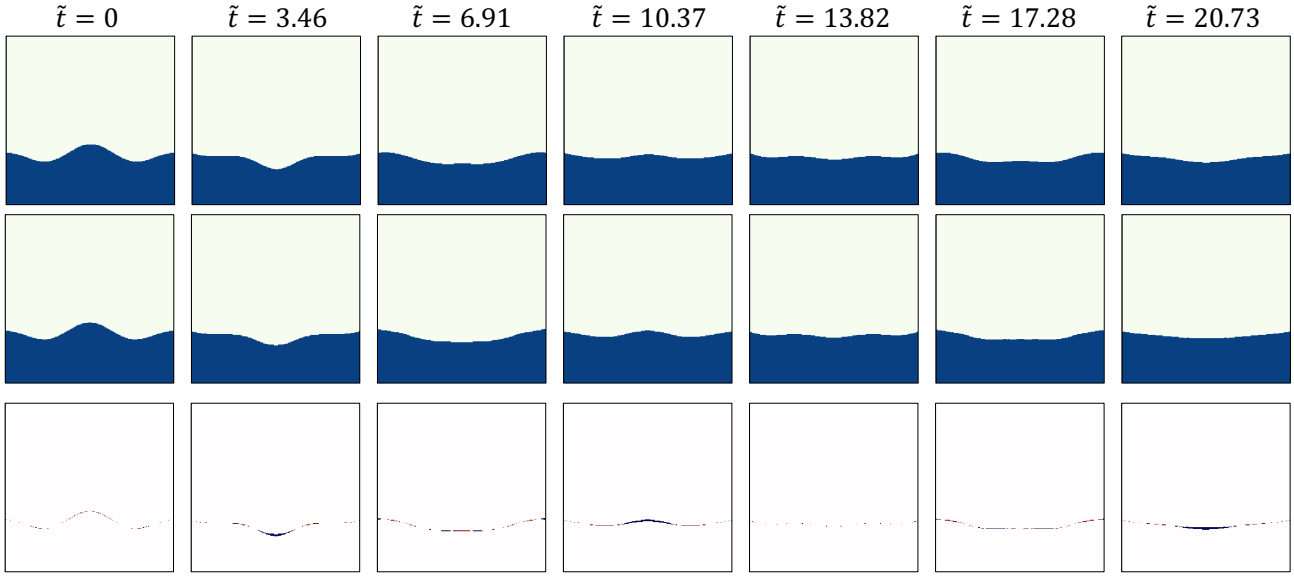

Figure 7.5: Comparison between original images from CFD simulations and predicted-reconstructed images at different dimensionless times for a sample case exhibiting fully damped behaviour, characterised by $\epsilon = 1.03$, $\rho_r = 3.06$, $\mu_r = 1.69$, $La = 1 \times 10^4$, and $Bo = 0$. The top row displays the original images, the middle row shows the predicted images, and the bottom row illustrates the differences between them. In both the original and predicted images, blue indicates the liquid phase ($\mathcal{H} = 1$) and white represents the gas phase ($\mathcal{H} = 0$). In the difference images, dark blue corresponds to a value of -1, and bright red corresponds to a value of 1

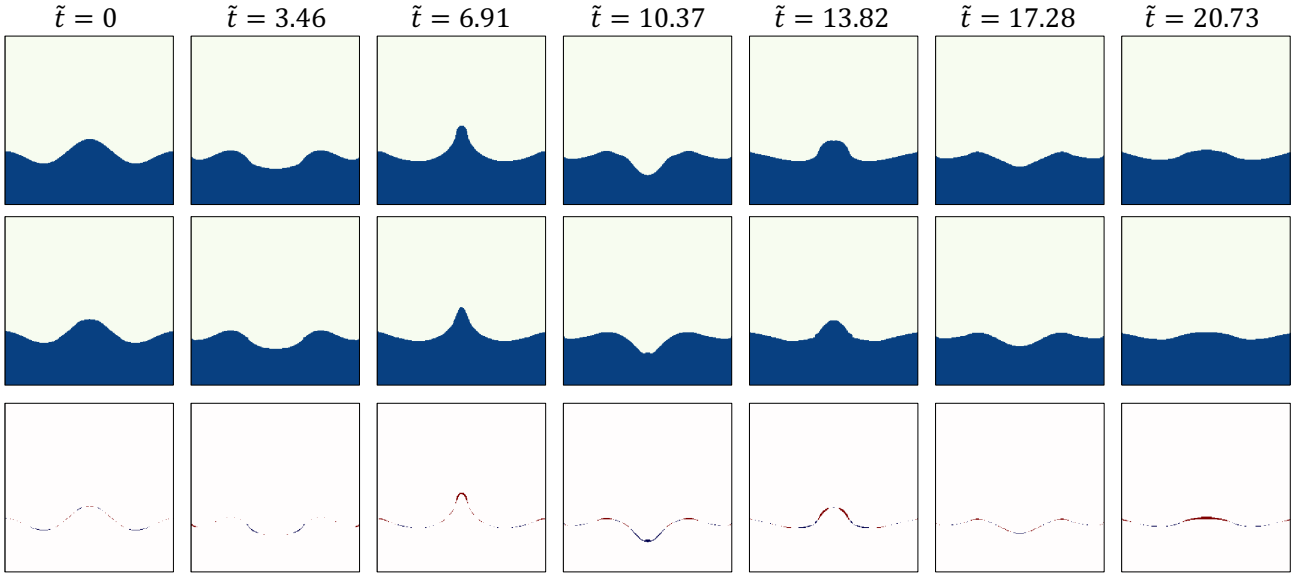

Figure 7.6: Comparison between original images from CFD simulations and predicted-reconstructed images at different dimensionless times for a sample case exhibiting simple jetting behaviour, characterised by $\epsilon = 1.46$, $\rho_r = 6.96$, $\mu_r = 3.49$, $La = 1 \times 10^4$, and $Bo = 10.2$. The top row displays the original images, the middle row shows the predicted images, and the bottom row illustrates the differences between them. In both the original and predicted images, blue indicates the liquid phase ($\mathcal{H} = 1$) and white represents the gas phase ($\mathcal{H} = 0$). In the difference images, dark blue corresponds to a value of -1, and bright red corresponds to a value of 1

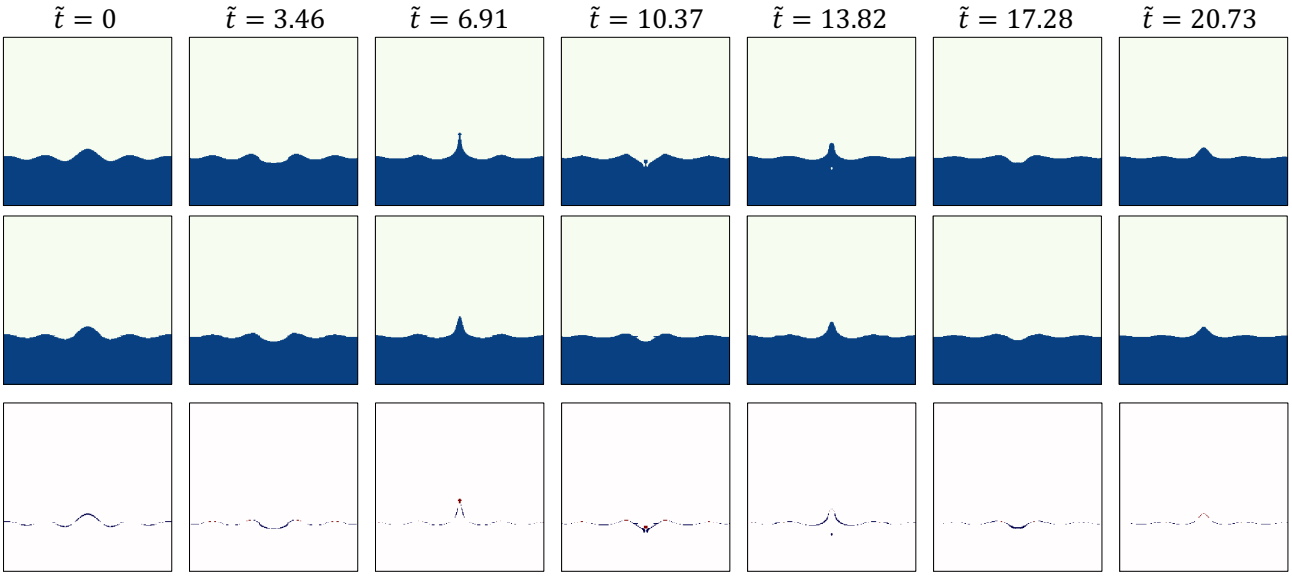

Figure 7.7: Comparison between original images from CFD simulations and predicted-reconstructed images at different dimensionless times for a sample case exhibiting complex jetting behaviour, characterised by $\epsilon = 1.46$, $\rho_r = 595.92$, $\mu_r = 661.10$, $La = 738.29$, and $Bo = 9.78$. The top row displays the original images, the middle row shows the predicted images, and the bottom row illustrates the differences between them. In both the original and predicted images, blue indicates the liquid phase ($\mathcal{H} = 1$) and white represents the gas phase ($\mathcal{H} = 0$). In the difference images, dark blue corresponds to a value of -1, and bright red corresponds to a value of 1

Bibliography

[1] T. Abadie. *Hydrodynamics of gas-liquid Taylor flow in microchannles*. Phd thesis, Université de Toulouse, November 2013.

[2] H.A. Abubakar and O.K. Matar. Linear stability analysis of Taylor bubble motion in downward flowing liquids in vertical tubes. *J. Fluid Mech.*, 941:A2, 6 2022.

[3] M.L Agrawal and R.D. Neuman. Surface diffusion in monomolecular films. *J. Colloid Interface Sci.*, 121(2):366–380, 2 1988. ISSN 00219797. doi: 10.1016/0021-9797(88)90440-7.

[4] E. Agunloye, L. Panariello, A. Gavriilidis, and L. Mazzei. A model for the formation of gold nanoparticles in the citrate synthesis method. *Chemical Engineering Science*, 191, 2018. ISSN 00092509. doi: 10.1016/j.ces.2018.06.046.

[5] M. N. Aktara, Sk. Nayim, N. K. Sahoo, and M. Hossain. The synthesis of thiol-stabilized silver nanoparticles and their application towards the nanomolar-level colorimetric recognition of glutathione. *New J. Chem.*, 43:13480–13490, 2019. doi: 10.1039/C9NJ01360A.

[6] M. T. Aljarrah, A. M. Alboull, M. S. Alharahsheh, A. Ashraf, and A. Khandakar. Parametric Study of Gold Nanoparticles Synthesis under Micro-Continuous Flow Conditions. *Molecules*, 27(24):8651, 2022. doi: 10.3390/molecules27248651.

[7] V. Alopaeus, M. Laakkonen, and J. Aittamaa. Solution of population balances with breakage and agglomeration by high-order moment-conserving method of classes. *Chemical Engineering Science*, 61(20), 2006. ISSN 00092509. doi: 10.1016/j.ces.2006.07.010.

[8] M. K. Alqadi, O. A. Abo Noqtah, F. Y. Alzoubi, J. Alzouby, and K. Aljarrah. PH effect on the aggregation of silver nanoparticles synthesized by chemical reduction. *Materials Science- Poland*, 32(1):107–111, 1 2014. ISSN 01371339. doi: 10.2478/s13536-013-0166-9.

[9] B. Ambravaneswaran and O. A. Basaran. Effects of insoluble surfactants on the nonlinear deformation and breakup of stretching liquid bridges. *Phys. Fluids.*, 11(5), 1999. ISSN 10706631. doi: 10.1063/1.869972.

[10] B. Ambravaneswaran, H.J. Subramani, S.D. Phillips, and O.A. Basaran. Dripping-jetting transitions in a dripping faucet. *Phys. Rev. Lett.*, 93(3):997–1015, 2004.

[11] A. Amirjani and D. F. Haghshenas. Modified Finke-Watzky mechanisms for the two-step nucleation and growth of silver nanoparticles. *Nanotechnology*, 29(50), 2018. ISSN 13616528. doi: 10.1088/1361-6528/aae3dd.

[12] B. Andersson, R. Andersson, L. Hakansson, M. Mortensen, R. Sudiyo, and B. van Wachem. *Computational Fluid Dynamics for Engineers*. Cambridge University Press, Cambridge, 2011. ISBN 9781139093590. doi: 10.1017/CBO9781139093590.

[13] M. Andredaki, A. Georgoulas, N. Miché, and M. Marengo. Accelerating Taylor bubbles within circular capillary channels: Break-up mechanisms and regimes. *Int. J. Multiph. Flow.*, 134:103488, 2021.

[14] A. Andrieux-Ledier, B. Tremblay, and A. Courty. Synthesis of silver nanoparticles using different silver phosphine precursors: Formation mechanism and size control. *The Journal of Physical Chemistry C*, 117(28):14850–14857, 2013. doi: 10.1021/jp4040248.

[15] C.R. Anthony, P.M. Kamat, M.T. Harris, and O.A. Basaran. Dynamics of contracting filaments. *Phys. Rev. Fluids.*, 4:093601, 2019.

[16] E. Antonopoulou, O. G. Harlen, M. Rump, T. Segers, and M. A. Walkley. Effect of surfactants on jet break-up in drop-on-demand inkjet printing. *Phys. Fluids.*, 33(7), 2021. ISSN 10897666. doi: 10.1063/5.0056803.

[17] O. Atasi, B. Haut, A. Pedrono, B. Scheid, and D. Legendre. Influence of Soluble Surfactants and Deformation on the Dynamics of Centered Bubbles in Cylindrical Microchannels. *Langmuir*, 34:10048–10062, 2018.

[18] P. Aussillous and D. Quéré. Quick deposition of a fluid on the wall of a tube. *Phys. Fluids.*, 12:2367–2371, 2000.

[19] R. Baber, L. Mazzei, N. T. K. Thanh, and A. Gavriilidis. Synthesis of silver nanoparticles in a microfluidic coaxial flow reactor. *RSC Adv.*, 5:95585–95591, 2015. doi: 10.1039/C5RA17466J.

[20] S. Babu Kalidindi, U. Sanyal, and B. R. Jagirdar. Chemical Synthesis of Metal Nanoparticles Using Amine-Boranes. *ChemSusChem*, 4(3):317–324, 2011. doi: 10.1002/cssc.201000318.

[21] V. Bal and R. Bandyopadhyaya. Generalized Model for Nano- and Submicron Particle Formation in Liquid Phase, Incorporating Reaction Kinetics and Hydrodynamic Interaction: Experiment, Modeling, and Simulation. *Journal of Physical Chemistry C*, 122(35), 2018. ISSN 19327455. doi: 10.1021/acs.jpcc.8b03521.

[22] V. Bal and R. Bandyopadhyaya. Mechanistic aspects in the formation of nano- and submicron particles in a batch and a continuous microfluidic reactor: Experiment, modeling

and simulation. *Chemical Engineering Journal*, 371:43–54, 9 2019. ISSN 13858947. doi: 10.1016/j.cej.2019.03.194.

[23] S. Balachandar and John K. Eaton. Turbulent dispersed multiphase flow, 1 2010. ISSN 00664189.

[24] B. V. Balakin, S. Lo, P. Kosinski, and A. C. Hoffmann. Modelling agglomeration and deposition of gas hydrates in industrial pipelines with combined CFD-PBM technique. *Chemical Engineering Science*, 153:45–57, 10 2016. ISSN 00092509. doi: 10.1016/j.ces.2016.07.010.

[25] D. Ballottin, S. Fulaz, F. Cabrini, J. Tsukamoto, N. Durán, O. L. Alves, and L. Tasic. Antimicrobial textiles: Biogenic silver nanoparticles against Candida and Xanthomonas. *Materials Science and Engineering C*, 75, 2017. ISSN 09284931. doi: 10.1016/j.msec.2017.02.110.

[26] S. Basak, P. K. Farsoiya, and R. Dasgupta. Jetting in finite-amplitude, free, capillary-gravity waves. *Journal of Fluid Mechanics*, 909:A3, 2021. doi: 10.1017/jfm.2020.851.

[27] N. Basha, R. Arcucci, Angeli P., C. Anastasiou, T. Abadie, C. Quilodrán Casas, J. Chen, S. Cheng, L. Chagot, F. Galvanin, C.E. Heaney, F. Hossein, J. Hu, N. Kovalchuk, M. Kalli, L. Kahouadji, M. Kerhouant, A. Lavino, F. Liang, K. Nathanael, L. Magri, P. Lettieri, M. Materazzi, M. Erigo, P. Pico, C.C Pain, M. Shams, M. Simmons, T. Traverso, J.P Valdes, Z. Wolffs, K. Zhu, Y. Zhuang, and O.K. Matar. Machine learning and physics-driven modelling and simulation of multiphase systems. *International Journal of Multiphase Flow*, 179:104936, 2024. ISSN 0301-9322. doi: 10.1016/j.ijmultiphaseflow.2024.104936.

[28] Neus G. Bastús, Florind Merkoçi, Jordi Piella, and Victor Puntes. Synthesis of highly monodisperse citrate-stabilized silver nanoparticles of up to 200 nm: Kinetic control and catalytic properties. *Chemistry of Materials*, 26(9), 2014. ISSN 15205002. doi: 10.1021/cm500316k.

[29] G. K. Batchelor. *An Introduction to Fluid Dynamics*. Cambridge Mathematical Library. Cambridge University Press, 2000.

[30] A. Batchvarov, L. Kahouadji, C. R. Constante-Amores, G. F. Noroes Gonçalves, S. Shin, J. Chergui, D. Juric, R. V. Craster, and O. K. Matar. Three-dimensional dynamics of falling films in the presence of insoluble surfactants. *J. Fluid Mech.*, 906, 2020. ISSN 14697645. doi: 10.1017/jfm.2020.796.

[31] A. Batchvarov, L. Kahouadji, M. Magnini, C. R. Constante-Amores, S. Shin, J. Chergui, D. Juric, R. V. Craster, and O. K. Matar. Effect of surfactant on elongated bubbles in capillary tubes at high Reynolds number. *Phys. Rev. Fluids.*, 5(9), 2020. ISSN 2469990X. doi: 10.1103/PhysRevFluids.5.093605.

[32] I.B. Bazhlekov, P.D. Anderson, and H.E.H. Meijer. Numerical investigation of the effect of insoluble surfactants on drop deformation and breakup in simple shear flow. *J. Colloid Interface Sci.*, 298(1):369–394, 2006.

[33] L. Bentea, M. A. Watzky, and R. G. Finke. Sigmoidal Nucleation and Growth Curves Across Nature Fit by the Finke-Watzky Model of Slow Continuous Nucleation and Autocatalytic Growth: Explicit Formulas for the Lag and Growth Times Plus Other Key Insights. *Journal of Physical Chemistry C*, 121(9), 2017. ISSN 19327455. doi: 10.1021/acs.jpcc.6b12021.

[34] A. Berny, L. Deike, T. Séon, and S. Popinet. Role of all jet drops in mass transfer from bursting bubbles. *Phys. Rev. Fluids.*, 5(3), 2020. ISSN 2469990X. doi: 10.1103/PhysRevFluids.5.033605.

[35] H. F. Bezdek and A. F. Carlucci. Surface Concentration of Marine Bacteria. *Limnology and Oceanography*, 17(4), 1972. ISSN 19395590. doi: 10.4319/lo.1972.17.4.0566.

[36] R.B. Bird, W.E. Stewart, and E.N. Lightfoot. *Transport Phenomena*. Number v. 1 in Transport Phenomena. Wiley, 2006. ISBN 9780470115398.

[37] D. C. Blanchard and L. D. Syzdek. Concentration of bacteria in jet drops from bursting bubbles. *J. Geophys. Res.*, 77(27), 1972. doi: 10.1029/jc077i027p05087.

[38] F. J. Blanco-Rodríguez and J. M. Gordillo. On the jets produced by drops impacting a deep liquid pool and by bursting bubbles. *J. Fluid Mech.*, 916, 2021. ISSN 14697645. doi: 10.1017/jfm.2021.207.

[39] A. Borhan and C.F. Mao. Effect of surfactants on the motion of drops through circular tubes. *Phys. Fluids. A.*, 4:2628–2640, 1992.

[40] D. Bothe, C. Stemich, and H. J. Warnecke. Fluid mixing in a T-shaped micro-mixer. *Chemical Engineering Science*, 61(9), 2006. ISSN 00092509. doi: 10.1016/j.ces.2005.10.060.

[41] J. M. Boulton-Stone and J. R. Blake. Gas bubbles bursting at a free surface. *J. Fluid Mech.*, 254:437–466, 1993. doi: 10.1017/S0022112093002216.

[42] C. F. Brasz, C. T. Bartlett, P. L.L. Walls, E. G. Flynn, Y. E. Yu, and J. C. Bird. Minimum size for the top jet drop from a bursting bubble. *Phys. Rev. Fluids.*, 7(3), 2018. ISSN 2469990X. doi: 10.1103/PhysRevFluids.3.074001.

[43] F. P. Bretherton. The motion of long bubbles in tubes. *J. Fluid Mech.*, 10(2):166 – 188, 1961.

[44] C.R. Carrigan and J.C. Eichelberger. Zoning of magmas by viscosity in volcanic conduits. *Nature*, 343:248–251, 1990.

[45] A.A. Castrejón-Pita, J.R. Castrejón-Pita, and I.M. Hutchings. Breakup of liquid filaments. *Phys. Rev. Lett.*, 108:074506, 2012.

[46] J.R Castrejón-Pita, A.A Castrejón-Pita, S.S Thete, K. Sambath, I.M. Hutchings, J. Hinch, J.R. Lister, and O.A. Basaran. Plethora of transitions during breakup of liquid filaments. *Proc. Natl. Acad. Sci. U.S.A.*, 112(15), 2015. ISSN 10916490. doi: 10.1073/pnas.1418541112.

[47] L. Champougny, B. Scheid, F. Restagno, J. Vermant, and E. Rio. Surfactant-induced rigidity of interfaces: a unified approach to free and dip-coated films. *Soft Matter*, 11: 2758–2770, 2015. doi: 10.1039/C4SM02661F.

[48] E. M. Chan, A. P. Alivisatos, and R. A. Mathies. High-temperature microfluidic synthesis of CdSe nanocrystals in nanoliter droplets. *Journal of the American Chemical Society*, 127 (40), 2005. ISSN 00027863. doi: 10.1021/ja051381p.

[49] H. Chen, Q. Meng, and J. Li. Thin lubrication film around moving bubbles measured in square microchannels. *Appl. Phys. Lett*, 107:141608, 2015.

[50] H. Chen, Z. Li, and J. Li. Thin-film profile around long bubbles in square microchannels measured by chromatic interference method. *Appl. Phys. Lett.*, 109:041604, 2016.

[51] S. Cheng, Y. Jin, S. P. Harrison, C. Quilodrán-Casas, I. C. Prentice, Y. K. Guo, and R. Arcucci. Parameter flexible wildfire prediction using machine learning techniques: Forward and inverse modelling. *Remote Sensing*, 14(13), 2022. ISSN 2072-4292. doi: 10.3390/rs14133228.

[52] A. J Chorin. Numerical solution of the navier-stokes equations. *Mathematics of Computation*, 22(104):745–762, 1968. ISSN 00255718, 10886842.

[53] K. N. Clayton, J. W. Salameh, S. T. Wereley, and T. L. Kinzer-Ursem. Physical characterization of nanoparticle size and surface modification using particle scattering diffusometry. *Biomicrofluidics*, 10(5), 2016. ISSN 19321058. doi: 10.1063/1.4962992.

[54] C. R. Constante-Amores, L. Kahouadji, A. Batchvarov, S. Shin, J. Chergui, D. Juric, and O. K. Matar. Dynamics of retracting surfactant-laden ligaments at intermediate Ohnesorge number. *Phys. Rev. Fluids.*, 5(8), 2020. ISSN 2469990X. doi: 10.1103/PhysRevFluids.5.084007.

[55] C. R. Constante-Amores, L. Kahouadji, A. Batchvarov, S. Shin, J. Chergui, D. Juric, and O. K. Matar. Dynamics of a surfactant-laden bubble bursting through an interface. *J. Fluid Mech.*, 911, 2021. ISSN 14697645. doi: 10.1017/jfm.2020.1099.

[56] C. R. Constante-Amores, T. Abadie, L. Kahouadji, S. Shin, J. Chergui, D. Juric, A. A. Castrejón-Pita, and O. K. Matar. Direct numerical simulations of turbulent jets: Vortex-interface-surfactant interactions. *J. Fluid Mech.*, 955, 2023. ISSN 14697645. doi: 10.1017/jfm.2022.1056.

[57] C. R. Constante-Amores, L. Kahouadji, S. Shin, J. Chergui, D. Juric, J. R. Castrejón-Pita, O. K. Matar, and A. A. Castrejón-Pita. Impact of droplets onto surfactant-laden thin liquid films. *J. Fluid Mech.*, 961, 2023. ISSN 14697645. doi: 10.1017/jfm.2023.224.

[58] C.R. Constante-Amores, A. Batchvarov, L. Kahouadji, S. Shin, J. Chergui, D. Juric, and O.K. Matar. Role of surfactant-induced Marangoni stresses in drop-interface coalescence. *J. Fluid Mech.*, 925, 2021.

[59] C.R. Constante-Amores, L. Kahouadji, A. Batchvarov, S. Shin, J. Chergui, D. Juric, and O.K. Matar. Direct numerical simulations of transient turbulent jets: Vortex-interface interactions. *J. Fluid Mech.*, 922:A6, 2021.

[60] R. V. Craster, O. K. Matar, and D. T. Papageorgiou. Pinchoff and satellite formation in compound viscous threads. *Phys. Fluids.*, 15(11), 2003. ISSN 10706631. doi: 10.1063/1.1611879.

[61] Clayton T. Crowe, John D. Schwarzkopf, Martin Sommerfeld, and Yutaka Tsuji. *Multiphase Flows with Droplets and Particles*. CRC Press, 8 2011. ISBN 9780429106392. doi: 10.1201/b11103.

[62] J. A. da Silva, M. R. Meneghetti, and C. M. Soares. Molecular Dynamics Simulations Suggest a Possible Role for NO in the Polyol Synthesis of Silver Nanostructures. *The Journal of Physical Chemistry C*, 124(44):24279–24288, 11 2020. ISSN 1932-7447. doi: 10.1021/acs.jpcc.0c08338.

[63] K. N.M. Dantas, L. R. Andrade, E. Lisboa, V. L. Santana, A. L.S. Santos, T. P. Mello, L. S. Sangenito, A. S. Lima, A. T. Fricks, A. F. Begnami, A. Cano, A. Zielinska, C. M.F. Soares, E. B. Souto, and P. Severino. Antimycotic nail polish based on humic acid-coated silver nanoparticles for onychomycosis. *Journal of Chemical Technology and Biotechnology*, 96(8), 2021. ISSN 10974660. doi: 10.1002/jctb.6676.

[64] S. Das, K. Bandyopadhyay, and M. M. Ghosh. Effect of stabilizer concentration on the size of silver nanoparticles synthesized through chemical route. *Inorganic Chemistry Communications*, 123:108319, 2021. ISSN 1387-7003. doi: doi.org/10.1016/j.inoche.2020.108319.

[65] R.F. Day, E.J. Hinch, and J.R. Lister. Self-similar capillary pinchoff of an inviscid fluid. *Phys. Rev. Lett.*, 80(4):704, 1998.

[66] A. de Ryck. The effect of weak inertia on the emptying of a tube. *Phys. Fluids.*, 14(7), 2002. ISSN 10706631. doi: 10.1063/1.1480267.

[67] W. M. Deen. *Analysis of Transport Phenomena*. Oxford University Press, USA, 2011.

[68] L. Deike, E. Ghabache, G. Liger-Belair, A. K. Das, S. Zaleski, S. Popinet, and T. Séon. Dynamics of jets produced by bursting bubbles. *Phys. Rev. Fluids.*, 3(1), 2018. ISSN 2469990X. doi: 10.1103/PhysRevFluids.3.013603.

[69] V. Demchenko, S. Riabov, S. Kobylinskyi, L. Goncharenko, N. Rybalchenko, A. Kruk, O. Moskalenko, and M. Shut. Effect of the type of reducing agents of silver ions in interpolyelectrolyte-metal complexes on the structure, morphology and properties of silver-containing nanocomposites. *Scientific Reports*, 10(1), 2020. ISSN 20452322. doi: 10.1038/s41598-020-64079-0.

[70] X. Dong, X. Ji, H. Wu, L. Zhao, J. Li, and W. Yang. Shape control of silver nanoparticles by stepwise citrate reduction. *Journal of Physical Chemistry C*, 113(16), 2009. ISSN 19327447. doi: 10.1021/jp900775b.

[71] X. Y. Dong, Z.W. Gao, K.F. Yang, W.Q. Zhang, and L.W. Xu. Nanosilver as a new generation of silver catalysts in organic transformations for efficient synthesis of fine chemicals. *Catalysis Science & Technology*, 5(5):2554–2574, 5 2015. ISSN 2044-4753. doi: 10.1039/C5CY00285K.

[72] T. Driessen, R. Jeurissen, H. Wijshoff, F. Toschi, and D. Lohse. Stability of viscous long liquid filaments. *Phys. Fluids.*, 25(6):062109, 2013.

[73] L. Dubitsky, O. McRae, and J. C. Bird. Enrichment of Scavenged Particles in Jet Drops Determined by Bubble Size and Particle Position. *Phys. Rev. Lett.*, 130(5), 2023. ISSN 10797114. doi: 10.1103/PhysRevLett.130.054001.

[74] L. Duchemin, S. Popinet, C. Josserand, and S. Zaleski. Jet formation in bubbles bursting at a free surface. *Phys. Fluids.*, 14(9), 2002. ISSN 10706631. doi: 10.1063/1.1494072.

[75] F. Durst, D. Miloievic, and B. Schönung. Eulerian and lagrangian predictions of particulate two-phase flows: a numerical study. *Applied Mathematical Modelling*, 8(2):101–115, 1984. ISSN 0307-904X. doi: doi.org/10.1016/0307-904X(84)90062-3.

[76] J. B. Edel, R. Fortt, J. C. DeMello, and A. J. DeMello. Microfluidic routes to the controlled production of nanoparticles. *Chemical Communications*, 2(10), 2002. ISSN 1364548X. doi: 10.1039/b202998g.

[77] R.K. Edvinsson and S. Irandoust. Finite-Element Analysis of Taylor Flow. *AIChE J.*, 42 (7), 1996.

[78] J. T. Edward. Molecular volumes and the Stokes-Einstein equation. *Journal of Chemical Education*, 47(4), 1970. ISSN 00219584. doi: 10.1021/ed047p261.

[79] J. Eggers. Universal pinching of 3D axisymmetric free-surface flow. *Phys. Rev. Lett.*, 71 (21), 1993. ISSN 00319007. doi: 10.1103/PhysRevLett.71.3458.

[80] J. Eggers and E. Villermaux. Physics of liquid jets. *Rep. Prog. Phys.*, 71(3), 2008. ISSN 00344885. doi: 10.1088/0034-4885/71/3/036601.

[81] J. Eggers, J.R. Lister, and H.A. Stone. Coalescence of liquid drops. *J. Fluid Mech.*, 401, 1999. ISSN 00221120. doi: 10.1017/S002211209900662X.

[82] C. D. Eggleton and K. J. Stebe. An adsorption–desorption-controlled surfactant on a deforming droplet. *Journal of Colloid and Interface Science*, 208(1):68–80, 1998. ISSN 0021-9797. doi: 10.1006/jcis.1998.5816.

[83] M.A. Erinin, C. Liu, X. Liu, W. Mostert, L. Deike, and J.H. Duncan. The effects of surfactants on plunging breakers. *Journal of Fluid Mechanics*, 972:R5, 2023. doi: 10.1017/jfm.2023.721.

[84] A. Etminan, Y.S. Muzychka, and K. Pope. A review on the hydrodynamics of taylor flow in microchannels: Experimental and computational studies. *Processes*, 9(5), 2021. ISSN 22279717. doi: 10.3390/pr9050870.

[85] P. K. Farsoiya, Y. S. Mayya, and R. Dasgupta. Axisymmetric viscous interfacial oscillations – theory and simulations. *Journal of Fluid Mechanics*, 826:797–818, 2017. doi: 10.1017/jfm.2017.443.

[86] A. Ferrari, M. Magnini, and J.R. Thome. Numerical analysis of slug flow boiling in square microchannels. *Int. J. Heat Mass Transf.*, 123, 2018. ISSN 00179310. doi: 10.1016/j.ijheatmasstransfer.2018.03.012.

[87] J. H. Ferziger and M. Perić. *Computational Methods for Fluid Dynamics*. Springer Berlin Heidelberg, Berlin, Heidelberg, 2002. ISBN 978-3-540-42074-3. doi: 10.1007/978-3-642-56026-2.

[88] A. Franci, I. De-Pouplana, G. Casas, M. Á. Celigueta, J. González-Usúa, and E. Oñate. PFEM–DEM for particle-laden flows with free surface. *Computational Particle Mechanics*, 7(1):101–120, 1 2020. ISSN 2196-4378. doi: 10.1007/s40571-019-00244-1.

[89] D. Frenkel and B. Smit. *Understanding Molecular Simulation: From Algorithms to Applications, Third Edition*. Elsevier Science, 2023. doi: 10.1016/C2009-0-63921-0.

[90] A. M. Gañán-Calvo. Revision of Bubble Bursting: Universal Scaling Laws of Top Jet Drop Size and Speed. *Phys. Rev. Lett.*, 119(20), 2017. ISSN 10797114. doi: 10.1103/PhysRevLett.119.204502.

[91] L. Ge, Q. Li, M. Wang, J. Ouyang, X. Li, and M.MQ Xing. Nanosilver particles in medical applications: synthesis, performance, and toxicity. *Int J Nanomedicine*, 9:2399–2407, 2014. doi: 10.2147/IJN.S55015.

[92] E. Ghabache. *Surface libre hors équilibre : de l'effondrement de cavité aux jets étirés*. PhD thesis, Université Pierre et Marie Curie Paris 6, Paris, 9 2015.

[93] E. Ghabache and T. Séon. Size of the top jet drop produced by bubble bursting. *Phys. Rev. Fluids.*, 1(5), 2016. doi: 10.1103/physrevfluids.1.051901.

[94] E. Ghabache, A. Antkowiak, C. Josserand, and T. Séon. On the physics of fizziness: How bubble bursting controls droplets ejection. *Phys. Fluids.*, 26(12), 2014. ISSN 10897666. doi: 10.1063/1.4902820.

[95] SN. Ghadiali and D.P. Gaver. The influence of non-equilibrium surfactant dynamics on the flow of a semi-infinite bubble in a rigid cylindrical capillary tube. *J. Fluid Mech.*, 478, 2003. ISSN 00221120. doi: 10.1017/S002211200200335X.

[96] M.D. Giavedoni and F.A. Saita. The rear meniscus of a long bubble steadily displacing a Newtonian liquid in a capillary tube. *Phys. Fluids.*, 11(4), 1999. ISSN 10706631. doi: 10.1063/1.869951.

[97] G.M. Ginley and C.J. Radke. Influence of soluble surfactants on the flow of long bubbles through a cylindrical capillary. In *ACS Symposium Series*, volume 396, 1989.

[98] H.L. Goldsmith and S.G. Mason. The flow of suspensions through tubes. II. Single large bubbles. *J. Colloid Sci.*, 18(3), 1963. ISSN 00958522. doi: 10.1016/0095-8522(63)90015-1.

[99] J. M. Gordillo and F. J. Blanco-Rodríguez. Theory of the jets ejected after the inertial collapse of cavities with applications to bubble bursting jets. *Phys. Rev. Fluids.*, 8(7), 2023. ISSN 2469990X. doi: 10.1103/PhysRevFluids.8.073606.

[100] J. M. Gordillo and J. Rodríguez-Rodríguez. Capillary waves control the ejection of bubble bursting jets. *J. Fluid Mech.*, 867, 2019. ISSN 14697645. doi: 10.1017/jfm.2019.161.

[101] R. Gupta, D.F. Fletcher, and B.S. Haynes. On the CFD modelling of Taylor flow in microchannels. *Chem. Eng. Sci.*, 64(12), 2009. ISSN 00092509. doi: 10.1016/j.ces.2009.03.018.

[102] Y. Han and N. Shikazono. Measurement of the liquid film thickness in micro tube slug flow. *Int. J. Heat Fluid Flow*, 30(5), 2009. ISSN 0142727X. doi: 10.1016/j.ijheatfluidflow.2009.02.019.

[103] D. R. Handwerk, P. D. Shipman, C. B. Whitehead, S. Özkar, and R. G. Finke. Mechanism-Enabled Population Balance Modeling of Particle Formation en Route to Particle Average Size and Size Distribution Understanding and Control. *Journal of the American Chemical Society*, 141(40), 2019. ISSN 15205126. doi: 10.1021/jacs.9b06364.

[104] D. R. Handwerk, P. D. Shipman, C. B. Whitehead, S. Özkar, and R. G. Finke. Particle Size Distributions via Mechanism-Enabled Population Balance Modeling. *Journal of Physical Chemistry C*, 124(8), 2020. ISSN 19327455. doi: 10.1021/acs.jpcc.9b11239.

[105] F. H. Harlow and J. E. Welch. Numerical calculation of time-dependent viscous incompressible flow of fluid with free surface. *The Physics of Fluids*, 8(12):2182–2189, 12 1965. ISSN 0031-9171. doi: 10.1063/1.1761178.

[106] H. S. Harned and C. L. Hildreth. The Diffusion Coefficient of Silver Nitrate in Dilute Aqueous Solution at 25°. *Journal of the American Chemical Society*, 73(7), 1951. ISSN 15205126. doi: 10.1021/ja01151a088.

[107] D.J.E. Harvie, J.J. Cooper-White, and M.R. Davidson. Deformation of a viscoelastic droplet passing through a microfluidic contraction. *Journal of Non-Newtonian Fluid Mechanics*, 155(1):67–79, 2008. ISSN 0377-0257. doi: 10.1016/j.jnnfm.2008.05.002.

[108] A.L. Hazel and M. Heil. The steady propagation of a semi-infinite bubble into a tube of elliptical or rectangular cross-section. *J. Fluid Mech.*, 470, 2002. ISSN 00221120. doi: 10.1017/S0022112002001830.

[109] Y. He, F. Wei, Z. Ma, H. Zhang, Q. Yang, B. Yao, Z. Huang, J. Li, C. Zeng, and Q. Zhang. Green synthesis of silver nanoparticles using seed extract of alpinia katsumadai, and their antioxidant, cytotoxicity, and antibacterial activities. *RSC Adv.*, 7:39842–39851, 2017. doi: 10.1039/C7RA05286C.

[110] M. Heil. Finite Reynolds number effects in the Bretherton problem. *Physics of Fluids*, 13 (9):2517–2521, 09 2001. ISSN 1070-6631. doi: 10.1063/1.1389861.

[111] M. Heil, A.L. Hazel, and J.A. Smith. The mechanics of airway closure. *Respiratory Physiology & Neurobiology*, 163(1-3):214–221, 11 2008. ISSN 15699048. doi: 10.1016/j.resp.2008.05.013.

[112] A. Henglein and M. Giersig. Formation of Colloidal Silver Nanoparticles: Capping Action of Citrate. *The Journal of Physical Chemistry B*, 103(44):9533–9539, 11 1999. ISSN 1520-6106. doi: 10.1021/jp9925334.

[113] J. C Heylmun. *Simulation methods for polydisperse, multiphase flows using moment methods*. PhD thesis, Iowa State University, 2019.

[114] C. Hirsch. Part III: The Analysis of Numerical Schemes. In *Numerical Computation of Internal and External Flows: The Fundamentals of Computational Fluid Dynamics*, pages 1–656. Elsevier, 1 2007. ISBN 9780750665940. doi: 10.1016/B978-0-7506-6594-0.X5037-1.

[115] J. Hoepffner and G. Paré. Recoil of a liquid filament: Escape from pinch-off through creation of a vortex ring. *J. Fluid Mech.*, 734, 2013. ISSN 14697645. doi: 10.1017/jfm.2013.472.

[116] W.A. Hyman and R. Skalak. Viscous flow of a suspension of liquid drops in a cylindrical tube. *Appl. Sci. Res.*, 26:27–52, 1972. doi: 10.1007/BF01897833.

[117] S. Iravani, H. Korbekandi, S. V. Mirmohammadi, and B. Zolfaghari. Synthesis of silver nanoparticles: chemical, physical and biological methods. *Research in pharmaceutical sciences*, 9(6):385–406, 12 2014. ISSN 1735-5362.

[118] M Iwamoto, K Kuroda, J Kanzow, S Hayashi, and F Faupel. Size evolution effect of the reduction rate on the synthesis of gold nanoparticles. *Advanced Powder Technology*, 16(2): 137–144, 2005. ISSN 0921-8831. doi: 10.1163/1568552053621669.

[119] E. Izak-Nau, A. Huk, B. Reidy, H. Uggerud, M. Vadset, S. Eiden, M. Voetz, M. Himly, A. Duschl, M. Dusinska, and I. Lynch. Impact of storage conditions and storage time on silver nanoparticles' physicochemical properties and implications for their biological effects. *RSC Adv.*, 5:84172–84185, 2015. doi: 10.1039/C5RA10187E.

[120] D. Izbassarov and M. Muradoglu. A computational study of two-phase viscoelastic systems in a capillary tube with a sudden contraction/expansion. *Phys. Fluids.*, 28(1):012110, 1 2016. ISSN 1070-6631. doi: 10.1063/1.4939940.

[121] A. Jahn, J. E. Reiner, W. N. Vreeland, D. L. DeVoe, L. E. Locascio, and M. Gaitan. Preparation of nanoparticles by continuous-flow microfluidics, 2008. ISSN 13880764.

[122] B. Ji, A. Singh, and J. Feng. Water-to-Air Transfer of Nano/Microsized Particulates: Enrichment Effect in Bubble Bursting Jet Drops. *Nano Lett.*, 22(13), 2022. ISSN 15306992. doi: 10.1021/acs.nanolett.2c01102.

[123] B. Ji, Z. Yang, Z. Wang, R. H. Ewoldt, and J. Feng. Secondary Bubble Entrainment via Primary Bubble Bursting at a Viscoelastic Surface. *Phys. Rev. Lett.*, 131(10), 2023. ISSN 10797114. doi: 10.1103/PhysRevLett.131.104002.

[124] V. John, I. Angelov, A. A. Öncül, and D. Thévenin. Techniques for the reconstruction of a distribution from a finite number of its moments. *Chemical Engineering Science*, 62(11), 2007. ISSN 00092509. doi: 10.1016/j.ces.2007.02.041.

[125] L. Kahouadji, E. Nowak, N. Kovalchuk, J. Chergui, D. Juric, S. Shin, M. J. H. Simmons, R. V. Craster, and O. K. Matar. Simulation of immiscible liquid–liquid flows in complex microchannel geometries using a front-tracking scheme. *Microfluidics and Nanofluidics*, 22 (11):126, 11 2018. ISSN 1613-4982. doi: 10.1007/s10404-018-2149-y.

[126] M. Kalli and P. Angeli. Effect of surfactants on drop formation flow patterns in a flow-focusing microchannel. *Chem. Eng. Sci.*, 253, 2022. ISSN 00092509. doi: 10.1016/j.ces.2022.117517.

[127] M. Kalli, L. Chagot, and P. Angeli. Comparison of surfactant mass transfer with drop formation times from dynamic interfacial tension measurements in microchannels. *J. Colloid Interface Sci.*, 605, 2022. ISSN 10957103. doi: 10.1016/j.jcis.2021.06.178.

[128] M. Kalli, P. Pico, L. Chagot, L. Kahouadji, S. Shin, J. Chergui, D. Juric, O.K. Matar, and P. Angeli. Effect of surfactants during drop formation in a microfluidic channel: a combined experimental and computational fluid dynamics approach. *J. Fluid Mech.*, 961:A15, 4 2023. ISSN 0022-1120. doi: 10.1017/jfm.2023.213.

[129] Ishara Dedunu Kamalanathan and Peter James Martin. Competitive adsorption of surfactant–protein mixtures in a continuous stripping mode foam fractionation column. *Chem. Eng. Sci.*, 146:291–301, 2016. ISSN 0009-2509. doi: 10.1016/j.ces.2016.03.002.

[130] P.M. Kamat, B.W. Wagoner, S.S. Thete, and O.A. Basaran. Role of Marangoni stress during breakup of surfactant-covered liquid threads: Reduced rates of thinning and microthread cascades. *Phys. Rev. Fluids.*, 3(4), 2018. ISSN 2469990X. doi: 10.1103/PhysRevFluids.3.043602.

[131] P.M. Kamat, B.W. Wagoner, A.A. Castrejón-Pita, J.R. Castrejón-Pita, C.R. Anthony, and O.A. Basaran. Surfactant-driven escape from endpinching during contraction of nearly inviscid filaments. *J. Fluid Mech.*, 899:A28, 2020. ISSN 14697645. doi: 10.1017/jfm.2020.476.

[132] T.G. Karayiannis and M.M. Mahmoud. Flow boiling in microchannels: Fundamentals and applications. *Appl. Therm. Eng.*, 115:1372–1397, 3 2017. ISSN 13594311. doi: 10.1016/j.applthermaleng.2016.08.063.

[133] O. Kašpar, A. H. Koyuncu, A. Pittermannová, P. Ulbrich, and V. Tokárová. Governing factors for preparation of silver nanoparticles using droplet-based microfluidic device. *Biomedical Microdevices*, 21(4):88, 12 2019. ISSN 1387-2176. doi: 10.1007/s10544-019-0435-4.

[134] V. Kathiravan, S. Ravi, and S. Ashokkumar. Synthesis of silver nanoparticles from melia dubia leaf extract and their in vitro anticancer activity. *Spectrochimica Acta Part A: Molecular and Biomolecular Spectroscopy*, 130:116–121, 2014. ISSN 1386-1425. doi: 10.1016/j.saa.2014.03.107.

[135] S. Kaviya, J. Santhanalakshmi, B. Viswanathan, J. Muthumary, and K. Srinivasan. Biosynthesis of silver nanoparticles using citrus sinensis peel extract and its antibacterial activity. *Spectrochimica Acta Part A: Molecular and Biomolecular Spectroscopy*, 79(3):594–598, 2011. ISSN 1386-1425. doi: 10.1016/j.saa.2011.03.040.

[136] L. Kayal, S. Basak, and R. Dasgupta. Dimples, jets and self-similarity in nonlinear capillary waves. *Journal of Fluid Mechanics*, 951:A26, 2022. doi: 10.1017/jfm.2022.854.

[137] S. A. Khan, A. Günther, M. A. Schmidt, and K. F. Jensen. Microfluidic synthesis of colloidal silica. *Langmuir*, 20(20), 2004. ISSN 07437463. doi: 10.1021/la0499012.

[138] Z. Khan, S. Al-Thabaiti Ahmed, Abdullah Yousif Obaid, and A.O. Al-Youbi. Preparation and characterization of silver nanoparticles by chemical reduction method. *Colloids and Surfaces B: Biointerfaces*, 82(2):513–517, 2011. ISSN 0927-7765. doi: 10.1016/j.colsurfb.2010.10.008.

[139] C. R Kharangate and I. Mudawar. Review of computational studies on boiling and condensation. *International Journal of Heat and Mass Transfer*, 108:1164–1196, 2017. ISSN 0017-9310. doi: doi.org/10.1016/j.ijheatmasstransfer.2016.12.065.

[140] S. Khodaparast, M. Magnini, N. Borhani, and J. R. Thome. Dynamics of isolated confined air bubbles in liquid flows through circular microchannels: an experimental and numerical study. *Microfluid. Nanofluidics*, 19(1), 2015. ISSN 16134990. doi: 10.1007/s10404-015-1566-4.

[141] S. Khodaparast, M.K. Kim, J.E Silpe, and H.A Stone. Bubble-Driven Detachment of Bacteria from Confined Microgeometries. *Environ. Sci. Technol.*, 51(3):1340–1347, 2 2017. ISSN 0013-936X. doi: 10.1021/acs.est.6b04369.

[142] D. Kim, S. Jeong, and J. Moon. Synthesis of silver nanoparticles using the polyol process and the influence of precursor injection. *Nanotechnology*, 17(16):4019, 2006. doi: 10.1088/0957-4484/17/16/004.

[143] Y. Kim, B. Lee Chung, M. Ma, W. J. M. Mulder, Z. A. Fayad, O. C. Farokhzad, and R. Langer. Mass Production and Size Control of Lipid–Polymer Hybrid Nanoparticles through Controlled Microvortices. *Nano Letters*, 12(7):3587–3591, 7 2012. ISSN 1530-6984. doi: 10.1021/nl301253v.

[144] T. Kisyelova, A. Novruzova, F. Hajiyeva, M. Ramazanov, and A. Chianese. Effect of the reactor configuration on the production of silver nanoparticles. *Chemical Engineering Transactions*, 47:121–126, May 2016. doi: 10.3303/CET1647021.

[145] W.B. Kolb and R.L. Cerro. Coating the inside of a capillary of square cross section. *Chem. Eng. Sci.*, 46(9), 1991. ISSN 00092509. doi: 10.1016/0009-2509(91)85119-I.

[146] J. Koplik and J. R. Banavar. Molecular dynamics of interface rupture. *Physics of Fluids A: Fluid Dynamics*, 5(3):521–536, 03 1993. ISSN 0899-8213. doi: 10.1063/1.858879.

[147] N. M. Kovalchuk and M. J. H. Simmons. Effect of soluble surfactant on regime transitions at drop formation. *Colloids and Surfaces A: Physicochemical and Engineering Aspects*, 545, 2018. ISSN 18734359. doi: 10.1016/j.colsurfa.2018.02.041.

[148] N. M. Kovalchuk, M. Reichow, T. Frommweiler, D. Vigolo, and M. J. H. Simmons. Mass transfer accompanying coalescence of surfactant-laden and surfactant-free drop in a microfluidic channel. *Langmuir*, 35(28):9184–9193, 2019. doi: 10.1021/acs.langmuir.9b00843.

[149] N.M. Kovalchuk, M. Sagisaka, K. Steponavicius, D. Vigolo, and M. J. H. Simmons. Drop formation in microfluidic cross-junction: jetting to dripping to jetting transition. *Microfluid Nanofluid*, 23(103):1–14, 2019. doi: 10.1007/s10404-019-2269-z.

[150] M. T. Kreutzer, F. Kapteijn, J. A. Moulijn, and J. J. Heiszwolf. Multiphase monolith reactors: Chemical reaction engineering of segmented flow in microchannels. *Chemical Engineering Science*, 60(22):5895–5916, 2005. ISSN 0009-2509. doi: 10.1016/j.ces.2005.03.022. 7th International Conference on Gas-Liquid and Gas-Liquid-Solid Reactor Engineering.

[151] M. T. Kreutzer, F. Kapteijn, J. A. Moulijn, C. R. Kleijn, and J. J. Heiszwolf. Inertial and interfacial effects on pressure drop of taylor flow in capillaries. *AIChE Journal*, 51(9): 2428–2440, 2005. doi: 10.1002/aic.10495.

[152] S. Krishnan, E. J. Hopfinger, and B. A. Puthenveettil. On the scaling of jetting from bubble collapse at a liquid surface. *J. Fluid Mech.*, 822, 2017. ISSN 14697645. doi: 10.1017/jfm.2017.214.

[153] N. Kumar, R. Bogireddy, Hoskote Anand Kiran Kumar, and Badal Kumar Mandal. Biofabricated silver nanoparticles as green catalyst in the degradation of different textile dyes. *Journal of Environmental Chemical Engineering*, 4(1):56–64, 2016. ISSN 2213-3437. doi: 10.1016/j.jece.2015.11.004.

[154] S. Kumar and S. Ganesan. Numerical simulation of nanocrystal synthesis in a microfluidic reactor. *Computers & Chemical Engineering*, 96:128–138, 1 2017. ISSN 00981354. doi: 10.1016/j.compchemeng.2016.10.004.

[155] J. S. Kuo and D. T. Chiu. Controlling mass transport in microfluidic devices. *Annual Review of Analytical Chemistry*, 4, 2011. ISSN 19361327. doi: 10.1146/annurev-anchem-061010-113926.

[156] D. Y. Kwak and J. S. Lee. Multigrid algorithm for the cell-centered finite difference method ii: discontinuous coefficient case. *Numerical Methods for Partial Differential Equations*, 20 (5):742–764, 2004. doi: doi.org/10.1002/num.20001.

[157] R. La Spina, D. Mehn, F. Fumagalli, M. Holland, F. Reniero, F. Rossi, and D. Gilliland. Synthesis of citrate-stabilized silver nanoparticles modified by thermal and ph preconditioned tannic acid. *Nanom. (Basel, Switzerland)*, 10:1–16, 2020. doi: 10.3390/nano10102031.

[158] C. Y. Lai, J. Eggers, and L. Deike. Bubble Bursting: Universal Cavity and Jet Profiles. *Phys. Rev. Lett.*, 121(14), 2018. ISSN 10797114. doi: 10.1103/PhysRevLett.121.144501.

[159] V. K. Lamer and R. H. Dinegar. Theory, Production and Mechanism of Formation of Monodispersed Hydrosols. *Journal of the American Chemical Society*, 72(11), 1950. ISSN 15205126. doi: 10.1021/ja01167a001.

[160] A. D. Lavino, M. Ferrari, A. A. Barresi, and D. Marchisio. Effect of different good solvents in flash nano-precipitation via multi-scale population balance modeling-CFD coupling approach. *Chemical Engineering Science*, 245, 2021. ISSN 00092509. doi: 10.1016/j.ces.2021.116833.

[161] L. L. Lazarus, C. T. Riche, B. C. Marin, M. Gupta, N. Malmstadt, and R. L. Brutchey. Two-phase microfluidic droplet flows of ionic liquids for the synthesis of gold and silver nanoparticles. *ACS Applied Materials & Interfaces*, 4(6):3077–3083, 2012. doi: 10.1021/am3004413. PMID: 22524284.

[162] K. J. Lee, B. H. Jun, T. H. Kim, and J. Joung. Direct synthesis and inkjetting of silver nanocrystals toward printed electronics. *Nanotechnology*, 17(9), 2006. ISSN 09574484. doi: 10.1088/0957-4484/17/9/060.

[163] H. Lhuissier and E. Villermaux. Bursting bubble aerosols. *J. Fluid Mech.*, 696, 2012. ISSN 14697645. doi: 10.1017/jfm.2011.418.

[164] G.-R. Li, H. Xu, X.F. Lu, J.X. Feng, Y.X Tong, and C.Y. Su. Electrochemical synthesis of nanostructured materials for electrochemical energy conversion and storage. *Nanoscale*, 5: 4056–4069, 2013. doi: 10.1039/C3NR00607G.

[165] K. Li, X. Jia, A. Tang, X. Zhu, H. Meng, and Y. Wang. Preparation of spherical and triangular silver nanoparticles by a convenient method. *Integrated Ferroelectrics*, 136(1): 9–14, 2012. doi: 10.1080/10584587.2012.686405.

[166] Y. Li and J.E. Sprittles. Capillary breakup of a liquid bridge: Identifying regimes and transitions. *J. Fluid Mech.*, 797, 2016. ISSN 14697645. doi: 10.1017/jfm.2016.276.

[167] Y.C Liao, E. I. Franses, and O. A. Basaran. Deformation and breakup of a stretching liquid bridge covered with an insoluble surfactant monolayer. *Phys. Fluids*, 18(2), 2006. ISSN 10706631. doi: 10.1063/1.2166657.

[168] I. M. Lifshitz and V. V. Slyozov. The kinetics of precipitation from supersaturated solid solutions. *Journal of Physics and Chemistry of Solids*, 19(1-2), 1961. ISSN 00223697. doi: 10.1016/0022-3697(61)90054-3.

[169] X. Z. Lin, A. D. Terepka, and H. Yang. Synthesis of silver nanoparticles in a continuous flow tubular microreactor. *Nano Letters*, 4(11), 2004. ISSN 15306984. doi: 10.1021/nl0485859.

[170] X. Z. Lin, A. D. Terepka, and H. Yang. Synthesis of silver nanoparticles in a continuous flow tubular microreactor. *Nano Lett.*, 4(11):2227–2232, 2004. doi: 10.1021/nl0485859.

[171] Y. Lin, K. Lee, and T. Matsoukas. Solution of the population balance equation using constant-number Monte Carlo. *Chemical Engineering Science*, 57(12), 2002. ISSN 00092509. doi: 10.1016/S0009-2509(02)00114-8.

[172] F. W. M. Ling, H. A. Abdulbari, and C. Sim-Yee. Effect of residence time on the morphology of silica nanoparticles synthesized in a microfluidic reactor. *Journal of Flow Chemistry*, 12 (1):17–30, 2022. ISSN 2063-0212. doi: 10.1007/s41981-021-00175-0.

[173] J.R. Lister, J.M. Rallison, A.A. King, L.J. Cummings, and O.E. Jensen. Capillary drainage of an annular film: The dynamics of collars and lobes. *J. Fluid Mech.*, 552, 2006. ISSN 14697645. doi: 10.1017/S0022112006008822.

[174] H. Liu, J. Li, D. Sun, T. Odoom-Wubah, J. Huang, and Q. Li. Modeling of Silver Nanoparticle Formation in a Microreactor: Reaction Kinetics Coupled with Population Balance Model

and Fluid Dynamics. *Industrial & Engineering Chemistry Research*, 53(11):4263–4270, 3 2014. ISSN 0888-5885. doi: 10.1021/ie4031314.

[175] H. Liu, H. Zhang, J. Wang, and J. Wei. Effect of temperature on the size of biosynthesized silver nanoparticle: Deep insight into microscopic kinetics analysis. *Arabian Journal of Chemistry*, 13(1), 2020. ISSN 18785352. doi: 10.1016/j.arabjc.2017.09.004.

[176] R. Liu, J. Tang, H. Yang, W. Jin, M. Liu, S. Liu, and J. Hu. In situ decoration of plasmonic silver nanoparticles on poly(vinylidene fluoride) membrane for versatile SERS detection. *New Journal of Chemistry*, 43(18), 2019. ISSN 13699261. doi: 10.1039/c9nj00439d.

[177] L. Lu, R. W. Y. Sun, R. Chen, C. K. Hui, C. M. Ho, J. M. Luk, G. K.K. Lau, and C. M. Che. Silver nanoparticles inhibit hepatitis B virus replication. *Antiviral Therapy*, 13(2), 2008. ISSN 13596535. doi: 10.1177/135965350801300210.

[178] Z.Y. Luo, X.L. Shang, and B.F. Bai. Effect of soluble surfactant on the motion of a confined droplet in a square microchannel. *Phys. Fluids.*, 31(11), 2019. ISSN 10897666. doi: 10.1063/1.5125949.

[179] M. Magnini and O.K. Matar. Morphology of long gas bubbles propagating in square capillaries. *Int. J. Multiph. Flow.*, 129, 2020. ISSN 03019322. doi: 10.1016/j.ijmultiphaseflow.2020.103353.

[180] M. Magnini, A. Ferrari, J.R. Thome, and H.A. Stone. Undulations on the surface of elongated bubbles in confined gas-liquid flows. *Phys. Rev. Fluids.*, 2(8), 2017. ISSN 2469990X. doi: 10.1103/PhysRevFluids.2.084001.

[181] M. Magnini, S. Khodaparast, O. K. Matar, H. A. Stone, and J. R. Thome. Dynamics of long gas bubbles rising in a vertical tube in a cocurrent liquid flow. *Phys. Rev. Fluids*, 4: 023601, Feb 2019. doi: 10.1103/PhysRevFluids.4.023601.

[182] M. Magnini, F. Municchi, I. El Mellas, and M. Icardi. Liquid film distribution around long gas bubbles propagating in rectangular capillaries. *Int. J. Multiph. Flow.*, 148, 2022. ISSN 03019322. doi: 10.1016/j.ijmultiphaseflow.2021.103939.

[183] P. R. Makgwane and S. S. Ray. Synthesis of nanomaterials by continuous-flow microfluidics: a review. *J. Nanosci. Nanotechnol.*, 14(2):1338–1363, 2014. doi: 10.1166/jnn.2014.9129.

[184] H. Manikantan and T. M. Squires. Surfactant dynamics: hidden variables controlling fluid flows. *J. Fluid Mech.*, 892:P1, 2020. doi: 10.1017/jfm.2020.170.

[185] D. L. Marchisio, A. A. Barresi, and R. O. Fox. Simulation of Turbulent Precipitation in a Semi-batch Taylor-Couette Reactor Using CFD. *AIChE Journal*, 47(3), 2001. ISSN 00011541. doi: 10.1002/aic.690470314.

[186] D. L. Marchisio, R. Dennis Vigil, and R. O Fox. Implementation of the quadrature method of moments in cfd codes for aggregation–breakage problems. *Chemical Engineering Science*, 58(15):3337–3351, 2003. ISSN 0009-2509. doi: 10.1016/S0009-2509(03)00211-2.

[187] D. L. Marchisio, R. O. Fox, and R. O. Fox. *Computational models for polydisperse particulate and multiphase systems*, volume 9780521858489. Cambridge University Press, 2010. doi: 10.1017/CBO9781139016599.

[188] L. Marciniak, M. Nowak, A. Trojanowska, B. Tylkowski, and R. Jastrzab. The Effect of pH on the Size of Silver Nanoparticles Obtained in the Reduction Reaction with Citric and Malic Acids. *Materials*, 13(23), 2020. ISSN 1996-1944. doi: 10.3390/ma13235444.

[189] M.J. Martinez and K.S. Udell. Axisymmetric creeping motion of drops through circular tubes. *J. Fluid Mech.*, 210(565), 1990.

[190] A. Martínez-Calvo, J. Rivero-Rodríguez, B. Scheid, and A. Sevilla. Natural break-up and satellite formation regimes of surfactant-laden liquid threads. *J. Fluid Mech.*, 883, 2020. ISSN 14697645. doi: 10.1017/jfm.2019.874.

[191] M.M.I. Masum, M.M. Siddiqa, K.A. Ali, Y. Zhang, Y. Abdallah, E. Ibrahim, W. Qiu, C. Yan, and B. Li. Biogenic synthesis of silver nanoparticles using phyllanthus emblica fruit extract and its inhibitory action against the pathogen acidovorax oryzae strain rs-2 of rice bacterial brown stripe. *Front Microbiol.*, 10(820):18, 2019. doi: 10.3389/fmicb.2019.00820.

[192] H. C. Mayer and R. Krechetnikov. Landau-Levich flow visualization: Revealing the flow topology responsible for the film thickening phenomena. *Phys. Fluids.*, 24(5), 2012. ISSN 10706631. doi: 10.1063/1.4703924.

[193] P. T. McGough and O. A. Basaran. Repeated formation of fluid threads in breakup of a surfactant-covered jet. *Phys. Rev. Lett.*, 96(5), 2006. ISSN 10797114. doi: 10.1103/PhysRevLett.96.054502.

[194] R. McGraw. Description of Aerosol Dynamics by the Quadrature Method of Moments. *Aerosol Science and Technology*, 27(2):255–265, 1 1997. ISSN 0278-6826. doi: 10.1080/02786829708965471.

[195] H.R. Moran, M. Magnini, C.N. Markides, and O.K. Matar. Inertial and buoyancy effects on the flow of elongated bubbles in horizontal channels. *Int. J. Multiph. Flow*, 135:103468, 2021. ISSN 0301-9322. doi: 10.1016/j.ijmultiphaseflow.2020.103468.

[196] F. Moukalled, L. Mangani, and M. Darwish. *The Finite Volume Method in Computational Fluid Dynamics*, volume 113 of *Fluid Mechanics and Its Applications*. Springer International Publishing, Cham, 2016. ISBN 978-3-319-16873-9. doi: 10.1007/978-3-319-16874-6.

[197] S. Mozaffari, W. Li, C. Thompson, S. Ivanov, S. Seifert, B. Lee, L. Kovarik, and A. M. Karim. Colloidal nanoparticle size control: Experimental and kinetic modeling investigation

of the ligand-metal binding role in controlling the nucleation and growth kinetics. *Nanoscale*, 9(36), 2017. ISSN 20403372. doi: 10.1039/c7nr04101b.

[198] M. Muradoglu and H. A. Stone. Mixing in a drop moving through a serpentine channel: A computational study. *Physics of Fluids*, 17(7):073305, 7 2005. ISSN 1070-6631. doi: 10.1063/1.1992514.

[199] M. Muradoglu and G. Tryggvason. Simulations of soluble surfactants in 3d multiphase flow. *J. Comput. Phys.*, 274, 2014. ISSN 10902716. doi: 10.1016/j.jcp.2014.06.024.

[200] Omid Naderi, May Nyman, Mehran Amiri, and Rahmat Sadeghi. Synthesis and characterization of silver nanoparticles in aqueous solutions of surface active imidazolium-based ionic liquids and traditional surfactants SDS and DTAB. *Journal of Molecular Liquids*, 273: 645–652, 2019. ISSN 0167-7322. doi: 10.1016/j.molliq.2018.10.046.

[201] R Nagarajan and T Alan Hatton. *Nanoparticles: Synthesis, Stabilization, Passivation, and Functionalization*, volume 996 of *ACS Symposium Series*. American Chemical Society, Washington, DC, 9 2008. ISBN 9780841269699. doi: 10.1021/bk-2008-0996.

[202] B. Nath, G. Biswas, A. Dalal, and K.C. Sahu. Migration of a droplet in a cylindrical tube in the creeping flow regime. *Phys. Rev. E*, 95(3), 2017. ISSN 24700053. doi: 10.1103/PhysRevE.95.033110.

[203] K. Nathanael, P. Pico, N. M. Kovalchuk, A. D. Lavino, M. J.H. Simmons, and O. K. Matar. Computational modelling and microfluidics as emerging approaches to synthesis of silver nanoparticles - A review. *Chemical Engineering Journal*, 436, 2022. ISSN 13858947. doi: 10.1016/j.cej.2022.135178.

[204] K. Nathanael, S. Cheng, N. M. Kovalchuk, R. Arcucci, and M.J.H. Simmons. Optimization of microfluidic synthesis of silver nanoparticles: a generic approach using machine learning. *Chemical Engineering Research and Design*, 2023. ISSN 02638762. doi: 10.1016/j.cherd.2023.03.007.

[205] K. Nathanael, F. Galvanin, N. M Kovalchuk, and M. J. H. Simmons. Development of a predictive response surface model for size of silver nanoparticles synthesized in a T-junction microfluidic device. *Chemical Engineering Science*, 279:118907, 2023. ISSN 0009-2509. doi: 10.1016/j.ces.2023.118907.

[206] B. Néel and L. Deike. Collective bursting of free-surface bubbles, and the role of surface contamination. *J. Fluid Mech.*, 917, 2021. ISSN 14697645. doi: 10.1017/jfm.2021.272.

[207] B. Néel, M. A. Erinin, and L. Deike. Role of Contamination in Optimal Droplet Production by Collective Bubble Bursting, 2022. ISSN 19448007.

[208] C. M. Ng, P. C. Chen, and S. Manickam. Green high-gravitational synthesis of silver nanoparticles using a rotating packed bed reactor (rpbr). *Ind. Eng. Chem. Res.*, 51(15): 5375–5381, 2012. doi: 10.1021/ie201795u.

[209] I. Nopens, C. A. Biggs, B. De Clercq, R. Govoreanu, B. M. Wilén, P. Lant, and P. A. Vanrolleghem. Modelling the activated sludge flocculation process combining laser light diffraction particle sizing and population balance modelling (PBM). *Water Science and Technology*, 45(6):41–49, 2002. ISSN 02731223. doi: 10.2166/wst.2002.0092.

[210] P.K. Notz and O.A. Basaran. Dynamics and breakup of a contracting liquid filament. *J. Fluid Mech.*, 512, 2004. ISSN 00221120. doi: 10.1017/S0022112004009759.

[211] W.L. Olbricht. Pore-Scale Prototypes of Multiphase Flow in Porous Media. *Annu. Rev. Fluid. Mech*, 28:187–213, 1996.

[212] W.L. Olbricht and D. M. Kung. The deformation and breakup of liquid drops in low Reynolds number flow through a capillary. *Phys. Fluids A*, 4(7), 1992. ISSN 08998213. doi: 10.1063/1.858412.

[213] U. Olgac and M. Muradoglu. Effects of surfactant on liquid film thickness in the Bretherton problem. *Int. J. Multiph. Flow.*, 48, 2013. ISSN 03019322. doi: 10.1016/j.ijmultiphaseflow.2012.08.007.

[214] S. Osher and J. A. Sethian. Fronts propagating with curvature-dependent speed: Algorithms based on hamilton-jacobi formulations. *Journal of Computational Physics*, 79(1):12–49, 1988. ISSN 0021-9991. doi: doi.org/10.1016/0021-9991(88)90002-2.

[215] I. Pan, L.R. Mason, and O.K Matar. Data-centric engineering: integrating simulation, machine learning and statistics. challenges and opportunities. *Chemical Engineering Science*, 249:117271, 2022. ISSN 0009-2509. doi: 10.1016/j.ces.2021.117271.

[216] A. Passalacqua, F. Laurent, E. Madadi-Kandjani, J.C. Heylmun, and R.O. Fox. An open-source quadrature-based population balance solver for OpenFOAM. *Chemical Engineering Science*, 176:306–318, 2 2018. ISSN 00092509. doi: 10.1016/j.ces.2017.10.043.

[217] A. Passalacqua, J. Heylmun, M.o Icardi, E. Madadi, P. Bachant, X. Hu, and J. Weaver. OpenQBMM/OpenQBMM: OpenQBMM 6.0.0 for OpenFOAM-v2006, 8 2020.

[218] S. V. Patankar. *Numerical heat transfer and fluid flow*. CRC Press, 1980. doi: 10.13182/nse81-a20112.

[219] S. Paul, P. Basak, R. Majumder, A. Mukherjee, J. Ghosh, S. Patra, and N. K. Jana. Biochemical estimation of Moringa oleifera leaf extract for synthesis of silver nanoparticle mediated drug delivery system. *Journal of Plant Biochemistry and Biotechnology*, 29(1), 2020. ISSN 09741275. doi: 10.1007/s13562-019-00517-z.

[220] P.F. Pelz, T. Keil, and T.F. Groß. The transition from sheet to cloud cavitation. *J. Fluid Mech.*, 817:439–454, 4 2017. ISSN 0022-1120. doi: 10.1017/jfm.2017.75.

[221] S. R. K. Perala and S. Kumar. On the two-step mechanism for synthesis of transition-metal nanoparticles. *Langmuir*, 30(42), 2014. ISSN 15205827. doi: 10.1021/la503199m.

[222] C. S. Peskin. Numerical analysis of blood flow in the heart. *J. Comput. Phys.*, 25(3), 1977. ISSN 10902716. doi: 10.1016/0021-9991(77)90100-0.

[223] C. S. Peskin and D. M. McQueen. A general method for the computer simulation of biological systems interacting with fluids. *Symposia of the Society for Experimental Biology*, 49:265–276, 1995.

[224] P. Pico, K. Nathanael, A. D. Lavino, N. M. Kovalchuk, M. J.H. Simmons, and O. K. Matar. Silver nanoparticles synthesis in microfluidic and well-mixed reactors: A combined experimental and pbm-cfd study. *Chemical Engineering Journal*, 474:145692, 2023. ISSN 1385-8947. doi: doi.org/10.1016/j.cej.2023.145692.

[225] P. Pico, L. Kahouadji, S. Shin, J. Chergui, D. Juric, and O. K. Matar. Drop encapsulation and bubble bursting in surfactant-laden flows in capillary channels. *Phys. Rev. Fluids.*, 9 (3):034001, 3 2024. ISSN 2469-990X. doi: 10.1103/PhysRevFluids.9.034001.

[226] P. Pico, L. Kahouadji, S. Shin, J. Chergui, D. Juric, and O. K. Matar. Surfactant-laden bubble bursting: Dynamics of capillary waves and worthington jet at large bond number. *Phys. Rev. Fluids*, 9:083606, Aug 2024. doi: 10.1103/PhysRevFluids.9.083606.

[227] J. Pierre, M. Poujol, and T. Séon. Influence of surfactant concentration on drop production by bubble bursting. *Phys. Rev. Fluids.*, 7(7), 2022. ISSN 2469990X. doi: 10.1103/PhysRevFluids.7.073602.

[228] J. Polte. Fundamental growth principles of colloidal metal nanoparticles - a new perspective. *CrystEngComm*, 17(36), 2015. ISSN 14668033. doi: 10.1039/c5ce01014d.

[229] J. Polte, X. Tuaev, M. Wuithschick, A. Fischer, A. F. Thuenemann, K. Rademann, R. Kraehnert, and F. Emmerling. Formation mechanism of colloidal silver nanoparticles: Analogies and differences to the growth of gold nanoparticles. *ACS Nano*, 6(7):5791–5802, 2012. doi: 10.1021/nn301724z.

[230] C. Pozrikidis. The buoyancy-driven motion of a train of viscous drops within a cylindrical tube. *J. Fluid Mech.*, 237(627), 1992. ISSN 14697645. doi: 10.1017/S0022112092003550.

[231] A. Prosperetti and G. Tryggvason. *Computational Methods for Multiphase Flow*. Cambridge University Press, 2007.

[232] Y. Qin, X. Ji, J. Jing, H. Liu, H. Wu, and W. Yang. Size control over spherical silver nanoparticles by ascorbic acid reduction. *Colloids and Surfaces A: Physicochemical and Engineering Aspects*, 372(1-3):172–176, 12 2010. ISSN 09277757. doi: 10.1016/j.colsurfa.2010.10.013.

[233] C. Quintero-Quiroz, N. Acevedo, J. Zapata-Giraldo, L. E. Botero, J. Quintero, D. Zárate-Triviño, J. Saldarriaga, and V. Z. Pérez. Optimization of silver nanoparticle synthesis

by chemical reduction and evaluation of its antimicrobial and toxic activity. *Biomaterials Research*, 23(1):27, 2019. doi: 10.1186/s40824-019-0173-y.

[234] A. D. Radadia. Microfluidics for Biochemical and Chemical Reactions. In *Encyclopedia of Microfluidics and Nanofluidics*. Springer New York, 2008. doi: 10.1007/978-0-387-48998-8{_}948.

[235] M. Rahil Hasan, N. Anzar, M. Tyagi, N. Yadav, and J. Narang. 8 - lab-on-a-chip devices—advancement in the designing of biosensors. In Chaudhery Mustansar Hussain, Sudheesh K. Shukla, and Girish M. Joshi, editors, *Functionalized Nanomaterials Based Devices for Environmental Applications*, Micro and Nano Technologies, pages 175–198. Elsevier, 2021. ISBN 978-0-12-822245-4. doi: doi.org/10.1016/B978-0-12-822245-4.00005-2.

[236] O. Ramírez-Soto, V. Sanjay, D. Lohse, J. T. Pham, and D. Vollmer. Lifting a sessile oil drop from a superamphiphobic surface with an impacting one. *Science Advances*, 6(34), 2020. ISSN 23752548. doi: 10.1126/sciadv.aba4330.

[237] D. Ramkrishna. The Framework of Population Balance. In D. Ramkrishna, editor, *Population Balances*, chapter 2, pages 7–45. Elsevier, 1 2000. ISBN 9780125769709. doi: 10.1016/b978-012576970-9/50003-5.

[238] D. Ramkrishna and M. R. Singh. Population balance modeling: current status and future prospects. *Annual review of chemical and biomolecular engineering*, 5:123–46, 2014. ISSN 1947-5438. doi: 10.1146/annurev-chembioeng-060713-040241.

[239] K. Ranoszek-Soliwoda, E. Tomaszewska, E. Socha, P. Krzyczmonik, A. Ignaczak, P. Orlowski, M. Krzyzowska, G. Celichowski, and J. Grobelny. The role of tannic acid and sodium citrate in the synthesis of silver nanoparticles. *Journal of Nanoparticle Research*, 19(8):273, 8 2017. ISSN 1388-0764. doi: 10.1007/s11051-017-3973-9.

[240] B. E. Rapp. Conservation of Mass: The Continuity Equation. In B. E. Rapp, editor, *Microfluidics: Modelling, Mechanics and Mathematics*, chapter 10, pages 265–271. Elsevier, 1 2017. ISBN 9781455731411. doi: 10.1016/B978-1-4557-3141-1.50010-1.

[241] M. U. Rashid, Md. K. H. Bhuiyan, and M. E. Quayum. Synthesis of Silver Nano Particles (Ag-NPs) and their uses for Quantitative Analysis of Vitamin C Tablets. *Dhaka University Journal of Pharmaceutical Sciences*, 12(1):29–33, 9 2013. doi: 10.3329/dujps.v12i1.16297.

[242] L. Rayleigh. On the capillary phenomenon of jets, 1879.

[243] Jane Y. Rempel, Moungi G. Bawendi, and Klavs F. Jensen. Insights into the kinetics of semiconductor nanocrystal nucleation and growth. *Journal of the American Chemical Society*, 131(12), 2009. ISSN 00027863. doi: 10.1021/ja809156t.

[244] Pedro Jose Rivero, Javier Goicoechea, Aitor Urrutia, and Francisco Javier Arregui. Effect of both protective and reducing agents in the synthesis of multicolor silver nanoparticles. *Nanoscale Research Letters*, 8(1):101, 2013. ISSN 1556-276X. doi: 10.1186/1556-276X-8-101.

[245] M.J. Rosen and J.T. Kunjappu. *Characteristic Features of Surfactants*, chapter 1, pages 1–38. John Wiley & Sons, Ltd, 2012. ISBN 9781118228920. doi: 10.1002/9781118228920.ch1.

[246] A. Roucoux, J. Schulz, and H. Patin. Reduced transition metal colloids: A novel family of reusable catalysts? *Chemical Reviews*, 102(10), 2002. ISSN 00092665. doi: 10.1021/cr010350j.

[247] Seungwon S., S.I. Abdel-Khalik, V. Daru, and D. Juric. Accurate representation of surface tension using the level contour reconstruction method. *Journal of Computational Physics*, 203(2):493–516, 2005. ISSN 0021-9991. doi: doi.org/10.1016/j.jcp.2004.09.003.

[248] H. E. Sandoe, M. A. Watzky, and S. A. Diaz. Experimental probes of silver metal nanoparticle formation kinetics: Comparing indirect versus more direct methods. *International Journal of Chemical Kinetics*, 51(11), 2019. ISSN 10974601. doi: 10.1002/kin.21315.

[249] V. Sanjay, D. Lohse, and M. Jalaal. Bursting bubble in a viscoplastic medium. *J. Fluid Mech.*, 922, 2021. ISSN 14697645. doi: 10.1017/jfm.2021.489.

[250] Udishnu Sanyal and Balaji R Jagirdar. Metal and Alloy Nanoparticles by Amine-Borane Reduction of Metal Salts by Solid-Phase Synthesis: Atom Economy and Green Process. *Inorganic Chemistry*, 51(23):13023–13033, 12 2012. ISSN 0020-1669. doi: 10.1021/ic3021436.

[251] M. Sauzade and T. Cubaud. Initial microfluidic dissolution regime of CO2 bubbles in viscous oils. *Phys. Rev. E*, 88(5), 2013. ISSN 15393755. doi: 10.1103/PhysRevE.88.051001.

[252] M. Sauzade and T. Cubaud. Bubble deformations and segmented flows in corrugated microchannels at large capillary numbers. *Phys. Rev. Fluids*, 3(3), 2018. ISSN 2469990X. doi: 10.1103/PhysRevFluids.3.034202.

[253] T. Schikarski, M. Avila, H. Trzenschiok, A. Güldenpfennig, and W. Peukert. Quantitative modeling of precipitation processes. *Chemical Engineering Journal*, 444:136195, 9 2022. ISSN 1385-8947. doi: 10.1016/J.CEJ.2022.136195.

[254] L.W. Schwartz, H.M. Princen, and A.D. Kiss. On the motion of bubbles in capillary tubes. *J. Fluid Mech.*, 172(-1):259–275, 11 1986. ISSN 14697645. doi: 10.1017/S0022112086001738.

[255] L.E. Scriven. Dynamics of a fluid interface equation of motion for newtonian surface fluids. *Chemical Engineering Science*, 12(2):98–108, 1960. ISSN 0009-2509. doi: 10.1016/0009-2509(60)87003-0.

[256] R. Seemann, M. Brinkmann, T. Pfohl, and S. Herminghaus. Droplet based microfluidics. *Reports on Progress in Physics*, 75(1):016601, dec 2011. doi: 10.1088/0034-4885/75/1/016601.

[257] T. Séon and G. Liger-Belair. Effervescence in champagne and sparkling wines: From bubble bursting to droplet evaporation, 2017. ISSN 19516401.

[258] T. Serra, J. Colomer, and X. Casamitjana. Aggregation and breakup of particles in a shear flow. *Journal of Colloid and Interface Science*, 187(2), 1997. ISSN 00219797. doi: 10.1006/jcis.1996.4710.

[259] D. Shalom, R. C. R. Wootton, R. F. Winkle, B. F. Cottam, R. Vilar, A. J. deMello, and C. P. Wilde. Synthesis of thiol functionalized gold nanoparticles using a continuous flow microfluidic reactor. *Materials Letters*, 61(4-5), 2007. ISSN 0167577X. doi: 10.1016/j.matlet.2006.06.072.

[260] N. Shembekar, C. Chaipan, R. Utharala, and C. A. Merten. Droplet-based microfluidics in drug discovery, transcriptomics and high-throughput molecular genetics. *Lab on a Chip*, 16 (8):1314–1331, 2016. ISSN 1473-0197. doi: 10.1039/C6LC00249H.

[261] M. Shiea, A. Buffo, M. Vanni, and D. Marchisio. Numerical Methods for the Solution of Population Balance Equations Coupled with Computational Fluid Dynamics. *Annual Review of Chemical and Biomolecular Engineering*, 11(1):339–366, 6 2020. ISSN 1947-5438. doi: 10.1146/annurev-chembioeng-092319-075814.

[262] S. Shim, J. Wan, S. Hilgenfeldt, P.D. Panchal, and H.A. Stone. Dissolution without disappearing: Multicomponent gas exchange for CO 2 bubbles in a microfluidic channel. *Lab Chip*, 14(14), 2014. ISSN 14730189. doi: 10.1039/c4lc00354c.

[263] S. Shin and D. Juric. Modeling three-dimensional multiphase flow using a level contour reconstruction method for front tracking without connectivity. *J. Comput. Phys.*, 180(2), 2002. ISSN 00219991. doi: 10.1006/jcph.2002.7086.

[264] S. Shin and D. Juric. High order level contour reconstruction method. *Journal of Mechanical Science and Technology*, 21(2):311–326, 2007. doi: doi.org/10.1007/BF02916292.

[265] S. Shin and D. Juric. A hybrid interface method for three-dimensional multiphase flows based on front tracking and level set techniques. *Int. J. Numer. Methods Fluids*, 60(7): 753–778, 7 2009.

[266] S. Shin, I. Yoon, and D. Juric. The local front reconstruction method for direct simulation of two- and three-dimensional multiphase flows. *Journal of Computational Physics*, 230 (17):6605–6646, 2011. ISSN 0021-9991. doi: doi.org/10.1016/j.jcp.2011.04.040.

[267] S. Shin, J. Chergui, and D. Juric. A solver for massively parallel direct numerical simulation of three-dimensional multiphase flows. *J. Mech. Sci. Technol.*, 31(4):1739–1751, 2017. doi: 10.1007/s12206-017-0322-y.

[268] S. Shin, J. Chergui, D. Juric, L. Kahouadji, O. K. Matar, and R. V. Craster. A hybrid interface tracking – level set technique for multiphase flow with soluble surfactant. *J. Comput. Phys.*, 359, 2018. ISSN 10902716. doi: 10.1016/j.jcp.2018.01.010.

[269] C. W. Shu and S. Oshert. Efficient implementation of essentially non-oscillatory shock-capturing schemes, ii. *J. Comput. Phys.*, 83(1), 1989. ISSN 10902716. doi: 10.1016/0021-9991(89)90222-2.

[270] D. Shukla, A. A. Joshi, and A. Mehra. Modeling of formation of nanoparticles in reverse micellar systems: Ostwald ripening of silver halide particles. *Langmuir*, 25(6):3786–3793, 2009. doi: 10.1021/la803684y.

[271] K. S. Siddiqi, A. Husen, and R. A. K. Rao. A review on biosynthesis of silver nanoparticles and their biocidal properties. *Journal of Nanobiotechnology*, 16(1):14, 12 2018. ISSN 1477-3155. doi: 10.1186/s12951-018-0334-5.

[272] S. K. Sivaraman, I. S. Elango, S. Kumar, and V. Santhanam. A green protocol for room temperature synthesis of silver nanoparticles in seconds. *Current Science*, 97:1055–1059, 2009.

[273] S. E. Skrabalak, B. J. Wiley, M. Kim, E. V. Formo, and Y. Xia. On the polyol synthesis of silver nanostructures: Glycolaldehyde as a reducing agent. *Nano Letters*, 8(7):2077–2081, 2008. doi: 10.1021/nl800910d.

[274] A. Sobczak-Kupiec, D. Malina, Z. Wzorek, and M. Zimowska. Influence of silver nitrate concentration on the properties of silver nanoparticles. *Micro and Nano Letters*, 6(8), 2011. ISSN 17500443. doi: 10.1049/mnl.2011.0152.

[275] D. E. Spiel. On the births of jet drops from bubbles bursting on water surfaces. *J. Geophys. Res.*, 100(C3), 1995. ISSN 01480227. doi: 10.1029/94JC03055.

[276] D. E. Spiel. More on the births of jet drops from bubbles bursting on seawater surfaces. *J. Geophys. Res. Oceans*, 102(C3), 1997. ISSN 01480227. doi: 10.1029/96JC03582.

[277] K. J. Stebe, S-Y Lin, and C. Maldarelli. Remobilizing surfactant retarded fluid particle interfaces. i. stress-free conditions at the interfaces of micellar solutions of surfactants with fast sorption kinetics. *Physics of Fluids A: Fluid Dynamics*, 3(1):3–20, 01 1991. ISSN 0899-8213. doi: 10.1063/1.857862.

[278] H. A. Stone. A simple derivation of the time-dependent convective-diffusion equation for surfactant transport along a deforming interface. *Physics of Fluids A: Fluid Dynamics*, 2 (1):111–112, 01 1990. ISSN 0899-8213. doi: 10.1063/1.857686.

[279] M. Sussman and E. Fatemi. An efficient, interface-preserving level set redistancing algorithm and its application to interfacial incompressible fluid flow. *SIAM Journal on Scientific Computing*, 20(4):1165–1191, 1999. doi: 10.1137/S1064827596298245.

[280] M. Sussman and E. G. Puckett. A coupled level set and volume-of-fluid method for computing 3d and axisymmetric incompressible two-phase flows. *Journal of Computational Physics*, 162(2):301–337, 2000. ISSN 0021-9991. doi: doi.org/10.1006/jcph.2000.6537.

[281] M. Sussman, E. Fatemi, P. Smereka, and S. Osher. An improved level set method for incompressible two-phase flows. *Comput. Fluids*, 27(5-6), 1998.

[282] Y. Tagawa, S. Takagi, and Y. Matsumoto. Surfactant effect on path instability of a rising bubble. *J. Fluid Mech.*, 738:124–142, 2014. doi: 10.1017/jfm.2013.571.

[283] T. Taha and Z.F. Cui. CFD modelling of slug flow inside square capillaries. *Chem. Eng. Sci.*, 61(2), 2006. ISSN 00092509. doi: 10.1016/j.ces.2005.07.023.

[284] M. Takesue, T. Tomura, M. Yamada, K. Hata, S. Kuwamoto, and T. Yonezawa. Size of elementary clusters and process period in silver nanoparticle formation. *Journal of the American Chemical Society*, 133(36), 2011. ISSN 00027863. doi: 10.1021/ja202815y.

[285] G.I Taylor. Deposition of a viscous fluid on a plane surface. *J. Fluid Mech.*, 9(2):218–224, 10 1960. ISSN 0022-1120. doi: 10.1017/S0022112060001055.

[286] N. T. K. Thanh, N. Maclean, and S. Mahiddine. Mechanisms of nucleation and growth of nanoparticles in solution. *Chemical Reviews*, 114(15):7610–7630, 2014. doi: 10.1021/cr400544s. PMID: 25003956.

[287] Y. Toba. Drop production by bursting of air bubbles on the sea surface (ii) theoretical study on the shape of floating bubbles. *Journal of the Oceanographical Society of Japan*, 15(3):121–130, 1959. doi: 10.5928/kaiyou1942.15.121.

[288] M. Tokuyama, K. Kawasaki, and Y. Enomoto. Kinetic equations for ostwald ripening. *Physica A: Statistical Mechanics and its Applications*, 134(2):323–338, 1986. ISSN 0378-4371. doi: 10.1016/0378-4371(86)90053-1.

[289] G. Tryggvason, B. Bunner, A. Esmaeeli, D. Juric, N. Al-Rawahi, W. Tauber, J. Han, S. Nas, and Y.-J. Jan. A front-tracking method for the computations of multiphase flow. *Journal of Computational Physics*, 169(2):708–759, 2001. ISSN 0021-9991. doi: 10.1006/jcph.2001.6726.

[290] G. Tryggvason, R. Scardovelli, and S. Zaleski. *Direct Numerical Simulations of Gas–Liquid Multiphase Flows*. Cambridge University Press, 2011.

[291] T.M. Tsai and M.J. Miksis. Dynamics of a Drop in a Constricted Capillary Tube. *J. Fluid Mech.*, 274, 1994. ISSN 14697645. doi: 10.1017/S0022112094002090.

[292] M. Tsuji, Y. Nishizawa, K. Matsumoto, M. Kubokawa, N. Miyamae, and T. Tsuji. Effects of chain length of polyvinylpyrrolidone for the synthesis of silver nanostructures by a microwave-polyol method. *Materials Letters*, 60(6):834–838, 3 2006. ISSN 0167577X. doi: 10.1016/j.matlet.2005.10.027.

[293] K. Y. Tung, C. C. Li, and J. T. Yang. Mixing and hydrodynamic analysis of a droplet in a planar serpentine micromixer. *Microfluidics and Nanofluidics*, 7(4):545–557, 10 2009. ISSN 1613-4982. doi: 10.1007/s10404-009-0415-8.

[294] H.S Udaykumar, R Mittal, and Wei Shyy. Computation of solid–liquid phase fronts in the sharp interface limit on fixed grids. *Journal of Computational Physics*, 153(2):535–574, 1999. ISSN 0021-9991. doi: doi.org/10.1006/jcph.1999.6294.

[295] T. Ung, M. Giersig, D. Dunstan, and P. Mulvaney. Spectroelectrochemistry of colloidal silver. *Langmuir*, 13(6), 1997. ISSN 07437463. doi: 10.1021/la960863z.

[296] M. Vanni. Approximate population balance equations for aggregation-breakage processes. *Journal of Colloid and Interface Science*, 221(2), 2000. ISSN 00219797. doi: 10.1006/jcis.1999.6571.

[297] E.J. Vega and J.M. Montanero. Influence of a surfactant on bubble bursting. *Exp. Therm. Fluid Sci.*, 151:111097, 2 2024. ISSN 0894-1777. doi: 10.1016/J.EXPTHERMFLUSCI.2023.111097.

[298] F. Veron. Ocean spray, 2015. ISSN 00664189.

[299] E. Villermaux, X. Wang, and L. Deike. Bubbles spray aerosols: Certitudes and mysteries. *PNAS Nexus*, 1(5), 2022. ISSN 27526542. doi: 10.1093/pnasnexus/pgac261.

[300] E. C. Vreeland, J. Watt, G. B. Schober, B. G. Hance, M. J. Austin, A. D. Price, B. D. Fellows, T. C. Monson, N. S. Hudak, L. Maldonado-Camargo, A. C. Bohorquez, C. Rinaldi, and D. L. Huber. Enhanced nanoparticle size control by extending lamer's mechanism. *Chemistry of Materials*, 27(17):6059–6066, 2015. doi: 10.1021/acs.chemmater.5b02510.

[301] C. Wagner. Theorie der alterung von niederschlägen durch umlösen (ostwald-reifung). *Zeitschrift für Elektrochemie, Berichte der Bunsengesellschaft für physikalische Chemie*, 65(7-8):581–591, 1961. doi: 10.1002/bbpc.19610650704.

[302] P. L.L. Walls, L. Henaux, and J. C. Bird. Jet drops from bursting bubbles: How gravity and viscosity couple to inhibit droplet production. *Phys. Rev. E*, 92(2), 2015. ISSN 15502376. doi: 10.1103/PhysRevE.92.021002.

[303] F. Wang, F.P. Contò, N. Naz, J.R. Castrejón-Pita, A.A. Castrejón-Pita, C.G. Bailey, W. Wang, J.J. Feng, and Y. Sui. A fate-alternating transitional regime in contracting liquid filaments. *J. Fluid Mech.*, 860, 2019. ISSN 14697645. doi: 10.1017/jfm.2018.855.

[304] H. Wang, X. Qiao, J. Chen, and S. Ding. Preparation of silver nanoparticles by chemical reduction method. *Colloids and Surfaces A: Physicochemical and Engineering Aspects*, 256 (2):111–115, 2005. ISSN 0927-7757. doi: 10.1016/j.colsurfa.2004.12.058.

[305] S. Wang, Y. Zhong, and H. Fang. Deformation characteristics of a single droplet driven by a piezoelectric nozzle of the drop-on-demand inkjet system. *J. Fluid Mech.*, 869, 2019. ISSN 14697645. doi: 10.1017/jfm.2019.242.

[306] Y.X. Wang and J.M. Wen. Gear method for solving differential equations of gear systems. *J. Phys. Conf. Ser.*, 48(1), 2006. ISSN 17426596. doi: 10.1088/1742-6596/48/1/026.

[307] Z. Wang, A.C. Bovik, H.R. Sheikh, and E.P. Simoncelli. Image quality assessment: from error visibility to structural similarity. *IEEE Transactions on Image Processing*, 13(4): 600–612, 2004. doi: 10.1109/TIP.2003.819861.

[308] I. A. Wani, S. Khatoon, A. Ganguly, J. Ahmed, and T. Ahmad. Structural characterization and antimicrobial properties of silver nanoparticles prepared by inverse microemulsion method. *Colloids and Surfaces B: Biointerfaces*, 101:243–250, 2013. ISSN 0927-7765. doi: 10.1016/j.colsurfb.2012.07.001.

[309] M. A. Watzky and R. G. Finke. Transition metal nanocluster formation kinetic and mechanistic studies. A new mechanism when hydrogen is the reductant: Slow, continuous nucleation and fast autocatalytic surface growth. *Journal of the American Chemical Society*, 119(43), 1997. ISSN 00027863. doi: 10.1021/ja9705102.

[310] H. Wee, B.W. Wagoner, V. Garg, P.M. Kamat, and O.A. Basaran. Pinch-off of a surfactant-covered jet. *J. Fluid Mech.*, 908:A38, 2 2021. ISSN 0022-1120. doi: 10.1017/jfm.2020.801.

[311] F. Wei, X. Zhao, C. Li, and X. Han. A novel strategy for water disinfection with a Ag-NPs/gelatin sponge filter. *Environmental Science and Pollution Research*, 25(20), 2018. ISSN 16147499. doi: 10.1007/s11356-018-2157-1.

[312] J. C. Wheeler. Modified moments and gaussian quadratures. *Rocky Mountain Journal of Mathematics*, 4(2), 1974. ISSN 00357596. doi: 10.1216/RMJ-1974-4-2-287.

[313] C. B. Whitehead, S. Özkar, and R. G. Finke. Lamer's 1950 model of particle formation: a review and critical analysis of its classical nucleation and fluctuation theory basis, of competing models and mechanisms for phase-changes and particle formation, and then of its application to silver halide, semiconductor, metal, and metal-oxide nanoparticles. *Mater. Adv.*, 2:186–235, 2021. doi: 10.1039/D0MA00439A.

[314] C. R. Wilke and Pin Chang. Correlation of diffusion coefficients in dilute solutions. *AIChE Journal*, 1(2), 1955. ISSN 15475905. doi: 10.1002/aic.690010222.

[315] M. Wojnicki, T. Tokarski, V. Hessel, K. Fitzner, and M. Luty-Błocho. Continuous, monodisperse silver nanoparticles synthesis using microdroplets as a reactor. *J. Flow. Chem.*, 9: 1–7, 2019. doi: 10.1007/s41981-018-0025-2.

[316] Marek Wojnicki, Magdalena Luty-Błocho, Magdalena Kotańska, Magdalena Wytrwal, Tomasz Tokarski, Anna Krupa, Marcin Kołaczkowski, Adam Bucki, and Marcin Kobielusz.

Novel and effective synthesis protocol of AgNPs functionalized using L-cysteine as a potential drug carrier. *Naunyn-Schmiedeberg's Archives of Pharmacology*, 391(2):123–130, 2018. ISSN 1432-1912. doi: 10.1007/s00210-017-1440-x.

[317] H. Wong, C.J. Radke, and S. Morris. The motion of long bubbles in polygonal capillaries. Part 2. Drag, fluid pressure and fluid flow. *J. Fluid Mech.*, 292:95–110, 6 1995.

[318] Ke-Jun Wu, Geoffroy Michet De Varine Bohan, and Laura Torrente-Murciano. Synthesis of narrow sized silver nanoparticles in the absence of capping ligands in helical microreactors. *React. Chem. Eng.*, 2(2):116–128, 2017. doi: 10.1039/C6RE00202A.

[319] Z. Wu, W. Zhou, C. Pang, W. Deng, Changliang Xu, and X. Wang. Multifunctional chitosan-based coating with liposomes containing laurel essential oils and nanosilver for pork preservation. *Food Chemistry*, 295, 2019. ISSN 18737072. doi: 10.1016/j.foodchem.2019.05.114.

[320] Y. Xie, R. Ye, and H. Liu. Synthesis of silver nanoparticles in reverse micelles stabilized by natural biosurfactant. *Colloids and Surfaces A: Physicochemical and Engineering Aspects*, 279(1):175–178, 2006. ISSN 0927-7757. doi: 10.1016/j.colsurfa.2005.12.056.

[321] L. Xu, J. Peng, M. Yan, D. Zhang, and A.Q. Shen. Droplet synthesis of silver nanoparticles by a microfluidic device. *Chemical Engineering and Processing: Process Intensification*, 102:186–193, 2016. ISSN 0255-2701. doi: 10.1016/j.cep.2016.01.017.

[322] Q. Xu, Y.C. Liao, and O. A. Basaran. Can surfactant be present at pinch-off of a liquid filament? *Phys. Rev. Lett.*, 98(5), 2007. ISSN 00319007. doi: 10.1103/PhysRevLett.98.054503.

[323] A.A. Yaqoob, K. Umar, and M.N.M Ibrahim. Silver nanoparticles: various methods of synthesis, size affecting factors and their potential applications–a review. *Applied Nanoscience*, 10:1369–1378, 2020. doi: 10.1007/s13204-020-01318-w.

[324] G. H. Yeoh and J. Tu. *Computational Techniques for Multiphase Flows*. Elsevier, 2010. ISBN 9780080467337. doi: 10.1016/C2009-0-16604-7.

[325] G.-S. Yeom. Correlations and asymptotic behaviors of the shape parameters of floating bubbles using an improved numerical procedure. *Applied Sciences*, 12(4), 2022. ISSN 2076-3417. doi: 10.3390/app12041804.

[326] S. Yoo, D. H. Nam, T. I. Singh, G. Leem, and S. Lee. Effect of reducing agents on the synthesis of anisotropic gold nanoparticles. *Nano Convergence*, 9(1):5, 2022. ISSN 2196-5404. doi: 10.1186/s40580-021-00296-1.

[327] X. Yu, H. Gu, S. Gupta, Q. Ma, L. Cheng, Y. Zhou, and H. Liang. Bubble floatation, burst, drainage, and droplet release characteristics on a free surface: A review, 2023. ISSN 10897666.

[328] C. Yuan. *Quadrature-based moment methods for polydisperse multiphase flow modeling*. PhD thesis, Iowa State University, 2013.

[329] M. Zahoor, N. Nazir, M. Iftikhar, S. Naz, I. Zekker, J. Burlakovs, F. Uddin, A. W. Kamran, A. Kallistova, N. Pimenov, and F. Ali Khan. A review on silver nanoparticles: Classification, various methods of synthesis, and their potential roles in biomedical applications and water treatment. *Water*, 13(16), 2021. ISSN 2073-4441. doi: 10.3390/w13162216.

[330] B. W. Zeff, B. Kleber, J. Fineberg, and D. P. Lathrop. Singularity dynamics in curvature collapse and jet eruption on a fluid surface. *Nature*, 403(6768), 2000. ISSN 00280836. doi: 10.1038/35000151.

[331] H. Zhang and Q. Liu. Numerical investigation on performance of moisture separator by Lagrangian-Eulerian strategy: Physical mechanisms, theoretical models, and advanced algorithms, 2020. ISSN 18732100.

[332] W. Zhang, X. Qiao, and J. Chen. Synthesis of nanosilver colloidal particles in water/oil microemulsion. *Colloids and Surfaces A: Physicochemical and Engineering Aspects*, 299 (1-3):22–28, 5 2007. ISSN 09277757. doi: 10.1016/j.colsurfa.2006.11.012.

[333] W. Zhang, X. Qiao, and J. Chen. Formation of silver nanoparticles in sds inverse microemulsions. *Materials Chemistry and Physics*, 109(2):411–416, 2008. ISSN 0254-0584. doi: 10.1016/j.matchemphys.2007.12.009.

[334] I. P. Zwar, C. d. V. Trotta, A. B. S. Ziotti, M. Lima Neto, W. L. Araújo, I. S. de Melo, C. A. Ottoni, and A. O. de Souza. Biosynthesis of silver nanoparticles using actinomycetes, phytotoxicity on rice seeds, and potential application in the biocontrol of phytopathogens. *Journal of Basic Microbiology*, 63(1):64–74, 1 2023. ISSN 0233-111X. doi: 10.1002/jobm.202200439.

Appendix A

Derivation of the Finke-Watzky expression

The forthcoming appendix elaborates on the derivation of the algebraic equation that correlates precursor concentration with time (Eq. (2.14) in §2.3.3) by solving the ordinary differential equation proposed by Watzky and Finke [309] (Eq. (2.13)). Despite its straightforward nature, this solution is not readily available in its entirety within the existing literature.

Let us begin with Eq. (2.13), herein replicated for clarity:

$$\frac{\mathrm{d}[A]}{\mathrm{d}t} = -k_1[A] - k_2[A]([A]_0 - [A]), \tag{A.1}$$

where $[A]$ denotes precursor concentration in time, $[A]_0$ is the concentration at $t = 0$, and k_1 and k_2 represent the kinetic constants of nucleation and growth.

Upon applying separation of variables, reorganising, and integrating both sides, Eq. (A.1) transforms into Eq. (A.2):

$$\int \frac{1}{[A](k_2[A] - k_2[A]_0 - k_1)}\,\mathrm{d}[A] = \int \mathrm{d}t, \tag{A.2}$$

which is solved via partial fractions decomposition. Decomposing the expression on the RHS of the above equation, Eq. (A.3) arises:

$$\frac{1}{[A](k_2[A] - k_2[A]_0 - k_1)} = \frac{a}{[A]} + \frac{b}{k_2[A] - k_2[A]_0 - k_1}, \tag{A.3}$$

which is multiplied by $[A](k_2[A] - k_2[A]_0 - k_1)$ such that Eq. (A.4) is obtained:

$$1 = a(k_2[A] - k_2[A]_0 - k_1) + [A]b. \tag{A.4}$$

By grouping the constant and linear terms, the values of a and b are determined as follows:

$$a = \frac{1}{-k_2[A]_0 - k_1}, \qquad b = \frac{-k_2}{-k_2[A]_0 - k_1}. \tag{A.5}$$

By reverting back to Eq. (A.2) and replacing the partial fractions expression, Eq. (A.6) is obtained:

$$\frac{1}{-k_2[A]_0 - k_1} \int \frac{1}{A}\, \mathrm{d}A + \frac{-k_2}{-k_2[A]_0 - k_1} \int \frac{1}{k_2[A] - k_2[A]_0 - k_1}\, \mathrm{d}A = \int \mathrm{d}t, \tag{A.6}$$

which upon integration becomes Eq. (A.7):

$$\ln|[A]| - \ln|k_2[A] - k_2[A]_0 - k_1| = t(-k_2[A]_0 - k_1) + c(-k_2[A]_0 - k_1), \tag{A.7}$$

where c corresponds to the integration constant, found by applying the initial condition $[A] = [A]_0$ at $t = 0$:

$$c = \frac{\ln|[A]_0| - \ln|-k_1|}{-k_2[A]_0 - k_1}. \tag{A.8}$$

By replacing c and into Eq. (A.7), the following intermediate equation is found:

$$[A] = \exp(t(-k_2[A]_0 - k_1)) \left(\frac{[A]_0}{-k_1}\right) (k_2[A] - k_2[A]_0 - k_1), \tag{A.9}$$

which, upon simplification and reorganisation, becomes the well-known form of the Finke-Watzky expression of Eq. (A.10):

$$[A] = \frac{[A]_0 + k_1/k_2}{1 + (k_1/k_2[A]_0)\exp(t(k_2[A]_0 + k_1))}. \tag{A.10}$$

Appendix B

Literature PSD predictions using higher-order reconstructions

This appendix provides evidence indicating that a significant portion of the large deviations observed in the work of Perala and Kumar [221] when employing the F-W two-step mechanism (refer to §2.3.3) to predict the particle size distribution (PSD) of iridium nanoparticles (IrNPs) in a well-mixed reactor can be attributed to the moment set used to reconstruct the distribution.

Figure 4.2 of chapter 4 depicts a replication of the numerical results of Perala and Kumar [221] for the synthesis of IrNPs to validate the implementation of the proposed model in open-source code. In their volume-based PBM, the average diameter, d, and standard deviation, σ^{SD}, of the PSD are calculated using Eq. (4.6) of chapter 4 and Eq.(B.1), respectively:

$$\sigma_V^{SD}(t) = \left(\left[\left(\frac{1}{k_V} \right)^{1/3} \frac{m_{1/3,V}(t)}{m_{0,V}(t)} \right]^2 - \left(\frac{1}{k_V} \right)^{2/3} \frac{m_{2/3,V}(t)}{m_{0,V}(t)} \right)^{1/2}. \tag{B.1}$$

Using a length-based PBM approach, these expressions become, respectively, Eq. (4.7) of chapter 4 and Eq. (B.2):

$$\sigma_L^{SD}(t) = \left(\left(\frac{m_{1,L}}{m_{0,L}} \right)^2 - \frac{m_{2,L}}{m_{0,L}} \right)^{1/2}. \tag{B.2}$$

As mentioned previously, this section elucidates how part of the $\approx 150\%$ deviation against the experimental data of Watzky and Finke [309] seen in Perala and Kumar [221] in terms of σ^{SD} is due to the selection of lower-order moments to represent the average diameter of the distribution. To do so, figure B.1 first shows the notably varied outcomes that can be achieved by using different combinations of moments to compute d under the conditions of figure 4.2 of

chapter 4. Figures B.1(a)-(b) clearly demonstrate how an increase in the order of the moments tends to increase (decrease) d (σ^{SD}), as expected. This is because higher-order-moment averages are more sensitive to the largest particles in the dispersion.

Considering the notable σ^{SD} over-predictions obtained by employing the lower-order-moment calculations of Perala and Kumar [221], the use of $m_{4,L}/m_{3,L}$ (the volume-weighted or De Brouckere mean diameter) is proposed to represent d, which is a common approach in solid-liquid applications. Figure B.2 portrays the temporal evolution of $d_{4,3}$ and $\sigma^{SD}_{4,3}$ obtained by re-fitting the value of d_{crit} to predict the final experimental d data point, as in the work of Perala and Kumar [221]. The marked improvement in the prediction of σ^{SD} ($\approx$ 150% error to 18.5% at the final time) by only tuning d_{crit} and without losing accuracy in predicting d and $[C]$ is an indication of the suitability of volume-weighted averages for this application as opposed to number- or area-weighted averages.

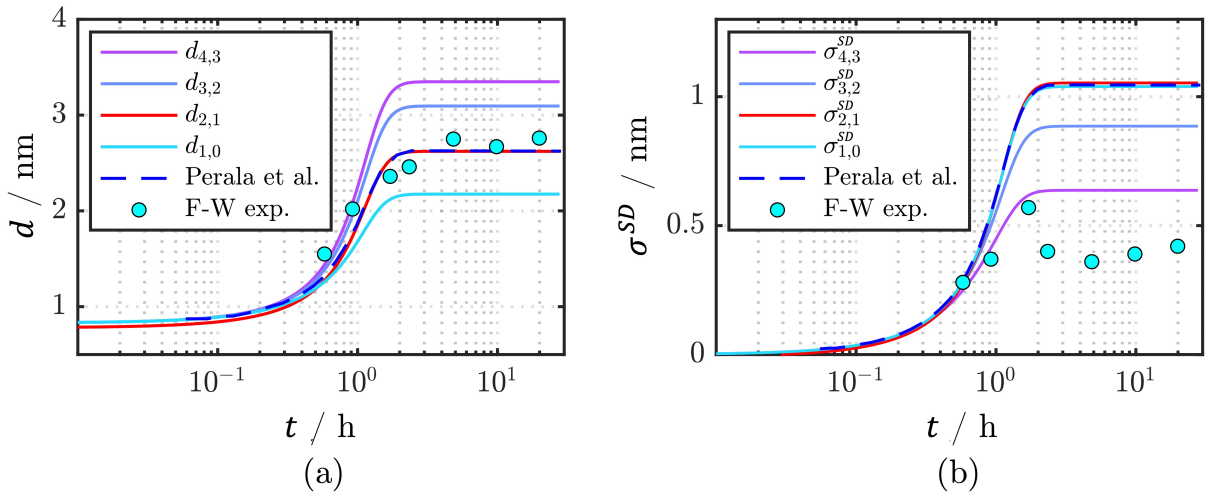

Figure B.1: Influence of the order of the moments selected to compute d and σ^{SD} using the conditions of Perala and Kumar [221]: (a) temporal evolution of d; (b) temporal evolution of σ^{SD}. The marks correspond to the experimental measurements of Watzky and Finke [309], and the discontinuous blue line to the calculations of Perala and Kumar [221] (see Eq.(4.6) - (B.2) of chapter 4). For this case, $[A]_0 = 1.2$ mM, $[B]_0 = 0.0$ mM, $[C]_0 = 1650$ mM, $k_1 = 0.0282$ h^{-1}, $k_2 = 3.379 \times 10^3$ M^{-1}h^{-1} ($[A]_0 k_2/k_1 = 159.52$), $d_{crit} = 0.83$ nm, $d_m = 0.272$ nm

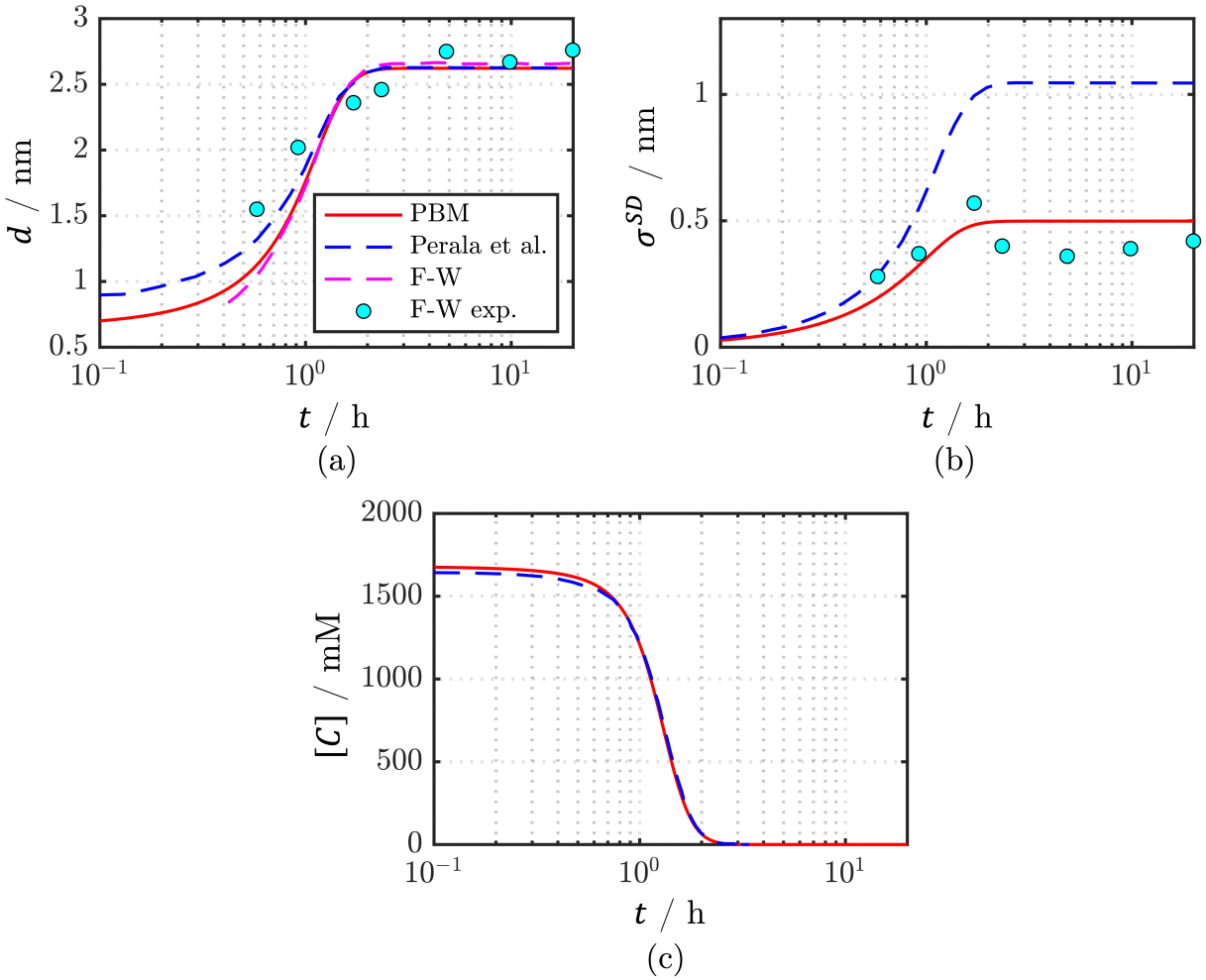

Figure B.2: Temporal evolution of (a) d, (b) σ^{SD}, and (c) precursor concentration, obtained by using a volume-weighted mean, showcasing how a much closer prediction of PSD to the experimental data is obtained without deteriorating the precursor consumption predictions. The marks correspond to the experimental measurements of Watzky and Finke [309], and the discontinuous blue line to the calculations of [221] (see Eq.(4.6) - (B.2) of chapter 4). For this case, $[A]_0 = 1.2$ mM, $[B]_0 = 0.0$ mM, $[C]_0 = 1650$ mM, $k_1 = 0.0282$ h^{-1}, $k_2 = 3.379 \times 10^3$ M^{-1}h^{-1} ($[A]_0 k_2/k_1 = 159.52$), $d_{crit} = 0.65$ nm, $d_m = 0.272$ nm